PROCEEDINGS OF PP1594: TOPOLOGICAL ENGINEERING OF ULTRASTRONG GLASSES

EDITED BY: Lothar Wondraczek, Joachim Deubener, Jürgen Horbach, Tanguy Rouxel and Jürgen Eckert

PUBLISHED IN: Frontiers in Materials

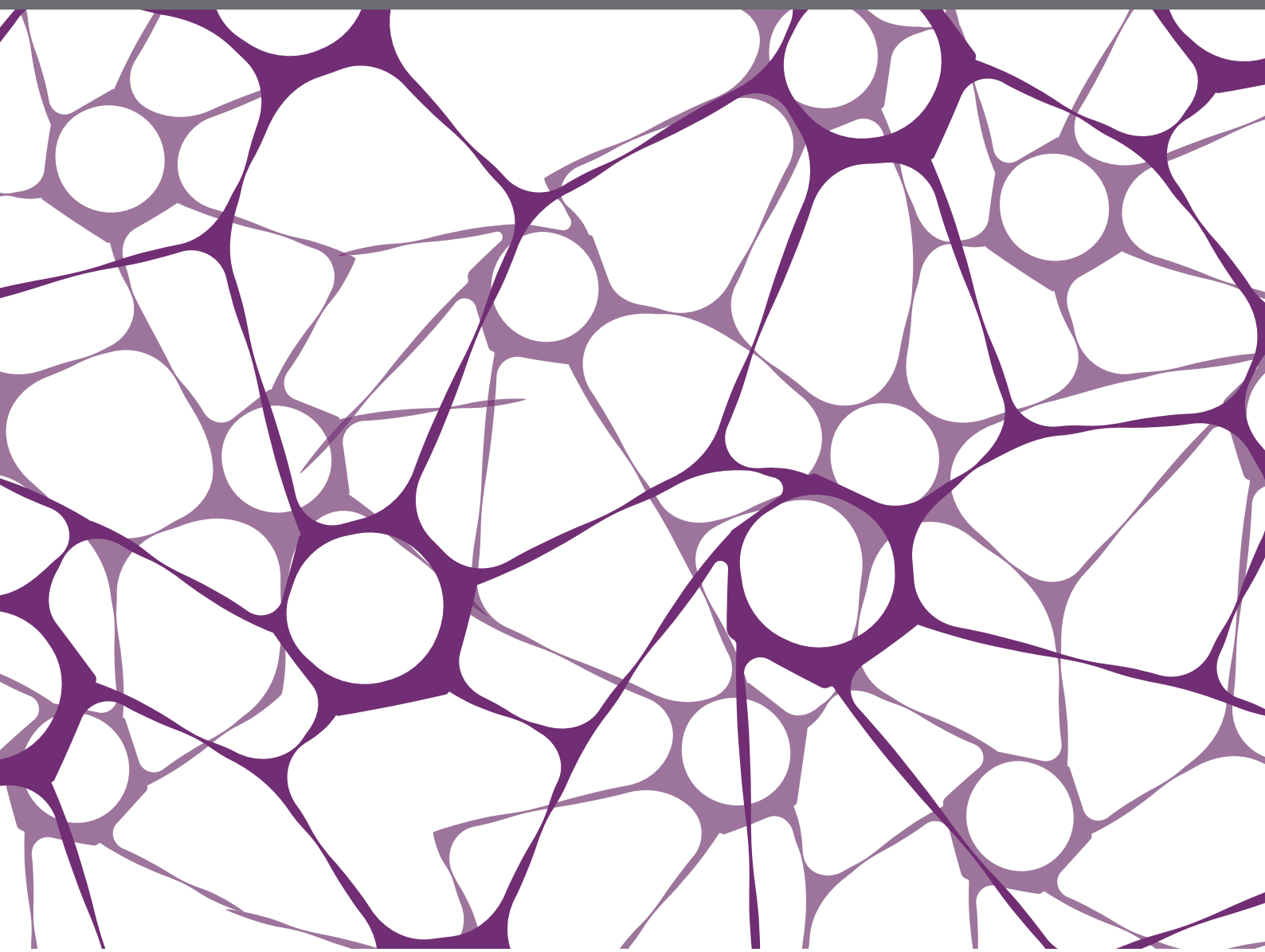

frontiers Research Topics

frontiers

ISSN 1664-8714
ISBN 978-2-88966-512-9
DOI 10.3389/978-2-88966-512-9

About Frontiers

Frontiers is more than just an open-access publisher of scholarly articles: it is a pioneering approach to the world of academia, radically improving the way scholarly research is managed. The grand vision of Frontiers is a world where all people have an equal opportunity to seek, share and generate knowledge. Frontiers provides immediate and permanent online open access to all its publications, but this alone is not enough to realize our grand goals.

Frontiers Journal Series

The Frontiers Journal Series is a multi-tier and interdisciplinary set of open-access, online journals, promising a paradigm shift from the current review, selection and dissemination processes in academic publishing. All Frontiers journals are driven by researchers for researchers; therefore, they constitute a service to the scholarly community. At the same time, the Frontiers Journal Series operates on a revolutionary invention, the tiered publishing system, initially addressing specific communities of scholars, and gradually climbing up to broader public understanding, thus serving the interests of the lay society, too.

Dedication to Quality

Each Frontiers article is a landmark of the highest quality, thanks to genuinely collaborative interactions between authors and review editors, who include some of the world's best academicians. Research must be certified by peers before entering a stream of knowledge that may eventually reach the public - and shape society; therefore, Frontiers only applies the most rigorous and unbiased reviews.
Frontiers revolutionizes research publishing by freely delivering the most outstanding research, evaluated with no bias from both the academic and social point of view. By applying the most advanced information technologies, Frontiers is catapulting scholarly publishing into a new generation.

What are Frontiers Research Topics?

Frontiers Research Topics are very popular trademarks of the Frontiers Journals Series: they are collections of at least ten articles, all centered on a particular subject. With their unique mix of varied contributions from Original Research to Review Articles, Frontiers Research Topics unify the most influential researchers, the latest key findings and historical advances in a hot research area! Find out more on how to host your own Frontiers Research Topic or contribute to one as an author by contacting the Frontiers Editorial Office: frontiersin.org/about/contact

PROCEEDINGS OF PP1594: TOPOLOGICAL ENGINEERING OF ULTRASTRONG GLASSES

Topic Editors:
Lothar Wondraczek, Friedrich Schiller University Jena, Germany
Joachim Deubener, Clausthal University of Technology, Germany
Jürgen Horbach, Heinrich Heine University of Düsseldorf, Germany
Tanguy Rouxel, University of Rennes 1, France
Jürgen Eckert, Erich Schmid Institute of Materials Science (ESI), Austria

Citation: Wondraczek, L., Deubener, J., Horbach, J., Rouxel, T., Eckert, J., eds. (2021). Proceedings of PP1594: Topological Engineering of Ultrastrong Glasses. Lausanne: Frontiers Media SA. doi: 10.3389/978-2-88966-512-9

Table of Contents

frontiers in Materials

ORIGINAL RESEARCH
published: 25 March 2020
doi: 10.3389/fmats.2020.00066

Crack Growth in Hydrous Soda-Lime Silicate Glass

Tina Waurischk[1], Ralf Müller[1], Stefan Reinsch[1], Philipe Kiefer[2], Joachim Deubener[2], Robert Balzer[3] and Harald Behrens[3]*

[1] Bundesanstalt für Materialforschung und -prüfung (BAM), Berlin, Germany, [2] Clausthal University of Technology, Institute for Non-Metallic Materials, Clausthal-Zellerfeld, Germany, [3] Leibniz University Hanover, Institute of Mineralogy, Hanover, Germany

Stable crack growth was measured for nominal dry and water-bearing (6 wt%) soda-lime silicate glasses in double cantilever beam geometry and combined with DMA studies on the effects of dissolved water on internal friction and glass transition, respectively. In vacuum, a decreased slope of logarithmic crack growth velocity versus stress intensity factor is evident for the hydrous glass in line with an increase of β-relaxation intensity indicating more energy dissipation during fracture. Further, inert crack growth in hydrous glass is found to be divided into sections of different slope, which indicates different water related crack propagation mechanism. In ambient air, a largely extended region II is observed for the hydrous glass, which indicates that crack growth is more sensitive to ambient water.

Keywords: soda-lime silicate glass, water content, stable crack growth, DCB geometry, stress intensity factor, internal friction

OPEN ACCESS

Edited by:
Randall Youngman, Corning Inc., United States

Reviewed by:
Jared Seaman Aaldenberg, Corning Inc., United States
Minoru Tomozawa, Rensselaer Polytechnic Institute, United States

***Correspondence:**
Ralf Müller
ralf.mueller@bam.de

Specialty section:
This article was submitted to Ceramics and Glass, a section of the journal Frontiers in Materials

Received: *06 January 2020*
Accepted: *03 March 2020*
Published: *25 March 2020*

Citation:
Waurischk T, Müller R, Reinsch S, Kiefer P, Deubener J, Balzer R and Behrens H (2020) Crack Growth in Hydrous Soda-Lime Silicate Glass. Front. Mater. 7:66. doi: 10.3389/fmats.2020.00066

INTRODUCTION

Glass strength and fatigue are controlled by the presence and propagation of surface microcracks (Ciccotti, 2009; Wiederhorn et al., 2013a). Focusing mainly on commercial glasses, crack velocity was studied in liquids (Wiederhorn and Bolz, 1970; Simmons and Freiman, 1981; Gehrke et al., 1987a; Gehrke et al., 1990; Gehrke et al., 1991; Dunning et al., 1994), humid air (Wiederhorn, 1967; Richter, 1983; Evans and Johnson, 1975; Gehrke et al., 1987b; Muraoka and Abe, 1996; Freiman et al., 2009), and vacuum (Pukh et al., 2009; Wiederhorn et al., 1974), where ambient water proved to be the key accelerant for slow crack propagation (Wiederhorn, 1967). Stress corrosion is therefore widely accepted as the underlying mechanism, assuming that water molecules break strained Si-O-Si network bonds at the crack tip into silanol groups (Charles, 1958; Hilling and Charles, 1965; Michalske and Freiman, 1982).

However, more recent studies indicate that crack propagation is affected by other phenomena and that a simple $\equiv$ Si-O-Si $\equiv$ + H_2O reaction (Michalske and Freiman, 1982) is unlikely to be the stress corrosion reaction (Ito and Tomozawa, 1981; Tomozawa, 2007; Ciccotti, 2009; Wiederhorn et al., 2013c). In contrast to Michalske and Freiman (1982) it was found that compressive instead of tensile stress promote glass dissolution at the crack tip (Ito and Tomozawa, 1981). Further, glass dissolution and reprecipitation at different curvature can cause crack tip blunting (Ito and Tomozawa, 1982a). Sodium can be enriched at the fractured glass surface (Langford et al., 1991; Celarie et al., 2007), dissolve into the narrow water film at the crack tip (Wiederhorn, 1967) and cause ion exchange related swelling and compressive stress (Lanford et al., 1979). In fused silica, swelling at the crack tip was also found and attributed to stress-induced water diffusion into the glass surface (Tomozawa, 1996; Fett et al., 2005; Wiederhorn et al., 2013a) as it was previously

stated (Nogami and Tomozawa, 1984; Han and Tomozawa, 1991). Water penetration and swelling were later described in Wiederhorn et al. (2013a) explaining why the strength of fused silica fibers is increased by soaking in water as reported in Ito and Tomozawa (1982a).

Alternatively, water-induced toughening can be explained by water induced stress relaxation as found for fused silica, E-glass and soda-lime silicate glass fibers (Lezzi and Tomozawa, 2015; Seaman et al., 2015). These experiments on bend fused silica fibers, held under subcritical tensile stress at low water pressure below T_g, indicate that molecular water can cause stress relaxation as a very mobile species. This conclusion was derived from the surface profiles of the IR reflection peak position at ≈1120 cm^{-1}, which indicates structural relaxation, and that of the Si-OH concentration. The latter profile was found to be 10 times less extended than the peak position profile (Lezzi and Tomozawa, 2015).

It is reasonable to assume that stress enhanced water diffusion into the strained silicate network (Nogami and Tomozawa, 1984; Han and Tomozawa, 1991; Wiederhorn et al., 2013b) can change local mechanical properties as well (Tomozawa, 2007). Thus, water is known to influence viscosity (Deubener et al., 2003), hardness (Marsh, 1964; Takata et al., 1982), and elastic moduli (Le Parc et al., 2006; Ito and Tomozawa, 1982b). Water was also proved to increase internal friction as e.g., shown for low water bearing (<0.3 wt%) phosphate (Day and Stevels, 1974), sodium silicate and borate glasses (Day, 1974). More recently, internal friction studies on high water bearing (<8 wt%) soda-lime silicate glasses (Reinsch et al., 2013) and sodium borosilicate glasses (Behrens et al., 2018) demonstrated that water strongly affects the temperature range and the intensity of sub-T_g relaxation.

These water-related effects, however, are difficult to be measured directly at the crack tip as the water influenced region is very limited in size (Wiederhorn et al., 2011). Even for slow crack growth in fused silica, the D_2O penetration depth at half-height was found to be ≈6–8 nm at an average crack velocity of $4{\cdot}10^{-6}$ m s^{-1} (Lechenault et al., 2011). These values are slightly larger than those for water in fused silica more previously measured with resonant nuclear reaction analysis at 10^{-7} m s^{-1} (Han and Tomozawa, 1991).

With this in mind, we tried to mimic the effect of water on mechanical properties and crack propagation by studying high water-bearing glass samples. For this purpose, oxide glasses containing up to 8 wt% water were synthesized by melting at high pressure according to Behrens and Stuke (2003). In this way, water speciation and its influence on glass network structure could be investigated for numerous hydrous glasses including soda-lime-borate, sodium borosilicate (Bauer et al., 2017; Behrens et al., 2018), silicoborate (Balzer et al., 2019a), phosphate (Balzer et al., 2019b), and microscope slide glasses (Kiefer et al., 2019). Analogous studies on other soda-lime glasses have been published previously (Behrens and Stuke, 2003).

Recently, measurements of density, molar volume of water, water speciation, elastic moduli, and hardness of water-bearing microscope slide glasses were reported (Kiefer et al., 2019). The present paper focuses on stable crack growth in ambient air and vacuum as well as on internal friction in these glasses.

EXPERIMENTAL

Glass Synthesis and Glass Transition Temperature

Commercial microscope slide glass (VEB, Ilmenau, Germany) of a previous study (Kiefer et al., 2019) was used. In particular, the sample 0W-MSG0 is the nominal dry glass (water content = 0.039 wt%), whereas the samples 3W-MSG500 and 6W-MSG500 are hydrous glasses, which has been, respectively mixed with nominal 3 and 6 wt% water and remelted in a internal pressure vessel at 500 MPa. Synthesis conditions, determination of the water content and the resulted water speciation are reported in Kiefer et al. (2019). The glass transition temperatures (T_g) are 812 K (0W-MSG0), 598 K (3W-MSG500), and 517 K (6W-MSG500) as measured by means of DTA (±5 K, TAG 24, Setaram, Caluire, France) and following the protocol given in Bauer et al. (2015).

Crack Growth in Double Cantilever Beam Geometry (DCB)

Crack growth measurements were made at room temperature in a self-built double cantilever beam device in ambient air at 20% rh (5600 ppmv), 24% rh (6750 ppmv), 40% rh (11300 ppmv), and in a vacuum of $2.8{\cdot}10^{-3}$ mbar (10^{-5} ppmv). Samples had been prepared with a diamond saw. A narrow groove, 600 μm broad and half of the sample thickness in depth, was cutted along the center line of the top surface to guide the crack. Samples of 60 mm × 22 mm × 1 mm and 30 mm × 17 mm × 2 mm in size were used for nominally dry and hydrous glasses, respectively. The stress intensity factor, K_I, was estimated according to Wiederhorn and Bolz (1970):

$$K_I = \frac{PL}{(wa)^{1/2}b^{3/2}}\left(3.47 + 2.32\frac{b}{L}\right) \quad (1)$$

with P = applied load, L = crack length, $2b$ = width of the glass slide, w = its thickness, and a is the remaining thickness of the glass slide beneath the groove. Eq. 1 is valid for $L/b > 1.5$. To ensure a sharp crack tip for DCB measurements, a pre-crack was thermally initiated. Afterward, the load was slightly increased until the crack length has reached $1.5{\cdot}b$. For measurements in vacuum, crack initiation and minimum growth were performed in air. Maintaining a small load preventing crack recombination, the DCB chamber was then evacuated. The maximum uncertainty of K_I obtained from repeated experiments on different samples of the same glass was ± 0.05 $MPa{\cdot}m^{0.5}$.

The crack length, L, was measured with a digital microscope (DinoLite, Digital Microscope) using the software DinoCapture2.0. Below 10^{-4} m s^{-1}, the crack velocity, v, was calculated from the time required for certain crack elongation steps. These steps were set to 0.1 and 0.3 mm for $v <$ and $> 10^{-7}$ m s^{-1}, respectively. Based on the accuracy of crack length (ΔL = 9 μm) and time measurement (Δt = 1 s), the uncertainty of v was estimated to $\Delta v \approx 3{\cdot}10^{-6}$ and $9{\cdot}10^{-9}$ m s^{-1} for $v = 10^{-4}$ and 10^{-7} m s^{-1}, respectively, and error bars would not exceed the symbol size.

Above 10^{-4} m s^{-1}, v was measured by high frequency (f = 5 kHz) modulation during crack growth according

to Kerkhof (1970); Ullner and Gehrke (1990). When crack propagation is affected by superimposed periodic stress, fracture surfaces exhibit a certain waviness and v can be concluded from f and the distance between neighbored wave peaks. This distance was measured with light microscopy using the software LEXT OLS (Olympus corporation, Tokyo, Japan) within 2 µm accuracy. For comparison, $v > 10^{-4}$ m s^{-1} was recorded with a Bonito high speed camera CL-400 (Allied Vision Technologies GmbH, Stadtroda, Germany) using the software Epix® Pixci® E8, XCAP V 3.8 (Epix Inc., Buffalo Groove, IL, United States) with a frame rate of up to 13000 fps. Applying these different techniques, v could be measured within 10 orders of magnitude.

Crack growth velocity data as a function of the stress intensity were analyzed using the empirical relation (Gehrke et al., 1987b).

$$v = v_0 K_I^n \tag{2}$$

where the limiting velocity v_0 and the crack growth exponent n (also called fatigue parameter) are adjustable parameters, which depend on the environmental condition of the DCB experiment and the chemical resistance of the glass, respectively.

Internal Friction (DMA)

Internal friction was measured with dynamic mechanical analysis (Eplexor 150N and Eplexor 25N, Gabo, Ahlden, Germany) in asymmetric three point bending mode on polished 25 mm × 5 mm × 2 mm samples. 3 N static and 1.5 N dynamic force components were applied and measured with a 25 N force detector with 0.1% accuracy. Displacement was recorded with an inductive displacement transducer. Force, displacement and phase shift, δ, were recorded in temperature-frequency sweep mode switching between 0.2, 2 and 20 Hz before stepping up by 5 K at ≈1.5 K min^{-1}. One frequency cycle took ≈13 min and the average heating rate was ≈0.3 K min^{-1}. Results are presented in terms of tanδ versus temperature in 5 K accuracy. OriginPro2015 (OriginLab, 2019) was used for data analysis. Spectra were smoothed averaging over 15 data points. This procedure reduced the scatter of tanδ to $<5{\cdot}10^{-4}$. For clarity, spectra were set zero at their minimum.

RESULTS

Crack Propagation Rates

In order to test the applied experimental procedure, **Figure 1** compares crack velocity data of the dry microscope slide (red symbols) with literature data on similar glasses (gray symbols). Glass compositions and crack growth exponents n (Eq. 2), which represent the slope of *log v* versus log K_I, are listed in **Table 1** for regions I (stress corrosion regime) and III (inert growth) (Ciccotti, 2009).

In *region I*, v strongly depends on humidity. Thus, log $v(K_I)$ shifts to lower K_I by approx. 0.05 MPa m$^{0.5}$ with increasing humidity from 24% rh (full red circles) to 40% rh (red open circles). This shift and the slope of the log $v(K_I)$-curve well confirm previous literature. Crack arrest at $K_{I0} \approx 0.32$ MPa m$^{0.5}$ is indicated for 40% rh.

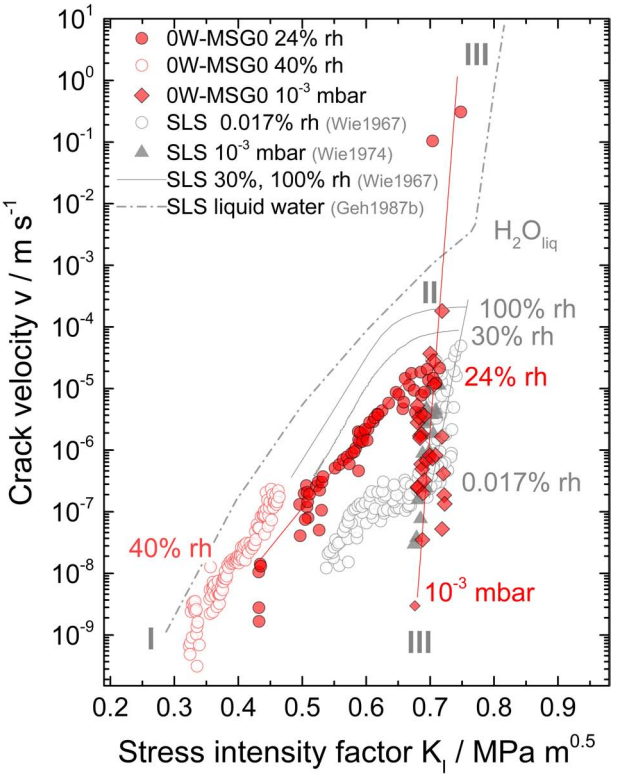

FIGURE 1 | Crack velocity, v, versus stress intensity factor, K_I, of the nominal dry microscope slide glass (red) compared to literature data on similar glasses (gray, **Table 1**). Red lines are best fits of Eq. 2. Full red circles: 24% rh, open red circles: 40% rh, full red diamonds: 10^{-3} mbar. Gray open circles: Microscope slide glass at 0.017% rh (Wiederhorn, 1967), gray triangles: Microscope slide glass at 10^{-3} mbar (Wiederhorn et al., 1974), solid gray lines: (Wiederhorn, 1967), gray dash-dot curve: Float glass in liquid water (e.g. Gehrke et al., 1987b).

In *region II*, the transition from region I to inert crack growth (region III) appears within a narrow range of K_I exhibiting large data scatter. Nevertheless, a slope is difficult to estimate in sufficent accuracy for this region.

In *region III*, crack growth is too fast to be affected by ambient water or occurs in vacuum. In both cases, inert crack growth is expected. Actually, fast crack growth data measured in air (full red circles, $v > 10^{-4}$ m s^{-1}) of this study coincide well with those measured under vacuum at 10^{-3} mbar (full red diamonds). The slope in region III is very steep ($n_{III}/n_I \approx 9$) and substantial crack extension proceeds in a narrow range of K_I. Although the slope appears slightly larger, measured values of fast crack propagation well confirm previous literature. Summing up, **Figure 1** provides confidence in the applied DCB protocol within 10 orders of magnitude of v.

Figure 2 compares crack propagation in the nominal dry microscope slide glass measured in air (red circles) and in vacuum (red diamonds) with that in the hydrous microscope slide glass containing 6 wt% water measured in air (blue circles) and in vacuum (blue diamonds). **Table 1** lists slopes n, for different regions of crack propagation.

TABLE 1 | Glass composition in mol% and crack growth exponents for regions I and III. n_I and n_{III} are best fits of the data in **Figures 1**, **2** with Eq. 2.

	SiO_2	Al_2O_3	Na_2O	K_2O	MgO	CaO	H_2O	n_I		n_{III}	
0W-MSG0 (Kiefer et al., 2019)	73.2	0.5	13.3	0.2	6.2	6.6	0.13	(24–40%) rh	$16 \pm 1^{\#}$	(vac.)	148
SLS (Gehrke et al., 1987b)	70.5[a]	0.3[a]	13.3[a]	0.1[a]	5.9[a]	9.9[a]	≈0.1	(H_2O_{liq})	15 ± 1	(nonane)	130 ± 13
SLS (Wiederhorn, 1967)	71.4[b]	1.2[b]	13.5[b]	0.6[b]	5.9[b]	7.4[b]	≈0.1	(10^{-2}–100%) rh	$17 \pm 4^{\#}$	(0.017% rh)	88
SLS (Wiederhorn et al., 1974)	71.4	1.2	13.5	0.6	5.9	7.4	≈0.1	–		(vac.)	96
6W-MSG500 (Kiefer et al., 2019)	60.7	0.4	11.0	0.2	5.1	5.5	17.1	(24% rh)	14 ± 3	(vac.)	16, 26, 55

The composition for the hydrous glass 6W-MSG500 is calculated from the composition of the dry glass considering the amount of water measured by means of IR in Kiefer et al. (2019). Data and keys: SLS: soda-lime silicate glass. –: not reported. [a]: as no composition of the float glass in Gehrke et al. (1987b) is given, a float glass composition reported in Deubener et al. (1992) is shown. [b]: taken from Tomozawa (2007). H_2O_{liq}: in liquid water. rh: relative humidity. vac.: in reduced pressure ($\leq 10^{-3}$ mbar). [#]: averaged over different humidity.

In *region I* (humid air), crack growth in the hydrous glass occurs at lower K_I than those observed for the dry glass. For instance, $v \approx 10^{-7}$ m s^{-1} measured in air of similar humidity occurs at $K_I \approx 0.50$ and 0.40 MPa m$^{0.5}$ for the dry and the hydrous glass, respectively. Eventhough, the slope of log $v(K_I)$ for the hydrous glass is rather similar to that of the dry glass. It is interesting to note that humidity much stronger promotes the crack growth in the hydrous glass. This effect causes a much broader K_I range of *region II*, which is shown by the shift of K_I at $v \approx 10^{-7}$ ms^{-1} down to ≈0.40 MPa m$^{0.5}$, as low as measured for float glass in liquid water [gray dash-dot line (Gehrke et al., 1987b)].

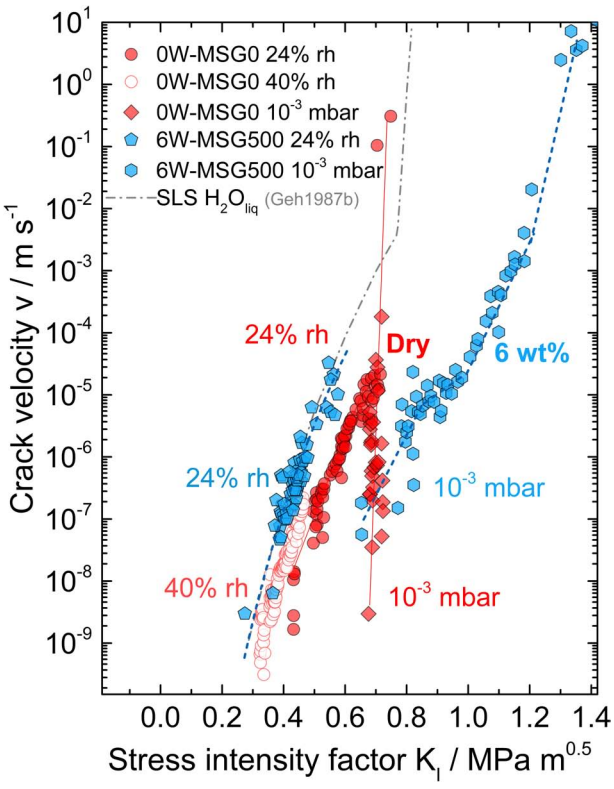

FIGURE 2 | Crack growth velocity, v, versus stress intensity factor, K_I, for nominal dry (red) and hydrous microscope slide glass (6 wt% water, blue). Dashed blue line: guide for the eye. Red symbols and gray dash-dot curve (e.g. Gehrke et al., 1987b) are taken from **Figure 1**. Blue pentagons: 20% rh, blue hexagons: 10^{-3} mbar (≈ 0.00002% rh).

In *region III* (vacuum), crack growth in the hydrous glass (blue hexagons) considerably differs from that observed for the dry glass (red diamonds). Most notably, the slope of log $v(K_I)$ is significantly decreased and, since slow crack growth (10^{-7} ms^{-1}) occurs at similar K_I for both glasses, crack growth in the hydrous glass mostly occurs at higher stress intensity. This effect indicates that dissolved water acts as a toughening agent, at least for $v > 10^{-7}$ m s^{-1}. Moreover, the graph of log $v(K_I)$ can be devided into sections of different slope. Thus, $n_{III} \approx 16$, 26 and 55 occurs for $v \approx 10^{-7}$–10^{-5} m s^{-1}, $v \approx 10^{-5}$–10^{-3} m s^{-1} and $> 3{\cdot}10^{-3}$ m s^{-1}, respectively (**Table 1**). The maximum slope at $v > 10^{-3}$ m s^{-1} is slightly lower than that observed in Gehrke et al. (1987b) for float glass in liquid water. The kink at $v \approx 3{\cdot}10^{-3}$ m s^{-1}, however, coincides with that reported in Gehrke et al. (1987b) (gray dash-dot curve), where inert crack growth is reached. This similarity and different slopes, which might indicate different crack growth mechanisms, make it questionable to assign all sections to the inert crack growth (region III).

DMA

Mechanical loss spectra for different water-bearing glasses obtained by dynamic mechanical analysis are shown in **Figure 3**. Fitted curve parameters are given in **Table 2**. According to Brueckner (1964), three different relaxation peaks can appear. α-*relaxation* at high temperature (long dashed curves) is caused by network relaxation phenomena, e.g., related to viscosity. Its maximum temperature reflects the frequency dependency of glass transition and can not be approached closer than 20 K during the DMA experiment in order to avoid a change of sample geometry. β-*relaxation* peaks at medium temperature (short dashed curves) are caused by complex regional co-operative movements of alkali and alkaline earth or water ions whereas γ-*relaxation* peaks at low temperature (arrow) relate to local alkali movements, i.e., Na^+ jumps.

For the dry glass, a weak γ-relaxation peak at 329 K (γ_d, arrow) and a weak β-relaxation at 605 K (β_{dOH}) are evident. Above 700 K, α-relaxation dominates.

For the glass containing 3 wt% water, a strong temperature decrease of α-relaxation is evident. This effect resembles the decrease in T_g measured with DTA. Further, a pronounced β-relaxation peak, shifted to 537 K, occurs (β_{3OH}). A closer look also reveals a small secondary β-relaxation peak at 441 K

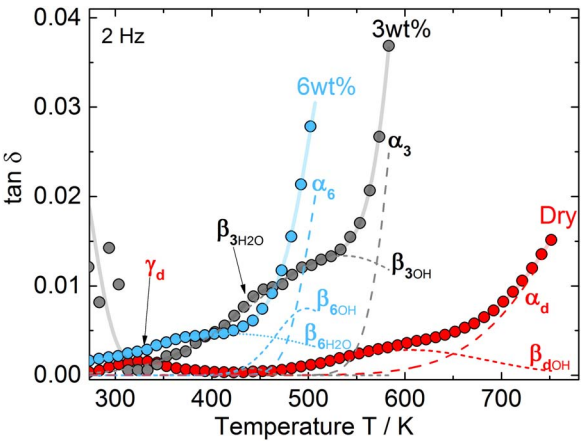

FIGURE 3 | Mechanical loss spectra in dry and water-bearing microscope slide glass samples for f = 2 Hz. Red circles: nominal dry glass (0W-MSG0), gray circles: 3 wt% water (3W-MSG500), blue circles: 6 wt% water (6W-MSG500). Dashed curves: deconvoluted Gaussian fits for γ-, β_{H2O}-, β_{OH}-, and α-relaxation.

(β_{3H2O}, arrow). The explanation of this effect can be based on similar findings reported in Reinsch et al. (2013) on soda-lime silicate glass, where two β-relaxation peaks have been attributed to molecular (β_{H2O}) and dissociated (β_{OH}) water. In fact, as a ratio of dissociated to molecular water [OH]/[H_2O] ≈ 1:1 was detected for the microscope slide glass containing 3 wt% water (Kiefer et al., 2019), a significant amount of molecular water is present. In this sense, the β-relaxation peaks at 537 K and 441 K can be attributed to β_{OH}- and β_{H2O}-relaxation peaks, respectively. As expected for samples with increased β-relaxation (Brueckner, 1964), the γ-relaxation peak disappeared. The relaxation peak near 273 K is probably caused by ice formation at the sample holder.

For the glass containing 6 wt% water, the ratio of dissociated to molecular water [OH]/[H_2O] further decreases to 1:2 (Kiefer et al., 2019). Confirming the strong shift of T_g measured by DTA, α-relaxation further shifts to lower T. The β_{OH}-relaxation peak also shifts to lower T (≈ 500 K) and decreases in intensity. β_{H2O}-relaxation, however, strongly increases in intensity while shifting to 422 K.

DISCUSSION

Crack Growth Exponent in Vacuum

Figure 2 reveals largely different crack propagation behavior of the nominal dry and the hydrous microscope slide glass in vacuum. Most strikingly, a much smaller crack growth exponent $n_{III} < 55$ is evident for the hydrous glass (blue diamonds), wheras $n_{III} \approx 150$ occurs for the dry glass. n_{III} of the hydrous glass is also smaller than those obtained from literature data in region III in other nominal dry silicate glasses ranging between 88 and 130 (**Table 1**).

The significantly lowered value of n_{III} for the hydrous glass indicates more energy dissipation during fracture. Thus, for ideal

TABLE 2 | Parameters of DMA peak analysis.

Glass	Peak temperature (K)			Peak height (tan δ·10^3)			Peak area (K)		
	γ	β_{H2O}	β_{OH}	γ	β_{H2O}	β_{OH}	γ	β_{H2O}	β_{OH}
0W-MSG0	329	–	605	1.49	–	2.84	0.13	–	0.55
3W-MSG500	–	441	537	–	0.79	13.39	–	0.03	3.11
6W-MSG500	–	422	499	–	7.48	4.65	–	1.15	0.60

brittle fracture, linear elastic fracture mechanics predicts a steep curve of log $v(K_I)$ at $K_I = K_{IC}$ depending on tensile stress, σ, Young's modulus, E, and the surface energy, γ_S (Griffith, 1921):

$$\frac{K_I^2(L,\sigma)}{E} = 2\gamma_S \tag{3}$$

If crack propagation is complicated by subsidiary energy dissipation, E and γ_S must be treated as a function of time in terms of Eq. 3 since energy dissipation is always related to relaxation phenomena (Ciccotti, 2009). Following this concept, different approaches in literature could show that energy dissipation results in a decrease of n.

(i) Liang and Zhou (1997), introduced a time depending compliance to model crack growth in viscoelastic solids:

$$\frac{1}{E(t)} = \frac{1}{E_1} + \frac{1}{E_2}[1 - \exp(-t/\tau)] \tag{4}$$

where τ and t denominate relaxation time and the time required for passing the plastic zone length for a given v, respectively. In this approach, which assumes energy dissipation throughout the whole sample body, $E(t) \approx E_1 \cdot (E_2/(E_1 + E_2))$ for slow crack growth or fast relaxation ($\tau \ll t$). It increases to $E(t) \approx E_1$ for fast crack growth or slow relaxation ($\tau \gg t$). As K_I for a certain value of v increases with E according to Eq. 3, this increase of E with v will reduce n.

Alternatively, (ii) Maugis (1985) proposed Eq. 5 as the stability criterium for crack growth in viscoelastic solids,

$$\frac{K_I^2}{E} = 2\gamma_S[1 + \alpha\Phi(v)] \tag{5}$$

where α is a constant depending on temperature, and Φ depends on v. In his approach, Maugis assumes that kinetic energy terms are negligible, viscous drag is proportional to the surface energy, γ_S, and energy dissipation is restricted to the vicinity of the crack tip. With $\Phi = v^m$ and $2E\gamma_S \ll K_I^2$, Eq. 5 gives the empirical power law of slow crack growth (Maugis, 1985):

$$v = \left(\frac{1}{2E\gamma_S\alpha}\right)^{\frac{1}{m}} K_I^{\frac{2}{m}} \tag{6}$$

where $2/m$ equals n in Eq. 2. For larger m, Φ (and hence γ_S in Eq. 3) more strongly increases with v, which, in turn, decreases n.

The above discussion makes it reasonable to assume that the low values of n_{III} in the hydrous glass seen in **Figure 2** indicate that dissolved water promotes energy dissipation during fracture. Such effect would match the well-known influence

of water on viscosity (Deubener et al., 2003) and stress relaxation (Lezzi and Tomozawa, 2015). Similarly, static fatigue studies on differently annealed silica samples show that n, which is also a fatigue parameter, decreases with increasing water content (Han and Tomozawa, 1991; cited in Tomozawa, 2007). Furthermore, the decrease of Knoop hardness of binary soda silicate glasses with increasing water content indicates that dissolved water promotes deformation by plastic flow (Takata et al., 1982).

Confirmingly, **Figure 3** could indicate increased internal friction during fracture in the hydrous glass. Thus, increased mechanical loss at room temperature can be expected from the temperature decrease of α- and β-relaxation and from the intensity increase of β-relaxation. Note that β-relaxation in the 6 wt% water-bearing glass is dominated by water molecules due to the given water speciation ratio $[OH]/[H_2O] \approx 1{:}2$ (Kiefer et al., 2019). Water molecules have been discussed in Lezzi and Tomozawa (2015) as a very mobile species causing structure relaxation more rapidly than silanol formation. The large mobility of molecular water is already known from diffusion studies in fused silica (Tomozawa et al., 1994). A large mobility of molecular water in the 6 wt% water-bearing glass is also indicated by the low β_{H2O}-relaxation maximum temperature at ≈422 K, not far above of the γ-relaxation of sodium at 329 K measured in the dry glass and the increased peak area (**Table 2**).

Figure 3 further indicates that internal friction in the hydrous glass would largely increase if the crack tip temperature increases during fracture. However, Weichert and Schönert (1973) estimated a moderate tip temperature increase of less than 300 K even assuming rapid crack propagation (soda-lime silicate glass, $v = 10^3$ m s^{-1}, heat production $2{\cdot}10^{-3}$ J m^{-2}). Also, **Figure 3** merely reflects the global viscoelastic response of the sample whereas energy dissipation is widely assumed to mainly occur in the vicinity of the crack tip. The latter assumption is supported by AFM studies revealing large fluctuations in v and a strong scatter in crack surface curvature in a nanometer scale (Marliere et al., 2003), whereas beyond 10 nm from the crack tip, the material appears fully elastic (Wiederhorn et al., 2011). Since internal friction and energy dissipation during fracture should be based on similar structural relaxation phenomena, however, internal friction and crack propagation data may be compared with each other at least qualitatively.

Different Sections of log $v(K_I)$ for Crack Growth in the Hydrous Glass in Vacuum

It is also worth noting that in contrast to the dry sample, log $v(K_I)$ for crack growth in vacuum in the hydrous sample reveals sections of different slopes (**Table 1**). In terms of section "Crack Growth Exponent in Vacuum," this effect is plausible due to the kinetic nature of energy dissipation. When its relaxation time becomes large compared to the time required for fast crack propagation, log $v(K_I)$ becomes steeper possibly causing a kink. This effect is inherently involved in Eq. 4 and also discussed by Maugis (1985) in terms of limiting crack speeds for certain slope segments. Therefore, n generally tends to increase with v (or K_I) as it is shown in **Figure 2**.

The first slope section, exhibiting the lowest slope of log $v(K_I)$ in **Figure 2** ($n = 16$), is limited by a shoulder at $v \approx 10^{-5}$ m s^{-1} beyond which the slope increases to $n = 26$. The crack velocity range of this shoulder seems to resemble that of region II for the nominal dry glass in ambient air, where it indicates the kinetic transition between water affected and water-independent crack propagation. Since this transition is even caused by trace amounts of water (Ciccotti, 2009), the similarity between the shoulders for the dry and hydrous glass seen in **Figure 2** might indicate similar underlying mechanisms. However, the shoulder at 10^{-3} mbar should occur at lower v. This is indicated by **Figure 1**, where region II for the dry glass shifts to much lower v with decreasing humidity (e.g., shifting down to $v = 10^{-7}$ m s^{-1} for crack growth in 0.017% rh) (Wiederhorn, 1967). At 10^{-3} mbar, this shoulder might fall below the range of v measured in this study. On the other hand, the high concentration of water in the hydrous glass [17 mol% (Kiefer et al., 2019)] makes it reasonable to assume that water readily escapes from the freshly fractured surface increasing the local vapor pressure at the crack tip. This effect might resemble the stress-induced emission of sodium during the fracture of soda-lime silicate glass (Lanford et al., 1979). The resulting micro climate might promote stress corrosion related crack propagation as for the dry glass in ambient air. The resulting shoulder in the hydrous glass would thus represent the kinetic limit of the this effect. The similar slopes n_I for region I in the dry and n_{III} for the first slope section in the hydrous glass in vacuum of 16 (**Table 1**), may also indicate a similar stress corrosion based mechanism. In this case, it would be difficult to apply the term "inert crack growth" or "region III" for this slope section.

The second slope section, exhibiting a slope of $n = 26$ (**Figure 2**), is limited by a kink at $v \approx 3{\cdot}10^{-3}$ m s^{-1} beyond which the slope increases to 55. It is interesting to note that this kink resembles the one found by Gehrke et al. (1987b) for crack growth in float glass measured in liquid water. In this case, the limiting effect of (ambient) water transport to the crack tip can be assumed to reach its minimum influence. For crack propagation in the hydrous glass measured in vacuum, however, this explanation seems questionable. Remaining traces of ambient water should cause a shoulder at much lower v and, assuming this effect is promoted by the micro climate at the crack tip, would contradict the above given explanation for the shoulder at $v \approx 10^{-5}$ m s^{-1}. Instead, the kink could be assumed to reflect the kinetic limit of Si-OH formation at the crack tip according to Michalske and Freiman (1982). This assumption would explain the kink at $v \approx 3{\cdot}10^{-3}$ m s^{-1} for the dry glass in liquid water as well as why dissolved water can not further promote crack propagation even though 17 mol% (Kiefer et al., 2019) of dissolved water is present in the hydrous glass. This hypothesis would allow to assume that water molecules might still diffuse toward the crack tip causing energy dissipation. This might also explain the fact that the slope of log $v(K_I)$ above $v \approx 10^{-3}$ m s^{-1} is smaller for the hydrous glass than for the dry glass.

As an alternative hypothesis, the shoulder at $v \approx 10^{-5}$ m s^{-1} might be explained as discussed above being related to a micro climate at the crack tip whereas the kink at $v \approx 10^{-3}$ m s^{-1} could reflect the kinetic limit of the diffusion of dissolved water toward the crack tip. This latter mechanism resembles the penetration of ambient water molecules into the glass as discussed for crack propagation in air (Tomozawa, 1996; Fett et al., 2005; Wiederhorn et al., 2013a). This effect seems plausible due to the high concentration of water given in the hydrous glass as well as due to the known effect of tensile stress on water diffusivity (Nogami and Tomozawa, 1984; Han and Tomozawa, 1991; Lechenault et al., 2011; Larché and Voorhees, 1996; Mehrer, 1996; Lechenault et al., 2011).

As a further hypothesis, the shoulder at $v \approx 10^{-5}$ m s^{-1} and the kink at 10^{-3} m s^{-1} could, respectively indicate the kinetic limit of diffusion of dissolved molecular water to the crack tip and the Si-OH formation. This interpretation implies that molecular water diffusion to the crack tip is slower than Si-OH-formation. At first glance, this assumption seems to contradict findings reported in Lezzi and Tomozawa (2015). This study shows that molecular water in fused silica can cause stress relaxation more rapidly than Si-OH-formation. A large mobility of molecular water is also indicated by the low peak temperature of β_{H2O} in **Figure 3**. It seems possible, however, that Si-OH formation could be largely promoted by high tensile stresses at the crack tip. Furthermore, the low temperature mobility of molecular water in soda-lime silicate glass is expected to be less than that in fused silica as demonstrated in Muller et al. (2005).

In any case, all hypotheses discussed above need more detailed studies to get better understanding of the underlying mechanism. In particular, the crack growth measurement of the hydrous glass shown here are based on two DCB samples of sufficient size and homogeneity to ensure straight and smooth crack growth along the groove. As the slope of log $v(K_I)$ for the hydrous glass (n = 55) is still smaller than that of the dry glass (n = 148, see **Table 1**), even at $v \approx 1$ m s^{-1}, fractographic studies on fast crack growth might be helpful to reveal the kinetic limit of the related energy dissipation mechanism. Such studies would also be very interesting inasmuch other dissipating mechanism could be expected for rapid crack growth. Thus, Kerkhof (1970) found that high humidity can dalay fast crack growth in soda-lime silicate glass above v = 10 ms^{-1} due to the adhesion between the fractured surfaces of sufficiantly narrow cracks. On the other hand, it would be interesting to study slow crack growth for $v < 10^{-8}$ m s^{-1} in the hydrous glass. In this case, however, the applicability of Eq. 1 has to be carefully considered with respect to a possible crack tip blunting promoted by the large amount of dissolved water.

Average Shift of log $v(K_I)$

As seen from Eq. 3, log $v(K_I)$ will shift right or left along the K_I axis if E and γ_S increases or decreases, respectively. If the change in E and γ_S is not kinetically affected during fracture, K_I equally shifts for any v.

Dissolved water and the resulting decrease of E near the crack tip is discussed as a possible mechanism of stress corrosion (Tomozawa, 2007; Wiederhorn et al., 2013a). In this sense, significant amounts of water dissolved in the hydrous glass during melting should shift log $v(K_I)$ for the inert crack growth to the left. However, the opposite is shown in **Figure 2**, at least for $v > 10^{-7}$ m s^{-1}, where dissolved water obiously acts as a toughening agent. Furthermore, the effect of dissolved water in the hydrous glass on E, seems not enough to explain any strong shift of log $v(K_I)$ in **Figure 2**. Thus, Eq. 3 includes a rather moderate effect ($K_I \sim E^{0.5}$) and almost similar values $E \approx 71$ GPa and 68 GPa were measured for the dry and the hydrous glass in Kiefer et al. (2019), respectively. Confirming this slight decrease in E, log $v(K_I)$ of the hydrous glass is slightly shifted to the left with respect to the dry glass for the slowest crack propagation rates in vacuum.

According to Eq. 3, log $v(K_I)$ can also shift to the left if γ_S is decreased by the presence of water. Such a shift is clearly caused by *ambient water*. Thus, $v = 10^{-7}$ m s^{-1} occurs at $K_I \approx 0.40$ and 0.67 MPa $m^{0.5}$ for the hydrous glass in ambient and vacuum conditions, respectively. This shift is stronger than that observed for the dry glass measured in similar conditions. This effect is most vividly seen in **Figure 2** by the strongly extended K_I range of region II for the hydrous glass. This behavior indicates that ambient water is far more effective than water dissolved in the glass bulk during pressure melting. This way, the toughening effect of dissolved water was overcompensated. One possible reason might be an even higher water concentration near the surface as proved in Han and Tomozawa (1991) for the outermost layer of fractured fused silica glass surfaces. Also, more molecular water is expected since water speciation equilibrium cannot be reached at the low temperature and short times available for ambient water to dissolve to the crack near glass region. Nevertheless, *dissolved water* may further decrease γ_S since slow crack growth in the hydrous glass in air occurs at lower K_I as in the dry glass.

SUMMARY

Crack propagation in nominal dry and hydrous microscope slide glasses containing 6 wt% water was studied in double cantilever beam geometry and was backed up with dynamic mechanical analysis and DTA. Water enrichment of hydrous glass has been achieved by high-pressure melting of glass powder - water mixtures at 500 MPa.

For crack growth in vacuum, dissolved water strongly decreases the slope of log $v(K_I)$ indicating more energy dissipation during fracture. Thus, although slow crack growth ($v = 10^{-7}$ m s^{-1}) is not strongly affected by dissolved water occurring at $K_I \approx 0.7$ MPa $m^{0.5}$ as for the dry glass, fast crack growth ($v = 10^{1}$ m s^{-1}) occurs at $K_I \approx 1.4$ MPa $m^{0.5}$. Consequently, crack growth in hydrous glass occurs at larger stress intensity factor and dissolved water may be regarded as a toughening agent.

However, in ambient air slow crack growth in the hydrous glass was found to occur at lower stress intensity than in the dry one. $v = 10^{-7}$ ms^{-1}, e.g., is, respectively reached at $K_I \approx 0.4$ and 0.5 MPa $m^{0.5}$ for the hydrous and the dry glass. Consequently, region II is much more extended for the hydrous glass. This effect

gives clear evidence that ambient water acts as a strong weakening agent overriding the toughening effect of dissolved water.

DATA AVAILABILITY STATEMENT

The raw data supporting the conclusions of this article will be made available by the authors, without undue reservation, to any qualified researcher upon request.

AUTHOR CONTRIBUTIONS

TW and RM wrote the first draft of the manuscript. SR and TW did the experiments and analysis. TW, RM, RB, HB, JD, and PK contributed to the conception and to critical interpretation of data for the work. All authors contributed to manuscript revision, read and approved the submitted version.

FUNDING

Financial support by the Deutsche Forschungsgemeinschaft (DFG) through its priority program SPP 1594 - Topological Engineering of Ultrastrong Glasses (MU 963/14-2, DE598/22-2, and Be1720/31-2) is gratefully acknowledged.

ACKNOWLEDGMENTS

The authors wish to thank all colleagues at division 5.6 Glass at BAM, in particular A. Marek for sample preparation. Additionally, R. Falkenberg is greatfully acknowledged for fruitfull discussions.

REFERENCES

Balzer, R., Behrens, H., Reinsch, S., and Fechtelkord, M. (2019a). Structural investigation of hydrous phosphate glasses. *Phys. Chem. Glass. Eur. J. Glass Sci. Technol. B* 60, 49–61. doi: 10.13036/17533562.60.2.041

Balzer, R., Behrens, H., Schuth, S., Waurischk, T., Reinsch, S., and Muller, R. (2019b). The influence of H2O and SiO2 on the structure of silicoborate glasses. *J. Non Cryst. Solids* 519, 38–51.

Bauer, U., Behrens, H., Fechtelkord, M., Reinsch, S., and Deubener, J. (2015). Water- and boron speciation in hydrous soda-lime-borate glasses. *J. Non Cryst. Solids* 423, 58–67. doi: 10.1016/j.jnoncrysol.2015.05.004

Bauer, U., Behrens, H., Reinsch, S., Morin, E. I., and Stebbins, J. F. (2017). Structural investigation of hydrous sodium borosilicate glasses. *J. Non Cryst. Solids* 465, 39–48. doi: 10.1016/j.jnoncrysol.2017.03.023

Behrens, H., Bauer, U., Reinsch, S., Kiefer, P., Muller, R., and Deubener, J. (2018). Structural relaxation mechanisms in hydrous sodium borosilicate glasses. *J. Non Cryst. Solids* 497, 30–39. doi: 10.1016/j.jnoncrysol.2018.05.025

Behrens, H., and Stuke, A. (2003). Quantification of H2O contents in silicate glasses using IR spectroscopy - a calibration based on hydrous glasses analyzed by Karl-Fischer titration. *Glass Sci. Technol.* 76, 176–189.

Brueckner, R. (1964). Charakteristische physikalische Eigenschaften der oxydischen Hauptglasbildner und ihre Beziehung zur Struktur der Gläser. Teil IV: deutung und strukturelle Schlußfolgerungen. *Glastechnol. Ber.* 37, 536–548.

Celarie, F., Ciccotti, M., and Marliere, C. (2007). Stress-enhanced ion diffusion at the vicinity of a crack tip as evidenced by atomic force microscopy in silicate glasses. *J. Non Cryst. Solids* 353, 51–68. doi: 10.1016/j.jnoncrysol.2006.09.034

Charles, R. J. (1958). Static fatigue of glass .2. *J. Appl. Phys.* 29, 1554–1560.

Ciccotti, M. (2009). Stress-corrosion mechanisms in silicate glasses. *J. Phys. D Appl. Phys.* 42:21.

Day, D. E. (1974). The Internal Friction of Glasses Containing Water. *Wiss. Zeitschr. Friedrich Schiller Univ. Jena Math. Nat. R.* 23, 293–305.

Day, D. E., and Stevels, J. M. (1974). Effect of dissolved water on internal-friction of glass. *J. Non Cryst. Solids* 14, 165–177. doi: 10.1016/0022-3093(74)90027-1

Deubener, J., Bruckner, R., and Hessenkemper, H. (1992). Nucleation and crystallization kinetics on float glass surfaces. *Glastechn. Ber. Glass Sci. Technol.* 65, 256–266.

Deubener, J., Muller, R., Behrens, H., and Heide, G. (2003). Water and the glass transition temperature of silicate melts. *J. Non Cryst. Solids* 330, 268–273. doi: 10.1016/s0022-3093(03)00472-1

Dunning, J., Douglas, B., Miller, M., and Mcdonald, S. (1994). The role of the chemical environment in frictional deformation - stress-corrosion cracking and comminution. *Pure Appl. Geophys.* 143, 151–178. doi: 10.1007/bf00874327

Evans, A. G., and Johnson, H. (1975). Fracture stress and its dependence on slow crack growth. *J. Mater. Sci.* 10, 214–222. doi: 10.1007/bf00540345

Fett, T., Guin, J. P., and Wiederhorn, S. M. (2005). Interpretation of effects at the static fatigue limit of soda-lime-silicate glass. *Eng. Fract. Mech.* 72, 2774–2791. doi: 10.1016/j.engfracmech.2005.07.002

Freiman, S. W., Wiederhorn, S. M., and Mecholsky, J. J. (2009). Environmentally enhanced fracture of glass: a historical perspective. *J. Am. Ceram. Soc.* 92, 1371–1382. doi: 10.1111/j.1551-2916.2009.03097.x

Gehrke, E., Hahnert, M., and Ullner, C. (1987a). Influence of dissolution rate on crack-growth and fatique of Na2O-Al2O3-B2O3-SiO2 glasses. *J. Mater. Sci.* 22, 1682–1686. doi: 10.1007/bf01132392

Gehrke, E., Ullner, C., and Hahnert, M. (1987b). Correlation between multistage crack-growth and time-dependent strength in commercial silicate-glasses .1. Influence of ambient media and types of initial cracks. *Glastechn. Ber. Glass Sci. Technol.* 60, 268–278.

Gehrke, E., Ullner, C., and Hahnert, M. (1990). Effect of corrosive media on crack-growth of model glasses and commercial silicate-glasses. *Glastechn. Ber. Glass Sci. Technol.* 63, 255–265.

Gehrke, E., Ullner, C., and Hahnert, M. (1991). Fatigue limit and crack arrest in alkali-containing silicate-glasses. *J. Mater. Sci.* 26, 5445–5455. doi: 10.1007/bf02403942

Griffith, A. A. (1921). The phenomena of rupture and flow in solids. *Philos. Trans. R. Soc. Lond. Ser. A* 221, 163–198.

Han, W. T., and Tomozawa, M. (1991). Effect of residual water in silica glass on static fatigue. *J. Non Cryst. Solids* 127, 97–104. doi: 10.1016/0022-3093(91)90405-u

Hilling, W. B., and Charles, R. J. (1965). "Surfaces, stress-dependent surface reactions, and strength," in *High Strength Materials*, ed. V. F. Zackay (New York, NY: John Wiley and Sons).

Ito, S., and Tomozawa, M. (1981). Stress-corrosion of silica glass. *J. Am. Ceram. Soc.* 64, C160–C160.

Ito, S., and Tomozawa, M. (1982a). Crack blunting of high-silica glass. *J. Am. Ceram. Soc.* 65, 368–371. doi: 10.1111/j.1151-2916.1982.tb10486.x

Ito, S., and Tomozawa, M. (1982b). Dynamic fatigue of sodium-silicate glasses with high water-content. *J. Phys.* 43, 611–614.

Kerkhof, F. (1970). *Bruchvorgänge in Gläsern*. Frankfurth: Verlag der Deutschen Glastechnischen Gesellschaft.

Kiefer, P., Balzer, R., Deubener, J., Behrens, H., Waurischk, T., Reinsch, S., et al. (2019). Density, elastic constants and indentation hardness of hydrous soda-lime-silica glasses. *J. Non Cryst. Solids* 521:119480. doi: 10.1016/j.jnoncrysol.2019.119480

Lanford, W. A., Davis, K., Lamarche, P., Laursen, T., Groleau, R., and Doremus, R. H. (1979). Hydration of soda-lime glass. *J. Non Cryst. Solids* 33, 249–266. doi: 10.1016/j.scitotenv.2018.04.178

Langford, S. C., Jensen, L. C., Dickinson, J. T., and Pederson, L. R. (1991). Alkali emission accompanying fracture of sodium-silicate glasses. *J. Mater. Res.* 6, 1358–1368. doi: 10.1557/jmr.1991.1358

Larché, F. C., and Voorhees, P. W. (1996). Diffusion and stresses: basic thermodynamics. *Defect Diffus. Forum* 12, 31–36. doi: 10.4028/www.scientific.net/ddf.129-130.31

Le Parc, R., Levelut, C., Pelous, J., Martinez, V., and Champagnon, B. (2006). Influence of fictive temperature and composition of silica glass on anomalous elastic behaviour. *J. Phys. Condens. Matter* 18, 7507–7527. doi: 10.1088/0953-8984/18/32/001

Lechenault, F., Rountree, C. L., Cousin, F., Bouchaud, J. P., Ponson, L., and Bouchaud, E. (2011). Evidence of deep water penetration in silica during stress corrosion fracture. *Phys. Rev. Lett.* 106:165504.

Lezzi, P. J., and Tomozawa, M. (2015). An overview of the strengthening of glass fibers by surface stress relaxation. *Int. J. Appl. Glass Sci.* 6, 34–44. doi: 10.1111/ijag.12108

Liang, R. Y., and Zhou, J. (1997). Energy based approach for crack initiation and propagation in viscoelastic solid. *Eng. Fract. Mech.* 58, 71–85. doi: 10.1016/s0013-7944(97)00072-6

Marliere, C., Prades, S., Celarie, F., Dalmas, D., Bonamy, D., Guillot, C., et al. (2003). Crack fronts and damage in glass at the nanometre scale. *J. Phys. Condens. Matter* 15, S2377–S2386.

Marsh, D. M. (1964). Plastic flow in glass. *Proc. R. Soc. Lond. Ser. A Math. Phys. Sci.* 279, 420–474.

Maugis, D. (1985). Subcritical crack-growth, surface-energy, fracture-toughness, stick slip and embrittlement. *J. Mater. Sci.* 20, 3041–3073. doi: 10.1007/bf00545170

Mehrer, H. (1996). The effect of pressure on diffusion. *Defect Diffus. Forum* 12, 57–76. doi: 10.4028/www.scientific.net/ddf.129-130.57

Michalske, T. A., and Freiman, S. W. (1982). A molecular interpretation of stress-corrosion in silica. *Nature* 295, 511–512. doi: 10.1038/295511a0

Muller, R., Gottschling, P., and Gaber, M. (2005). Water concentration and diffusivity in silicates obtained by vacuum extraction. *Glass Sci. Technol.* 78, 76–89.

Muraoka, M., and Abe, H. (1996). Subcritical crack growth in silica optical fibers in a wide range of crack velocities. *J. Am. Ceram. Soc.* 79, 51–57. doi: 10.1111/j.1151-2916.1996.tb07879.x

Nogami, M., and Tomozawa, M. (1984). Effect of stress on water diffusion in silica glass. *J. Am. Ceram. Soc.* 67, 151–154. doi: 10.1111/j.1151-2916.1984.tb09634.x

OriginLab (2019). *OriginLab Releases Origin 2015 Data Analysis and Graphing Software 2014*. Available online at: https://www.originlab.com/index.aspx?go=Company/NewsAndEvents/PressRoom&pid=2141 (accessed September 30, 2019).

Pukh, V. P., Baikova, L. G., Kireenko, M. F., and Tikhonova, L. V. (2009). On the kinetics of crack growth in glass. *Glass Phys. Chem.* 35, 560–566. doi: 10.1134/s1087659609060029

Reinsch, S., Muller, R., Deubener, J., and Behrens, H. (2013). Internal friction of hydrated soda-lime-silicate glasses. *J. Chem. Phys.* 139:174506. doi: 10.1063/1.4828740

Richter, H. (1983). Zum Einfluß umgebender Medien auf die Rißausbreitung in Glas in einem Zwischenbereich von Bruchgeschwindigkeiten. *Glastech. Ber.* 56, 402–407.

Seaman, J. H., Lezzi, P. J., Blanchet, T. A., and Tomozawa, M. (2015). Modeling slow crack growth behavior of glass strengthened by a subcritical tensile stress using surface stress relaxation. *J. Am. Ceram. Soc.* 98, 3075–3086. doi: 10.1111/jace.13710

Simmons, C. J., and Freiman, S. W. (1981). Effect of corrosion processes on subcritical crack-growth in glass. *J. Am. Ceram. Soc.* 64, 683–686. doi: 10.1111/j.1151-2916.1981.tb15870.x

Takata, M., Tomozawa, M., and Watson, E. B. (1982). Effect of water content on mechanical properties of Na2O-SiO2 glasses. *J. Am. Ceram. Soc.* 65, C156–C157.

Tomozawa, M. (1996). Fracture of glasses. *Annu. Rev. Mater. Sci.* 26, 43–74.

Tomozawa, M. (2007). "Role of water in fracture of glass," in *Proceedings of the 4th International Workshop on Fracture and Flow of Advanced Glasses FAAG*, Troy, NY.

Tomozawa, M., Li, H., and Davis, K. M. (1994). Water diffusion, oxygen vacancy annihilation and structural relaxation in silica glasses. *J. Non Cryst. Solids* 179, 162–169. doi: 10.1016/0022-3093(94)90693-9

Ullner, C., and Gehrke, E. (1990). Mechanism of mechanical strength increase of soda lime glass by aging - comment. *J. Am. Ceram. Soc.* 73, 1461–1463. doi: 10.1111/j.1151-2916.1990.tb05229.x

Weichert, R., and Schönert, K. (1973). On the temperature rise at the tip of a fast running crack. *J. Phys. Mech. Sol.* 22, 127–133. doi: 10.1016/0022-5096(74)90018-0

Wiederhorn, S. M. (1967). Influence of water vapor on crack propagation in soda-lime glass. *J. Am. Ceram. Soc.* 50, 407–414. doi: 10.1111/j.1151-2916.1967.tb15145.x

Wiederhorn, S. M., and Bolz, L. H. (1970). Stress corrosion and static fatigue of glass. *J. Am. Ceram. Soc.* 53, 543–548. doi: 10.1111/j.1151-2916.1970.tb15962.x

Wiederhorn, S. M., Diness, A. M., and Heuer, A. H. (1974). Fracture of glass in vacuum. *J. Am. Ceram. Soc.* 57, 336–341.

Wiederhorn, S. M., Fett, T., Guin, J. P., and Ciccotti, M. (2013a). Griffith cracks at the nanoscale. *Int. J. Appl. Glass Sci.* 4, 76–86. doi: 10.1111/ijag.12025

Wiederhorn, S. M., Fett, T., Rizzi, G., Hoffmann, M. J., and Guin, J. P. (2013b). The effect of water penetration on crack growth in silica glass. *Eng. Fract. Mech.* 101, 3–16. doi: 10.1016/j.engfracmech.2012.04.026

Wiederhorn, S. M., Fett, T., Rizzi, G., Hoffmann, M. J., and Guin, J. P. (2013c). Water penetration-its effect on the strength and toughness of silica glass. *Metall. Mater. Trans. A Phys. Metall. Mater. Sci.* 44A, 1164–1174. doi: 10.1007/s11661-012-1333-z

Wiederhorn, S. M., Guin, J. P., and Fett, T. (2011). The use of atomic force microscopy to study crack tips in glass. *Metall. Mater. Trans. A Phys. Metall. Mater. Sci.* 42A, 267–278. doi: 10.1007/s11661-010-0411-3

Conflict of Interest: The authors declare that the research was conducted in the absence of any commercial or financial relationships that could be construed as a potential conflict of interest.

frontiers in Materials

REVIEW
published: 17 April 2020
doi: 10.3389/fmats.2020.00089

Review on Quantum Mechanically Guided Design of Ultra-Strong Metallic Glasses

Simon Evertz[1], Volker Schnabel[1], Mathias Köhler[2], Ines Kirchlechner[2], Paraskevas Kontis[2], Yen-Ting Chen[1], Rafael Soler[2], B. Nagamani Jaya[2], Christoph Kirchlechner[2], Denis Music[1], Baptiste Gault[2,3], Jochen M. Schneider[1], Dierk Raabe[2] and Gerhard Dehm[2]*

[1] Materials Chemistry, RWTH Aachen University, Aachen, Germany, [2] Max-Planck-Institut für Eisenforschung, Düsseldorf, Germany, [3] Department of Materials, Royal School of Mines, Imperial College London, London, United Kingdom

Quantum mechanically guided materials design has been used to predict the mechanical property trends in crystalline materials. Thereby, the identification of composition-structure-property relationships is enabled. However, quantum mechanics based design guidelines and material selection criteria for ultra-strong metallic glasses have been lacking. Hence, based on an *ab initio* model for metallic glasses in conjunction with an experimental high-throughput methodology geared toward revealing the relationship between chemistry, topology and mechanical properties, we propose principles for the design of tough as well as stiff metallic glasses. The main design notion is that a low fraction of hybridized bonds compared to the overall bonding in a metallic glass can be used as a criterion for the identification of damage-tolerant metallic glass systems. To enhance the stiffness of metallic glasses, the bond energy density must be increased as the bond energy density is the origin of stiffness in metallic glasses. The thermal expansion, which is an important glass-forming identifier, can be predicted based on the Debye-Grüneisen model.

Keywords: metallic glass, *ab initio*, quantum mechanical materials design, toughness, stiffness, micro-mechanics

OPEN ACCESS

Edited by:
Jürgen Horbach, Heinrich Heine University of Düsseldorf, Germany

Reviewed by:
Roger Jay Loucks, Alfred University, United States
Haizheng Tao, Wuhan University of Technology, China

****Correspondence:***
Simon Evertz
evertz@mch.rwth-aachen.de

Specialty section:
This article was submitted to Ceramics and Glass, a section of the journal Frontiers in Materials

Received: *06 February 2020*
Accepted: *25 March 2020*
Published: *17 April 2020*

Citation:
Evertz S, Schnabel V, Köhler M, Kirchlechner I, Kontis P, Chen Y-T, Soler R, Jaya BN, Kirchlechner C, Music D, Gault B, Schneider JM, Raabe D and Dehm G (2020) Review on Quantum Mechanically Guided Design of Ultra-Strong Metallic Glasses. Front. Mater. 7:89. doi: 10.3389/fmats.2020.00089

INTRODUCTION

Today, 60 years after metallic glasses were first introduced by Klement et al. (1960), a large number of metallic glass compositions have been identified (Li et al., 2017) and their characteristic topological, magnetic, corrosive and mechanical properties have been widely explored (Ashby and Greer, 2006). Metallic glasses are amorphous alloys, lacking long-range order and microstructure (Ashby and Greer, 2006). They are produced by rapid quenching below the glass transition temperature T_g, where kinetic limitations prevent crystallization. Therefore, they are frozen in a local minimum of the energy landscape, exhibiting higher energy than their crystalline counterparts and are hence metastable (Stillinger, 1995; Debenedetti and Stillinger, 2001).

Traditionally, three rules are followed in designing metallic glasses with a high glass forming ability (Inoue, 2000). These rules require for a metallic glass: (a) a multi-component system with more than three constituents; (b) a large atomic size difference between

the main constituents, i.e., larger than 12%; (c) negative enthalpies of mixing between the main constituents (Greer, 1993; Inoue, 2000; Greer, 2009). However, deviations from these rules have been found, for instance in the Pd-(Cu)-Ni-P system. Despite not following the empirical rules, a high glass forming ability was reported to be due to the coexistence of two types of short-range ordered clusters in these glasses, namely trigonal prisms and tetragonal dodecahedra in case of the Pd-Cu-Ni-P glass that hinder atomic rearrangements in this material (Inoue, 2000).

Due to their amorphous nature, mechanical properties such as hardness, yield strength, and toughness of metallic glasses are often promising for structural applications (Ashby and Greer, 2006). Metallic glasses can exhibit high resilience together with low damping (Ashby and Greer, 2006), allowing the efficient storage and release of elastic energy. In addition, metallic glasses cover a wide range of fracture toughness together with a high yield strength (Ashby and Greer, 2006; Demetriou et al., 2011). However, tough metallic glasses appear to fail in a brittle manner as shear is concentrated in shear bands leading to work softening (Greer, 2009; Greer et al., 2013). Confinement of shear bands can prohibit catastrophic failure from a single shear band (Greer, 2009; Kumar et al., 2011). Mechanical properties depend on the chemistry but also on sample dimensions and processing history (Greer, 2009; Greer et al., 2013). Processing influences the atomic configuration and especially the free volume in the glass (Li et al., 2007; Cheng and Ma, 2011). The fracture toughness, which is a crucial material parameter for any load-bearing structural material, is enhanced as the free volume is increased (Xu et al., 2010). While intrinsic toughening of metallic glasses focuses on crack initiation, extrinsic toughening strategies focus on crack propagation and utilize finely dispersed phase fractions (Xu et al., 2010) to counteract brittle failure of the material.

Next to their mechanical properties, the soft-magnetic properties of metallic glasses favor their application in transformer sheets and electronic communication (Inoue et al., 2004; Chen et al., 2018). The magnetic moment in metallic glasses is weakened by the introduction of metalloids due to hybridizing bonds (Hostert et al., 2012).

In this review on quantum-mechanically guided design of metallic glasses, we focus on the influence of chemical composition on the electronic structure as well as on the mechanical properties of metallic glasses, especially on stiffness and toughness in monolithic metallic glasses. We investigate composition induced changes in the electronic structure and relate those to property changes to derive design principles that are more precise than the traditional empirical rules. To validate our design approach, we combine *ab initio* modeling with experimental high-throughput characterization methods to investigate the chemistry-topology relationship and probe the validity of the predicted mechanical properties on the most promising samples thereof.

In the following sections, we review our work on *ab initio* modeling of metallic glasses as well as on high throughput methods to characterize metallic glasses. Finally, we show that fracture toughness is related to the fraction of hybridized bonds on the overall bonding and stiffness of metallic glasses originates in the bond energy density.

AB INITIO MOLECULAR DYNAMICS MODEL OF METALLIC GLASSES

Due to the dense packing and the formation of short-range ordered clusters of atoms in metallic glasses, the modeling of metallic glasses needs to take chemical effects and many-body interactions into account (Greer, 2009). As the selection of reliable interatomic potentials for classical, semi-empirical potential molecular dynamics (MD) is challenging due to the anharmonicity in metallic glasses (Lambson et al., 1986; Crespo et al., 2016; Aitken et al., 2018), density functional theory-based *ab initio* MD has been used to calculate the properties of a vast number of materials as it does not require the input of interatomic potentials while being able to cover many-body interactions. By *ab initio* modeling, an in-depth analysis of the structure-property relationship of metallic glasses is possible that is otherwise challenging to probe only by experimental means, including parameters such as the partial pair correlations (Qin et al., 2007; Ganesh and Widom, 2008; Hui et al., 2008b, 2009; Fang et al., 2009; Tian et al., 2011; Zhang et al., 2015; Hunca et al., 2016; Yu et al., 2016), coordination polyhedra (Ganesh and Widom, 2008; Fang et al., 2009; Fujita et al., 2009; Hui et al., 2009; Hirata et al., 2011; Tian et al., 2011; Kumar et al., 2011; Durandurdu, 2012; Wu et al., 2012; Zhang et al., 2015; Huang et al., 2016; Yu et al., 2016) and bonding (Kumar et al., 2011; Hunca et al., 2016). However, modeling the dynamics involved in relaxation and rejuvenation phenomena is out of reach for *ab initio* molecular dynamics due to the limitations of time steps and cell size as discussed below.

To reveal the structure-property relationship in metallic glasses and predict stiffness and toughness based on the electronic structure, we performed large scale *ab initio* calculations in the past years. This allows for an in-depth analysis of the electronic structure, which cannot be obtained by classical molecular dynamical calculations. However, the aim of predicting mechanical properties of metallic glasses from *ab initio* calculations raises two major challenges: First, while the elastic properties and thermal expansion can be directly calculated from *ab initio* configurations, mechanical properties involving the rearrangement of atoms such as fracture toughness cannot be predicted directly. This requires new predictor functions and their validation. Second, the *ab initio* configuration has to be representative of the corresponding synthesized materials. Hence, high-throughput synthesis and characterization of topology and microstructure by pair distribution functions and atom probe tomography are employed to compare the synthesized material with the configuration obtained by *ab initio* calculations. Finally, the predictor functions need to be validated by extracting the mechanical properties by experimental means such as micro-mechanical bending tests. Specifically, we define a cubic supercell with specific chemical composition and obtain an amorphous structure by *ab initio* heating-quenching cycles. From this glassy cell, mechanical properties are calculated either

directly or by the introduction of new predictor functions. These introduced predictor functions are then validated experimentally and revisited to improve their predictive power.

Our *ab initio* approach starts with a cubic supercell containing in the order of 115 atoms (Hostert et al., 2011), which is in line with the typical size of a supercell for glassy structures found in literature (Hui et al., 2008b; Fang et al., 2009; Fujita et al., 2009; Hirata et al., 2011; Tian et al., 2011; Kumar et al., 2011; Galván-Colín et al., 2015; Zhang et al., 2015; Huang et al., 2016) and represents the lower limit required for physically significant models (Holmström et al., 2010). This cell is then annealed at an extremely high temperature such as 4000 K for 400 fs (Hostert et al., 2011), then quenched to 0 K (Hostert et al., 2011; Schnabel et al., 2015) or room temperature (Zhang et al., 2015) with infinite quenching rate. At the final temperature, the atomic structure is equilibrated (Hostert et al., 2011; Zhang et al., 2015; Yu et al., 2016). The heating – quenching – equilibration cycle is done once (Fang et al., 2009; Fujita et al., 2009; Galván-Colín et al., 2015; Zhang et al., 2015) or repeatedly until the volume is self-consistent (Hostert et al., 2011).

Alternative approaches to obtain an amorphous configuration include: stepwise cooling to simulate a cooling rate (Hui et al., 2008b; Fang et al., 2009; Fujita et al., 2009; Hirata et al., 2011; Tian et al., 2011; Kumar et al., 2011; Durandurdu, 2012; Wu et al., 2012; Hunca et al., 2016; Yu et al., 2016); cooling a supercell from melt, equilibration below the melting point and subsequent cooling to room temperature with an imposed cooling rate (Qin et al., 2007; Jakse and Pasturel, 2008; Hui et al., 2009; Huang et al., 2016); or by conducting several tempering steps (Ganesh and Widom, 2008; Hui et al., 2008a). Thereby, structures consistent with physical samples can be achieved (Galván-Colín et al., 2015). The *ab initio* models are probed for consistency with physical samples by comparison with experimentally obtained X-ray scattering data (Ganesh and Widom, 2008; Hui et al., 2009; Hirata et al., 2011; Hostert et al., 2011; Wu et al., 2012; Galván-Colín et al., 2015; Huang et al., 2016; Yu et al., 2016), extended X-ray absorption fine structure (EXAFS) (Fujita et al., 2009; Kumar et al., 2011), electron nano-beam diffraction (Hirata et al., 2011), density (Hostert et al., 2011) and coordination numbers (Fang et al., 2009).

To obtain an amorphous structure *in silico*, one option to reconstruct the structure from experimental topology data (X-ray scattering, neutron scattering, EXAFS) is the use of Reverse Monte Carlo modeling (RMC) (Jóvári et al., 2007; Mattern et al., 2009; Senkov et al., 2010). In RMC, a starting configuration with N atoms is iteratively fitted to the available experimental data. In every iteration, the difference X^2_0 of the structure factor of the starting configuration and the experimental structure factor is calculated. Then, one atom is randomly moved. The move is rejected, if it results in an atomic distance smaller than a predefined cut-off distance. After the move, the difference X^2_N between the structure factor of the new configuration and the experimental structure is calculated. If $X^2_N < X^2_0$, the move is accepted. Otherwise, it is accepted with a probability of $\exp(-(X^2_N - X^2_0)/2)$. This iteration is repeated until X^2 reaches an equilibrium value (McGreevy, 2001).

We investigated the influence of the quenching rate for the Co-Ta-Fe-B system (Hostert et al., 2011). Comparing supercells quenched with 1014 and 1016 K s^{-1} and infinite cooling rate, the total energy differences between the two finite and the infinite quenching rates are −0.5% for 1016 K s^{-1} quenching rate and −1.2% for 1014 K s^{-1} quenching rate (Hostert et al., 2011). The comparison of Young's modulus and mass density of the infinitely fast quenched *ab initio* configuration is consistent with values obtained experimentally from a sample synthesized by magnetron sputtering. To compare the topology of the simulated material with a physical sample, the total pair distribution function (PDF) obtained for the simulated material with an infinite quenching rate is shown in **Figure 1** together with the experimental PDF obtained by high-energy X-ray scattering. The calculated PDF shows the same features as the experimental PDF (Hostert et al., 2011). The calculated principal peak indicating the first coordination shell coincides very well with the experimental first coordination shell, while the agreement between theory and experiment of the second and third coordination shell is weaker due to the limited size of the calculated supercell (Hostert et al., 2011).

HIGH-THROUGHPUT CHARACTERIZATION

To validate the representativeness of the *ab initio* configuration and the properties predicted directly by *ab initio* calculations, a high-throughput synthesis and characterization route is required. To explore a large compositional range, the use of sample libraries with spatially resolved analysis techniques has been proven efficient (Sakurai et al., 2007.; Deng et al., 2007; Li et al., 2008, 2017, 2019; Aono et al., 2010, 2011; Guo et al., 2011; Sakurai et al., 2011; Wang et al., 2011; Ding et al., 2012, 2014; Gregoire et al., 2012; Tsai and Flores, 2014, 2016; Liu et al., 2016;

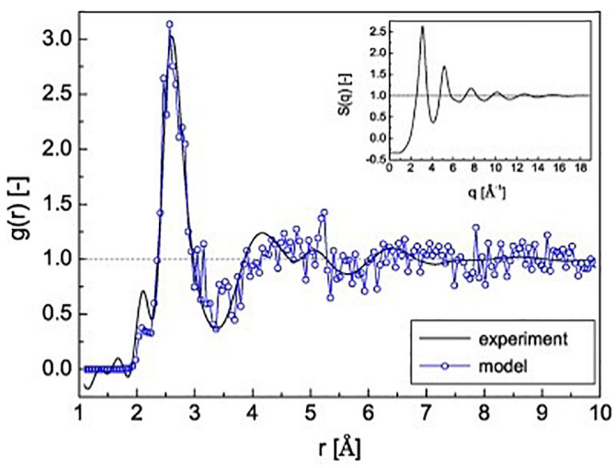

FIGURE 1 | Pair distribution function g(r) of experimentally and *ab initio* calculated $Co_{45.5}Fe_{24}Ta_6B_{24.5}$. Inset: structure factor S(q) of the experimental sample (Hostert et al., 2011). © IOP Publishing. Reproduced from Hostert et al. (2011) with permission from IOP. All rights reserved.

Schnabel et al., 2016b; Bordeenithikasem et al., 2017; Ren et al., 2018; Zhang et al., 2018; Zheng et al., 2019). Examples of synthesis routes for combinatorial samples are physical vapor deposition (Sakurai et al., 2007, 2011; Deng et al., 2007; Li et al., 2008, 2017, 2019; Aono et al., 2011; Guo et al., 2011; Wang et al., 2011; Ding et al., 2012, 2014; Gregoire et al., 2012; Liu et al., 2016; Schnabel et al., 2016b; Bordeenithikasem et al., 2017; Ren et al., 2018; Zhang et al., 2018; Zheng et al., 2019) or laser additive manufacturing (Tsai and Flores, 2014, 2016) of metallic glasses.

Our high-throughput approach to correlate chemistry, topology and mechanical properties is based on magnetron sputtering of combinatorial samples with the same sputtering parameters on silicon and polyimide substrates, enabling to screen samples with in-plane chemical gradients (scheme shown in **Figure 2**) by energy-dispersive X-ray spectroscopy, high-energy X-ray scattering, atom-probe tomography (APT) and nanoindentation (Schnabel et al., 2016b). The analysis of the Co-Ta-Zr-B system (**Figure 2**) shows a chemically induced bond weakening of the metal-metal bonds (i.e., increase of bond distances, 1st bond distances correspond predominantly to Co-Co bonds, while 2nd bond distances correspond predominantly to Zr-Zr bonds) with increasing boron content as inferred from a shift in peak positions in the pair distribution function (Schnabel et al., 2016b). However, due to the increased B content, the stiffness is enhanced along the Co-B gradient (Schnabel et al., 2016b). With increasing Zr content, the presence of two Co- and Zr-rich amorphous phases is suggested from the PDF (not shown here, c.f. Schnabel et al., 2016b) and confirmed on selected samples by APT. The periodicity is 20–30 nm independent of composition (Schnabel et al., 2016b). The correlation between composition and mechanical properties can also be revealed by studying thin film metallic glasses on micro-cantilever arrays (Guo et al., 2011).

In addition to mechanical properties, topology, and composition, the glass forming ability can be investigated by high-throughput methods. Ding et al. placed a gas releasing agent below combinatorial magnetron sputtered thin film metallic glasses to investigate thermoplastic formability by blow molding along the concentration gradient (Ding et al., 2014). Sheet resistivity (Li et al., 2019), resistivity (Zhang et al., 2018, Zheng et al., 2019), thermography (Aono et al., 2010, 2011), laser spike annealing (Bordeenithikasem et al., 2017) and image contrast (Ding et al., 2012) have been employed to explore glass forming ability. The use of nanocalorimetry allows the determination of glass transition temperature and glass transition enthalpy (Gregoire et al., 2012). Combinatorial synthesis and characterization are also used to investigate corrosion (Sakurai et al., 2011; Li et al., 2017), antibacterial properties (Liu et al., 2016) and biocompatibility of metallic glasses (Li et al., 2017).

While magnetron sputtering allows for high cooling rates that enable the synthesis of a large range of amorphous compositions, laser deposition allows the high-throughput synthesis via melting which is closer to synthesis conditions of bulk metallic glasses (Tsai and Flores, 2014, 2016). In contrast to magnetron sputtering, this allows the screening of alloys for glass forming ability and mechanical properties as shown by Tsai and Flores for Cu-Zr (Tsai and Flores, 2014) and Cu-Zr-Ti (Tsai and Flores, 2016). However, this method requires more preparation for the investigation of topological changes along the gradients, as samples have to be taken out of the gradient for electron or X-ray scattering experiments.

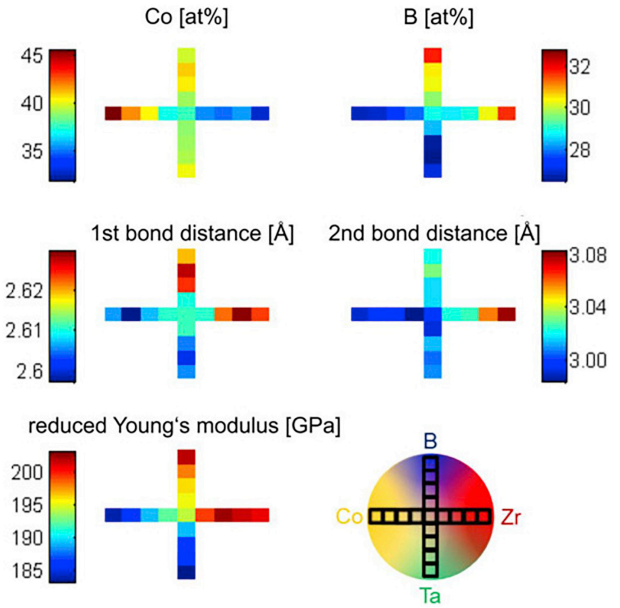

FIGURE 2 | Co and B concentration, 1st and 2nd bond distance and Young's modulus along the composition gradients of a combinatorial Co-Zr-Ta-B metallic glass as sketched in the lower right scheme of a combinatorial sample. The color scheme indicates the value of the quantity shown along the respective gradients. Each box in the gradient correlates to the measurement location on the investigated sample. Reproduced from Schnabel et al. (2016b) with permission from Elsevier.

Despite experimental high-throughput methods, systematic screening by *ab initio* and experimental means of all possible metallic glass compositions based on the elements in the periodic table would take extremely long. Hence, Ren et al. introduced a machine learning model to predict the glass forming ability (Ren et al., 2018). Starting with a limited amount of data, the predictions of the machine learning model are validated by combinatorial magnetron sputtered samples. The experimental results are fed back into the machine learning model, thereby improving the model (Ren et al., 2018). By the combination of machine learning and combinatorial testing, Ren et al. accelerate the screening of ternary alloys by 100 times compared to traditional methods.

ORIGIN OF STIFFNESS IN METALLIC GLASSES

The stiffness in terms of bulk modulus of metallic glasses is defined by the chemical composition and topology (Davis et al., 1982). Bulk modulus is usually lower in the amorphous structure compared to the crystal structure. This is proposed to originate

from strongly bonded metal-metalloid clusters connected by weaker bonds in the amorphous structure (Davis et al., 1982). The lower bulk modulus in the glass compared to the corresponding crystal infers a lower internal bond energy density of the glass compared to the crystal (Gilman, 1975). It has been reported that the bond stiffness and bond strength critically affect the elastic moduli (Zhao et al., 2016). Other work claims variations in bulk modulus are a density effect (Cheng and Ma, 2009). In terms of electronic structure, the origin of stiffness is the valence electron density (Gilman, 2008; Pang et al., 2013), if covalent bonding does not prevail (Pang et al., 2013). The elastic constants can be calculated on the continuum scale from the curvature of the total energy-volume curve of the supercell (Zhang, 2013). As the elastic constants originate from the atomic bonding, they reflect the topology (Davis et al., 1976) and atomic bond strength on a macroscopic scale (Zhang, 2013).

We found, however, that the valence electron density does not scale universally with bulk modulus for metallic glasses (Schnabel et al., 2017). Schnabel et al. (2017) report two different linear relations between B and valence electron density for metal-metal glasses and for metal-metalloid glasses. The comparison of density, electronic structure, and bond energy, obtained by integration of the crystal orbital Hamilton population (Dronskowski and Bloechl, 1993), with bulk moduli of different metal-metal and metal-metalloid metallic glasses indicates the bond energy density as the origin of stiffness in metallic glasses (Schnabel et al., 2017). This underlines the early notion by Gilman that the internal energy density of a glass correlates with the elastic moduli (Gilman, 1975). The fit of bulk modulus as a function of bond energy density (**Figure 3**) shows the universality of this correlation for metallic glasses. Thereby, the bond energy density is consistent with previous literature as it combines the notions of strong metal-metalloid bonds and the valence electron density.

QUANTUM MECHANICAL DESIGN PROPOSAL FOR FRACTURE TOUGHNESS

Next to stiffness, the combination of the mutually exclusive properties strength and toughness (Ritchie, 2011), also referred to

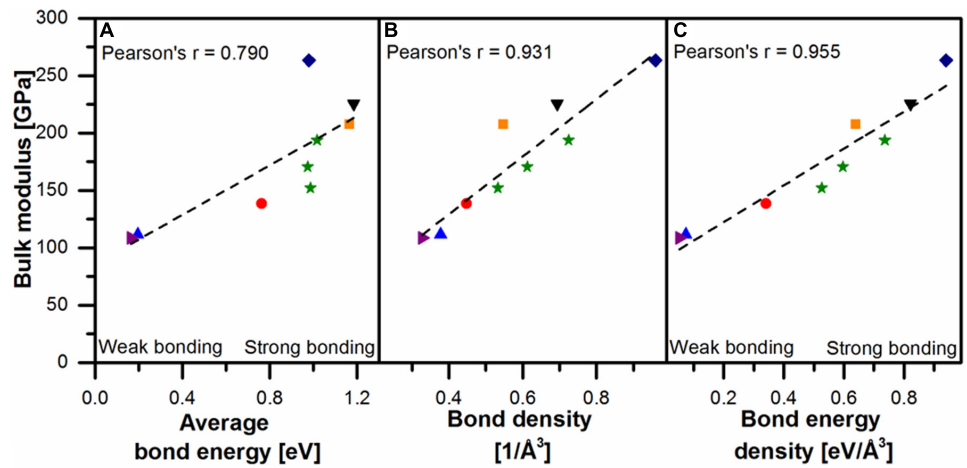

D

Composition	Average bond energy eV	Bond density 1/Å³	Bond energy density eV/Å³	Molar density mol/cm³	B GPa	G GPa	E GPa
◆ $Co_{33.0}Ta_{3.5}B_{63.5}$	0.98	0.96	0.94	0.207	263	118	307
★ $Co_{41.7}Fe_{23.5}Y_{3.5}B_{31.3}$	1.02	0.72	0.74	0.163	194	82	215
★ $Co_{45.2}Fe_{23.4}Y_{7.0}B_{24.3}$	0.97	0.61	0.60	0.148	171	71	188
★ $Co_{42.6}Fe_{25.2}Y_{11.3}B_{20.9}$	0.98	0.53	0.53	0.137	152	63	165
▼ $Co_{58.4}Fe_{7.0}B_{34.6}$	1.18	0.69	0.82	0.181	225	92	244
▲ $Cu_{70}Zr_{30}$	0.20	0.38	0.07	0.104	112	36	98
● $Co_{65}Zr_{35}$	0.76	0.45	0.34	0.113	138	39	106
■ $Co_{42.0}Fe_{13.2}Zr_{10.7}Ta_{6.6}B_{27.5}$	1.17	0.55	0.64	0.150	208	100	258
▶ $Au_{49.0}Ag_{5.5}Pd_{2.3}Cu_{26.9}Si_{16.3}$	0.16	0.33	0.05	0.096	109	29	81

FIGURE 3 | Comparison of bulk modulus as a function of average bond energy **(A)**, bond density **(B)** and bond energy density **(C)** based on *ab initio* calculations. The table **(D)** summarizes chemical composition, average bond energy, bond density, bond energy density, molar density, bulk, shear and Young's modulus of data points shown in **(A–C)**. B is the bulk modulus, G shear modulus and E Young's modulus.

as damage tolerance, is of importance for structural applications. While the elastic constants can be directly calculated from the *ab initio* configuration, for the fracture toughness new predictor functions have to be developed. Therefore, the origin of fracture toughness in metallic glasses needs to be understood. In metallic glasses, a large bulk to shear modulus ratio (B/G) favors damage tolerance, as a low shear modulus facilitates the formation of multiple shear transformation zones, while a high bulk modulus prevents cavity formation inside the glass (Demetriou et al., 2011; Ritchie, 2011). As B/G is proportional to the Poisson's ratio, a brittle to ductile transition at a Poisson's ratio of 0.31–0.32 was proposed by Lewandowski et al. (2005). This brittle-to-ductile transition has been proven not to be universal for all metallic glass systems (Raghavan et al., 2009; Zhu et al., 2011; He et al., 2012; Schnabel et al., 2016a). Instead, the shear modulus, the homologous temperature T_{room}/T_g (Zhu et al., 2011), and the free volume content (Raghavan et al., 2009) are proposed as design guidelines for tough metallic glasses.

Shear transformation zones and free volume are considered as defects in metallic glasses (Spaepen, 2006) and determine the plasticity of metallic glasses (Sun and Wang, 2015). Hence, the toughness of metallic glasses is sensitive to the composition and topology, such as geometrically unfavored structural motifs (Greer et al., 2013; Xu and Ma, 2014). Temperature rises in shear bands are large for brittle and small for tough metallic glasses (Yang et al., 2016). Local fluctuations in the elastic properties are found for metallic glasses with macroscopic plasticity, while they are lacking for brittle metallic glasses (Wang et al., 2009; Stoica et al., 2010). The influence of free volume content on shear band evolution can be observed in nanoindentation (Li et al., 2007). Wang et al. (2010) report a critical free volume content of 2.4% as the onset of yielding for metallic glasses. However, most investigations on the mechanism of plasticity in metallic glasses focus on the topology, whereas the focus should be on the chemical bonding – being the basis of atomic cohesion and hence mechanical properties.

Thus, based on *ab initio* calculations, the fraction of hybridized bonds has been proposed as a qualitative fingerprint for fracture toughness in metallic glasses (Schnabel et al., 2016a). Comparing the electronic density of states (DOS) of $Cu_{70}Zr_{30}$ and $Pd_{57}Al_{24}Cu_{11}Y_8$ metallic glasses exhibiting fracture toughness of 2.7 and 49.0 MPa.m$^{0.5}$, respectively, a larger band overlap and hence stronger hybridization has been observed between Cu and Zr compared to the major constituents Pd and Al

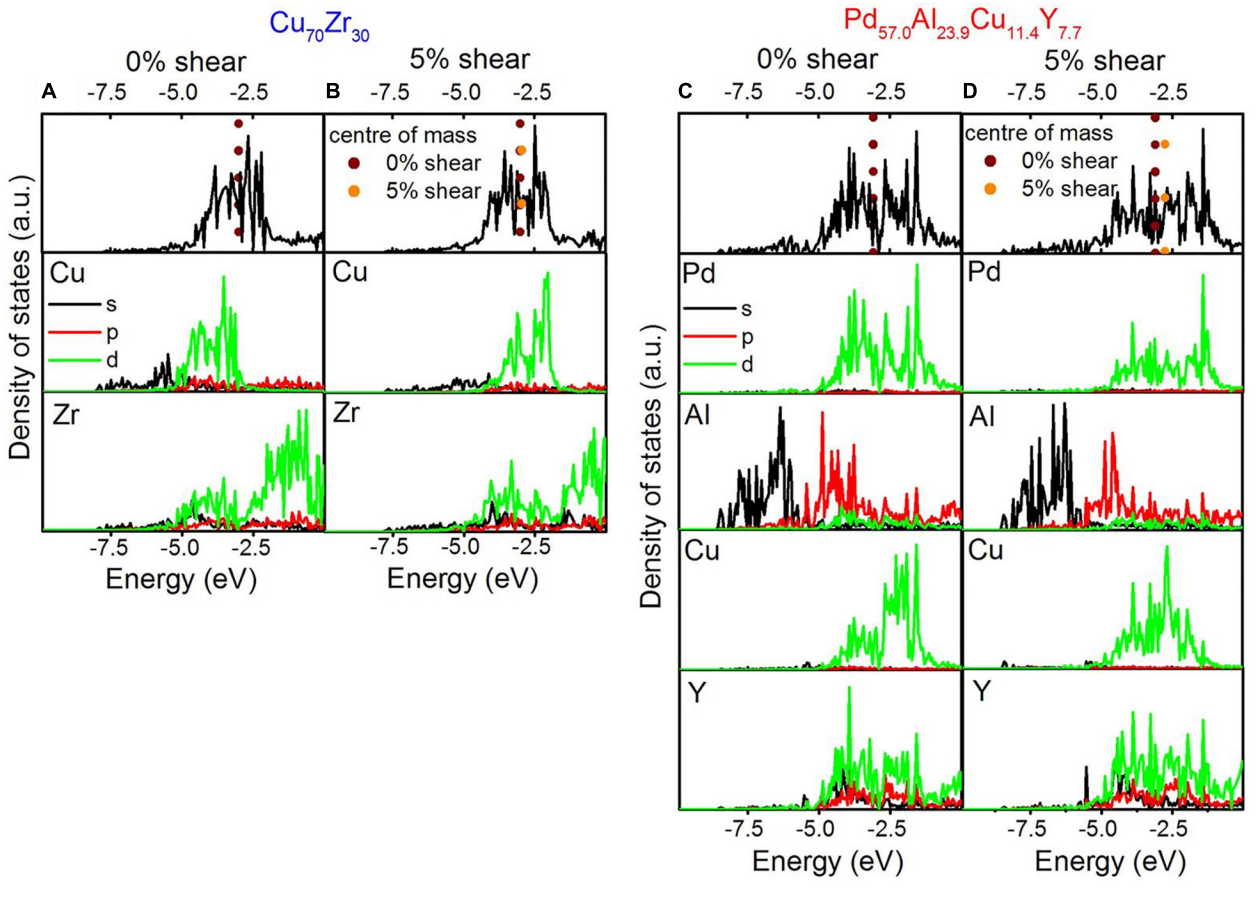

FIGURE 4 | Electronic density of states of $Cu_{70}Zr_{30}$ **(A,B)** and $Pd_{57.0}Al_{23.9}Cu_{11.4}Y_{7.7}$ **(C,D)**. The density of states for the simulation cells without shear is shown in **(A,C)** and with 5% shear in **(B,D)**. The Fermi level is set to 0 eV. Reproduced from Schnabel et al. (2016a) under the Creative Commons CC BY license.

(**Figure 4**). This is consistent with the analysis of bonding states via crystal orbital Hamilton populations (COHP), where the Pd-based glass shows more anti-bonding states than $Cu_{70}Zr_{30}$ and hence weaker bonding (Schnabel et al., 2016a). A lower fraction of hybridized bonds hence promotes shear relaxation and enhances toughness by easing the formation of shear transformation zones (Schnabel et al., 2016a). In a sheared metallic glass, the DOS is shifted toward the Fermi level. Therefore, the bonds become weaker and the glass softer. This is consistent with the effects of micro-alloying that affects the hybridization of the constituents (Sun and Wang, 2015).

Based on the notion that the toughness of metallic glasses is defined by the electronic structure (Schnabel et al., 2016a), we predicted quantitatively that the fracture toughness of metallic glasses is maximized as the fraction metallic bonds is maximized (Evertz et al., 2020). However, as it is not possible to quantify the metallic bonds, focusing on the minimization of hybridized bonds enables the quantitative prediction of fracture toughness. Calculating the bond overlap by means of crystal orbital overlap populations (COOP) (Hoffmann, 1987), the hybridized bonds can be analyzed. In a pure metallically bonded material, all electrons at the Fermi level E_f are delocalized and shared in a free electron gas. Hence, the ideal metallic glass in terms of toughness has a $COOP(E_f) = 0$.

The experimental fracture toughness of metallic glasses scales with $COOP(E_f)$ as shown in (**Figure 5A**) (Evertz et al., 2020). Considering the $COOP(E_f)$ for a metallic glass with unknown fracture toughness such as $Pd_{57.4}Al_{23.5}Y_{7.8}Ni_{11.3}$, which has a low fraction of hybridized bonds based on a qualitative analysis of the density of states (Evertz et al., 2020), the fracture toughness can be predicted based on the fit of the data in **Figure 5A**. This results in a fracture toughness of 95 ± 20 MPa.m$^{0.5}$ for $Pd_{57.4}Al_{23.5}Y_{7.8}Ni_{11.3}$. Thereby, not only the fraction of hybridized bonds is crucial, but also the antibonding bonding character at E_f, as antibonding states increase the total energy of the system and promote bond separation (Smith, 2000; Evertz et al., 2020). Comparing the COOPs of the glasses shown in **Figure 5A** (**Figure 5B**), a bonding to antibonding transition is observed for all metallic glasses between -5 and -3 eV, while the amount of states at E_f differs significantly. However, the difference in the $COOP(E_f)$ depends mainly on the major constituent of the alloy (Evertz et al., 2020). By this, the design guideline based on the Poisson's ratio (Lewandowski et al., 2005) may be understood as a useful indicator of the major constituent of tough metallic glasses, while the quantitative prediction of fracture toughness requires the analysis of the electronic structure.

To appraise critically the predicted fracture toughness of 95 ± 20 MPa.m$^{0.5}$ for $Pd_{57.4}Al_{23.5}Y_{7.8}Ni_{11.3}$ and the new predictor function introduced in Evertz et al. (2020), micro-mechanical beam bending experiments were employed. In these experiments, the $Pd_{57.9}Al_{25.0}Y_{4.9}Ni_{12.2}$ metallic glass cantilever did not break while showing the formation of multiple shear bands that are confined by the stress gradient in the bent cantilever (Evertz et al., 2020). Moreover, since no crack extension has been observed, the fracture toughness exceeds the boundaries of micro-mechanical fracture experiments (Evertz et al., 2020). This is consistent with the high fracture toughness predicted based on the electronic structure (Evertz et al., 2020).

PREDICTION OF THERMAL EXPANSION

The thermal expansion is important for dimensional accuracy and thermal stresses during near net shape processing of metallic glasses (Telford, 2004; Schroers, 2010). The thermal expansion of metallic glasses is similar to that of crystalline metals such as steel (Telford, 2004). Due to the lack of a first-order phase transition, the volume shrinkage is already reduced to a minimum compared with crystalline materials (Schroers, 2010) but the maximum thermal expansion before T_g is only 25% of the expansion of metals before melting. Thermal expansion is related to the glass transition, as the product of thermal expansion coefficient and T_g is constant (Kato et al., 2008) and can hence be employed to predict the glass forming ability (Li et al., 2009). Experimentally, the thermal expansion of metallic glasses can be measured by high energy X-ray scattering as it is connected to the shift of the principal peak in the structure factor during heating (Mattern et al., 2003, 2004, 2012; Hajlaoui et al., 2004; Yavari et al., 2005; Louzguine-Luzgin et al., 2006; Louzguine-Luzgin and Inoue, 2007; Bednarcik et al., 2011) or by dilatometry (Nishiyama et al., 2000; Gonchukova and Drugov, 2003; Jing, 2003; Jing et al., 2007; Kato et al., 2008; Li et al., 2009).

The coefficient of thermal expansion had been predicted by the volume change of an *ab initio* configuration as a function of the temperature (Hunca et al., 2016), which is rather expensive in terms of computational resources. Theoretically, the thermal expansion coefficient of metallic glasses can be predicted by the Debye-Grüneisen model. For $Pd_{57.4}Al_{23.5}Y_{7.8}Ni_{11.3}$ the thermal expansion coefficient has been predicted to be $3.4 \cdot 10^{-5}$ K^{-1} at room temperature, which is in agreement with the experimental value $3.5 \cdot 10^{-5}$ K^{-1} obtained by high energy X-ray scattering (**Figure 6**; Evertz et al., 2017). However, the prediction of thermal expansion for higher temperatures is only possible as long as no structural changes appear. The deviation between predicted and measured thermal expansion coefficient does indicate structural relaxation or rejuvenation in the physical sample (Evertz et al., 2017). The time scales of the relaxation and rejuvenation processes are too large to cover with *ab initio* calculations and computational resources which are available today. However, after complete relaxation, the thermal expansion is reversible (Bednarcik et al., 2011) and could hence be covered by *ab initio* calculations.

The nature of the thermal expansion for metallic glasses is not associated with an increase of interatomic distances but rather with an increase in free volume content between the short-range ordered clusters (Bar'yakhtar et al., 1989; Qu et al., 2011). This is because the principle peak of the structure factor describes medium to long-range order, as can be observed by comparing pair distribution functions calculated from the principal peak of the structure factor and from the complete structure factor (Bednarcik et al., 2011). However, more recent studies report that the thermal expansion is not equal to changes in free volume,

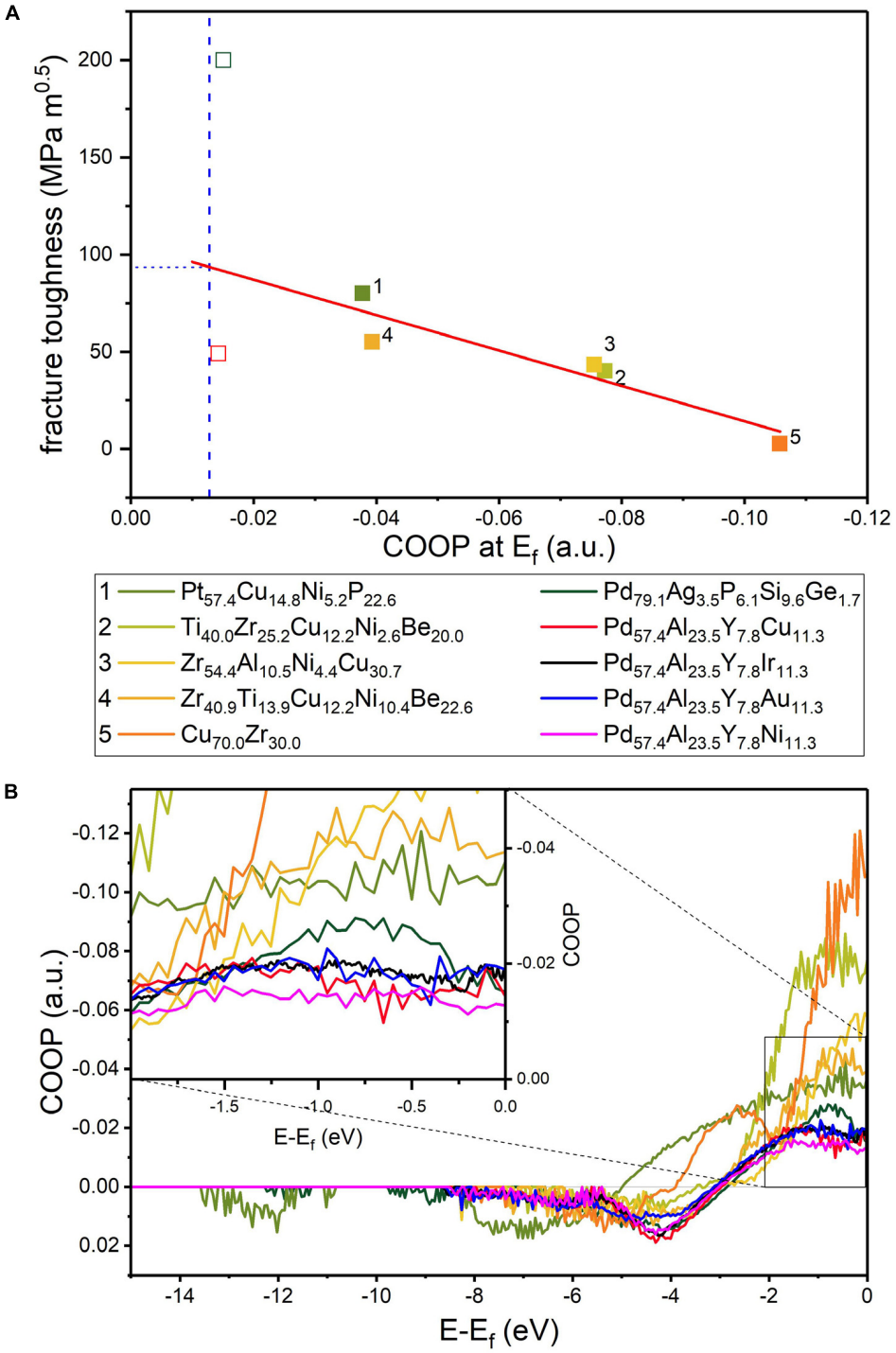

FIGURE 5 | (A) Fracture toughness as a function of COOP at the Fermi level. Open symbols are not included in the fit as they may be sample size dependent (Evertz et al., 2020). The vertical dashed blue line indicates the COOP of $Pd_{57.4}Al_{23.5}Y_{7.8}Ni_{11.3}$ **(B)** COOP of the glasses shown in **(A)**. Reproduced from Evertz et al. (2020) under the Creative Commons CC BY license.

as free volume is annihilated during annealing (structural relaxation) by atomic rearrangements in the glass (Chen, 1978; Nishiyama et al., 2000; Jing, 2003; Hajlaoui et al., 2004; Meng et al., 2006). Especially above T_g atomic rearrangements are no longer negligible, hence the volume change in the supercooled and liquid states cannot be attributed to pure thermal expansion (Mattern et al., 2003, 2012; Georgarakis et al., 2011). The change of thermal expansion, thereby, can serve as an indicator of the

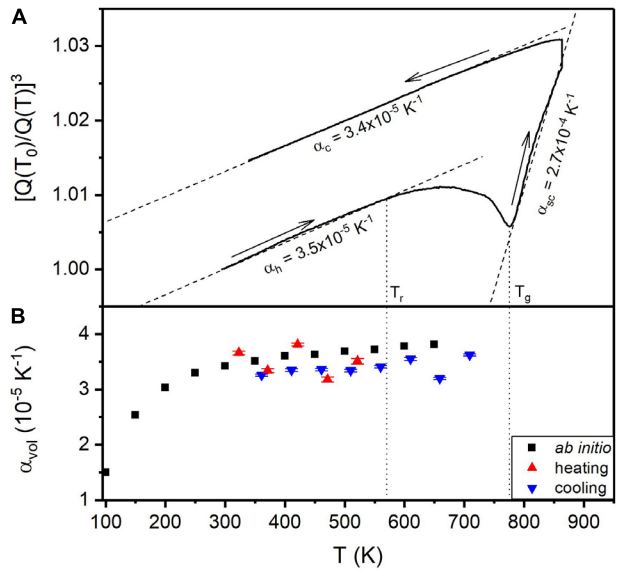

FIGURE 6 | Shift of the principal peak of the structure factor of $Pd_{62.1}Al_{27.3}Y_{4.2}Ni_{6.4}$ **(A)**, an indicator of volume expansion. **(B)** Coefficient of thermal expansion calculated *ab initio* by the Debye-Grüneisen model (black) in comparison with experimental values (red and blue). Reproduced from Evertz et al. (2017) under the Creative Commons CC BY license.

fragility of the glass (Bendert et al., 2013). This can be understood in terms of an energy landscape, where at low temperature the glassy state is dominated by local energy minima or basins (Debenedetti and Stillinger, 2001). At high temperatures, the glass can sample the whole potential energy landscape due to enhanced atomic mobility. Hence, in the landscape dominated region, thermal vibrations dominate thermal expansion, while in the high temperature range, structural changes are more important (Bendert et al., 2012) and surpass thermal expansion.

DISCUSSION

Based on the literature discussed above, *ab initio* calculations are the state of the art to investigate the structure and topology of metallic glasses in depth. The protocols to create a glassy structure representing real physical glasses are thereby similar while differing in the number of cooling steps, heating rates, and heating-quenching cycles. To evaluate the relevance of the *ab initio* structures, the topology of the simulated samples is compared to the topology of the experimental samples. If the overall topologies are consistent, the structural analysis of the prediction often yields more detail than experimental studies (Qin et al., 2007; Ganesh and Widom, 2008; Hui et al., 2008b; Fang et al., 2009; Fujita et al., 2009; Hui et al., 2009; Hirata et al., 2011; Tian et al., 2011; Kumar et al., 2011; Durandurdu, 2012; Wu et al., 2012; Zhang et al., 2015; Huang et al., 2016; Hunca et al., 2016; Yu et al., 2016). However, the electronic structure of metallic glasses is analyzed in only few studies (Hostert et al., 2011; Kumar et al., 2011; Hunca et al., 2016; Schnabel et al., 2016a, 2017).

High-throughput characterization techniques have been applied for metallic glasses to investigate glass forming ability, thermoplastic formability, composition, topology, and mechanical properties. However, most high-throughput studies are purely experimental, relying on trial and error (Sakurai et al., 2007, 2011; Deng et al., 2007; Aono et al., 2010, 2011; Guo et al., 2011; Wang et al., 2011; Ding et al., 2012, 2014; Gregoire et al., 2012; Tsai and Flores, 2014, 2016; Liu et al., 2016; Bordeenithikasem et al., 2017; Li et al., 2017, 2019; Zhang et al., 2018; Zheng et al., 2019); or empirical, such as machine learning approaches (Ren et al., 2018). In recent years, we combined *ab initio* calculations with high-throughput characterization techniques. Therefore, we propose quantum-mechanically based design guidelines of crucial properties for structural applications of metallic glasses (Schnabel et al., 2016a, 2017; Evertz et al., 2017, 2020). These quantum mechanical design proposals are: a) the fraction of hybridized bonds is the fingerprint for damage tolerance in metallic glasses (Schnabel et al., 2016a); b) the bond energy density is proposed to be the origin of the stiffness of metallic glasses (Schnabel et al., 2017); and c) the Debye-Grüneisen model is suitable to predict thermal expansion (Evertz et al., 2017).

However, *ab initio* calculations still have some drawbacks due to their high computational cost, leading to the analysis of some hundred atoms only, which means that only the short-range order, but not the medium-range order in metallic glasses can be studied. Moreover, *ab initio* produced metallic glasses are exposed to very high cooling rates (Hostert et al., 2011), originating in the small time scales accessible by *ab initio* methods. Hence, the simulation of structural relaxation and rejuvenation in metallic glasses is not achievable with conventional DFT codes and available resources today, which might result in different free volume contents compared to physical samples, affecting the mechanical properties (Li et al., 2007; Wang et al., 2010; Sun and Wang, 2015), especially plastic deformations. No systematic *ab initio* studies on the correlation between free volume and electronic structure are known to the authors so far. Hence, the effects of free volume on the electronic structure remain an open question for future studies.

CONCLUSION

Ab initio calculations have been used to explore composition induced changes of the topology and properties of metallic glasses. In recent years, we correlated theoretical and experimental approaches to propose design guidelines for fracture toughness and stiffness of metallic glasses. These predictions have been validated experimentally by micro-mechanical experiments. One grand future challenge is that the effect of free volume has to be included in the *ab initio* models to enhance the quantum-mechanical design for metallic glasses. Further, the formation of shear bands has not been understood and the role of the electronic structure for the onset of shear bands needs to be investigated.

AUTHOR CONTRIBUTIONS

All authors contributed to the conception of the review, manuscript revision, read, and approved the submitted version. SE wrote the first draft of the manuscript.

FUNDING

Financial support of the German Research Foundation within the SPP 1594 "Topological Engineering of Ultrastrong Glasses" is acknowledged (DE 796/9-2, SCHN 735/22-2, and RA 659/18-2).

REFERENCES

Aitken, Z. H., Jafary-Zadeh, M., Lewandowski, J. J., and Zhang, Y.-W. (2018). Anharmonic model for the elastic constants of bulk metallic glass across the glass transition. *Phys. Rev. B* 97:014101. doi: 10.1103/PhysRevB.97.014101

Aono, Y., Sakurai, J., Ishida, T., Shimokohbe, A., and Hata, S. (2010). High-throughput measurement method for time–temperature-transformation diagram of thin film amorphous alloys. *Appl. Phys. Express* 3:125601. doi: 10.1143/APEX.3.125601

Aono, Y., Sakurai, J., Shimokohbe, A., and Hata, S. (2011). High-throughput characterization method for crystallization temperature of integrated thin film amorphous alloys using thermography. *Jpn. J. Appl. Phys.* 50:55601. doi: 10.1143/JJAP.50.055601

Ashby, M., and Greer, A. L. (2006). Metallic glasses as structural materials. *Scr. Mater.* 54, 321–326. doi: 10.1016/j.scriptamat.2005.09.051

Bar'yakhtar, V. G., Mikhailova, L. E., Il'inskii, A. G., Romanova, A. V., and Khristenko, T. M. (1989). Thermal expansion of liquid metals. *Zh. Eksp. Teor. Fiz.* 95, 1404–1411.

Bednarcik, J., Michalik, S., Sikorski, M., Curfs, C., Wang, X. D., Jiang, J. Z., et al. (2011). Thermal expansion of a La-based bulk metallic glass: insight from in situ high-energy x-ray diffraction. *J. Phys. Condens. Matter* 23:254204. doi: 10.1088/0953-8984/23/25/254204

Bendert, J. C., Blodgett, M. E., Gangopadhyay, A. K., and Kelton, K. F. (2013). Measurements of volume, thermal expansion, and specific heat in Zr 57 Cu 15.4 Ni 12.6 Al 10 Nb 5 and Zr 58.5 Cu 15.6 Ni 12.8 Al 10.3 Nb 2.8 liquids and glasses. *Appl. Phys. Lett.* 102:211913. doi: 10.1063/1.4808030

Bendert, J. C., Gangopadhyay, A. K., Mauro, N. A., and Kelton, K. F. (2012). Volume expansion measurements in metallic liquids and their relation to fragility and glass forming ability: an energy landscape interpretation. *Phys. Rev. Lett.* 109:185901. doi: 10.1103/PhysRevLett.109.185901

Bordeenithikasem, P., Liu, J., Kube, S. A., Li, Y., Ma, T., Scanley, B. E., et al. (2017). Determination of critical cooling rates in metallic glass forming alloy libraries through laser spike annealing. *Sci. Rep.* 7:7155. doi: 10.1038/s41598-017-07719-2

Chen, H., Dong, B., Zhou, S., Li, X., and Qin, J. (2018). Structural, magnetic, and electronic properties of Fe82Si4B10P4 metallic glass. *Sci Rep* 8:1331. doi: 10.1038/s41598-018-23952-9

Chen, H. S. (1978). The influence of structural relaxation on the density and Young's modulus of metallic glasses. *J. Appl. Phys.* 49, 3289–3291. doi: 10.1063/1.325279

Cheng, Y. Q., and Ma, E. (2009). Configurational dependence of elastic modulus of metallic glass. *Phys. Rev. B* 80:611. doi: 10.1103/PhysRevB.80.064104

Cheng, Y. Q., and Ma, E. (2011). Atomic-level structure and structure–property relationship in metallic glasses. *Prog. Mater. Sci.* 56, 379–473. doi: 10.1016/j.pmatsci.2010.12.002

Crespo, D., Bruna, P., Valles, A., and Pineda, E. (2016). Phonon dispersion relation of metallic glasses. *Phys. Rev. B* 94:144205. doi: 10.1103/PhysRevB.94.144205

Davis, L. A., Chou, C.-P., Tanner, L. E., and Ray, R. (1976). Strenghts and stiffnesses of metallic glasses. *Scr. Metallurg.* 10, 937–940. doi: 10.1016/0036-9748(76)90217-9

Davis, L. A., Yeow, Y. T., and Anderson, P. M. (1982). Bulk stiffnesses of metallic glasses. *J. Appl. Phys.* 53, 4834–4837. doi: 10.1063/1.331313

Debenedetti, P. G., and Stillinger, F. H. (2001). Supercooled liquids and the glass transition. *Nature* 410, 259–267. doi: 10.1038/35065704

Demetriou, M. D., Launey, M. E., Garrett, G., Schramm, J. P., Hofmann, D. C., Johnson, W. L., et al. (2011). A damage-tolerant glass. *Nat. Mater.* 10, 123–128. doi: 10.1038/NMAT2930

Deng, Y. P., Guan, Y. F., Fowlkes, J. D., Wen, S. Q., Liu, F. X., Pharr, G. M., et al. (2007). A combinatorial thin film sputtering approach for synthesizing and characterizing ternary ZrCuAl metallic glasses. *Intermetallics* 15, 1208–1216. doi: 10.1016/j.intermet.2007.02.011

Ding, S., Gregoire, J., Vlassak, J. J., and Schroers, J. (2012). Solidification of Au-Cu-Si alloys investigated by a combinatorial approach. *J. Appl. Phys.* 111:114901. doi: 10.1063/1.4722996

Ding, S., Liu, Y., Li, Y., Liu, Z., Sohn, S., Walker, F. J., et al. (2014). Combinatorial development of bulk metallic glasses. *Nat. Mater.* 13, 494–500. doi: 10.1038/nmat3939

Dronskowski, R., and Bloechl, P. E. (1993). Crystal orbital hamilton populations (COHP): energy-resolved visualization of chemical bonding in solids based on density-functional calculations. *J. Phys. Chem.* 97, 8617–8624. doi: 10.1021/j100135a014

Durandurdu, M. (2012). Ab initio modeling of metallic Pd80Si20 glass. *Comp. Mater. Sci.* 65, 44–47. doi: 10.1016/j.commatsci.2012.06.040

Evertz, S., Kirchlechner, I., Soler, R., Kirchlechner, C., Kontis, P., Bednarcik, J., et al. (2020). Electronic structure based design of thin film metallic glasses with superior fracture toughness. *Mater. Des.* 186:108327. doi: 10.1016/j.matdes.2019.108327

Evertz, S., Music, D., Schnabel, V., Bednarcik, J., and Schneider, J. M. (2017). Thermal expansion of Pd-based metallic glasses by ab initio methods and high energy X-ray diffraction. *Sci. Rep.* 7:15744. doi: 10.1038/s41598-017-16117-7

Fang, H. Z., Hui, X., Chen, G. L., and Liu, Z. K. (2009). Al-centered icosahedral ordering in Cu46Zr46Al8 bulk metallic glass. *Appl. Phys. Lett.* 94:91904. doi: 10.1063/1.3086885

Fujita, T., Konno, K., Zhang, W., Kumar, V., Matsuura, M., Inoue, A., et al. (2009). Atomic-scale heterogeneity of a multicomponent bulk metallic glass with excellent glass forming ability. *Phys. Rev. Lett.* 103:75502. doi: 10.1103/PhysRevLett.103.075502

Galván-Colín, J., Valladares, A. A., Valladares, R. M., and Valladares, A. (2015). Short-range order in ab initio computer generated amorphous and liquid Cu–Zr alloys: a new approach. *Phys. B Condens. Matter* 475, 140–147. doi: 10.1016/j.physb.2015.07.027

Ganesh, P., and Widom, M. (2008). Ab initio simulations of geometrical frustration in supercooled liquid Fe and Fe-based metallic glass. *Phys. Rev. B* 77:467. doi: 10.1103/PhysRevB.77.014205

Georgarakis, K., Louzguine-Luzgin, D. V., Antonowicz, J., Vaughan, G., Yavari, A. R., Egami, T., et al. (2011). Variations in atomic structural features of a supercooled Pd–Ni–Cu–P glass forming liquid during in situ vitrification. *Acta Mater.* 59, 708–716. doi: 10.1016/j.actamat.2010.10.009

Gilman, J. J. (1975). Mechanical behavior of metallic glasses. *J. Appl. Phys.* 46, 1625–1633. doi: 10.1063/1.321764

Gilman, J. J. (2008). *Electronic Basis of the Strength of Materials*. Cambridge: Cambridge University Press.

Gonchukova, N. O., and Drugov, A. N. (2003). Thermal expansion of amorphous alloys. *Glass Phys. Chem.* 29, 184–187. doi: 10.1023/A:1023463210498

Greer, A. L. (1993). Confusion by design. *Nature* 366, 303–304. doi: 10.1038/366303a0

Greer, A. L. (2009). Metallic glasses on the threshold. *Mater. Today* 12, 14–22. doi: 10.1016/s1369-7021(09)70037-9

Greer, A. L., Cheng, Y. Q., and Ma, E. (2013). Shear bands in metallic glasses. *Mater. Sci. Eng. R* 74, 71–132. doi: 10.1016/j.mser.2013.04.001

Gregoire, J. M., McCluskey, P. J., Dale, D., Ding, S., Schroers, J., and Vlassak, J. J. (2012). Combining combinatorial nanocalorimetry and X-ray diffraction techniques to study the effects of composition and quench rate on Au–Cu–Si metallic glasses. *Scr. Mater.* 66, 178–181. doi: 10.1016/j.scriptamat.2011.10.034

Guo, Q., Zhang, L., Zeiger, A. S., Li, Y., van Vliet, K. J., and Thompson, C. V. (2011). Compositional dependence of Young's moduli for amorphous Cu–Zr films measured using combinatorial deposition on microscale cantilever arrays. *Scr. Mater.* 64, 41–44. doi: 10.1016/j.scriptamat.2010.08.061

Hajlaoui, K., Benameur, T., Vaughan, G., and Yavari, A. R. (2004). Thermal expansion and indentation-induced free volume in Zr-based metallic glasses measured by real-time diffraction using synchrotron radiation. *Scr. Mater.* 51, 843–848. doi: 10.1016/j.scriptamat.2004.07.008

He, Q., Shang, J. K., Ma, E., and Xu, J. (2012). Crack-resistance curve of a Zr–Ti–Cu–Al bulk metallic glass with extraordinary fracture toughness. *Acta Mater.* 60, 4940–4949. doi: 10.1016/j.actamat.2012.05.028

Hirata, A., Guan, P., Fujita, T., Hirotsu, Y., Inoue, A., Yavari, A. R., et al. (2011). Direct observation of local atomic order in a metallic glass. *Nat. Mater.* 10, 28–33. doi: 10.1038/NMAT2897

Hoffmann, R. (1987). How chemistry and physics meet in the solid state. *Angew. Chem. Int. Ed. Engl.* 26, 846–878. doi: 10.1002/anie.198708461

Holmström, E., Bock, N., Peery, T., Chisolm, E., Lizárraga, R., de Lorenzi-Venneri, G., et al. (2010). Structure discovery for metallic glasses using stochastic quenching. *Phys. Rev. B* 82:024203. doi: 10.1103/PhysRevB.82.024203

Hostert, C., Music, D., Bednarcik, J., Keckes, J., Kapaklis, V., Hjorvarsson, B., et al. (2011). Ab initio molecular dynamics model for density, elastic properties and short range order of Co-Fe-Ta-B metallic glass thin films. *J. Phys. Condens. Matter* 23:475401. doi: 10.1088/0953-8984/23/47/475401

Hostert, C., Music, D., Bednarcik, J., Keckes, J., and Schneider, J. M. (2012). Quantum mechanically guided design of Co43Fe20Ta(5.5)X(31.5) (X=B, Si, P, S) metallic glasses. *J. Phys. Condens. Matter* 24:175402. doi: 10.1088/0953-8984/24/17/175402

Huang, Y., Huang, L., Wang, C. Z., Kramer, M. J., and Ho, K. M. (2016). Ab initio molecular dynamics simulations of short-range order in $Zr_{50}Cu_{45}Al_5$ and $Cu_{50}Zr_{45}Al_5$ metallic glasses. *J. Phys. Condens. Matter* 28:85102. doi: 10.1088/0953-8984/28/8/085102

Hui, X., Fang, H. Z., Chen, G. L., Shang, S. L., Wang, Y., and Liu, Z. K. (2008a). Icosahedral ordering in Zr41Ti14Cu12.5Ni10Be22.5 bulk metallic glass. *Appl. Phys. Lett.* 92:201913. doi: 10.1063/1.2931702

Hui, X., Fang, H. Z., Chen, G. L., Shang, S. L., Wang, Y., Qin, J. Y., et al. (2009). Atomic structure of Zr41.2Ti13.8Cu12.5Ni10Be22.5 bulk metallic glass alloy. *Acta Mater.* 57, 376–391. doi: 10.1016/j.actamat.2008.09.022

Hui, X., Gao, R., Chen, G. L., Shang, S. L., Wang, Y., and Liu, Z. K. (2008b). Short-to-medium-range order in Mg65Cu25Y10 metallic glass. *Phys. Lett. A* 372, 3078–3084. doi: 10.1016/j.physleta.2008.01.031

Hunca, B., Dharmawardhana, C., Sakidja, R., and Ching, W.-Y. (2016). Ab initio calculations of thermomechanical properties and electronic structure of vitreloy Zr41.2Ti13.8Cu12.5Ni10Be22.5. *Phys. Rev. B* 94:144207. doi: 10.1103/PhysRevB.94.144207

Inoue, A. (2000). Stabilization of metallic supercooled liquid and bulk amorphous alloys. *Acta Mater.* 48, 279–306. doi: 10.1016/S1359-6454(99)00300-6

Inoue, A., Shen, B. L., Koshiba, H., Kato, H., and Yavari, A. R. (2004). Ultra-high strength above 5000 MPa and soft magnetic properties of Co? Fe?Ta?B bulk glassy alloys. *Acta Mater.* 52, 1631–1637. doi: 10.1016/j.actamat.2003.12.008

Jakse, N., and Pasturel, A. (2008). Local order and dynamic properties of liquid and undercooled CuxZr1-x alloys by ab initio molecular dynamics. *Phys. Rev. B* 78:425. doi: 10.1103/PhysRevB.78.214204

Jing, G., Xiufang, B., Tao, L., Yan, Z., Li, T., Bo, Z., et al. (2007). Formation and interesting thermal expansion behavior of novel Sm-based bulk metallic glasses. *Intermetallics* 15, 929–933. doi: 10.1016/j.intermet.2006.11.003

Jing, Q. (2003). Thermal expansion behavior and structure relaxation of ZrTiCuNiBe bulk amorphous alloy. *Scr. Mater.* 49, 111–115. doi: 10.1016/S1359-6462(03)00240-9

Jóvári, P., Saksl, K., Pryds, N., Lebech, B., Bailey, N. P., Mellergård, A., et al. (2007). Atomic structure of glassy Mg60Cu30Y10 investigated with EXAFS, x-ray and neutron diffraction, and reverse Monte Carlo simulations. *Phys. Rev. B* 76:42. doi: 10.1103/PhysRevB.76.054208

Kato, H., Chen, H.-S., and Inoue, A. (2008). Relationship between thermal expansion coefficient and glass transition temperature in metallic glasses. *Scr. Mater.* 58, 1106–1109. doi: 10.1016/j.scriptamat.2008.02.006

Klement, W., Willens, R. H., and Duwez, P. O. L. (1960). Non-crystalline structure in solidified Gold–Silicon alloys. *Nature* 187, 869–870. doi: 10.1038/187869b0

Kumar, G., Desai, A., and Schroers, J. (2011). Bulk metallic glass: the smaller the better. *Adv. Mater.* 23, 461–476. doi: 10.1002/adma.201002148

Kumar, V., Fujita, T., Konno, K., Matsuura, M., Chen, M. W., Inoue, A., et al. (2011). Atomic and electronic structure of Pd 40 Ni 40 P 20 bulk metallic glass from ab initio simulations. *Phys. Rev. B* 84:134204. doi: 10.1103/PhysRevB.84.134204

Lambson, E. F., Lambson, W. A., Macdonald, J. E., Gibbs, M. R., Saunders, G. A., and Turnbull, D. (1986). Elastic behavior and vibrational anharmonicity of a bulk Pd40Ni40P20 metallic glass. *Phys. Rev. B* 33, 2380–2385. doi: 10.1103/physrevb.33.2380

Lewandowski, J. J., Wang, W. H., and Greer, A. L. (2005). Intrinsic plasticity or brittleness of metallic glasses. *Phil. Mag. Lett.* 85, 77–87. doi: 10.1080/09500830500080474

Li, G. H., Wang, W. M., Bian, X. F., Zhang, J. T., Li, R., and Qin, J. Y. (2009). Correlation between thermal expansion coefficient and glass formability in amorphous alloys. *Mater. Chem. Phys.* 116, 72–75. doi: 10.1016/j.matchemphys.2009.02.041

Li, J., Gittleson, F. S., Liu, Y., Liu, J., Loye, A. M., McMillon-Brown, L., et al. (2017). Exploring a wider range of Mg-Ca-Zn metallic glass as biocompatible alloys using combinatorial sputtering. *Chem. Commun. (Cambridge, England)* 53, 8288–8291. doi: 10.1039/c7cc02733h

Li, M.-X., Zhao, S.-F., Lu, Z., Hirata, A., Wen, P., Bai, H.-Y., et al. (2019). High-temperature bulk metallic glasses developed by combinatorial methods. *Nature* 569, 99–103. doi: 10.1038/s41586-019-1145-z

Li, N., Liu, L., Chen, Q., Pan, J., and Chan, K. C. (2007). The effect of free volume on the deformation behaviour of a Zr-based metallic glass under nanoindentation. *J. Phys. D Appl. Phys.* 40, 6055–6059. doi: 10.1088/0022-3727/40/19/043

Li, Y., Guo, Q., Kalb, J. A., and Thompson, C. V. (2008). Matching glass-forming ability with the density of the amorphous phase. *Science (New York, N.Y.)* 322, 1816–1819. doi: 10.1126/science.1163062

Li, Y., Zhao, S., Liu, Y., Gong, P., and Schroers, J. (2017). How many bulk metallic glasses are there? *ACS Combinat. Sci.* 19, 687–693. doi: 10.1021/acscombsci.7b00048

Liu, Y., Padmanabhan, J., Cheung, B., Liu, J., Chen, Z., Scanley, B. E., et al. (2016). Combinatorial development of antibacterial Zr-Cu-Al-Ag thin film metallic glasses. *Sci. Rep.* 6:26950. doi: 10.1038/srep26950

Louzguine-Luzgin, D. V., and Inoue, A. (2007). Thermal expansion of an amorphous alloy. Reciprocal-space versus real-space distribution functions. *Physica B Condens. Matter* 388, 290–293. doi: 10.1016/j.physb.2006.06.143

Louzguine-Luzgin, D. V., Inoue, A., Yavari, A. R., and Vaughan, G. (2006). Thermal expansion of a glassy alloy studied using a real-space pair distribution function. *Appl. Phys. Lett.* 88:121926. doi: 10.1063/1.2187955

Mattern, N., Hermann, H., Roth, S., Sakowski, J., Macht, M.-P., Jovari, P., et al. (2003). Structural behavior of Pd40Cu30Ni10P20 bulk metallic glass below and above the glass transition. *Appl. Phys. Lett.* 82, 2589–2591. doi: 10.1063/1.1567457

Mattern, N., Jóvári, P., Kaban, I., Gruner, S., Elsner, A., Kokotin, V., et al. (2009). Short-range order of Cu–Zr metallic glasses. *J. Alloys Compd.* 485, 163–169. doi: 10.1016/j.jallcom.2009.05.111

Mattern, N., Kühn, U., Hermann, H., Roth, S., Vinzelberg, H., and Eckert, J. (2004). Thermal behavior and glass transition of Zr-based bulk metallic glasses. *Mater. Sci. Eng.* 375–377, 351–354. doi: 10.1016/j.msea.2003.10.125

Mattern, N., Stoica, M., Vaughan, G., and Eckert, J. (2012). Thermal behaviour of Pd40Cu30Ni10P20 bulk metallic glass. *Acta Mater.* 60, 517–524. doi: 10.1016/j.actamat.2011.10.032

McGreevy, R. L. (2001). Reverse monte carlo modelling. *J. Phys. Condens. Matter* 13, R877–R913. doi: 10.1088/0953-8984/13/46/201

Meng, Q. G., Zhang, S. G., Li, J. G., and Bian, X. F. (2006). Dilatometric measurements and glass-forming ability in Pr-based bulk metallic glasses. *Scr. Mater.* 55, 517–520. doi: 10.1016/j.scriptamat.2006.05.036

Nishiyama, N., Horino, M., and Inoue, A. (2000). Thermal expansion and specific volume of Pd40Cu30Ni10P20 alloy in various states. *Mater. Trans. JIM* 41, 1432–1434. doi: 10.2320/matertrans1989.41.1432

Pang, J. J., Tan, M. J., and Liew, K. M. (2013). On valence electron density, energy dissipation and plasticity of bulk metallic glasses. *J. Alloys Compd.* 577, S56–S65. doi: 10.1016/j.jallcom.2012.03.036

Qin, J., Gu, T., Yang, L., and Bian, X. (2007). Study on the structural relationship between the liquid and amorphous Fe78Si9B13 alloys by ab initio molecular dynamics simulation. *Appl. Phys. Lett.* 90:201909. doi: 10.1063/1.2737937

Qu, D., Liss, K.-D., Yan, K., Reid, M., Almer, J. D., Wang, Y., et al. (2011). On the atomic anisotropy of thermal expansion in bulk metallic glass. *Adv. Eng. Mater.* 13, 861–864. doi: 10.1002/adem.201000349

Raghavan, R., Murali, P., and Ramamurty, U. (2009). On factors influencing the ductile-to-brittle transition in a bulk metallic glass. *Acta Mater.* 57, 3332–3340. doi: 10.1016/j.actamat.2009.03.047

Ren, F., Ward, L., Williams, T., Laws, K. J., Wolverton, C., Hattrick-Simpers, J., et al. (2018). Accelerated discovery of metallic glasses through iteration of machine learning and high-throughput experiments. *Sci. Adv.* 4:eaaq1566. doi: 10.1126/sciadv.aaq1566

Ritchie, R. O. (2011). The conflicts between strength and toughness. *Nat. Mater.* 10, 817–822. doi: 10.1038/NMAT3115

Sakurai, J., Hata, S., Yamauchi, R., and Shimokohbe, A. (2007). Searching for novel Ru-based thin film metallic glass by combinatorial Arc plasma deposition. *Jpn. J. Appl. Phys.* 46, 1590–1595. doi: 10.1143/jjap.46.1590

Sakurai, J., Kozako, H., Mukai, N., Ohnuma, Y., Takahashi, T., and Hata, S. (2011). Combinatorial search for Ni–Nb–Ti thin film amorphous alloys with high corrosion resistances. *Jpn. J. Appl. Phys.* 50:87201. doi: 10.1143/JJAP.50.087201

Schnabel, V., Evertz, S., Ruess, H., Music, D., and Schneider, J. M. (2015). Stiffness and toughness prediction of Co-Fe-Ta-B metallic glasses, alloyed with Y, Zr, Nb, Mo, Hf, W, C, N and O by ab initio molecular dynamics. *J. Phys. Condens. Matter* 27:105502. doi: 10.1088/0953-8984/27/10/105502

Schnabel, V., Jaya, B. N., Kohler, M., Music, D., Kirchlechner, C., Dehm, G., et al. (2016a). Electronic hybridisation implications for the damage-tolerance of thin film metallic glasses. *Sci. Rep.* 6:36556. doi: 10.1038/srep36556

Schnabel, V., Köhler, M., Evertz, S., Gamcova, J., Bednarcik, J., Music, D., et al. (2016b). Revealing the relationships between chemistry, topology and stiffness of ultrastrong Co-based metallic glass thin films: a combinatorial approach. *Acta Mater.* 107, 213–219. doi: 10.1016/j.actamat.2016.01.060

Schnabel, V., Köhler, M., Music, D., Bednarcik, J., Clegg, W. J., Raabe, D., et al. (2017). Ultra-stiff metallic glasses through bond energy density design. *J. Phys. Condens. Matter* 29:265502. doi: 10.1088/1361-648X/aa72cb

Schroers, J. (2010). Processing of bulk metallic glass. *Adv. Mater.* 22, 1566–1597. doi: 10.1002/adma.200902776

Senkov, O. N., Miracle, D. B., Barney, E. R., Hannon, A. C., Cheng, Y. Q., and Ma, E. (2010). Local atomic structure of Ca-Mg-Zn metallic glasses. *Phys. Rev. B* 82:193. doi: 10.1103/PhysRevB.82.104206

Smith, D. W. (2000). The antibonding effect. *J. Chem. Educ.* 77:780. doi: 10.1021/ed077p780

Spaepen, F. (2006). Homogeneous flow of metallic glasses: a free volume perspective. *Scr. Mater.* 54, 363–367. doi: 10.1016/j.scriptamat.2005.09.046

Stillinger, F. H. (1995). A topographic view of supercooled liquids and glass formation. *Science (New York, N.Y.)* 267, 1935–1939. doi: 10.1126/science.267.5206.1935

Stoica, M., Das, J., Bednarèik, J., Wang, G., Vaughan, G., Wang, W. H., et al. (2010). Mechanical response of metallic glasses: insights from in-situ high energy X-ray diffraction. *JOM* 62, 76–82. doi: 10.1007/s11837-010-0037-3

Sun, B. A., and Wang, W. H. (2015). The fracture of bulk metallic glasses. *Prog. Mater. Sci.* 74, 211–307. doi: 10.1016/j.pmatsci.2015.05.002

Telford, M. (2004). The case for bulk metallic glass. *Mater. Today* 7, 36–43. doi: 10.1016/S1369-7021(04)00124-5

Tian, H., Zhang, C., Wang, L., Zhao, J., Dong, C., Wen, B., et al. (2011). Ab initio molecular dynamics simulation of binary $Cu_{64}Zr_{36}$ bulk metallic glass: validation of the cluster-plus-glue-atom model. *J. Appl. Phys.* 109:123520. doi: 10.1063/1.3599882

Tsai, P., and Flores, K. M. (2014). A combinatorial strategy for metallic glass design via laser deposition. *Intermetallics* 55, 162–166. doi: 10.1016/j.intermet.2014.07.017

Tsai, P., and Flores, K. M. (2016). High-throughput discovery and characterization of multicomponent bulk metallic glass alloys. *Acta Mater.* 120, 426–434. doi: 10.1016/j.actamat.2016.08.068

Wang, J. G., Zhao, D. Q., Pan, M. X., Shek, C. H., and Wang, W. H. (2009). Mechanical heterogeneity and mechanism of plasticity in metallic glasses. *Appl. Phys. Lett.* 94:31904. doi: 10.1063/1.3073985

Wang, J. G., Zhao, D. Q., Pan, M. X., Wang, W. H., Song, S. X., and Nieh, T. G. (2010). Correlation between onset of yielding and free volume in metallic glasses. *Scr. Mater.* 62, 477–480. doi: 10.1016/j.scriptamat.2009.12.015

Wang, Z. T., Zeng, K. Y., and Li, Y. (2011). The correlation between glass formation and hardness of the amorphous phase. *Scr. Mater.* 65, 747–750. doi: 10.1016/j.scriptamat.2011.06.043

Wu, S., Kramer, M. J., Fang, X. W., Wang, S. Y., Wang, C. Z., Ho, K. M., et al. (2012). Icosahedral short-range order in amorphous Cu80Si20 by ab initio molecular dynamics simulation study. *Intermetallics* 30, 122–126. doi: 10.1016/j.intermet.2012.03.018

Xu, J., and Ma, E. (2014). Damage-tolerant Zr–Cu–Al-based bulk metallic glasses with record-breaking fracture toughness. *J. Mater. Res.* 29, 1489–1499. doi: 10.1557/jmr.2014.160

Xu, J., Ramamurty, U., and Ma, E. (2010). The fracture toughness of bulk metallic glasses. *JOM* 62, 10–18. doi: 10.1007/s11837-010-0052-4

Yang, G. N., Shao, Y., and Yao, K. F. (2016). The material-dependence of plasticity in metallic glasses: an origin from shear band thermology. *Mater. Des.* 96, 189–194. doi: 10.1016/j.matdes.2016.02.007

Yavari, A. R., Le Moulec, A., Inoue, A., Nishiyama, N., Lupu, N., Matsubara, E., et al. (2005). Excess free volume in metallic glasses measured by X-ray diffraction. *Acta Mater.* 53, 1611–1619. doi: 10.1016/j.actamat.2004.12.011

Yu, Q., Wang, X. D., Lou, H. B., Cao, Q. P., and Jiang, J. Z. (2016). Atomic packing in Fe-based metallic glasses. *Acta Mater.* 102, 116–124. doi: 10.1016/j.actamat.2015.09.001

Zhang, H., Lee, D., Shen, Y., Miao, Y., Bae, J., Liu, Y., et al. (2018). Combinatorial temperature resistance sensors for the analysis of phase transformations demonstrated for metallic glasses. *Acta Mater.* 156, 486–495. doi: 10.1016/j.actamat.2018.07.012

Zhang, S. G. (2013). Signature of properties in elastic constants of no-metalloid bulk metallic glasses. *Intermetallics* 35, 1–8. doi: 10.1016/j.intermet.2012.11.017

Zhang, X., Li, R., and Zhang, T. (2015). Ab initio molecular dynamics simulation of the surface composition of Co 54 Ta 11 B 35 metallic glasses. *J. Non Cryst. Solids* 425, 199–206. doi: 10.1016/j.jnoncrysol.2015.04.013

Zhao, W., Cheng, J. L., Feng, S. D., Li, G., and Liu, R. P. (2016). Intrinsic correlation between elastic modulus and atomic bond stiffness in metallic glasses. *Mater. Lett.* 175, 227–230. doi: 10.1016/j.matlet.2016.03.037

Zheng, J., Zhang, H., Miao, Y., Chen, S., and Vlassak, J. J. (2019). Temperature-resistance sensor arrays for combinatorial study of phase transitions in shape memory alloys and metallic glasses. *Scr. Mater.* 168, 144–148. doi: 10.1016/j.scriptamat.2019.04.027

Zhu, Z.-d, Jia, P., and Xu, J. (2011). Optimization for toughness in metalloid-free Ni-based bulk metallic glasses. *Scr. Mater.* 64, 785–788. doi: 10.1016/j.scriptamat.2010.12.047

Conflict of Interest: The authors declare that the research was conducted in the absence of any commercial or financial relationships that could be construed as a potential conflict of interest.

frontiers in Materials

ORIGINAL RESEARCH
published: 12 May 2020
doi: 10.3389/fmats.2020.00115

Tailoring the Mechanical Properties of Metaluminous Aluminosilicate Glasses by Phosphate Incorporation

*Thilo Grammes[1], René Limbach[1], Sebastian Bruns[2], Leo van Wüllen[3], Dominique de Ligny[4], Efstratios I. Kamitsos[5], Karsten Durst[2], Lothar Wondraczek[1] and Delia S. Brauer[1]**

[1] Otto Schott Institute of Materials Research, Friedrich Schiller University Jena, Jena, Germany, [2] Physical Metallurgy, Technical University of Darmstadt, Darmstadt, Germany, [3] Institute of Physics, Augsburg University, Augsburg, Germany, [4] Department of Materials Science and Engineering, Institute of Glass and Ceramics, Friedrich Alexander University Erlangen-Nürnberg, Erlangen, Germany, [5] Theoretical and Physical Chemistry Institute, National Hellenic Research Foundation, Athens, Greece

The characterization of aluminosilicate glasses is highly relevant in geosciences and for engineering applications such as reinforcement fibers or touchscreen covers. The incorporation of phosphate as a third network-forming species into these glasses offers unique opportunities for fine-tuning glass properties via changes in glass structure and polymerization. In this work, we studied melt-quenched aluminosilicate glasses within the system SiO_2-Al_2O_3-Na_2O-P_2O_5 with 50–70 mol% SiO_2 and up to 7.5 mol% P_2O_5. All glasses were metaluminous (Al:Na = 1) in order to maximize the degree of polymerization. Increasing the phosphate content at the expense of $NaAlO_2$ led to reduced glass polymerization and density, resulting in a decrease in elastic moduli and hardness and an increase in strain-rate sensitivity. When increasing the silica content by substituting SiO_4 for AlO_4 tetrahedra, network polymerization remained mostly unchanged, as confirmed by nearly constant hardness. Densification upon indentation was analyzed by Raman spectroscopy and finite element analysis. We find that the elastic properties and hardness of metaluminous phospho-aluminosilicate glasses are governed by changes in density and network polymerization. Other mechanical properties underlie more complex changes in glass structure.

Keywords: glass, mechanical properties, density, aluminosilicate, phosphate, elastic properties, hardness, densification

OPEN ACCESS

Edited by:
Ashutosh Goel, Rutgers, The State University of New Jersey, United States

Reviewed by:
Timothy Michael Gross, Corning Inc., United States
Nicholas Stone-Weiss, Rutgers, The State University of New Jersey, United States

***Correspondence:**
Delia S. Brauer
delia.brauer@uni-jena.de

Specialty section:
This article was submitted to Ceramics and Glass, a section of the journal Frontiers in Materials

Received: *10 January 2020*
Accepted: *15 April 2020*
Published: *12 May 2020*

Citation:
Grammes T, Limbach R, Bruns S, van Wüllen L, de Ligny D, Kamitsos EI, Durst K, Wondraczek L and Brauer DS (2020) Tailoring the Mechanical Properties of Metaluminous Aluminosilicate Glasses by Phosphate Incorporation. Front. Mater. 7:115. doi: 10.3389/fmats.2020.00115

INTRODUCTION

The mechanical properties of aluminosilicate glasses have been valued by humans since ancient times, as obsidian, a natural aluminosilicate glass vitrified from lava, found use in the fabrication of tools (Cann and Renfrew, 1964; Ericson et al., 1975; Bellot-Gurlet et al., 2004). In the early days of fracture mechanics, the high intrinsic strength of aluminosilicate glasses was demonstrated (Griffith, 1920), paving the way for their use as reinforcement fibers in composites (Botev et al., 1999; Dibenedetto, 2001; Nkurunziza et al., 2005; Sathishkumar et al., 2014). More recently, damage resistant aluminosilicate glasses have been evolving (Bechgaard et al., 2016; Zeng et al., 2016). Understanding the underlying structural origin of their response to mechanical load provides tools for tailoring glass properties (Wondraczek et al., 2011). As an ultimate objective,

introducing microscopic ductility as a route to dissipate mechanical energy would enable glasses with unprecedented practical strength (Wondraczek, 2019).

Metaluminous aluminosilicate glasses are highly polymerized as aluminum is present in the form of network-forming AlO_4 tetrahedra, charge-balanced by alkali metal cations such as sodium (Al:Na = 1). While the high degree of polymerization already yields favorable mechanical properties, small amounts of additional glass components may allow for fine-tuning.

The use of P_2O_5 as a third network-forming oxide besides SiO_2 and Al_2O_3 is such an option. Phosphate forms tetrahedral structural units similar to those of SiO_4 and AlO_4. However, phosphate tetrahedra are connected to the surrounding network structure by less than four bridging oxygen bonds (Dupree et al., 1988; Kosinski et al., 1988; Gan and Hess, 1992; Toplis and Schaller, 1998) and may thus reduce glass polymerization. On the other hand, a preferential association of phosphate with Al^{3+} and Na^+ (Ryerson and Hess, 1980; Gan and Hess, 1992; Mysen, 1998) may additionally affect glass structure and properties.

Up to now, few studies have been reported on the effects of phosphate on the mechanical properties of aluminosilicate glasses (Lönnroth and Yue, 2009; Zeng et al., 2016; Tarragó et al., 2018a,b). These studies concerned only with an excess of alkaline ions over aluminum rather than highly polymerized metaluminous glasses. Furthermore, while all of these studies investigated glass hardness, none of them reported on the elastic properties.

The aim of this work was therefore to provide a comprehensive mechanical characterization of phosphate-containing metaluminous aluminosilicate glasses and to identify the structural origin of these data. For this purpose, the model glass system of SiO_2-Al_2O_3-Na_2O-P_2O_5 was investigated. Three glass series were compared: one series with increasing P_2O_5 content from 0 to 7.5 mol% and constant 60 mol% SiO_2 and two series with increasing SiO_2 content from 50 to 70 mol% and constant P_2O_5 content of either 0 or 7.5 mol%. The study focused on elastic properties and hardness, complemented by investigations of density, densification upon indentation, strain-rate sensitivity and crack resistance.

TABLE 1 | Nominal and (in brackets) analyzed glass compositions (mol%).

Glass		SiO_2	P_2O_5	Al_2O_3	Na_2O
Series i:	Si60P0[a]	60	-	20	20
		(57.8 ± 2.0)	(-)	(20.8 ± 1.0)	(21.4 ± 1.6)
	Si60P2.5	60	2.5	18.75	18.75
		(59.1 ± 1.2)	(1.6 ± 1.0)	(19.8 ± 1.3)	(19.5 ± 0.4)
	Si60P5	60	5	17.5	17.5
		(59.4 ± 1.7)	(4.1 ± 0.1)	(18.8 ± 1.8)	(17.7 ± 0.9)
	Si60P6.25	60	6.25	16.875	16.875
		(59.2 ± 1.1)	(5.4 ± 0.6)	(18.1 ± 1.4)	(17.2 ± 0.7)
	Si60P7.5	60	7.5	16.25	16.25
		(58.3 ± 1.2)	(6.8 ± 0.7)	(17.1 ± 1.4)	(17.8 ± 0.7)
Series ii:	Si50P0	50	-	25	25
		(48.1 ± 1.7)	(-)	(26.2 ± 1.4)	(25.6 ± 0.7)
	Si60P0	60	-	20	20
		(57.8 ± 2.0)	(-)	(20.8 ± 1.0)	(21.4 ± 1.6)
	Si70P0	70	-	15	15
		(68.2 ± 1.6)	(-)	(15.9 ± 1.2)	(15.9 ± 0.4)
Series iii:	Si50P7.5	50	7.5	21.25	21.25
		(48.7 ± 1.4)	(6.6 ± 0.7)	(22.4 ± 1.6)	(22.3 ± 0.6)
	Si55.5P7.5	55.5	7.5	18.5	18.5
		(54.4 ± 1.2)	(6.6 ± 0.8)	(20.1 ± 1.4)	(19.0 ± 0.6)
	Si60P7.5	60	7.5	16.25	16.25
		(58.3 ± 1.2)	(6.8 ± 0.7)	(17.1 ± 1.4)	(17.8 ± 0.7)
	Si70P7.5	70	7.5	11.25	11.25
		(68.7 ± 0.7)	(6.9 ± 0.8)	(12.2 ± 1.0)	(12.2 ± 0.7)

[a] *In the notation used here the first number indicates the nominal SiO_2 content and the second number the nominal P_2O_5 content in mol%.*

MATERIALS AND METHODS

Glass Synthesis

Three series of metaluminous (Al:Na = 1) aluminosilicate glasses of the system $xSiO_2$-yP_2O_5-0.5(100-x-y)Al_2O_3-0.5(100-x-y)Na_2O were prepared by melt-quenching: (i) x = 60 mol%, y = 0, 2.5, 5, 6.25 and 7.5 mol%, (ii) x = 50, 60 and 70 mol%, y = 0 mol%, (iii) x = 50, 55.5, 60 and 70 mol%, y = 7.5 mol%. **Table 1** provides an overview of nominal and analyzed glass compositions. Raw materials for synthesis were high purity powders of SiO_2 (Carl Roth, Karlsruhe, Germany), $Al(OH)_3$ (Merck, Darmstadt, Germany), Na_2CO_3 (Carl Roth), and $NaPO_3$ (Carl Roth). After thorough mixing, the batches were heated up to 1,650°C at a rate of 5 K/min in alumina crucibles using an electrically heated furnace (HTK 16/17 FL, Thermconcept Dr. Fischer GmbH & Co. KG, Bremen, Germany). The melts were maintained at this temperature for 1 h before transferring the melt inside the crucible to an annealing furnace preheated to temperatures 20 K above the respective glass transition temperature, T_g, to reduce residual stresses. At 1 h at this temperature, the crucibles were slowly cooled down to room temperature by switching off the furnace. Glass monoliths were retrieved by breaking the alumina crucible walls: glasses were not cast from platinum crucibles and quenched because of high melt viscosity. From the monoliths, coplanar glass samples were cut and polished on both sides.

As leaching of alumina from the crucibles could not be excluded, longer melting times were avoided and sections close to the crucible walls were omitted during sample cutting. The protocol described here allowed for comparable synthesis conditions for all glasses except Si50P0. For this glass, owing to its high Na_2O content of 25 mol%, crystallization could only be prevented by reducing the annealing temperature to T_g-40 K. However, tests with various annealing temperatures showed that even such reduced cooling temperature had no significant effect on glass properties (results not shown).

Compositional Analysis

Actual chemical compositions of all glasses were analyzed by energy-dispersive X-ray spectroscopy (EDX). For each glass the composition was calculated as mean value of four EDX measurements. Errors represent standard deviations. Using

different specimens, three of these four measurements were performed with the same scanning electron microscope (Phenom pro X, Phenomworld, Eindhoven, NL). The fourth EDX measurement was performed with a different instrument (Neon 60, Zeiss, Jena, Germany, combined with X-Max X-Ray Detector 80 mm^2, Oxford Instruments, High Wycombe, UK) at a different laboratory.

Density and Related Properties

Glass density, ρ, was determined as the arithmetic mean out of ten measurements on a single specimen, using a helium pycnometer (AccuPyc 1330, Micromeritics GmbH, Mönchengladbach, Germany). Powder samples with a particle size of 125–250 µm were used to minimize the influence of bubbles. The experimental error is ±0.01 g/cm^3. Molar volume, V_m, was calculated from density and molar weight, M_i, of each glass component weighted by its nominal molar fraction, f_i.

$$V_m = \frac{1}{\rho}\sum_i f_i M_i \tag{1}$$

All calculations presented here were based on nominal glass compositions, justified by a good agreement with the analyzed compositions (**Table 1**).

Atomic packing density, C_g, was estimated using the following equation (Makishima and Mackenzie, 1973):

$$C_g = \rho\frac{\sum_i f_i V_i}{\sum_i f_i M_i} \tag{2}$$

Here, $V_i = 4/3\pi N\left(xr_A^3 + yr_B^3\right)$ represents the molar volume occupied by an oxide A_xB_y. N is Avogadro's number and r_A as well as r_B are the ionic radii of the corresponding cations and anions, respectively. Effective ionic radii were employed (Shannon, 1976), considering Si^{4+} (r_{Si} = 26 pm), Al^{3+} (r_{Al} = 39 pm), and P^{5+} (r_P = 17 pm) species in tetrahedral coordination, Na^{2+} (r_{Na} = 102 pm) in octahedral coordination and O^{2-} (r_O = 135 pm) in two-fold coordination. It is noted that the radius of oxygen ions may vary depending on the coordinated cations and may be determined by the cation-oxygen bond lengths (Duffy, 1990; Zeidler et al., 2014). However, in the absence of quantitative data on the amount of bridging and non-bridging oxygen species and the connectivity between different polyhedral species, a constant ionic radius of oxygen was chosen for the sake of simplicity. Consequences of this assumption will be addressed in the discussion.

Oxygen packing density, ρ_{ox}, was calculated as the molar amount of oxygen per unit volume of glass (Ray, 1974; Fredholm et al., 2010).

$$\rho_{ox} = \frac{1}{V_m}\sum_i f_i N_{ox,i} \tag{3}$$

$N_{ox,i}$ is the stoichiometric number of oxygen atoms provided by each glass component, i.e., 2 for SiO_2, 5 for P_2O_5, 3 for Al_2O_3 and 1 for Na_2O. Errors of molar volume, packing density and oxygen packing density were estimated by error propagation calculation.

Ultrasonic Echometry and Brillouin Spectroscopy

The longitudinal and transversal sound velocities, v_L and v_T, were measured by ultrasonic echometry and Brillouin spectroscopy. On that basis, elastic properties were calculated, including shear modulus, G, Young's modulus, E, bulk modulus, K, and Poisson's ratio, ν, under the assumption of isotropic symmetry in the glasses (Rouxel, 2007). Experimental uncertainties were estimated by error propagation.

$$G = \rho v_T^2 \tag{4}$$

$$K = \rho\left(v_L^2 - \frac{4}{3}v_T^2\right) \tag{5}$$

$$E = \rho\left(\frac{3v_L^2 - 4v_T^2}{\left(\frac{v_L}{v_T}\right)^2 - 1}\right) \tag{6}$$

$$\nu = \frac{v_L^2 - 2v_T^2}{2\left(v_L^2 - v_T^2\right)} = \frac{E}{2G} - 1 \tag{7}$$

Ultrasonic echometry was performed on coplanar, optically-polished samples of ∼2 mm thickness using an echometer (Echometer 1077, Karl Deutsch GmbH & Co. KG, Wuppertal, Germany) equipped with piezoelectric transducers operating at frequencies of 8–12 MHz. Values of v_T and v_T were derived from sound propagation times, which were recorded with an accuracy of ±1 ns, and from the exact thickness of the 2 mm thick coplanar, optically-polished specimen, as measured with an accuracy of ±2 µm using a micrometer screw.

Brillouin spectroscopy was performed at room temperature on coplanar, optically-polished samples of 200–300 µm thickness using a custom-built optical setup as described previously (Veber et al., 2018). Brillouin shifts were averaged between the Stokes and anti-Stokes signals to account for instrumental non-zero position of the Rayleigh line. Experiments were performed in backscattering geometry (through a microscope, 50x magnification, 0.42 numerical aperture) as well as platelet geometry (45° incidence angle).

In backscattering geometry, v_L was determined as $v_L = f{\cdot}\lambda/(2n)$ (Rabia et al., 2016), where λ (488 nm) is the wavelength of the continuous wave sapphire laser used, and f is the Brillouin shift of the longitudinal acoustic mode, which was determined with an accuracy of ±0.012 GHz. The glasses' refractive index, n, at 488 nm was deduced by linear interpolation between refractive indices at 480 and 546.1 nm as determined by Pulfrich refractometry (PR2, Carl Zeiss, Jena, Germany) with an experimental uncertainty of ±0.001.

In platelet geometry, v_L and v_T were determined from the Brillouin shifts of the longitudinal and transversal acoustic modes, f_L and f_T, as $v_{L/T} = f_{L/T} \cdot \lambda/(\sqrt{2})$ (Whitfield et al., 1976). Although the platelet geometry delivered both v_L and v_T, the v_L value from backscattering geometry is normally more precise because of sample surfaces not being perfectly coplanar and because of precision on the 45° angle in platelet geometry. The values of v_L from backscattering geometry were therefore

preferred and further used to correct v_T from platelet geometry ($v_{T,corrected} = v_T \times v_{L,backscatter}/v_{L,platelet}$).

Calculation of Elastic Properties

In addition to experimental results, we employed the model of Makishima and Mackenzie (1973) to predict the compositional dependence of Young's modulus. Following this approach, Young's modulus of a glass is determined from the atomic packing density and volume density of bonding energy, $<U_0/V_m>$.

$$E = 2C_g \left\langle \frac{U_0}{V_m} \right\rangle \tag{8}$$

Note that $<U_0/V_m>$ was calculated by means of the actual glass density rather than the density of the individual components in their crystalline state (Limbach et al., 2017). The average bond energy, $U_0 = \sum f_i \Delta H_{ai}$, was calculated from molar dissociation enthalpies, ΔH_{ai}, of the glass components, weighted by their nominal molar fractions, f_i. Values of ΔH_{ai} were determined from molar heats of formation, ΔH_f, of each oxide component A_xB_y in its crystalline state and the constituent atoms in gaseous state (Inaba et al., 1999).

$$\Delta H_{ai} = x\Delta H_f\left(A, gas\right) + y\Delta H_f\left(B, gas\right) - \Delta H_f(A_xB_y, crystal) \tag{9}$$

Values of ΔH_f were taken from Lide (2006), except for $\Delta H_f(P_2O_5) = -306.4$ kJ/mol, which was calculated from the dissociation energy of P_2O_5, $\Delta H_{ai}/V_m = 62.8$ kJ/cm^3, available from literature (Inaba et al., 1999) and using Equations (1) and (9). The error of the calculated modulus was estimated by error propagation.

Indentation

Nanoindentation

Instrumented indentation experiments were carried out using a nanoindenter (Nano Indenter G200, Schaefer Technology GmbH, Langen, Germany) equipped with a three-sided Berkovich diamond tip (Synton-MDP, Port, Switzerland) and operating in continuous stiffness measurement (CSM) mode (applying an oscillation of amplitude $\Delta h = 2$ nm and frequency $f = 45$ Hz). Values of Young's modulus and hardness, H, were determined from indentations with a depth limit, h, of 2 µm created at constant strain-rate, $\dot{\varepsilon}$, of 0.05 s^{-1}, following the method proposed by Oliver and Pharr (1992). For statistical relevance, the values of E and H were averaged over at least 15 individual indentation experiments.

Time-dependent indentation deformation was analyzed in a nanoindentation strain-rate jump test, as described in detail elsewhere (Maier et al., 2011; Limbach et al., 2014). This test initially comprises a first segment, where the Berkovich indenter tip penetrates the glass surface to a depth of 500 nm at a constant strain-rate of 0.05 s^{-1}. Afterwards, with further increasing indenter displacement, the strain-rate is changed in intervals of 250 nm while monitoring the accompanied changes in hardness using the CSM equipment of the nanoindentation setup ($\Delta h =$ 5 nm, $f = 45$ Hz). In this study, a total number of at least eight strain-rate jump tests were evaluated on each sample with strain-rates of 0.05, 0.007, and 0.001 s^{-1} (in descending order). The strain-rate sensitivity, m, was calculated from the slope of the logarithmic plot of the hardness, lnH, over the indentation strain-rate, $\ln \dot{\varepsilon}_i$, where, $\dot{\varepsilon}_i$ is equal to $\dot{\varepsilon}/2$ for materials with a depth-independent hardness value (Maier et al., 2011, 2013; Limbach et al., 2014; Zehnder et al., 2017).

$$m = \frac{\partial lnH}{\partial ln\dot{\varepsilon}_i} \tag{10}$$

Error bars show standard deviations from averaging over all evaluated indentation experiments.

Vickers Hardness

Vickers hardness, H_v, was determined using a Vickers microhardness tester (Duramin-1, Struers GmbH, Willich, Germany). On each sample, 25 indentations with a load, P, of 981 mN were created. Loading duration and dwell time were set to 15 and 10 s, respectively. H_v was calculated from the load in N and the length of the projected indentation diagonals, d, in µm according to $H_v = 1.8544(P/d^2)$ (Tabor, 1970). Error bars show standard deviations.

Crack Resistance

Crack resistance was analyzed by Vickers indentation. Indents with stepwise increasing loads from 981 mN up to 19.6 N were created in air under ambient conditions using a constant loading duration of 15 s and dwell time of 10 s. After unloading, the number of median-radial cracks occurring at the corners (illustrated by inset in **Figure 1**) of the residual Vickers hardness imprints was counted. On each sample, 25 indentations were performed per load applied and the probability of crack initiation, PCI, was calculated from the number of corners with cracks divided by the total number of corners.

The load dependence of PCI is exemplarily shown for glass Si60P7.5 in **Figure 1**. The experimental data follows the typical sigmoidal trend (orange dashed line) as reported previously (Limbach et al., 2015b). The load value of the fitted sigmoidal curve at 50% PCI was taken as crack resistance, CR, i.e. the load at which on average two cracks were formed. A detailed description of the procedure used for assessing the experimental uncertainty of this method is given in the Discussion.

Densification Analysis

Raman Spectroscopy

To characterize glass densification, the low frequency region of Raman spectra was analyzed using the method presented by Deschamps et al. (2011, 2013). After indentation, the low frequency Raman region (blue line in **Figure 2**), including its center of gravity, COG (dash-dotted gray line in **Figure 2**), was shifted (illustrated by arrow in **Figure 2**) toward higher wavenumbers. This COG shift upon indentation was used to quantify densification.

The low frequency envelopes of Raman spectra measured before (black spectrum in **Figure 2**) and after indentation (orange

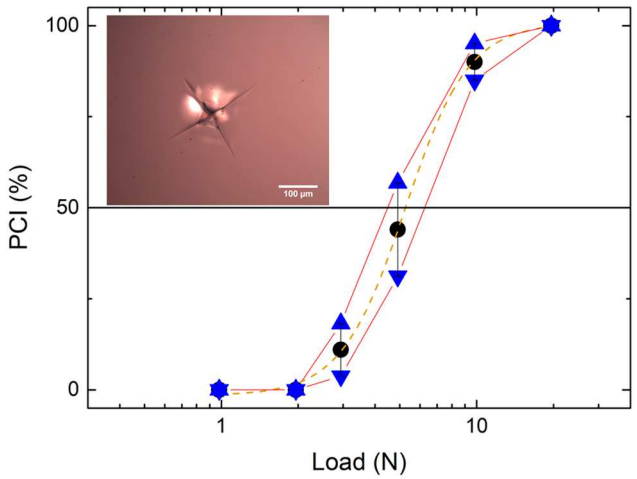

FIGURE 1 | Probability of crack initiation (PCI) as a function of the applied Vickers indentation load for glass Si60P7.5. The inset shows the typical crack pattern observed after Vickers indentation (load 19.6 N). The orange dashed line illustrates the sigmoidal fit used to determine crack resistance (defined as the load at PCI = 50%). Connecting the end points of the PCI error bars creates an approximated error envelope. The intersections of this error envelope with the 50% PCI line were used to estimate the experimental uncertainty in crack resistance.

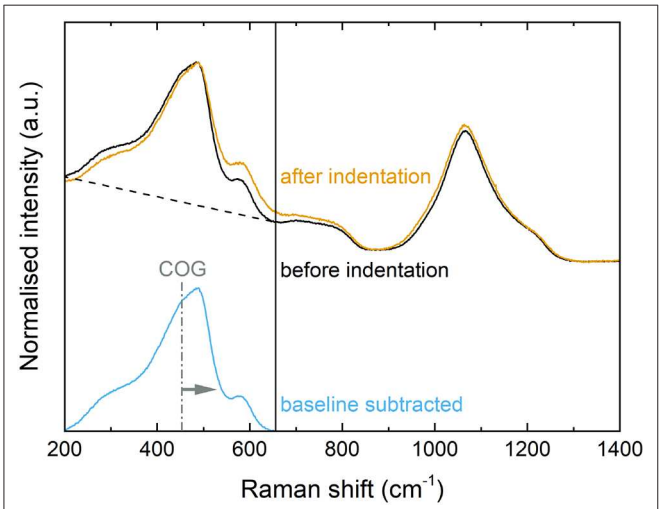

FIGURE 2 | Raman spectra of a glass before (black) and after (orange) densification by Vickers indentation. The blue spectrum shows the low frequency region after subtraction of a baseline (dashed black line) and was used to calculate that region's center of gravity (COG, gray dash-dotted line). The densification shifted intensities in the low frequency region. This was quantified by determining the shift of the COG (arrow, not to scale).

spectrum in **Figure 2**) were integrated to obtain their respective COG using the following equation.

$$\frac{\int_{low}^{COG} I(\omega)\, d\omega}{\int_{low}^{up} I(\omega)\, d\omega} = \frac{1}{2} \tag{11}$$

Here, the COG is the wavenumber which divides the integrated region into two parts of equal area. I(ω) is the Raman intensity and ω the Raman shift in cm^{-1}. The lower and upper integration limits are *low* and *up*, respectively. The limits were chosen at the positions of the intensity minima which confined the low frequency Raman region.

Following the procedure by Deschamps et al. (2011), a linear baseline as illustrated in **Figure 2** was subtracted from the low frequency Raman region prior to COG calculation. Furthermore, the use of this baseline was compared to another post-processing routine involving a linear baseline fitted to the signal-free high frequency end of the Raman spectra to remove luminescence, followed by a data reduction by the Long equation (Long, 1977, 2002).

$$I_{reduced} = I_{measured}\ \omega_0^3 \frac{\omega}{(\omega_0 - \omega)^4}\left[1 - exp\left(\frac{-\hbar\omega}{k_B T}\right)\right] \tag{12}$$

Here, ω_0 is the wavenumber of the excitation laser, $\hbar$ is the reduced Planck constant, k_B the Boltzmann constant and T the absolute temperature. The Long reduction required a change of the lower integration limit because it shifted the corresponding intensity minimum to the lowest measured frequency. This enlarged the integrated range for datasets that underwent the Long reduction. However, the impact of the changed integration limits on the COG calculation was considered low as Raman intensities in the affected wavenumber regime dropped significantly during Long reduction.

Raman spectra were measured in the centers of each of five residual Vickers hardness imprints (load 981 mN) per sample, as well as five reference spectra of the pristine glasses. Obtained COG shifts were averaged, error bars show standard deviations. Raman measurements were carried out using a Raman microscope (invia Raman Microscope, Renishaw, Wotton-under-Edge, UK). Measurements were performed at room temperature using the 488 nm line of an argon ion laser and a microscope objective lens with 50× magnification and a 0.50 numerical aperture. Spectra were measured in the range from 150 to 1,550 cm^{-1}. The acquisition time per spectrum was 225 s, summarized over several scans.

Finite Element Analysis

Finite Element Analysis (FEA) was performed using the software package ABAQUS, similar to earlier studies (Bruns et al., 2017, 2020). The indentation process was modeled in a two-dimensional (2D) axisymmetric way using the Berkovich equivalent cone, which exhibits an opening angle of 70.3°. The indenter/material contact was assumed to be frictionless. All material properties were presumed to represent rate insensitive room temperature values. The series with constant 60 mol% SiO_2 content (Si60Px) was selected as model system, whose corresponding elastic properties (isotropy assumed) can be found in the Results section.

The yield surface of this series was mapped with Drucker-Prager-Cap plasticity according to Bruns et al. (2020). The yield strength under hydrostatic pressure relied on densification hardening curves usually recorded in diamond anvil cell (DAC)

experiments. Since corresponding data are not available for the system studied here, the densification capacity was estimated according to Rouxel's model predictions based on Poisson's ratio (Rouxel et al., 2008). For $\nu = 0.22$ (constant value found for the entire Si60Px series) a densification capacity of 8.6 ± 2.5% can be estimated. The experimental densification hardening curve of fused silica (Rouxel et al., 2008; Sonneville et al., 2012; Deschamps et al., 2013) was then compressed to the saturation level determined earlier (8.6%, **Figure 3A**) and serves as input for cap hardening along hydrostatic axis.

The yield strength under pure shear was fitted based on experimental nanoindentation load-displacement curves using the extrema of the Si60Px series with 0 and 7.5 mol% P_2O_5. Since the densification prediction does not exhibit the sensitivity to account for those chemical variations, only one representative yield surface for this series was constructed (**Figure 3B**).

RESULTS

Compositional Analysis

Deviations from the nominal compositions are listed in **Table 1**. Almost all values measured are similar to the nominal compositions within error limit. It can be noticed however that SiO_2 and P_2O_5 content were systematically lower and Al_2O_3 and Na_2O content higher than nominal composition. The overall good agreement justifies the utilization of the nominal compositions for the theoretical considerations on packing efficiency or bond energy density.

Density and Related Properties

Density (ρ) and atomic packing density (C_g) decreased, while molar volume (V_m) and oxygen packing density (ρ_{ox}) increased for glasses with increasing P_2O_5 content and constant SiO_2 content (**Figures 4A,C,E,G**). For increasing SiO_2 content and constant P_2O_5 content of either 0 or 7.5 mol% density and atomic packing density decreased, and oxygen packing density increased (**Figures 4B,F,H**). For phosphate-free glasses the decrease of packing density was within the error limit at lower silica contents (**Figure 4F**). At 50 mol% SiO_2, the incorporation of P_2O_5 did not notably change packing density. The molar volume only slightly decreased for increasing SiO_2 content and remained almost constant for glasses with 7.5 mol% P_2O_5 (**Figure 4D**).

Elastic Properties

Compositional variations in elastic properties, including shear (G), bulk (K) and Young's moduli (E) as well as Poisson's ratio (ν), as obtained from the different experimental methods are illustrated in **Figures 5–7**. Trends described in the following apply to all methods employed.

For glasses with constant 60 mol% SiO_2 and increasing phosphate content (**Figure 5**), the values of G, K and E decreased while ν remained constant within error limits.

For increasing silica content in phosphate-free glasses (**Figure 6**) as well as glasses with 7.5 mol% P_2O_5 (**Figure 7**), the trends were less clear. G remained roughly constant while K and E decreased with increasing silica content, regardless of the phosphate content. The decrease in E was weak, but K showed a decrease of a similar magnitude as the one observed with increasing phosphate content. Poisson's ratio appeared to decrease with increasing silica content.

Elastic properties obtained by ultrasonic echometry and Brillouin spectroscopy were in good agreement (**Figures 5–7**), reflecting the fact that both methods rely on the propagation of sound waves. The only exception was glass Si60P5 (5 mol% P_2O_5, **Figure 5**), where slightly higher values of G, K and E were probed by Brillouin spectroscopy as compared to ultrasonic echometry.

The trends for E obtained by nanoindentation (green triangles in **Figures 5–7**) agreed well with the trends determined by ultrasonic echometry and Brillouin spectroscopy. Here again, the sample with 5 mol% P_2O_5 was slightly off the trend, indicating an outlier. Values for E obtained by nanoindentation were systematically lower by up to 5 GPa than those obtained by

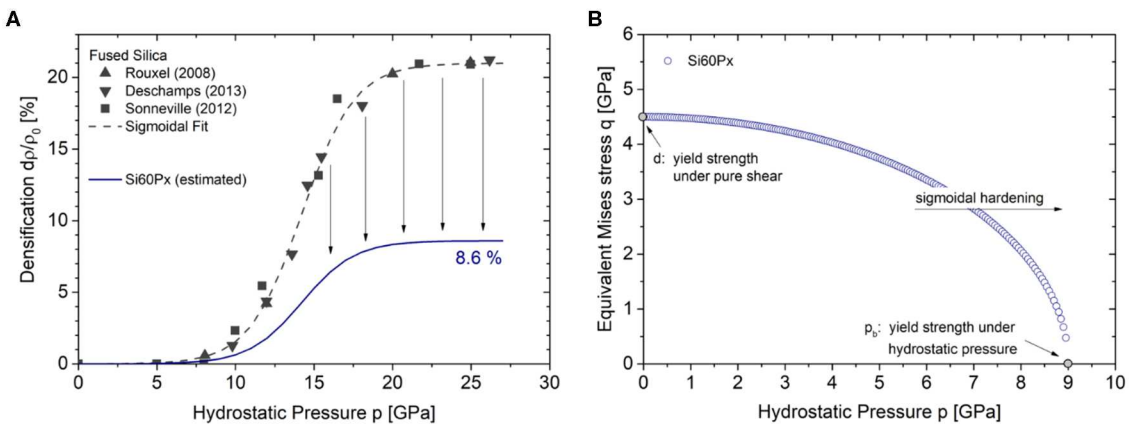

FIGURE 3 | (A) Densification hardening curve for the series with constant 60 mol% SiO_2 (Si60Px, dark blue) based on model predictions and experimental data on fused silica (open symbols). It serves as input for determination of the yield surface. The yield surface, shown in **(B)**, was used for FEA analysis of the Si60Px series (applies to all x values from 0 to 7.5 mol% P_2O_5 because all glasses had similar Poisson's ratio, see text).

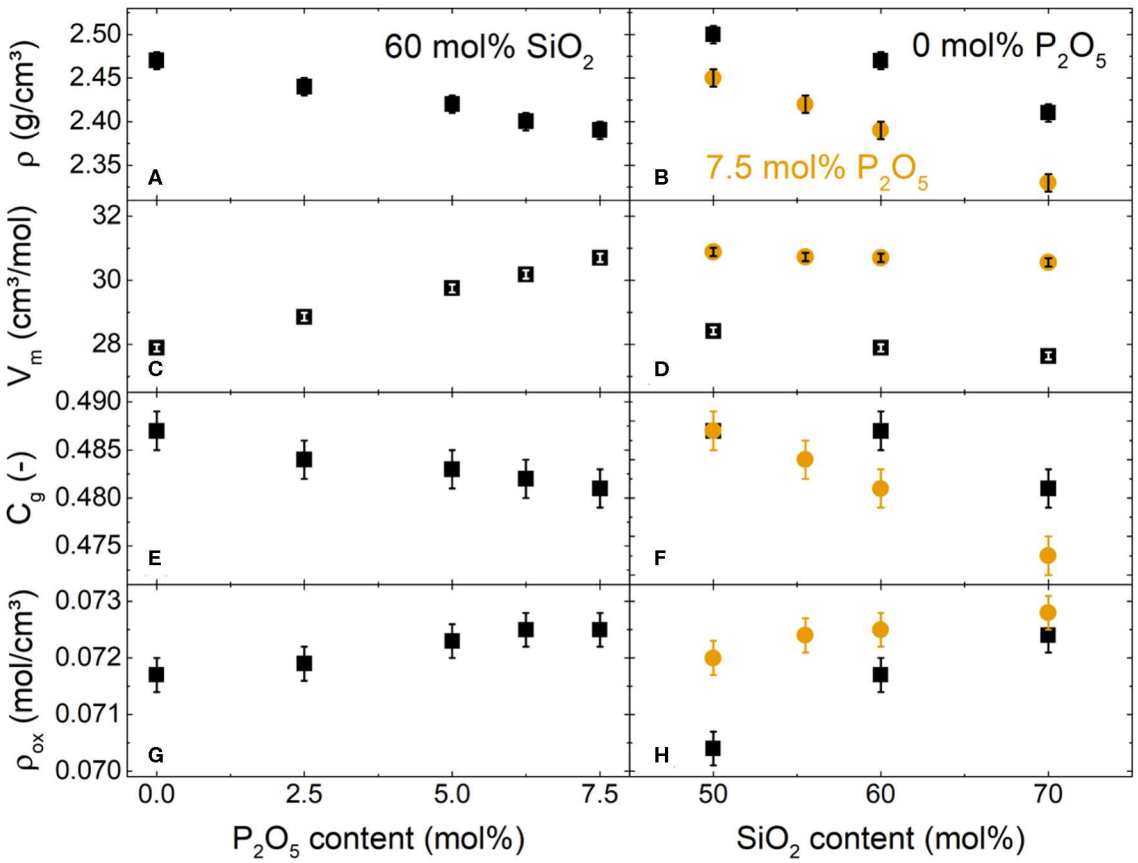

FIGURE 4 | Density **(A,B)**, molar volume **(C,D)**, packing density **(E,F),** and oxygen packing density **(G,H)** of the glasses with **(A,C,E,G)** 60 mol% SiO_2, **(B,D,F,H)** 0 mol% P_2O_5 (black squares) or 7.5 mol% P_2O_5 (orange circles).

the other two methods. This small discrepancy results from differences in testing conditions and may originate from sink-in effects or a piling-up of material at the periphery of the indenter (Limbach et al., 2015a, 2017).

Young's modulus as calculated by the model of Makishima-Mackenzie (E_{M+M}) was relatively close to the values measured by echometry (**Figure 8**); however, the model systematically underestimated the experimentally determined values by about 2–8 GPa.

Hardness

Compositional trends in the hardness as obtained from micro- and nanoindentation agreed well, yielding decreasing hardness values with increasing phosphate content (**Figures 9A,C**). With increasing silica content (**Figures 9B,D**), hardness remained roughly constant for both methods, regardless of the phosphate content. However, Vickers hardness (H_v) showed a slight decrease for increasing silica content in phosphate-free glasses. The hardness values measured by nanoindentation (H) were systematically higher than the corresponding Vickers hardness by ∼1 GPa. This may be attributed to differences between the two methods: Vickers microindentation probes plastic deformation only, while nanoindentation probes the combined elastic-plastic response of a material, yielding higher hardness values for materials with a pronounced elastic contribution to the indentation deformation (Oliver and Pharr, 1992).

Crack Resistance

Crack resistance did not show any trend for increasing phosphate content (**Figure 10A**). Data scattered between values of 4 and 8 N. By contrast, two different trends were found for the glasses with 0 and 7.5 mol% P_2O_5, respectively, when increasing the silica content (**Figure 10B**). The crack resistance of glasses with 0 mol% P_2O_5 slightly increased for increasing silica content. For the glasses with 7.5 mol% P_2O_5, crack resistance decreased markedly from 50 to 55.5 mol% SiO_2 and then remained constant within error limit for further increasing silica content.

Densification From Raman Analysis

Densification upon indentation resulted in a COG shift by 12–24 cm^{-1} of the low frequency Raman region in the considered spectral range of 200–650 cm^{-1} (exemplified in **Figure 2**, black spectrum before indentation, orange spectrum after indentation). For the two post-processing routes used, i.e., Long data reduction and baseline subtraction (filled and open symbols in **Figures 10C,D**), the COG shifts upon indentation showed

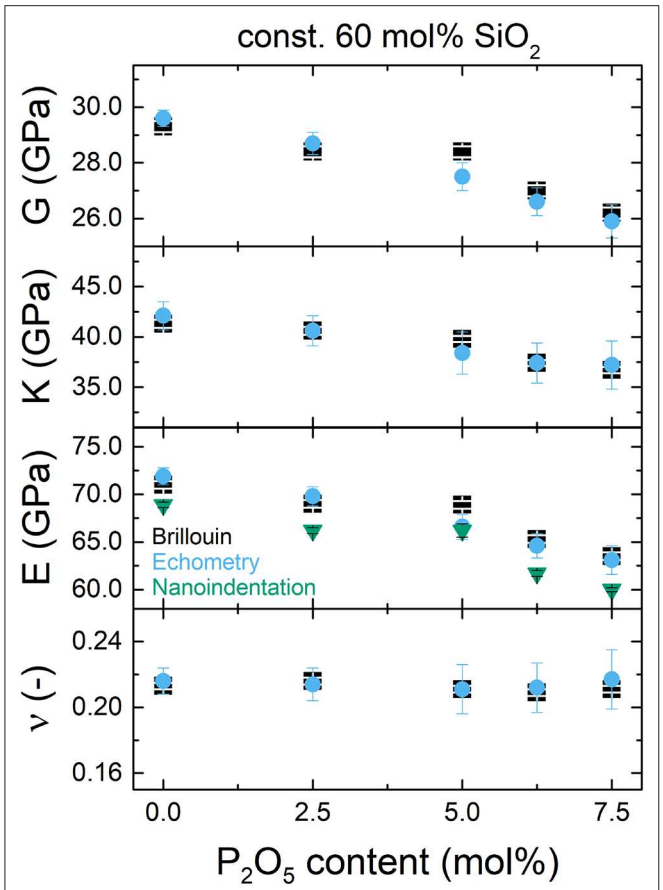

FIGURE 5 | Elastic properties obtained by Brillouin spectroscopy (black squares), ultrasonic echometry (blue circles) and nanoindentation (green triangles, only E) for glasses with 60 mol% SiO_2 and varying phosphate content: (from top to bottom) shear modulus (G), bulk modulus (K), Young's modulus (E) and Poisson's ratio (ν).

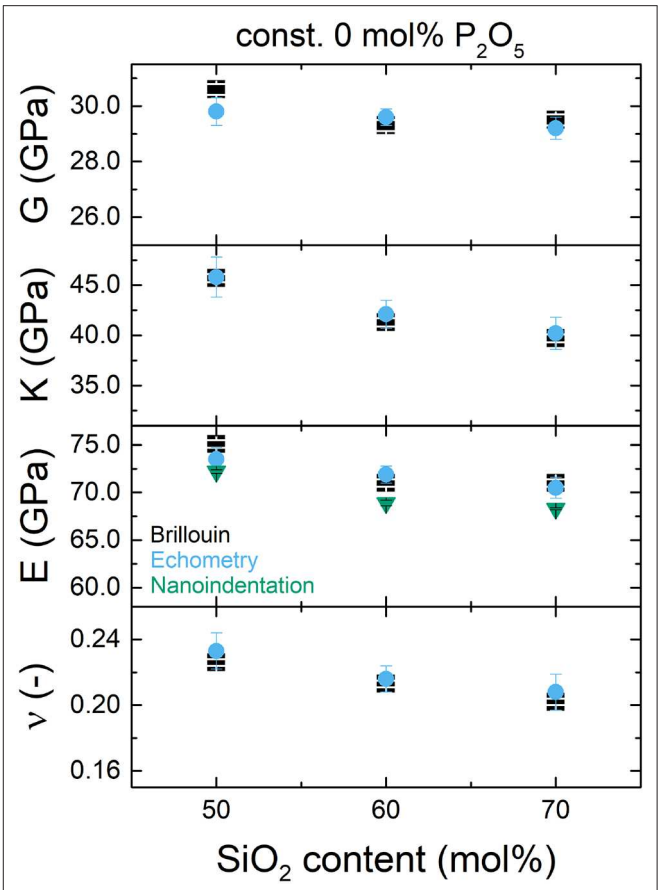

FIGURE 6 | Elastic properties obtained by Brillouin spectroscopy (black squares), ultrasonic echometry (blue circles) and nanoindentation (green triangles, only E) for glasses with 0 mol% P_2O_5 and varying silica content: (from top to bottom) shear modulus (G), bulk modulus (K), Young's modulus (E) and Poisson's ratio (ν).

little variation (<2 cm^{-1}). For increasing phosphate content (**Figure 10C**) the COG shift increased to a maximum value and then slightly decreased toward 7.5 mol% P_2O_5, independent of the data processing. For increasing silica content (**Figure 10D**), the COG shift increased for both glass series. This increase appeared to be linear within the error range for the series with 7.5 mol% P_2O_5 (**Figure 10D**, orange circles), while it was non-linear for the series with 0 mol% P_2O_5 (**Figure 10D**, black squares).

As an additional observation, an increase in phosphate content did not significantly affect the COG shift for the glasses with 50 mol% SiO_2 (**Figure 10D**), regardless of the data processing.

Densification From FEA

Previous studies indicate that densification saturation cannot be achieved using indentation testing (Bruns et al., 2020). The predicted saturation densification of 8.6% (see section Finite Element Analysis in the Materials and Methods section) will likely not be achieved in the indentation center. An experimental determination of densification based on the COG shift upon indentation requires correlation factors, usually determined in DAC experiments accompanied by Raman spectroscopy. Those factors are rarely available for glasses, except for fused silica (Sonneville et al., 2012; Deschamps et al., 2013), and it remains unclear if they are applicable to other glasses, such as the aluminosilicate glasses investigated here. In the absence of such data an alternative strategy needs to be proposed.

FEA offers the opportunity to fill this gap and to provide information on the densification field for a glass from the Si60Px series having a Poisson's ratio of 0.22 (**Figure 11**). Densification is exported from ABAQUS using the parameter PEQC4, a measure for the total volumetric inelastic strain. In this manner, a maximum densification of 5.88 ± 1.39% can be observed in the indentation center.

Strain-Rate Sensitivity

For increasing phosphate content (**Figure 10E**) the strain-rate sensitivity slightly increased. For increasing silica content (**Figure 10F**) the strain-rate sensitivity appears to increase first up to a maximum value in the range between 50 and 60 mol%

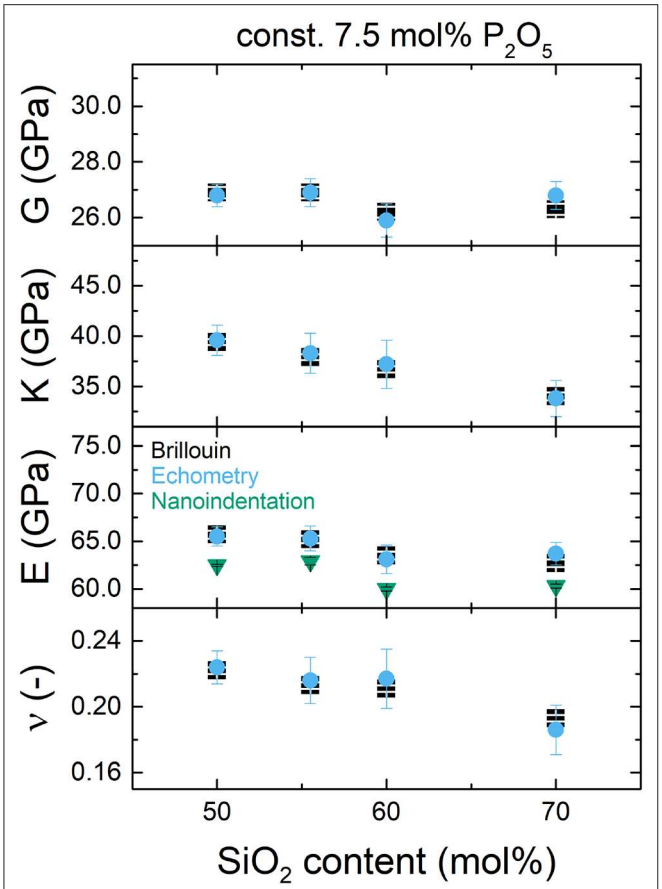

FIGURE 7 | Elastic properties obtained by Brillouin spectroscopy (black squares), ultrasonic echometry (blue circles) and nanoindentation (green triangles, only E) for glasses with 7.5 mol% P_2O_5 and varying silica content: (from top to bottom) shear modulus (G), bulk modulus (K), Young's modulus (E) and Poisson's ratio (ν).

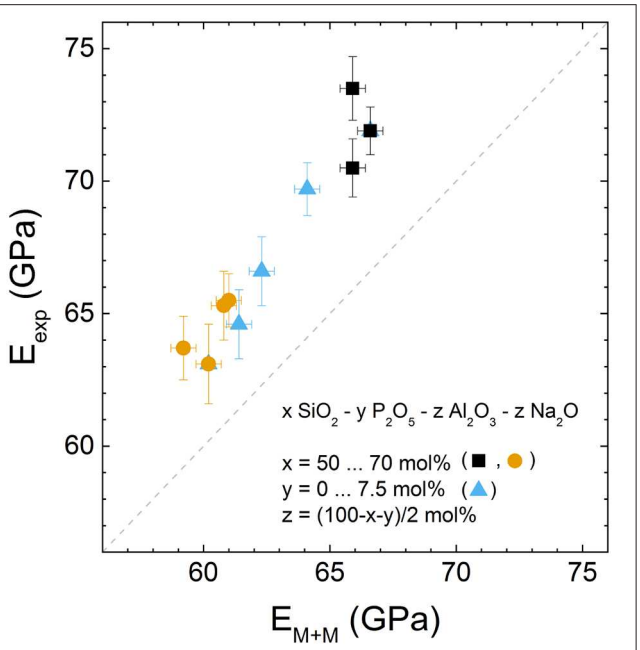

FIGURE 8 | Comparison of Young's moduli determined by ultrasonic echometry (E_{exp}) and by the Makishima-Mackenzie model (E_{M+M}). The dashed line marks the ideal case of complete agreement. The Makishima-Mackenzie model slightly underestimates the measured values.

SiO_2, followed by a slight decrease with further increasing SiO_2 content for both glass series.

DISCUSSION

Compositional Analysis

The observed slight increase in Al_2O_3 content and decrease in SiO_2 content compared to the nominal composition (**Table 1**) can be attributed to Al_2O_3 crucible corrosion (Barz et al., 1996; Smith et al., 2014; Palles et al., 2016). The amount of Al_2O_3 incorporation found here is less than for (silico-)phosphate and tellurite glasses, which have been found to incorporate about 3–9 mol% Al_2O_3 during melting (Palles et al., 2016; Tagiara et al., 2017; Griebenow et al., 2018; Sawangboon et al., 2020). This difference may be explained by the high melt viscosity of the present glasses.

The lower P_2O_5 content may originate from P_2O_5 evaporation during melting (Griebenow et al., 2018; Sawangboon et al., 2020), but P_2O_5 losses are small considering the high melting temperature. This confirms a previous finding that P_2O_5 is not likely to leave metaluminous melts (London et al., 1993).

Density and Related Properties

The decreasing density and atomic packing density as well as the increasing molar volume with increasing phosphate content (**Figure 4**) may be explained by the fact that phosphate was incorporated by substituting P_2O_5 for $NaAlO_2$, i.e., substituting two phosphate tetrahedra for one aluminate tetrahedron charge-balanced by sodium. We note that all aluminate tetrahedra are supposed to have four bridging oxygen atoms (BO) because of the metaluminous composition (Al:Na = 1). Phosphate tetrahedra, on the other hand, may bear fewer BO. Phosphate groups have been reported to partially assume Q^4_P state by forming Al-O-P bonds (Ryerson and Hess, 1980; Gan and Hess, 1992; Kirkpatrick and Brow, 1995). Such bonds between tetrahedral aluminate and phosphate groups have been shown by a bond valence approach to be stable in the absence of an alkaline charge-compensator. In this approach, the Al^{3+} provides 0.75 valence units (cation oxidation number / coordination number) to the bridging oxygen, while the P^{5+} provides 1.25 valence units. Therefore, the nominal −2 charge of the bridging oxygen is compensated (Brow et al., 1993; Bertmer et al., 2000). Al-O-P bond formation was supported also by heteronuclear dipolar solid state NMR experiments (Nizamutdinova et al., 2020). Formation of these bonds should liberate Na^+ ions to create new non-bridging oxygen atoms (NBO) rather than charge-balancing aluminate tetrahedra. As a consequence, the progressive substitution of P_2O_5 for $NaAlO_2$ introduces more tetrahedral units per mole

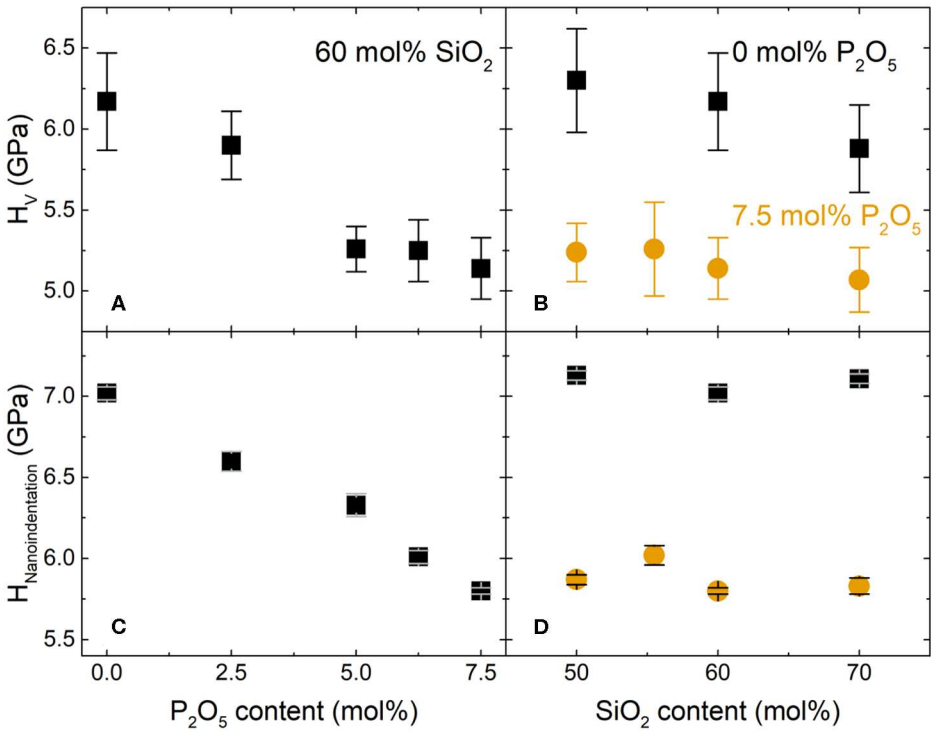

FIGURE 9 | Compositional dependence of **(A,B)** Vickers hardness, H_v, and **(C,D)** hardness as determined by nanoindentation, H: **(A,C)** increasing P_2O_5 content and constant 60 mol% SiO_2, **(B,D)** increasing SiO_2 content and constant P_2O_5 contents of 0 (black squares) or 7.5 mol% (orange circles).

and simultaneously reduces the average number of BO per tetrahedron. An increase in phosphate content therefore involves a decreasing network polymerization. This depolymerisation was supported by recent results derived from a solid-state ^{31}P MAS NMR spectroscopic analysis (Nizamutdinova et al., 2020). A glass network with fewer cross-links and a higher number of tetrahedra per mole is likely to be less compact. The observed decrease in density and atomic packing density as well as the increase in molar volume may be attributed to this decreased network polymerization, but also to the decreasing amount of interstitial sodium ions with increasing P_2O_5 content and, with regard to the molar volume, to a higher number of tetrahedral species per mole. A similar decrease in density has been observed in basaltic glasses (Tarragó et al., 2018b).

For increasing silica content, silica tetrahedra (SiO_4) were substituted for aluminate tetrahedra charge-balanced by sodium ($Na^+[AlO_4]^-$). As both tetrahedral units bear four BO each, the overall network polymerization is assumed to remain unchanged. This appears to correlate with the nearly constant molar volume, but the latter may also be explained by the constant number of tetrahedral groups, regardless of their degree of polymerization. The decrease in density and atomic packing density for increasing silica content is caused by the requirement for charge-balancing Na^+ ions in the vicinity of $[AlO_4]^-$ tetrahedra. Considering the similar ionic radii of Si^{4+} (r_{Si} = 26 pm) and Al^{3+} (r_{Al} = 39 pm) (Shannon, 1976), their corresponding tetrahedra will also be of comparable size, but a network with more aluminate tetrahedra is likely to occupy more inter-tetrahedral space for the accommodation of the charge-balancing sodium ions. Therefore, both density (ρ) and atomic packing density (C_g) changed, even though the molar volume remained roughly constant.

The invariance of C_g within the error limits for all glasses with 50 mol% SiO_2 and for the phosphate-free glass with 60 mol% SiO_2, even though ρ changed, is attributed to the C_g model assumption of densely packed spheres. This model is strongly affected by the selected ionic radii and does not take into account directional bonds and NBO which may be present.

The trend observed for oxygen packing density (ρ_{ox}) was opposite to that for density (**Figure 4**). This is counter intuitive for oxide glasses with oxygen as the most abundant element. The concept of oxygen packing density, i.e., the amount of oxygen atoms per defined volume of glass, has been introduced by Ray (1974), who emphasized its usefulness for weakly polymerized alkali silicate glasses with alkaline ions acting as network modifier. The glasses studied here, however, are highly polymerized, and sodium ions take a charge-balancing role rather than a modifying one. Equivalent to C_g, the calculation of ρ_{ox} is based on the assumption of densely packed spheres and does not take the directional, covalent character of the oxygen bridging bonding into account. The dependence of oxygen packing density on stoichiometric numbers appears to be a disadvantage in the presence of three different network-forming oxides, all of them with different stoichiometric numbers of oxygen. Oxygen

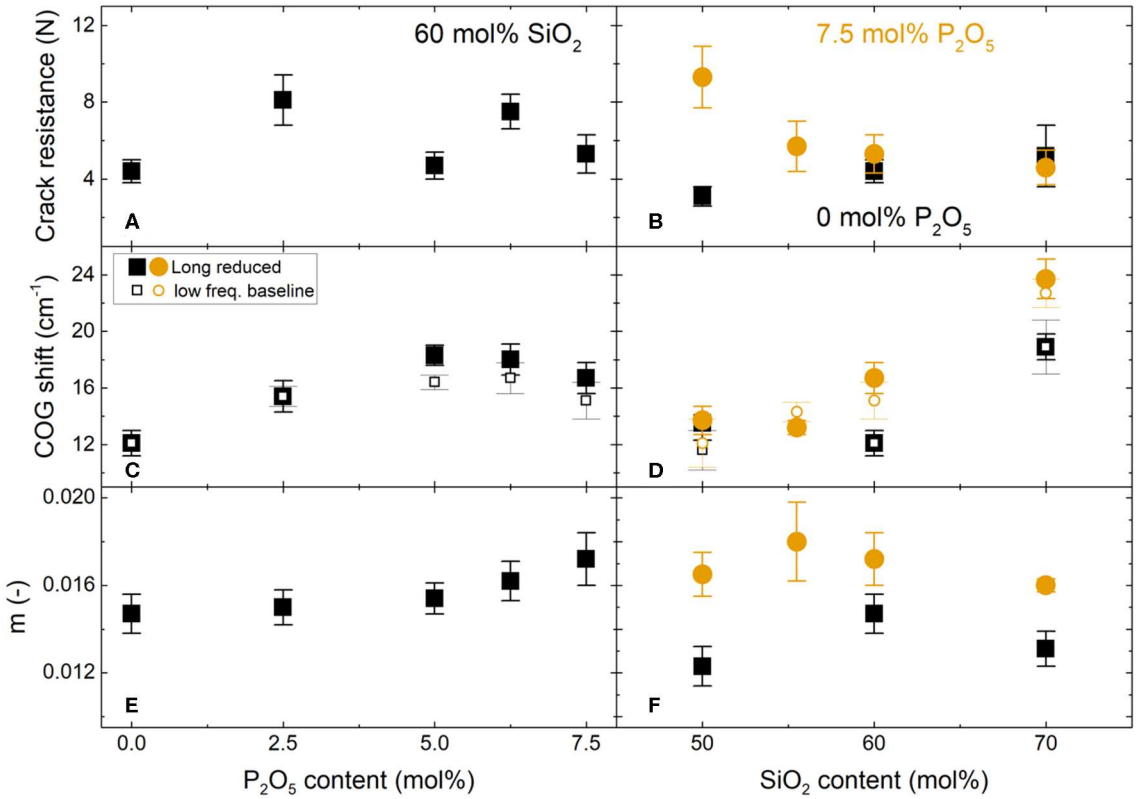

FIGURE 10 | Compositional dependence of **(A,B)** crack resistance, **(C,D)** indentation-induced (981 mN) shift in the low frequency Raman center of gravity (COG) and **(E,F)** strain-rate sensitivity (m): **(A,C,E)** increasing P_2O_5 content and constant 60 mol% SiO_2, **(B,D,F)** increasing SiO_2 content and constant P_2O_5 contents of 0 (black squares) or 7.5 mol% (orange circles). Only for **(C,D)**: Filled symbols show COG shift after data reduction by the Long equation, preceded by a baseline correction at the high frequency end of the spectra. Open symbols show COG shift after subtraction of a linear baseline from the low frequency spectral region.

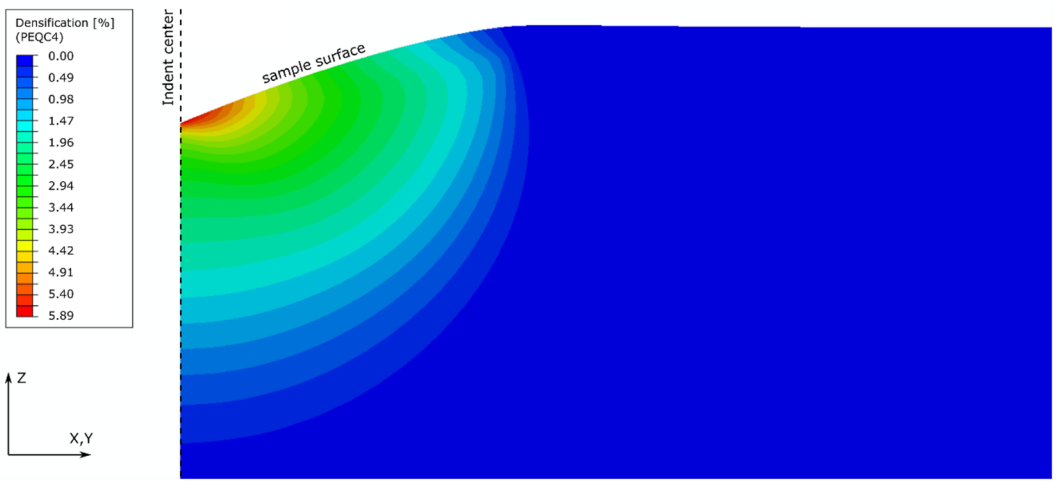

FIGURE 11 | FEA densification field for the system with constant 60 mol% SiO_2, beneath the residual impression of a Berkovich equivalent conical indentation. As the indenter shape is self-similar, the shape of the densification field is independent from indentation depth. Therefore, no scale is required for the axes X,Y,Z. Densification is exported from ABAQUS using the PEQC4 parameter.

packing density is most useful for glass series with constant numbers of oxygen atoms per formula unit (Tylkowski and Brauer, 2013; Mandlule et al., 2014). Oxygen packing density has been found to depend on the coordination number of the cations (Zeidler et al., 2014; Salmon and Zeidler, 2015). However, recent solid-state MAS NMR spectroscopic

investigations indicated that Si, Al and P remained in fourfold coordination in all studied glasses (Grammes et al., in preparation; Nizamutdinova et al., 2020).

Results for packing density and oxygen packing density may additionally be affected by the assumption of a constant ionic radius for oxygen ($r_O = 135$ pm). The ionic radius of oxygen is known to vary depending on the adjacent cationic species (Duffy, 1990; Zeidler et al., 2014). Therefore, values found here could be erroneous. In general, a lower oxygen radius should enable a higher packing density and oxygen packing density. However, once the oxygen is surrounded by cations from more than one species, determination of an exact ionic radius becomes difficult if no quantitative data are available from bond-length measurements. We note that the calculation of oxygen packing density according to Equation (3) does not involve the ionic radius of oxygen [in contrast to the equation used by Zeidler et al. (2014) which requires an a-priori knowledge of the exact bond-lengths] while the packing density calculation via Equation (2) does require the oxygen radius. This may also be a reason for the opposing trends between those two properties. As stated above, the trend in packing density appears more valid as it correlates with the measured density. Therefore, the oxygen packing density will not be taken into account in further analyses here.

Elastic Properties

The elastic properties determined for phosphate-free metaluminous glasses agreed well with available literature data on similar compositions. For Si50P0 and Si60P0 glasses, values of Young's modulus ranging from 72 to 74 GPa have been reported (here: 71–75 GPa for Brillouin spectroscopy and ultrasonic echometry) as well as Poisson's ratios from 0.200 to 0.228 (here: 0.213–0.233) (Tiegel et al., 2015; Weigel et al., 2016). To our knowledge, elastic properties have not yet been reported on comparable phospho-aluminosilicate glass compositions. Only peralkaline basaltic glasses with negligible phosphate contents of 0.2 mol% have been investigated (Lönnroth and Yue, 2009). The decrease in E, G and K for increasing phosphate content (**Figure 5**) may indicate a decrease in network polymerization. This trend may also be related to a decrease in atomic packing density upon phosphate incorporation, as suggested by Makishima and Mackenzie (1973). According to Rouxel, the packing density shows a non-linear correlation with elastic properties for a wide range of glass types (Rouxel, 2006, 2007).

For increasing silica content here, polymerization should remain unchanged, at least in the phosphate-free glasses. For the phosphate-containing glasses, interactions between Na, P and Al may slightly influence polymerization. If little to no change in polymerization is assumed, the elastic properties should remain largely constant. This assumption is well confirmed by the results for G and possibly for E (**Figures 6**, **7**). Results show a clear difference in the trends for G and E with increasing silica content, showing minor changes only, and much more pronounced changes for increasing phosphate content. Despite constant network polymerization with increasing silica content, a clear decrease of K is observed in addition to the very minor decreases of G and E. These decreasing moduli may possibly be explained by the decrease in packing density (**Figure 4**). The decrease in packing density with increasing silica content indicates an increase in free volume. A glass with more free volume will be more compliant toward elastic deformation as indicated by the trend observed for K (and, possibly, G and E). To conclude, both network polymerization and atomic packing density appear to contribute to modulus changes, but only the change in packing density may explain all measured trends.

Poisson's ratio remained practically constant for increasing P_2O_5 content (**Figure 5**) and decreasing polymerization, even though Rouxel (2006) indicated an increase of ν for glasses with lower degree of cross-linking. However, his data showed large scattering for highly polymerized glasses. Rouxel's observations also include a decrease in Poisson's ratio with decreasing packing density. The results shown here do not confirm this observation, however, as the packing density showed a clear decrease with increasing phosphate content, while Poisson's ratio remained constant. By contrast, the slight decrease of ν for increasing SiO_2 content (**Figures 6**, **7**) matches the relationship found by Rouxel (2006). There is actually a simple mathematical explanation for the constant values observed for ν, as it was calculated by dividing E by G. As E and G showed comparable changes with composition, no change in ν is observed. One additional observation may be noted, though. Rouxel's observation of a correlation between ν and packing density (Rouxel, 2006) was confirmed here when substituting SiO_4 for $Na^+[AlO_4]^-$, i.e., when the overall amount of network-forming units did not change. With increasing phosphate content, by contrast, this correlation was not observed, most likely because the overall amount of network-forming units increased, as $NaAlO_2$ was replaced by P_2O_5. However, to really test whether the overall ratio of network formers to network modifiers correlates with ν, one would need to test over a much wider range of glass compositions.

Young's moduli calculated using the Makishima-Mackenzie model showed a comparable trend to the experimental values (**Figure 8**), although the calculated values were lower than the experimental ones. The relatively good agreement in trend highlights that, despite its simplicity, the model provides a useful estimate of elastic properties. This is in agreement with an earlier study of the model on simple silicate, borate and phosphate glasses (Inaba et al., 1999). The deviation between experimental and model values may be caused by various factors.

First of all, the Makishima-Mackenzie model assumes that all elements in the glass have the same coordination as in their corresponding oxide components. This is not true for aluminum which should be present mainly in fourfold coordination in the studied metaluminous glasses, while the Makishima-Mackenzie calculation is based on the dissociation energy of Al_2O_3, in which aluminum is exclusively sixfold coordinated. The cation packing fraction of aluminum in fourfold and sixfold coordination is similar, yet the charge of Al^{3+} is shared among fewer oxygens in fourfold coordination (She et al., 2019). This is in agreement with early work by Sun (1947) suggesting that the dissociation energy of Al-O bonds is higher when Al is in fourfold coordination compared to sixfold coordination. Therefore, an adjustment of the model

taking into account Al coordination may potentially yield larger calculated values of E, leading to better agreement with experimental data.

Secondly, the Makishima-Mackenzie model presents a mean-field approximation. Using quantitative data on the work of deformation and its comparison to predicted bulk modulus, it has recently been shown for a wide range of glassy materials that this is overly simplified (Sawamura and Wondraczek, 2018). Instead, the mechanical response of glasses is strongly dependent on their respective structural heterogeneity (Benzine et al., 2018).

Another shortcoming of the Makishima-Mackenzie model is its implicit assumption that all bonds are bridging oxygen bonds. Neither non-bridging oxygen nor terminal oxygen are taken into account. Inaba et al. (1999) found this to affect the model values for phosphate glasses and successfully adjusted the model to take non-bridging oxygen atoms into account. However, in the present study the model underestimated the experimental values. An adjustment of the model to include non-bridging oxygens connected to phosphate groups would further decrease the calculated moduli, leading to even higher deviation from experimental values.

A further factor influencing the moduli may be bonds between mixed network-forming units, such as Al-O-P bonds, which are not taken into account by the Makishima-Mackenzie model either. A comparison between the molar heats of formation of $AlPO_4$ (−1733.8 kJ/mol, only Al-O-P bonds) and Al_2O_3 (−1675.7 kJ/mol, only Al-O-Al bonds) (Lide, 2006) suggests that mixed bonds are stronger than non-mixed ones. This may partially explain why experimental moduli are higher than the calculated ones. An adjustment of the model to take mixed bonds into account would require detailed knowledge of the glass structure, however, to determine the relative amount of each type of bond.

A minor contribution to the deviation between model and experimental data may also result from actual glass composition slightly deviating from the nominal values used in the model. Furthermore, ionic radii used for the calculation of packing density were found to have a major influence on the results of the Makishima-Mackenzie model. For example, the two different sets of "effective ionic radii" and "crystal radii" provided by Shannon (1976) led to differences of more than 10 GPa in the calculated moduli. For this reason, the effective ionic radii used here were chosen as they yielded the best agreement with experimental data.

Hardness

The decrease in hardness with increasing phosphate content can be explained by lower network polymerization, caused by P_2O_5 incorporation. The constant hardness for increasing silica content may be explained by constant network polymerization upon substitution of SiO_4 for $Na^+[AlO_4]^-$ tetrahedra.

Lönnroth and Yue (2009) have noted a weak correlation between hardness and density in peralkaline aluminosilicate glasses. Results here showed a correlation of hardness with packing density (Makishima and Mackenzie, 1973) with increasing P_2O_5 content but not with increasing SiO_2 content. Instead, the constant hardness with increasing silica content could be related to the constant molar volume (**Figures 4D, 9B,D**). The decreasing hardness with increasing P_2O_5 content (**Figures 9A,C**) was accompanied by increasing molar volume, indicating a relationship between large molar volume and low hardness for the present system. A similar decrease in hardness with increasing phosphate content up to more than 8 mol% has been reported for basaltic glasses (Tarragó et al., 2018b). Zeng et al. (2016) found hardness values between 5 and 5.5 GPa for peralkaline glasses with 5 mol% P_2O_5. This range agrees with the Vickers hardness of most phosphate-containing glasses presented here. The hardness values found for the phosphate-free glasses (6 to 6.3 GPa for microindentation) are in good agreement with a value of about 6 GPa reported by Tiegel et al. (2015) for a glass of the Si60P0 composition. Other literature hardness values of metaluminous glasses with various alkaline constituents ranged from 5.6 to 7.4 GPa (Smedskjaer et al., 2013; Tiegel et al., 2015; Bechgaard et al., 2016).

Crack Resistance

To estimate the error of the crack resistance, a method was developed here based on the PCI error bars. In **Figure 1**, PCI error bars represent the 95% confidence interval after evaluation of 25 indentations (up to 100 potential median-radial cracks) per load. The error of the crack resistance has to be found in the load dimension (horizontal axis). Therefore, the end points of the PCI error bars (blue triangles) were connected by linear segments to create an estimated error envelope of the PCI (red lines in **Figure 1**). This error envelope intersects the 50% PCI line at two loads above and below the crack resistance, generating two horizontal error bars (not shown) of different length (because of logarithmic axis). The larger error bar out of the two was chosen as the estimated error of the crack resistance.

The slight increase in crack resistance with increasing silica content in phosphate-free glasses (**Figure 10B**) confirms previous findings available in the literature (Gross et al., 2009; Hermansen et al., 2013). Bechgaard et al. (2016) have recently reported crack resistances between 1 and 3 N for a glass of Si50P0 composition. This agrees with the value found here (3.1 ± 0.5 N). For metaluminous calcium aluminosilicate glasses with SiO_2 content increasing from 60 to 80 mol%, Gross et al. found an increase in crack resistance with values comparable to those obtained in this study (Gross et al., 2009). However, for >80 mol% SiO_2, this trend is reverted as cracking changed to silica-like anomalous behavior with different crack systems becoming active. Up to now, there is no literature data available on the crack resistance of phospho-aluminosilicate glasses.

Higher crack resistances have previously been linked to higher silica content in the case of soda-lime silicate glasses (Hermansen et al., 2013), indicating the influence of network polymerization. For phosphate-free sodium aluminosilicate glasses, on the other hand, crack resistance was reported to decrease when increasing the Al/Na ratio from 0 to 1 (Bechgaard et al., 2016), even though this means approaching metaluminous composition and thus increasing polymerisation.

The range of data scattering observed for increasing phosphate content (**Figure 10A**) is similar to the range spanned by the crack resistance trends for increasing silica content

(**Figure 10B**). Therefore, the apparent trends in **Figure 10B** may be coincidental and will not be discussed further.

To increase reliability of crack resistance measurements, an even higher number of indentations would be needed to improve statistics. Also, atmospheric humidity may affect the measurements and should be avoided by measuring under protective atmosphere or in vacuum.

Densification

Changes in the low frequency Raman region have been correlated with bond angle changes and thus with density changes (Galeener, 1979; Rouxel et al., 2008; Deschamps et al., 2011; Cornet et al., 2017). In case of densification, this region shifts toward higher wavenumbers; however, the theoretical basis for this correlation has only been strictly defined for one-component glasses such as vitreous silica (Sen and Thorpe, 1977; Galeener, 1979). The phospho-aluminosilicate glasses studied here carry three different network formers, all of them possessing different Raman scattering cross-sections. This may influence the spectral shifts to a currently unpredictable degree. Even so, in the past the analysis of densification with Raman spectroscopy has not only been exercised on vitreous silica (Kailer et al., 1999; Hehlen, 2010; Cornet et al., 2017), but also on soda-lime silicate glasses (Deschamps et al., 2011; Kassir-Bodon et al., 2012), borosilicate glasses (Winterstein-Beckmann et al., 2014) and aluminosilicate glasses (Poe et al., 2001; Bechgaard et al., 2016). All of these studies correlated changes of the low frequency Raman region with densification. Even the studies on borosilicate and aluminosilicate glasses have not tackled the issue of having more than one network former. Instead, a phenomenological approach has been chosen for these glass systems. As long as silica remained the main network former, the shape of the low frequency Raman envelope was close enough to that of vitreous silica to assume similar behavior. The same assumption will be considered valid for the phospho-aluminosilicate glasses studied here, because of their high degree of polymerisation and the clearly observable changes of the low frequency Raman region upon indentation.

Changes in the medium frequency region [Raman band at 700 cm^{-1} in **Figure 2**, assigned to $[AlO_4]^-$ stretching (Iwamoto et al., 1978; McMillan and Piriou, 1982; Kamitsos et al., 1994)] were not taken into account here. This band would be affected by a change of Al coordination, but there was no reason to assume such a coordination change in the present metaluminous glasses. The formation of higher-coordinated aluminum upon compression is likely for peralkaline compositions but not for metaluminous ones (Hochella and Brown, 1985; Bechgaard et al., 2016). Instead, a weak intensity increase in the medium frequency region upon densification is assumed to be caused by partial overlap with the low frequency bands.

When analyzing densification by Raman spectroscopy, a comparison between the baseline method by Deschamps et al. (2011) and the Long data reduction seemed worthwhile since the use of the Long data reduction is popular in Raman analysis of glasses, yet changes markedly the shape of the low frequency Raman region (Seifert et al., 1982; Neuville and Mysen, 1996; Mysen, 1999; Mysen and Toplis, 2007; Le Losq and Neuville, 2013; Neuville et al., 2014; Rabia et al., 2016). Thus, the comparison allowed to test whether the Long data reduction affected the densification analysis. Concluding from the good agreement between the two tested post-processing routes (open and filled symbols in **Figures 10C,D**), different ways of determining the COG shift may still lead to comparable results regarding densification. Both tested post-processing routes may be regarded as equally applicable.

Raman spectroscopy allowed to track differences in densification between the different compositions, based on different COG shifts. The increasing COG shift upon phosphate incorporation in glasses with 60 mol% SiO_2 (**Figure 10C**) indicates higher densification upon indentation. This may be explained by the lower density of the phosphate-containing glasses (**Figure 4**). When equally loaded, a less densely packed glass should be more readily densified than a densely packed one. The maximum trend of the COG shift with increasing P_2O_5 content (**Figure 10C**) may be related to increasing glass depolymerisation upon increasing P_2O_5 content. As shown by Bechgaard et al. (2016), the degree of polymerisation may affect the deformation mechanism of aluminosilicate glasses.

The increasing COG shift with increasing silica content (**Figure 10D**) may be explained by the lower packing density of the high-silica glasses. The apparent non-linearity of this trend may potentially be caused by underlying changes of the deformation mechanism. The slightly higher values of Poisson's ratio for the glasses with lower silica content (**Figures 6**, **7**) support a lower degree of densification and a higher degree of shearing for the low-silica glasses, following Sellappan et al. (2013).

The transformation of COG shifts into absolute values of densification is established for vitreous silica (Deschamps et al., 2013) and soda-lime silicate glass (Deschamps et al., 2011) only. For more complex glass systems such as the given phospho-aluminosilicate glass series no direct correlation is available in the literature. In the present study the degree of densification was estimated using FEA for the 60 mol% SiO_2 glass series and a maximum indentation densification of 5.88 $\pm$ 1.39% was observed (**Figure 11**). The FEA input is strongly linked to Poisson's ratio, which is almost constant around 0.22 for the 60 mol% SiO_2 glass series (**Figure 5**). Therefore, the FEA approach does not exhibit the precision to reproduce the compositional influences as they have been found for the COG shift in the given test series. Both approaches should be considered together. The sensitive COG shifts provide insight into how compositional changes lead to relative differences in densification upon indentation. FEA provides a rough idea of the absolute level of indentation densification on which those changes take place.

Raman signal is gathered not only from the sample surface but also from below, where densification is lower (**Figure 11**) (Bruns et al., 2020). COG shifts therefore correspond to a densification averaged over signal depth. Compositional trends of COG shift should not be affected by this because indent size, load, and Raman depth of field were roughly equal for all samples.

Strain-Rate Sensitivity

All strain-rate sensitivities found here fit well within the relationship between strain-rate sensitivity and Poisson's ratio for glasses shown by Limbach et al. (2014). The strain-rate

sensitivities ranged from 0.012 to 0.018 for values of ν between 0.20 and 0.24, agreeing with similar values for soda-lime silicate glasses (Limbach et al., 2014, 2017). These strain-rate sensitivities are rather low, yet common over many different glass systems (Limbach et al., 2014). The slightly increasing strain-rate sensitivity for increasing phosphate content (**Figure 10E**) may potentially be explained by the decreasing packing density and network polymerisation upon phosphate incorporation. Both trends should account for more free volume within the glass. This additional free volume together with the lower degree of cross-linking may facilitate local structural rearrangements when subjected to sudden changes in strain-rate. Nevertheless, a complete structural explanation of the increased strain-rate sensitivity has to be more complex. For increasing silica content, the results show no correlation between strain-rate sensitivity and density. Here, the non-linearity of strain-rate sensitivity correlates with no other property. A tentative structural hint may be obtained from metaluminous minerals of stoichiometry comparable to that of the phosphate-free glasses. Glass Si50P0 has the same stoichiometric composition as the mineral nepheline ($NaAlSiO_4$). The composition of glass Si60P0 lies between nepheline and jadeite ($NaAlSi_2O_6$), the latter corresponding to 66.67 mol% SiO_2. The composition of glass Si70P0 lies between jadeite and albite ($NaAlSi_3O_8$), with albite corresponding to 75 mol% SiO_2. The crystal structures of nepheline, jadeite and albite are hexagonal, monoclinic and triclinic, respectively, see e.g., the RRUFF mineral database, entries R040025.1, R050220 and R040068.1 (Lafuente et al., 2015). Potentially, the maximum in strain-rate sensitivity upon increasing silica content may correspond to an underlying change within the glasses' medium-range structure which bears similarities to the change of the corresponding crystal structure. However, this is a mere hypothesis and requires further study.

CONCLUSIONS

This work has reported the synthesis and study of mechanical properties of glasses in the metaluminous (Al:Na = 1) system SiO_2-Al_2O_3-Na_2O-P_2O_5. The incorporation of phosphate into such aluminosilicate glasses by substituting P_2O_5 for $NaAlO_2$ resulted in decreasing packing density. A simultaneous decrease in hardness and elastic moduli and increase in strain-rate sensitivity could be attributed to this packing density decrease, and to depolymerisation of the glass network.

Regarding glass densification upon indentation, glasses with lower initial density showed higher shifts of the correlated Raman spectral region, indicating higher densification. The results were non-linear over glass composition, which was tentatively attributed to a change in deformation mechanism.

Variation of the silica content by substituting SiO_4 for $Na^+[AlO_4]^-$ tetrahedra was assumed to maintain nearly constant network polymerisation. This was supported by constant hardness. Simultaneous changes in elastic moduli correlated with packing density, while changes in Poisson's ratio were small. Only in case of increasing SiO_2 content they could be correlated with packing density changes.

Taken together, the findings of this first comprehensive mechanical analysis of metaluminous phospho-aluminosilicate glasses provides a basis for tailoring mechanical properties by simply varying the P_2O_5 or SiO_2 content. Non-linearities found in densification and strain-rate sensitivity hint toward more complex changes in glass structure, opening up possibilities for further study of the interplay between the three network formers.

DATA AVAILABILITY STATEMENT

The datasets generated for this study are available on request to the corresponding author.

AUTHOR CONTRIBUTIONS

TG, DB, LvW, and DL designed the glass series and the experiments. TG synthesized the samples, performed density, microindentation and Raman spectroscopy experiments, contributed to Makishima-Mackenzie calculations, analyzed and interpreted the results, and wrote the manuscript. RL performed nanoindentation and ultrasonic echometry measurements and contributed to Makishima-Mackenzie calculations, interpretation of mechanical properties, and writing of the manuscript. SB performed the FEA analysis and contributed to the interpretation of glass densification and to writing the corresponding part of the manuscript. LvW, DL, EK, KD, LW, and DB contributed to the interpretation of the results and writing of the manuscript.

FUNDING

Financial support by the German Research Foundation (DFG project SPP 1594) is gratefully acknowledged. We also acknowledge financial support for open access publishing by the German Research Foundation and the Publication Fund of the Thueringer Universitaets- und Landesbibliothek Jena (project number 433052568).

ACKNOWLEDGMENTS

We would like to thank Alexander Veber (formerly Friedrich Alexander University Erlangen-Nürnberg) for Brillouin measurements, Johannes Buchheim (Institute of Technical and Environmental Chemistry, Friedrich Schiller University Jena) as well as Detlef Schelle (Institute of Applied Physics, Friedrich Schiller University Jena) for EDX measurements, Timothy Oshiobughie Imogore (Friedrich Schiller University Jena) for implementing the center of gravity calculation into MATLAB, Tadiyos Tarekegn Alemayehu (formerly Friedrich Schiller University Jena) for assistance with crack resistance measurements and two reviewers for their valuable comments. The majority of data shown here, with exception of the Makishima-Mackenzie calculations and the FEA simulation of densification, was published in TG's Ph.D. thesis (Grammes, 2020).

REFERENCES

Barz, A., Haase, T., Meyer, K., and Stachel, D. (1996). Corrosion of crucible materials and their influence on structure of phosphate glasses. *Phosphorus Res. Bull.* 6, 331–336. doi: 10.3363/prb1992.6.0_331

Bechgaard, T., Goel, A., Youngman, R., Mauro, J., Rzoska, S., Bockowski, M., et al. (2016). Structure and mechanical properties of compressed sodium aluminosilicate glasses: role of non-bridging oxygens. *J. Non Crystal. Solids* 441, 49–57. doi: 10.1016/j.jnoncrysol.2016.03.011

Bellot-Gurlet, L., Le Bourdonnec, F.-X., Poupeau, G., and Dubernet, S. (2004). Raman micro-spectroscopy of western Mediterranean obsidian glass: one step towards provenance studies? *J. Raman Spectr.* 35, 671–677. doi: 10.1002/jrs.1195

Benzine, O., Bruns, S., Pan, Z., Durst, K., and Wondraczek, L. (2018). Local deformation of glasses is mediated by rigidity fluctuation on nanometer scale. *Adv. Sci.* 5:1800916. doi: 10.1002/advs.201800916

Bertmer, M., Züchner, L., Chan, J., and Eckert, H. (2000). Short and medium range order in sodium aluminoborate glasses. 2. site connectivities and cation distributions studied by rotational echo double resonance NMR spectroscopy. *J. Phys. Chem. B* 104, 6541–6553. doi: 10.1021/jp9941918

Botev, M., Betchev, H., Bikiaris, D., and Panayiotou, C. (1999). Mechanical properties and viscoelastic behavior of basalt fiber-reinforced polypropylene. *J. Appl. Polymer Sci.* 74, 523–531. doi: 10.1002/(SICI)1097-4628(19991017)74:3<523::AID-APP7>3.0.CO;2-R

Brow, R., Kirkpatrick, R., and Turner, G. (1993). Nature of alumina in phosphate glass: ii, structure of sodium aluminophosphate glass. *J. Am. Ceramic Soc.* 76, 919–928. doi: 10.1111/j.1151-2916.1993.tb05316.x

Bruns, S., Johanns, K., Rehman, H., Pharr, G., and Durst, K. (2017). Constitutive modeling of indentation cracking in fused silica. *J. Am. Ceramic Soc.* 100, 1928–1940. doi: 10.1111/jace.14734

Bruns, S., Uesbeck, T., Fuhrmann, S., Tarragó, M., Wondraczek, L., De Ligny, D., et al. (2020). Indentation densification of fused silica assessed by Raman spectroscopy and constitutive finite element analysis. *J. Am. Ceramic Soc.* 103, 3076–3088. doi: 10.1111/jace.17024

Cann, J., and Renfrew, C. (1964). The Characterization of Obsidian and its application to the Mediterranean region. *Proceedings of the Prehistoric Society* 30, 111–133. doi: 10.1017/S0079497X00015097

Cornet, A., Martinez, V., De Ligny, D., Champagnon, B., and Martinet, C. (2017). Relaxation of densified silica glass. *J. Chem. Phys.* 146, 094504. doi: 10.1063/1.4977036

Deschamps, T., Kassir-Bodon, A., Sonneville, C., Margueritat, J., Martinet, C., De Ligny, D., et al. (2013). Permanent densification of compressed silica glass: a Raman-density calibration curve. *J. Phys. Cond. Matter.* 25:025402. doi: 10.1088/0953-8984/25/2/025402

Deschamps, T., Martinet, C., Bruneel, J. L., and Champagnon, B. (2011). Soda-lime silicate glass under hydrostatic pressure and indentation: a micro-Raman study. *J. Phys. Cond. Matter.* 23:035402. doi: 10.1088/0953-8984/23/3/035402

Dibenedetto, A. (2001). Tailoring of interfaces in glass fiber reinforced polymer and composites: a review. *Mater. Sci. Eng. A* 302, 74–82. doi: 10.1016/S0921-5093(00)01357-5

Duffy, J. A. (1990). *Bonding, Energy Levels & Bands in inorganic Solids*. London, UK: Longman Scientific & Technical.

Dupree, R., Holland, D., and Mortuza, M. (1988). The role of small amounts of P2O5 in the structure of alkali disilicate glasses. *Phys. Chem. Glass.* 29, 18–21.

Ericson, J., Makishima, A., Mackenzie, J., and Berger, R. (1975). Chemical and Physical Properties of Obsidian: A Naturally Occurring Glass. *J. Non Crystal. Solids* 17, 129–142. doi: 10.1016/0022-3093(75)90120-9

Fredholm, Y., Karpukhina, N., Law, R., and Hill, R. (2010). Strontium containing bioactive glasses: Glass structure and physical properties. *J. Non Crystal. Solids* 356, 2546–2551. doi: 10.1016/j.jnoncrysol.2010.06.078

Galeener, F. (1979). Band limits and the vibrational spectra of tetrahedral glasses. *Phys. Rev. B* 19, 4292–4297. doi: 10.1103/PhysRevB.19.4292

Gan, H., and Hess, P. C. (1992). Phosphate speciation in potassium aluminosilicate glasses. *Am. Mineral.* 77, 495–506.

Grammes, T. (2020). *Structure and mechanical properties of aluminosilicate glasses* (Dissertation), Friedrich Schiller University Jena, Jena, Germany.

Griebenow, K., Bragatto, C., Kamitsos, E., and Wondraczek, L. (2018). Mixed-modifier effect in alkaline earth metaphosphate glasses. *J. Non Crystal. Solids* 481, 447–456. doi: 10.1016/j.jnoncrysol.2017.11.041

Griffith, A. (1920). The Phenomena of rupture and flow in solids. *Phil. Trans. Roy. Soc. London A* 221, 163–198. doi: 10.1098/rsta.1921.0006

Gross, T., Tomozawa, M., and Koike, A. (2009). A glass with high crack initiation load: Role of fictive temperature-independent mechanical properties. *J. Non Crystal. Solids* 355, 563–568. doi: 10.1016/j.jnoncrysol.2009.01.022

Hehlen, B. (2010). Inter-tetrahedra bond angle of permanently densified silicas extracted from their Raman spectra. *J. Phys. Cond. Matter.* 22:025401. doi: 10.1088/0953-8984/22/2/025401

Hermansen, C., Matsuoka, J., Yoshida, S., Yamazaki, H., Kato, Y., and Yue, Y. (2013). Densification and plastic deformation under microindentation in silicate glasses and the relation to hardness and crack resistance. *J. Non Crystal. Solids* 364, 40–43. doi: 10.1016/j.jnoncrysol.2012.12.047

Hochella, M., and Brown, Jr., G. (1985). The structures of albite and jadeite composition glasses quenched from high pressure. *Geochimica et Cosmochimica Acta* 49, 1137–1142. doi: 10.1016/0016-7037(85)90004-3

Inaba, S., Fujino, S., and Morigana, K. (1999). Young's Modulus and Compositional Parameters of Oxide Glasses. *J. Am. Ceramic Soc.* 82, 3501–3507. doi: 10.1111/j.1151-2916.1999.tb02272.x

Iwamoto, N., Tsunawaki, Y., Hattori, T., and Mitsuishi, A. (1978). Raman spectra of Na_2O-SiO_2-Al_2O_3 and K_2O-SiO_2-Al_2O_3 glasses. *Phys. Chem. Glass.* 19, 141–143.

Kailer, A., Nickel, K. G., and Gogotsi, Y. G. (1999). Raman microspectroscopy of nanocrystalline and amorphous phases in hardness indentations. *J. Raman Spectr.* 30, 939–946. doi: 10.1002/(SICI)1097-4555(199910)30:10<939::AID-JRS460>3.0.CO;2-C

Kamitsos, E., Kapoutsis, J., Jain, H., and Hsieh, C. (1994). Vibrational study of the role of trivalent ions in sodium trisilicate glass. *J. Non Crystal. Solids* 171, 31–45. doi: 10.1016/0022-3093(94)90030-2

Kassir-Bodon, A., Deschamps, T., Martinet, C., Champagnon, B., Teisseire, J., and Kermouche, G. (2012). Raman mapping of the indentation-induced densification of a soda-lime-silicate glass. *Int. J. Appl. Glass Sci.* 3, 29–35. doi: 10.1111/j.2041-1294.2012.00078.x

Kirkpatrick, R., and Brow, R. (1995). Nuclear magnetic resonance investigation of the structures of phosphate and phosphate-containing glasses: a review. *Solid State Nuclear Magn. Reson.* 5, 9–21. doi: 10.1016/0926-2040(95)00042-O

Kosinski, S., Krol, D., Duncan, T., Douglass, D., Macchesney, J., and Simpson, J. (1988). Raman and NMR Spectroscopy of SiO_2 Glasses Co-Doped with Al_2O_3 and P_2O_5. *J. Non Crystal. Solids* 105, 45–52. doi: 10.1016/0022-3093(88)90336-5

Lafuente, B., Downs, R. T., Yang, H., and Stone, N. (2015). "The power of databases: the RRUFF project," in *Highlights in Mineralogical Crystallography*, eds. T. Armbruster and R. M. Danisi (Berlin, DE: Walter De Gruyter GmbH), 1–30. doi: 10.1515/9783110417104-003

Le Losq, C., and Neuville, D. (2013). Effect of the Na/K mixing on the structure and the rheology of tectosilicate silica-rich melts. *Chem. Geol.* 346, 57–71. doi: 10.1016/j.chemgeo.2012.09.009

Lide, D. (2006). *CRC Handbook of Chemistry and Physics*. Boca Raton, FL: CRC Press.

Limbach, R., Karlsson, S., Scannell, G., Mathew, R., Edén, M., and Wondraczek, L. (2017). The effect of TiO2 on the structure of Na_2O-CaO-SiO_2 glasses and its implications for thermal and mechanical properties. *J. Non Crystal. Solids* 471, 6–18. doi: 10.1016/j.jnoncrysol.2017.04.013

Limbach, R., Rodrigues, B., Möncke, D., and Wondraczek, L. (2015a). Elasticity, deformation and fracture of mixed fluoride-phosphate glasses. *J. Non Crystal. Solids* 430, 99–107. doi: 10.1016/j.jnoncrysol.2015.09.025

Limbach, R., Rodrigues, B., and Wondraczek, L. (2014). Strain-rate sensitivity of glasses. *J. Non Crystal. Solids* 404, 124–134. doi: 10.1016/j.jnoncrysol.2014.08.023

Limbach, R., Winterstein-Beckmann, A., Dellith, J., Möncke, D., and Wondraczek, L. (2015b). Plasticity, crack initiation and defect resistance in alkali-borosilicate glasses: from normal to anomalous behavior. *J. Non Crystal. Solids* 417–418, 15–27. doi: 10.1016/j.jnoncrysol.2015.02.019

London, D., Morgan Vi, G., Babb, H., and Loomis, J. (1993). Behavior and effects of phosphorus in the system Na_2O-K_2O-Al_2O_3-SiO_2-P_2O_5-H_2O at 200 MPa (H_2O). *Contrib. Mineral. Petrol.* 113, 450–465. doi: 10.1007/BF00698315

Long, D. A. (1977). *Raman Spectroscopy*. New York, NY: McGraw-Hil.

Long, D. A. (2002). *The Raman Effect: A Unified Treatment of the Theory of Raman Scattering by Molecules. West Sussex, UK: John Wiley & Sons Ltd. doi: 10.1002/0470845767*

Lönnroth, N., and Yue, Y. (2009). Influence of chemical composition on the physical properties of basaltic glasses. *Glass Technol.* 50, 165–173.

Maier, V., Durst, K., Mueller, J., Backes, B., Höppel, H., and Göken, M. (2011). Nanoindentation strain-rate jump tests for determining the local strain-rate sensitivity in nanocrystalline Ni and ultrafine-grained Al. *J. Mater. Res.* 26, 1421–1430. doi: 10.1557/jmr.2011.156

Maier, V., Merle, B., Göken, M., and Durst, K. (2013). An improved long-term nanoindentation creep testing approach for studying the local deformation processes in nanocrystalline metals at room and elevated temperatures. *J. Mater. Res.* 28, 1177–1177. doi: 10.1557/jmr.2013.39

Makishima, A., and Mackenzie, J. (1973). Direct calculation of young's modulus of glass. *J. Non Crystal. Solids* 12, 35–45. doi: 10.1016/0022-3093(73)90053-7

Mandlule, A., Döhler, F., Van Wüllen, L., Kasuga, T., and Brauer, D. (2014). Changes in structure and thermal properties with phosphate content of ternary calcium sodium phosphate glasses. *J. Non Crystal. Solids* 392–393, 31–38. doi: 10.1016/j.jnoncrysol.2014.04.002

McMillan, P., and Piriou, B. (1982). The structures and vibrational spectra of crystals and glasses in the silica-alumina system. *J. Non Crystal. Solids* 53, 279–298. doi: 10.1016/0022-3093(82)90086-2

Mysen, B. (1998). Phosphorus solubility mechanisms in haplogranitic aluminosilicate glass and melt: Effect of temperature and aluminum content. *Contrib. Mineral. Petrol.* 133, 38–50. doi: 10.1007/s004100050435

Mysen, B. (1999). Structure and properties of magmatic liquids: From haplobasalt to haploandesite. *Geochimica et Cosmochimica Acta* 63, 95–112. doi: 10.1016/S0016-7037(98)00273-7

Mysen, B., and Toplis, M. (2007). Structural behavior of Al^{3+} in peralkaline, metaluminous, and peraluminous silicate melts and glasses at ambient pressure. *Am. Mineral.* 92, 933–946. doi: 10.2138/am.2007.2334

Neuville, D., De Ligny, D., and Henderson, G. (2014). Advances in Raman SPECTROSCOPY APPLIED TO EARTH AND MATERIAL SCIENCES. *Rev. Mineral. Geochem.* 78, 509–541. doi: 10.2138/rmg.2013.78.13

Neuville, D., and Mysen, B. (1996). Role of aluminium in the silicate network: *in situ*, high-temperature study of glasses and melts on the join SiO2-NaAlO2. *Geochimica et Cosmochimica Acta* 60, 1727–1737. doi: 10.1016/0016-7037(96)00049-X

Nizamutdinova, A., Uesbeck, T., Grammes, T., Brauer, D.S., and Van Wüllen, L. (2020). Structural role of phosphate in metaluminous sodium aluminosilicate glasses as studied by solid state NMR spectroscopy. *J. Phys. Chem. B* 124, 2691–2701. doi: 10.1021/acs.jpcb.9b11403

Nkurunziza, G., Debaiky, A., Cousin, P., and Benmokrane, B. (2005). Durability of GFRP bars: a critical review of the literature. *Prog. Struc. Eng. Mater.* 7, 194–209. doi: 10.1002/pse.205

Oliver, W., and Pharr, G. (1992). An improved technique for determining hardness and elastic modulus using load and displacement sensing indentation experiments. *J. Mater. Res.* 7, 1564–1583. doi: 10.1557/JMR.1992.1564

Palles, D., Konidakis, I., Varsamis, C., and Kamitsos, E. (2016). Vibrational spectroscopic and bond valence study of structure and bonding in Al_2O_3-containing AgI - $AgPO_3$ glasses. *RSC Adv.* 6, 16697–16710. doi: 10.1039/C6RA00162A

Poe, B., Romano, C., Zotov, N., Cibin, G., and Marcelli, A. (2001). Compression mechanisms in aluminosilicate melts: Raman and XANES spectroscopy of glasses quenched from pressures up to 10 GPa. *Chem. Geol.* 174, 21–31. doi: 10.1016/S0009-2541(00)00304-1

Rabia, M., Degioanni, S., Martinet, C., Le Brusq, J., Champagnon, B., and Vouagner, D. (2016). A-thermal elastic behavior of silicate glasses. *J. Phys. Cond. Matter.* 28:075402. doi: 10.1088/0953-8984/28/7/075402

Ray, N. (1974). Composition-property relationships in inorganic oxide glasses. *J. Non Crystal. Solids* 15, 423–434. doi: 10.1016/0022-3093(74)90148-3

Rouxel, T. (2006). Elastic properties of glasses: a multiscale approach. *Comptes Rendus Mécanique* 334, 743–753. doi: 10.1016/j.crme.2006.08.001

Rouxel, T. (2007). Elastic properties and short-to medium-range order in glasses. *J. Am. Ceramic Soc.* 90, 3019–3039. doi: 10.1111/j.1551-2916.2007.01945.x

Rouxel, T., Ji, H., Hammouda, T., and Moréac, A. (2008). Poisson's ratio and the densification of glass under high pressure. *Phys. Rev. Lett.* 100:225501. doi: 10.1103/PhysRevLett.100.225501

Ryerson, F., and Hess, P. (1980). The role of P_2O_5 in silicate melts. *Geochimica et Cosmochimica Acta* 44, 611–624. doi: 10.1016/0016-7037(80)90253-7

Salmon, P., and Zeidler, A. (2015). Networks under pressure: the development of *in situ* high-pressure neutron diffraction for glassy and liquid materials. *J. Phys. Cond. Matter.* 27:133201. doi: 10.1088/0953-8984/27/13/133201

Sathishkumar, T., Satheeshkumar, S., and Naveen, J. (2014). Glass fiber-reinforced polymer composites - a review. *J. Reinforced Plastics Composites* 33, 1258–1275. doi: 10.1177/0731684414530790

Sawamura, S., and Wondraczek, L. (2018). Scratch hardness of glass. *Phys. Rev. Mater.* 2:092601. doi: 10.1103/PhysRevMaterials.2.092601

Sawangboon, N., Nizamutdinova, A., Uesbeck, T., Limbach, R., Meechoowas, E., Tapasa, K., et al. (2020). Modification of silicophosphate glass composition, structure and properties via crucible material and melting conditions. *Int. J. Appl. Glass Sci.* 11, 46–57. doi: 10.1111/ijag.13958

Seifert, F., Mysen, B., and Virgo, D. (1982). Three-dimensional network structure of quenched melts (glass) in the systems SiO_2-$NaAlO_2$, SiO_2-$CaAl_2O_4$ and SiO_2-$MgAl_2O_4$. *Am. Mineral.* 67, 696–717.

Sellappan, P., Rouxel, T., Celarie, F., Becker, E., Houizot, P., and Conradt, R. (2013). Composition dependence of indentation deformation and indentation cracking in glass. *Acta Materialia* 61, 5949–5965. doi: 10.1016/j.actamat.2013.06.034

Sen, P., and Thorpe, M. (1977). Phonons in AX2 glasses: From molecular to band-like modes. *Phys. Rev. B* 15, 4030–4038. doi: 10.1103/PhysRevB.15.4030

Shannon, R. (1976). Revised effective ionic radii and systematic studies of interatomic distances in halides and chalcogenides. *Acta Crystallographica A* 32, 751–767. doi: 10.1107/S0567739476001551

She, J., Sawamura, S., and Wondraczek, L. (2019). Scratch hardness of rare-earth substituted calcium aluminosilicate glasses. *J. Non Crystal. Solids X* 1:100010. doi: 10.1016/j.nocx.2019.100010

Smedskjaer, M., Mauro, J., Kjeldsen, J., and Yue, Y. (2013). Microscopic origins of compositional trends in aluminosilicate glass properties. *J. Am. Ceramic Soc.* 96, 1436–1443. doi: 10.1111/jace.12298

Smith, C., Brow, R., Montagne, L., and Revel, B. (2014). The structure and properties of zinc aluminophosphate glasses. *J. Non Crystal. Solids* 386, 105–114. doi: 10.1016/j.jnoncrysol.2013.11.042

Sonneville, C., Mermet, A., Champagnon, B., Martinet, C., Margueritat, J., De Ligny, D., Deschamps, T., and Balima, F. (2012). Progressive transformations of silica glass upon densification. *J. Chem. Phys.* 137, 124505. doi: 10.1063/1.4754601

Sun, K.-H. (1947). Fundamental Condition of Glass Formation. *J. Am. Ceramic Soc.* 30, 277–281. doi: 10.1111/j.1151-2916.1947.tb19654.x

Tabor, D. (1970). The hardness of solids. *Rev. Phys. Technol.* 1, 145–179. doi: 10.1088/0034-6683/1/3/I01

Tagiara, N., Palles, D., Simandiras, E., Psycharis, V., Kyritsis, A., and Kamitsos, E. (2017). Synthesis, thermal and structural properties of pure TeO_2 glass and zinc-tellurite glasses. *J. Non Crystal. Solids* 457, 116–125. doi: 10.1016/j.jnoncrysol.2016.11.033

Tarragó, M., Esteves, H., Garcia-Valles, M., Martínez, S., and Neuville, D. (2018a). Effect of Ca in P-doped basaltic glass-ceramics: application to waste inertization. *Mater. Lett.* 220, 266–268. doi: 10.1016/j.matlet.2018.03.020

Tarragó, M., Garcia-Valles, M., Martínez, S., and Neuville, D. (2018b). Phosphorus solubility in basaltic glass: limitations for phosphorus immobilization in glass and glass-ceramics. *J. Environ. Manag.* 220, 54–64. doi: 10.1016/j.jenvman.2018.04.079

Tiegel, M., Hosseinabadi, R., Kuhn, S., Herrmann, A., and Rüssel, C. (2015). Young's modulus, vickers hardness and indentation fracture toughness of alumino silicate glasses. *Ceramics Int.* 41, 7267–7275. doi: 10.1016/j.ceramint.2015.01.144

Toplis, M., and Schaller, T. (1998). A MAS NMR study of glasses in the system xNa_2O-$(1-x)Al_2O_3$-$2SiO_2$-yP_2O_5. *J. Non Crystal. Solids* 224, 57–68. doi: 10.1016/S0022-3093(97)00458-4

Tylkowski, M., and Brauer, D. (2013). Mixed alkali effects in Bioglass® 45S5. *J. Non Crystal. Solids* 376, 175–181. doi: 10.1016/j.jnoncrysol.2013.05.039

Veber, A., Cicconi, M. R., Reinfelder, H., and De Ligny, D. (2018). Combined differential scanning calorimetry, Raman and brillouin spectroscopies: a

multiscale approach for materials investigation. *Analytica Chimica Acta* 998, 37–44. doi: 10.1016/j.aca.2017.09.045

Weigel, C., Le Losq, C., Vialla, R., Dupas, C., Clément, S., Neuville, D. R., et al. (2016). Elastic moduli of $XAlSiO_4$ aluminosilicate glasses: effects of charge-balancing cations. *J. Non Crystal. Solids* 447, 267–272. doi: 10.1016/j.jnoncrysol.2016.06.023

Whitfield, C., Brody, E., and Bassett, W. (1976). Elastic moduli of NaCl by Brillouin scattering at high pressure in a diamond anvil cell. *Rev. Sci. Inst.* 47, 942–947. doi: 10.1063/1.1134778

Winterstein-Beckmann, A., Möncke, D., Palles, D., Kamitsos, E., and Wondraczek, L. (2014). Raman spectroscopic study of structural changes induced by micro-indentation in low alkali borosilicate glasses. *J. Non Crystal. Solids* 401, 110–114. doi: 10.1016/j.jnoncrysol.2013.12.038

Wondraczek, L. (2019). Overcoming glass brittleness. *Science* 366, 804–805. doi: 10.1126/science.aaz2127

Wondraczek, L., Mauro, J., Eckert, J., Kühn, U., Horbach, J., Deubener, J., et al. (2011). Towards ultrastrong glasses. *Adv. Mater.* 23, 4578–4586. doi: 10.1002/adma.201102795

Zehnder, C., Bruns, S., Peltzer, J.-N., Durst, K., Korte-Kerzel, S., and Möncke, D. (2017). Influence of cooling rate on cracking and plastic deformation during impact and indentation of borosilicate glasses. *Front. Mater.* 4:5. doi: 10.3389/fmats.2017.00005

Zeidler, A., Salmon, P., and Skinner, L. (2014). Packing and the structural transformations in liquid and amorphous oxides from ambient to extreme conditions. *Proceedings of the National Academy of Sciences of the United States of America* 111, 10045–10048. doi: 10.1073/pnas.1405660111

Zeng, H., Wang, L., Ye, F., Yang, B., Chen, J., Chen, G., and Sun, L. (2016). Mechanical-Structural Investigation of Chemical Strengthening Aluminosilicate Glass through Introducing Phosphorus Pentoxide. *Front. Mater.* 3:53. doi: 10.3389/fmats.2016.00053

Conflict of Interest: The authors declare that the research was conducted in the absence of any commercial or financial relationships that could be construed as a potential conflict of interest.

frontiers in Materials

ORIGINAL RESEARCH
published: 15 May 2020
doi: 10.3389/fmats.2020.00085

Water in Alkali Aluminosilicate Glasses

Robert Balzer[1], Harald Behrens[1], Tina Waurischk[2], Stefan Reinsch[2], Ralf Müller[2], Philipe Kiefer[3], Joachim Deubener[3] and Michael Fechtelkord[4]*

[1] Institute of Mineralogy, Leibniz University Hannover, Hanover, Germany, [2] Bundesanstalt für Materialforschung und -prüfung (BAM), Division Glass, Berlin, Germany, [3] Institute of Non-Metallic Materials, Clausthal University of Technology, Clausthal-Zellerfeld, Germany, [4] Mineralogy and Geophysics, Institute of Geology, Ruhr-University Bochum, Bochum, Germany

To understand the influence of water and alkalis on aluminosilicate glasses, three polymerized glasses with varying ratios of Na/K were synthesized [(22. 5-*x*)Na_2O-*x*K_2O-22.5 Al_2O_3-55 SiO_2 with $x = 0$, 7.5, and 11.25]. Subsequently, these glasses were hydrated (up to 8 wt% H_2O) in an internally heated gas pressure vessel. The density of hydrous glasses linearly decreased with water content above 1 wt%, consistent with the partial molar volume of H_2O of 12 cm^3/mol. Near-infrared spectroscopy revealed that hydroxyl groups are the dominant species at water content of <4 wt%, and molecular water becomes dominating at water content of >5 wt%. The fraction of OH is particularly high in the pure Na-bearing glass compared to the mixed alkali glasses. ^{27}Al magic angle spinning-NMR spectroscopy shows that aluminum is exclusively fourfold coordinated with some variations in the local geometry. It appears that the local structure around Al becomes more ordered with increasing K/Na ratio. The incorporation of H_2O reinforces this effect. The differential thermal analysis of hydrous glasses shows a significant mass loss in the range of glass transition already during the first upscan, implying the high mobility of water in the glasses. This observation can be explained by the open structure of the aluminosilicate network and by the low dissociation enthalpy of H_2O in the glasses (≈ 8 kJ/mol). The effect of the dissolved H_2O on the glass transition temperature is less pronounced than for other aluminosilicate glasses, probably because of the large fraction of Al in the glasses.

Keywords: alkali aluminosilicate glasses, water speciation, glass transition, infrared spectroscopy, NMR spectroscopy

OPEN ACCESS

Edited by:
Randall Youngman, Corning Inc., United States

Reviewed by:
Jonathan Stebbins, Stanford University, United States
Jingshi Wu, Corning Inc., United States

***Correspondence:**
Harald Behrens
h.behrens@mineralogie.uni-hannover.de

Specialty section:
This article was submitted to Ceramics and Glass, a section of the journal Frontiers in Materials

Received: *10 January 2020*
Accepted: *24 March 2020*
Published: *15 May 2020*

Citation:
Balzer R, Behrens H, Waurischk T, Reinsch S, Müller R, Kiefer P, Deubener J and Fechtelkord M (2020) Water in Alkali Aluminosilicate Glasses. Front. Mater. 7:85. doi: 10.3389/fmats.2020.00085

INTRODUCTION

Alkali aluminosilicate glasses are a class of materials that is widely used in commercial applications as chemical strengthened cover glass for consumer electronics (Scholze, 1988; Ellison and Gomez, 2010; Varshneya, 2010a,b; Allan et al., 2013). Furthermore, these systems constitute more than 50% of natural rhyolitic and granitic magmas (Tuttle and Bowen, 1958; Johannes and Holtz, 1996). Of particular interest is the Na_2O-Al_2O_3-SiO_2 (NAS) system because, on the one hand, sodium ions are highly mobile in ion-exchange processes used for chemical strengthening and, on the other hand, this system contains a number of geologically important minerals such as albite, jadeite, and nepheline (Toplis et al., 1997a). Thus, it has often been used as a model system for granitic magmas.

The structure and thus the related properties of aluminosilicate glasses and melts mainly depend on the ratio between Al and the charge-balancing network modifier (e.g., Na) as this determines the

degree of polymerization of the structure (Mysen and Richet, 2018). In subaluminous compositions (Na/Al = 1), all Al^{3+} is charge-balanced by alkali, and the structure basically consists of a fully polymerized network of SiO_4 and AlO_4 tetrahedra (Mysen et al., 1981; Toplis et al., 2000). However, as shown by ^{17}O NMR spectroscopy for K_2O-Al_2O_3-SiO_2 (KAS) glasses with 60 mol% SiO_2, the subaluminous compositions may contain non-bridging oxygen on the 1% level (Thompson and Stebbins, 2011).

In peralkaline compositions (Na/Al > 1), the excess of alkali relative to aluminum causes a depolymerization of the network with formation of non-bridging oxygen (Toplis et al., 1997a). In peraluminous compositions (Na/Al < 1), the amount of alkali is insufficient for the charge compensation of Al^{3+} in tetrahedral coordination, and aluminum can have a network-modifying role as indicated by the highly coordinated AlO_5 and AlO_6 species (Mysen et al., 1981; Toplis et al., 1997a; Doweidar, 1998). Additionally, as suggested by Lacy (1963) and others (Toplis et al., 2000; Kuryaeva, 2004; Xue and Kanzaki, 2007), the excess Al^{3+} may form triclusters with three AlO_4 tetrahedra sharing a common oxygen atom. Furthermore, it was found that the type of charge-balancing cation affects the formation of non-bridging oxygen and thus the degree of polymerization. For instance, for subaluminous compositions, it was found that the abundance of non-bridging oxygen increases in alkaline earth aluminosilicates compared to that in alkali aluminosilicate glasses (Wu and Stebbins, 2009; Mysen and Richet, 2018).

Dissolving water in glasses and melts can dramatically affect their physical and mechanical properties. For example, small amounts of water can strongly reduce the viscosity and enhance the rates of structural relaxation and phase separation in melts (Zhang et al., 2003; Whittington et al., 2004; Del Gaudio et al., 2007; Zietka et al., 2007). Furthermore, the mechanical strength and fatigue resistance of glasses can be lowered (Wiederhorn, 1967; Lee and Tomozawa, 1999). In silicates and aluminosilicates, the effect of water on physical properties was found to be rather similar to that of alkali oxides (Shaw, 1963; Dingwell et al., 1996). On the other hand, in borate glasses, protons play a very different role compared to alkali cations due to the weaker Si-O-B bonds compared to the Si-O-Al bonds and due to the strong localization of protons at single oxygen (Reinsch et al., 2016).

It is well known that water in glasses occurs as hydroxyl groups and as molecular water (Scholze, 1960; Stolper, 1982a; Stuke et al., 2006). In melts, the interaction between molecular water and hydroxyl groups can be described by the following homogeneous reaction:

$$H_2O_{(melt)} + O_{(melt)} \leftrightarrow 2OH_{(melt)} \quad (1)$$

where O is an anhydrous oxygen. Assuming an ideal mixing of H_2O, O, and OH species, the equilibrium constant K for the above reaction is:

$$K = \frac{[OH]^2}{[H_2O][O]} \quad (2)$$

where the square brackets indicate mole fractions calculated on a single-oxygen basis. As shown in several papers on aluminosilicates, the measured water speciation in glasses at room temperature corresponds to the equilibrium water speciation in the melt, frozen-in at the fictive temperature (T_f) during cooling (Dingwell and Webb, 1990; Zhang et al., 1995; Behrens and Stuke, 2003).

The OH and H_2O species behave differently within the network structure of glasses and melts (Behrens et al., 2007). Therefore, not only the quantification of water species but also the understanding of the mechanisms of incorporation of water in the silicate structure is of great importance for both material and earth sciences.

The present study is devoted to the investigation of the influence of different charge-balancing cations as well as the effect of water on the structure of aluminosilicate glasses. Three different glasses (22.5-x)Na_2O-xK_2O-22.5Al_2O_3-55SiO_2 (x = 0, 7.5, and 11.25) were prepared, wherein Na_2O was successively substituted by K_2O. These glasses have high Al/Si ratios, close to 1. A comparison with literature data for other polymerized glasses with low Al/Si ratios [*e. g.*, albite ($NaAlSi_3O_8$) with Al/Si = 0.33 or the natural alkali aluminosilicate rhyolite with Al/Si ≈ 0.20] allows conclusions about the effect of Al/Si ratio on glass and melt properties. The variation of water content of these highly polymerized glasses was achieved by high pressure–high temperature synthesis using an internally heated pressure vessel (IHPV). Fourier-transform infrared (FTIR) spectroscopy and nuclear magnetic resonance (NMR) spectroscopy were performed to analyze the speciation of dissolved water and the structural changes of the glass network upon hydration. The glass transition was studied using differential thermal analysis (DTA), providing also information about the mobility of hydrous species in the glass structure. These findings about the interaction of water with the glass structures may improve our understanding of corrosion as well as the crack propagation mechanisms of glasses.

EXPERIMENTAL AND ANALYTICAL METHODS

Starting Materials

Three aluminosilicate glasses were prepared using Na_2CO_3, K_2CO_3, Al_2O_3, and SiO_2 powders. These powders were carefully mixed using a 3D shaker mixer (Turbula®, WAB, Switzerland) and filled into a Pt-Rh10 crucible before melting in a chamber furnace. The temperature was raised to 1,973 K (NAS glass) and 2,023 K (NKAS glasses), respectively, and kept for 2 h. Afterwards, the melts were quenched by pouring them into water. To achieve good homogeneity, the glasses were crushed, re-melted, and quenched–poured onto a graphite plate. Clear bubble-free glasses were obtained by this method.

The bulk composition of the air-melted glasses was analyzed by X-ray fluorescence spectrometry (XRF; PANalytical MagiX PRO, Almelo, Netherlands) equipped with a 4-kW Rh tube. For calibration, standard glasses NIST 1412, NIST 1411, NRS 93a, NBS 620, and BAM S005b were used.

To verify the XRF analyses, the bulk compositions were additionally measured using electron microprobe analyses (EMPA). The measurements were performed using a Cameca

SX-100 microprobe, and each glass was analyzed at 50 different positions to probe its homogeneity. The measurement conditions included a beam current of 15 nA, an acceleration voltage of 15 kV, a defocused beam of 5-μm spot size, and counting times of 10 to 20 s. Similar values were obtained by both analytical methods (**Table S1**) and revealed that all glasses have a slight excess of alkalis [(Na+K)/Al ratio >1]. The EMPA measurements further provide evidences that the glasses are homogeneous over several millimeters.

Synthesis of Hydrated and Compacted Glasses

Hydrated glasses with H_2O contents up to 8 wt% were synthesized in platinum capsules (25 mm in length and inner diameter of 6 mm). The water contents were always below the solubility limits at synthesis conditions. To achieve homogeneous initial water distribution, glass powder, and distilled water were alternately filled into the capsules. The powder–water mixture was compacted with a steel piston between loading steps to minimize air bubble inclusion. To obtain a cylindrical shape, round platinum lids were welded onto the open end of the capsules after loading. The capsules were heated in a drying oven at 373 K for several hours and subsequently weighed to test for possible leakage.

Syntheses were performed in an IHPV at 500 MPa and 1,523–1,873 K for 20 h using Ar as pressure medium. Two different setups were used depending on the desired water content of the glasses. For water-poor glass (up to 4 wt% H_2O), a high temperature (HT) equipment was used and single capsules were hung up with a platinum wire in the hot zone of the sample holder (controlled by S-type thermocouples). The liquidus of the water-rich glasses (> 4 wt% H_2O) is low enough that these samples could be synthesized in the normal temperature (NT) device controlled by K-type thermocouples. Here up to three capsules have been placed in the hot zone of the sample holder. In both cases, the samples were quenched isobarically to avoid pressure-induced structural changes and to prevent water loss from the hydrated glasses. The cooling rates in the glass transition region were 6–7 K/s for the HT device and ∼3.5 K/s for the NT device. A detailed description of the vessel and procedures is given by Berndt et al. (2002).

All hydrous glass cylinders were transparent and contained neither bubbles nor crystals. To check for homogeneity of the water distribution in the glasses, ∼5-mm-thick slices were cut from both ends of the cylinders and subsequently analyzed by Karl–Fischer titration (KFT).

To study the effect of pressurization on glass properties, the anhydrous glasses were compacted in the range of glass transition using a cold seal pressure vessel (CSPV) with Ar as pressure medium (Wondraczek and Behrens, 2007). Producing such compacted water-poor glasses from melts in an IHPV was not possible due to the high melting temperatures (1,973–2,023 K). For compaction, cylindrical samples were drilled out of the glasses and placed in a CSPV. Pressure of 500 MPa was applied to the samples before the pre-heated furnace was pulled over the autoclave. The temperature was increased to 15 K above T_g (based on DTA measurements on starting glasses) and kept for 30 min. Afterwards, the autoclave was removed from the furnace and cooled with a compressed air bell whereby the pressure was kept constant by manual pumping. The initial cooling rate was typically 3 K/s for this procedure. All compacted glass cylinders were transparent and show no visible changes to their appearance.

Density Determination

The density of dry and of hydrous glasses was determined by the buoyancy method. In doing so, the weight of single pieces (100–500 mg in mass) was measured in air and in ethanol.

Karl–Fischer Titration

The total water content of hydrous glasses was determined by pyrolysis and subsequently by KFT as described in Behrens (1995), Behrens et al. (1996), and Behrens and Stuke (2003). For the analysis, ca. 10–15 mg of glass fragments was loaded into small platinum crucibles and heated up rapidly to 1,573 K. To avoid an explosive release of H_2O during heating, they were pressed firmly together at the top. The results are shown in **Table S2**.

Differential Thermal Analysis

The fictive temperature, T_f, and the glass transition temperature, T_g, were determined by DTA in air using 10–20 mg of glass pieces placed in Pt crucibles (thermobalance TAG 24 Setaram, Caluire, France). In order to register a possible loss of water, the thermal gravimetric (TG) signal was simultaneously recorded during DTA measurements. The same type of analysis and data evaluation was applied, e.g., to hydrous borate (Bauer et al., 2015; Reinsch et al., 2016) and phosphate (Balzer et al., 2019) glasses.

In general, four heating and cooling cycles at 10 K min^{-1} were applied. The first heating cycle was used to determine the fictive temperature T_f of the glasses since the initial state of the glasses represents the cooling history during synthesis. The T_g of nominally dry glasses was determined by the following three cycles. The definition of T_f and T_g is based on the onset of the endothermic step in the DTA curve according to Mazurin (2007) and Mazurin and Gankin (2007). For hydrous samples, only T_f could be determined because a massive loss of water occurred during the first upscan. The T_f values and the average values of T_g (anhydrous glasses) are shown in **Table S2** and are similar to the values of albite glasses (1,007–1,068 K) reported in Arndt and Häberle (1973), Toplis et al. (1997b), and Whittington et al. (2004). The large scatter of the T_g values of albite glasses is probably due to the small deviations from Na/Al =1.

Infrared Spectroscopy

The network structure of the glasses was investigated by mid-infrared (MIR) spectroscopy of KBr-pressed pellets in the range from 370 to 4,000 cm^{-1} using an FTIR spectrometer (Bruker Vertex 80v). The spectrometer is equipped with a globar light source, a KBr beam splitter, and a pyroelectric deuterated, L-alanine-doped triglycerine sulfate detector. One milligram of glass powder and 199 mg KBr were mixed and pressed into a pellet at 100 kN. A pure KBr pellet was measured as reference

to examine the contribution of contamination of KBr to the spectrum in the range of OH stretching vibrations.

Additionally, mid-infrared spectra have been measured on glass sections polished on both sides using an FTIR spectrometer (Bruker IFS 88) to investigate the fundamental OH stretching vibrations. The spectrometer is linked with an IR microscope Bruker IR scope II equipped with a mercury–cadmium–tellurium detector. Absorption spectra were measured in the range between 600 and 6,000 cm^{-1} with a spectral resolution of 2 cm^{-1} using a KBr beam splitter and a globar light source. For each sample and background (air) measurement, 50 scans were accumulated.

Near-infrared (NIR) spectra were recorded on thick sections (ca. 300 μm) to analyze the speciation of dissolved water in the glasses. The same setup was applied as for the MIR measurements on thin sections, except that a tungsten light source and a CaF_2 beam splitter were used. The spectral resolution was 4 cm^{-1}, and 100 scans were accumulated for each spectrum. To test the homogeneity of water distribution, sections were prepared from the top and the bottom of the synthesized glass body, and each sample was analyzed at least three times at different positions. Sample thickness was determined using a digital micrometer (Mitutoyo Absolute) with a precision of ±2 μm.

^{27}Al Magic Angle Spinning-NMR Spectroscopy

To analyze the Al coordination in the glasses, ^{27}Al magic angle spinning (MAS)-NMR spectra were acquired on selected samples (anhydrous and with 8 wt% H_2O) at room temperature using a Bruker ASX 400 WB spectrometer. Measurements were performed at a Larmor frequency of 104.27 MHz using a standard Bruker 4-mm probe with a spinning speed of 12.5 kHz. $AlCl_3$ (1 M) was processed as a secondary reference standard. To ensure homogeneous excitation, a single pulse duration of 0.6 μs was applied. The recycle delay was 0.1 s, and 16,000 scans were accumulated. ^{27}Al spectra were processed using the DMFit 2015 program (Massiot et al., 2002).

RESULTS

Water Distribution in the Glasses

The difference in water content at the bottom and at the top of the glass body is small for glasses with <4 wt% H_2O and often close to the analytical error (**Table S2**). In contrast, the deviation is more distinct in some samples with water content above 4 wt%. These deviations could be the result of an initial inhomogeneous water distribution during the sample preparation. The diffusion data reviewed by Zhang and Ni (2010) indicate that water diffusion in aluminosilicate melts is too slow to achieve a homogeneous water distribution over distances longer than 1 cm within the synthesis times.

In the following, we refer to the average of the KFT data for a discussion of the results of bulk methods (e.g., density and NMR spectroscopy). For methods with high spatial resolution (i.e., IR spectroscopy), however, the KFT measurements on adjacent pieces are used.

Density

The densities of anhydrous glasses compacted at 500 MPa are about 1% higher than the glasses melted at ambient pressure (**Table S2**, **Figure 1A**). This increase in density upon compression is similar to that of silicate and aluminosilicate glasses reported by Wondraczek and Behrens (2007), Wondraczek et al. (2009). The addition of 1 wt% H_2O induced a slight increase in the density of NAS and NKAS(1:1) glasses but a small decrease in the case of NKAS(2:1) glass. At higher water content, all three glasses show a linear dependence of density on water content, consistent with the ideal mixing of oxide component with H_2O component. According to Richet et al. (2000), the partial molar volume of water can be directly obtained by extrapolation of the tangents in **Figure 1B** to 100 mol% H_2O. The derived molar volumes (NAS: 11.8 ± 0.1 cm^3 mol^{-1}, NKAS(2:1): 12.0 ± 0.1 cm^3 mol^{-1}, and NKAS(1:1): 12.1 ± 0.2 cm^3 mol^{-1}) are in excellent agreement with the values reported for silicate and aluminosilicate glasses (11.5–12.5 cm^3 mol^{-1}; Richet et al., 2000).

Differential Thermal Analysis-Thermal Gravimetric Measurements

Repeated DTA–TG measurements on dry glasses show good reproducibility, although the endothermic step at the glass transition is very weak. An example is given in **Figure 2A**. Due to the less pronounced effects at the glass transition, the determination of T_f and T_g has higher uncertainty than commonly reported for other glasses. Based on reproducibility, we estimate the error to be below ±10 K.

As mentioned above, only the fictive temperatures could be determined for hydrous glasses because of the dramatic decrease in the TG signal in the regime of T_f or shortly above. Microscopic inspection gives evidence for bubble formation in some of the post-DTA samples, but not in all. Another mechanism for water release may be spontaneous crack formation as observed with hydrous albitic glasses during heating below the glass transition (Indris et al., 2005).

Results for NKAS(2:1) are displayed in **Figure 2**. A T_f value of 984 K was determined for the glass containing 1 wt% H_2O. At already 10 K above this temperature, a dramatic decrease in TG by around 0.5 wt% occurred within a very small temperature interval. At 2 wt% H_2O, T_f was found to be at 864 K and the massive decrease of TG starts immediately (**Figure 2C**). At 4 wt% (**Figure 2D**) and 6 wt% H_2O (**Figure 2E**), T_f is at 707 and 634 K, respectively, and the loss of mass is around 20 K higher. Here it can be possible to distinguish between the endothermic step of T_f and the endothermic peak caused by the release of water. Similar trends were observed in the other hydrous glasses [NAS and NKAS(1:1)]. At higher water content (8 wt%), the DTA curves show large irregularities and T_f cannot be constrained. Considering these problems, it is clear that the fictive temperature of hydrous glasses has a very large error, which we estimate to be about 15%.

Mid-Infrared Spectroscopy

The MIR spectra of the aluminosilicate glasses [NAS, NKAS(2:1), and NKAS(1:1)] in KBr-pressed pellets are shown in **Figure 3**.

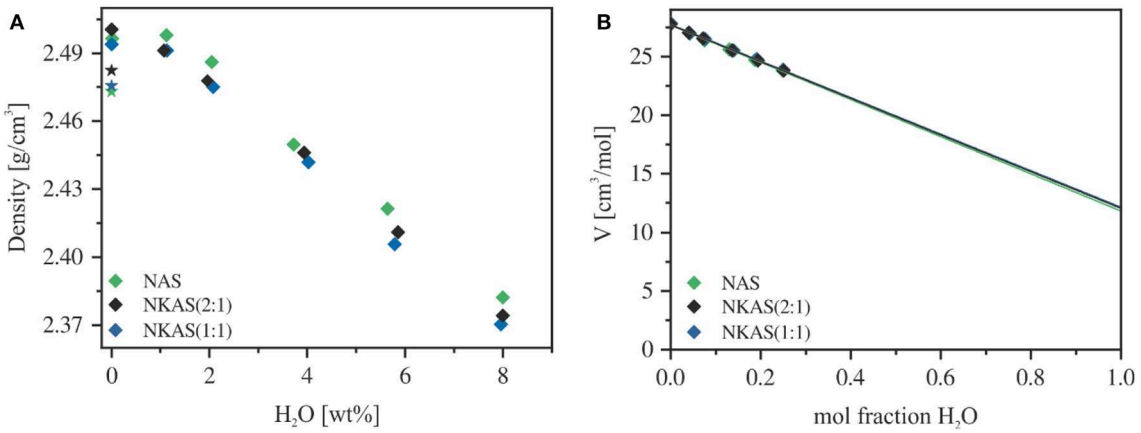

FIGURE 1 | Density **(A)** and molar volume **(B)** of aluminosilicate glasses. The air-melted glasses are represented by a star and the compacted glasses (500 MPa) by diamonds. Errors are smaller than the symbol size.

The spectra can be divided into two regions. The first region comprises lattice vibrations in the range between 400 and 1,250 cm^{-1}, while the second region originates from OH stretching vibration in the range between 3,250 and 3,700 cm^{-1} (Stolper, 1982a,b).

In the first region, three main bands are clearly visible. The absorption band at ∼450 cm^{-1} is related to the bending vibrations of Si–O–Si and Si–O–Al linkages (Handke and Mozgawa, 1993; Sroda and Paluszkiewicz, 2008). The ∼700 cm^{-1} band is caused by the symmetric stretching vibrations of Si–O–Al bonds between SiO_4 and AlO_4 tetrahedra (Tarte, 1967; Handke and Mozgawa, 1993; Handke et al., 1994; Sroda and Paluszkiewicz, 2008), while the band at ∼1,000 cm^{-1} corresponds to the asymmetric stretching vibration of Si–O–Al bonds (Handke and Mozgawa, 1993; Handke et al., 1994; Stoch and Sroda, 1999; Sroda and Paluszkiewicz, 2008).

A closer look at the band structures in this region reveals some differences in peak position and shape. For instance, the bands at ∼450 and ∼700 cm^{-1} in anhydrous glasses shift slightly to lower wavenumbers when Na is substituted by K. On the other hand, the position of the 1,000 cm^{-1} band is the same in all three anhydrous glasses.

The addition of water results in some changes in the structure of the MIR bands. In pure sodium aluminosilicate glasses (**Figure 3A**), the peak at 458 cm^{-1} (dry glass) shifts to 448 cm^{-1} (8 wt%) and its intensity decreases, while the peak at 702 cm^{-1} (dry glass) shifts to 708 cm^{-1} (8 wt%). The intensity of the latter remains unchanged. The peak position and the intensity of the 1,000 cm^{-1} band is constant, but at water contents above 4 wt% a shoulder at ∼854 cm^{-1} appears that is probably related to SiOH groups (Acocella et al., 1984; Rüscher et al., 2011). In addition, a small peak at 575 cm^{-1} evolves at water contents above 4 wt%. According to Tarte (1967), Handke et al. (1994), and Sroda and Paluszkiewicz (2008), this peak is related to the stretching vibrations of the four- and the six-membered ring systems of Si–O and Al–O tetrahedra.

Similar trends upon hydration are visible in NKAS(2:1) and NKAS(1:1) glasses (**Figures 3B,C**). The addition of water results in a peak shift and a decrease of intensity of the 456 cm^{-1} band (dry glass) to 446 cm^{-1} (8 wt%) [NKAS(2:1)] and from 454 to 444 cm^{-1} [NKAS(1:1)], respectively. In NKAS(2:1) glasses, the band of the symmetric stretching vibration of Si–O–Al bonds shifts from 698 cm^{-1} (dry glass) to 706 cm^{-1} (8 wt%). In NKAS(1:1) glasses, this peak shifts from 696 cm^{-1} (dry glass) to 704 cm^{-1} (8 wt%). At 4 wt% H_2O, the SiOH-related shoulder is visible at 852 cm^{-1} [NKAS(2:1)] and 850 cm^{-1} [NKAS(1:1)], respectively, while the peak position and the intensity of the main absorption band at 996 cm^{-1} do not change. As in NAS glasses, a peak at 575 cm^{-1} becomes visible. These features are more pronounced in the mixed alkali glasses (**Figures 3B,C**) than in the sodium aluminosilicate glasses (**Figure 3A**).

As the water content increases, a small peak near 1,650 cm^{-1} appears, which becomes more pronounced with growing water content. According to Scholze (1960), Bartholomew et al. (1980), and Stolper (1982b), this peak is caused by the bending vibration of H_2O molecules. In the high wavenumber range, broadbands between 3,250 and 3,700 cm^{-1} are visible in all glasses, with a maximum at 3,400 cm^{-1} and a small shoulder toward lower wavenumbers. These bands are related to the OH stretching vibrations of weakly to moderately H-bound hydrous species (Scholze, 1959; Zarubin, 1999) and become more pronounced with increasing water content. However, in some cases, noticeable deviations from this trend are visible in **Figure 3**. A comparison of these bands to the spectra of pure KBr pellets shows that the pressed pellets are sensitive to water adsorption during sample preparation. This effect cannot be eliminated by the subtraction of a spectrum of pure KBr pellets since the interfaces between glass powder and salt may contribute significantly to the spectra in this range. Thus, using KBr-pressed pellets, we cannot obtain reliable information about the shape of the OH stretching vibration bands.

The spectra of thin sections (∼80 μm) do not suffer from this problem (**Figure 4**). However, due to high absorbances

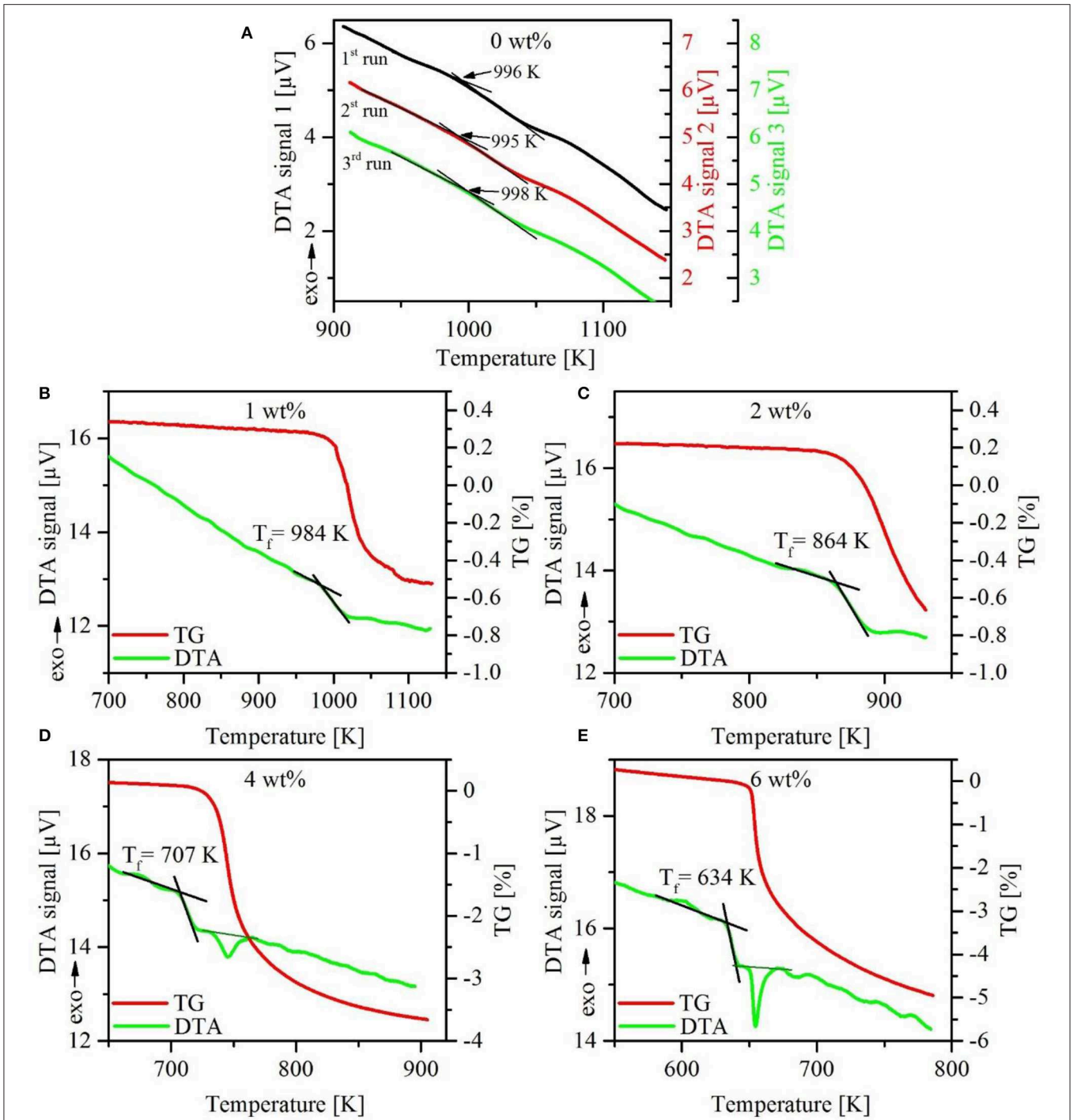

FIGURE 2 | Comparison of the first three upscans of DTA measurements on dry NKAS(2:1)$_{start}$ glass. Note the very weak endothermic signal at the glass transition **(A)**. First upscan of DTA–TG analysis of hydrous NKAS(2:1) glasses with DTA curves (green solid lines) and corresponding mass loss (red solid lines) **(B–E)**. Note the onset of dehydration close to T_f.

and difficulties in preparing sections <40 µm, the MIR spectra could be obtained only for glasses containing up to 2 wt% H_2O. In the range of OH stretching vibrations, the absorption spectra of hydrous NAS glasses resemble the spectra of other aluminosilicate glasses, (e.g., Stolper, 1982a; Jewell et al., 1993; Tamic et al., 2001; Behrens et al., 2004; Robert et al., 2013) with the peak maximum near 3,500 cm^{-1} and an asymmetric tailing toward a lower wavenumber. These features are characteristic for

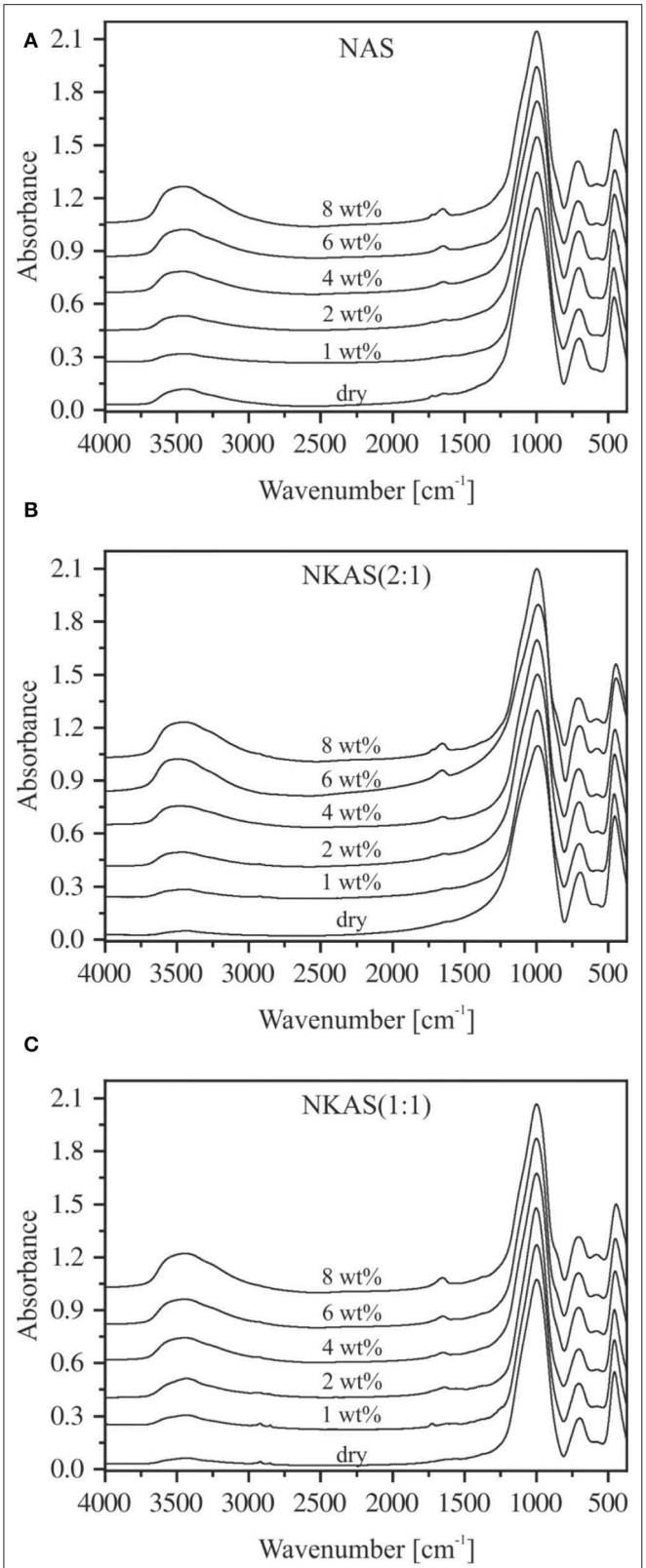

FIGURE 3 | MIR spectra of KBr-pressed pellets of NAS **(A)**, NKAS(2:1) **(B)**, and NKAS(1:1) **(C)**. The spectra were normalized to the absorption peak of ~996 cm^{-1} and shifted vertically for clarity. Nominal water contents are indicated.

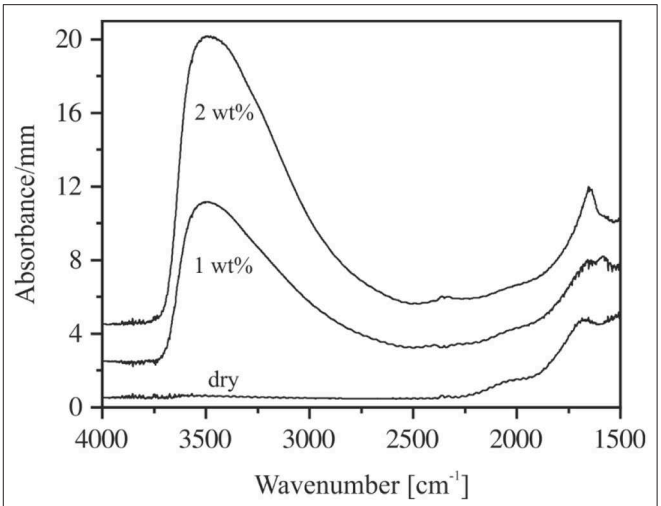

FIGURE 4 | MIR spectra of thin sections of NAS containing 0–2 wt% H_2O. The irregularities at 2,350 cm^{-1} are due to differences in CO_2 during background and sample measurements. The spectra are shifted vertically for clarity. Nominal water contents are indicated.

weakly H-bonded hydrous species in glasses (Franz and Kelen, 1966; Zarubin, 1999). At water contents above 1 wt%, the sharp bend of the bending vibrations of H_2O molecules develops at 1,650 cm^{-1}, which is superimposed by a wide broadband system originating from glass network vibrations (Bartholomew et al., 1980; Stolper, 1982a,b; Newman et al., 1986; Behrens and Stuke, 2003). The MIR spectra of NKAS(2:1) and NKAS(1:1) glasses are similar to those of NAS glasses.

In order to separate the water-related peaks from the network vibration features, the spectrum of each dry glass was subtracted from the spectra of water-bearing glasses, as shown in **Figure 5**. For glasses containing ca. 1 wt% H_2O, the peak at 1,650 cm^{-1} has noticeable intensity only for the NAS glass (**Figure 5A**). In glasses containing 2 wt% H_2O, the intensity of the H_2O bending peak is similar in all glasses.

To quantify the water contents of the nominally dry glasses (**Table 2**), the linear molar absorption coefficient for the band at 3,500 cm^{-1} (ε_{3500}) was determined using the hydrous glasses with up to 2 wt% H_2O. The basic assumption is that the absorbance at the peak maximum represents the total water content measured by KFT. This approach is justified since the shape of the OH stretching vibration does not depend on the water content. The total water content of c_{H2Ot} is given as

$$c_{H_2O_t} = \frac{1802 \cdot A_{3500}}{\rho \cdot d \cdot \varepsilon_{3500}} \quad (3)$$

where A_{3500} refers to the absorbance of the band at 3,500 cm^{-1}, ρ refers to the density in g L^{-1}, and d refers to the sample thickness (in cm). The values of ε_{3500} decrease when K is substituted for Na (**Table 1**). Compared to other aluminosilicate glasses, the ε_{3500} values are relatively low. For instance, in fully polymerized albite glasses, Silver and Stolper (1989) and Yamashita et al. (1997) determined a value for ε_{3500} of 70 L mol^{-1} cm^{-1}. For rhyolite

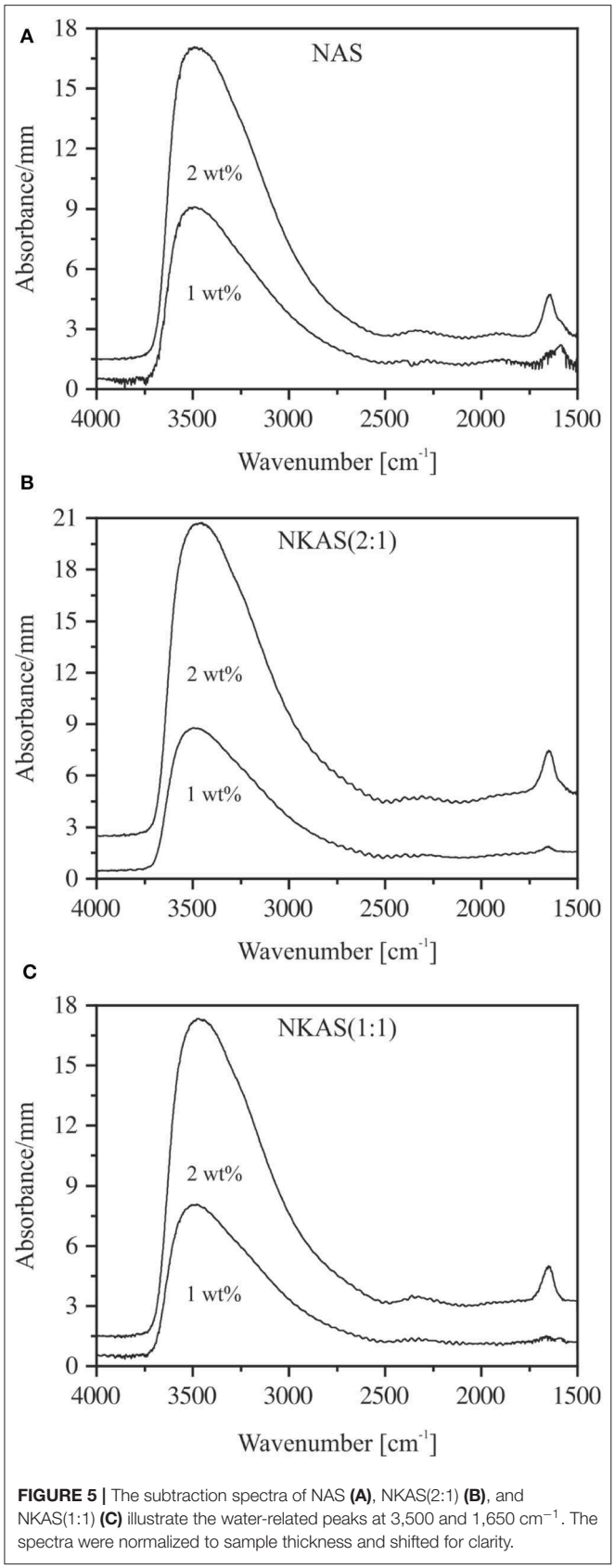

FIGURE 5 | The subtraction spectra of NAS **(A)**, NKAS(2:1) **(B)**, and NKAS(1:1) **(C)** illustrate the water-related peaks at 3,500 and 1,650 cm^{-1}. The spectra were normalized to sample thickness and shifted for clarity.

TABLE 1 | Average values of the linear molar absorption coefficient ε for water-related bands in aluminosilicate glasses.

	MIR		NIR	
	ε_{3500} (L mol^{-1} cm^{-1})	ε_{4050} (L mol^{-1} cm^{-1})	ε_{4500} (L mol^{-1} cm^{-1})	ε_{5200} (L mol^{-1} cm^{-1})
NAS	52.7 ± 2.7	0.20 ± 0.02	0.62 ± 0.15	1.03 ± 0.07
NKAS(2:1)	50.7 ± 1.9	0.18 ± 0.04	0.88 ± 0.09	0.91 ± 0.09
NKAS(1:1)	41.9 ± 3.1	0.15 ± 0.03	0.72 ± 0.06	0.90 ± 0.05

Errors represent the standard deviation (n = 3).

TABLE 2 | Full-width at half-maximum (FWHM) of ^{27}Al MAS-NMR signals (in ppm) and Hz for anhydrous and hydrous glasses.

	Nominally dry		8 wt% H_2O	
	ppm	FWHM (Hz)	Ppm	FWHM (Hz)
NAS	21.8	2,273	14.6	1,526
NKAS(2:1)	20.8	2,115	13.6	1,418
NKAS(1:1)	19.6	2,048	13.2	1,376

compositions, ε_{3500} values between 88 and 100 L mol^{-1} cm^{-1} are reported (Newman et al., 1986; Yamashita et al., 1997; Leschik et al., 2004), and for basaltic compositions, values of 65 L mol^{-1} cm^{-1} are also reported (Yamashita et al., 1997; Shishkina et al., 2010). On the other hand, the ε_{3500} values of our glasses are similar to those for float glass and soda lime silicate glasses (∼40 L mol^{-1} cm^{-1}) as determined by Harder et al. (1998) and others (Behrens and Stuke, 2003; Suzuki et al., 2015).

In part, the differences in ε_{3500} can be explained by the degree of polymerization of the glasses, i.e., ε_{3500} becomes smaller as the ratio of non-bridging oxygen over tetrahedral cations (NBO/T) increases. However, at constant NBO/T, an increased Al/Si ratio appears to lower ε_{3500}, as indicated by the comparison of our data to albite composition. Furthermore, the nature of the charge-compensating cation also seems to play an important role.

Using these ε_{3500} values, the water contents of the air-melted glasses are 0.015 ± 0.002 wt% (NAS), 0.019 ± 0.005 wt% NKAS(2:1), and 0.013 ± 0.003 wt% NKAS(1:1). Such contents are typical for aluminosilicate glasses melted at air (Scholze, 1960). Compaction of the glass bodies near T_g in the cold seal pressure vessel does not change the water content. Water diffusivity is too slow at these temperatures to equilibrate the glass cylinders with the pressure medium.

Near-Infrared Spectroscopy

The NIR spectra of NAS, NKAS(2:1), and NKAS(1:1) containing up to 8 wt% H_2O are shown in **Figure 6**. Strong absorption bands at ∼5,200, ∼4,500, and ∼4,050 cm^{-1} are visible in the plotted range between 6,000 and 3,700 cm^{-1}. Analogous to silicate glasses, the band at 4,050 cm^{-1} is attributed to the combination of OH stretching vibration with a low wavenumber

lattice vibration (Wu, 1980; Stolper, 1982a; Bauer et al., 2015, 2017). The absorption band near 4,500 cm^{-1} represents the combination of stretching and bending vibrations of hydroxyl groups connected to tetrahedrally coordinated silicon (Si–OH) (Wu, 1980; Stolper, 1982a; Nowak and Behrens, 1995; Behrens et al., 1996). This assignment is supported by the MIR spectra, i.e., the band at 4,500 cm^{-1} originates from a combination of OH stretching vibration at 3,500 cm^{-1} and a Si–OH stretching vibration near 1,000 cm^{-1} (**Figure 3**). The absorption band at 5,200 cm^{-1} is related to the combination of stretching and bending modes of H_2O molecules (Bartholomew et al., 1980; Behrens and Stuke, 2003; Stuke et al., 2006).

All these NIR bands are visible at water contents >1 wt%, whereby their intensities increase with increasing water content. The peaks of ∼4,050, ∼4,500, and ∼5,200 cm^{-1} shift toward a lower wavenumber when K_2O is substituted for Na_2O. A noticeable peak shift upon hydration is not observed for any of these peaks (**Table 2**).

To use the NIR bands for the determination of the species concentration and the total water content of the glasses, the choice of baseline is crucial. As discussed by Withers and Behrens (1999), the highest reproducibility for aluminosilicate glasses can be achieved using tangential baselines. This method of baseline correction is illustrated in **Figure 7**.

As shown in **Figure S1**, the absorbance of the 4,050 cm^{-1} band, normalized to sample thickness and density, is proportional to the total water content. The linear correlation indicates that both the OH groups and the H_2O molecules contribute to this band. The linear molar absorption coefficient (ε_{4050}) of this band was derived by the slope of data points and decreases when Na is replaced by K (**Table 3**). The ε_{4100} values are much lower than those determined for rhyolite (0.68 L mol^{-1} cm^{-1}), basalt (0.51 L mol^{-1} cm^{-1}), and albite (0.94 L mol^{-1} cm^{-1}) glasses (Stolper, 1982a; Withers and Behrens, 1999), consistent with the low ε_{3500} values of the Al-rich alkali aluminosilicate glasses.

Assuming that the combination bands at ∼4,500 and ∼5,200 cm^{-1} represent the total water content and that the absorption coefficients are independent of the water content, a simple calibration can be performed to determine the linear molar absorption coefficient for both bands (Equations 4–6) (Newman et al., 1986; Behrens et al., 1996; Withers and Behrens, 1999; Balzer et al., 2019):

$$c_{H_2O_t} = c_{OH} + c_{H_2O} \quad (4)$$

$$c_{OH} = \frac{1802 \cdot A_{4500}}{\rho \cdot d \cdot \varepsilon_{4500}} \quad (5)$$

$$c_{H_2O} = \frac{1802 \cdot A_{5200}}{\rho \cdot d \cdot \varepsilon_{5200}} \quad (6)$$

where c_{OH} denotes the content of water dissolved as OH groups and c_{H2O} denotes the content of molecular H_2O. The linear molar absorption coefficients ε can be derived by a linear regression of Equation (7) which is obtained by the combination of Equations (4–6):

$$\frac{1802 \cdot A_{5200}}{d \cdot \rho \cdot C_{H_2O_t}} = \varepsilon_{5200} - \frac{\varepsilon_{5200}}{\varepsilon_{4450}} \cdot \frac{1802 \cdot A_{4450}}{d \cdot \rho \cdot C_{H_2O_t}} \quad (7)$$

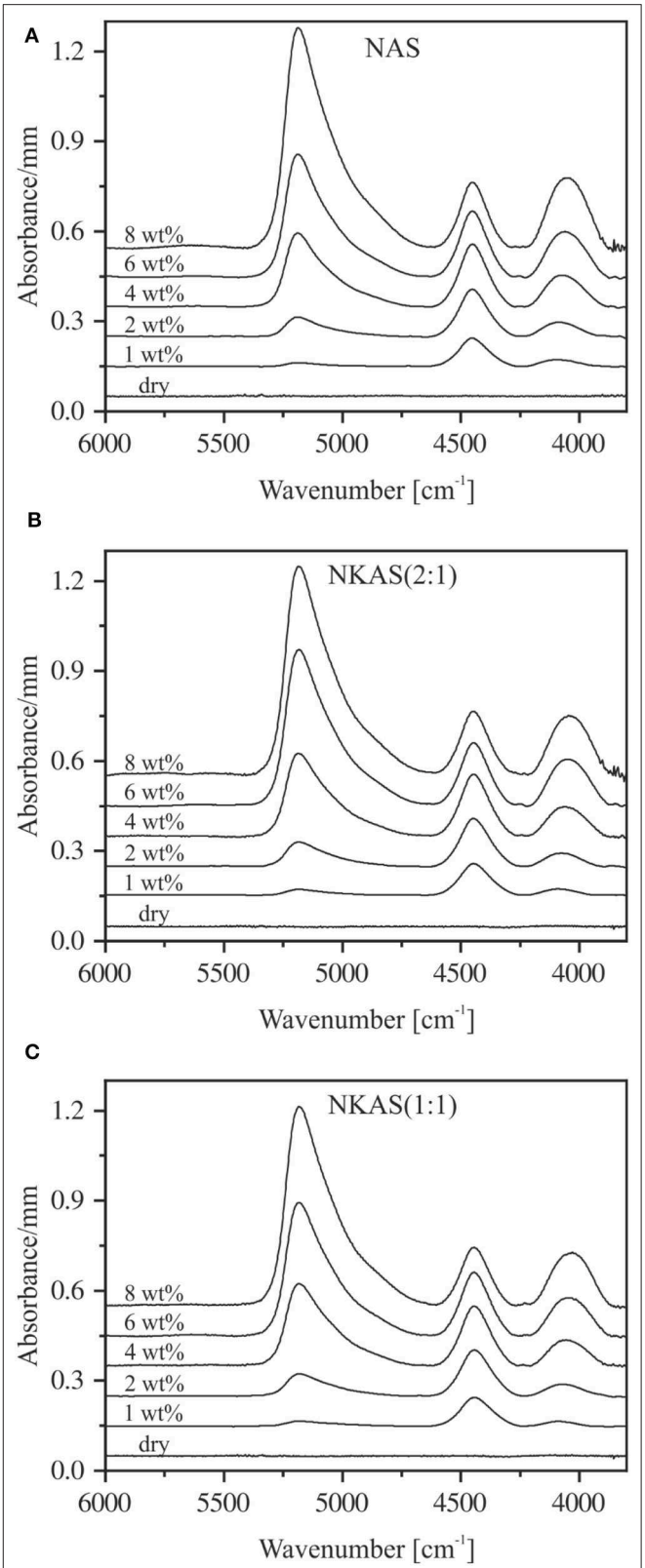

FIGURE 6 | Baseline-corrected near-infrared spectra of NAS **(A)**, NKAS(2:1) **(B)**, and NKAS(1:1) **(C)** containing 0–8 wt% H_2O. The spectra were normalized to sample thickness and vertically shifted for clarity. Nominal water contents are indicated.

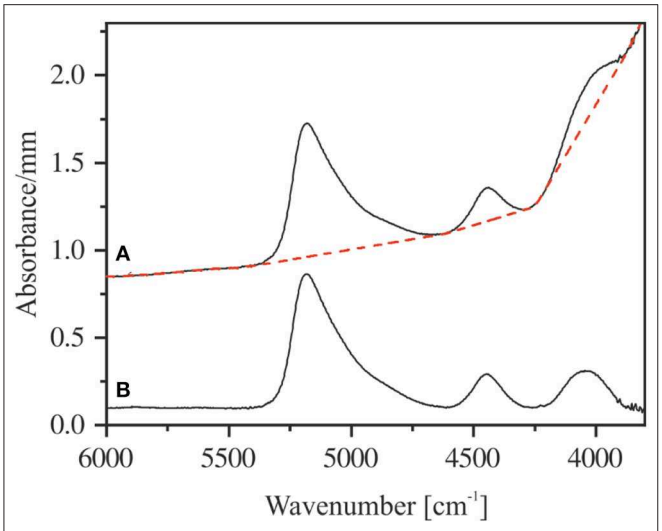

FIGURE 7 | Measured near-infrared spectrum of NKAS(2:1) 8-I with the applied tangential baseline (red dashed line) (A). Corresponding baseline-corrected spectrum (B). The spectra are shifted for clarity.

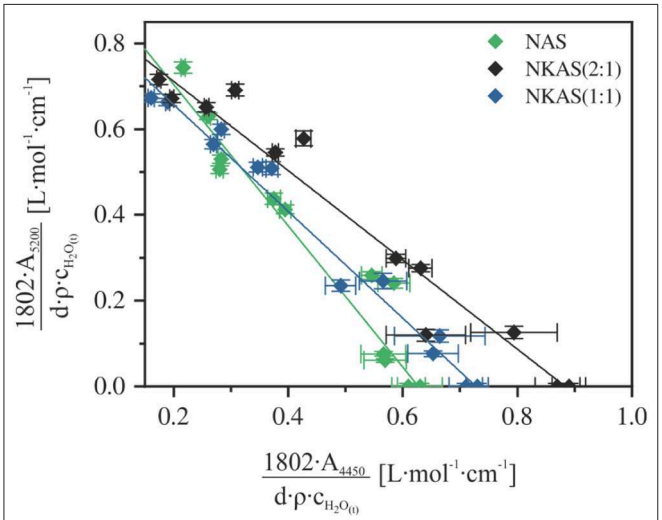

FIGURE 8 | Calibration plot for the determination of the linear molar absorption coefficient of the near-infrared bands at 4,450 and 5,200 cm^{-1} in aluminosilicate glasses.

In a graphical representation of this relationship (**Figure 8**), the linear molar absorption coefficients of the NIR absorption bands are given by the intercepts with the corresponding axis. This approach was successfully applied to a variety of glass systems, e.g., silicates (Stuke et al., 2006; Yamashita et al., 2008), aluminosilicate (Nowak and Behrens, 1995; Behrens et al., 1996; Ihinger et al., 1999; Schmidt et al., 2001), borosilicates (Bauer et al., 2017), borates (Bauer et al., 2015), and phosphates (Balzer et al., 2019).

Values of ε_{4500} and ε_{5200} resulting from this approach are shown in **Table 1**. The ε_{4500} value increases when 7.5 mol% K_2O is incorporated at the expense of 7.5 mol% Na_2O. This behavior is consistent with the findings on other aluminosilicate glasses (Behrens et al., 1996). However, a further substitution of Na_2O by K_2O leads to a decrease of ε_{4500}. In contrast, ε_{5200} continuously decreases with the K_2O content.

The linear molar absorption coefficients of ε_{4500} and ε_{5200} in our glasses are much lower compared to those of other aluminosilicate glasses, e.g., albite glasses as reported by Withers and Behrens (1999). They obtained values of 1.21 L mol^{-1} cm^{-1} (ε_{4450}) and 1.46 L mol^{-1} cm^{-1} (ε_{5200}), respectively, choosing the same baseline correction for their spectra. This comparison shows that higher alkali contents in polymerized aluminosilicate glasses lead to lower absorption coefficients. These findings are consistent with those of the investigations on sodium silicate glasses made by Yamashita et al., where a decrease of the molar absorption coefficient with the Na_2O content of the glasses was observed (Yamashita et al., 2008).

^{27}Al Magic Angle Spinning-NMR Spectroscopy

The ^{27}Al MAS-NMR spectra of NAS, NKAS(2:1), and NKAS(1:1) exhibit similar features (**Figure 9**). The main resonance of the central transition in the spectra of nominally dry NAS glass is centered at 55.9 ppm, with the typical asymmetric extension toward lower values resulting from the distribution of quadrupolar parameters of ^{27}Al arising from the disordered nature of the glass (Zeng et al., 2000; Wu and Stebbins, 2009) (**Figures 10A,C**). According to previous studies (Engelhardt and Michel, 1987; Merzbacher, 1990; Stebbins and Farnan, 1992; Toplis et al., 1997a, 2000; Sen et al., 1998; Schmidt et al., 2000; Xue and Kanzaki, 2007; Wu and Stebbins, 2009; Sukenaga et al., 2010; Stebbins et al., 2013), this peak is assigned to tetrahedrally coordinated Al (Al^{IV}). In the range of 13 ppm, a weakly pronounced shoulder is visible. Typically, this resonance is caused by octahedral coordinated Al (Al^{VI}). The first spinning sidebands of the main resonance are located at 178 and−62 ppm.

In anhydrous mixed alkali glasses [NKAS(2:1) and NKAS(1:1)], the main resonance shifts by 0.4 ppm to higher values (**Figures 10A,C**). With increasing substitution of K for Na, a decrease of the full-width at half maximum occurs (**Table 2**). The shoulder at 13 ppm becomes more pronounced when Na_2O is exchanged for K_2O.

According to Stebbins and Farnan (1992), Stebbins et al. (2013) and others (Toplis et al., 2000; Neuville et al., 2006; Xue and Kanzaki, 2007; Wu and Stebbins, 2009), a fivefold coordinated aluminum (Al^V) produces a signal at around 30–40 ppm in aluminosilicate glasses. Such a high Al coordination was found not only in glasses with divalent modifier cations, e.g., CAS (CaO-Al_2O_3-SiO_2) (Neuville et al., 2004) and MAS (MgO-Al_2O_3-SiO_2) (Toplis et al., 2000) but also in binary Al_2O_3-SiO_2 glasses (Stebbins and Farnan, 1992). Al^V species were also found in NAS (Na_2O–Al_2O_3-SiO_2) and KAS (K_2O–Al_2O_3-SiO_2) glasses quenched from melts at pressures above 10 GPa (Stebbins et al., 2013). We do not observe such species in our spectra, but the presence of a small fraction of Al^V cannot be ruled out as the signal could be covered by the broad tail of the Al^{IV} peak.

The signals of the hydrous glasses containing 8 wt% H_2O (**Figures 9B,D**) are more symmetric and significantly narrower compared to the anhydrous glasses, which are also documented by the smaller FWHM (**Table 2**). The main resonance in all three

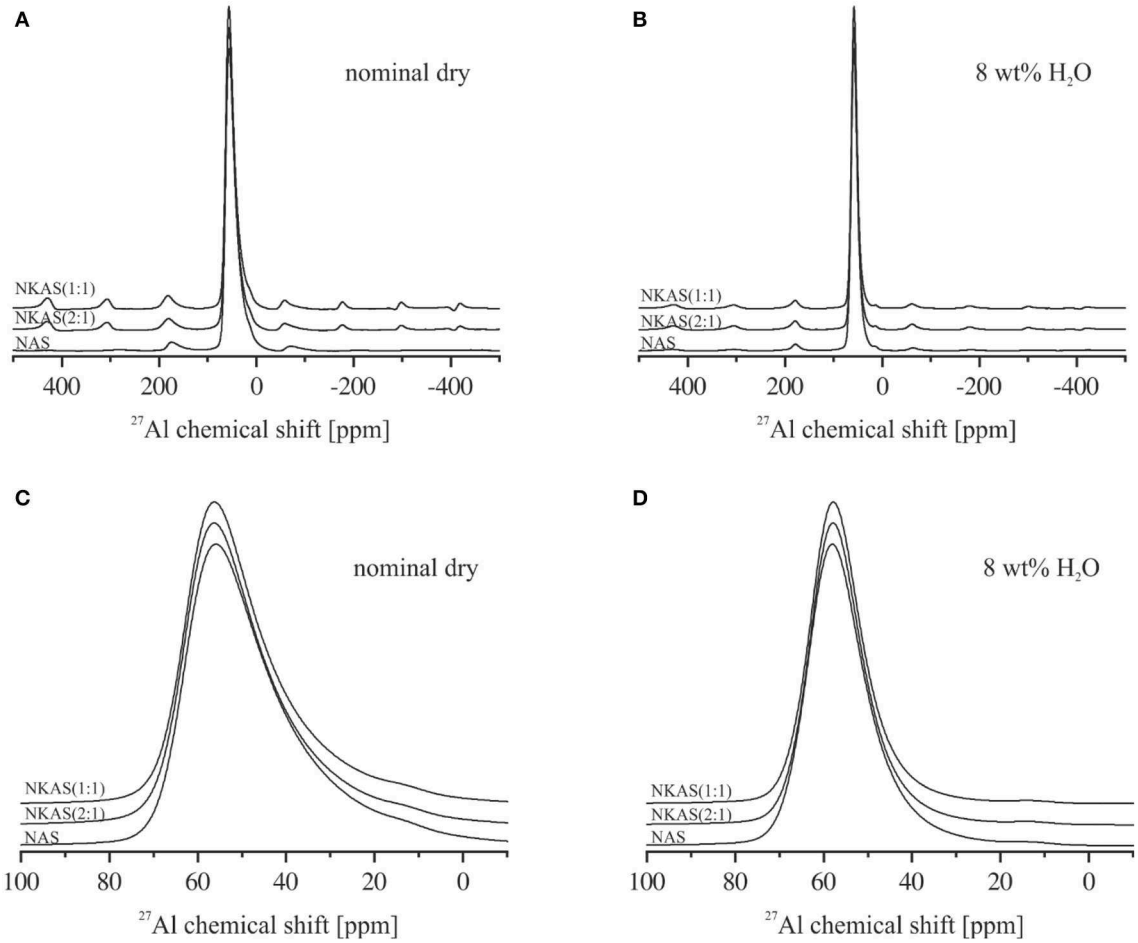

FIGURE 9 | ^{27}Al magic angle spinning (MAS)-NMR spectra of anhydrous glasses **(A)** and magnification of the main resonance of the central transition between 100 and −10 ppm **(C)**. ^{27}Al MAS-NMR spectra of hydrous glasses bearing 8 wt% **(B)** and magnification of the main resonance between 100 and −10 ppm **(D)**. All spectra are normalized to the Al^{IV} resonance (∼55 ppm) and shifted vertically for comparison.

compositions, attributed to Al^{IV}, is slightly shifted to higher values and is located at 58 ppm. As the main resonance becomes narrower, the signal at 13 ppm becomes better resolved, but its intensity does not seem to have changed. In their ^{27}Al MAS-NMR study on hydrous sodium aluminosilicate glasses, Zeng et al. (2000) also observed a small signal near 13 ppm. They suggest that this signal originates from the surface reaction during sample preparation. Since the peak does not change significantly with glass composition for our samples, we agree with this statement. Another explanation would be a small percentage of crystalline relics such as corundum, but a microscopic examination gave no indication for the presence of crystalline phases.

DISCUSSION

Effect of Water on the Fictive Temperature

The T_f values of anhydrous glasses are very similar and do not differ from the subsequent T_g determinations by more than 12 K (**Table S2**). Thus, we conclude that the fictive temperatures are directly comparable to the T_g values reported in literature. Upon hydration, the fictive temperature of the glasses continuously decreases, which is consistent with literature data for other aluminosilicate glasses (Zhang et al., 2003; Whittington et al., 2004; Bouhifd et al., 2006; Del Gaudio et al., 2007). However, the initial effect of addition of water is much weaker than that observed for albite and rhyolite glasses (**Figure 10**). The data plotted for rhyolite are calculated using the viscosity model of Zhang et al. (2003). The model is based on data for 11 natural and synthetic aluminosilicate compositions which have in common a low Al/Si (0.18–0.25), a high excess of alkali compared to alkaline earth elements, and an almost subaluminous composition (NKC/Al of 0.86–1.04). Parallel plate viscometry was used by Whittington et al. (2004) to measure the viscosity of albite glasses (Al/Si = 0.32) containing up to 2 wt% H_2O. At higher water contents, this method failed for the hydrous albite glass because of the rapid water loss of the samples. Since water loss is even more severe for our Al-rich glasses, we did not try to experimentally determine the melt viscosity.

The development of T_f upon hydration can be approximated for our aluminosilicate glasses by straight lines. Deviations from this trend reflect the possible error of DTA measurements. The T_f values of NAS glasses are systematically higher compared

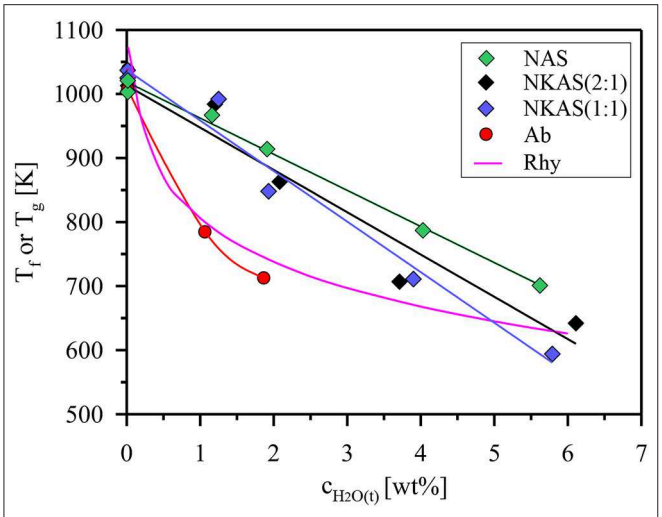

FIGURE 10 | Fictive temperature (T_f) of Al-rich alkali aluminosilicate glasses as a function of the total water content. For comparison, trends of glass transition temperatures (T_g) defined by a viscosity of 10^{12} Pas are shown for rhyolite (Rhy) and albite (Ab) composition (Zhang et al., 2003; Whittington et al., 2004).

to NKAS(2:1) and NKAS(1:1), *i. e.*, the effect of water on the reduction of T_f is stronger for the mixed alkalis. Compared to the rhyolite composition, the effect of added water is weaker for water-poor glasses (<1.5 wt% H_2O) but stronger for water-rich glasses (>2 wt% H_2O). These changes are most likely associated with structural modifications by an increase of the Al/Si ratio and the alkali content of the glasses.

Structure of Aluminosilicate Glasses

The nominal composition of our glasses is subaluminous, but all glasses contain a small excess of charge-balancing cations (e.g. Na^+, K^+) which shifts the melt into the peralkaline region. The NBO/T ratio based on EMPA data is still very close to 0 [NAS: 0.039 ± 0.001, NKAS(2:1): 0.052 ± 0.002, and NKAS(1:1): 0.027 ± 0.002]. In such glasses, Al is in tetrahedral coordination (Engelhardt and Michel, 1987; Kohn et al., 1989; Mysen, 1990; Neuville et al., 2004; Xue and Kanzaki, 2007; Wu and Stebbins, 2009; Mysen and Richet, 2018), which is also evidenced by the ^{27}Al MAS-NMR spectra of our anhydrous glasses. Assuming that the Al avoidance principle (Loewenstein rule) is obeyed (Loewenstein, 1954; Yildirim and Dupree, 2004) and ignoring the small amount of NBO, each AlO_4 tetrahedron is connected to four SiO_4 tetrahedra. However, the broadness of the ^{27}Al MAS-NMR signal and its asymmetric tail toward a lower chemical shift indicate large variations in the local geometry of the AlO_4 tetrahedra. The SiO_4 tetrahedra can be linked to four AlO_4 tetrahedra [Q^4(4 Al)] or to three AlO_4 tetrahedra and one SiO_4 tetrahedra [Q^4(3 Al)]. Based on the EMPA data, the Al/Si ratio in our glasses is about 0.77. Thus, based on composition, we expect the ratio of Q^4(4 Al)/(Q^4(3 Al) to be close to 1. This is of course a simplifying approach. ^{17}O NMR spectroscopy gives evidence that $NaAlSiO_4$ glass has roughly 10% each of Al–O–Al and Si–O–Si, but in this glass with Al/Si of 1:1 the tendency to form Al–O–Al is probably particularly pronounced (Lee and Stebbins, 2000).

In principle, the ^{29}Si MAS-NMR spectra could provide information about the Q species in the glasses. However, for aluminosilicates, the signals are typically very broad and the contributions from different species cannot be separated properly (Kohn et al., 1992; Zhang and Ni, 2010). Therefore, we did not perform ^{29}Si MAS-NMR spectroscopy on our glasses.

The decrease in FWHM (**Table 2**) of the AlO_4 resonance, when Na_2O is exchanged for K_2O, can be explained by the higher cation field strength of Na^+ compared to that of K^+. The higher cation field strength of Na^+ in NAS glasses causes a higher degree of disorder than in the mixed alkali glasses (Navrotsky et al., 1985; Romano et al., 2001) since Na^+ has a higher interaction with T–O–T bonds which results in the distortion of the tetrahedra geometry (Navrotsky et al., 1985; Stebbins and Farnan, 1992).

The ^{27}Al MAS-NMR spectra give clear evidence that after hydration Al is still in tetrahedral coordination. The question is whether the hydrolysis of the T–O–T bonds generates Al connected to an OH group and three SiO_4 tetrahedra (Q^3AlOH species) or all Al still connected to SiO_4 tetrahedra (Q^4Al). The shift of the Al^{IV} signal toward higher frequency and the decrease in the FWHM upon hydration are very similar to that found by Kohn et al. (1989) and Zeng et al. (2000) for albite glass. Based on spectra simulations, Zeng et al. (2000) concluded that the change of the lineshape of the ^{27}Al MAS-NMR spectra of $NaAlSi_3O_8$ glasses with increasing water content does not preclude the formation of Q^3AlOH, but the narrowing of the linewidth can be attributed to the ordering of Q^4Al with increasing water content. Such "ordering" can occur, for instance, through the elimination of highly strained Q^4Al sites by reaction with water. On the other hand, according to Zeng et al. (2000), the shift of the signal is consistent with the formation of Q^3AlOH species. They proposed a water dissolution mechanism in which both SiOH and AlOH groups are formed, the ratio depending on the Al/Si ratio of the glass. According to their prediction, for the NAS glass with Al/Si = 0.77, the AlOH/SiOH should be close to 1. However, the model of Zeng et al. (2000) suggests that NaOH groups are also formed upon water dissolution in the melts. According to Xue and Kanzaki (2007), free hydroxyls (OH groups which are not bound to tetrahedral cations) are favored by more depolymerized melts and alkaline earth cations as network-modifying cations. Thus, free hydroxyl groups are not expected for the glasses under investigation here.

The decrease of disorder with increasing water content is probably only in part the effect of the re-arrangement of the tetrahedral units after the hydrolysis of the T–O–T bond. The frozen-in temperature also decreases with water content, and the disorder of the structure increases with rising temperature (Dubinsky, 2006; Stebbins, 2008).

Water Speciation in Aluminosilicate Glasses

As a common feature, in oxide glasses OH groups are dominating at low water contents, but the fraction of molecular water continuously increases with the total water content. This trend

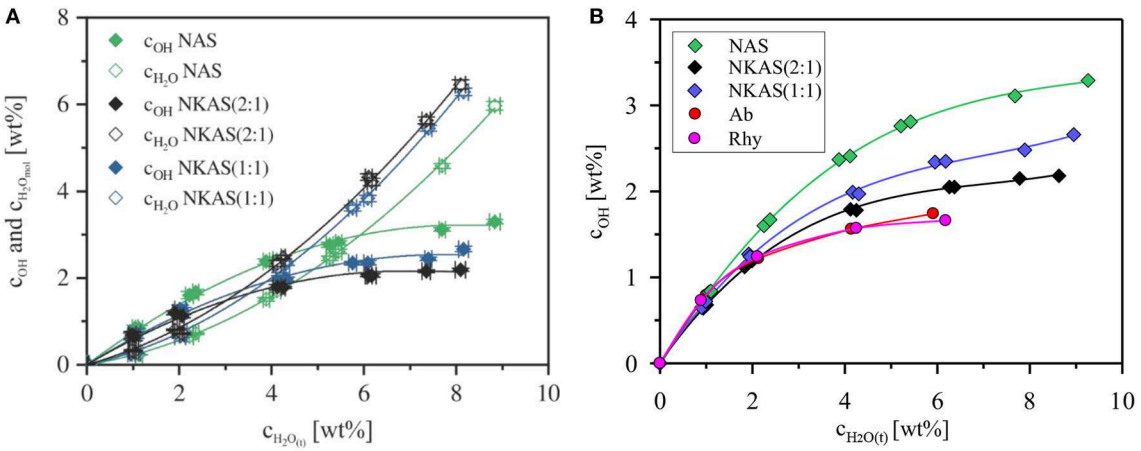

FIGURE 11 | Water species concentration in the glasses NAS, NKAS(2:1), and NKAS(1:1) in function of total water content **(A)**. Comparison of the content of dissociated H_2O with albite and rhyolite glasses synthesized and quenched at similar conditions as the glasses of our study (Withers and Behrens, 1999) **(B)**.

is caused by the decrease of the fictive temperature with total water content (**Figure 10**) and the increase of the equilibrium fraction of the OH groups with increasing temperature (Nowak and Behrens, 2001; Behrens and Nowak, 2003). The fictive temperature represents the apparent equilibrium temperature for the speciation frozen in the glass (Behrens and Nowak, 2003). As known from literature, the total water content, at which the contents of dissociated H_2O and molecular H_2O are the same, depends on the glass composition. For instance, in soda-lime borate glasses, the OH groups are the dominant species even at very high water content (∼8 wt%) (Bauer et al., 2015). In borosilicate glasses, the intersection point, where the concentration of dissociated water and molecular H_2O are the same, is at about 6–7 wt% H_2O (Bauer et al., 2017). In (alumino)silicate glasses, this intersection point was found between 3 and 4 wt% H_2O (Silver et al., 1990; Schmidt et al., 2001; Behrens and Stuke, 2003; Stuke et al., 2006).

Our data for NKAS(2:1) and NKAS(1:1) are consistent with previous data for aluminosilicate glasses, with intersection points at total water contents of 3.0 and 3.8 wt%, respectively (**Figure 11A**). The NAS glasses contain a higher fraction of OH groups with the intersection point at 5.9 wt% H_2O. Compared with other polymerized alkali aluminosilicates, the fraction of dissociated H_2O is higher in our Al-rich glasses (Al/Si≈0.77) than those in albite (Al/Si ≈ 0.32) and in rhyolite (Al/Si ≈ 0.20) glass (**Figure 11B**). All these glasses were synthesized in the same type of IHPV, and the quench rate was the same, at least, for the water-rich glasses. Hence, differences in thermal history of the samples cannot explain the high OH contents in the Al-rich glasses. However, different fictive temperatures at the same water content (**Figure 10**) may partially explain this finding.

To test this hypothesis, we have used the fictive temperature concept to determine the equilibrium water speciation in function of temperature. The kinetics of water species conversion in polymerized aluminosilicate melts is controlled by structural relaxation of the network and, hence, by melt viscosity (Dingwell and Webb, 1990; Zhang et al., 1995; Behrens and Nowak, 2003). Thus, the fictive temperature of glass represents the equilibrium temperature for the speciation of H_2O measured in the glasses. Behrens and Nowak (2003) have demonstrated the applicability of this concept for a rhyolite-like composition. The equilibrium constants for speciation of dissolved water in the melts derived by the concept of fictive temperature were consistent with *in situ* measurement in melts at high pressure and temperature as well as with experiments in which the glasses were equilibrated for longer times in the range of glass transition and subsequently rapidly cooled to room temperature. **Figure 12** compares the equilibrium constant for water speciation (Equations 2) with other data for aluminosilicate melts. The water speciation data published so far cover a narrow range in the ln K *vs.* $1/T$ space. Considering the compositions given in **Table 3**, there is little effect of composition on equilibrium water speciation in the melt within the Al/Si range of 0.19–0.36, the Na/K range of 0.84–∞, and the $(Na_2O + K_2O)/(CaO + MgO)$ range of 0–∞. The only clear trend from literature data is the decrease of ln K when Ca^{2+} is substituted for 2 Na^+ in melts with Al/Si = 0.31 (Ohlhorst et al., 2000).

The data for the Al-rich alkali aluminosilicate melts fit well to the data for the other compositions at high temperature. However, with increasing water content and, hence, decreasing temperature, the data determined in our study deviate more and more from the other data. The slope m of the straight lines is connected to the standard enthalpy ΔH^0 of the water speciation reaction as $\Delta H^0 = Rm$, where R is the universal gas constant (Nowak and Behrens, 1995, 2001; Sowerby and Keppler, 1999). Linear regressions for the alkali aluminosilicate glasses were performed only for water contents from 2 to 6 wt%. At lower water content, the error of C_{OH} is very high; at higher water content $T_f$could not be measured due to rapid water loss. Errors of ΔH^0 were estimated assuming an error of T_f of ±15 K and an error of ln K of ±0.1. The derived ΔH^0 values of the three alkali aluminosilicate glasses agree within error: 7.0 ± 3.5

TABLE 3 | Compositional data in wt% of the aluminosilicate melts plotted in **Figure 12**.

	Rhy, Ih99	Rhy, S&K99	AOQ, N&B01 B&N03	Dac, Liu04	And, Bo06	Ab, Oh00	$Qz_{33}Ab_{33}An_{33}$, Oh00	$Qz_{50}An_{50}$, Oh00
SiO_2	76.40	74.13	76.14	65.18	57.44	69.48	71.25	70.24
TiO_2				0.65	1.06			
Al_2O_3	12.30	13.92	13.53	15.93	17.53	18.48	18.54	18.92
B_2O_3								
FeO^{tot}	1.00			4.37	7.20			
MnO					0.12			
MgO		1.01		2.15	4.31			
CaO	0.50	1.16		5.05	7.42		6.71	10.21
Na_2O	3.80	2.90	4.65	3.73	3.32	12.03	4.13	
K_2O	4.80	5.24	5.68	2.69	1.61	0.01		
Total	98.80	98.36	100.00	99.75	100.01	100.00	100.63	99.37
Al/Si	0.19	0.22	0.21	0.29	0.36	0.31	0.31	0.32
Na/K	1.20	0.84	1.24	2.11	3.13	∞	∞	-
$(Na_2O+K_2O)/(CaO+MgO)$	12.6	2.2	∞	0.6	0.3	∞	0.6	0.0

Ih99, (Ihinger et al., 1999); S&K99, (Sowerby and Keppler, 1999); N&B01, (Nowak and Behrens, 2001); B&N03, (Behrens and Nowak, 2003); Liu04, (Liu et al., 2004); Bo06, (Botcharnikov et al., 2006); Oh00, (Ohlhorst et al., 2000).

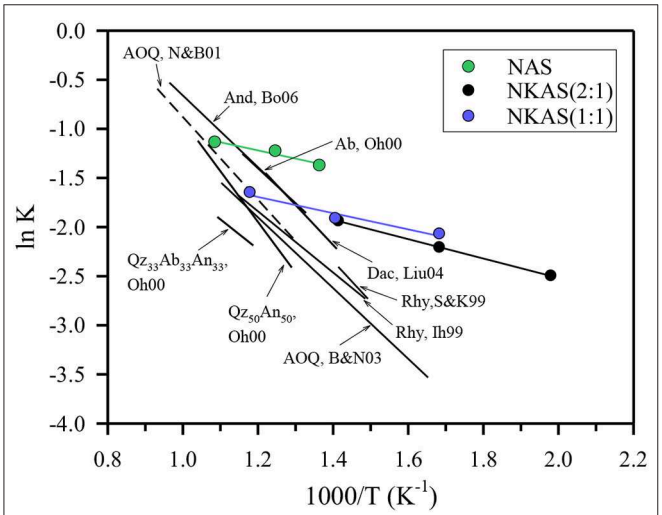

FIGURE 12 | Comparison of the equilibrium constants for water speciation in aluminosilicate. The composition of the reference data are given in **Table 3**.

kJ mol^{-1} for NAS, 8.2 ± 4.1 kJ mol^{-1} for NKAS(2:1), and 6.9 ± 3.4 kJ mol^{-1} for NKAS(1:1). Thus, lower OH contents at the same temperature in the mixed alkali glasses compared to the pure Na aluminosilicate glasses are not caused by different enthalpies for the dissociation reaction. These differences may be explained by the higher cation field strength of Na^+ compared to K^+, which facilitates the breaking of neighboring Al–O–Si bonds.

The ΔH^0 values are much lower for the Al-rich aluminosilicate than for all the other compositions reported in **Table 3**. For instance, Nowak and Behrens determined ΔH^0 = 35.0 ± 1.2 kJ mol^{-1} for the rhyolite-like AOQ composition and Ohlhorst et al. (2000) determined ΔH^0 = 33.8 ± 3.6 kJ mol^{-1} for the albite composition. Our interpretation of these trends is that the relative abundance of Si–O–Si and Si–O–Al linkages in the network determines the hydrolysis behavior. In the Al-rich aluminosilicates, there are seven times as many Si–O–Al linkages than Si–O–Si linkages. In the other aluminosilicates, the abundance of both is similar (for And, Bo06 in **Figure 12**) or Si–O—Si linkages predominate. This implies that the Si–O–Al connections are stabilized against hydrolysis by neighboring Si–O–Si.

CONCLUSION

Al-rich alkali aluminosilicate glasses consist of an alternating network of AlO_4 and SiO_4 tetrahedra, which is strongly strained as indicated by ^{27}Al MAS-NMR spectroscopy. Replacing Na^+ with K^+ reduces the internal tension to some extent, but much more efficient is the incorporation of H_2O into the structure, which depolymerizes the network through the formation of SiOH and AlOH groups. The enthalpy of the water dissociation reaction is much lower for the Al-rich melts (Al/Si = 0.77) compared to melts with a low fraction of aluminum (Al/Si <0.40). This implies that Si–O–Si connections are crucial for the stabilization of the network against hydrolysis. As a consequence, the initial decrease of the fictive temperature with the addition of water content is relatively weak in Al-rich alkali aluminosilicates.

Another important finding of our study is the tremendous increase of water mobility in the range of glass transition. According to Behrens and Nowak (1997), water can migrate through polymerized aluminosilicate structures either by the direct jumps of H_2O molecules or by the transient reaction of H_2O molecules with bridging oxygen forming OH group pairs. Both mechanisms are favored by the fact that the Al–O–Si bonds can be broken more easily than the Si–O–Si bonds. Thus, how

large the fraction of the SiO_4 tetrahedra connected to the four AlO_4 tetrahedra is of crucial importance.

These observations, although mainly constrained for the range of glass transition, may have also implications for the mechanical behavior of glasses at ambient conditions, e.g., for the crack growth behavior. As demonstrated by Waurischk et al. (this issue), larger forces are required for inert crack growth in hydrous microscope slide glass compared to the dry glass. Thus, dissolved water in the glass may act as a toughening agent. A possible explanation is a local stress relief by breaking up the strained bonds through reaction with water species. For Al-rich glasses, one would expect this difference between dry and hydrous glasses to be even more pronounced.

DATA AVAILABILITY STATEMENT

All datasets generated for this study are included in the article/**Supplementary Material**.

AUTHOR CONTRIBUTIONS

This paper is a joint project of the research groups in Hannover, Berlin, Clausthal, and Bochum. Syntheses of hydrous glasses were done by RB and HB in Hannover. Dry glasses and DTA measurements were done by TW, SR, and RM in Berlin. Discussion include contributions of PK and JD from Clausthal. MF performed the NMR measurements.

ACKNOWLEDGMENTS

Financial support by the Deutsche Forschungsgemeinschaft (DFG) through its priority program SPP 1594—Topological Engineering of Ultrastrong Glasses (MU 963/14-2, DE598/22-2, and Be1720/31-2) is gratefully acknowledged. This research is part of the Ph.D. thesis of RB at Leibniz University of Hannover (Balzer, 2019), but the data were re-evaluated and re-interpreted for publication in Frontiers. The authors thank Jonathan Stebbins and a second reviewer for their fruitful comments.

SUPPLEMENTARY MATERIAL

The Supplementary Material for this article can be found online at: https://www.frontiersin.org/articles/10.3389/fmats.2020.00085/full#supplementary-material

REFERENCES

Acocella, J., Tomozawa, M., and Watson, E. B. (1984). The Nautre of dissolved water in sodium silicate glasses and its effect on various properties. *J. Non-Crystalline Solids* 65, 355–372. doi: 10.1016/0022-3093(84)90058-9

Allan, D. C., Ellison, A. J., and Gomez, S. (2013). "Glass with compressive surface for consumer applications" in *United States Patent*. Corning, NY: Corning Incorporated.

Arndt, J., and Häberle, F. (1973). Thermal expansion and glass transition temperatures of synthetic glasses of plagiclase-like compositions. *Contrib. Mineral. Petrol.* 39, 175–183. doi: 10.1007/BF00375739

Balzer, R. (2019). *Interaction of water with oxide glass structures, in Institut für Mineralogie*. Hannover: Gottfried Wilhelm Leibniz Universität Hannover. p. 111.

Balzer, R., Behrens, H., Reinsch, S., and Fechtelkord, M. (2019). Structural investigation of hydrous phosphate glasses. *Phys. Chem. Glasses* 60, 49–61. doi: 10.13036/17533562.60.2.041

Bartholomew, R. F., Butler, B. L., Hoover, H. L., and Wu, C. K. (1980). Infrared spectra of a water-containing glass. *J. Am. Ceramic Soc.* 63, 481–485. doi: 10.1111/j.1151-2916.1980.tb10748.x

Bauer, U., Behrens, H., Fechtelkord, M., Reinsch, S., and Deubener, J. (2015). Water- and boron speciation in hydrous soda-lime-borate glasses. *J. Non-Crystalline Solids* 423–424, 58–67. doi: 10.1016/j.jnoncrysol.2015.05.004

Bauer, U., Behrens, H., Reinsch, S., Morin, E. I., and, J. F., Stebbins (2017). Structural investigation of hydrous sodium borosilicate glasses. *J. Non-Crystalline Solids* 465, 39–48. doi: 10.1016/j.jnoncrysol.2017.03.023

Behrens, H. (1995). Determination of water solubilities in high-viscosity melts-an experimental study on NaAlSi3O8 and KAlSi3O8 melts. *Eur. J. Mineral.* 7, 905–920. doi: 10.1127/ejm/7/4/0905

Behrens, H., and Nowak, M. (1997). The mechanisms of water diffusion in polymerized silicate melts. *Contrib. Mineral. Petrol.* 126, 377–385. doi: 10.1007/s004100050257

Behrens, H., and Nowak, M. (2003). Quantification of H2O speciation in silicate glasses and melts by IR spectroscopy -in situ versus quench techniques. *Phase Transitions* 76, 45–61. doi: 10.1080/0141159031000076048

Behrens, H., Romano, C., Nowak, M., Holtz, F., and Dingwell, D. B. (1996). Near-infrared spectroscopic determination of water species in glasses of the system MAlSI3O8 (M=Li,Na,K)-an intralaboratory study. *Chem. Geol.* 128, 41–63. doi: 10.1016/0009-2541(95)00162-X

Behrens, H., and Stuke, A. (2003). Quantification of H2O contents in silicate glasses using IR spectroscopy - a calibration based on hydrous glasses analyzed by Karl-Fischer titration. *Glass Sci. Technol.* 76, 176–189.

Behrens, H., Tamic, N., and Holtz, F. (2004). Determination of the molar absorption for the infrared absorption band of CO2 in rhyolitic glasses. *Am. Mineral.* 89, 301–306. doi: 10.2138/am-2004-2-307

Behrens, H., Zhang, Y., Leschik, M., Wiedenbeck, M., Heide, G., Frischat, G. H. (2007). Molecular H2O as carrier for oxygen diffusion in hydrous silicate melts. *Earth Planet. Sci. Lett.* 254, 69–76. doi: 10.1016/j.epsl.2006.11.021

Berndt, J., Liebske, C., Holtz, F., Freise, M., Nowak, M., Ziegenbein, D., et al. (2002). A combined rapid-quench and H2-membrane setup for internally heated pressure vessels-Description and application for water solubility in basaltic melts. *Am. Mineral.* 87, 1717–1726. doi: 10.2138/am-2002-11-1222

Botcharnikov, R. E., Behrens, H., and Holtz, F. (2006). Solubility and speciation of C-O-H fluids in andesitic melt at T = 1,100–1,300°C and *P* = 200 and 500 MPa. *Chem. Geol.* 229, 125–143. doi: 10.1016/j.chemgeo.2006.01.016

Bouhifd, M. A., Whittington, A., Roux, J., and Richet, P. (2006). Effect of water on the heat capacity of polymerized aluminosilicate glasses and melts. *Geochim. Cosmochim. Acta* 70, 711–722. doi: 10.1016/j.gca.2005.09.012

Del Gaudio, P., Behrens, H., and Deubener, J. (2007). Viscosity and glass transition temperature of hydrous float glass. *J. Non-Crystalline Solids* 353, 223–236. doi: 10.1016/j.jnoncrysol.2006.11.009

Dingwell, D. B., Romano, C., and Hess, K. U. (1996). The effect of water on the viscosity of a haplogranitic melt under P-T-Xconditions relevant to silicic volcanism. *Contrib. Mineral. Petrol.* 124, 19–28. doi: 10.1007/s004100050170

Dingwell, D. B., and Webb, S. L. (1990). Relaxation in silicate melts. *Eur. J. Mineral.* 2, 427–449. doi: 10.1127/ejm/2/4/0427

Doweidar, H. (1998). Density - structure correlations in Na2O-Al2O3-SiO2 glasses. *J. Non-Crystalline Solids* 240, 55–65. doi: 10.1016/S0022-3093(98)00719-4

Dubinsky, E. V. (2006). Quench rate and temperature effects on framework ordering in aluminosilicate melts. *Am. Mineral.* 91, 753–761. doi: 10.2138/am.2006.2039

Ellison, A. J., and Gomez, S. (2010). *Down-drawable, chemically strengthened glass for cover plate*, U.S. Patent, Editor. Corning, NY: Corning Incorporate.

Engelhardt, G., and Michel, D. (1987). *High Resolution Solid State NMR of Silicates and Zeolites.* Chichester; New York; Brisbane; Toronto; Singapore: John Wiley & Sons, 485.

Franz, H., and Kelen, T. (1966). Erkenntnisse über die Struktur von Alkalisilicatgläsern und -schmelzen aus dem Einbau von OH-Gruppen Glastechnischer Bericht. *Glastechnische Berichte*. 40, 141–148.

Handke, M., and Mozgawa, W. (1993). Vibrational spectroscopy of the amorphous silicates. *Vibrat. Spectroscopy* 5, 75–84. doi: 10.1016/0924-2031(93)87057-Z

Handke, M., Mozgawa, W., and Nocun, M. (1994). Specific features of the IR spectra of silicate glasses. *J. Mol. Struct.* 325, 129–136. doi: 10.1016/0022-2860(94)80028-6

Harder, U., Geißler, H., Gaber, M., and Hähnert, M. (1998). Determination of the water content of alkali lime silica glasses by IR spectroscopy using nuclear reaction analysis for calibration. *Glass Sci. Technol.* 71, 12–18.

Ihinger, P. D., Zhang, Y., and Stolper, E. M. (1999). The specitation of dissolved water in rhyolitic melt. *Geochim. Cosmochim. Acta* 63, 3567–3578. doi: 10.1016/S0016-7037(99)00277-X

Indris, S., Heitjans, P., Behrens, H., Zorn, R., and Frick, B. (2005). Fast dynamics of H2Oin hydrous aluminosilicate glasses studied with quasielastic neutron scattering. *Phys. Rev. B* 71:e064205. doi: 10.1103/PhysRevB.71.064205

Jewell, J. M., Shaw, C. M., and Shelby, J. E. (1993). Effects of water content an aluminosilicate glasses and the relatio to strong-fragile liquid theory. *J. Non-Crystalline Solids* 152, 32–41. doi: 10.1016/0022-3093(93)90441-Y

Johannes, W., and Holtz, F. (1996). *Petrogenesis and Experimental Petrology of Granitic Rocks. Vol. 22*. Berlin: Springer. doi: 10.1007/978-3-642-61049-3

Kohn, S. C., Dupree, R., and Golam Mortuza, M. (1992). The interaction between water and aluminosilicate magmas. *Chem. Geol.* 96, 399–409. doi: 10.1016/0009-2541(92)90068-G

Kohn, S. C., Dupree, R., and Smith, M. E. (1989). A multinuclear magnetic resonance study of the strucutre of hydrous albite glasses. *Geochim. Cosmochim. Acta* 53, 2925–2935. doi: 10.1016/0016-7037(89)90169-5

Kuryaeva, R. G. (2004). Degree of polymerization of aluminosilicate glasses and melts. *Glass Phys. Chem.* 30, 157–166. doi: 10.1023/B:GPAC.0000024000.19443.f6

Lacy, E. D. (1963). Aluminum in glasses and melts. *Phys. Chem. Glasses* 4, 234–238.

Lee, S. K., and Stebbins, J. F. (2000). Al-O-AL and Si-O-Si sites in framework aluminosilicate glasses with Si/Al=1: quantification of framework disorder. *J. Non-Crystalline Solids* 270, 260–264. doi: 10.1016/S0022-3093(00)00089-2

Lee, Y.-K., and Tomozawa, M. (1999). Effect of water content in phosphate glasses on slow crack growth rate. *J. Non-Crystalline Solids* 248, 203–210. doi: 10.1016/S0022-3093(99)00146-5

Leschik, M., Heide, G., and Frischat, G. H. (2004). Determination of H2O and D2O contents in rhyolithic glasses. *Phys. Chem. Glasses* 45, 238—251.

Liu, Y., Zhang, Y., and Behrens, H. (2004). H2O diffusion in dacitic melts. *Chem. Geol.* 209, 327–340. doi: 10.1016/j.chemgeo.2004.06.019

Loewenstein, W. (1954). The distribution of aluminum in the tetrahedra of silicates and aluminates. *Am. Mineral.* 39, 92–96.

Massiot, D., Fayon, F., Capron, M., King, I., Le Calv, S., Alonso, B., et al. (2002). Modelling one- and two-dimensional solid-state NMR spectra. *Magnet. Resonance Chem.* 40, 70–76. doi: 10.1002/mrc.984

Mazurin, O. V. (2007). Problems of compability of the values of glass transition temperatures published in the world literature. *Glass Phys. Chem.* 33, 22–36. doi: 10.1134/S108765960701004X

Mazurin, O. V., and Gankin, Y. V. (2007). "Glass transition temperature: problems of measurements and analysis of the existing data"; Proceedings, International Congress on Glass, July 1-6, 2007, Strasbourg, France.

Merzbacher, C. I. (1990). A high-resolution 29Si and 27Al NMR study of alkaline earth aluminosilicate glasses. *J. Non-Crystalline Solids* 124, 194–206. doi: 10.1016/0022-3093(90)90263-L

Mysen, B. O. (1990). Role of Al in depolymerized, peralkaline aluminosilicate melts in the systems Li2O-Al2O3-SiO2, Na2O-Al2O3-SiO2, K2O-Al2O3-SiO2. *Am. Mineral.* 75, 120–134.

Mysen, B. O., and Richet, P. (2018). *Silicate Glasses and Melts, 2nd Edn. Elsevier Science,* 720.

Mysen, B. O., Virgo, D., and Kushiro, I. (1981). The structural role of aluminum in silicate melts-a Raman spectroscopic study at 1 atmosphere. *Am. Mineral.* 66, 678–701.

Navrotsky, A., Geisinger, K. L., McMillan, P., and Gibbs, G. V. (1985). The tetrahedral framework in glass and melts - inferences from molecular orbital calculations and implications for structure, thermodynamics, and physical properties. *Phys. Chem. Minerals* 11, 284–298. doi: 10.1007/BF00307406

Neuville, D. R., Cormier, L., and Massiot, D. (2004). Al environment in tectosilicate and peraluminous glasses: A 27Al MQ-MAS NMR, Raman, and XANES investigation. *Geochim. Cosmochim. Acta* 68, 5071–5079. doi: 10.1016/j.gca.2004.05.048

Neuville, D. R., Cormier, L., and Massiot, D. (2006). Al coordination and speciation in calcium aluminosilicate glasses: Effects of composition determined by 27Al MQ-MAS NMR and Raman spectroscopy. *Chem. Geol.* 229, 173–185. doi: 10.1016/j.chemgeo.2006.01.019

Newman, S., Stolper, E. M., and Epstein, S. (1986). Measurement of water in rhyolithic glasses Calibration of an infrared spectroscopic technique. *Am. Mineral.* 71, 1527–1541.

Nowak, M., and Behrens, H. (1995). The speciation of water in haplogranitic glasses and melts determined by in situ near-infrared spectroscopy. *Geochim. Cosmochim. Acta* 59, 3445–3450. doi: 10.1016/0016-7037(95)00237-T

Nowak, M., and Behrens, H. (2001). Water in rhyolitic magmas - getting a grip on a slippery problem. *Earth Planetary Sci. Lett.* 184, 515–522. doi: 10.1016/S0012-821X(00)00343-5

Ohlhorst, S., Behrens, H., Holtz, F., and Schmidt, B. C. (2000). "Water speciation in aluminosilicate glasses and melts," in *Applied Mineralogy in Research, Economy, Technology and Culture.* eds D. Rammlmair, J. Mederer, T. H. Oberthür, R. B. Heimann, and H. Pentinghaus. *Proc. 6th Int. Conf. Appl. Mineral*, (Rotterdam: Balkema), 193–196.

Reinsch, S., Roessler, C., Bauer, U., Müller, R., Deubener, J., Behrens, H., et al. (2016). Water the other network modifier in borate glasses. *J. Non-Crystalline Solids* 432, 208–217. doi: 10.1016/j.jnoncrysol.2015.10.010

Richet, P., Whittington, A., Holtz, F., Behrens, H., Ohlhorst, S., Wilke, M. (2000). Water and the density of silicate glasses. *Contrib. Mineral. Petrol.* 138, 337–347. doi: 10.1007/s004100050567

Robert, G., Whittington, A. G., Stechern, A., and Behrens, H. (2013). The effect of water on the viscosity of a synthetic calc-alkaline basaltic andesite. *Chem. Geol.* 346, 135–148. doi: 10.1016/j.chemgeo.2012.10.004

Romano, C., Poe, B., Mincione, V., Hess, K. U., and Dingwell, D. B. (2001). The viscosities of dry and anhydrous XAlSi3O8 (X = Li, Na, K, Ca0.5, Mg0.5) melts. *Chem. Geol.* 174, 115–132. doi: 10.1016/S0009-2541(00)00311-9

Rüscher, C. H., Mielcark, E. M, Wongpa, J., Jathrupitakkul, J., Jirasit, F., Lohaus, L. (2011). Silicate-, aluminosilicate and calciumsilicate gels for building materials: chemical and mechanical properties during ageing. *Eur. J. Mineral.* 23, 111–124. doi: 10.1127/0935-1221/2010/0022-2070

Schmidt, B. C., Behrens, H., Riemer, T., Kappes, R., and Dupree, R. (2001). Quantitative determination of water speciation in aluminosilicate glasses- a comparative NMR and IR spectroscopic study. *Chem. Geol.* 174, 195–208. doi: 10.1016/S0009-2541(00)00316-8

Schmidt, B. C., Riemer, T., Kohn, S. C., Behrens, H., and Dupree, R. (2000). Different water solubility mechanisms in hydrous glasses along the Qz-Ab Join-Evidence from NMR spectroscopy. *Geochim. Cosmochim. Acta* 64, 513–526. doi: 10.1016/S0016-7037(99)00331-2

Scholze, H. (1959). Der Einbau des Wassers in Gläsern. *Der Einfluss des im Glas gelösten Wassers auf das Ultrarot-Spektrum und die quantitative ultrarotspektroskopische Bestimmung des Wassers in Gläsern.* 32, *81–88*.

Scholze, H. (1960). Zur Frage der Unterscheidung zwischen H2O-Molekülen und OH-Gruppen in gläsern und Mineralen. *Die Naturwissenschaften* 47, 226–227. doi: 10.1007/BF00602759

Scholze, H. (1988). *Glas-Natur, Struktur, Eigenschaften Vol. 3*. Berlin; Heidelberg: Springer Verlag. doi: 10.1007/978-3-662-07495-4_2

Sen, S., Xu, Z., and Stebbins, J. F. (1998). Temperature dependent strucural changes in borate, borosilicare and Boroaluminate liquids high resolution 11B, 29Si, 27Al NMR studies. *J. Non-Crystalline Solids* 226, 29–40. doi: 10.1016/S0022-3093(97)00491-2

Shaw, H. R. (1963). Obsidian-H20 Viscosities at 1,000 and 2,000 bars in the temperature range 700°C to 900°C. *J. Geophys. Res.* 68, 6337–6343. doi: 10.1029/JZ068i023p06337

Shishkina, T. A., Botcharnikov, R. E., Holtz, F., Almeev, R. R., and Portnyagin, M. V. (2010). Solubility of H2O- and CO2-bearing fluids in tholeiitic basalts at pressures up to 500 MPa. *Chem. Geol.* 277, 115–125. doi: 10.1016/j.chemgeo.2010.07.014

Silver, L. A., Ihinger, P. D., and Stolper, E. (1990). The influence of bulk composition on the speciation of water in silicate glasses. *Contrib. Mineral. Petrol.* 104, 142–162. doi: 10.1007/BF00306439

Silver, L. A., and Stolper, E. (1989). Water in Albitic glasses. *J. Petrol.* 30, 667–709. doi: 10.1093/petrology/30.3.667

Sowerby, J. R., and Keppler, H. (1999). Water speciation in rhyolithic melt determined by *in-situ* infrared spectroscopy. *Am. Mineral.* 84, 1843–1849. doi: 10.2138/am-1999-11-1211

Sroda, M., and Paluszkiewicz, C. (2008). The structural role of alkaline earth ions in oxyfluoride aluminosilicate glasses-Infrared spectroscopy study. *Vibrat. Spectroscopy* 48, 246–250. doi: 10.1016/j.vibspec.2008.02.017

Stebbins, J. F. (2008). Temperature effects on the network structure of oxide melts and their consequences for configurational heat capacity. *Chem. Geol.* 256, 80–91. doi: 10.1016/j.chemgeo.2008.03.011

Stebbins, J. F., and Farnan, I. (1992). Effects of high temperature on silicate liquid strucutre - a multinuclear NMR study. *Science* 255, 586–589. doi: 10.1126/science.255.5044.586

Stebbins, J. F., Wu, J., and Thompson, L. M. (2013). Interactions between network cation coordination and non-bridiging oxygen abundance in oxide glasses and melts Insights from NMR spectroscopy. *Chem. Geol.* 346, 34–46. doi: 10.1016/j.chemgeo.2012.09.021

Stoch, L., and Sroda, M. (1999). Infrared spectroscopy in the investigation of oxide glasses structure. *J. Mol. Struct.* 511–512, 77–84. doi: 10.1016/S0022-2860(99)00146-5

Stolper, E. (1982a). Water in silicate glasses- an infrared Spectroscopic Study. *Contrib. Mineral. Petrol.* 81, 1–17. doi: 10.1007/BF00371154

Stolper, E. (1982b). The speciation of water in silicate melts. *Geochim. Cosmochim. Acta*, 46, 2609–2620. doi: 10.1016/0016-7037(82)90381-7

Stuke, A., Behrens, H., Schmidt, B. C., and Dupree, R. (2006). H2O speciation in float glass and soda lime silica glass. *Chem. Geol.* 229, 64–77. doi: 10.1016/j.chemgeo.2006.01.012

Sukenaga, S., Nagahisa, T., Kanehashi, K., Saito, N., and Nakashima, K. (2010). Reconsideration of Al coordination in CaO-SiO2-Al2O3-(R2O or RO) Glasses by using High Field Solid Sate 27 Al NMR Spectroscopy. *ISIJ Int.* 51, 333–335. doi: 10.2355/isijinternational.51.333

Suzuki, T., Konishi, J., Yamamoto, K., Ogura, S., Fukutani, K. (2015). IR practical extinction coefficients of water in Alkali lime silicate glasses determined by nuclear reaction analysis. *J. Am. Ceramic Soc.* 98, 1794–1798. doi: 10.1111/jace.13568

Tamic, N., Behrens, H., and Holtz, F. (2001). The solubility of H2O and CO2 in rhyolitic melts in equilibrium with a mixed CO2-H2O fluid phase. *Chem. Geol.* 174, 333–347. doi: 10.1016/S0009-2541(00)00324-7

Tarte, P. (1967). Infra-red spectra of inorganic aluminates and characteristic vibrational frequencies of AlO4 tetrahedra and AlO6 octahedra. *Spectrochim. Acta* 23A, 2127–2143. doi: 10.1016/0584-8539(67)80100-4

Thompson, L. M., and Stebbins, J. F. (2011). Non-bridging oxygen and high-coordinated aluminum in metaluminous and peraluminous calcium and potassium aluminosilicate glasses: High-resolution 17O and 27Al MAS NMR results. *Am. Mineral.* 96, 841–853. doi: 10.2138/am.2011.3680

Toplis, M. J., Dingwell, D. B., Hess, K.-U., and Tommaso, L. (1997b). Viscosity, fragility, and configurational entropy of melts along the join SiO2-NaAlSiO4. *Am. Mineral.* 82, 979–990. doi: 10.2138/am-1997-9-1014

Toplis, M. J., Dingwell, D. B., and Lenci, T. (1997a). Peraluminous viscosity maxima in Na2O-Al2O3-SiO2 liquids - The role of triclusters in tectosilicate melts. *Geochim. Cosmochim. Acta*, 61, 2605–2612. doi: 10.1016/S0016-7037(97)00126-9

Toplis, M. J., Kohn, S. C., and S.M. E., and, I. J. F., Poplett (2000). Fivefold-coordinated aluminum in tectosilicate glasses observed by triple quantum MAS NMR. *Am. Mineral.* 85, 1556–1560. doi: 10.2138/am-2000-1031

Tuttle, O. F., and Bowen, N. L. (1958). *Origin of Granite in the Light of Experimental Studies in the System NaAlSi3O8-KAlSi3O8-SiO2-H2O*. Geological Society of America.

Varshneya, A. K. (2010a). Chemical strengthening of glass: lessons learned and yet to be learned. *Int. J. Appl. Glass Sci.* 1, 131–142. doi: 10.1111/j.2041-1294.2010.00010.x

Varshneya, A. K. (2010b). The physics of chemical strengthening of glass: room for a new view. *J. Non-Crystalline Solids* 356, 2289–2294. doi: 10.1016/j.jnoncrysol.2010.05.010

Whittington, A., Richet, P., Behrens, H., Holtz, F., and Scaillet, B. (2004). Experimental temperature-X(H2O)-viscosity relationship for leucogranites and compariosn with synthetic silicic liquids. *Trans. Royal Soc. Edinburgh* 95, 59–71. doi: 10.1017/S0263593300000924

Wiederhorn, S. M. (1967). Influence of water vapor on crack propagation in soda-lime glass. *J. Am. Ceram. Soc.* 50, 407–414. doi: 10.1111/j.1151-2916.1967.tb15145.x

Withers, A. C., and Behrens, H. (1999). Temperature-induced changes in the NIR spectra of hydrous albitic and rhyolitic glasses between 300 and 100 K. *Phys. Chem. Minerals* 27, 119–132. doi: 10.1007/s002690050248

Wondraczek, L., and Behrens, H. (2007). Molar volume, excess enthalpy, and Prigogine-Defay ratio of some silicate glasses with different (P,T) histories. *J. Chem. Phys.* 127:2794745. doi: 10.1063/1.2794745

Wondraczek, L., Krolikowski, S., and Behrens, H. (2009). Relaxation and Prigogine-Defay ratio of compressed glasses with negative viscosity-pressure dependence. *J. Chem. Phys.* 130:3141382. doi: 10.1063/1.3141382

Wu, C.-K. (1980). Natrure of incorporated water in hydrated silicate glasses. *J. Am. Ceramic Soc.* 63, 453–457. doi: 10.1111/j.1151-2916.1980.tb10211.x

Wu, J., and Stebbins, J. F. (2009). Effects of cation field strength on the structure of aluminoborosilicate glasses: high-resolution 11B, 27Al and 23Na MAS NMR. *J. Non-Crystalline Solids* 355, 556–562. doi: 10.1016/j.jnoncrysol.2009.01.025

Xue, X., and Kanzaki, M. (2007). Al coordination and water speciation in hydrous aluminosilicate glasses: direct evidence from high-resolution heteronuclear 1H-27Al correlation NMR. *Solid State Nucl. Magn. Reson.* 31, 10–27. doi: 10.1016/j.ssnmr.2006.11.001

Yamashita, S., Behrens, H., Schmidt, B. C., and Dupree, R. (2008). Water speciation in sodium silicate glasses based on NIR and NMR spectroscopy. *Chem. Geol.* 256, 231–241. doi: 10.1016/j.chemgeo.2008.06.029

Yamashita, S., Kitamura, T., and Kusakabe, M. (1997). Infrared spectroscopy of hydrous glasses of arc magma compositions. *Geochem. J.* 31, 169–174. doi: 10.2343/geochemj.31.169

Yildirim, E., and Dupree, R. (2004). Investigation of Al-O-Al sites in an Na-aluminosilicate glass. *Bull. Mater. Sci.* 27, 269–272. doi: 10.1007/BF02708516

Zarubin, D. P. (1999). Infrared spectra of hydrogen bonded hydroxyl groups in silicate glasses. A re-interpretation. *Phys. Chem. Glasses* 40, 184–192.

Zeng, Q., Nekvasil, H., and Grey, C. P. (2000). In support of a depolymerization model for water in sodium aluminoslicate glasses: Information from NMR spectroscopy. *Geochim. Cosmochim. Acta* 64, 883–896. doi: 10.1016/S0016-7037(99)00352-X

Zhang, Y., and Ni, H. (2010). Diffusion of H, C, and O Components in Silicate Melts. *Rev. Mineral. Geochem.* 72, 171–225. doi: 10.2138/rmg.2010.72.5

Zhang, Y., Stolper, E. M., and Ihinger, P. D. (1995). Kinetics of the reaction H2O+O=2OH in rhyolitic and albitic glasses: Preliminary results. *Am. Mineral.* 80, 593–612. doi: 10.2138/am-1995-5-618

Zhang, Y., Xu, Z., and Liu, Y. (2003). Viscosity of hydrous rhyolitic melts inferred from kinetic experiments, and a new viscosity model. *Am. Mineral* 88, 1741–1752. doi: 10.2138/am-2003-11-1215

Zietka, S., Deubener, J., Behrens, H., and Müller, R. (2007). Glass transition and viscosity of hydrated silica glasses. *Phys. Chem. Glasses: Eur. J. Glass Sci. Technol. B*, 48, 380–387.

Conflict of Interest: The authors declare that the research was conducted in the absence of any commercial or financial relationships that could be construed as a potential conflict of interest.

frontiers in Materials

ORIGINAL RESEARCH
published: 19 May 2020
doi: 10.3389/fmats.2020.00144

Shear Bands in Monolithic Metallic Glasses: Experiment, Theory, and Modeling

René Hubek[1], Sven Hilke[1], Farnaz A. Davani[1], Mehrdad Golkia[2], Gaurav P. Shrivastav[2,3], Sergiy V. Divinski[1], Harald Rösner[1], Jürgen Horbach[2] and Gerhard Wilde[1]*

[1] *Institute of Materials Physics, University of Münster, Münster, Germany,* [2] *Institut für Theoretische Physik II - Soft Matter, Heinrich-Heine-Universität Düsseldorf, Universitätsstraße 1, Düsseldorf, Germany,* [3] *Institute for Theoretical Physics, TU Wien, Wien, Austria*

For applications, metallic glasses need to retain their high strength over enhanced strain ranges. However, many metallic glasses show catastrophic failure, even in or close to the end of the regime that conventionally has been thought to be elastic. Recent observations of irreversible events at low strains shed some doubt on this nomenclature. In fact, these observations indicate that although the macroscopic response indicates elastic behavior, the microscopic processes might at least partially be irreversible and time-dependent. In that respect, shear bands as the result of shear localization and as the cause of shear softening play a decisive role with respect to the performance of metallic glasses under mechanical load. Therefore, in this work, we are aiming at understanding the correlations between glass structure, glass properties and the thermomechanical history of the glass including the shear bands on one hand and the plastic yielding on the other hand. Various attempts have been made to explain or model the response of metallic glasses to externally applied shear stresses. Hypotheses have been put forward concerning the impact of materials parameters or structural aspects that might favor homogeneous plastic flow. Additionally, scenarios have been suggested for the early stages of anelastic and plastic deformation as well as for the transition to localization and shear band formation/activation. In this contribution, we present a focused viewpoint both from theory and modeling as well as an experimental perspective set on the structure and properties of glasses under shear, with a special focus on shear banding. We also discuss the impact of the local structure of glasses (that depend on the synthesis and processing path-way) in terms of their medium range order. The impact of chemical composition (including microalloying effects) on kinetic properties of shear bands and elasto-plastic properties (Poisson's ratio and three-point bending) is evaluated. These aspects have seen relatively sparse coverage, but are of far-reaching consequences concerning the properties of glasses under mechanical stress. Moreover, these aspects can reveal new insight into the underlying dominant mechanisms and, equally important, allow also to infer about the early stages of strain localization and to analyze the impact of structural heterogeneity or processing conditions on plastic yielding.

Keywords: bulk metallic glass, shear band, shear band diffusion, relaxation, deformation, microalloying

OPEN ACCESS

Edited by:
Vardan Galstyan,
University of Brescia, Italy

Reviewed by:
Matteo Valt,
University of Ferrara, Italy
Garth W. Scannell,
Corning Inc., United States

****Correspondence:***
Jürgen Horbach
horbach@thphy.uni-duesseldorf.de

Specialty section:
This article was submitted to Ceramics and Glass, a section of the journal Frontiers in Materials

Received: *12 March 2020*
Accepted: *24 April 2020*
Published: *19 May 2020*

Citation:
Hubek R, Hilke S, Davani FA, Golkia M, Shrivastav GP, Divinski SV, Rösner H, Horbach J and Wilde G (2020) Shear Bands in Monolithic Metallic Glasses: Experiment, Theory, and Modeling. Front. Mater. 7:144. doi: 10.3389/fmats.2020.00144

1. INTRODUCTION

Bulk metallic glasses (BMGs), being the youngest member of the materials group of glasses, present a combination of properties that renders them favorable as real-world representatives of model glassy materials with structures and properties that are dominated by local topology and packing fraction (Ashby and Greer, 2006). With respect to mechanical properties and plasticity, as this presents the focus of the present article, metallic glasses as other glasses too show macroscopically homogeneous or inhomogeneous flow, depending on the applied deformation parameters and boundary conditions (i.e., strain rate and temperatures) (Lewandowski et al., 1993; Kumar et al., 2013).

However, upon straining at low homologous temperatures, with the glass transition temperature as a metric, metallic glasses in contrast to covalent glasses, have an extended regime where macroscopic shear stresses are accommodated by localized inhomogeneous flow. Thus, metallic glasses provide conditions that allow to access more easily the investigation of deformation localization than other glassy systems.

Although most glasses, including metallic glasses, do not suffer from low strength and while specifically metallic glasses present a large macroscopically elastic regime, it is still their mechanical performance, which makes them unattractive for applications. In fact, due to the formation of plate-like mesoscopic defects that are termed shear bands, work softening occurs during plastic deformation that leads to catastrophic failure under tension at the latest at the end of the elastic regime. On the other hand, metallic glasses can sustain large macroscopic strain before catastrophic failure if external shear stresses are applied or if the deformation proceeds under (partially) confined conditions. To compare experiment and simulation, it should be noted that the experimental application of an external shear stress, as e.g., during rolling, in almost all cases involves also a significant hydrostatic (pressure) component of the stress tensor.

The commonly accepted picture of plastic deformation of metallic glasses involves structural response on different length and time scales. The initial response involves local yielding of localized regions that involve a group of tens of atoms that undergo a local structural transformation under an applied stress. Such regions that preferentially yield have originally been termed "shear transformation zones" (STZ). Since the early work by Argon (1979) several different terms for related local entities have been coined that describe the local response to an applied shear stress on the basis of a rather similar physical picture. The local shear transformation of a group of atoms then creates a quadrupolar stress field in the adjacent regions, similar to an Eshelby inclusion in an elastic continuum. These stress fields grow, overlap and align upon continuous straining such that percolating shear bands (SB) are formed. In metallic glasses, a broad spectrum of STZs seems to exist (Maaß et al., 2014), which display a rather broad range of activation energies. Some STZs can show rather early activation at low stress within the range that classically has been thought of as reacting purely elastic.

Inherent to this description is the local irreversible response already during macroscopically elastic deformation, due to the broad distribution of activation barriers for the unit shear transformation of a STZ. Thus, strictly speaking glasses have no truly elastic regime, if the microscopic response is taken into account.

Once SBs have formed, deformation proceeds in a localized, inhomogeneous fashion under work softening conditions. Depending on the deformation geometry, the deformation parameters and boundary conditions as well as the specific material, catastrophic failure through fracture will present the final stage of the glass response to the external strain. Even in cases where for a bulk specimen only one major shear band was present and active, slip proceeds often in a stick-slip manner giving rise to the typical "serrated flow" behavior (Klaumünzer et al., 2011). Non-serrated flow behavior can be observed if deformation proceeds at lower temperatures. These observations point toward the importance of relaxation of the glass within the shear bands.

Without regarding specific details or differences between different model descriptions of glass plasticity, it seems clear that the applicability of glasses as structural materials would benefit from enhancing the macroscopic toughness, not necessarily the strength, in order to avoid early failure. For this reason, the response to externally applied stresses needs to be understood from the initial local response of localized groups of atoms to the macroscopic yielding along system-spanning shear bands. In particular, although metallic glasses are rather isotropic, it is necessary to take the atomistic nature of matter into account, since the local STZ activity depends on the local atomic structure and the flow properties of material within the shear band regions are also affected by their atomic structure and the related mechanical properties.

Shear bands have been shown to present a range of values concerning their properties, such as width or specific volume (Klaumünzer et al., 2011; Maaß et al., 2014). Our own work has shown that even for a single shear band, properties such as the specific volume, chemical composition, and atomic configurations may vary along the shear band. In fact, these results indicate unambiguously that both, densification or dilatation occurs, which are probably inherent for stick-slip deformation behavior. Measurements of the atomic diffusion inside shear bands of a metallic glass indicate strongly accelerated diffusion and an intricate dependence on the relaxation of the glass after deformation (Bokeloh et al., 2011). These results render tracer diffusion as a unique and extremely sensitive tool for a detailed investigation of structural changes in shear bands induced by deformation and heat treatment, including the impact of chemical heterogeneity.

Thus, the focus of the present work is on the analysis of the local atomic structures in the glass and on their dependence on strain as well as on the spatio-temporal dynamics of atoms in glasses under strain. Complementing investigations based on experiments and on molecular dynamics simulations have been carried out to elucidate the local response in detail. With this study, we are focusing on generic features of glassy systems and thus provide also a link between metallic and inorganic glasses with respect to their mechanical responses.

2. METHODOLOGY

2.1. Sample Preparation

Experimentally, glassy samples of $Pd_{40}Ni_{40}P_{20}$ (in at.%) were prepared by alloying the appropriate amounts of pure Pd (99.995 wt.% purity) with the compound Ni_2P (99.99 wt.% purity) under partial Argon pressure in an arc melting facility. The resulting crystalline ingot of a few (2–6) grams in weight was repeatedly molten and solidified inside a B_2O_3 flux to extract impurities from the material that are likely to form catalytically potent nucleation sites (Wilde et al., 2000, 2006). Subsequently the metallic alloy was inductively molten inside a SiO_2 crucible that was equipped with a nozzle. At a temperature of about 1,100 K, the melt was blown out through the nozzle by a pressure difference of about 200 mbar of Argon and vitrified inside a massive Cu mold that was kept at room temperature. Estimations concerning the cooling rate during glass synthesis result in about $\left(dT/dt\right)_{eff} \approx$ 300 K/s.

The resulting massive samples of glassy $Pd_{40}Ni_{40}P_{20}$ were then checked for the absence of any detectable crystalline fractions. If the absence of detectable crystallinity was confirmed, then the samples were further used for the analysis.

In cases where samples have been annealed, the concept of the limiting fictive temperature according to Tool and Eichlin (1931) has been applied to define the relaxation state on a common basis.

Deformation was applied by cold rolling at room temperature, which amounts to about half of the glass temperature by different means. A macroscopic strain rate of the order of 10^{-1} was utilized to apply a macroscopically uniform deformation on an entire sample. If the quasi-elastic limit was exceeded, then shear bands formed under an angle of about 40–45° with respect to the rolling direction. The total strain was 5–10% measured through the thickness reduction of the plate-like sample.

The amorphous state of each sample was carefully characterized by X-ray diffraction (Siemens D5000) using a Cu cathode, an α-monochromator and a rotating sample holder in the 2θ-geometry. The chemical composition after casting was analyzed by energy dispersive X-ray spectroscopy (EDS) using a Nova Nano SEM 230 (FEI) scanning electron microscope and verified by atomic absorption spectroscopy (Mikroanalytische Labor Pascher, Germany).

Differential scanning calorimetry (DSC) was performed using a Perkin-Elmer Diamond DSC with a typical heating rate of 20 K/min. It was proven that different parts of the same ingots are characterized by almost identical DSC signals verifying the reliability of the data.

Transmission electron microscopy (TEM) was performed using a Titan Themis G3 300 TEM (FEI). Electron-transparent TEM samples were prepared by either electropolishing ($Al_{88}Y_7Fe_5$) or focused ion beam (FIB) preparation (Vit105 and $Pd_{40}Ni_{40}P_{20}$). More details are given in Rösner et al. (2014), Schmidt et al. (2015), and Hieronymus-Schmidt et al. (2017). We used high-angle annular dark-field (HAADF) imaging for the investigations of the shear bands since their visibility is better under these imaging conditions compared to conventional BF/DF imaging. This is because the materials' contrast (Z-contrast) is maximized and the imaging is largely independent of diffraction contrast. For the fluctuation electron microscopy (FEM) analyses, the information was calculated from usually more than 80 individual nanobeam diffraction patterns to have significant good statistics for the variance signal. Sampling with different parallel coherent probe sizes, R, gives insight into the structural ordering length scale and provides a semi-quantitative measure of volume fraction of the medium-range order (peak height or peak integral). This is called VR-FEM (Treacy and Gibson, 1996; Treacy et al., 2005) and was used to extract information on the medium-range order size.

The details of the diffusion measurements are provided in Bokeloh et al. (2011), Binkowski et al. (2016), and Hieronymus-Schmidt et al. (2017). The measurements are performed on macroscopically large samples (typical diameter is about 8 mm) providing sample-averaged concentration–depth profiles over 100 and more microns. The tracer diffusion coefficients are determined using an appropriate solution of the diffusion problem. A typical uncertainty of diffusion measurements is below 50% of the reported diffusion coefficient for the shallow parts of concentration profiles representing fast shear band diffusion. A scatter of the data between the different measurements on identical samples is within these limits.

The Poisson's ratios were determined using ultrasonic measurements carried out in an Olympus 38DL Plus device. A low scatter (several percents at most) has been observed between the data measured on separately cast samples. These deviations were less than the statistical uncertainty (error bars) between multiple measurements on the same sample.

The sample-to-sample variability was found to be low, particularly for the calorimetric, XRD, and ultrasonic measurements. In each case, at least two different samples were analyzed from each cast ingot and a comparison was made for samples produced from different ingots, too. No significant deviations between the measurements were observed.

2.2. Particle-Based Computer Simulation

To model glassforming $Ni_{80}P_{20}$ mixtures under mechanical load, we perform Molecular Dynamics (MD) simulation, i.e., we solve Newton's equations of motion for systems consisting typically of several thousands to about 10^6 particles. The effective interactions between the atoms are described in terms of a Lennard-Jones (LJ) model proposed by Kob and Andersen (1994), where the interaction between a particle of type α and one of type β ($\alpha, \beta =$ A, B with A = Ni and B = P), separated by a distance r from each other, is given by

$$u_{\alpha\beta}(r) = \phi_{\alpha\beta}(r) - \phi_{\alpha\beta}(r_c) - (r - r_c)\frac{d\phi_{\alpha\beta}}{dr}(r_c), \quad (1)$$

$$\phi_{\alpha\beta} = 4\varepsilon_{\alpha\beta}\left[\left(\frac{\sigma_{\alpha\beta}}{r}\right)^{12} - \left(\frac{\sigma_{\alpha\beta}}{r}\right)^{6}\right], \text{ for } r \le r_c \quad (2)$$

$$= 0, \text{ otherwise.} \quad (3)$$

The values of the interaction parameters are set to $\varepsilon_{AA} = 1.0$, $\varepsilon_{AB} = 1.5\varepsilon_{AA}$, $\varepsilon_{BB} = 0.5\varepsilon_{AA}$, $\sigma_{AA} = 1.0$, $\sigma_{AB} = 0.8\sigma_{AA}$, and $\sigma_{BB} = 0.88\sigma_{AA}$. In the simulations, the parameters ε_{AA} and σ_{AA} set the units for energy and length, respectively. The other parameters are chosen as $\varepsilon_{AB} = 1.5\varepsilon_{AA}$, $\varepsilon_{BB} = 0.5\varepsilon_{AA}$,

$\sigma_{AB} = 0.8\sigma_{AA}$, and $\sigma_{BB} = 0.88\sigma_{AA}$. The cut-off length for the potentials is $r_c = 2.5\sigma_{AA}$. The masses of both particle species are assumed to be equal, $m = m_A = m_B = 1$. Time is measured in units of $\tau_{LJ} = \sqrt{\frac{m\sigma_{AA}^2}{\varepsilon_{AA}}}$. The equations of motion are integrated with a time step $\delta t = 0.005\,\tau_{LJ}$. Note that in the original model used by Kob and Andersen, the third term on the right-hand side of Equation (1) was not introduced, leading to a discontinuity of the forces at r_c. Moreover, in their model the cut-off lengths for the potentials were set to $r_c^{\alpha\beta} = 2.5\sigma_{\alpha\beta}$, i.e., they used different cut-off lengths for AA, AB, and BB interactions.

To give an idea about the conversion to the experimental length, energy, and time scales, we can convert ε_{AA} and σ_{AA} to typical scales of a Ni-P alloy and set $\varepsilon_{AA} = 1,000\,k_B\,K$ and $\sigma_{AA} = 3.5\,Å$ (with k_B the Boltzmann constant). In these units, the LJ time scale is $\tau_{LJ} = 0.93\,ps$ (here, we have set m to the mass of Ni, $m = 97.431 \times 10^{-27}\,kg$). In the following, we consider systems at the mass density $\rho = 1.2\,m/\sigma_{AA}^3 = 2.73\,g/cm^3$. Systems in a cubic box geometry with a linear size $L = 30\,\sigma_{AA} = 105\,Å$ are considered. These systems contain 32,400 particles.

Typically, the protocol of our simulations is as follows: We equilibrate the system in the supercooled liquid state at a temperature $T = 0.44\,\varepsilon_{AA}/k_B = 440\,K$ over a time scale of $10^4\,\tau_{LJ} \approx 9.3\,ns$. Note that the mode coupling transition temperature for the considered binary LJ mixture is at $T_c = 0.435\,\varepsilon_{AA}/k_B = 435\,K$. Then, we perform a quench from the supercooled liquid to a glass state at $T = 0.2\,\varepsilon_{AA}/k_B = 200\,K$. Here, the sample is annealed for $t_w = 10^4\,\tau_{LJ}$, followed by the shearing of the system with a constant strain rate $\dot\gamma$. The shear is realized via Lees-Edwards boundary conditions (Lees and Edwards, 1972), imposing a planar Couette flow along the xz plane in the direction of x. The system's temperature is kept constant via dissipative particle dynamics which provides local momentum conservation and an unbiased thermostating of the system (Soddemann et al., 2003). The LAMMPS package (Plimpton, 1995) is used to perform the simulations. As a typical shear rate, we have chosen $\dot\gamma = 10^{-4}/\tau_{LJ} \approx 0.1\,ns^{-1}$. More details about details of the simulation can be found in Binkowski et al. (2016), Shrivastav et al. (2016a), Shrivastav et al. (2016b), and Golkia et al. (2020).

The response to an external shear is well understood for the case of a fluid in the Newtonian or linear response regime (Chhabra and Richardson, 2008), i.e., at sufficiently low shear rates $\dot\gamma$. In the steady state, one obtains a homogeneously flowing fluid, associated with a linear velocity profile in the considered planar Couette flow geometry. The steady-state shear stress in the Newtonian regime exhibits a linear dependence on shear rate, $\sigma_{ss} = \eta\dot\gamma$ with η the shear viscosity. When one decreases temperature toward the glass transition temperature in a glassforming fluid, the Newtonian regime shifts to smaller and smaller shear rates. Eventually, at the glass transition, the Newtonian regime is no longer accessible experimentally. So, below the glass transition, there is no linear response regime and the flow curve, i.e., σ_{ss} as a function of $\dot\gamma$, can be usually well-fitted by a Herschel-Bulkley law at low shear rates (Chhabra and Richardson, 2008; Ovarlez et al., 2013),

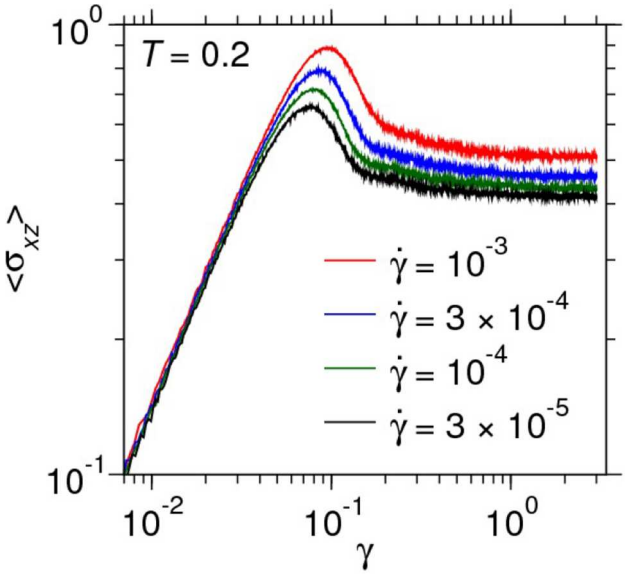

FIGURE 1 | Stress-strain relations, as obtained from the simulation, for different shear rates at the temperature $T = 0.2$, i.e., the initial states, before the shear is switched on, are glasses. Note that the shear rates are given in units of $1/\tau_{LJ}$.

$$\sigma_{ss} = \sigma_Y + A\dot\gamma^{\alpha} \tag{4}$$

with the yield stress σ_y, an amplitude A, and an exponent α which is usually in the range between 0.4 and 0.6. For a recent discussion of the Herschel-Bulkley law in glasses, we refer to Agoritsas and Martens (2017). It predicts the existence of a yield stress σ_Y which has, however, a purely kinetic origin. It is due to the inaccessibility of the Newtonian regime on the time scale of the experiment or simulation.

Both supercooled liquids in the non-Newtonian regime and glasses typically display a similar behavior with respect to the average shear stress (Zausch et al., 2008; Zausch and Horbach, 2009), $\langle\sigma\rangle$, as a function of the strain $\gamma = \dot\gamma t$. In **Figure 1**, stress-strain relations are shown for different shear rates at the temperature $T = 0.2$, i.e., the initial unsheared samples are in a glass state. Note that the results in **Figure 1** are obtained from an average over 250 independent runs for each shear rate. For $\gamma < 0.08$, there is an elastic response to the external shear where the stress increases linearly with increasing γ, $\langle\sigma_{xz}\rangle = G\gamma$ with G the shear modulus. The curves for the different shear rates are almost on top of each other which indicates that the shear modulus G has only a very weak dependence on $\dot\gamma$. The elastic regime is followed by a stress overshoot around a strain of the order of 0.1 from where the stress decays toward the steady-state shear stress. A characteristic feature in the latter transient regime is the occurrence of inhomogeneous flow patterns; in particular, there is the possibility of the formation of horizontal shear bands, i.e., bands of high mobility parallel to the flow direction. Although these horizontal bands are transient, they are relatively

long-lived. One observes a sublinear growth of their width as a function of strain (Alix-Williams and Falk, 2018; Golkia et al., 2020). The stress-strain relations of supercooled liquids in the non-Newtonian regime also show typically a maximum around $\gamma \approx 0.1$ and, at sufficiently low shear rates, inhomogeneous flow patterns (Golkia et al., 2020). As in glasses, there are also long-ranged strain correlations in supercooled liquids (Chattoraj and Lemaître, 2013; Hassani et al., 2018), similar to those caused by Eshelby inclusions in an elastic medium. However, horizontal shear bands have not been observed in supercooled liquids under shear (Golkia et al., 2020). Their appearance in simulated glasses under shear is discussed in more detail below.

3. STRUCTURE OF SHEAR BANDS

3.1. Microstructural Investigations Using Analytical Transmission Electron Microscopy (TEM) and Fluctuation Electron Microscopy (FEM)

Our experiments showed an alternation of higher and lower density regions along the propagation direction of the shear bands for three different metallic glasses (Rösner et al., 2014; Schmidt et al., 2015; Hieronymus-Schmidt et al., 2017; Hilke et al., 2019). The density changes along shear bands are correlated with small deflections along the propagation direction (see **Figure 2**), structural changes in the medium-range order (MRO) and in some incidences, with compositional changes. The observation of densification for the bright shear band regions was somewhat unexpected since macroscopic measurements reported dilation only (Lechner et al., 2010; Klaumünzer et al., 2011; Shao et al., 2013).

3.2. New Method Developed

A new method was developed to quantify the density changes using the intensity of the recorded electron micrographs (Rösner et al., 2014). A simple correlation was found for the intensity ratio of shear band and the matrix material (ISB/IM) with the relative density changes ($\Delta\rho/\rho$). Simulations confirmed the high precision of this approach (Radek et al., 2018), $\frac{\Delta\rho}{\rho} = \frac{I_{SB}}{I_M} - 1$.

3.3. Model Based on Continuum Mechanics Explaining the Observations of Density Oscillations With Smaller Positive and Larger Negative Amplitudes as Deformation Mechanism

A model was proposed based on the idea that the density changes in the shear bands are caused by an alignment of quadrupolar stress concentrators (Eshelby-like quadrupoles) (Dasgupta et al., 2012, 2013), which follow a $\propto \cos(4\theta)/r^3$ dependence (Hieronymus-Schmidt et al., 2017). This model provides the non-trivial connections between the different magnitudes for dilated and densified regions (see **Figure 2**) and the bulk modulus K. The difference in magnitude between the negative and positive amplitudes can be explained now since the amplitude height of the density variations scales with the compressibility $\kappa = 1/K$ of the material, which is the second derivative of the interatomic potential with respect to the volume or the curvature of the interatomic potential. Due to the asymmetry of the interatomic potential it is easier to achieve expansion than compression.

3.4. Topological Order (MRO) as the Structural Element in Glasses

The medium-range order of different metallic glasses was quantified using fluctuation electron microscopy (FEM) (Treacy and Gibson, 1996; Voyles and Muller, 2002; Treacy et al., 2005). FEM is a microscopic technique that is sensitive to MRO in disordered materials since it contains information about the four-body correlation of atom pairs (pair-pair correlation function). For this purpose, a statistical analysis of the diffracted intensities $I(\vec{k}, R, \vec{r})$ from nanometric volumes obtained either by tilted dark-field TEM or STEM microdiffraction was carried out. Sampling with different parallel coherent probe sizes, R, enhances the sensitivity to the structural ordering length scales and provides a semi-quantitative measure of the MRO volume fraction. This is called variable resolution FEM (VR-FEM).

This technique was applied to our metallic glass materials. The MRO of both as-cast and deformed states of different metallic glass [Al88Y7Fe5, Zr52.5Cu17.9Ni14.6Al10Ti5 (Vitreloy105), $Pd_{40}Ni_{40}P_{20}$ and α-Si] were analyzed using variable resolution fluctuation electron microscopy (VR-FEM). The investigated metallic glasses span the entire range of characteristic properties of metallic glasses [marginal to good glassforming ability (GFA) as well as brittle to ductile behavior]. After deformation we observe significant structural changes in the MRO inside the shear bands and the adjacent matrix; the MRO was altered in terms of types, size and volume fractions (Schmidt et al., 2015; Hilke et al., 2019). The changes in the matrix MRO upon deformation confirm the existence of a shear-affected zone around the shear band. The results are graphically illustrated in **Figure 3**.

The presence of MRO was also confirmed for amorphous Si (α-Si) (Radić et al., 2019), which in turn, span the range from metallic glasses to inorganic silica glasses. In essence, the MRO regions can also be seen as carriers of plasticity (like shear transformation zones) bridging the mechanical behavior of metallic glasses and silica glasses. This concept also suggests connections to the physics of granular materials and jammed systems with the MRO as granules.

4. CHARACTERIZATION OF SHEAR BANDS ON A MICROSCOPIC LEVEL

As we have mentioned above, our non-equilibrium molecular dynamics simulations of the $Ni_{80}P_{20}$ model show the occurrence of horizontal shear bands in the considered sheared glasses at the temperature $T = 0.2\,\varepsilon_{AA}/k_B$ (in real units, this corresponds to a temperature of the order of 200 K, see above). Now, we characterize the properties of horizontal shear bands and discuss the conditions under which they form.

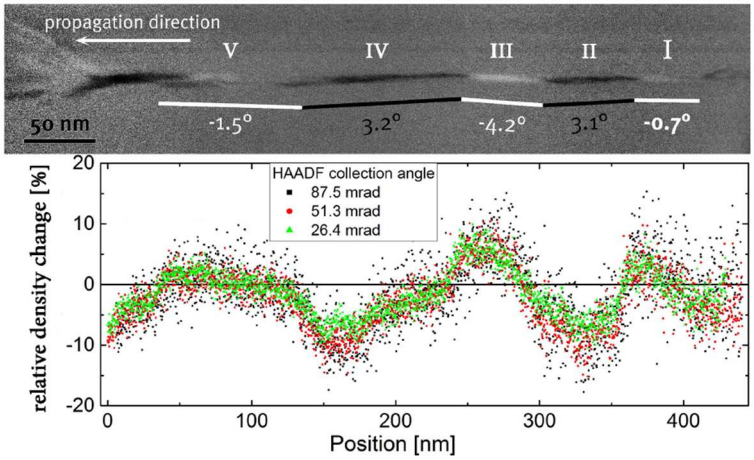

FIGURE 2 | (Top) Electron micrograph (HAADF-STEM) showing contrast changes (bright-dark-bright) in a shear band of cold-rolled $Al_{88}Y_7Fe_5$ metallic glass. **(Bottom)** Corresponding quantified density changes along the shear band. Note the difference in the amplitude height for the denser shear band segments.

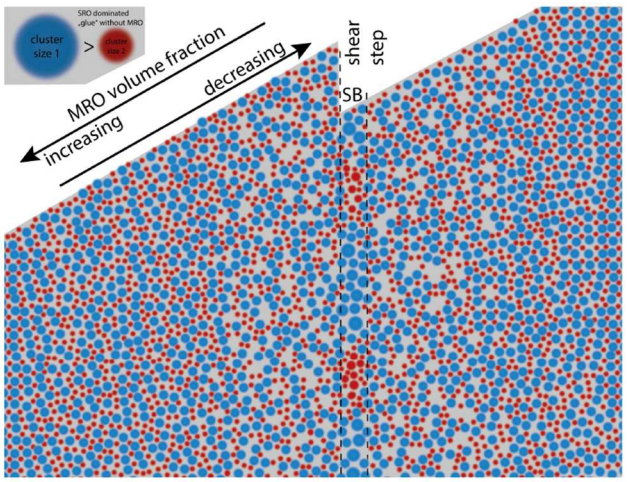

FIGURE 3 | Graphical illustration of the medium-range order (MRO) distribution around a shear band in a metallic glass as carriers for deformation accommodating the external stress.

Unlike the supercooled liquid state, the response of glasses to shear can be qualitatively different from sample to sample. In the transient regime after the stress overshoot, one can obtain different flow patterns when the shear is applied to glass samples with the same thermal history. This is exemplified in **Figure 4**. Here, **Figures 4a,b** show respectively the shear stress and the potential energy as a function of strain γ for two individual samples. While the stress-strain relations are similar for both samples, the potential energy shows significant differences with respect to the behavior between $\gamma_{\max} \approx 0.08$ (location of the stress maximum) and the steady state which is reached for both samples around $\gamma = 1.0$. In one sample (corresponding to the cyan curve in the figure), the potential energy has a shallow minimum after a local maximum at $\gamma_{\max}$, followed by an increase toward the steady-state value U_{ss}. The other sample (corresponding to the orange curve), on the contrary, increases monotonically toward U_{ss}. In fact, the two samples are associated with different flow patterns, one with two vertical bands (orange curve) and the other one with a horizontal band (cyan curve). This is illustrated for each case in the snapshots in **Figure 4** at the strains $\gamma = 0.2, 0.5, 1.0$, and 3.0. These snapshots show mobility color maps of single particle square displacements in z-direction (direction of the shear gradient), $\delta r_z^2(t) = (r_{iz}(t) - r_{iz}(0))^2$ with $r_{iz}(t)$ the z-component of the coordinate of particle i at time t. We can infer from the snapshots that the horizontal shear band (**Figure 4a**) has a longer lifetime than the vertical bands (**Figure 4b**).

An interesting question is about the connection of the type of shear band with structural heterogeneities in the initial quiescent glass sample. Is it predetermined by the initial configuration whether it will evolve into a vertical or a horizontal shear band? To analyze this issue, we have done shear simulations starting from the same sample, but using different initial random seeds for the DPD thermostat. In some cases, horizontal shear bands, albeit at different locations, are formed, while in other cases vertical bands are seen where the evolution toward the homogeneous steady-state flow is significantly faster. This indicates that the type of shear band and also its location is not predetermined by the initial undeformed glass. Note that our findings are in agreement with those of Gendelman et al. (2015) for a two-dimensional binary Lennard-Jones glass model in a confined geometry with circular shape. Their and our results challenge the assumption made in shear transformation zone (STZ) theory (Taub and Spaepen, 1980; Falk and Langer, 1998), according to which plastic events happen at some hot spots that are connected to structural heterogeneities in the glass state from which the shear is started.

The formation of horizontal shear bands becomes more likely with increasing system size (Golkia et al., 2020) and it becomes more pronounced also at very low temperature where the thermal motion of the particles is no longer relevant. Using an athermal

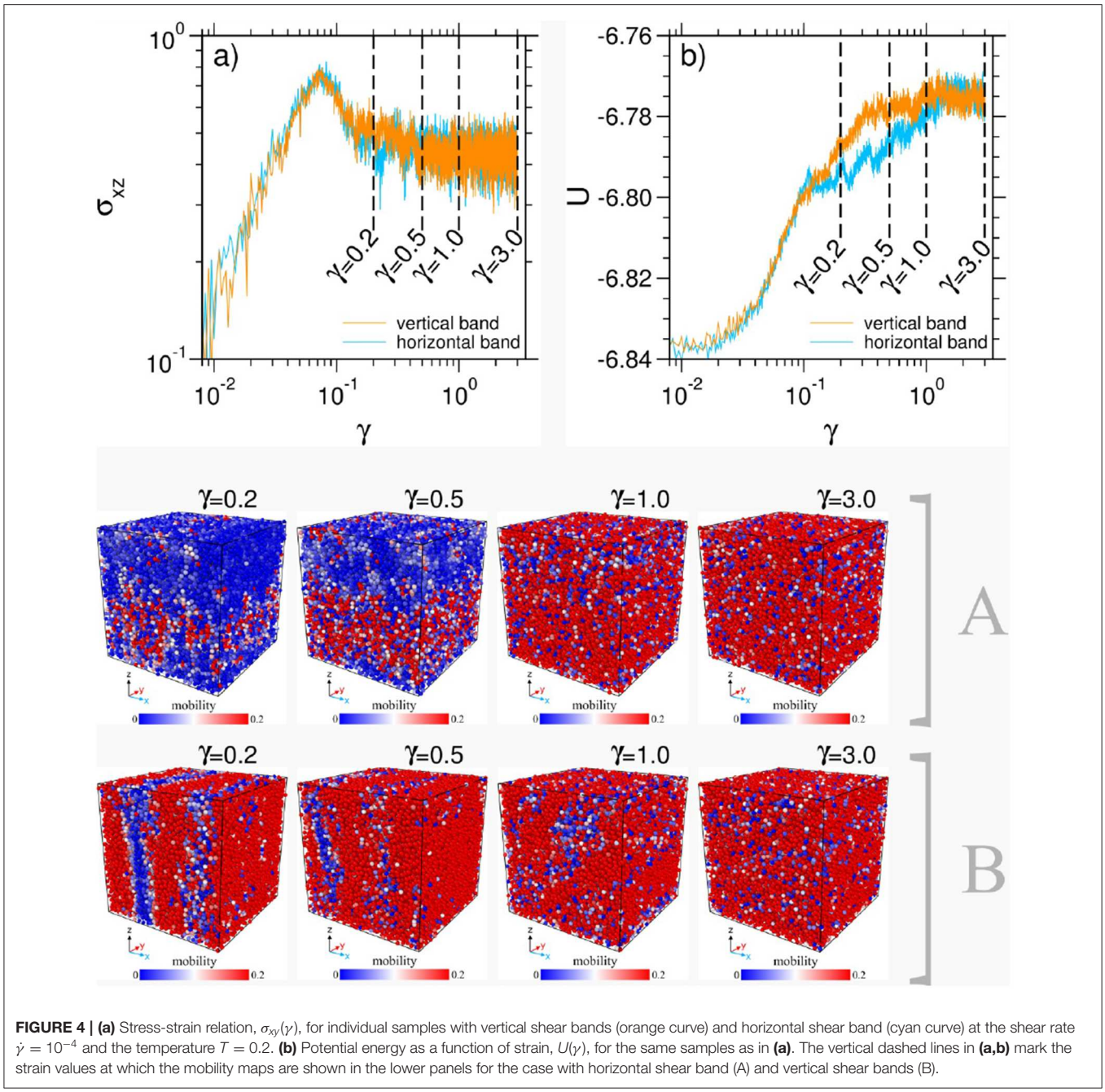

FIGURE 4 | (a) Stress-strain relation, $\sigma_{xy}(\gamma)$, for individual samples with vertical shear bands (orange curve) and horizontal shear band (cyan curve) at the shear rate $\dot{\gamma} = 10^{-4}$ and the temperature $T = 0.2$. **(b)** Potential energy as a function of strain, $U(\gamma)$, for the same samples as in **(a)**. The vertical dashed lines in **(a,b)** mark the strain values at which the mobility maps are shown in the lower panels for the case with horizontal shear band (A) and vertical shear bands (B).

quasi-static shear (aqs) protocol, Ozawa et al. (2018) have demonstrated that the formation of a shear band is intimately linked to the degree of annealing of the initially undeformed glass sample. Then, horizontal shear bands are associated with a very sharp stress drop that becomes sharper with increasing system size which is reminiscent of a first-order phase transition. In fact, the authors of Ozawa et al. (2018) argue that, under athermal conditions, the yielding of a well-annealed amorphous solid can be interpreted as a first-order non-equilibrium phase transition. It is also interesting that inhomogeneous states with horizontal shear bands can be stabilized via oscillatory shear. This has been recently demonstrated in a simulation study by Parmar et al. (2019).

Our work shows that the formation of horizontal shear bands is associated with a peculiar behavior of the system's potential energy. After the formation of such a band right after the occurrence of the stress drop in the stress-strain relation, the potential energy function $U(\gamma)$ has local minimum, followed by an increase of U with further deformation toward the steady state value. We note that this behavior becomes more pronounced with decreasing temperature as well as the degree of annealing of the initial unsheared glass state (Golkia et al., 2020). The findings

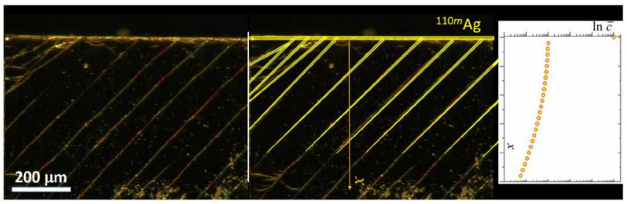

FIGURE 5 | Side-view of a cold-rolled PdNiP glass **(left)** with a sketch of an anticipated distribution of the ^{110m}Ag tracer atoms after diffusion annealing **(center)** and a hypothetical penetration profile measured by a parallel sectioning parallel to the specimen's surface **(right)**. It is assumed that a remnant activity on the surface is remaining. A single family of shear bands is seen with some irregularities. $\bar{c}$ is the layer concentration of the tracer and x is the penetration depth.

may also reveal what one sees on the typical experimental time and length scales which are both much larger than those of the simulation. In experiments of bulk metallic glasses, shear banded structures appear to maintain after yielding and a subsequent switch-off of the mechanical load. This is due to the efficient stress release in combination with the minimization of the system's potential energy via the formation of a shear band.

5. ATOMIC TRANSPORT ALONG SHEAR BANDS

Detailed calorimetric investigations substantiated an absence of any measurable changes of the calorimetric response of a bulk metallic glass, particularly of a model PdNiP one (Mitrofanov et al., 2014, 2015), on shear banding induced by cold rolling to low strain, about 10% of thickness reduction. All main calorimetric parameters, including glass transition temperature, T_g, crystallization temperature, total enthalpy, and low temperature heat capacity remain unchanged in the limits of typical experimental uncertainties (Mitrofanov et al., 2014, 2015).

However, the structure and local atomic configurations—as revealed by, e.g., the MRO parameter (Hilke et al., 2019)—are different in the shear bands from the surrounding matrix. The strain-induced differences in the atomic configurations might be traced by dedicated investigations of the atomic transport rates, and indeed the tracer diffusion measurements substantiated kinetic differences between the shear bands and the glassy matrix (Bokeloh et al., 2011).

5.1. Shear Bands as Short-Circuits for Enhanced Diffusion

In **Figure 5**, a side view on off-sets induced by shear band propagation is presented (left panel). Before the one-pass rolling to about 5%, the sample was polished to a mirror-like finish that allowed to visualize the shear bands.

In a typical radiotracer experiment (Paul et al., 2014), we are depositing a tiny amount of a suitable radioactive isotope on the polished surface and subjecting the specimen to a diffusion annealing treatment. In order to quantify the diffusion rates along the shear bands, the conditions of the diffusion treatment are typically chosen which corresponds to the absence of any volume diffusion in the glass (i.e., the corresponding diffusion depths, $\sqrt{D_v t}$, are smaller than an interatomic distance, with D_v and t being the volume diffusion coefficient and the diffusion time, respectively). An anticipated tracer distribution after such annealing is sketched in **Figure 5** (central panel). In this figure, one can recognize a remnant activity of the tracer material (in a particular case of the ^{110m}Ag isotope) on the surface, which correspond to not-diffused isotopes and some potential irregularities in the depth distribution of the tracer atoms due to heterogeneities of the shear banding. Formally, these diffusion conditions correspond to the C-type kinetic regime of diffusion along short circuits in crystalline solid after Harrison's classification (Harrison, 1961; Paul et al., 2014).

After diffusion annealing, the sample is sectioned by, e.g., precision mechanical grinding, parallel to the initial surface in thin slices and the *total* activity in the sections is measured. As a result, a penetration profile corresponding to the layer activity of the tracer, $\bar{c}$, vs. the penetration depth, x, is measured, **Figure 5**, right panel.

In some cases, we are applying a second tracer, e.g., the ^{57}Co to the sample surface after annealing just before sectioning. If there would be micro-cracks in the sample, the ^{57}Co isotope would be detectable to similar depths as ^{110m}Ag. Our experiments (Bokeloh et al., 2011) confirmed the absence of the second isotope at large depths and substantiated a deep penetration of the first isotope, which experienced a diffusion annealing treatment. Thus, the observed deep penetration of the ^{110m}Ag isotope is not due to deformation-induced cracks.

The shear band diffusion coefficients, D_{sb}, can be determined as (Paul et al., 2014)

$$D_{sb} = \frac{q}{4t}\left(-\frac{\partial \ln \bar{c}}{\partial x^2}\right)^{-1}. \quad (5)$$

Here, the factor q takes into account the orientation of the short-circuit path with respect to the normal to the sample surface and it is equal to about 2 since the shear bands are oriented at about 45° to the sample surface.

The determined shear band diffusion coefficients of Ag atoms, D_{sb}, turned out to be eight to nine orders of magnitude larger than the volume diffusion coefficients measured in as-cast PdNiP samples for Au (Duine et al., 1993) or Pd (Bartsch et al., 2010) tracers. At 473 K, the volume diffusion coefficients are less than 10^{-26} m^2/s at 473 K, while the shear band diffusion coefficients are of the order of 10^{-17} m^2/s at the same temperature (**Figure 6**).

These data substantiate the possibility to use tracer diffusion measurements in deformed glasses as a unique and very sensitive probe of changes of local atomic structures. Tracking the shear band diffusion in dependence of the annealing time in the same way as the as-quenched and deformed material indicates differences in structure of the matrix material as well as the shear band structure in the relaxed material.

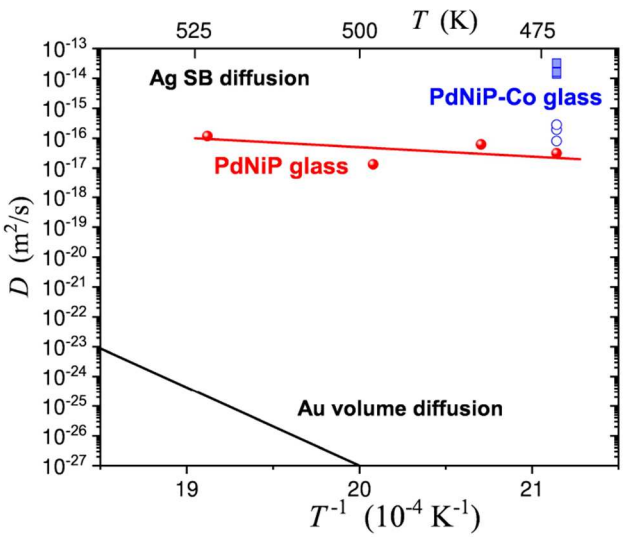

FIGURE 6 | Arrhenius plot for Ag diffusion along shear bands (red symbols Binkowski et al., 2016) in comparison to the extrapolation of the Arrhenius dependence measured for Au bulk diffusion (Duine et al., 1993) in PdNiP glass of nominally the same composition (black line). For comparison, the shear band diffusion coefficients measured for Ag diffusion in cold-rolled PdNiP-Co glass (Hubek et al., 2020) are shown (blue symbols).

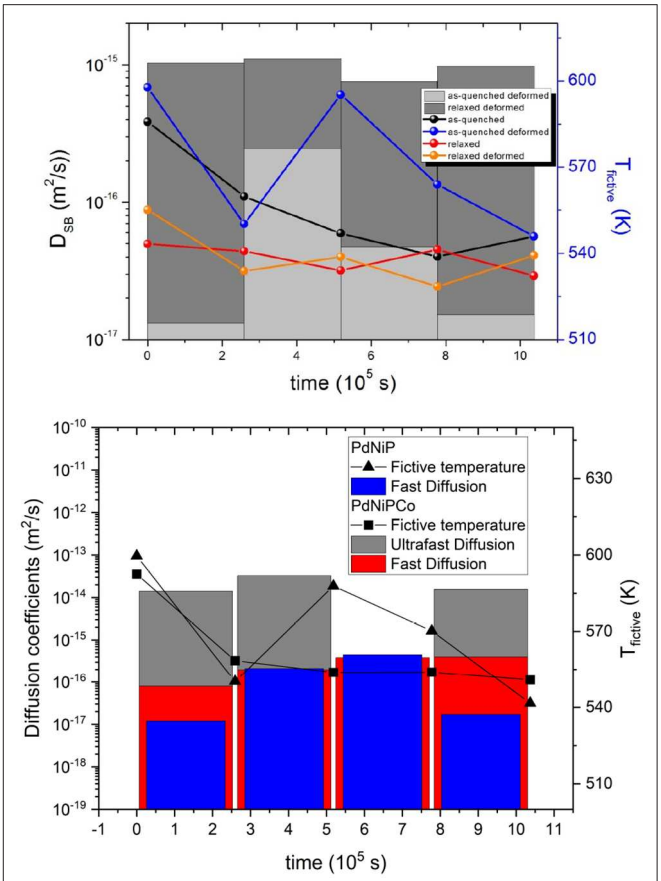

FIGURE 7 | Time dependence of diffusion enhancement in model PdNiP glass deformed by cold-rolling as compared to that in PdNiP preliminary relaxation annealed **(Top)** or to as-quenched Co-microalloyed PdNiP glass **(Bottom)**. Further, the time dependencies of the diffusion coefficients are compared with that of the fictive temperature $T_{fictive}$ of the BMGs. The systematic uncertainty of a single diffusion experiments can be approximated to be about 50%. These are not shown for better visibility of the graph.

5.2. Relaxation Behavior of Enhanced Shear Band Diffusion

The shear band diffusivities behave in an abnormal fashion (unlike expected when structural relaxation is considered to lower diffusivities) for the deformed as-quenched samples. Yet, this behavior is not observed for samples relaxed previously to deformation. In contrast to the deformed as-quenched metallic glass state, the deformed relaxed samples reach much earlier a metastable equilibrium state, in which the atomic mobility inside the shear bands is no longer time dependent.

In cold-rolled as-quenched Co-free PdNiP glass, fast shear band diffusion was measured (the diffusion coefficients are of the order of 10^{-17} m^2/s) and interpreted in terms of a single family of shear bands. A cross-over relaxation behavior of shear band diffusion is observed and explained as a counteraction of redistribution of excess free volume in deformation-modified volume and in shear bands.

Relaxation-annealed PdNiP at 503 K for 1 day reveal unexpectedly the existence of two kinds of short-circuit contributions with conventional fast (about 10^{-17} m^2/s) and ultra-fast diffusion (about 10^{-15} m^2/s) coefficients (**Figure 7**).

The ultra-fast shear band diffusivity in relaxed samples shows not only time-independent, but rather shows unexpectedly a diffusion enhancement in comparison to the deformed as-quenched state of about 1–2 orders of magnitude (**Figure 7**). Since atoms in general need less energy to move through a more open structure, the shear band structure in relaxed glasses differs to the shear bands in as-quenched glasses indicating the presence of an enhanced amount of free volume.

Similarly, the Co micro-alloyed glass reveals unambiguously two families of short circuits, namely the "fast" diffusion paths (essentially the same diffusion coefficients) and a second type of "ultrafast" paths (with diffusion coefficients of the order of 10^{-15}–10^{-14} m^2/s), correspondingly open and filled blue symbols in **Figure 6**. We are attributing this second path to a special type of shear band. Such shear bands are either absent in the as-quenched Co-free glass or their number density is below the detection limit of the applied radiotracer technique. There is a clear difference between the optically observable primary and secondary shear bands—available in fact in both types of the glassy systems—and the kinetically different shear bands. So far, it is a very first observation of this behavior.

Furthermore, the exceptional time-evolution of the glass transition observed in the heat flow curves of the deformed as-quenched glass is not observed for the relaxed and deformed glass. The macroscopically measurable atomic rearrangements during annealing are missing. Annealing treatments below the glass transition temperatures of glasses are known to

change the glassy structure causing physical aging. Free volume annihilates and "anneals out" as the structural relaxation occurs (Haruyama and Inoue, 2006). The more dense structure contains decreasingly sites for increased atomic movement known as STZ. Thus, taking the STZs as precursors for the formation of shear bands, shear band emergence is strongly decreased. The excess energy barrier to effectuate a shear transformation is much higher when lacking of adequate amount of free volume. If the amount of shear deformation is, however, high enough to provide the necessary energy, shear transformations are activated. An increase in input energy engenders an increase in release of energy during shear band formation and, as a resulting consequence, may force a more open structure of the resulting shear bands.

We may argue that shear banding in relaxed glass induces stronger variation of local configurations with respect to those in as-quenched glasses and, importantly, these stronger variations correspond to energy configurations being more stable with respect to their further structural relaxation. As a result, we may suggest that the shear bands induced in relaxed metallic glass represent a more stable, but different glassy configuration as the matrix itself that could be further investigated with respect to production of nano-glasses (Gleiter, 2013) by plastic deformation. These changes are strongly localized at the shear bands and the corresponding contribution is almost invisible in the DSC measurements.

5.3. Micro-Alloying

5.3.1. Structural Changes and Mechanical Response

Micro-alloying was performed on monolithic $Pd_{40}Ni_{40}P_{20}$ bulk metallic glass by adding small amounts of Co and Fe. The material was melted in a melt-spinner using induction melting and subsequently casted into Cu-molds (Nollmann et al., 2016) (see the flow chart of **Figure 8**). The amorphous state was confirmed by X-ray diffraction and it was further characterized by electron diffraction and differential scanning calorimetry, left and central panels in **Figure 8**, respectively. The 3-point bending tests were performed showing an improved ductility when Co was added, **Figure 8**, right panel. However, the addition of Fe led to embrittlement, whereas the ternary $Pd_{40}Ni_{40}P_{20}$ alloy showed quite some ductility. Recent microstructural investigations using fluctuation electron microscopy showed that a second larger MRO correlation length was observed in the ductile material (Davani et al., 2020), which explains the difference in the deformability.

5.3.2. Mechanical Properties (Poisson's Ratio) of Deformed BMGs

It is still a matter of debate, whether the ductility of bulk metallic glasses is related to their elastic constants. Here we present experiments on the Poisson's ratio of Pd-based BMG in dependence of the degree of deformation. For this purpose, $Pd_{40}Ni_{40}P_{20}$ was cold rolled up to 50% deformation and the elastic constants were subsequently determined from ultrasonic measurements (Nollmann et al., 2016). Our experiments (**Figure 9**) show that there is no measurable change in the Poisson's ratio, comparing undeformed with deformed metallic glass.

5.3.3. Shear Band Diffusion in Microalloyed State

The radiotracer measurements substantiated that cold-rolled Co-microalloyed PdNiP glasses reveal the existence of two families of shear bands, slow and fast ones (Hubek et al., 2020), see open and filled blue symbols in **Figure 6**. From the measurements with the ^{57}Co tracer the resulting ratio for the PdNiPCo profiles lies between 1:10 to 1:100 of ultrafast to fast diffusion paths.

Multiple kinds of shear bands, defined as primary and secondary (Schroers and Johnson, 2004; Chen and Lin, 2010) or "hot" and "cold" (Lewandowski and Greer, 2005) shear bands, were previously reported in the literature. While one could interpret the two measured shear band diffusion coefficients as indication for primary and secondary shear bands, this is not clearly the case.

In the present case of a low imposed deformation, mainly primary shear bands were detected (Hubek et al., 2020). However, a strong heterogeneity of shear band offsets was reported (Hubek et al., 2020) for Co-microalloyed PdNiP glass. Those results indicate a correlation between the distribution of shear band offsets and the existence of different families of short-circuit diffusion paths in the PdNiP-based metallic glasses. Although our measurements do not provide a direct verification that the ultra-fast diffusion paths are represented by the shear bands with large shear offsets, there is a direct correlation between the structure heterogeneity and the kinetic heterogeneity of the shear band properties. This finding is encouraging and demands further investigations.

The different shear band types were reported for different glasses, irrespective of their composition (Schroers and Johnson, 2004; Chen et al., 2010). Thus it is important to highlight that in Hubek et al. (2020), an increased heterogeneity of the shear band properties induced by micro-alloying was for the first time reported. Moreover, the tracer diffusion data document the existence of *kinetically different* classes of shear bands. The structural difference between these types has to be elucidated yet. It is probably not just different thickness of the shear bands, especially since the extensive structural and chemical TEM studies (Schmidt et al., 2015) have not revealed an abnormal variation of the shear band thickness which is about 10 nm or less.

One might suggest that porosity could be the origin of the fast diffusion path, but the experiments with the ^{57}Co tracer ruled out this explanation.

6. SUMMARY AND CONCLUSIONS

In this work, we have used a combination of experiment and molecular dynamics (MD) computer simulation to investigate the formation and properties of shear bands in bulk metallic PdNiP glasses under and after mechanical load. While the experiments focussed on the materials properties after shear band formation, in the MD simulation we were aiming at studying the shear band formation during shear on a microscopic level.

An important tool in the experiments is the measurement of tracer diffusion in shear-banded regions. In a cold-rolled

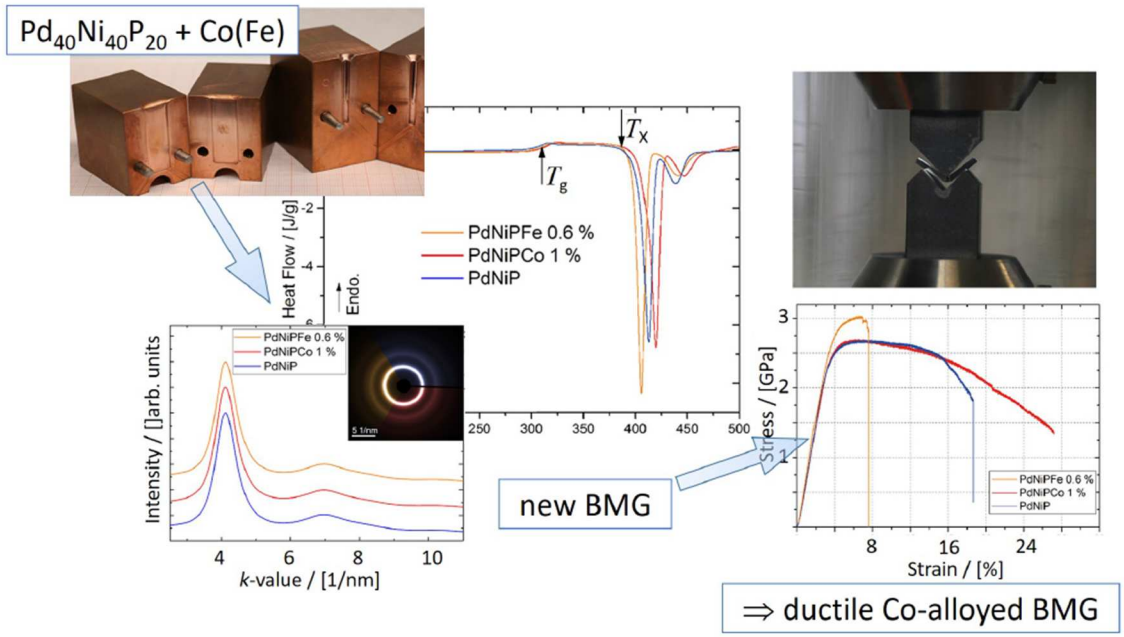

FIGURE 8 | Workflow showing the whole process of micro-alloying from casting panel, characterization to the mechanical testing, adopted from Nollmann (2018). First, the glasses is produced by casting into a copper mold **(top-left)**. Furthermore, the sample are tested for their amorphousness through X-ray diffraction **(bottom-left)** and differential scanning calorimetry **(center)** measurements. Finally, the sample is subjected to a three-point bending test **(right)**.

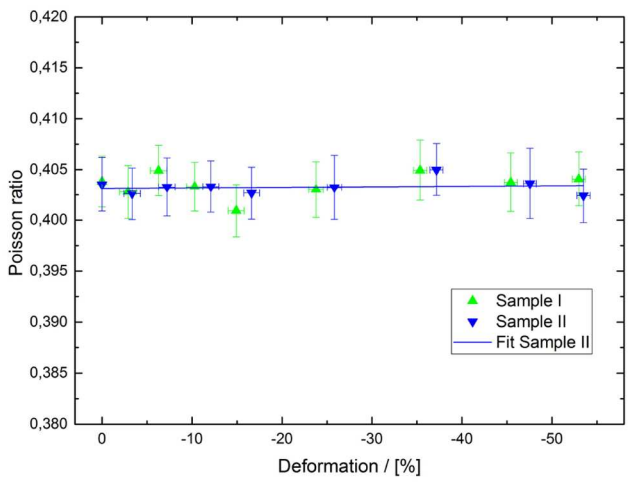

FIGURE 9 | Evolution of the Poisson's ratio in $Pd_{40}Ni_{40}P_{20}$ during cold-rolling. The error bars represent the standard deviation of a set of 10 measurements. Sample I and sample II are different casts of $Pd_{40}Ni_{40}P_{20}$ metallic glass to showcase the reproducibility of this experiment.

model PdNiP glass, significantly enhanced (akin short-circuit) shear band diffusion is determined at the temperatures at which volume diffusion in as-cast glass is frozen. A cross-over relaxation behavior of shear band diffusion is reported and explained as a counteraction to the redistribution of excess free volume in the deformation-modified volume and in the shear bands. The Co micro-alloyed glass reveals unambiguously the existence of at least two distinct families of short circuits, namely the "fast" diffusion paths (typically for Co-free PdNiP glasses) and a second type of "ultrafast" paths (with the diffusion coefficients higher by two orders of magnitude). The second path is attributed to a special type of shear bands. Such shear bands are either absent in the Co-free glass or their number density is below the detection limit of the applied radiotracer technique. There is a clear difference between the optically observable primary and secondary shear bands—available in fact in both types of the glassy systems—and the kinetically different shear bands. Co micro-alloying was unambiguously shown to enhance ductility of a model PdNiP glass, whereas addition of Fe or Cu increases brittleness. A correlation of the enhanced ductility, appearance of specific MRO motives and the existence of kinetically specific shear bands upon Co alloying is established. The diffusion enhancement in plastically deformed Co-alloyed glass shows specific response upon annealing below glass transition temperature with a cross-over type of behavior and the different time scales of relaxation for kinetically different types of shear bands.

In the MD simulations, we consider a binary Lennard-Jones model that can be considered as a model for $Ni_{80}P_{20}$. Shear at a constant shear rate is imposed on this system using a planar Couette flow geometry. The sheared glasses show the typical stress-strain relations with an overshoot around a strain of $\gamma = 0.08$, marking the onset of plastic flow. Right after the stress overshoot, prior to the steady state, there is the emergence of inhomogeneous flow patterns. Both vertical and horizontal shear

bands are observed. While the vertical bands lead to a relatively quick approach of the steady state, the horizontal bands are associated with a local potential energy minimum and a slow growth with increasing strain (we note that the width of the shear band increases in a subdiffusive manner; Golkia et al., 2020). The emergence of horizontal shear bands is intimately linked to the level of annealing of the initial undeformed glass state and the the applied strain rate (Golkia et al., 2020). Well-annealed glasses in combination with low shear rates exhibit a high affinity to form horizontal shear bands. This finding indicates why, on the experimental scales, shear banding appears to be a common feature in BMGs.

Another issue that we have addressed in our work is the question whether one can infer the plastic response of BMGs from their elastic properties. The evolution of the Poisson's ratio of $Pd_{40}Ni_{40}P_{20}$ BMG during deformation was measured by ultrasonic measurements revealing no detectable changes. These findings are supported by the MD simulations. Thus, we conclude that the value of the Poisson's ratio cannot be used as an unambiguous criterion of the ductility of any BMG. As the MD simulation indicates, this is also true for other elastic properties Golkia et al.. We propose that the specific changes of MRO parameters and the kinetic response of deformed glasses are key features for adequate description of deformation phenomena both in BMGs as well as in inorganic glasses. The comparison of plastic flow in BMGs to that in inorganic glasses such as silica will be a theme of forthcoming studies.

DATA AVAILABILITY STATEMENT

The raw data supporting the conclusions of this article will be made available by the authors, without undue reservation, to any qualified researcher.

AUTHOR CONTRIBUTIONS

SD, HR, JH, and GW designed the research. RH, SH, FD, MG, GS, SD, and HR performed the research. SD, HR, JH, GW, RH, SH, FD, MG, and GS analyzed the data. SD, HR, JH, and GW wrote the paper.

ACKNOWLEDGMENTS

We gratefully acknowledge financial support by the German Science Foundation (DFG) via SPP 1594 *Topological engineering of ultra-strong glasses*, projects WI 1899/27-2 and HO 2231/8-2, and for TEM equipment via the Major Research Instrumentation Programme under INST 211/719-1 FUGG.

REFERENCES

Agoritsas, E., and Martens, K. (2017). Non-trivial rheological exponents in sheared yield stress fluids. *Soft Matter* 13:4653. doi: 10.1039/c6sm02702d

Alix-Williams, D. D., and Falk, M. L. (2018). Shear band broadening in simulated glasses. *Phys. Rev. E* 98:053002. doi: 10.1103/PhysRevE.98.053002

Argon, A. S. (1979). Plastic deformation in metallic glasses. *Acta Metallur.* 27:47.

Ashby, M. F., and Greer, A. L. (2006). Metallic glasses as structural materials. *Scrip. Mater.* 54, 321–326. doi: 10.1016/j.scriptamat.2005.09.051

Bartsch, A., Rätzke, K., Meyer, A., and Faupel, F. (2010). Dynamic arrest in multicomponent glass-forming alloys. *Phys. Rev. Lett.* 104:195901. doi: 10.1103/PhysRevLett.104.195901

Binkowski, I., Shrivastav, G. P., Horbach, J., Divinski, S. V., and Wilde, G. (2016). Shear band relaxation in a deformed bulk metallic glass. *Acta Mater.* 109, 330–340. doi: 10.1016/j.actamat.2016.02.061

Bokeloh, J., Divinski, S. V., Reglitz, G., and Wilde, G. (2011). Accelerated diffusion along shear bands in metallic glass. *Phys. Rev. Lett.* 107:235503. doi: 10.1103/PhysRevLett.107.235503

Chattoraj, J., and Lemaître, A. (2013). Elastic signature of flow events in supercooled liquids under shear. *Phys. Rev. Lett.* 111:066001. doi: 10.1103/PhysRevLett.111.066001

Chen, K.-W., and Lin, J.-F. (2010). Investigation of the relationship between primary and secondary shear bands induced by indentation in bulk metallic glasses. *Int. J. Plast.* 26, 1645–1658. doi: 10.1016/j.ijplas.2010.03.003

Chen, N., Martin, L., Luzguine-Luzgin, D. V., and Inoue, A. (2010). Role of alloying additions in glass formation and properties of bulk metallic glasses. *Materials* 3, 5320–5339. doi: 10.3390/ma3125320

Chhabra, R. P., and Richardson, J. F. (2008). *Non-Newtonian Flow and Applied Rheology, 2nd Edn.* Oxford: Elsevier Butterworth-Heinemann.

Dasgupta, R., Hentschel, H. G. E., and Procaccia, I. (2012). Microscopic mechanism of shear bands in amorphous solids. *Phys. Rev. Lett.* 109:255502. doi: 10.1103/PhysRevLett.109.255502

Dasgupta, R., Hentschel, H. G. E., and Procaccia, I. (2013). Yield strain in shear banding amorphous solids. *Phys. Rev. E* 87:022810. doi: 10.1103/PhysRevE.87.022810

Davani, F. A., Hilke, S., Rösner, H., Geisler, D., Gebert, A., and Wilde, G. (2020). What renders bulk metallic glass ductile/brittle? - New insight from the medium-range order. *arXiv [Preprint]. arXiv*:2003.01368.

Duine, P. A., Sietsma, J., and Beukel, A. v. d. (1993). Atomic transport in amorphous $Pd_{40}Ni_{40}P_{20}$ near the glass-transition temperature: Au diffusivity and viscosity. *Phys. Rev. B* 48:6957. doi: 10.1103/PhysRevB.48.6957

Falk, M. L., and Langer, J. S. (1998). Dynamics of viscoplastic deformation in amorphous solids. *Phys. Rev. E* 57:7192. doi: 10.1103/PhysRevE.57.7192

Gendelman, O., Jaiswal, P. K., Procaccia, I., Gupta, B. S., and Zylberg, J. (2015). Shear transformation zones: state determined or protocol dependent? *Europhys. Lett.* 109:16002. doi: 10.1209/0295-5075/109/16002

Gleiter, H. (2013). Nanoglasses: a new kind of noncrystalline materials. *Beilstein J. Nanotechnol.* 4:517. doi: 10.3762/bjnano.4.61

Golkia, M., Shrivastav, G. P., Chaudhuri, P., and Horbach, J. (2020) Flow heterogeneities in supercooled liquids and glasses under shear. *arXiv [Preprint]. arXiv*:2004.02868.

Golkia, M., Shrivastav, G. P., Nollmann, N., Hieronymus-Schmidt, V., Rösner, H., Wilde, G., et al. (2020). preprint.

Harrison, L. G. (1961). Influence of dislocations on diffusion kinetics in solids with particular reference to the alkali halides. *Trans. Faraday Soc.* 57, 1191–1199. doi: 10.1039/tf9615701191

Haruyama, O., and Inoue, A. (2006). Free volume kinetics during sub-T_g structural relaxation of a bulk $Pd_{40}Ni_{40}P_{20}$ metallic glass. *Appl. Phys. Lett.* 88:131906. doi: 10.1063/1.2189833

Hassani, M., Zirdehi, E. M., Kok, K., Schall, P., Fuchs, M., and Varnik, F. (2018). Long-range strain correlations in 3D quiescent glass forming liquids. *Europhys. Lett.* 124:18003. doi: 10.1209/0295-5075/124/18003

Hieronymus-Schmidt, V., Rösner, H., Wilde, G., and Zaccone, A. (2017). Shear banding in metallic glasses described by alignments of Eshelby quadrupoles. *Phys. Rev. B* 95:134111. doi: 10.1103/PhysRevB.95.134111

Hilke, S., Rösner, H., Geissler, D., Gebert, A., Peterlechner, M., and Wilde, G. (2019). The influence of deformation on the medium-range order of a Zr-based bulk metallic glass characterized by variable resolution fluctuation electron microscopy. *Acta Mater.* 171:275–281. doi: 10.1016/j.actamat.2019.04.023

Hubek, R., Seleznev, M., Binkowski, I., Peterlechner, M., Divinski, S. V., and Wilde, G. (2020). Intrinsic heterogeneity of shear banding: hints from diffusion and

relaxation measurements of Co micro-alloyed PdNiP-based glass. *J. Appl. Phys.* 127:115109. doi: 10.1063/1.5142162

Klaumünzer, D., Lazarev, A., Maaß, R., Dalla Torre, F., Vinogradov, A., and Löffler, J. F. (2011). Probing shear-band initiation in metallic glasses. *Phys. Rev. Lett.* 107:185502. doi: 10.1103/PhysRevLett.107.185502

Kob, W., and Andersen, H. C. (1994). Scaling behavior in the β-relaxation regime of a supercooled Lennard-Jones mixture. *Phys. Rev. Lett.* 73, 1376–1379. doi: 10.1103/PhysRevLett.73.1376

Kumar, G., Neibecker, P., Liu, Y. H., and Schroers, J. (2013). Critical fictive temperature for plasticity in metallic glasses. *Nat. Commun.* 4:1536. doi: 10.1038/ncomms2546

Lechner, W., Puff, W., Wilde, G., and Würschum, R. (2010). Vacancy-type defects in amorphous and nanocrystalline Al alloys: variation with preparation route and processing. *Scripta Mater.* 62, 439–442. doi: 10.1016/j.scriptamat.2009.11.037

Lees, A. W., and Edwards, S. F. (1972). The computer study of transport processes under extreme conditions, *J. Phys. C* 5:1921.

Lewandowski, J. J., and Greer, A. L. (2005). Temperature rise at shear bands in metallic glasses. *Nat. Mater.* 5, 15–18. doi: 10.1038/nmat1536

Lewandowski, J. J., Wang, W. H., and Greer, A. L. (1993). Intrinsic plasticity of brittleness of metallic glasses. *Philos. Mag. Lett.* 85, 77–87. doi: 10.1080/09500830500080474

Maaß, R., Samwer, K., Arnold, W., and Volkert, C. A. (2014). A single shear band in a metallic glass: local core and wide soft zone. *Appl. Phys. Lett.* 105:171902. doi: 10.1063/1.4900791

Mitrofanov, Y. P., Peterlechner, M., Binkowski, I., Zadorozhnyy, M. Y., Golovin, I. S., Divinski, S. V., et al. (2015). The impact of elastic and plastic strain on relaxation and crystallization of PdNiP-based bulk metallic glasses. *Acta Mater.* 90:318. doi: 10.1016/j.actamat.2015.03.001

Mitrofanov, Y. P., Peterlechner, M., Divinski, S. V., and Wilde, G. (2014). Impact of plastic deformation and shear band formation on the boson heat capacity peak of a bulk metallic glass. *Phys. Rev. Lett.* 112:135901. doi: 10.1103/PhysRevLett.112.135901

Nollmann, N. (2018). *Plastische Deformation und mechanische Eigenschaften von Palladium-basierten metallischen Gläsern* (Ph.D. thesis). Münster University, Münster, Germany.

Nollmann, N., Binkowski, I., Schmidt, V., Rösner, H., and Wilde, G. (2016). Impact of micro-alloying on the plasticity of Pd-based bulk metallic glasses. *Scripta Mater.* 111, 119–122. doi: 10.1016/j.scriptamat.2015.08.030

Ovarlez, G., Cohen-Addad, S. Krishan, K., Goyon, J., and Coussot, P. (2013). On the existence of a simple yield stress fluid behavior. *J. Non-Newton. Fluid Mech.* 193, 68–79. doi: 10.1016/j.jnnfm.2012.06.009

Ozawa, M., Berthier, L., Biroli, G., Rosso, A., and Tarjus, G. (2018). Random critical point separates brittle and ductile yielding transitions in amorphous materials. *Proc. Natl. Acad. Sci. U.S.A.* 115, 6656–6661. doi: 10.1073/pnas.1806156115

Parmar, A. D. S., Kumar, S., and Sastry, S. (2019). Strain localization above the yielding pont in cyclically deformed glasses. *Phys. Rev. X* 9:021018. doi: 10.1103/PhysRevX.9.021018

Paul, A., Laurila, T., Vuorinen, V., and Divinski, S. V. (2014). *Thermodynamics, Diffusion and the Kirkendall Effect in Solids* . Heidelberg: Springer.

Plimpton, S. (1995). Fast parallel algorithms for short-range molecular dynamics. *J. Comput. Phys.* 117, 1–19. doi: 10.1006/jcph.1995.1039

Radek, M., Tenberge, J.-G., Hilke, S., Wilde, G. and Peterlechner, M. S (2018). TEMclA multi-GPU multislice algorithm for simulation of large structure and imaging parameter series. *Ultramicroscopy* 188, 24–30. doi: 10.1016/j.ultramic.2018.02.004

Radić, D., Hilke, S., Peterlechner, M., Posselt, M., and Bracht, H. (2019). Fluctuation electron microscopy on silicon amorphized at varying self ion-implantation conditions. *J. Appl. Phys.* 126:095707. doi: 10.1063/1.5107494

Rösner, H., Peterlechner, M., Kübel, C., Schmidt, V., and Wilde, G. (2014). Density changes in shear bands of a metallic glass determined by correlative analytical transmission electron microscopy. *Ultramicroscopy* 142, 1–9. doi: 10.1016/j.ultramic.2014.03.006

Schmidt, V., Rösner, H., Peterlechner, M., Wilde, G., and Voyles, P. M. (2015). Quantitative measurement of density in a shear band of metallic glass monitored along its propagation direction. *Phys. Rev. Lett.* 115:035501. doi: 10.1103/PhysRevLett.115.035501

Schroers, J., and Johnson, W. L. (2004). Ductile bulk metallic glass. *Phys. Rev. Lett.* 93:255506. doi: 10.1103/PhysRevLett.93.255506

Shao, H., Xu, Y., Shi, B., Yu, C., Hahn, H., Gleiter, H., et al. (2013). High density of shear bands and enhanced free volume induced in $Zr_{70}Cu_{20}Ni_{10}$ metallic glass by high-energy ball milling. *J. Alloys Compounds* 548, 77–81. doi: 10.1016/j.jallcom.2012.08.132

Shrivastav, G. P., Chaudhuri, P., and Horbach, J. (2016a). Heterogeneous dynamics during yielding of glasses: effect of aging. *J. Rheol.* 60, 835–847. doi: 10.1122/1.4959967

Shrivastav, G. P., Chaudhuri, P., and Horbach, J. (2016b). Yielding of glass under shear: a directed percolation transition precedes shear-band formation. *Phys. Rev. E* 94:042605. doi: 10.1103/PhysRevE.94.042605

Soddemann, T., Dünweg, B., and Kremer, K. (2003). Dissipative particle dynamics: a useful thermostat for equilibrium and nonequilibrium molecular dynamics simulations. *Phys. Rev. E* 68:046702. doi: 10.1103/PhysRevE.68.046702

Taub, A. I., and Spaepen, F. (1980). The kinetics of structural relaxation of a metallic glass. *Acta Metallur.* 28, 1781–1788. doi: 10.1016/0001-6160(80)90031-0

Tool, A. Q., and Eichlin, C. G. (1931). Variations caused in heating curves of glass by heat treatment. *J. Am. Ceram. Soc.* 14, 276–308. doi: 10.1111/j.1151-2916.1931.tb16602.x

Treacy, M. M. J., and Gibson, J. M. (1996). Variable coherence microscopy: a rich source of structural information from disordered materials. *Acta Crystallogr. Sect. A* 52:212.

Treacy, M. M. J., Gibson, J. M., Fan, L., Paterson, D. J., and McNulty, I. (2005). Fluctuation microscopy: a probe of medium range order. *Rep. Prog. Phys.* 68:2899. doi: 10.1088/0034-4885/68/12/R06

Voyles, P., and Muller, D. (2002). Fluctuation microscopy in the STEM. *Ultramicroscopy* 93, 147–159. doi: 10.1016/S0304-3991(02)00155-9

Wilde, G., Görler, G. P., Willnecker, R., and Fecht, H. J. (2000). Calorimetric thermomechanical and rheological characterizations of bulk metallic glassforming: $Pd_{40}Ni_{40}P_{20}$, *J. Appl. Phys.* 87:1141. doi: 10.1063/1.371991

Wilde, G., Sebright, J. L., and Perepezko, J. H. (2006). Bulk liquid undercooling and nucleation in gold. *Acta Mater.* 54, 4759–4769. doi: 10.1016/j.actamat.2006.06.007

Zausch, J., and Horbach, J. (2009). The build-up and relaxation of stresses in a glassforming soft-sphere mixture under shear: a computer simulation study. *Europhys. Lett.* 88:60001. doi: 10.1209/0295-5075/88/60001

Zausch, J., Horbach, J., Laurati, M., Egelhaaf, S. U., Brader, J. M., Voigtmann, T., et al. (2008). From equilibrium to steady state: the transient dynamics of colloidal liquids under shear. *J. Phys.: Condens. Matter* 20:404120. doi: 10.1088/0953-8984/20/40/404210

Conflict of Interest: The authors declare that the research was conducted in the absence of any commercial or financial relationships that could be construed as a potential conflict of interest.

frontiers in Materials

ORIGINAL RESEARCH
published: 29 May 2020
doi: 10.3389/fmats.2020.00126

Deformation and Fracture of Silica Glass Fiber Under Sharp Wedge-Indentation

*Roman Sajzew, Rene Limbach and Lothar Wondraczek**

Otto Schott Institute of Materials Research, Friedrich Schiller University Jena, Jena, Germany

Fiber or fiber tapers are the material of choice when studying the mechanical properties and intrinsic load-response of glasses at highest sample quality and experimental repeatability. However, surface curvature strongly complicates meaningful analysis using local (sharp) contact probes. Wedge-indentation provides a means for overcoming some of the problems of normal indentation on curved glass surfaces. In particular, it enables testing in comparably homogenous, two-dimensional stress fields, avoiding the effects of the sharp edges of pyramidal indenters and facilitating auxiliary *in situ* or *ex situ* structural mapping, for example, by vibrational spectroscopy. Adjusting the wedge's opening angle, length and orientation relative to the fiber surface enables highly reproducible studies of material deformation, surface crack initiation, and effects of fiber anisotropy.

Keywords: silica glass, glass fiber, mechanical properties, nanoindentation, wedge-indentation, plasticity, fracture, hardness

OPEN ACCESS

Edited by:
Praveen Sekhar, Washington State University, United States

Reviewed by:
Yann Gueguen, University of Rennes 1, France
Guglielmo Macrelli, Isoclima SpA, Italy

***Correspondence:**
Lothar Wondraczek
lothar.wondraczek@uni-jena.de

Specialty section:
This article was submitted to Ceramics and Glass, a section of the journal Frontiers in Materials

Received: *10 March 2020*
Accepted: *17 April 2020*
Published: *29 May 2020*

Citation:
Sajzew R, Limbach R and Wondraczek L (2020) Deformation and Fracture of Silica Glass Fiber Under Sharp Wedge-Indentation. Front. Mater. 7:126. doi: 10.3389/fmats.2020.00126

INTRODUCTION

Despite superior intrinsic material properties, commercially available glass products usually exhibit very low practical strength. This is due to the defect susceptibility of glass surfaces. Paired with high brittleness, surface defects cause local stress amplification, and, hence, material failure (Wondraczek et al., 2011). Microscopic defects may already form during the manufacturing process (Varshneya, 2018), thus determining characteristic limits of practical strength for different glass products. For example, while untreated container glasses rarely reach tensile strength above 100 MPa, optical glass fiber may very well approach 10 GPa, or more (Kurkjian et al., 2003; Kurkjian et al., 2010). Defect susceptibility occurs across all length scales; ultimately, stress accumulation, and glass deformation are mediated by rigidity fluctuation which results from structural heterogeneity of the glass network itself (Benzine et al., 2018). The generation and growth of microscopic defects in glasses has been studied intensely over the past decades (Rouxel and Yoshida, 2017), in particular, using methods of micro or nanoindentation (Yoshida, 2019). However, indentation methods remain problematic and highly ambiguous when analyzing glass fracture and material toughness (Cook, 2020). Lateral indentation was introduced as a complementary method for assessing scratch hardness (Sawamura and Wondraczek, 2018; Sawamura et al., 2019) and surface cracking (Moayedi and Wondraczek, 2017), but requires flat and smooth specimen surfaces. On the other hand, fiber drawn from silica or aluminosilicate glass rods (Kurkjian et al., 2003; Kurkjian et al., 2010), or tapered silica (Brambilla and Payne, 2009) have been the closest in terms of reaching the limits of theoretical (intrinsic) glass strength in praxis. Carefully prepared glass fibers benefit from very high surface quality.

This prevents stress amplification at surface flaws and enables very high levels of applied stress before fracture occurs (Wondraczek, 2019). Such conditions do not only allow for observing intrinsic strength, but also facilitate studies of plastic deformation processes. For example, thin films of flawless a-Al_2O_3 have been observed to exhibit pronounced plasticity when sufficiently high levels of stress are reached (Frankberg et al., 2019). Indentation studies on glass fiber remain challenging, though. In particular, surface curvature makes conventional testing protocols impractical, leading to systematic overestimation of contact area (Lonnroth et al., 2008; McAllister et al., 2012), and very strong sensitivity to tip-surface alignment.

Here, we employ wedge-indentation as a means to overcome some of the problems of normal indentation on curved glass surfaces. In particular, such indentation experiments enable testing in comparably homogenous, two-dimensional stress fields, avoiding the effects of the sharp edges of pyramidal indenters. Adjusting the wedge's opening angle, length and orientation relative to the fiber surface provides for highly reproducible studies of material deformation, surface crack initiation, and effects of fiber anisotropy.

MATERIALS AND METHODS

Sample Preparation

The pristine silica glass fibers used for this study were provided by the Leibniz Institute of Photonic Technology (IPHT), Jena, Germany: individual glass fibers with diameters of d = 440 μm, 220 μm, and 125 μm, respectively, were drawn from a vitreous silica glass rod (Suprasil F300, Heraeus Quarzglas GmbH & Co. KG) on an optical fiber drawing tower. A flat slide of vitreous silica (Suprasil 2B, Heraeus Quarzglas GmbH & Co. KG) was included into the study for reference. Prior to the mechanical analysis, the polymeric fiber coating was removed by etching for 20 s at 100°C in concentrated sulfuric acid. After etching, the uncoated silica glass fibers were rinsed for 10 s with deionized water and subsequently dried in flowing nitrogen. Segments of the bare silica glass fibers (20 mm) were then glued on microscope slides (Carl Roth GmbH & Co. KG) in horizontal direction using a thin film of an acrylate adhesive (Verifix MV 760, Bohle AG, and Young's modulus E = 1.2 GPa). The adhesive was cured for 10 min under a UV-A lamp. To ensure that each fiber segment was glued to the substrate over its entire length, an auxiliary glass slide was temporarily placed on top of the fiber segment as a counter weight during UV exposure. After removing the supporting glass slide, the polymer was allowed to cure for another 12–16 h in laboratory air under ambient conditions before mechanical characterization was conducted.

Nanoindentation

Instrumented indentation testing was carried out using a nanoindentation platform (G200, KLA Co.) equipped with a high-load option for loads up to P = 10 N. Young's modulus E and hardness H were determined from indentation experiments with a Vickers diamond tip (Micro Star Technologies). On each glass sample, at least five indents were created with a maximum load of 2.94 N. The loading duration and dwell time were kept constant at 10 s and 5 s, respectively. The values of H were determined from the maximum load $P_{\max}$ divided by the projected contact area of the indenter tip A_c (Oliver and Pharr, 1992):

$$H = \frac{P_{\max}}{A_c} \tag{1}$$

The values of E were estimated from the combined elastic response of the diamond tip (E_i = 1141 GPa and ν_i = 0.07) and the material tested (Johnson, 1985):

$$E = \left(1 - \nu^2\right)\left(\frac{1}{E_r} - \frac{1 - \nu_i^2}{E_i}\right)^{-1} \tag{2}$$

with the reduced elastic modulus E_r (Pharr et al., 1992)

$$E_r = \frac{S}{2}\sqrt{\frac{\pi}{A_c}} \tag{3}$$

The parameter S denotes the contact stiffness, i.e., the initial slope of the load-displacement P-h curve upon unloading (Oliver and Pharr, 1992). The tip area function and instrument frame compliance were calibrated prior to the first experiments on a silica reference glass sample (Corning Code 7980, Corning Inc.). In order to derive the values of E from E_r (Eq. (2)), a constant Poisson's ratio of ν = 0.17 (Limbach et al., 2015) was assumed for all glass samples examined in this work. All Vickers indentations on the silica glass fibers were realized with one diagonal oriented parallel to the fiber axis.

Wedge-indentation experiments were conducted on the silica glass fibers using sharp wedge-shaped diamond tips (Synton-MDP, Switzerland; **Figure 1**). Two different wedge indenters were employed: (i) a tip with an opening angle of θ = 90° and an effective length of L = 215 μm and (ii) another tip with θ = 60° and L = 180 μm. Indentation experiments were conducted with defined indenter displacement h ranging from 0.5 to 10 μm in the high-load mode and with a constant strain-rate of $\dot{\varepsilon} = 0.05\ s^{-1}$ (defined as the loading rate dP/dt divided by the actual load). If not otherwise stated, wedge indentations were realized with the wedge tip aligned at 90° with respect to the fiber axis (see, e.g., **Figure 1**). All indentation experiments were carried out in laboratory air under ambient conditions and with thermal drift rates of <0.05 nm/s. After indentation, the residual imprints were analyzed by standard optical microscopy and widefield confocal microscopy (Smartproof 5, Zeiss AG).

Raman Spectroscopy

Raman spectroscopic analysis was carried out *post mortem* using a confocal Raman microscope (inVia, Renishaw Inc.) in scanning mode. Raman spectra were collected across a surface area of 30 μm × 10 μm with 1 μm spacing between individual measurement positions and a focal depth of 0–6 μm using an Argon laser (λ = 514.5 nm) and a 50× microscope objective. All spectra were recorded for wavenumbers ranging

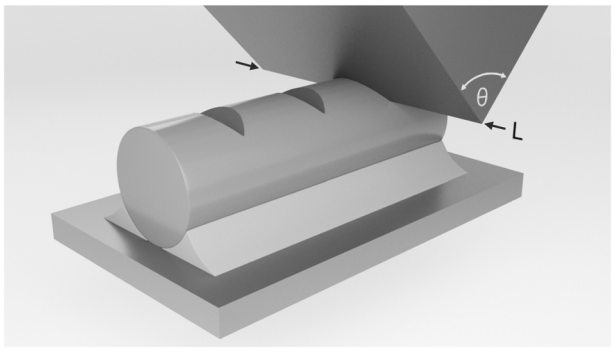

FIGURE 1 | Schematic representation of a nanoindentation experiment on a silica glass fiber using a wedge-shaped tip with the opening angle θ and the effective length *L*.

from 150 to 1500 cm^{-1} and with an accumulation time of 60 s per spectrum.

RESULTS

Vickers Indentation on Silica Glass Fiber

In this section, we first illustrate the differences in the contact behavior between a sharp pyramidal Vickers indenter tip and a flat (**Figure 2A**) or a curved glass surface (**Figure 2B**). Exemplary *P-h* curves recorded during nanoindentation experiments on silica glass fibers with d = 440; 220; and 125 µm, respectively, are shown in **Figure 2C**. Experimental data from Vickers indentation on a bulk silica glass sample is added for reference. Regardless of the surface curvature, reproducible and smooth parabolic *P-h* curves were obtained. However, at any given load, consistently higher indenter displacements are recorded on the silica glass fibers in comparison to the flat bulk glass specimen. The magnitude of this effect increases with increasing surface curvature, i.e., decreasing fiber diameter: at P_{max} = 245 mN, the values of h gradually increase from 1503 ± 4 nm (bulk silica glass) to 1520 ± 1 nm (d = 440 µm), 1528 ± 4 nm (d = 220 µm), and 1565 ± 1 nm (d = 125 µm), respectively. This trend is more obvious when P is plotted against h^2 (**Figure 2C**, inset). Since the slope of the P-h^2 curve directly scales with hardness H, this observation indicates that H is systematically underestimated with decreasing d. The same effect was observed for the whole load range up to 2.94 mN. For verification, the values of the apparent hardness H_a were estimated following the protocol described in section "Nanoindentation." The results of these calculations are shown in **Figure 2D**. Corresponding data on apparent Young's modulus E_a are provided for comparison. In accordance with a previous report (Lonnroth et al., 2008), both E_a and H_a scale linearly with $1/d$.

Wedge-Indentation on Silica Glass Fiber

In contrast to standard nanoindentation protocols on flat glass surfaces, where only the distance between the individual indents needs to be considered in order to avoid cross-interaction (Phani and Oliver, 2019), the mechanical characterization of silica glass fibers by instrumented indentation testing offers further challenges. This is not only due to surface curvature and its implications for the contact behavior (Lonnroth et al., 2008), but also because even small offsets between the tip position and the fiber apex may lead to strongly varying experimental results (Dabbs and Lawn, 1985; do Nascimento and Lepienski, 2006; Lonnroth et al., 2008; McAllister et al., 2012). We demonstrate this by intentionally misaligning the

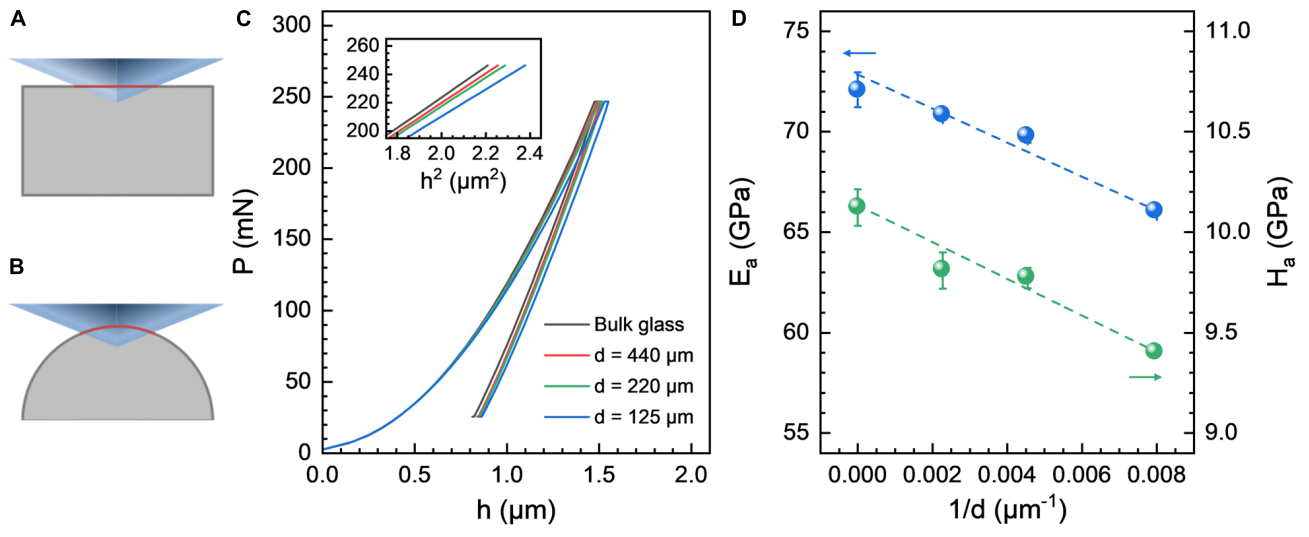

FIGURE 2 | (A) Schematic illustration of the contact behavior between a Vickers tip and **(A)** flat or **(B)** curved glass surfaces. The contact areas projected on the original surfaces are marked in red. **(C)** Representative load-displacement *P-h* curves as recorded from nanoindentation experiments on bulk vitreous silica and silica glass fibers of varying diameter d using a Vickers tip. The inset displays P as a function of h^2. **(D)** Apparent Young's modulus E_a and hardness H_a as a function of fiber diameter.

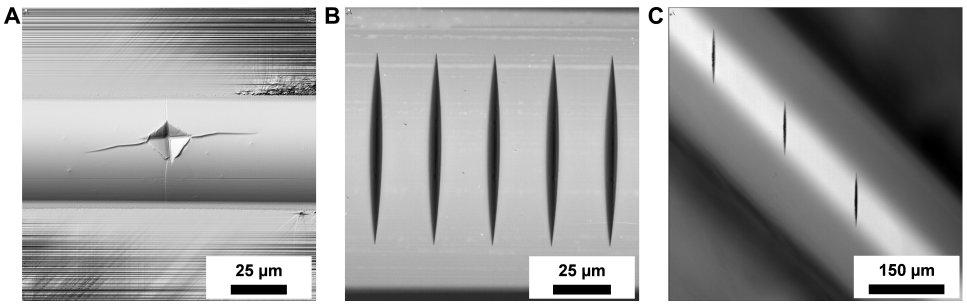

FIGURE 3 | (A) Surface visualization of a residual Vickers hardness imprint created at a normal load of 2.94 N on a 125 µm silica glass fiber. The asymmetric shape results from intentional misalignment of the Vickers tip relative to the fiber apex by about 7 µm. **(B–C)** Optical micrographs of residual imprints on a 440 µm silica glass fiber produced with a wedge-shaped tip with an opening angle of 90° and an effective length of 215 µm in **(B)** 90° and **(C)** 45° orientation relative to the fiber axis. The maximum loads were 3.62 N and 4.06 N, respectively.

Vickers indenter on a 125 µm silica glass fiber (**Figure 3A**): *post mortem* optical inspection of the residual imprint reveals a highly asymmetric shape (the micrographs recorded by widefield confocal microscopy only display the illuminated area which was in focus during image capture). Nanoindentation testing using a wedge-shaped tip, on the other hand, usually resulted in repeatable, highly symmetric indents (**Figure 3B**). Apparent *self-alignment* of the wedge indenter relative to the fiber apex occurs for as long as the effective length of the wedge-shaped tip exceeds the contact length L_c during indentation (e.g., $L_c \sim 83$ µm for a 3.26 N indent on a 440 µm silica glass fiber produced by a wedge indenter with $\theta = 90°$ and $L = 215$ µm). This provides for highly reproducible contact conditions for any given orientation between the wedge and the fiber axis (**Figure 3C**).

Representative *P-h* curves of wedge-indentation ($\theta = 90°$ and $L = 215$ µm on a 440 µm silica glass fiber, **Figure 3B**) are presented in **Figure 4**, recorded during indentation to maximum normal loads ranging from 290 mN up to 8.98 N. Similar to indentation with the sharp Vickers tip (**Figure 2C**), repeatable and smooth parabolic *P-h* curves were obtained over the full range of loads. This directly reflects the aforementioned *self-alignment* of the wedge indenter leading to highly reproducible contact conditions. Optical inspection of the residual imprints (**Figures 4B–E**) indicates a gradually increasing imprint size with increasing maximum load, on first view without any further variations in the overall material response. In particular, no cracking is observed up to $P_{max} = 8.98$ N [for reference, vitreous silica starts to crack at ~0.25 N (Li et al., 2019) to 1.50 N (Mound and Pharr, 2019) when sharp Vickers or Berkovich tips are used].

In **Figure 5**, *post mortem* Raman mapping data are presented for the imprint shown in **Figure 4E**, with exemplary individual scans in **Figure 5A** collected at the rim (red curve) and at a distance of 15 µm from the center of the indent (blue curve). For a qualitative assessment of spatial variations in the indentation-induced structural modifications, individual Raman spectra were evaluated in terms of the spectral center of gravity (COG). For this, each Raman spectrum was integrated over the

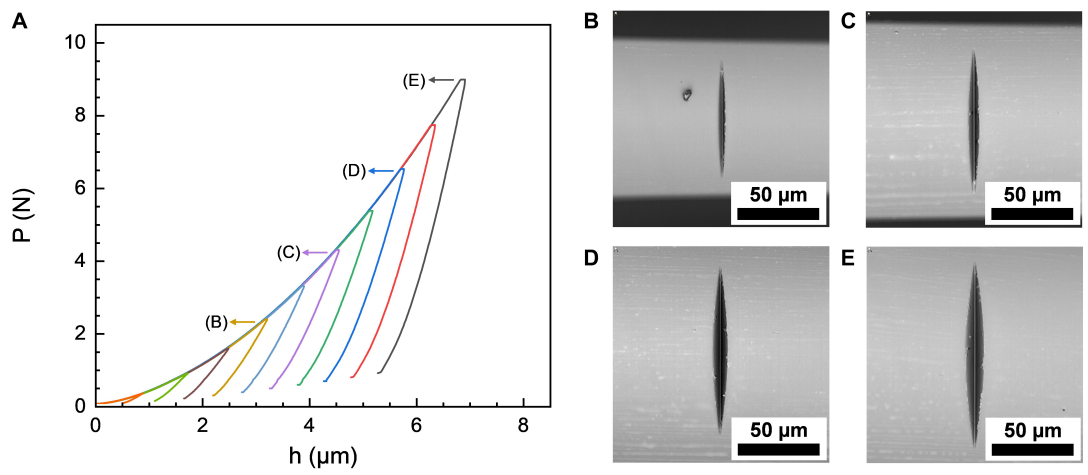

FIGURE 4 | (A) Representative load-displacement *P-h* curves recorded during wedge-indentation on a 440 µm silica glass fiber using a wedge with an opening angle of 90° and an effective length of 215 µm. Optical micrographs of the corresponding residual imprints (after unloading) are shown for indentations with maximum normal loads of **(B)** 2.34 N, **(C)** 4.26 N, **(D)** 6.52 N, and **(E)** 8.98 N.

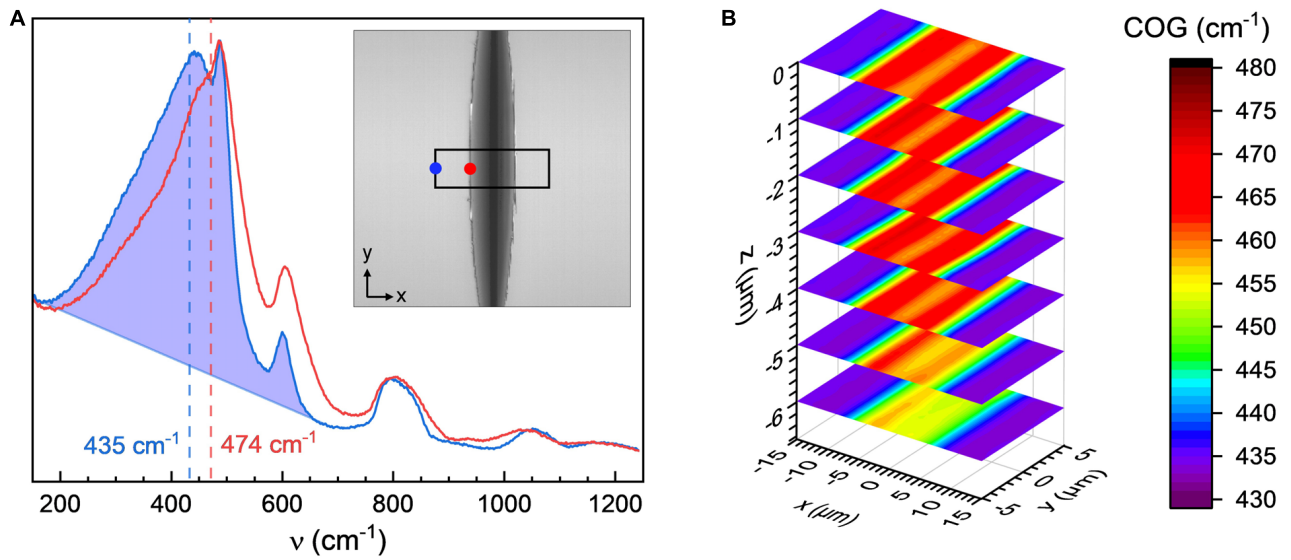

FIGURE 5 | Raman spectroscopic analysis of a residual imprint on a 440 μm silica glass fiber, produced under a normal load of 8.98 N with a wedge with an opening angle of 90° and an effective length of 215 μm. **(A)** Individual Raman spectra recorded at the rim (red curve; inset: red dot) and at a distance of 15 μm from the center of the imprint (blue curve; inset: blue dot), respectively. The shaded section on the blue curve shows an example of the determination of the spectral center of gravity (COG); COGs are marked with dashed lines. **(B)** Three-dimensional representation of the COG mapped across an area of 30 μm × 10 μm from the fiber surface (z = 0) and down to a depth of 6 μm.

spectral range of 200 to 700 cm^{-1} after baseline subtraction (**Figure 5A**, blue curve, and shaded area) following the protocol of Deschamps et al. (2013). Positive shifts in the COG of the silica Raman spectrum were previously assigned to congruent densification of the glass network during sharp contact loading (Bruns et al., 2020; Gerbig and Michaels, 2020). In the present case, the values of COG cover the range of 433 to 477 cm^{-1} (**Figure 5B**). The highest degree of densification is found in the flanks of the residual wedge imprint, gradually decreasing toward the value of bulk silica glass with increasing distance from the wedge apex. While we do not intend to go into detail here about the nature of structural densification in terms of the underlying molecular reactions, we note that wedge-indentation provides a homogeneous stress field, and resulting Raman map in the direction of the wedge over a length of several tens of μm. In comparison, the widely employed Vickers or Berkovich indentation studies (Winterstein-Beckmann et al., 2014a,b) produce significantly more complex stress fields and low spatial accuracy in the Raman spectroscopic evaluation of residual imprints (Bruns et al., 2020).

It is well-established from experiments (Yoshida et al., 2010; Gross, 2012; Mound and Pharr, 2019) and finite element simulation (Bruns et al., 2017, 2020) that sharper tips (pyramidal indenters with lower center-axis-to-face angle) produce higher local stress, thereby reducing the load threshold for indentation cracking in vitreous silica. In order to assess the influence of the opening angle of a wedge-shaped tip on the indentation response of curved glass surfaces, a second wedge indenter with θ = 60° and L = 180 μm was employed for comparison to the 90° wedge. Indents were created with maximum normal loads of up to 1.67 N on the same set of silica glass fibers as with the 90° wedge. While crack-free imprints were received from indentations with P_{max} = 8.98 N on a 440 μm silica glass fiber when θ = 90° (**Figure 4E**), on the same fiber, indentation-induced cracking was noticed already at loads ranging from 25 to 813 mN when using the wedge with θ = 60° (**Supplementary Figure S1**). Crack initiation was detected not only from *post mortem* optical inspection, but also reflected in the occurrence of sudden displacement bursts or "pop-ins" in the *P-h* curves recorded *in situ* during nanoindentation testing. This phenomenon is shown in **Figure 6** on the examples of two individual indentation experiments on a 220 μm silica glass fiber using a wedge-shaped tip with θ = 60°, i.e., for a crack-free indent (**Figure 6A**, blue curve) and for an indent where pronounced chipping was noticed (**Figure 6A**, green curve). Optical micrographs of the corresponding residual imprints are provided in **Figures 6B,C**, respectively. In the absence of cracking, a smooth, parabolic *P-h* curve was recorded during progressive increase of normal load up to P_{max} = 490 mN (**Figure 6A**, blue curve). Cracking materialized as an abrupt increase of the indenter displacement at almost constant load (in the shown example, this occurred at $P \sim 405$ mN, **Figure 6A**, and green curve). Furthermore, a large number of small serrations was observed in the *P-h* curve upon unloading (**Figure 6A**, green curve, and inset).

Following these observations, series of up to 25 indentations were created on silica glass fibers with d = 440 μm, 220 μm, and 125 μm, respectively, using the sharper wedge with θ = 60°. The corresponding *P-h* curves obtained on the 220 μm silica glass fiber are shown in **Figure 7A** (experimental data recorded for the 440 and 125 μm silica glass fibers are provided as supplementary

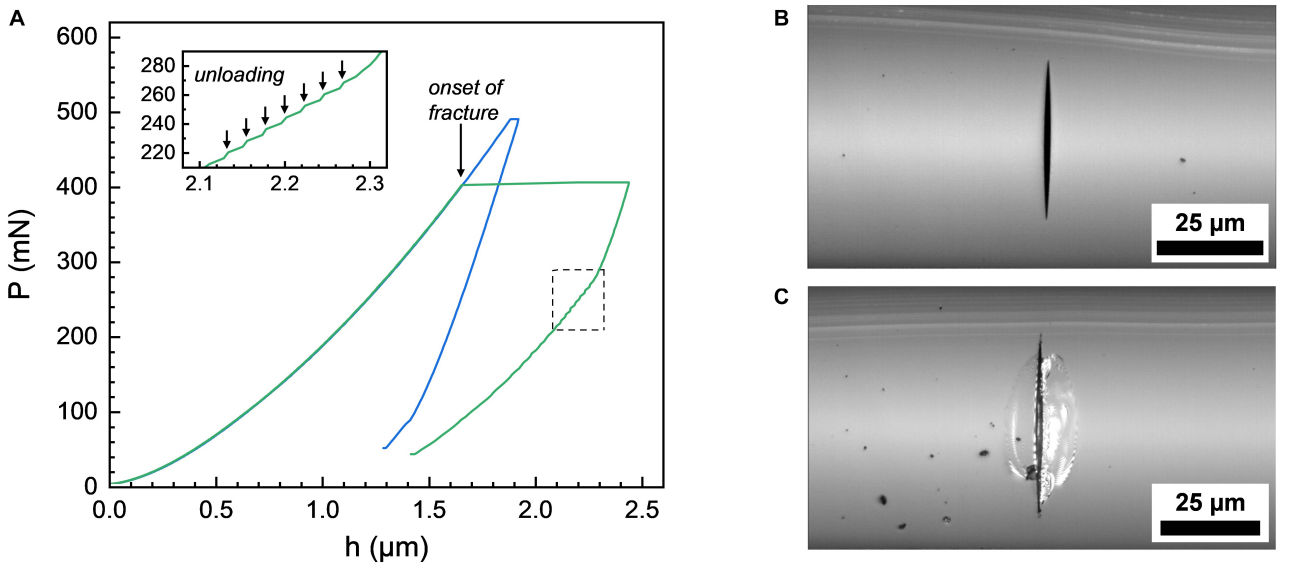

FIGURE 6 | (A) Representative load-displacement *P-h* curves as recorded from nanoindentation experiments on a 220 μm silica glass fiber using a wedge-shaped tip with an opening angle of 60° and an effective length of 180 μm. The sudden displacement burst at around 405 mN indicates the onset of fracture (green curve). In this case, multiple serrations occur upon unloading (green curve, inset). Corresponding optical micrographs of residual imprints are provided in **(B)** for the crack-free indent with a maximum load of 490 mN (blue curve), and **(C)** for the cracked specimen with a maximum load 405 mN (green curve).

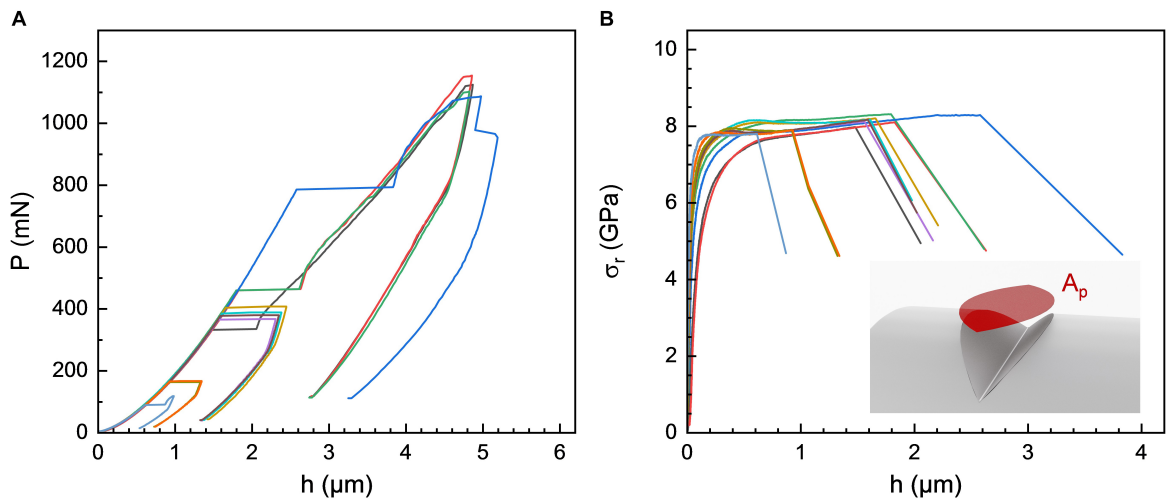

FIGURE 7 | (A) Examples of load-displacement *P-h* curves recorded from nanoindentation experiments on a 220 μm silica glass fiber using a wedge-shaped tip with an opening angle of 60° and an effective length of 180 μm. **(B)** Corresponding depth profiles of the representative mean indentation stresses σ_r. In **(B)**, data are presented up to the occurrence of the first pop-in event.

information in **Supplementary Figures S1, S2**, respectively). Even under identical experimental (ambient) conditions, there is a strong variability in the loads at which the first pop-in occurred, denoted $P_{\mathrm{pop-in}}$, as well as in the magnitude of the displacement bursts. For example, on the 220 μm fiber, the first pop-in was observed within a load range of 13–784 mN (**Figure 7A**). On first view, the magnitude of the displacement bursts seemed to scale with $P_{\mathrm{pop-in}}$ (**Figure 7A**), where larger pop-ins were found for higher values of $P_{\mathrm{pop-in}}$. The latter suggests a relation between $P_{\mathrm{pop-in}}$ and the size of the deformed volume. In order to emphasize this argument, the experimental values of P were converted into a representative mean indentation stress σ_r:

$$\sigma_r = \frac{P}{A_{\mathrm{p}}} \tag{4}$$

Neglecting the effects of sink-in and pile-up, A_p represents the projected contact area of the wedge indenter (**Figure 7B** and **Supplementary Figure S4A**),

$$A_p = \tan\left(\frac{\theta}{2}\right)\left[\frac{d^2}{2}arccos\left(1-\frac{2h}{d}\right)-(d-2h)\sqrt{dh-h^2}\right] \quad (5)$$

This approach resolves the apparent scatter in the P_{pop-in} data: when normalized to the projected contact area, the first pop-in event is observed within a relatively narrow range of representative stress, i.e., within 7–8 GPa (**Figure 7B**). Further evaluation will require accurate knowledge of the true contact area. In the absence of such knowledge, the above approach is employed for approximation. For low fiber curvature or low indentation depth, A_p is very close to the enveloping cylinder section A_s (i.e., the cylinder surface section opened by the wedge, see **Supplementary Figure S4**). The lateral contact area A relative to A_p is constant for any given wedge opening angle, e.g., $A/A_p = 2$ for $\theta = 60°$.

DISCUSSION

Evaluation of the deformation behavior and fracture processes in glasses by (nano) indentation testing typically relies on rigid, ideally sharp pyramidal Vickers or Berkovich tips penetrating a co-planar, and optically polished glass surface (Taylor, 1949; Rouxel, 2015; Sawamura and Wondraczek, 2018; Cook, 2019). In practice, however, indentation experiments are often performed on rough and slightly tilted surfaces (Xu and Li, 2007). Surface asperity usually leads to low data reproducibility (Kim et al., 2006). A tilted surface would cause a systematic deflection of the load-displacement curves recorded *in situ* during indentation (Oliver and Pharr, 2004; Wang and Liu, 2019); its effects can be analyzed *post mortem* on the shape of the residual imprints (Kashani and Madhavan, 2011). Accurate knowledge of the tilt angle allows for data correction in terms of the asymmetric contact between the indenter tip and the tested material (Kashani and Madhavan, 2011; Wang and Liu, 2019). On the other hand, such routines are not applicable to curved glass fiber surfaces, on which the "*local tilt angle*" continuously changes throughout the indentation experiment. It depends on fiber surface curvature, tip geometry, initial offset between tip position and fiber apex, and indenter displacement. For example, when the indenter tip is aligned optically, with a numerical aperture of 0.25 at an observation wavelength of ∼500 nm, an accuracy of ∼2 μm is achieved in tip positioning. For a fiber with a diameter of 125 μm, such an offset between the tip position and the fiber apex would already correspond to a local tilt angle of ∼3° at the initial point of contact (or ∼10° for a moderate offset of about 7 μm as illustrated in **Figure 3A**). Wedge-indentation overcomes this issue. Potential misalignments of the wedge indenter with respect to the fiber apex are negligible for as long as a contact between the corners of the wedge indenter and the glass surface is avoided (that is, when the contact length during indentation remains smaller than the effective length of the wedge). Highly symmetric indents were consistently generated on the surface of silica glass fibers of varying diameters throughout this study (**Figures 3B**, **4E,F**). On a side note, crack-free wedge imprints can be used as well-defined, highly reproducible defects for further studies of crack initiation, crack propagation and fracture toughness. Such artificial defects (mimicking naturally occurring surface flaws) are often generated with sharp pyramidal Vickers or Berkovich tips (Dabbs and Lawn, 1985; Donaghy and Dabbs, 1988; Jakus et al., 1988; Lin and Matthewson, 1996; do Nascimento and Lepienski, 2006; Cui et al., 2019). In view of precise tip alignment (Dabbs and Lawn, 1985; do Nascimento and Lepienski, 2006), using wedge-shaped tips appears to be more suitable for such experiments.

A primary feature of wedge-indentation is the unidirectional stress field produced by a wedge indenter and the accompanied homogeneous stress and strain distribution parallel to the wedge axis (**Figure 5B**). In previous experiments, the structural response of vitreous silica and other glasses to local mechanical contact was almost exclusively studied by *post mortem* Raman spectroscopic investigation of residual Vickers, Berkovich or cube-corner hardness imprints (Perriot et al., 2006; Winterstein-Beckmann et al., 2014a,b; Bruns et al., 2020). However, such analyses are strongly complicated by local stress amplification near the sharp edges of the pyramidal indenters (Perriot et al., 2006). Even more critical, the limited spatial resolution of the Raman probe leads to signal integration over regions with large property gradients (Bruns et al., 2020). For this reason, indentations with loads well beyond the onset of crack initiation are normally performed to create sufficiently large imprints and minimize the degree of structural averaging (Malchow et al., 2015; Bruns et al., 2020; Gerbig and Michaels, 2020). The presence of cracks is often supposed to be of minor importance for the structural analysis (Kassir-Bodon et al., 2012), but interactions with the Raman probe cannot safely be excluded (Bruns et al., 2020; Gerbig and Michaels, 2020). In order to obtain meaningful, unambiguous vibrational spectroscopic data on the indentation-induced structural changes in glasses, the availability of crack-free, and high-load indentations would be favorable. For example, this was partially realized by operating the (nano) indenter under inert atmospheres (Gross and Tomozawa, 2008). Wedge-indentation provided another option on the same line. Using a wedge-shaped tip with $\theta = 90°$ and $L = 215$ μm, we were able to generate reproducible, highly symmetric indents over a wide range of loads up to $P_{max} = 8.98$ N (**Figures 4B–E**). Remarkably, the indentations with the highest loads of $P_{max} = 8.98$ N remained crack-free (**Figure 4E**), even after storing the indented silica glass fibers for a period of 6 months in laboratory air under ambient conditions (supplementary information in **Supplementary Figure S3**). Aside *post mortem* structural analysis by vibrational spectroscopy, this feature has been motivating the use of wedge-indentation also for *in situ* analysis of the indentation-induced structural modifications in vitreous silica by small-angle X-ray scattering (Fuhrmann et al., 2020).

It remains to be explored if the unidirectional stress field produced by a wedge-shaped tip may also facilitate the in-depth analysis of the mechanical properties of anisotropic glasses (Endo et al., 2015). Although glasses are usually referred to as isotropic materials, structural anisotropy can be induced by frozen-in strain, e.g., during fiber drawing (Brückner et al., 1980; Stockhorst and Brückner, 1986; Inaba et al., 2015). The accessible degree of structural anisotropy depends on the

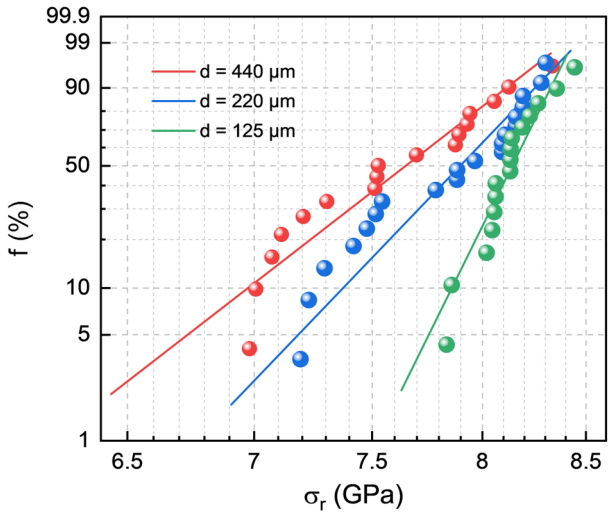

FIGURE 8 | Statistical analysis of the first pop-in for silica glass fibers with varying diameter *d*. The representative mean indentation stress σ_r associated with the occurrence of the first pop-in was taken from **Figure 7B** and **Supplementary Figures S1, S2**. Weibull probability data *f* were determined using median rank approximation (Moayedi and Wondraczek, 2017). Nanoindentation testing was performed using a wedge-shaped tip with an opening angle of 60° and an effective length of 180 µm.

molecular structure of the glass network and its propensity to self-organize into a preferential direction when subjected to large stress at temperatures above the glass transition (Inaba et al., 2015; Yang et al., 2017; Inaba et al., 2020). As a hypothesis, glasses with pronounced structural anisotropy respond differently to the unidirectional stress field produced by a wedge indenter as compared to isotropic materials. We may then speculate that variations in the orientation of the wedge indenter with respect to the fiber axis (as exemplarily illustrated in **Figures 3B,C**) can reveal potential differences in the mechanical behavior of anisotropic glasses.

Using a sharper wedge, surface cracks can be generated (**Figure 6C**). Such cracks are readily visible *in situ* as sudden displacement bursts (*pop-ins*) in the load-displacement curve (**Figures 6A**, **7A**). At first glance, these discontinuities display some similarities to fluctuations in the load-displacement curves which were observed in scratch-induced micro-abrasion on the surface of vitreous silica (Moayedi and Wondraczek, 2017; Sawamura et al., 2018; Sawamura et al., 2019), where material removal was supposed to occur abruptly via chipping (Lee et al., 2018). Indeed, in *post mortem* optical inspection, chipping also dominates the crack pattern on silica glass fibers indented by a wedge-shaped tip with an opening angle of 60° (**Figure 6C**). Once chipping occurs, there is a rapid loss of contact between the wedge indenter and the surrounding material, which is compensated by an abrupt increase in the indenter displacement (**Figures 6A**, **7A**). This assumes that the derived crack pattern indeed corresponds to the *in situ* observations. The fracture process continues during unloading (**Figure 6A**, inset) and (potentially) sample storage.

A statistical evaluation of the occurrence of the first *pop-in* is provided in **Figure 8** in the form of a Weibull probability distribution of the representative stress at which the first *pop-in* was observed for variable fiber diameter. We obtain effective (overall) Weibull moduli *m* of 20, 27, and 53 for fiber diameters of 440, 220, and 125 µm, respectively, whereby all data seem to converge in a high-strength mode with $m_h \sim 50$, and a low-strength mode with significantly lower m_l (broader distribution of chipping events in terms of σ_r). The latter regime is more pronounced for higher fiber thickness. The obtained values compare to an upper limit in the order of $m \sim 10^2$ for tensile testing of "perfect" (flawless) furnace-drawn silica fiber (d = 110 µm) with a protective polymer coating and a strength in the range of 5.6 GPa (Kurkjian and Paek, 1983), where the scatter in strength data was related to fluctuations in fiber diameter which occurred in the range of 0.4% (<0.5 µm). For higher diameter fluctuation (~2.6 µm), a modulus of $m \sim 25$ was found (Kurkjian and Paek, 1983). As for the present case, although fluctuations in the local fiber diameter between individual indentation sites will affect the estimated values of σ_r, their presence may not fully explain the actual magnitude of *m*. Assuming that the absence of a polymer coating has a minor effect for small-volume testing such as applied in the present study, we instead relate the present magnitude of *m* to the remaining variance in wedge alignment and surface detection, leading to over- or underestimation of the projected contact area. For the Weibull scale (σ_r at a failure probability of ~63%), we obtain 7.8, 8.0, and 8.2 GPa for fiber diameters of 440, 220, and 125 µm, respectively. As already noted, these absolute values are strongly dependent on the assumptions made for the contact area.

CONCLUSION

In summary, we used sharp wedge-shaped diamond tips with opening angles of 60–90° for testing the surface mechanical behavior of vitreous silica fiber with diameters of 125 to 440 µm. We chose a wedge length, which avoided corner surface contact, thus overcoming some of the limitations of sharp pyramidal indentation. Using a higher opening angle enabled the generation of highly reproducible crack-free imprints with a depth of up to 7 µm and a width of several tens of µm for loads reaching 8.98 N. The residual imprints can be used for accurate *post mortem* inspection of permanent deformation-induced material modification, e.g., by vibrational spectroscopic methods. With shaper wedge tips, chipping occurred for normal loads in the range of 10^2 mN. Fracture events were readily visible as sudden displacement bursts *in situ* during loading. Normalization to the projected contact area enabled a statistical evaluation of the representative stress which led to the first such *pop-in*. We obtained Weibull moduli depending on fiber diameter, increasing from ~20 (d = 440 µm) to ~50 (d = 125 µm), with representative stresses in the range of 8 GPa. The observed magnitude of *m* is only partially related to fluctuations in fiber diameter. Also the remaining variations in wedge alignment relative to the fiber axis and the accuracy of instrumented surface detection are important factors.

DATA AVAILABILITY STATEMENT

The datasets generated for this study are available on request to the corresponding author.

AUTHOR CONTRIBUTIONS

LW conceived of this study. RS prepared the samples and performed the optical characterization and Raman spectroscopic analysis. RL and RS designed and conducted the nanoindentation experiments. All authors jointly evaluated the data and wrote the manuscript.

FUNDING

Financial support by the German Science Foundation through the priority program PP 1594 (Grant No. WO1220/9-2) is gratefully acknowledged. Parts of the study received further support from the German Federal Ministry of Education and Research under the Entrepreneurial Regions research and innovation program.

ACKNOWLEDGMENTS

The authors gratefully acknowledge colleagues at the Leibniz IPHT, Jena, for providing the silica glass fibers used for this study. The authors would further like to thank Zhiwen Pan and Omar Benzine from the Otto Schott Institute of Materials Research, Friedrich Schiller University Jena, for their support in the Raman spectroscopic analysis.

SUPPLEMENTARY MATERIAL

The Supplementary Material for this article can be found online at: https://www.frontiersin.org/articles/10.3389/fmats.2020.00126/full#supplementary-material

FIGURE S1 | (A) Selected load-displacement *P-h* curves as recorded from nanoindentation experiments on a 440 μm silica glass fiber using a wedge-shaped tip with an opening angle of 60° and an effective length of 180 μm. **(B)** Corresponding depth profiles of the representative stress σ_r. Data in **(B)** are limited to the first pop-in event, as the incipient fracture violates the assumptions made for the calculation of the projected area by means of Equation (5).

FIGURE S2 | (A) Selected load-displacement *P-h* curves as recorded from nanoindentation experiments on a 125 μm silica glass fiber using a wedge-shaped tip with an opening angle of 60° and an effective length of 180 μm. **(B)** Corresponding depth profiles of the representative stress σ_r. Data in **(B)** are limited to the first pop-in event, as the incipient fracture violates the assumptions made for the calculation of the projected area by means of Equation (5).

FIGURE S3 | Optical micrograph of a residual imprint on a 440 μm silica glass fiber afterstorage for a period of six months in laboratory air under ambient conditions. The imprint was createdwith a maximum normal load of 8.98 N usinga wedge-shaped tip with an opening angle of 90° and an effective length of 215 μm.

FIGURE S4 | (A) Schematic visualization of thelateral contact area A, the enveloping cylinder surface section A_S and the projected contact area A_p during indentation of glass fibers with a wedge-shaped tip. **(B)** Calculated nominal areas A, A_S and A_p for indentation with a 60° wedge on a 125 μm fiber as a function of indenter displacement h perpendicular to the fiber axis.

REFERENCES

Benzine, O., Bruns, S., Pan, Z. W., Durst, K., and Wondraczek, L. (2018). Local deformation of glasses is mediated by rigidity fluctuation on nanometer scale. *Adv. Sci.* 5:1800916. doi: 10.1002/advs.201800916

Brambilla, G., and Payne, D. N. (2009). The ultimate strength of glass silica nanowires. *Nano Lett.* 9, 831–835. doi: 10.1021/nl803581r

Brückner, R., Sammet, M., and Stockhorst, H. (1980). Evidence of structural anisotropies in silicate glass fibres by ESR. *J. Non-Crystall. Solids* 40, 273–289. doi: 10.1016/0022-3093(80)90106-4

Bruns, S., Johanns, K. E., Rehman, H. U., Pharr, G. M., and Durst, K. (2017). Constitutive modeling of indentation cracking in fused silica. *J. Am. Ceram. Soc.* 100, 1928–1940. doi: 10.1111/jace.14734

Bruns, S., Uesbeck, T., Fuhrmann, S., Aymerich, M. T., Wondraczek, L., de Ligny, D., et al. (2020). Indentation densification of fused silica assessed by raman spectroscopy and constitutive finite element analysis. *J. Am. Ceram. Soc.* 103, 3076–3088. doi: 10.1111/jace.17024

Cook, R. F. (2019). Fracture sequences during elastic-plastic indentation of brittle materials. *J. Mater. Res.* 34, 1633–1644. doi: 10.1557/jmr.2019.112

Cook, R. F. (2020). A critical evaluation of indentation crack lengths in air. *J. Am. Ceram. Soc.* 103, 2278–2295. doi: 10.1111/jace.16925

Cui, Y. X., Chen, Y. X., and He, J. J. (2019). Equivalent initial flaw size model for fracture strength prediction of optical fibers with indentation flaws. *Eng. Fract. Mech.* 215, 36–48. doi: 10.1016/j.engfracmech.2019.04.021

Dabbs, T. P., and Lawn, B. R. (1985). Strength and fatigue properties of optical-glass fibers containing microindentation flaws. *J. Am. Ceram. Soc.* 68, 563–569. doi: 10.1111/j.1151-2916.1985.tb16156.x

Deschamps, T., Kassir-Bodon, A., Sonneville, C., Margueritat, J., Martinet, C., de Ligny, D., et al. (2013). Permanent densification of compressed silica glass: a Raman-density calibration curve. *J. Phys. Condens. Matter* 25:025402. doi: 10.1088/0953-8984/25/2/025402

do Nascimento, E. M., and Lepienski, C. M. (2006). Mechanical properties of optical glass fibers damaged by nanoindentation and water ageing. *J. Non-Cryst. Solids* 352, 3556–3560. doi: 10.1016/j.jnoncrysol.2006.02.114

Donaghy, F. A., and Dabbs, T. P. (1988). Subthreshold flaws and their failure prediction in long-distance optical fiber cables. *J. Lightw. Technol.* 6, 226–232. doi: 10.1109/50.3993

Endo, J., Inaba, S., and Ito, S. (2015). Mechanical properties of anisotropic metaphosphate glass. *J. Am. Ceram. Soc.* 98, 2767–2771. doi: 10.1111/jace.13682

Frankberg, E. J., Kalikka, J., Ferré, F. G., Joly-Pottuz, L., Salminen, T., Hintikka, J., et al. (2019). Highly ductile amorphous oxide at room temperature and high strain rate. *Science* 366, 864–869. doi: 10.1126/science.aav1254

Fuhrmann, S., de Macedo, G. N. B. M., Limbach, R., Krywka, C., Bruns, S., Durst, K., et al. (2020). Indentation-induced structural changes in vitreous silica probed by in-situ small-angle X-ray scattering. *Front. Mater.* 7 (in press). doi: 10.3389/fmats.2020.00173

Gerbig, Y. B., and Michaels, C. A. (2020). In-situ raman spectroscopic measurements of the deformation region in indented glasses. *J. Non-Cryst. Solids* 530:119828. doi: 10.1016/j.jnoncrysol.2019.119828

Gross, T. M. (2012). Deformation and cracking behavior of glasses indented with diamond tips of various sharpness. *J. Non-Cryst. Solids* 358, 3445–3452. doi: 10.1016/j.jnoncrysol.2012.01.052

Gross, T. M., and Tomozawa, M. (2008). Crack-free high load Vickers indentation of silica glass. *J. Non-Cryst. Solids* 354, 5567–5569. doi: 10.1016/j.jnoncrysol.2008.09.015

Inaba, S., Benino, Y., Kohara, S., Hosono, H., and Ito, S. (2020). Anisotropic structure of alkali metaphosphate glasses. *J. Am. Ceram. Soc.* 103, 3631–3641. doi: 10.1111/jace.17065

Inaba, S., Hosono, H., and Ito, S. (2015). Entropic shrinkage of an oxide glass. *Nat. Mater.* 14, 312–317. doi: 10.1038/NMAT4151

Jakus, K., Ritter, J. E., Choi, S. R., Lardner, T., and Lawn, B. R. (1988). Failure of fused-silica fibers with subthreshold flaws. *J. Non-Cryst. Solids* 102, 82–87. doi: 10.1016/0022-3093(88)90115-9

Johnson, K. L. (1985). *Contact Mechanics*. Cambridge: Cambridge University Press.

Kashani, M. S., and Madhavan, V. (2011). Analysis and correction of the effect of sample tilt on results of nanoindentation. *Acta Mater.* 59, 883–895. doi: 10.1016/j.actamat.2010.09.051

Kassir-Bodon, A., Deschamps, T., Martinet, C., Champagnon, B., Teisseire, J., and Kermouche, G. (2012). Raman mapping of the indentation-induced densification of a soda-lime-silicate glass. *Int. J. Appl. Glass Sci.* 3, 29–35. doi: 10.1111/j.2041-1294.2012.00078.x

Kim, J. Y., Lee, J. J., Lee, Y. H., Jang, J. I., and Kwon, D. (2006). Surface roughness effect in instrumented indentation: a simple contact depth model and its verification. *J. Mater. Res.* 21, 2975–2978. doi: 10.1557/Jmr.2006.0370

Kurkjian, C. R., Gupta, P. K., and Brow, R. K. (2010). The strength of silicate glasses: what do we know, what do we need to know? *Int. J. Appl. Glass Sci.* 1, 27–37. doi: 10.1111/J.2041-1294.2010.00005.X

Kurkjian, C. R., Gupta, P. K., Brow, R. K., and Lower, N. (2003). The intrinsic strength and fatigue of oxide glasses. *J. Non-Cryst. Solids* 316, 114–124. doi: 10.1016/S0022-3093(02)01943-9

Kurkjian, C. R., and Paek, U. C. (1983). Single-valued strength of perfect silica fibers. *Appl. Phys. Lett.* 42, 251–253. doi: 10.1063/1.93905

Lee, K., Marimuthu, K. P., Kim, C. L., and Lee, H. (2018). Scratch-tip-size effect and change of friction coefficient in nano/micro scratch tests using XFEM. *Tribol. Int.* 120, 398–410. doi: 10.1016/j.triboint.2018.01.003

Li, C. S., Zhang, L. C., Sun, L., Yang, S. M., Wu, C. H., Long, X. Y., et al. (2019). A quantitative analysis of the indentation fracture of fused silica. *J. Am. Ceram. Soc.* 102, 7264–7277. doi: 10.1111/jace.16645

Limbach, R., Winterstein-Beckmann, A., Dellith, J., Möncke, D., and Wondraczek, L. (2015). Plasticity, crack initiation and defect resistance in alkali-borosilicate glasses: from normal to anomalous behavior. *J. Non-Cryst. Solids* 41, 15–27. doi: 10.1016/j.jnoncrysol.2015.02.019

Lin, B., and Matthewson, M. J. (1996). Inert strength of subthreshold and post-threshold Vickers indentations on fused silica optical fibres. *Philos. Mag. A* 74, 1235–1244. doi: 10.1080/01418619608239723

Lonnroth, N., Muhlstein, C. L., Pantano, C., and Yue, Y. Z. (2008). Nanoindentation of glass wool fibers. *J. Non-Cryst. Solids* 354, 3887–3895. doi: 10.1016/j.jnoncrysol.2008.04.014

Malchow, P., Johanns, K. E., Möncke, D., Korte-Kerzel, S., Wondraczek, L., and Durst, K. (2015). Composition and cooling-rate dependence of plastic deformation, densification, and cracking in sodium borosilicate glasses during pyramidal indentation. *J. Non-Cryst. Solids* 419, 97–109. doi: 10.1016/j.jnoncrysol.2015.03.020

McAllister, Q. P., Gillespie, J. W., and VanLandingham, M. R. (2012). Nonlinear indentation of fibers. *J. Mater. Res.* 27, 197–213. doi: 10.1557/jmr.2011.336

Moayedi, E., and Wondraczek, L. (2017). Quantitative analysis of scratch-induced microabrasion on silica glass. *J. Non-Cryst. Solids* 470, 138–144. doi: 10.1016/j.jnoncrysol.2017.05.003

Mound, B. A., and Pharr, G. M. (2019). Nanoindentation of fused quartz at loads near the cracking threshold. *Exp. Mech.* 59, 369–380. doi: 10.1007/s11340-018-00446-3

Oliver, W. C., and Pharr, G. M. (1992). An improved technique for determining hardness and elastic modulus using load and displacement sensing indentation experiments. *J. Mater. Res.* 7, 1564–1583. doi: 10.1557/Jmr.1992.1564

Oliver, W. C., and Pharr, G. M. (2004). Measurement of hardness and elastic modulus by instrumented indentation: advances in understanding and refinements to methodology. *J. Mater. Res.* 19, 3–20. doi: 10.1557/Jmr.2004.19.1.3

Perriot, A., Vandembroucq, D., Barthel, E., Martinez, V., Grosvalet, L., Martinet, C., et al. (2006). Raman microspectroscopic characterization of amorphous silica plastic behavior. *J. Am. Ceram. Soc.* 89, 596–601. doi: 10.1111/j.1551-2916.2005.00747.x

Phani, P. S., and Oliver, W. C. (2019). A critical assessment of the effect of indentation spacing on the measurement of hardness and modulus using instrumented indentation testing. *Mater. Des.* 164, 107563. doi: 10.1016/j.matdes.2018.107563

Pharr, G. M., Oliver, W. C., and Brotzen, F. R. (1992). On the generality of the relationship among contact stiffness, contact area, and elastic modulus during indentation. *J. Mater. Res.* 7, 613–617. doi: 10.1557/Jmr.1992.0613

Rouxel, T. (2015). Driving force for indentation cracking in glass: composition, pressure and temperature dependence. *Philos. Trans. R. Soc. A* 373:20140140. doi: 10.1098/rsta.2014.0140

Rouxel, T., and Yoshida, S. (2017). The fracture toughness of inorganic glasses. *J. Am. Ceram. Soc.* 100, 4374–4396. doi: 10.1111/jace.15108

Sawamura, S., Limbach, R., Behrens, H., and Wondraczek, L. (2018). Lateral deformation and defect resistance of compacted silica glass: quantification of the scratching hardness of brittle glasses. *J. Non-Cryst. Solids* 481, 503–511. doi: 10.1016/j.jnoncrysol.2017.11.035

Sawamura, S., Limbach, R., Wilhelmy, S., Koike, A., and Wondraczek, L. (2019). Scratch-induced yielding and ductile fracture in silicate glasses probed by nanoindentation. *J. Am. Ceram. Soc.* 102, 7299–7311. doi: 10.1111/jace.16679

Sawamura, S., and Wondraczek, L. (2018). Scratch hardness of glass. *Phys. Rev. Mater.* 2:092601. doi: 10.1103/PhysRevMaterials.2.092601

Stockhorst, H., and Brückner, R. (1986). Structure sensitive measurements on phosphate glass fibers. *J. Non-Cryst. Solids* 85, 105–126. doi: 10.1016/0022-3093(86)90083-9

Taylor, E. W. (1949). Plastic deformation of optical glass. *Nature* 163:323. doi: 10.1038/163323a0

Varshneya, A. K. (2018). Stronger glass products: lessons learned and yet to be learned. *Int. J. Appl. Glass Sci.* 9, 140–155. doi: 10.1111/ijag.12341

Wang, L., and Liu, X. P. (2019). Correlation analysis of surface tilt effect on its mechanical properties by nano-indentation. *Int. J. Precis. Eng. Manuf.* 20, 327–335. doi: 10.1007/s12541-019-00061-9

Winterstein-Beckmann, A., Möncke, D., Palles, D., Kamitsos, E. I., and Wondraczek, L. (2014a). Raman spectroscopic study of structural changes induced by micro-indentation in low alkali borosilicate glasses. *J. Non-Cryst. Solids* 401, 110–114. doi: 10.1016/j.jnoncrysol.2013.12.038

Winterstein-Beckmann, A., Möncke, D., Palles, D., Kamitsos, E. I., and Wondraczek, L. (2014b). A raman-spectroscopic study of indentation-induced structural changes in technical alkali-borosilicate glasses with varying silicate network connectivity. *J. Non-Cryst. Solids* 405, 196–206. doi: 10.1016/j.jnoncrysol.2014.09.020

Wondraczek, L. (2019). Overcoming glass brittleness. *Science* 366, 804–805. doi: 10.1126/science.aaz2127

Wondraczek, L., Mauro, J. C., Eckert, J., Kühn, U., Horbach, J., Deubener, J., et al. (2011). Towards ultrastrong glasses. *Adv. Mater.* 23, 4578–4586. doi: 10.1002/Adma.201102795

Xu, Z. H., and Li, X. (2007). Effect of sample tilt on nanoindentation behaviour of materials. *Philos. Mag.* 87, 2299–2312. doi: 10.1080/14786430601175516

Yang, X., Scannell, G., Jain, C., Rodrigues, B. P., Schmidt, M. A., and Wondraczek, L. (2017). Permanent structural anisotropy in a hybrid fiber optical waveguide. *Appl. Phys. Lett.* 111:201901. doi: 10.1063/1.4999048

Yoshida, S. (2019). Indentation deformation and cracking in oxide glass –toward understanding of crack nucleation. *J. Non-Cryst. Solids X* 1:100009. doi: 10.1016/j.nocx.2019.100009

Yoshida, S., Sawasato, H., Sugawara, T., Miura, Y., and Matsuoka, J. (2010). Effects of indenter geometry on indentation-induced densification of soda-lime glass. *J. Mater. Res.* 25, 2203–2211. doi: 10.1557/Jmr.2010.0287

Conflict of Interest: The authors declare that the research was conducted in the absence of any commercial or financial relationships that could be construed as a potential conflict of interest.

frontiers in Materials

ORIGINAL RESEARCH
published: 02 June 2020
doi: 10.3389/fmats.2020.00128

Studies on Stress Corrosion Cracking of Vit 105 Bulk Metallic Glass

Annett Gebert[1], David Geissler[1], Stefan Pilz[1], Margitta Uhlemann[1], Farnaz A. Davani[2], Sven Hilke[2], Harald Rösner[2] and Gerhard Wilde[2]*

[1] Institute for Complex Materials, Leibniz IFW Dresden, Dresden, Germany, [2] Institut für Materialphysik, Westfälische Wilhelms-Universität Münster, Münster, Germany

The project "Stress Corrosion Cracking of Zr-based Bulk Metallic Glasses" (SCC of Zr-BMGs) within PP1594 mainly dealt with mechanical–corrosive interactions and failure of this class of metastable materials. It focused on one of the most application-relevant zirconium (Zr)-BMG, Vit(reloy) 105, with composition $Zr_{52.5}Cu_{17.9}Ni_{14.6}Al_{10}Ti_5$ (at.%). Even though this BMG is known as an extraordinary glass former, the metallurgical processing is still a critical issue. In contrast to conventional processing, i.e., arc melting of master alloy ingots from single constituents, a different route using binary pre-alloys for the master alloys production was applied and led to superior mechanical properties upon mechanical testing under tensile and three-point-bending (3PB) conditions in air. As a reference and for a detailed understanding of failure, fracture, and cracking of Zr-based BMG in air, notched specimen 3PB experiments with *in situ* microscopic observation were done and the still controversial interpretation of the mechanical behavior of BMG in the framework of fracture mechanics was addressed. The specimen from the *in situ* 3PB tests served for transmission electron microscopy (TEM) investigations on the structural nature of shear bands in BMG on the atomistic scale. Altogether, complete crack paths could be observed and analyzed, and based on this, details of the shear band-driven crack growth are described. While in first SCC studies using a newly developed setup full cross section (3PB) bars were investigated, in recent *in situ* experiments, notched specimens were tested in 0.01 M NaCl, yielding strong evidence for a catastrophic failure due to hydrogen embrittlement (HE). The known susceptibility to pitting corrosion in halide-containing environments is only the initial stage for failure under SCC conditions. Once pitting is initiated, the local electrode potential is severely reduced. Further, the hydrolysis reaction of oxidized Zr^{4+} to zirconyl ions ZrO^{2+} during local BMG dissolution produces H^+ and, thus, a local acidic environment that enables proton reduction and hydrogen absorption in the stressed BMG region. The peculiar failure and fracture surface characteristics as well as the proven local reduction of the pH value in the vicinity of the notch during *in situ* experiments clearly account for the proposed HE-SCC failure mechanism.

Keywords: bulk metallic glass, zirconium alloy, cracking, shear bands, pitting, hydrogen, corrosion

OPEN ACCESS

Edited by:
Tanguy Rouxel,
University of Rennes 1, France

Reviewed by:
Jie Wang,
Corning Inc., United States
Zhongzhi Tang,
Corning Inc., United States

****Correspondence:***
Annett Gebert
a.gebert@ifw-dresden.de

Specialty section:
This article was submitted to Ceramics and Glass, a section of the journal Frontiers in Materials

Received: *09 January 2020*
Accepted: *20 April 2020*
Published: *02 June 2020*

Citation:
Gebert A, Geissler D, Pilz S, Uhlemann M, Davani FA, Hilke S, Rösner H and Wilde G (2020) Studies on Stress Corrosion Cracking of Vit 105 Bulk Metallic Glass. Front. Mater. 7:128. doi: 10.3389/fmats.2020.00128

INTRODUCTION

Among the bulk metallic glass (BMG)-forming systems, multicomponent zirconium (Zr)-based alloys are most prominent and best investigated regarding glass formation, mechanical performance, and chemical reactivity. Impressive mechanical properties of those alloys, like $Zr_{55}Cu_{30}Al_{10}Ni_5$, $Zr_{57}Cu_{15.4}Ni_{12.6}Al_{10}Nb_5$ (Vit 106), $Zr_{41.2}Ti_{13.8}Cu_{12.5}Ni_{10}Be_{22.5}$ (Vit 1), and $Zr_{52.5}Cu_{17.9}Ni_{14.6}Al_{10}Ti_5$ (Vit 105), are comparatively very high fracture strength values of 1,400–1,900 MPa, Young's modulus values of 70–96 GPa, and typical $\leq$2% elongation at yielding. These alloys have been mostly employed in fundamental studies of the deformation behavior of metallic glasses and basic mechanisms comprising processes of shear band nucleation and propagation were described. This knowledge is used for new strategies toward enhanced mechanical properties (Cheng et al., 2008; Trexler and Thadhani, 2010; Suryanarayana and Inoue, 2011). Optimization of casting techniques (Suryanarayana and Inoue, 2011; Yokoyama, 2015) and new concepts for additive manufacturing (Deng et al., 2019) allow for the fabrication of BMGs with larger dimensions or with complex shapes. This has opened the door for commercial production of those BMGs and for prospective engineering applications, e.g., hardware casings, sportive goods, watches and jewelry, and biomedical products (Suryanarayana and Inoue, 2011). Nevertheless, questions regarding long-term durability under application-relevant conditions, i.e., the superposition of mechanical loading and (often humid) environment remained scarcely addressed so far. With our fundamental studies on fracture toughness and on stress corrosion phenomena, we contribute to the understanding of failure mechanisms of this innovative class of glass-forming alloys.

Bulk metallic glasses are ideally single-phase, i.e., theoretically, they do not contain structural or chemical defects. This is alike the basic characteristics of inorganic glasses. Their composition is often complex and atypical in comparison to conventional crystalline alloys. (B) MGs have unique short- and medium-range order (SRO/MRO) structures, their topology yields outstanding properties and determines their response to mechanical load (Wondraczek et al., 2011). For example, synchrotron diffraction studies and computational analyses of the atomistic structure and stress effects of Zr-Cu(-Al) glasses revealed that their SRO has interpenetrating icosahedral-like clusters forming superclusters. Under tensile or compressive deformation, the topological and chemical SRO change results in dynamic cluster-destruction-recreation processes and reorganization of superclusters (Almyras et al., 2010; Zhang et al., 2011; Lekka et al., 2012).

Metallic glasses are basically expected to show "ideal brittle fracture" performance due to the absence of strain hardening and barriers for crack propagation. Their structural nature cannot yield the conditions to reduce high stress levels in the regions of crack tips. Such an ideal brittle behavior must result in a lack of plastic deformation and in very low toughness (Schuh et al., 2007). Nevertheless, Lewandowski et al. (2005) derived – also based on empirical data – critical levels for the Poisson's ratio ν, and this classifies BMGs according to a certain glass toughness. Hence, cast Zr-based glasses are comparatively "tough"; they show local plasticity due to multiple shear band formation. Together with high strength, this results in a significant fracture toughness.

Fracture toughness and fatigue resistance of glass-forming alloys have to be critically assessed, but they are far from being comprehensively understood (Schuh et al., 2007). Only for selected Zr-based BMG studies on these issues have been conducted. Firstly, Gilbert et al. (1997) determined for amorphous $Zr_{41.2}Ti_{13.8}Cu_{12.5}Ni_{10}Be_{22.5}$ CT-specimens a fracture toughness of K_{Ic} ~55 MPa$\sqrt{m}$ which is comparable to that of a high-strength steel. Under cyclic loading, fatigue crack growth rates comparable to those of ductile crystalline alloys were determined. Flores and Dauskardt (1999) fundamentally analyzed fatigue pre-cracked, single-edge notched tension samples of this BMG. *In situ* microscopic observations under tensile loading conditions revealed remarkable plastic deformation in crack tip regions which is indicative for high facture toughness. The local generation of shear bands and the branching of cracks cause an energy-dissipating region, and this determines crack growth. Recently, Madge (2015) reviewed the current state of research regarding toughness of BMGs and emphasized that even less tough metallic glasses are tougher than oxide glasses. But already among Zr-based glasses, a wide variability in fracture toughness and fatigue resistance data was evidenced, which is obviously related to the capability of the glass specimen to form a shear banding zone at a crack tip region. This is determined by experimental conditions (e.g., notch dimension, type of experiment, sample size) but is also strongly correlated with the alloy chemistry. Kruzic (2011) assessed the parameters which can affect the fracture and fatigue behavior of BMGs. The glass composition determining the SRO/MRO, the structural relaxation state (residual stress state), and the nature of surface and bulk defects are main important factors. Moreover, a high sensitivity for environmental influences, i.e., the test medium, was emphasized.

Owing to their ideally single-phase chemically homogeneous nature, metallic glasses are often considered as highly corrosion-resistant materials. Indeed, Zr-Cu-based BMGs can exhibit excellent passivity in a wide pH value range which is due to their valve-metal components Zr, Ti, Nb, or Al. However, in chloride-containing media, they are prone to pitting corrosion with low re-passivation ability. Our studies revealed that this has to be attributed to their high Cu content and selective constituent dissolution (Gostin et al., 2015a). Further, chemical and morphological defects determine the pitting susceptibility of BMG specimens which were fabricated under actual conditions (Scully et al., 2007). We also demonstrated that corrosive reactions interact with mechanically induced defects like shear bands (Gebert et al., 2012). It was predictable that those phenomena will be strongly accelerated under crevice-like conditions, i.e., in a crack tip zone. On the other hand, in our project, an approach for exploiting those mechano-corrosive interactions for the *in situ* electrochemical analysis of deformation processes was developed (Grell et al., 2015). When a quasi-static mechanical test is conducted in an inert salt solution with the BMG sample as an electrode, early stages

of plastic deformation can be detected *via* its electrochemical response which is much more sensitive than the macroscopic mechanical signal. The generation of first shear bands is accompanied by a local breakdown of the passive film at the BMG surface, yielding characteristic discontinuous changes of the electrode potential. There is a great potential for further developing this method.

Meanwhile, more and more studies are published which emphasize the high sensitivity of Zr-based BMGs for stress corrosion cracking (SCC) and corrosion fatigue (CF) phenomena. We have summarized those in a recent review (Gostin et al., 2015b). Pit formation is the typical first step, and in the following, cracks are initiated at those surface defects. A rapid crack growth is mostly ascribed to active dissolution in the region of the crack tip. Also, a few studies claim hydrogen damage to be responsible for crack propagation. Zr-based BMGs are excellent hydrogen absorbers. Investigations on pre-charged samples showed that hydrogen influences the shear band formation at notches and reduces the limit of the intensity factor. Upon continuous or cyclic loading, hydrogen inhibits the crack growth. Altogether, the complex SCC and CF mechanisms in Zr-based BMGs are by far not understood and have to be considered – similar to crystalline metals – from the viewpoint of both, metal dissolution and hydrogen-related effects as driving force for crack propagation and material failure. So far, due to the limited availability of appropriate glassy sample sizes and comparatively fast crack propagation rates, SCC and CF testing of BMGs was often not possible according to ASTM/DIN standard testing conditions. New setups and protocols have to be developed, enabling the analysis of those complex damage processes for smaller sample dimensions to clarify the impact of BMG alloy chemistry and particular structural states.

The present paper reviews highlight results of the SCC of Zr-BMG project starting with effects of different casting routes for BMG fabrication on their basic mechanical performance under tensile and 3PB conditions *via in situ* analysis of shear band-driven crack propagation upon 3PB in air up to SCC analyses with (un)/notched 3PB specimen under potential control in chloride-containing electrolytes. For these studies, the $Zr_{52.5}Cu_{17.9}Ni_{14.6}Al_{10}Ti_5$ (VIT 105) alloy was chosen as an example since it is well known as one of the best glass formers among the Zr-based alloys and one with highest application potential.

MATERIALS AND METHODS

Bulk Metallic Glass Sample Preparation

As many studies have already shown (Gebert et al., 2012; Yokoyama, 2015), element purity as well as melting and casting conditions are extremely decisive factors determining the quality of BMG samples in terms of achieving single-phase chemically homogeneous glassy states. In order to address this issue, we employed two different arc melting routes for $Zr_{52.5}Cu_{17.9}Ni_{14.6}Al_{10}Ti_5$ (Vit 105) ingot production:

Route (A) This follows the common procedure for BMG preparation. An appropriate mixture of single constituent elements Zr, Cu, Ni, Al, and Ti with very high purity (purity ≥99.9%) was used for arc melting on a Cu hearth under highly purified Ti-gettered Ar atmosphere. To ensure a homogeneous chemical composition, the ingots with a mass of 20 g were re-melted at least three times (Gostin et al., 2015c).

But large differences of the temperatures of melting varying from 933.5 K (Al) to 2,125 K (Zr) cause difficulties to obtain homogeneous master alloys. Therefore, a new procedure was established:

Route (B) This route is based on four binary pre-alloys in appropriate compositions which were prepared separately and used as starting material. The final $Zr_{52.5}Cu_{17.9}Ni_{14.6}Al_{10}Ti_5$ master alloy was re-melted in several steps for homogenization. All details of the process are provided in Geissler et al. (2019).

Then, flat BMG specimens (3 mm × 10 mm × 85 mm size) were cast using the master alloy ingots by means of suction casting into a copper mold. Resulting sample types are nominated as "A" and "B."

Material Characterization

The cast plates were chemically analyzed by inductively coupled plasma-optical emission spectrometry (ICP-OES) (SPECTRO ARCOS MV). For these samples, an approximate weight of 150 mg was taken from three different sections of one plate (top, center, bottom). The relative standard deviation (RSD) represents the error of the measurement and the homogeneity of material. It results from four times repeated measurements of three parallel weights of about 50 mg. Further, carrier gas hot extraction was employed to determine the impurity level, especially the oxygen concentration (LECO TC-436DR). The freshly etched samples which were taken from the different sections of a plate were mixed, and from that, average values of three repeated measurements were determined. The structure of BMG plates was investigated by X-ray diffraction (XRD) with a Philips Panalytical X'PERT-Pro MPD system with Co-Kα radiation in Bragg-Brentano geometry with theta–theta focusing. The thermal behavior was studied by differential scanning calorimetry (DSC) using a PerkinElmer DSC Diamond at 40 K/min under Ar. Polished as well as fractured surfaces were investigated by scanning electron microscopy (SEM) with a Leo 1530 Field Emission Gun SEM with Zeiss Gemini column operated at 20 kV. Microstructural investigations [transmission electron microscopy (TEM)] were performed using a Thermo Fisher Scientific FEI Themis 300 G3 transmission electron microscope. A more detailed description for the experimental setup is given by Hilke et al. (2019).

In situ Analysis of Cracking in Air

For *in situ* observation of fracture and failure in air, three-point-bending (3PB) tests were conducted using a Kammrath & Weiss Tensile-Compressive testing device equipped with an in-house developed 3PB kit as illustrated in **Figure 1A**. For these tests notched bars were employed. To fit to the used outer support span of S = 18 mm, the cast BMG

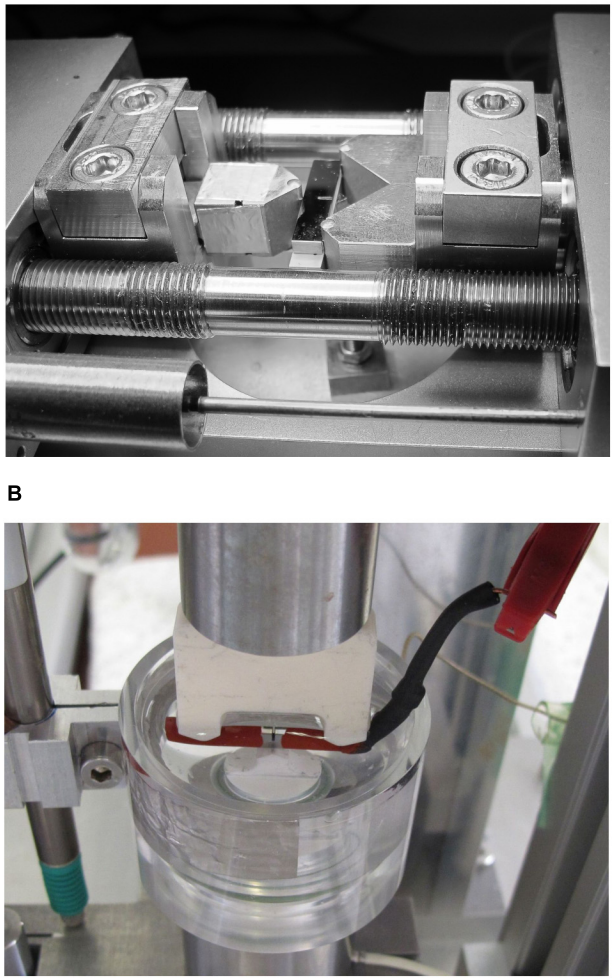

FIGURE 1 | (A) Three-point-bending (3PB) test in air with notched Vit 105 bulk metallic glass (BMG) sample in a Kammrath &Weiss tensile-compressive testing device with 3PB kit and **(B)** setup for 3PB-stress corrosion cracking (SCC) testing in 0.01 M NaCl with notched Vit 105 BMG sample, Pt counter, and SCE reference electrodes in an electrolyte cell.

plates were cut into bars with appropriate size and with a geometry that is close to recommendations of ASTM E399, E1820, ISO12135, cf. SEN(B) specimen (Geissler et al., 2018). Each side of a pre-cut slug beam was prepared to the desired size by standard metallographic procedures (Geissler et al., 2019). The final outer geometry of a sample was $S < L = 20.5$ mm, $W = 4.33$ mm, and $B = 2.243$ mm. A chevron edge notch was introduced in the middle of the bending bar by electrodischarge machining that was finally sharpened by a razor blade. The 3PB test was monitored and recorded *in situ* with a microDAC strain measurement device (Chemnitzer Werkstoffmechanik GmbH). A 5-kN load cell was used for the load measurement during the experiment. Further details are given in Geissler et al. (2019). In addition, *tensile tests* were done using the same Kammrath & Weiss Tensile-Compressive Testing device. The developed tensile testing setup for small-sized samples in Dogbone geometry was used. From cast BMG plates, appropriate sample dimensions were obtained by means of electrodischarge machining. The sample surface preparation was performed by standard metallographic procedures. The final sample had a thickness of about 1 mm, a gauge length of 5 mm, and a width of about 1 mm. Sample and fracture surfaces were as well analyzed by (SEM).

Stress Corrosion Cracking

For the analysis of SCC phenomena, rectangular bars were abrasively cut and metallographically prepared (0.25 μm finish) from cast BMG plates. For first studies with un-notched samples of alloy type "A," their dimensions were 2.50 mm^3 × 2.00 mm^3 × 27.00 mm^3 (Gostin et al., 2015c). Later in the project, straight-through edge notched bar samples with $S = 20$ mm were made from alloy types "A" and "B," respectively, as described in section "*In Situ* Analysis of Cracking in Air" and in Geissler et al. (2019). A setup for SCC testing of those small BMG samples was designed and built in-house, the test cell is shown in **Figure 1B**. A BMG 3PB sample was electrically connected and employed as working electrode. A container was added to the lower anvil and comprised 0.01 M NaCl ± 0.01 M Na_2SO_4 solution and the Pt counter electrode. An saturated calomel electrode (SCE) reference [E(SHE) = 0.241 V] with a Haber–Luggin capillary was used. The electrochemical cell was connected to a Potentiostat/Galvanostat PGU 10 V–100 mA from IPS Elektroniklabor GmbH & Co. KG. *In situ* pH value measurements at the notch root were conducted with an Orion PerpHecT ROSS Combination pH Micro Electrode from Thermo Scientific. The mechanical loading of the bending bars was realized by hand. Such a setup records simultaneously force, deflection, current, and potential and, separately, the pH value. The SCC experiment is described in very detail in Geissler et al. (2019) and comprised (a) an immersion period with recording of the open-circuit potential (OCP), (b) the adjustment of an elastic load level, (c) the recording of the OCP at the attained deflection, (d) a potentiostatic polarization at a selected anodic potential, and (e) the measurement of the OCP after anodic polarization and fracture. This principle test protocol was already established and firstly applied to un-notched bending bars in Gostin et al. (2015c).

RESULTS AND DISCUSSION

Analysis of Mechanical Performance and Crack Propagation in Air

Impact of Sample Homogeneity on Tensile and Bending Deformation of Vit 105

Vit 105 samples which were obtained from casting routes "A" and "B" were subjected to careful chemical analysis to assess the accuracy of the attained alloy composition, the impurity level, and the homogeneity. **Table 1** summarizes exemplary results

TABLE 1 | Results of chemical analyses of Vit 105 BMG samples prepared by routes A and B: element analysis (ICP-OES in at.%) and carrier gas hot extraction oxygen analysis (in wt.%).

Composition	Zr	Cu	Ni	Al	Ti	O
Nominal	52.50	17.90	14.60	10.00	5.00	–
sample A	52.55	17.85	14.50	10.10	5.00	0.029
sample A RSD	1.25	1.30	1.10	0.75	1.25	0.002
sample B	52.56	17.90	14.57	9.97	5.00	0.028
sample B RSD	0.05	0.05	0.06	0.13	0.06	0.003

BMG, bulk metallic glass; ICP-OES, inductively coupled plasma-optical emission spectrometry; RSD, relative standard deviation.

gained from ICP-OES for metallic constituent analysis as well as carrier gas hot extraction for the determination of the oxygen content. For both sample types A and B, the presented absolute element concentrations show very good approximation to the nominal values. However, the RSD values which express the relative standard deviation for multiple measurements differ significantly. In case of sample type A, for all constituents, RSD values are much larger, i.e., up to two orders of magnitude, than those determined in case of sample B. This implies some fluctuations of the chemical composition within one sample when it is processed *via* the common casting route A which starts with arc melting of the single constituents instead of selected binary pre-alloys. However, despite multiple arc-melting steps and final suction casting, the oxygen contents for both sample types are quite similar and comparatively low which are important for suppressing oxygen-induced crystallization upon slow cooling from the melt (Gebert et al., 1998).

Exemplary XRD patterns of a Vit 105 plate sample of type A are shown in **Figure 2**. Those were similarly measured for cast samples of type B. After surface polishing to remove the outermost plate regions with some unidentifiable crystalline phases (up to ∼100 μm depth), in all cases, only the broad diffuse diffracted intensity maxima which are characteristic for

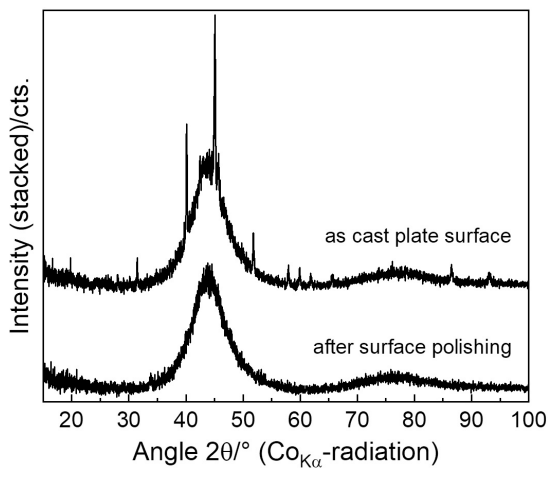

FIGURE 2 | X-ray diffraction (XRD) pattern of Vit 105 bulk metallic glass (BMG) samples of type A, as cast and after surface polishing.

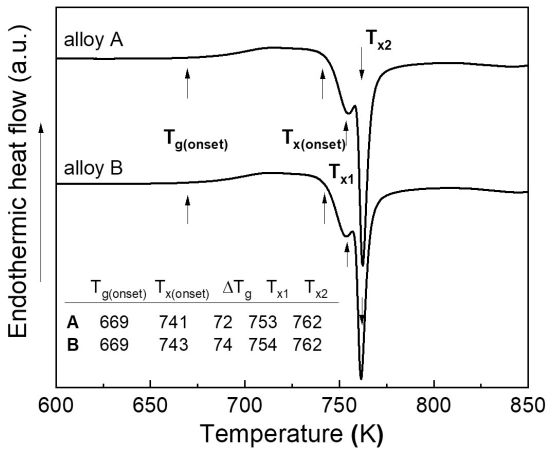

FIGURE 3 | Differential scanning calorimetry (DSC) curves of Vit 105 bulk metallic glass (BMG) samples of types A and B recorded at a heating rate of 40 K/min.

an amorphous phase were detected (Gostin et al., 2015c). Micro-CT of several cast specimens detected a limited number of small pores with sizes <50 μm. However, this XRD analysis cannot resolve possible crystalline second phases with volume fractions <2. . .5%.

The thermal behavior of a metallic glass sample is usually a sensitive indicator for its initial structural state after solidification since the glass-forming ability correlates with the extension of the undercooled liquid region and the exothermic crystallization events provide hints regarding the homogeneity and purity of the quenched state (Gebert et al., 1998). Characteristic DSC traces of cast Vit 105 samples of types A and B are shown in **Figure 3**. Both sample types exhibit a very similar thermal behavior with undercooled liquid ranges of 72–74 K and a two-step crystallization sequence starting at 753–754 K. Thus, in the present study, neither differences in chemical homogeneity nor important differences in crystallite levels and so in the mechanical behavior (as presented later) can be inferred from the nearly identical DSC measurement results.

Mechanical properties of both sample types were characterized by 3PB as well as tensile testing in air. For the 3PB experiments, chevron-notched samples were used. Typical recorded and corrected 3PB stress–deflection curves for samples of types A and B are shown in **Figure 4A**. For a comparison of the results of bending tests in air and in the SCC situation (section "Stress corrosion analysis"), the maximum bending stress (3PB) was calculated and used (Geissler et al., 2018). The obtained maximum tensile stress values of about 2,300 MPa at the onset of plastic deformation match very good to those data obtained for un-notched $Zr_{52.5}Cu_{17.9}Ni_{14.6}Al_{10}Ti_5$ samples of A-type (Gostin et al., 2015c). So, this way of stress estimation (Geissler et al., 2018) is applied in the following studies.

In contrast to the thermal behavior, a distinctly different mechanical behavior was observed between the samples of routes A and B. Specimens from cast plates of route B reach much higher fracture stress levels, as demonstrated in **Figure 4A**

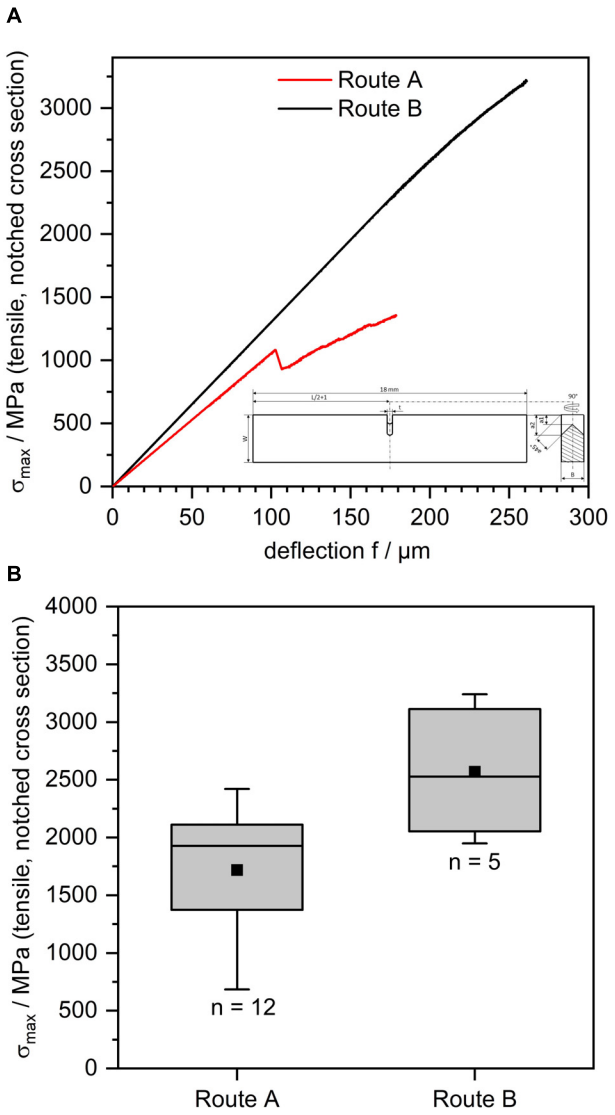

FIGURE 4 | Three-point-bending (3PB) tests of chevron-notched samples of routes A and B in air. **(A)** Stress deflection curves and **(B)** boxplots of the maximum bending stress on the remaining ligament at fracture (*n* = number of tested samples).

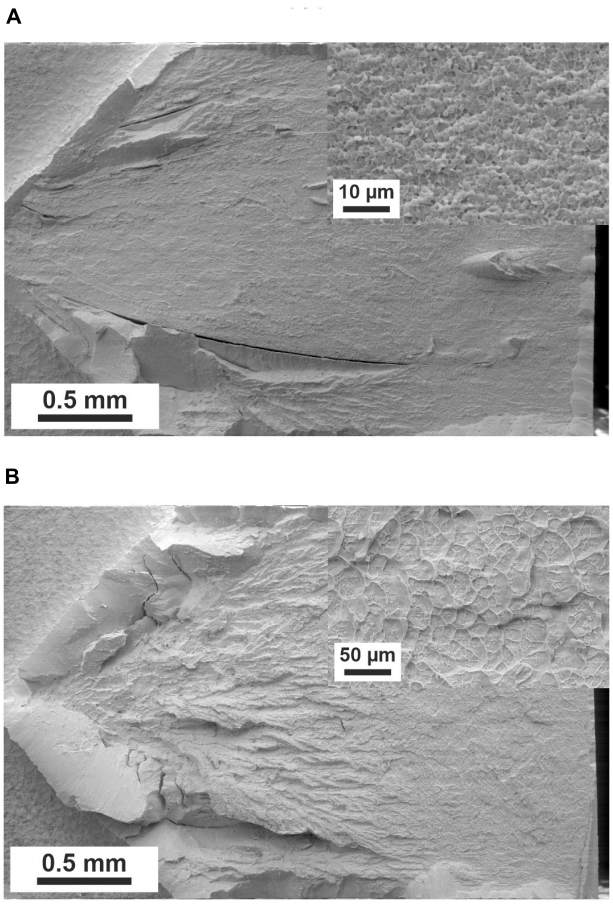

FIGURE 5 | (A) Scanning electron microscopy (SEM) fracture surface images of the samples corresponding to the stress deflection curve in **Figure 4A** fracture surface of sample type A, **(B)** fracture surface of sample type B.

comparing two example curves for 3PB specimens of the two types. The B-sample reached typical values of fracture stress of $\gtrsim$3,200 MPa tensile and 2,400 MPa compressive. In contrast, those data are much lower for the A-type BMG sample which is less homogeneous. In this case, the sample began to fracture at much lower tensile stresses ($\sigma \gtrsim$ 1,100 MPa). In the course of this comparative study with several samples of each type, selected A-type BMG 3PB specimen failed already at very low stresses, i.e., in a range of $\gtrsim$685 MPa (tensile), as it was obvious from the boxplots in **Figure 4B**. On the other side, the lowest bending fracture stress observed for a specimen of route B was $\gtrsim$1,900 MPa. Particles are the reason for the worse mechanical performance of the specimens from route A (**Figure 5A**) which accumulate to create sheetlike "inner surfaces" (Morrison et al., 2007). When those are located in the middle of the 3PB bending bar, i.e., in the notched zone, they can cause early failure at small stresses. In case of specimens prepared by the new route B, the probability of such detrimental particle aggregations is very low. The images of the fracture surface in **Figures 5A,B** that correspond to the 3PB samples in **Figure 4A** confirm this observation. For the specimen of route A, massive flaws are present in the fracture surface. In contrast to that, the fracture surface of the specimen of route B (**Figure 5B**) shows only features which were reported for bulk glassy samples subjected to similar deformation processes [e.g., Hull (1999); Morrison et al. (2007)]. The surface comprises rim regions with rough vein patterns corresponding to evident stress states and more delicate patterns in the center regions which relate to dominant strain states.

The findings of the 3PB experiments are further supported by results of conducted tensile tests. Representative stress strain curves of tensile specimens fabricated from cast plates of route A and route B are shown in **Figure 6A**. As already discussed for 3PB, specimens of route B possess notably higher fracture stress values

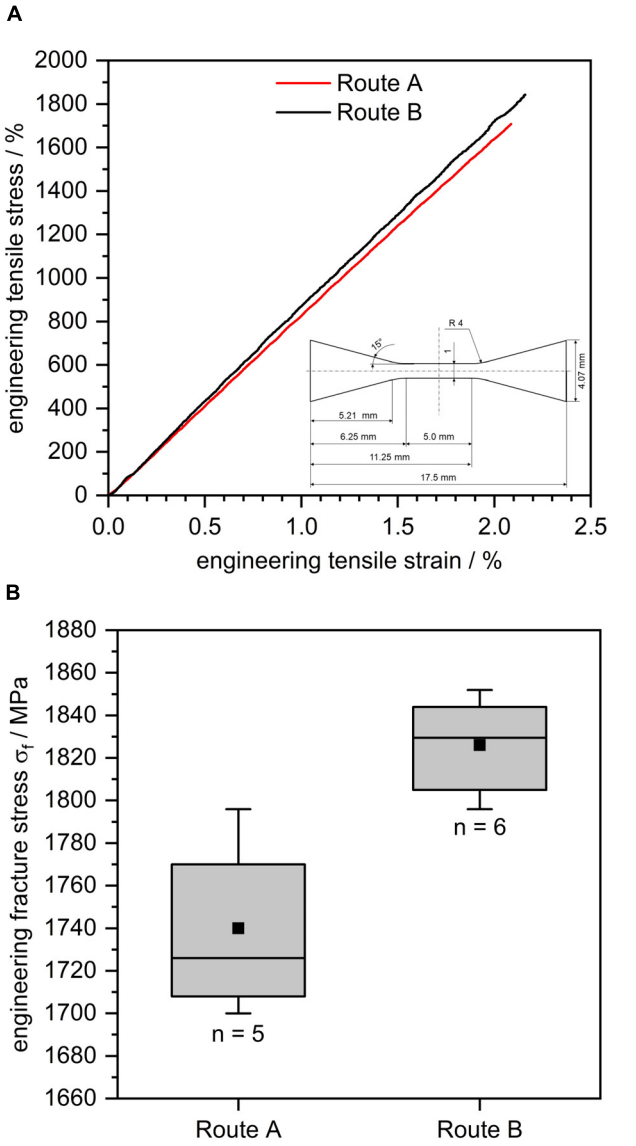

FIGURE 6 | Tensile tests of samples of routes A and B in air. **(A)** Exemplary stress strain curves and **(B)** boxplots of the fracture stress (*n* = number of tested samples).

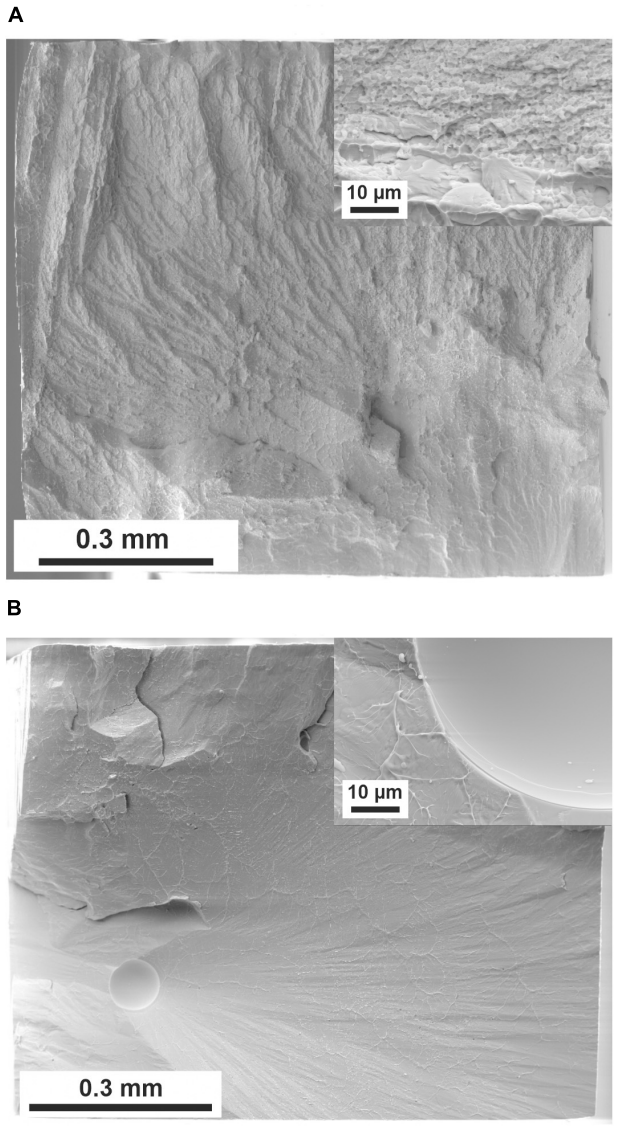

FIGURE 7 | Scanning electron microscopy (SEM) fracture surface images of the samples corresponding to the stress strain curves depicted in **Figure 6A**: **(A)** fracture surface of sample type A, **(B)** fracture surface of sample type B.

and lower scattering of those. Thereby, samples from route B reached values between 1,800 and 1,845 MPa, whereas samples of route A failed between 1,710 and 1,800 MPa (**Figure 6B**). Tensile samples of both casting routes fractured not at or near the clamping, and for both routes, multiple fractures occurred for some samples. SEM evaluations after fracture showed in both cases cracks as well as shear bands that were not catastrophic. A notable difference is seen in the images of the fractured faces of the two BMG types. Specimens of route A show again particles and sheetlike delaminations at the fracture surface besides typical vein pattern parts (**Figure 7A**). In contrast, for samples of route B, these defects are not present, but only the typical vein patterns (see inset in **Figure 7B**). Furthermore, the depicted sample of route B showed even with the present pore (**Figure 7B**) a higher fracture strength than the samples of route A.

In situ Analysis of Crack Propagation in Vit 105 Under Three-Point-Bending Conditions

In the following section, the crack propagation under 3PB bending conditions (S = 10 mm) will be described for a pre-notched Vit 105 specimen (route A) in air. Images were recorded *in situ* with a microDAC strain measurement system and *ex situ* using a field emission gun (FEG)-SEM. The complete crack path after testing as well as selected *in situ* images visualizing the crack propagation and shear band development are given in **Figure 8**. The force deflection curve of the sample is shown in **Figure 9A**. First crack initiation and propagation from the

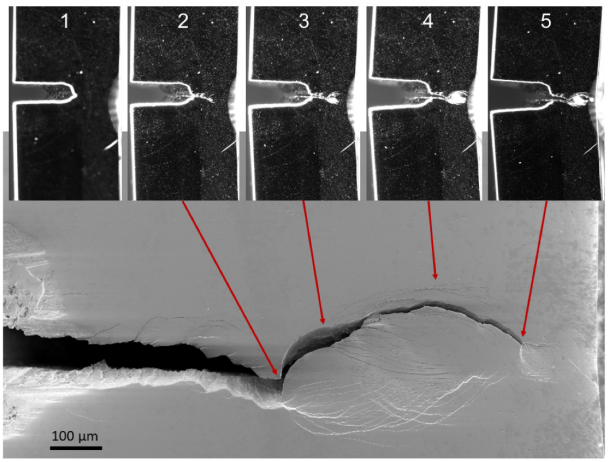

FIGURE 8 | Crack propagation of pre-notched Vit 105 sample under three-point-bending (3PB) conditions.

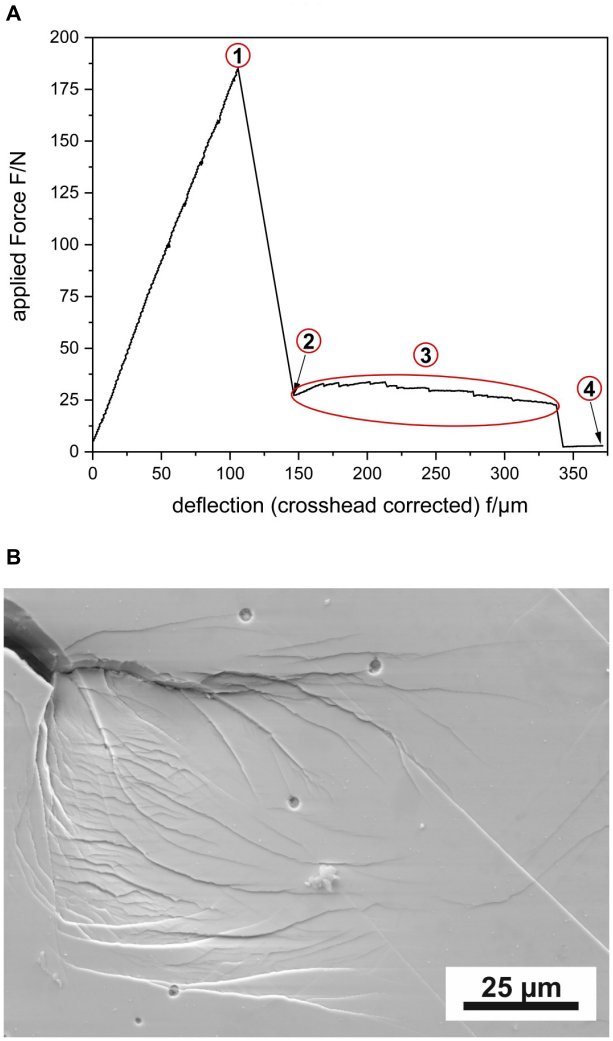

FIGURE 9 | (A) Force deflection curve of pre-notched three-point-bending (3PB) sample in air (images of corresponding crack propagation are depicted in **Figure 8** and **(B)** scanning electron microscopy (SEM) image of the crack tip after testing.

existing notch occurred at a load of 185 N and corresponds to a maximum tensile stress of about 1,670 MPa in the remaining cross section. At point 2 of the load deflection curve, the crack propagation stopped due to the extensive shear banding. The shear bands follow the theoretical solution of the fan-shaped Prandtl slip-line fields for a notched bending specimen (Green and Hundy, 1956; McClintock, 1971; Flores and Dauskardt, 1999; Chakrabarty, 2006; Zhu and Joyce, 2012; Geissler et al., 2018). In this first part, the crack propagation is fairly straight, and only small curvatures are existing due to crack deflections (**Figure 8**, image 2). The formation of shear bands along the crack path and in front of the crack tip is clearly visible in the *in situ* and SEM images. Based on the SEM images, the shear band zone has a size of about 100 µm in this first region. With ongoing deflection, further crack growth occurred at maximum tensile stress which is about 1,140 MPa in the remaining cross section. The *in situ* image (**Figure 8**, image 3) and the SEM image demonstrate the extensive formation of shear band patterns in front of the crack tip resembling the aforementioned fan-shaped slip-line field solutions. These shear band patterns correspond to the Prandtl-type slip-line fields that denote the maximum shear stress and shear velocity and demonstrate complete plastic behavior due to non-hardening or strain softening of bulk glassy alloys (Geissler et al., 2018). High normal stresses are also present orthogonal to these slip-line traces, and therefore, further crack events follow either the one or the other trace along a shear band. Thereby, the crack is deflected from its straight propagation direction. With ongoing deformation, a new slip-line field develops in front of the crack tip of the arrested crack due to partial unloading and leads again to comparatively large-scale plastic deformation and later a crack deflection. To emphasize, the formation of shear band patterns according to slip-line field solutions indicates more a plastic collapse behavior beyond the classical KI- or J-integral fracture mechanics framework (Geissler et al., 2018). This behavior is nicely visible in the *in situ* images (**Figure 8**, images 3 and 4) corresponding to part 3 of the load deflection curve. The crack propagation takes place mainly along separated shear band planes. The formed shear band zone in this sample area is even larger than 100 µm. The final crack tip after the stopped bending experiment (**Figure 8**, image 5; **Figure 9A**, region 4) at this stage is depicted in **Figure 9B** and demonstrates again nicely the slip-line field-like arrangement of shear bands.

An electron-transparent sample was prepared by FIB from a notched three-point bending test containing four shear bands (1–4) and subsequently imaged using high-angle annular dark-field scanning transmission electron microscopy (HAADF-STEM) (Hilke et al., 2019). Alternating contrast changes along their propagation direction can be noticed for three of them (**Figure 10**). The contrast changes are caused by differences in the density along the shear band and have also been observed for $Pd_{40}Ni_{40}P_{20}$ (Hieronymus-Schmidt et al., 2017) and

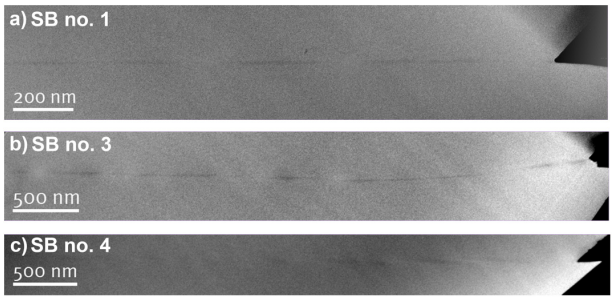

FIGURE 10 | Contrast-enhanced high-angle annular dark-field scanning transmission electron microscopy (STEM-HAADF) micrographs showing shear bands in Vit 105 with alternating contrast changes. **(a)** shows a shear band (no. 1) that is aligned edge-on to the electron beam; **(b)** shows a shear band (no. 3) that bends toward the surface; and **(c)** shows shear band (no. 4) that is twisted and thus misaligned to the electron beam.

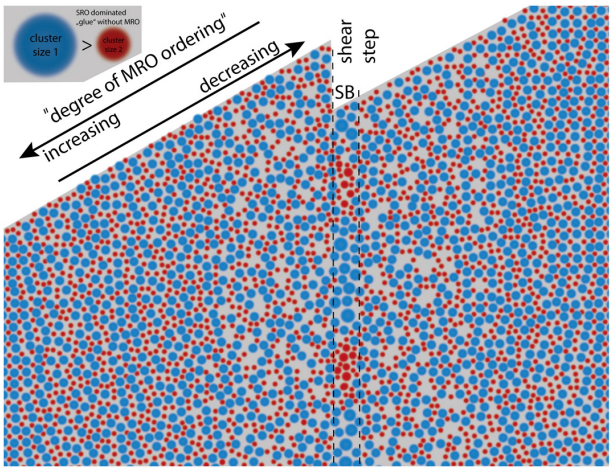

FIGURE 11 | Schematic illustration of the medium-range order (MRO) distribution in and around a shear band indicating the influence of the deformation.

$Al_{88}Y_7Fe_5$ (Rösner et al., 2014; Schmidt et al., 2015). Moreover, the microstructure of the amorphous state was analyzed with respect to MRO using variable resolution fluctuation electron microscopy (VR-FEM). FEM is sensitive to MRO of disordered materials. It uses the correlation of atom pairs (pair–pair correlation function). A statistical analysis of the variance V(k, R) from diffracted intensities of nanometric volumes obtained by nano-diffraction was used to extract this information. Sampling with different parallel probe sizes, R, gives information of the structural ordering length scale. Moreover, the height of the first variance peak provides a semiquantitative measure of the MRO volume fraction. From individual nano-beam diffraction patterns (NBDPs) taken from different regions (shear band and matrix), this statistical information was extracted prior to and after deformation. Strikingly, the MRO of the matrix was strongly affected after deformation (peak height reduction). For the details, we refer to Figure 3 in Hilke et al. (2019). **Figure 11** is an illustration based on the observed changes in the matrix MRO after deformation indicating the existence of a shear band-affected zone (SBAZ) (Pan et al., 2001; Maaß et al., 2014; Shen et al., 2018).

Stress Corrosion Analysis

In the project, a detailed study of the SCC process was carried out on cast $Zr_{52.5}Cu_{17.9}Al_{10}Ni_{14.6}Ti_5$ (Vit 105) BMG samples. In 3PB tests with an environment comprising near-neutral water-based NaCl solutions, *in situ* recordings of stress and current density and later of the local pH value were performed, and afterward, the fractured surfaces of the samples were inspected. So, the impact of solution, electrode potential, and applied elastic load on the initiation and growth of cracks could be assessed and discussed under consideration of their particular microstructure.

First studies were conducted with un-notched rectangular bar samples of type A. In order to determine appropriate testing conditions, quasi-static bending tests in air were conducted by means of the SCC setup (section "Stress Corrosion Cracking"), and two stress levels in the elastic regime were selected, i.e., 30% and 50% of the $R_{p0.2}$. Further, potentiodynamic anodic polarization curves with re-passivation loops were recorded on embedded and polished sample cross sections in the test electrolyte 0.01 M Na_2SO_4 + 0.01 M NaCl and suitable potentials in the region ($E_{repass} < E_{anodic} < E_{pit}$), i.e., $E_{anodic} = -50$; 0; 50 mV versus SCE have been selected. With these parameters, SCC tests were performed (Gostin et al., 2015c). From each test, a collection of data, i.e., the duration for the initiation of pitting, the initiation time for SCC and that for SCC propagation, as well as the total duration to fracture, was obtained. Results regarding the latter are shown in **Figure 12A**. Though there is an obvious scattering of the data, two principal trends can be derived. Firstly, for a defined load level of 50% $R_{p0.2}$ and with increasing potential, the fracture duration is reduced, and therefore, the resistance to stress corrosion declines. Further, at a given potential of +50 mV versus SCE, a lower applied load of 30% $R_{p0.2}$ causes increased durations to fractures. Also, the studies revealed the stage when the dominance of pitting changes toward a dominance of cracking which occurs earlier at an increased stress level. From those experiments, average crack growth rates were roughly estimated. For example, the rate was about 14 $\mu m \cdot s^{-1}$ for a test conducted at an initial stress of 50% of $R_{p0.2}$ and an electrode potential of 0 mV versus SCE. The value was estimated by employing SEM analysis which revealed the total length of the fractured region due to crack propagation, and this was divided by the propagation time (Gostin et al., 2015b,c).

A typical example of a fracture surface is shown in **Figure 12B**. Fractography of numerous samples revealed that multiple pits are typically present and are mostly located along the sample edges. Due to their sharp geometry, these edges are most preferred sites at the BMG electrode surface for chloride ion attack. This confirms critical conclusions made in earlier corrosion fatigue studies on 4PB Vit 105 samples (Morrison et al., 2007). Altogether, our SEM investigations disclosed that cracks usually started at locally corroded zones. This was similarly observed

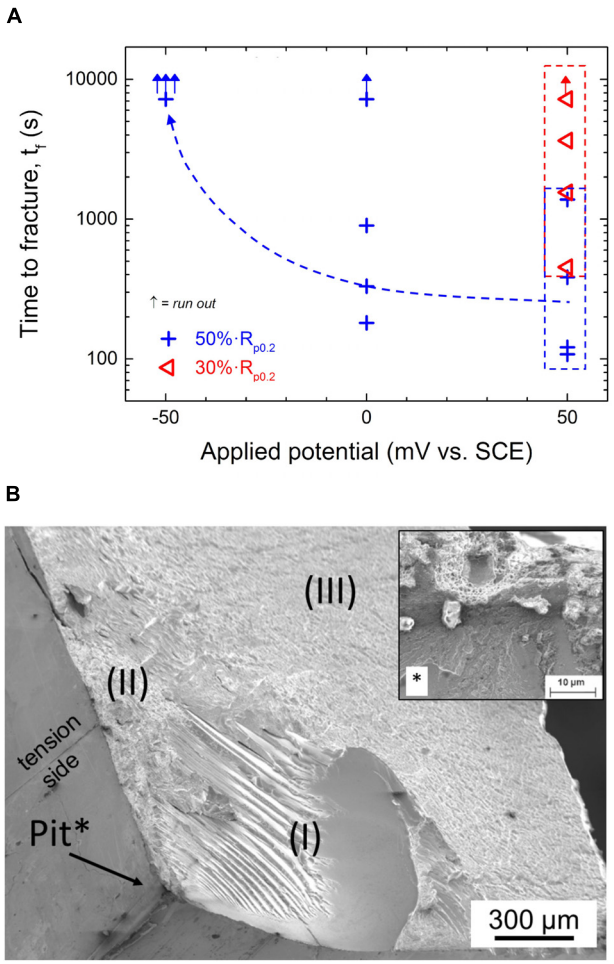

FIGURE 12 | (A) Stress corrosion cracking (SCC) test results-total time to fracture versus applied anodic potential E_{anodic} for un-notched Vit 105 bars in 0.01 M Na_2SO_4 + 0.01 M NaCl, starting σ_{max} = 1,301 MPa (50% of $R_{p0.2}$) and **(B)** scanning electron microscopy (SEM) image of fracture surface of un-notched Vit 105 sample after SCC testing (for I–III, see text).

in corrosion fatigue tests which were conducted in the present project employing the same sample type A of Vit 105 3PB samples (Grell et al., 2017). The randomness of the pitting process is one reason explaining the scattering of the final times to fracture. The zones I and II correspond to different crack propagation stages. At these early stages of our studies, the features in the zone I were interpreted as indications for a crack growth with multiple superimposed processes comprising unstable but permanent brittle propagation at the rim regions of the bulk glassy sample. Toward the center of a sample, this changed to a stepped growth mode with shearing and dissolution in the crack tip zone. The characteristics of zone II were ascribed to anodic dissolution during crack propagation (Gostin et al., 2015c). However, our subsequent analyses led to new interpretations as will be also explained below (Geissler et al., 2019). Nevertheless, it is emphasized that the relative area ratio of zone I to zone II was not always the same in each experiment. For example, samples tested at the highest stress level and at the most positive electrode potential (50%·$R_{p0.2}$ and 50 mV) failed mostly at their middle region. There, the fracture surface was very smooth indicating that a zone II type characteristic governed the process. The observed relation between the site of the initiation of a crack and the resulting features of the fracture surface were attributed to stress fields which are present at the crack tip. We supposed that only zone II is created by true SCC, whereas zone I evolves by only superimposed mechanical fracture steps. The last period of the fracture process causes zone III which exhibits mainly vein patterns. For BMGs, those are indications for unstable growth of cracks based on shear banding (Gostin et al., 2015c). Based on those observations, a first model mechanism for the SCC process in this Zr-based BMG was proposed which comprised (i) pit formation at sample edges, (ii) pit to crack transition–cracking initiation, (iii) crack growth with increase of the stress intensity factor; a reduction of stress concentration by the formation of shear bands which can lead to a significant inhibition of the propagation of the crack, (iv) many crack branches may form due to enhanced dissolution at the shear bands, and (v) when the stress level surpasses a threshold at a tip of a generated branch, the formation of shear bands sets in again and this leads to further blunting at the crack (Gostin et al., 2015c).

However, with view to the high sensitivity of those SCC tests, the criticality of employing un-notched 3PB samples and the difficulties of having limited reproducibility of BMG sample quality were emphasized. Moreover, in a few earlier studies, there were first suggestions that hydrogen as corrosion product may play a significant role (Kawashima et al., 2010; Gostin et al., 2015b). Commonly, in the case of anodic SCC, corrosive dissolution is locally triggered by stress or plastic deformation. Indeed, many stress corrosion and corrosion fatigue analyses that were done so far on bulk glass-forming Zr alloys end with a discussion of the results only under consideration of local dissolution as driving process for the crack initiation and growth [see for example, Ritchie et al. (2000); Schroeder and Ritchie (2006); Morrison et al. (2007)]. However, corrosion reactions as steps of an SCC process can also yield hydrogen species which can be easily absorbed by metals and alloys such as Zr-based materials. Therefore, also for those amorphous alloys, effects of hydrogen embrittlement (HE) or hydrogen-induced SCC (HISCC) have to be taken into account. Kawashima et al. (2010) conducted tensile tests of Zr-BMG samples exposed to NaCl electrolytes and Nakai and Yoshioka (2010) performed deformation studies with CT samples in such environments. In both studies, the deformation test data and the analysis of the characteristics of the fracture surface led to the conclusion that hydrogen, i.e., HE, plays a crucial role in the early failure of the material. Moreover, the corrosion-assisted cracking behavior and the hydrogen sensitivity of crystalline Zr and Zircaloy-2 and -4 should also be taken into these considerations. Though they exhibit a relatively high passivation ability, a high tendency for local corrosion is given in chloride electrolytes in particular when iron or copper ions are involved. SCC processes were observed and were often attributed to embrittlement effects in consequence of the generation of Zr hydrides. On the other hand,

from several studies, it was concluded that HE and SCC can take place without the accumulation of significant Zr hydrides in the deformed regions of a crack tip (Majumdar and Scully, 1979; Cox, 1990; Rebak, 2000; Farina et al., 2003). Thus, one has to take into account that there are some similarities in the hydrogen-driven mechanical behavior of crystalline and amorphous Zr-based alloys, and those have to be considered in the discussion of experimental observations gained in stress corrosion and fatigue corrosion analysis of these newer bulk glass-forming systems.

Altogether, in the subsequent 3PB-SCC tests on $Zr_{52.5}Cu_{17.9}Al_{10}Ni_{14.6}Ti_5$, Vit 105 specimens were conducted with special emphasis on the identification of hydrogen-related phenomena (Geissler et al., 2019). All experiments were performed with notched bar specimen, and larger sample surface areas were coated with a paint, as shown in **Figure 1B**, in order to localize the expected degradation events in the middle of the notched bar. This was also the site for potential and pH value measurement. Both BMG sample types A and B were investigated, and no significant differences regarding the SCC mechanism were noticed. **Figure 13** shows a typical result of an *in situ* SCC experiment with a straight-through edge notched Vit 105 3PB specimen (type B) in 0.01 M NaCl solution, i.e., the evolution of the sample response in terms of load, electrode potential, current, and pH value in dependence of time (Geissler et al., 2019). In these tests, a 0.01 M NaCl solution with pH 5.6 was employed. The free corrosion potential *OCP* was measured during the initial step at small pre-load F_0(10N) and varied only slightly between −100 and −50 mV versus SCE. Next, under *OCP* conditions, the load level was slowly raised to adjust the maximum load F_{max} which controlled a small deflection f_{exp}. Here, F_{max} was 177 N which is equivalent to an estimated maximum tensile stress of ≥365 MPa (Geissler et al., 2018). This is less than 12% of the value of >2,300 MPa for a 3PB(-SCC) chevron-notched specimen tested in air (see section "Analysis of Mechanical Performance and Crack Propagation in Air"; **Figure 4A**). When applying the load, the OCP decreased to below −400 mV. This is attributable to a breakdown of the passive film which locally exposes the free metal surface. After this initial drop down, the *OCP* gradually increased again, indicating a healing trend (re-passivation) of the metal surface. In a next step, the electrode potential was increased with constant rate from *OCP* to a potential of *AP* of −50 mV at the deflection f_{exp}. When keeping *AP* constant, the current started to gradually rise, and the pH value decreased. From an abrupt and then stepwise load drop, a beginning cracking with several propagation steps had to be concluded. In all SCC tests, failures of the BMG specimen occurred within very short time spans, i.e., only within about a minute. Also, after the full fracture, the *AP* was still applied whereby the current increase and the pH value decrease continued. It is remarkable that pH values as low as pH < 4 were measured near the originally notched center region of the BMG specimen. In a last step, the external potential was switched off, and thus, the OCP and the pH value recovered gradually. However, in similar SCC experiments

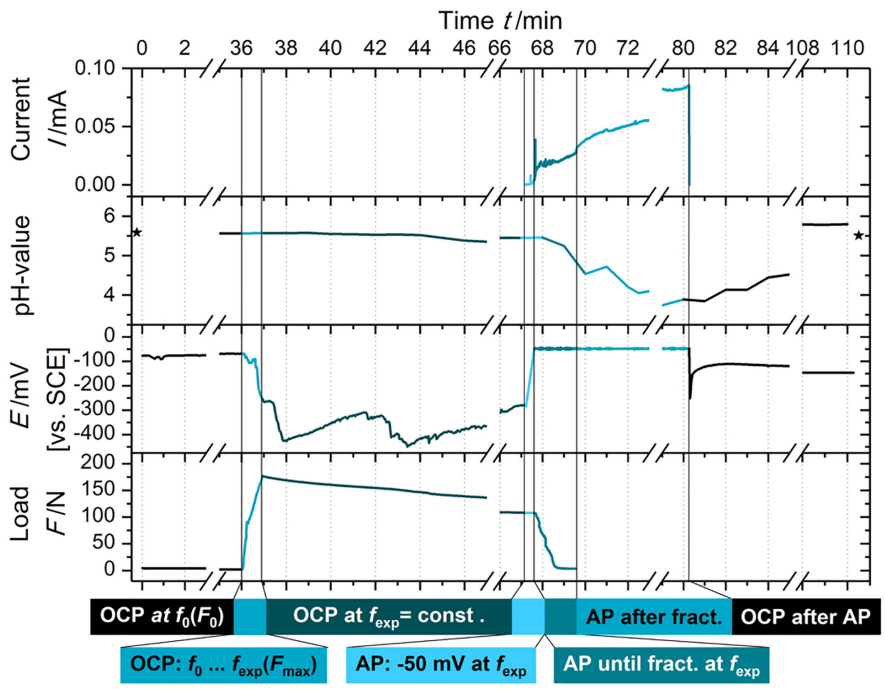

FIGURE 13 | Stress corrosion cracking (SCC) test with a straight-through edge notched Vit 105 three-point-bending (3PB) specimen (type B) in 0.01 M NaCl solution: evolution of load, electrode potential, current, and pH value in dependence of exposure time (Geissler et al., 2019, open-access article with Elsevier user license CC BY 4.0).

[not shown here but in Geissler et al. (2019)], the 3PB BMG samples started to fail already in the early period of open circuit conditions with constant deflection f_{exp}. Also, in those cases, a significant acidification of the solution near the sample surface was measured.

After those SCC experiments, the test electrolytes were analyzed regarding metal release with ICP-OES, and large amounts of Zr species and Al, Ti, and Ni species and to a lesser extent Cu species were detected. Detailed microscopic fractography was done after all SCC tests, and typical examples are shown in **Figure 14A** for the sample subjected to the SCC test plotted in **Figure 13** and in **Figure 14B** for a Vit 105 sample that failed already during loading under OCP immersion.

In comparison to 3PB overload failure in air (section "Analysis of Mechanical Performance and Crack Propagation in Air"), after testing under SCC conditions in 0.01 M NaCl solution, the fracture surface appearances are completely different. This was already evident upon visual inspection of the fractured specimen. From typical surface images that are exemplarily shown in **Figure 14A**, a conchoidal fracture has to be derived which is typical for very brittle materials (Hull, 1999). In 3PB SCC tests which were conducted at higher applied loads, also mixed fracture modes occurred. Those comprised in addition smaller regions with characteristics of overload fractures which were observed and described for fracture surfaces generated in air. This is exemplarily shown in **Figure 14B** for a notched BMG bar specimen which partially fractured already during exposure under open circuit conditions and applied load. The insets of **Figures 14A,B** reveal that pitlike corrosion damages occurred at the outer edges of the specimens and also at the bottoms of the notches. Close to those, the morphologies of the fracture surface are indicative for a change from local corrosion to conchoidal fracture. This appears to be a typical characteristic of the stress corrosion process of Zr-based BMGs.

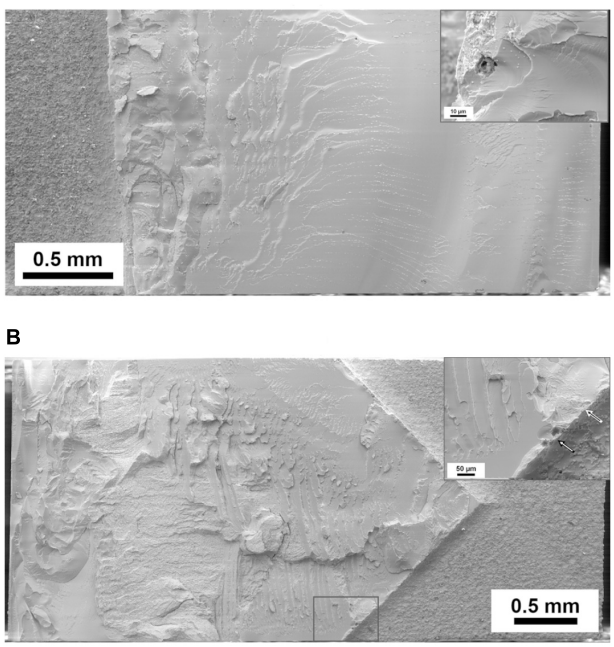

FIGURE 14 | (A) Scanning electron microscopy (SEM) image of a fracture surface of straight-through edge notched Vit 105 three-point-bending (3PB) specimen after stress corrosion cracking (SCC) test in **Figure 13**, inset: site of pitting and most plausible crack initiation and **(B)** SEM image of a fracture surface of a chevron-notched Vit 105 3PB specimen which failed upon SCC testing at open-circuit potential (OCP) condition, inset and lower box: pitting and possible crack initiation.

Finally, when analyzing the basic morphologies of corroded areas in pits as reported in various publications [e.g., in Gostin et al. (2015a,c)] and under consideration of the typical fracture surface features which were observed in the present study as well in an earlier report (Kawashima et al., 2010), it has to be concluded that a main reason for macroscopic failure upon SCC testing of Zr-based BMGs even under free corrosion and anodic control is HE or hydrogen-induced SCC (HISCC).

A reason why hydrogen-related effects are mostly excluded during corrosion testing of Zr-based BMG samples in near-neutral water-based tests electrolytes is that relevant electrode potentials seem to be by far too positive, i.e., too far away from the cathodic hydrogen reduction potential. However, if only small actively corroding sites like pits or cracks are present on an otherwise passive metal surface, a mixed electrode potential is measured. Thus, the potential of an active site is unknown but must be very negative in the present case. In the SCC tests, this was obvious from the significant drops of the OCP by several hundreds of millivolts upon mechanical loading (**Figure 13**) which is due to the rupture of the natural passive film or even first pitting. Similar as reported in some earlier works, our present studies on $Zr_{52.5}Cu_{17.9}Al_{10}Ni_{14.6}Ti_5$ (Vit 105) 3PB samples in NaCl solutions under OCP or anodic conditions revealed that local anodic dissolution (pitting) is the typical initial step of a stress corrosion process. Similar to other Zr-based BMG alloys (Gostin et al., 2015a), the major constituent Zr mainly dissolves whereby hardly soluble Cu compounds remain enriched as residues in the corroded surface areas. Zr is a strong base metal, its standard electrode potential is $E = -1.8$ V – this is far below the stability range of water which is ∼1.5 V more positive. Thus, in solutions with pH < 6.6, the Zr metal tends to dissolve and the Zr^{4+} ions are subjected to complex hydrolysis reactions, leading to zirconyl ions ZrO^{2+} and protons H^+ (Pourbaix, 1966). Our *in situ* pH value measurements during SCC testing revealed significant acidification (**Figure 13**), and this indicated that those processes can occur also in case of a Zr-based metallic glass. When the main alloy component Zr actively dissolves in localized areas such as a pit or crack, this can cause instantaneously the generation of hydrogen atoms. Those can be reduced at the very negative bare BMG surface site, and finally, adsorbed hydrogen atoms will be absorbed. Fundamental studies regarding hydrogen uptake of Zr-based glass-forming alloys revealed that the hydrogen solubility and diffusivity can be remarkable (Eliaz and Eliezer, 1999; Ismail et al., 2002). Hydrogen atoms can be incorporated in the (un-deformed) SRO/MRO structure of the metallic glass by successively occupying interstitial tetrahedral sites of different energy levels (Bankmann et al., 2003; Gostin et al., 2015b). *In situ* generated and absorbed hydrogen atoms

in a crack tip region will have significant effects on shear band-driven crack propagation and on the local SRO/MRO structure. It should be a matter of further studies to analyze those local structural changes in the presence of interstitial hydrogen atoms and to clarify consequences for shear band formation and propagation. Nonetheless, from our macroscopic test results, we have sufficient evidence for hydrogen-driven catastrophic failure of the Vit 105 3PB SCC samples. This seems to be to a certain extent contradictive to results of studies where mechanical properties of Zr-based BMG samples were analyzed under sustained or cyclic loading conditions and cathodic hydrogen (pre-)charging (Gostin et al., 2015b). Our experimental findings elucidated that corrosion processes such as chloride-induced pitting or local dissolution as a consequence of mechanical passive film rupture are the first steps to start hydrogen-related cracking processes (HE, HISCC).

SUMMARY AND CONCLUSION

Though $Zr_{52.5}Cu_{17.9}Ni_{14.6}Al_{10}Ti_5$ (Vit 105) is one of the known Zr-based alloys with the highest glass-forming ability, the casting conditions for BMG sample production persist a critical issue finally influencing the mechanical and corrosion performances. A new approach of a copper mold casting process using binary pre-alloys as starting materials yields more homogeneous and reproducible bulk amorphous sample qualities. In consequence, upon quasi-static 3PB (notched specimen) and tensile testing in air, those BMG types exhibited generally notably higher fracture stress levels and only fracture surface features which are typical for single-phase glassy states. In contrast, BMG types, classically produced by using single constituent elements as starting materials, contained partially segregated small particles (crystallites) that caused early failure at lower stresses.

In situ analysis during 3PB of pre-notched BMG samples in air revealed a complex crack propagation mechanism mainly driven by shear banding. The extensive formation of shear band patterns in front of the crack tip resembled fan-shaped slip-line field solutions. These patterns correspond to the Prandtl-type slip-line fields that denote the maximum shear stress and shear velocity and elucidate fully plastic behavior in result of the non-hardening or even strain softening of BMGs. High normal stresses are also present orthogonal to these slip-line traces, and therefore, further crack events follow either the one or the other trace along a shear band. Thereby, the crack is deflected from its straight propagation direction. With ongoing deformation, a new slip-line field develops in front of the crack tip of the arrested crack due to partial unloading and leads again to comparatively large-scale plastic deformation and later a crack deflection. Shear band regions resulting from such a 3PB test were imaged and analyzed by HAADF-STEM and VR-FEM. These observations manifest significant structural changes induced by deformation. Such changes are not only limited to the shear bands but also affected their immediate environment by altering the MRO of the matrix and thus confirm the existence of shear-affected zones around shear bands (SBAZ).

Corrosive aqueous environments have a great detrimental effect on the mechanical performance of those Zr-based BMGs, which largely exceeds impacts of above-stated different sample qualities. The focus of this project was on the detailed analysis of SCC phenomena for Vit 105 samples in selected chloride-containing electrolytes. First, 3PB tests with un-notched bar specimen in solution under *in situ* control of the electrochemical response revealed significant effects of increasing applied elastic load levels and increasing anodic potentials toward a reduction of the total time to fracture. Further SCC tests with notched 3PB specimen conducted in 0.01 M NaCl solution demonstrated that due to corrosive attack comprising not only metal dissolution but also hydrogen formation, the applied load to attain material failure load is much smaller than that determined when similar tests were performed in air. SEM fractography revealed characteristic surface morphologies which are typical for conchoidal fractures of very brittle materials.

In summary of all experimental observations, it is concluded that pitting at surface defects is the typical initiation step followed by a mainly HISCC process, which leads to catastrophic failure. The chemical composition of Vit 105 with Zr and Cu as main constituents appears to be problematic as those facilitate the pitting process and enable the local generation of hydrogen. It is known that hydrogen atoms can be incorporated in the SRO/MRO structure of a Zr-based metallic glass by successively occupying interstitial sites of different energy levels. It is expected that *in situ* generated and absorbed hydrogen atoms in a stressed crack tip region will have significant effects on the local SRO/MRO structure and on the shear band-driven crack propagation. This should be a matter of further detailed analytical studies. However, according to our present state of knowledge, the catastrophic stress corrosion failure evidenced for Vit 105 BMG samples must be generalized to Zr–Cu-based BMG types with similar compositions. In conclusion, this supports our opinion that this BMG family is not applicable in corrosive environments.

DATA AVAILABILITY STATEMENT

All datasets generated for this study are included in the article/supplementary material.

AUTHOR CONTRIBUTIONS

DG planned and conducted the experimental work on alloy preparation and characterization, mechanical testing, *in situ* crack analysis in air, and stress corrosion cracking analysis. SP helped him with the analysis, discussion, and manuscript presentation of the mechanical testing results and the *in situ* crack analysis. MU contributed to hydrogen analysis and the discussion of hydrogen-induced stress corrosion cracking. AG was the PI of this project with two funding periods and was involved in the experimental planning and discussion of experimental results, prepared main parts of this manuscript which reviews

the highlight results of the project. All authors from Münster contributed equally to this manuscript.

FUNDING

DG and AG gratefully acknowledge the financial support by the German Research Foundation (DFG) under grant GE 1106/11 (project 224063632) as well as the Materials Physics Group of G. Wilde under grant WI 1899/27 (project 325408982). The DFG is further acknowledged for funding the TEM equipment in Münster *via* the Major Research Instrumentation Program under INST 211/719-1 FUGG. P.F. Gostin from IFW Dresden and E. Kerscher and D. Grell from the University of Kaiserslautern (grant KE 1426/4) are gratefully acknowledged for their scientific contributions to this project within the first funding period.

ACKNOWLEDGMENTS

The authors are grateful to J. Freudenberger, T.G. Woodcock, H. Wendrock, S. Oswald, and C. Damm from IFW Dresden and M. Zimmermann from TU Dresden for fruitful scientific discussions and for analytical support. Further technical assistance of T. Sturm, S. Donath, B. Gebel, L. Ewenz K. Hennig, M. Johne A. Voß, R. Buckan, H. Bußkamp, S. Kaschube, and the Research Technology Division of IFW Dresden is appreciated. P. Schrems from IPS Elektroniklabor GmbH & Co. KG is acknowledged for technical help.

REFERENCES

Almyras, G. A., Lekka, C. E., Mattern, N., and Evangelakis, G. A. (2010). On the microstructure of the Cu65Zr35 and Cu35Zr65 metallic glass. *Scripta Mater.* 62, 33–36. doi: 10.1016/j.scriptamat.2009.09.019

Bankmann, J., Pundt, A., and Kirchheim, R. (2003). Hydrogen loading behaviour of multi-component amorphous alloys: model and experiment. *J. Alloys Compd.* 356-357, 566–569. doi: 10.1016/S0925-8388(02)01278-1

Chakrabarty, J. (2006). *Theory of Plasticity*. Burlington: Elsevier Butterworth-Heinemann.

Cheng, Y. Q., Cao, A. J., Sheng, H. W., and Ma, E. (2008). Local order influences initiation of plastic flow in metallic glass: effects of alloy composition and sample cooling history. *Acta. Mater.* 56, 5263–5275. doi: 10.1016/j.actamat.2008.07.011

Cox, B. (1990). Environmentally-induced cracking of zirconium alloys - a review. *J. Nucl. Mater.* 170, 1–23. doi: 10.1016/0022-3115(90)90321-D

Deng, L., Gebert, A., Zhang, L., Chen, H. Y., Gu, D. D., Kuehn, U., et al. (2019). Mechanical performance and corrosion behaviour of Zr-based bulk metallic glass produced by selective laser melting. *Mater. Design* 189:108532. doi: 10.1016/j.matdes.2020.108532

Eliaz, N., and Eliezer, D. (1999). An overview of hydrogen interaction with amorphous alloys. *Adv. Perform. Mater.* 6, 5–31. doi: 10.1023/A:1008748627295

Farina, S., Duffo, G., and Galvele, J. (2003). Stress corrosion cracking of zirconium and Zircaloy-4 in halide aqueous solutions. *Corros. Sci.* 45, 2497–2512. doi: 10.1016/S0010-938X(03)00075-1

Flores, K. M., and Dauskardt, R. H. (1999). Enhanced toughness due to stable crack tip damage zones in bulk metallic glasses. *Scripta Mater.* 41, 937–943. doi: 10.1016/S1359-6462(99)00243-2

Gebert, A., Eckert, J., and Schultz, L. (1998). Effect of oxygen on phase formation and thermal stability of slowly cooled Zr65Cu17.5*Al*7.5Ni10 metallic glass. *Acta Mater.* 46, 5475–5482. doi: 10.1016/S1359-6454(98)00187-6

Gebert, A., Gostin, P. F., Uhlemann, M., Eckert, J., and Schultz, L. (2012). Interactions between mechanically generated defects and corrosion phenomena of Zr-based bulk metallic glasses. *Acta Mater.* 60, 2300–2309. doi: 10.1016/j.actamat.2011.12.044

Geissler, D., Freudenberger, J., Wendrock, H., Zimmermann, M., and Gebert, A. (2018). On sample size effects in fracture toughness determination of bulk metallic glasses. *Eng. Frac. Mech.* 202, 500–507. doi: 10.1016/j.engfracmech.2018.09.020

Geissler, D., Uhlemann, M., and Gebert, A. (2019). Catastrophic stress corrosion failure of Zr-base bulk metallic glass through hydrogen embrittlement. *Corros. Sci.* 159:108057. doi: 10.1016/j.corsci.2019.06.012

Gilbert, C. J., Ritchie, R. O., and Johnson, W. L. (1997). Fracture toughness and fatigue-crack propagation in a Zr-Ti-Ni-Cu-Be bulk metallic glass. *Appl. Phys. Lett.* 71, 476–478. doi: 10.1063/1.119610

Gostin, P. F., Eigel, D., Grell, D., Eckert, J., Kerscher, E., and Gebert, A. (2015a). Comparing the pitting corrosion behavior of prominent Zr-based bulk metallic glasses. *J. Mater. Res.* 30, 233–241. doi: 10.1557/jmr.2014.371

Gostin, P. F., Eigel, D., Grell, D., Uhlemann, M., Kerscher, E., Eckert, J., et al. (2015b). Stress corrosion cracking of a Zr-based bulk metallic glass. *Mater. Sci. Engg. A* 639, 681–690. doi: 10.1016/j.msea.2015.05.049

Gostin, P. F., Eigel, D., Grell, D., Uhlemann, M., Kerscher, E., Eckert, J., et al. (2015c). Stress-corrosion interactions in Zr-based bulk metallic glasses. *Metals* 5, 1262–1278. doi: 10.3390/met5031262

Green, A. P., and Hundy, B. B. (1956). Initial plastic yielding in notch bend test. *J. Mech. Phys. Solids.* 4, 128–144. doi: 10.1016/0022-5096(56)90085-0

Grell, D., Gostin, P. F., Eckert, J., Gebert, A., and Kerscher, E. (2015). In situ electrochemical analysis during deformation of a Zr-based bulk metallic glass: a sensitive tool revealing early shear banding. *Adv. Eng. Mater.* 17, 1532–1535. doi: 10.1002/adem.201500273

Grell, D., Wilkin, Y., Gostin, P. F., Gebert, A., and Kerscher, E. (2017). Corrosion fatigue studies on bulk glassy Zr-based alloy under three-point bending. *Front. Mater.* 3:60. doi: 10.3389/fmats.2016.00060

Hieronymus-Schmidt, V., Rösner, H., Wilde, G., and Zaccone, A. (2017). Shear banding in metallic glasses described by alignments of Eshelby quadrupoles. *Phys. Rev. B* 95:134111. doi: 10.1103/PhysRevB.95.134111

Hilke, S., Roesner, H., Geissler, D., Gebert, A., Peterlechner, M., and Wilde, G. (2019). The influence of deformation on the medium-range order of a Zr-based bulk metallic glass characterized by variable resolution fluctuation electron microscopy. *Acta Mater.* 171, 275–281. doi: 10.1016/j.actamat.2019.04.023

Hull, D. (1999). *Fractography: Observing, Measuring and Interpreting Fracture Surface Topography*. Cambridge, MA: University Press.

Ismail, N., Uhlemann, M., Gebert, A., Eckert, J., and Schultz, L. (2002). The electrochemical hydrogen sorption behaviour of Zr-Cu-Al-Ni metallic glasses. *Mater. Trans.* 43, 1133–1137. doi: 10.2320/matertrans.43.1133

Kawashima, A., Yokoyama, Y., and Inoue, A. (2010). Zr-based bulk glassy alloy with improved resistance to stress corrosion cracking in sodium chloride solutions. *Corros. Sci.* 52, 2950–2957. doi: 10.1016/j.corsci.2010.05.007

Kruzic, J. J. (2011). Understanding the problem of fatigue in bulk metallic glasses. *Metall. Mater. Trans. A* 42, 1516–1523. doi: 10.1007/s11661-010-0413-1

Lekka, C. E., Bokas, G. B., Almyras, G. A., Papgeorgiou, D. G., and Evangelakis, G. A. (2012). Clustering, microalloying and mechanical properties in Cu/Zr-based glassy models by molecular dynamics simulation and ab-initio computation. *J. Alloys Compd.* 536, 65–69. doi: 10.1016/j.jallcom.2011.11.038

Lewandowski, J. J., Wang, W. H., and Greer, A. L. (2005). Intrinsic plasticity or brittleness of metallic glasses. *Phil. Mag. Lett.* 85, 77–87. doi: 10.1080/09500830500080474

Maaß, R., Samwer, K., Arnold, W., and Volkert, C. (2014). A single shear band in a metallic glass: local core and wide soft zone. *Appl. Phys. Lett.* 105:171902. doi: 10.1063/1.4900791

Madge, S. V. (2015). Toughness of bulk metallic glasses. *Metals* 5, 1279–1305. doi: 10.3390/met5031279

Majumdar, P., and Scully, J. (1979). Reversible embrittlement in zircaloy-2. *Corros. Sci.* 19, 141–145. doi: 10.1016/0010-938X(79)90047-7

McClintock, F. A. (1971). "Plasticity aspects of fracture," in *Fracture - An Advanced Treatise*, ed. H. Liebowitz (New York: Academic Press), 48–225.

Morrison, M. L., Buchanan, R. A., Liaw, P. K., Green, B. A., Wang, G. Y., Liu, C. T., et al. (2007). Corrosion-fatigue studies of the Zr-based Vitreloy 105 bulk metallic glass. *Mater. Sci. Eng. A* 467, 198–206. doi: 10.1016/j.msea.2007.03.106

Nakai, Y., and Yoshioka, Y. (2010). Stress corrosion and corrosion fatigue crack growth of Zr- based bulk metallic glass in aqueous solutions. *Metall. Mater. Trans. A* 41, 1792–1798. doi: 10.1007/s11661-009-9945-7

Pan, J., Chen, Q., Liu, L., and Li, Y. (2001). Softening and dilatation in a single shear band. *Acta Mater.* 59, 5146–5158. doi: 10.1016/j.actamat.2011.04.047

Pourbaix, M. (1966). *Atlas of Electrochemical Equilibria in Aqueous Solutions*. Oxford: Pergamon Press.

Rebak, R. B. (2000). *Corrosion and Environmental Degradation, volume 2*. Weinheim: Wiley-VCH.

Ritchie, R. O., Schroeder, V., and Gilbert, C. (2000). Fracture, fatigue and environmentally-assisted failure of a Zr-based bulk amorphous metal. *Intermetallics* 8, 469–475. doi: 10.1016/S0966-9795(99)00155-7

Rösner, H., Peterlechner, M., Kübel, C., Schmidt, V., and Wilde, G. (2014). Density changes in shear bands of a metallic glass determined by correlative analytical transmission electron microscopy. *Ultramicroscopy* 142, 1–9. doi: 10.1016/j.ultramic.2014.03.006

Schmidt, V., Rösner, H., Peterlechner, M., Wilde, G., and Voyles, P. M. (2015). Quantitative measurement of density in a shear band of metallic glass monitored along its propagation direction. *Phys. Rev. Lett.* 115:035501. doi: 10.1103/PhysRevLett.115.035501

Schroeder, V., and Ritchie, R. O. (2006). Stress-corrosion fatigue-crack growth in a Zr-based bulk amorphous metal. *Acta Mater.* 54, 1785–1794. doi: 10.1016/j.actamat.2005.12.006

Schuh, C. A., Hufnagel, T. C., and Ramamurty, U. (2007). Mechanical behaviour of amorphous alloys. *Acta Mater.* 55, 4067–4109. doi: 10.1016/j.actamat.2007.01.052

Scully, J. R., Gebert, A., and Payer, J. H. (2007). Corrosion and related mechanical properties of bulk metallic glasses. *J. Mater. Res.* 22, 302–313. doi: 10.1557/jmr.2007.0051

Shen, L., Luo, P., Hu, Y., Bai, H., Sun, Y., Sun, B., et al. (2018). Shear-band affected zone revealed by magnetic domains in a ferromagnetic metallic glass. *Nat. Commun.* 9:4414. doi: 10.1038/s41467-018-06919-2

Suryanarayana, C., and Inoue, A. (2011). *Bulk Metallic Glasses*. New York, NY: CRC Press.

Trexler, M. M., and Thadhani, N. N. (2010). Mechanical properties of bulk metallic glasses. *Prog. Mater. Sci.* 55, 759–839. doi: 10.1016/j.pmatsci.2010.04.002

Wondraczek, L., Mauro, J. C., Eckert, J., Kühn, U., Horbach, J., Deubener, J., et al. (2011). Towards ultrastrong glasses. *Adv. Mater.* 23, 4578–4586. doi: 10.1002/adma.201102795

Yokoyama, Y. (2015). Development of an automatic fabrication system for cast glassy alloys. *Metall. Mater. Trans. B* 46, 893–905.

Zhang, Y., Mattern, N., and Eckert, J. (2011). Effect of uniaxial loading on the structural anisotropy and the dynamics of atoms of Cu50Zr50 metallic glasses within the elastic regime studied by molecular dynamic simulation. *Acta Mater.* 59, 4303–4313. doi: 10.1016/j.actamat.2011.03.054

Zhu, X.-K., and Joyce, J. A. (2012). Review of fracture toughness (G, K, J, CTOD, CTOA) testing and standardization. *Eng. Fract. Mech.* 85, 1–46. doi: 10.1016/j.engfracmech.2012.02.001

Conflict of Interest: The authors declare that the research was conducted in the absence of any commercial or financial relationships that could be construed as a potential conflict of interest.

frontiers in Materials

ORIGINAL RESEARCH
published: 09 June 2020
doi: 10.3389/fmats.2020.00173

Indentation-Induced Structural Changes in Vitreous Silica Probed by *in-situ* Small-Angle X-Ray Scattering

Sindy Fuhrmann [1,2], Guilherme N. B. M. de Macedo [1], René Limbach [1], Christina Krywka [3,4], Sebastian Bruns [5], Karsten Durst [5] and Lothar Wondraczek [1]*

[1] Otto Schott Institute of Materials Research, Friedrich Schiller University Jena, Jena, Germany, [2] Institute of Ceramic, Glass and Construction Materials, TU Bergakademie Freiberg, Freiberg, Germany, [3] Institute of Materials Research, Helmholtz-Zentrum Geesthacht, Outstation at DESY, Geesthach, Germany, [4] Institute of Experimental and Applied Physics, Christian Albrechts University, Kiel, Germany, [5] Physical Metallurgy, TU Darmstadt, Darmstadt, Germany

The transient (or permanent) structural modifications which occur during local deformation of oxide glasses are typically studied on the basis of short-range data, for example, obtained through vibrational spectroscopy. This is in contrast to macroscopic observations, where variations in material density can usually not be explained using next-neighbor correlations alone. Recent experiments employing low-frequency Raman spectroscopy have pointed-out this issue, emphasizing that the deformation behavior of glasses is mediated through structural heterogeneity and drawing an analogy to granular media. Here, we provide additional support to this understanding, using an alternative experimental method. Structural modification of vitreous silica in the stress field of a sharp diamond indenter tip was monitored by *in-situ* small-angle X-ray scattering. The influenced zone during loading and after unloading was compared, demonstrating that changes in the position of the first sharp diffraction peak (FSDP) directly in the center of the indent are of permanent character. On the other hand, variations in the amplitude of electron density fluctuations (AEDF) appear to fully recover after load release. The lateral extent of the modifications and their relaxation are related to the short- to intermediate-range structure and elastic heterogeneity pertinent to the glass network. With support from Finite Element Analysis, we suggest that different structural length scales govern shear deformation and isotropic compaction in vitreous silica.

Keywords: *in-situ* indentation, SAXS, vitreous silica, glass, heterogeneity, density fluctuation, densification

OPEN ACCESS

Edited by:
Randall Youngman, Corning Inc., United States

Reviewed by:
Liping Huang, Rensselaer Polytechnic Institute, United States
Ling Cai, Corning Inc., United States

****Correspondence:***
Sindy Fuhrmann
sindy.fuhrmann@ikgb.tu-freiberg.de

Specialty section:
This article was submitted to Ceramics and Glass, a section of the journal Frontiers in Materials

Received: *12 February 2020*
Accepted: *11 May 2020*
Published: *09 June 2020*

Citation:
Fuhrmann S, de Macedo GNBM, Limbach R, Krywka C, Bruns S, Durst K and Wondraczek L (2020) Indentation-Induced Structural Changes in Vitreous Silica Probed by in-situ Small-Angle X-Ray Scattering. Front. Mater. 7:173. doi: 10.3389/fmats.2020.00173

INTRODUCTION

Investigations of liquids and glasses by Small-Angle X-ray Scattering (SAXS) usually address the characterization of physical heterogeneity, e.g., dispersed nanoparticles or pores. Besides, SAXS provides quantitative data on local density fluctuations. While early research in this field focused on polymers, the technique was successfully adapted for the characterization of inorganic glasses (Pierre et al., 1972; Rathje and Ruland, 1976; Fischer and Dettenmaier, 1978; Wiegand and Ruland, 1979; Golubkov et al., 1980; Roe and Curro, 1983; Tanabe et al., 1984): spatial density fluctuations are a universal feature of glassy materials. For example, fluctuations in chemical composition may be caused by the presence of different chemical compounds with non-random (selective) bonding such as introduced by Greaves as an essential feature of the Modified Random Network

Model for glass structure (Greaves et al., 1981; Greaves, 1985). Physical fluctuations such as in network topology manifests in variations within the atomic arrangement, e.g., local network rigidity or packing density. The latter may depend on the thermal history of the glass, for example, quenching rates (Levelut et al., 2002, 2005, 2007; Brüning and Cottrell, 2003; Watanabe et al., 2003; Brüning et al., 2005, 2007) or pressure (Reibstein et al., 2011; Cornet et al., 2019). These frozen-in fluctuations typically occur at nanometer scale. Their assessment provides useful insight at the intermediate- to long-range structural characteristics of glasses (Greaves et al., 2008). As such density fluctuations are not strictly defined in shape or size (Golubkov, 1996; Bakai and Fischer, 2004; Ozhovan, 2006; Huang et al., 2018), they do not cause distinct, sharp scattering signals. Instead, their presence manifests in the overall scattering intensity at low scattering angles q, i.e., the extrapolated SAXS intensity to zero scattering angle $I(0)$.

In particular for metallic glasses, significant efforts have been undertaken in order to relate the occurrence of structural heterogeneity to mechanical behavior. This draws on the understanding of plastic flow in these materials, where localized shear transformation zones (STZs) are a primary factor in overall material deformation [e.g., (Yang et al., 2010; Huo et al., 2013; Li et al., 2015; Limbach et al., 2017; Zhu et al., 2018; Hilke et al., 2019)]. For inorganic glasses, the understanding of structural heterogeneity in the context of mechanical behavior remains less developed and mostly phenomenological, e.g., for material response to (nano)indentation (Benzine et al., 2018a; Poletto Rodrigues et al., 2019) or scratching (de Macedo et al., 2018; Sawamura and Wondraczek, 2018; Sawamura et al., 2019). In such experiments, the structural consequence of deformation is typically studied by well-established *ex-situ* (post-deformation) vibrational spectroscopy (Perriot et al., 2006; Koike and Tomozawa, 2007; Deschamps et al., 2011; Kassir-Bodon et al., 2012; Kato et al., 2012; Tran et al., 2012; Yoshida et al., 2012; Winterstein-Beckmann et al., 2014a,b; Januchta et al., 2017; Kilymis et al., 2017) and related to numerical stress field analysis (Kermouche et al., 2008; Gadelrab et al., 2012; Bruns et al., 2017, 2020a,b; Molnár et al., 2017). However, such an approach has various shortcomings. It provides only indirect information on the deformation process; transient (non-permanent) effects must be studied *in-situ* (Yoshida et al., 2019; Gerbig and Michaels, 2020). Longer-range structural information requires vibrational spectroscopy in the THz regime, which is still a challenge to do *in-situ* (Benzine et al., 2018b).

Here, we report on using Small-Angle X-ray Scattering with a customized nanoindentation set-up to evaluate the short- as well as intermediate- to long-range structural response of vitreous silica during loading with a sharp, wedge-shaped diamond indenter. For mapping experiments, we employ the P03 beamline at the German Synchrotron Facility DESY at PETRA III (Krywka et al., 2013; Gamcová et al., 2016; Zeilinger et al., 2016), offering low spot size and low beam opening angle for 2-dimensional mapping at a lateral resolution of about 1 μm.

MATERIALS AND METHODS

Commercial-grade vitreous silica (Herasil, Heraeus Quarzglas GmbH & Co. KG) was used for this study. The glass specimen was initially cut into a rectangular slice of 13 mm length and 3 mm height. All sides were polished to optical grade, with plane-parallel opposing faces. Afterwards, the specimen thickness was gradually reduced down to 467 μm to account for the transmission requirements of the scattering experiment. The glass specimen was glued on one side to the sample holder using a thermoplastic polymer (Crystal bond, Aremco Products Inc.), with the upper 1 mm being free-standing to avoid shadowing effects in the SAXS experiments (schematic drawing in **Supplementary Figure 1**).

Small-Angle X-ray Scattering (SAXS) experiments were carried out at the Nanofocus Endstation of the P03 beamline at PETRA III synchrotron, DESY, Hamburg, Germany (Krywka et al., 2012), using monochromatic X-rays with an energy of 15 keV. The beam was focused by a set of elliptical mirrors to achieve a beam size of 800 nm and an opening angle of 0.002 rad. A 2D detector (Dectris Pilatus 1M) with a detector field of 168.7 × 179.4 mm² was positioned at a distance of 750 mm behind the sample. The scattering vector q was calibrated using silver behenate. The direct beam was detected by means of a semi-transparent beamstop, which was made of multiple layers of a thin silver foil up to a total nominal thickness of 330 μm.

The indentation set-up at P03 is realized with a multi-stage motor stack, which enables precise alignment of the indenter tip and the sample with six geometric degrees of freedom (x, y, z, χ, ϕ, ϑ) and the movement of the whole relative to the X-ray beam for spatially resolved SAXS data acquisition (schematic drawing in **Supplementary Figure 1**). The scattering contribution is accumulated through the specimen thickness. Thus, a sharp wedge-shaped diamond indenter tip (Synton-MDP Inc.) with a length of 490 μm and an opening angle of 60° was used. A careful alignment procedure of beam and tip as well as sample to beam was carried out. This is to provide a homogeneous strain distribution along the beam path through the sample and to prevent the averaging-out of structural changes. However, the surface topography of the sample itself introduced averaging effects, which results in not quantitative comparable loading conditions (see below). Within the indentation set-up a frame decouples the sample positioning motors from the indenter tip. A stepwise increase of the load is achieved by moving the glass specimen upwards against the indenter tip. The applied load P was monitored by means of a capacitive force sensor (Kistler Instrumente GmbH) with a sensitivity of 10.55 pC/N, attached to the indenter tip. The maximum load must be limited to ∼3 N due to the low load-tolerance of the hexapods and the piezoelectric positioners used. Two independent loadings were carried out. For indent 1 an initial maximum load of circa 2.4 N and for indent 2 an initial maximum load of circa 2.7 N were applied. The contact situation was checked by *post-mortem* analysis with wide-field confocal optical microscopy (Smartproof 5, Zeiss with a nominal lateral resolution of (0.13 ± 0.1) μm and a nominal accuracy in depth with ± 0.1 μm for the C Epiplan-APOCHROMAT

50 x /0.95 objective). **Figure 1** images the resulting imprints. Please note the curvature of the sample with a flattening and rounding of the face edges due to the manual preparation of the glass slides (U-shape in cross section). This results in gradually decreasing imprint depths, from ∼300 nm in the center of the sample to ∼60 nm toward the edges. The mean depth for indent 1 is ∼175 nm and for indent 2 ∼150 nm. This, in turn, implies different contact situations for the two indents, such that indent 2 exhibits an average lower indentation depth during loading, despite the higher maximum load recorded by the capacitive force sensor, which must be considered when comparing the SAXS data of indent 1 and 2. SAXS data were collected in transmission mode for the pristine sample, after loading, as well as after unloading. In each indentation experiment, a 2D SAXS map with step widths of 2 μm in horizontal *x*- and 1 μm in vertical *y*-direction relative to the indenter tip, covering a total area of ∼12 × 22 μm^2, was acquired (refer to schematic drawing in **Supplementary Figure 1**). The scattered photons were accumulated for 60 s at each spot. During the accumulation of the SAXS data (∼4.5 h for each imprint) a load decrease to ∼2.2 N (indent 1) and ∼2.4 N (indent 2), respectively, were observed. This decrease can primarily be attributed to relaxation processes occurring during the time of the SAXS measurement. Recent studies have shown that indentation relaxation in the order of ∼10 % is likely to happen for such a period of time (Baral et al., 2019).

Data processing was carried-out using the software FIT2D (Hammersley et al., 1996). Each detector image was carefully checked before evaluation. No anisotropy effect due to an inhomogeneous deformation from an inclined diamond wedge or damage of the sample could be detected. In a first step, each detector image was masked to eliminate areas such as the beamstop, dead pixels, detector segments, or scattering and reflection contributions from the diamond indenter tip or sample surface. The data were then integrated azimuthally to generate curves of scattering intensity I as a function of scattering angle or scattering vector q. To extract information on the direct transmission, the beamstop area was selected and the intensity values of each pixel were summed-up. The scattering curves were normalized for the incident intensity decay of the PETRA III X-ray beam and their respective transmission value and thickness. Due to the beamstop located close to the detector, a large contribution from air scattering superimposes the low-angle scattering of the glass. In order to extract the scattering originating from the sample, multiple empty measurements (no sample installed, same set-up and measurement conditions) were collected and used to normalize the transmission scaled scattering intensities.

The stress field beneath the indenter tip was simulated via Finite Element Analysis using the software package (Abaqus 2016 Online Documentation, 2015). The indentation process was modeled according to previous reports (Bruns et al., 2017, 2020a,b) using a friction coefficient of 0.15 as suggested in literature (Johnson, 1970). The wedge-shaped indenter tip was approximated with a 2D representation, using the experimental tip area function as reference. All material parameters were assumed to represent isotropic and rate-insensitive room temperature values. A Young's modulus of 70 GPa and a Poisson's ratio of 0.18 were used for vitreous silica (Limbach et al., 2014). The plastic material response was modeled using the cap section of Drucker-Prager-Cap plasticity to replicate the elliptical yield surface of vitreous silica (Kermouche et al., 2008). In this context a yield strength under pure shear of 7.5 GPa and a hydrostatic yield strength of 8 GPa were assumed. Sigmoidal densification hardening was implemented based on experimental diamond anvil cell data from literature (Rouxel et al., 2008; Deschamps et al., 2012; Sonneville et al., 2012). Details on this procedure are reported elsewhere (Bruns et al., 2017, 2020b).

RESULTS

Spatially Resolved *in-situ* Small-Angle X-Ray Scattering

The comparably short sample to detector distance in the SAXS set-up allowed to observe the First Sharp Diffraction Peak (FSDP, also refer to **Supplementary Figure 3**). Its position relative to the sample surface and the indenter tip is shown in **Figure 2** for the two loadings (**Figures 2A,C**), together with the respective maps after unloading (**Figures 2B,D**). The indentation center (indenter tip) is located at $(x,y) = (0,0)$. As we expect a symmetric indentation profile, in order to reduce the required scanning time, only one half the deformation field was captured. The FSDP maximum is located around $q_{FSDP} = 15.2$ nm^{-1}, in good accordance with literature (Warren et al., 1936; Elliott, 1991; Brüning and Cottrell, 2003). A rather small deviation of ± 0.1 nm^{-1} was found within the bulk glass sample. Below the indenter tip, the FSDP is shifted toward higher scattering angles by about 0.6 nm^{-1}. As only half of the indent was mapped, a possible misalignment of the scan field cannot fully be excluded. Nevertheless, from the results presented in **Figure 2A** we can conclude that the position of the FSDP for indent 1 is affected within an area extending to at least 4 μm in lateral dimension from the loading axis and ∼7 μm in depth.

The FSDP analysis shown in **Figure 2** indicates mostly elastic (reversible) effects. The complementary *post-mortem* inspection of the indented area by confocal optical microscopy revealed the creation of permanent imprints of about 1.5 ± 0.3 μm in width (see **Figure 1**). Thus, not only elastic deformation, but also inelastic deformation in terms of either shear flow and/or permanent densification occurred during the experiment, which agrees with the expected indentation response of vitreous silica. The spatial resolution of the SAXS mappings is too low to resolve the residual imprint. Additionally, the obtained SAXS data results from a longitudinal view parallel to the wedge axis; hence, it integrates over any variations in indentation depth (which are different for both indents). The quantitative comparison of both indents shows obvious differences. Despite the nominal higher maximum load recorded for indent 2, a smaller FSDP shift as well as a more blurred shape of the stressed region can be noted in comparison to indent 1.

The further analysis of the SAXS data is based on the diffuse scattering level at low scattering angles, which represents the amplitude of electron density fluctuations (AEDF) in liquids and glasses (Porod, 1982). Since the investigated glass is pure

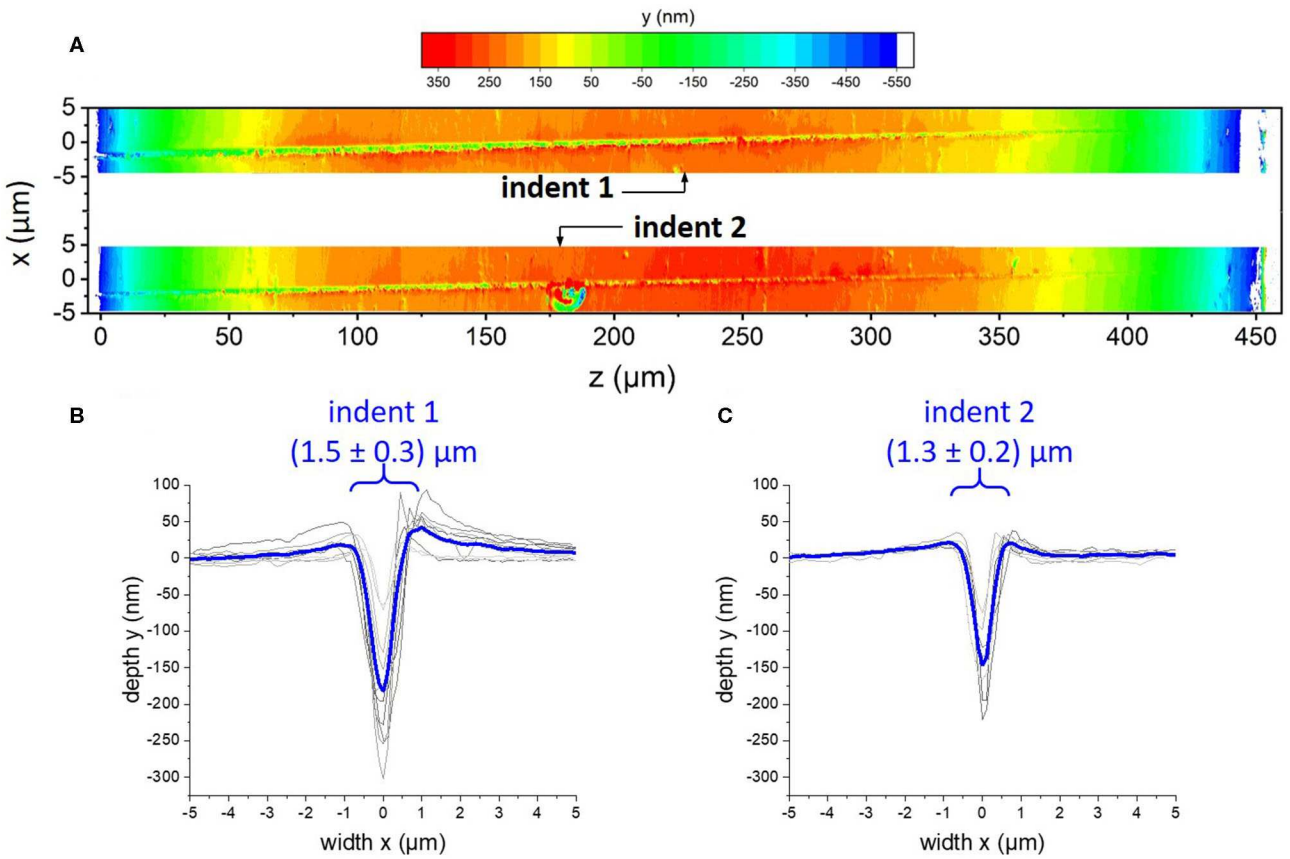

FIGURE 1 | (A) Wide-field confocal microscopic images showing the topography of the residual wedge imprints on vitreous silica after unloading. The coordinate system is adapted from the beamline experimental set-up, displaying the height variances in *y*-direction with the color code shown in the top. **(B,C)** show cross-profiles in *x*-direction at different positions *z* along the imprint (gray curves) and their average (blue curve) for indent 1 in **(B)** and indent 2 in **(C)**.

SiO_2, changes of the AEDF upon deformation are only related to physical heterogeneity (no chemical fluctuations) (Levelut et al., 2002, 2005, 2007; Reibstein et al., 2011). In the present experiment, the AEDF reflects stress-induced modifications of the topological heterogeneity of the silica network *in-situ*. The scattering intensity at zero angle, $I_0 = I(q = 0)$, is employed as a measure of the low-angle scattering level. To extrapolate to I_0, the scattering data obtained from the interval of $\sim 1.7 < q < 2.7$ nm^{-1} were linearized by plotting $\ln[I(q)]$ over q^2; I_0 was deduced from the intersection of a fitted straight line with the *y*-axis (Tanabe et al., 1984). This procedure is illustrated in **Supplementary Figure 3**. The absolute value of I_0 can vary depending on the chosen fitting range due to interference from the low-angle tail of the FSDP (Levelut et al., 2002). Data interpretation is therefore made under the assumption that the influence of the low angle scattering tail of the FSDP is equal for all data points in the chosen fitting range. The extrapolated values were normalized to the I_0^{bulk} of the pristine, bulk glass specimen. Data obtained in this way are presented in **Figure 3** as functions of the distance from the specimen surface in *y*-direction for various distances *x* relative to the loading axis. A two-dimensional representation is provided exemplarily for indent 2 in the **Supplementary Figures S2C,D**.

When comparing the variation of the AEDF under load (**Figures 3A,C**) and after unloading (**Figures 3B,D**), it is obvious that the presence of a local stress field strongly influences the level of scattering at low angles, whereas the data after unloading indicate much less variation (circa ± 1%). The data recorded under load indicate for both indents a decrease in I_0 during indentation. Although the applied loads are relatively close, some differences are seen in their comparison, probably indicating the accuracy and reproducibility of the present method. This observation was already expected from the different topography of the imprints (see **Figure 1**). At indent 1 (**Figure 3A**), the normalized scattering intensity is consistently reduced by about 3–4% at distances up to 8 µm relative to the loading axis and for the full measurement depths down to $y = 21$ µm. In the vicinity of the indenter tip ($x = 0$ µm) the reduction in the normalized scattering intensity increases gradually down to a depth of ~10 µm. In a distance of $x = -10$ µm from the indent center, no variations are found

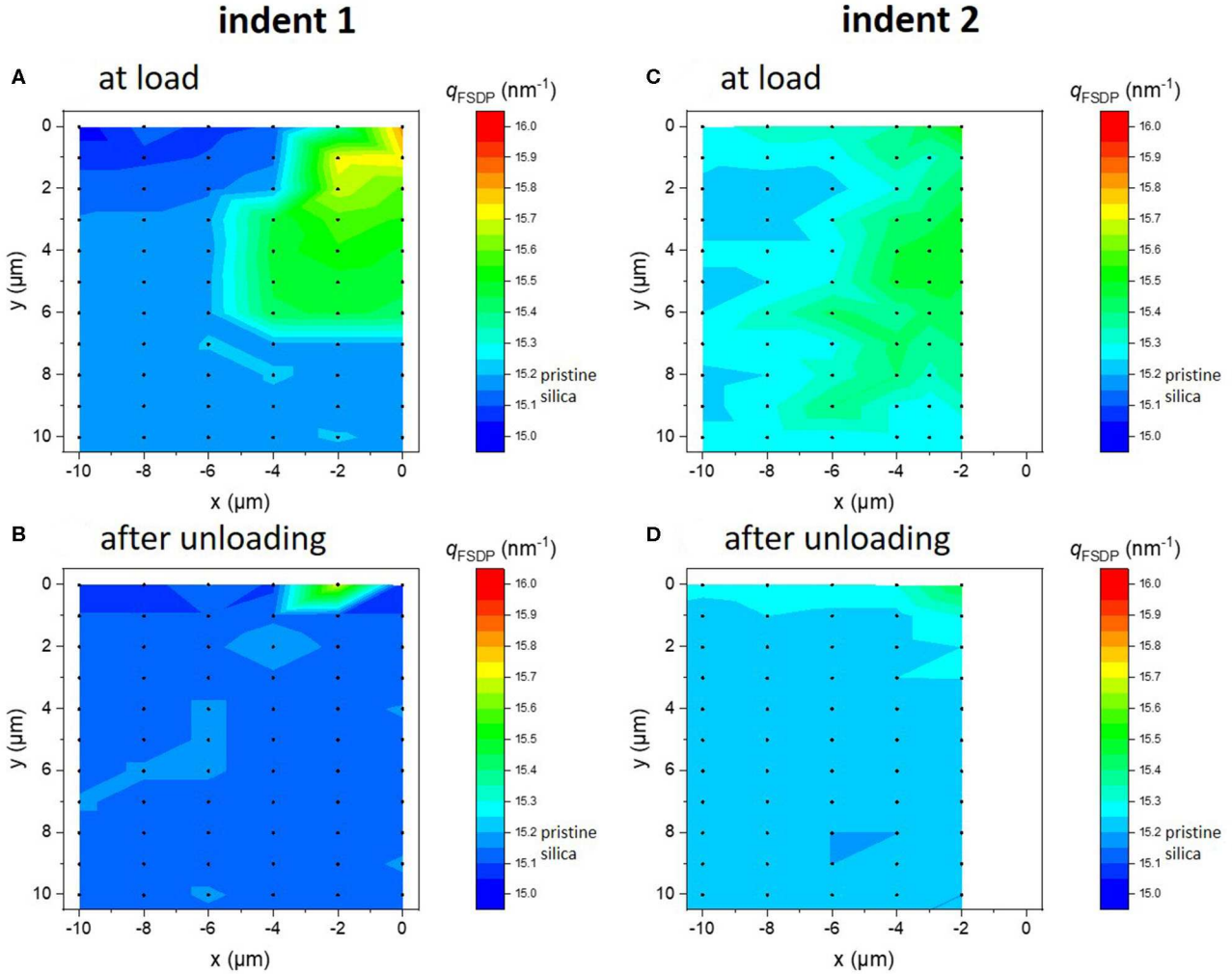

FIGURE 2 | Spatial variation of the maximum position of the First Sharp Diffraction Peak (FSDP), q_{FSDP}, of vitreous silica monitored as function of depth relative to the sample surface, *y*, and for different distances relative to the diamond tip, *x*. Black points indicate points of data acquisition. The color map was obtained from linear interpolations between data points. Data were recorded during loading **(A,C)** with a wedge-shaped diamond tip, as well as directly after unloading **(B,D)**.

in the AEDF. An overall smaller reduction of the normalized scattering intensity by ∼2 % (**Figure 3C**) is observed for indent 2 with the nominal higher peak load. However, this corresponds well to the overall smaller deformation (see **Figure 1C**). The aforementioned reduced normalized scattering intensity at the indent center is not reproduced. The scattering intensity rather seems to increase with increasing depth and would presumably reach the bulk value at a depth of about 27 µm. The depth profiles recorded at larger distances from the indenter tip all scatter within a narrow interval of ± 1% and thus are not significantly influenced by the presence of the local stress field. It is nevertheless worth noting, that the data recorded down to depths of ∼3–4 µm display strong scattering and exhibit large positive values.

Characterization of the Magnitude and Directionality of the Stress Field by FEA

Finite Element Analysis (FEA) was carried out in order to quantify the stress field below the indentation, using the geometry of the wedge-shaped diamond indenter tip as an input parameter in the 2D analysis. The simulations were performed under displacement control, until a similar residual indentation depth as found in the experiments was achieved. **Figure 4** depicts the von Mises equivalent stress (defined as J2, second invariant of stress deviator), the hydrostatic stress component p (defined as $\rho = -\sigma_{ii}/3$) as well as the densification (given as the volumetric inelastic strain) at maximum indentation depth under load. The von Mises equivalent stress $\sigma_{\text{equ.Mises}}$ in **Figure 4A** reveals a symmetric, ellipsoidal-shaped distribution with a radius of about

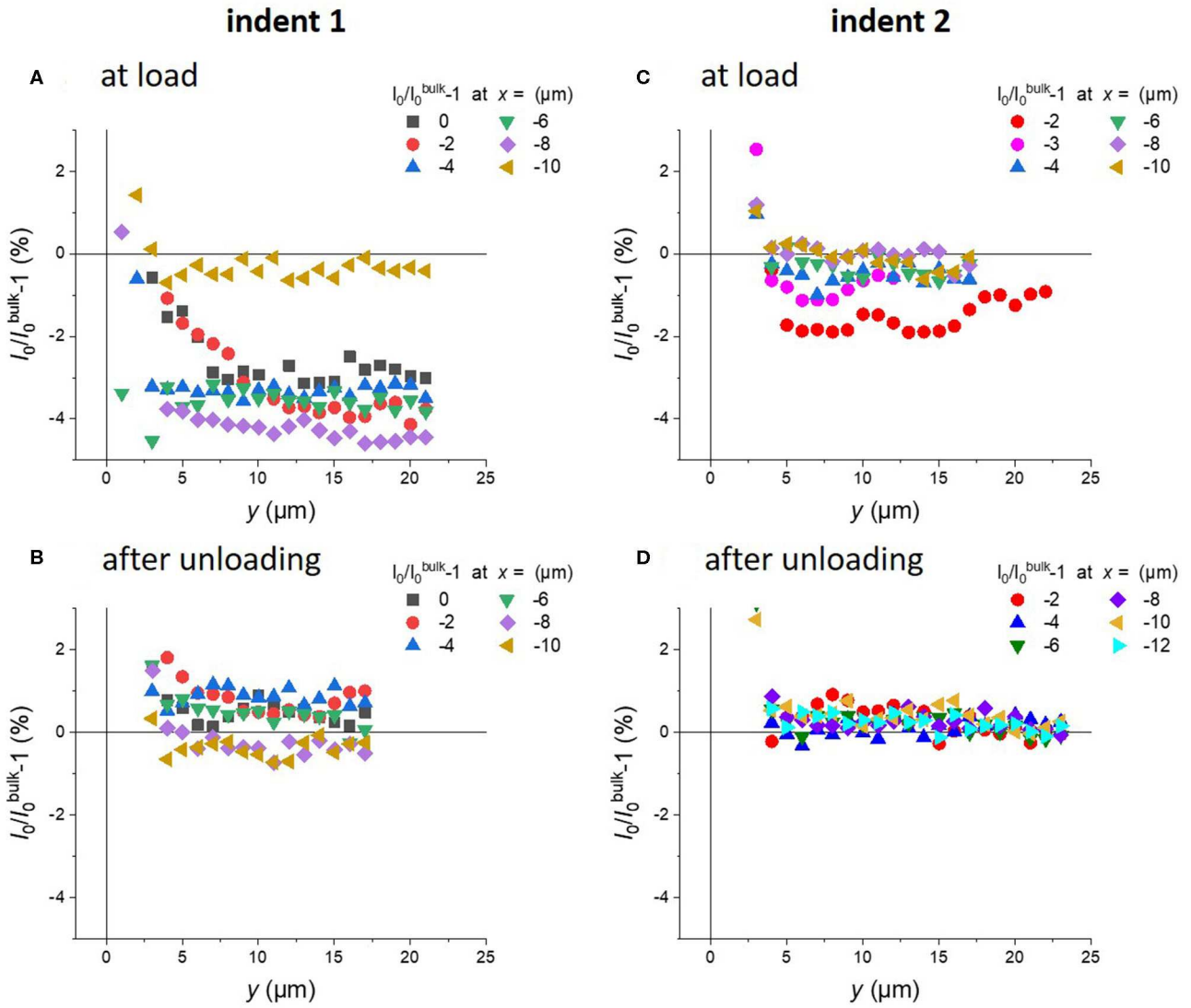

FIGURE 3 | Variation of the scattering intensity I_0 for vitreous silica during loading **(A,C)** and after unloading **(B,D)**. For comparability, the values of I_0 were normalized to the level of the pristine bulk glass, I_0^{bulk}. Experimental data are shown as functions of the distance from the specimen surface in *y*-direction for various distances *x* relative to the loading axis (see **Figure 2** for details).

12 μm. Highest stresses occur directly at the indenter tip with a maximum of $\sigma_{equ.Mises} = 7.5$ GPa, according to the employed yield criterion. The hydrostatic stress field below the indenter is much smaller in dimension, but exhibits a similar shape as the von Mises stress field. It extends laterally up to $x \sim -5\,\mu m$, whereas in depth a non-zero pressure stress is still calculated for $y = 8\,\mu m$. The shear stress together with the hydrostatic pressure component induces a gradual densification in the plastic zone with a maximum of ~16 % at the indent center (**Figure 4C**, inset).

After unloading, a permanent imprint with a width of ~2 μm and a depth of ~0.7 μm is formed on the glass surface (**Figure 4C**). The permanent densification, however, only occurs within a small region which corresponds roughly to the direct contact zone. It spreads until $x \sim -1.5\,\mu m$ in width and $y \sim 2\,\mu m$ in depth. The densification (**Figure 4C**) was calculated based on the density of pristine vitreous silica, i.e., $\rho(\text{v-SiO}_2) = 2.21\ \text{gcm}^{-3}$, and the density distribution as derived from FEA.

DISCUSSION

Short- to Intermediate-Range Structural Response of Vitreous Silica to Indentation

The FSDP in glasses originates from local variations in structural order. In vitreous silica the FSDP reflects the distribution of the SiO_4 inter-tetrahedral distances and Si-O-Si bond angles (Elliott, 1991; Brüning and Cottrell, 2003). The correlated real

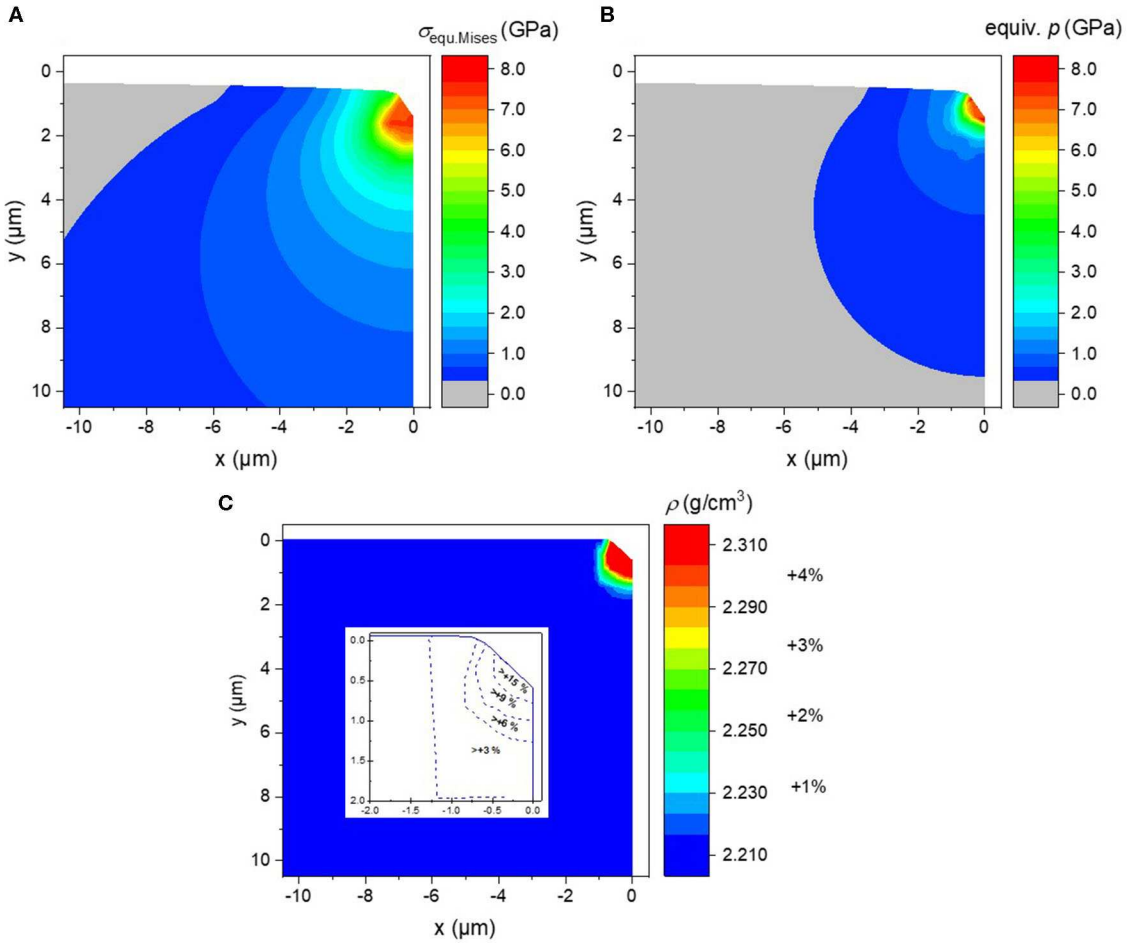

FIGURE 4 | FEA results of a wedge indentation experiment on vitreous silica in 2D representation. Indentation was performed to a similar penetration depth as in the SAXS-experiments. The contour plots show **(A)** the lateral distribution of the equivalent van Mises stress $\sigma_{equMises}$, **(B)** the corresponding hydrostatic stress p and **(C)** the resulting density distribution ρ within the glass sample after unloading. The inset in **(C)** displays the densification in the vicinity of the indenter tip calculated using FEA data and the density of pristine vitreous silica, *i.e.*, $\rho(\text{v-SiO}_2) = 2.21$ gcm^{-3}. In all plots, the y-direction depicts the depth relative to the sample surface and the x-direction represents the lateral distance relative to the loading axis [indent center is located at $(x,y) = (0,0)$].

space length, $d = 2\pi/q$, for the intensity maximum of the pristine bulk glass calculates to ∼4.1 Å. The observed positive shift of the FSDP maximum (**Figures 2A,C**) indicates a decrease of the real space length during loading, and thus, a decrease in the inter-tetrahedral distances and bond angles. This observation is in agreement with similar reports on densified glasses (Elliott, 1991). When the structure compacts, distances and bond angles decrease. According to Tan and Arndt (Tan and Arndt, 1999), the maximum position of the FSDP in vitreous silica follows a linear trend with the glass density via the following empirical relation:

$$\rho = 1.621 + 41.9(1/d^3) \quad (1)$$

Using the above expression and the results from the FSDP (**Figures 2A,C**), a density map for indent 1 *in-situ* under applied load (**Figure 5A**) and after unloading (**Figure 5B**) is constructed. The densification during loading reaches its maximum of about 3 % in the vicinity of the indenter tip and the affected area extends up to roughly x ∼ 6 µm. This compares well with the FEA results (**Figure 4B**). When releasing the stress, the major part of the FSDP variation is recovered, leaving only a slight trace of residual modification (**Figure 5B**). At first glance, this observation appears to be contradictory to the FEA, which predicts a maximum densification of about 15% directly below the indenter tip (**Figure 4C**). However, the spatial resolution of the X-ray scattering experiment does presently not allow for further interpretation. The SAXS investigation is not only affected by the curvature of the surface (**Figure 1A**), but also strongly influenced by a signal averaging effect over a structural gradient at the imprint center (Bruns et al., 2020b). Both FEA and SAXS, however, agree in that the size of the permanent densified material below the indent is confined to a local area of ∼2 × 2 µm^2 in dimension.

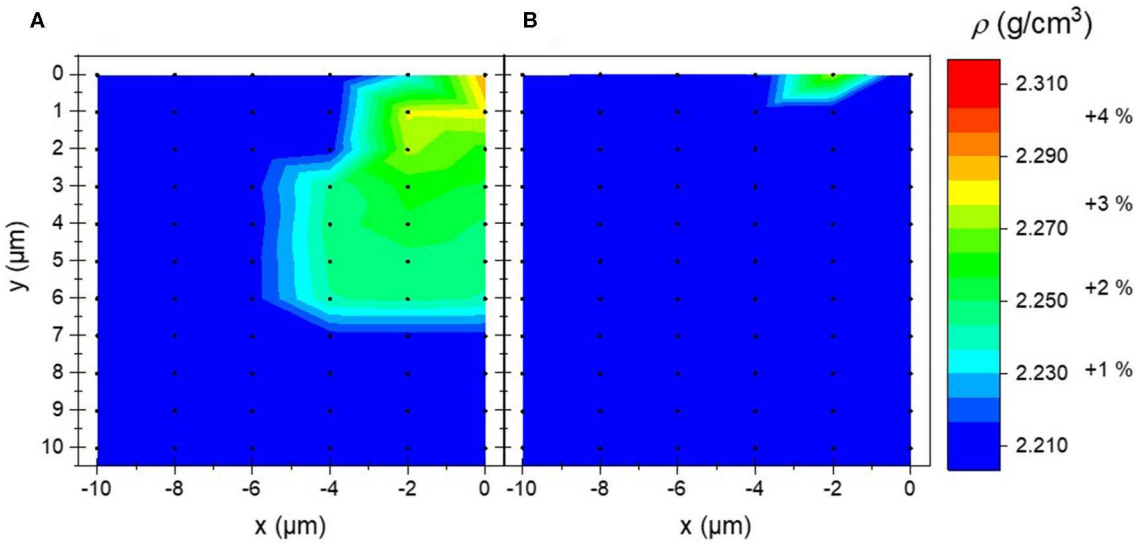

FIGURE 5 | Density map as derived from the maximum position of the FSDP for indent 1 using the calibration curve in Eq. 1 (Tan and Arndt, 1999): **(A)** *in-situ* during indentation; **(B)** after unloading. Contour diagrams of density ρ were constructed from interpolation between the individual measurement positions (black points).

Evaluation of Structural Heterogeneity in Vitreous Silica During Indentation

The densification of about 3% during loading (**Figure 5A**), which was determined from the positive shift of the FSDP to higher scattering angles (**Figure 2A**), coincides very well with the relative reduction of the AEDF compared to the bulk value of about 3–4% (**Figure 3A**). It appears that the local stress-field produced by the wedge-shaped diamond indenter tip induces comparable extents of structural modification across all length scales (as reflected by the changes in the position of the FSDP and by the variations in the AEDF, which are directly correlated to the longer-range structural heterogeneity on the scale of a few nanometers). Under load, the overall AEDF was reduced and thus, the material became more homogeneous. Interestingly, while structural variations at short- to intermediate-length scales are confined within a narrow volume in the vicinity of the indent center and for depths down to ∼6.5 µm (**Figure 2**, **Figure 5A**, respectively), it appears that modifications in the topological heterogeneity as derived from the AEDF (**Figure 3**) are achieved in a considerably larger volume spreading to about 8 µm in radial direction (x) and more than 22 µm in depth (y). We note, that similar observations were made for indent 2 (see **Supplementary Figure 2**), although the different loading conditions impede a quantitative comparison between both indents. The size of the AEDF field corresponds well to the FEA equivalent van Mises stress field beneath the indenter tip (**Figure 4A**), whereas the extent of the FSDP field corresponds well to the FEA isostatic equivalent pressure stress field (**Figure 4B**). We therefore conclude that the reduction of the AEDF and the shift in the FSDP are induced by different stress components and that they are not necessarily directly correlated to each other. On high pressure derived glasses it has been recognized that pressure-induced modifications at the short-range structural order may not be sufficient to explain the variations in density (Wondraczek and Behrens, 2007; Wondraczek et al., 2007; Wu et al., 2009), but the increase in long-range structural homogeneity has a major contribution as well (Reibstein et al., 2011). These observations indicate that the topological heterogeneity at longer-range is more sensitive to the shear stress component than the short- to intermediate-range structure of a glass. This becomes evident from the good correlation between the affected area in the AEDF analysis and the FEA equivalent von Mises stress field, which contains shear stress components. It should be noted, that both the FSDP shift and the reduction of the AEDF only persist upon loading, i.e., when the glass is exposed to the stress field of the indenter tip. Major parts of the glassy structure relax without permanent structural modifications upon the relief of the stresses at unloading.

CONCLUSION

In summary, we presented *in-situ* SAXS as a complementary method to study structural modification induced by local material deformation on intermediate length scale. Such investigations allow for relating macroscopic observations (e.g., material compaction or stress fields) to structural heterogeneity. They may help to elucidate the discrepancies between observations made on short (molecular) length scale and physical property variations toward an improved understanding of the reactions which lead to glass deformation. In vitreous silica subjected to wedge indentation, structural motives with a correlation length of ∼0.4 nm show permanent, irreversible

changes, whereas the longer-range structure (≥ 1 nm) fully recovers upon stress release. From the comparison of the affected region with FEA of the stress field, we found that shear and non-permanent densification seem to act as the primary factors on the longer-range structure. This should be investigated systematically at higher load and in glass systems with higher Poisson's ratio, where shear is more pronounced over pure densification. For this, it will be necessary to optimize the indentation set-up at the beamline to increase load tolerance and frame stiffness as well as to perform experiments with higher scanning resolution (i.e., spatial resolution).

DATA AVAILABILITY STATEMENT

The datasets generated for this study are available on request to the corresponding author.

AUTHOR CONTRIBUTIONS

SF and LW conceived of the study. The experimental design, the conduction of the SAXS experiment and data interpretation were made by SF, GM, RL, and CK. RL performed the mechanical analysis and stiffness calibration. SB and KD set and performed Finite Element Analysis. All authors participated in manuscript writing, revision, and final approval.

FUNDING

The authors gratefully acknowledge the Deutsches Elektronen-Synchrotron (DESY, Hamburg, Germany) a member of the Helmholtz Association HGF for assigning beamtime (I-20150108, I-20140502) and supporting travel expenses. This project is funded through the priority program 1594 of the German Science Foundation by the starting-ramp funding through grant no. WO1220/8-1 and project grant nos. DU424/8-2 and FU1018/1-2.

ACKNOWLEDGMENTS

We acknowledge DESY (Hamburg, Germany), a member of the Helmholtz Association HGF, for the provision of experimental facilities. Major parts of this research were carried out at PETRA III at P03 MINAXS. We thank OSIM technician Christian Zeidler for his help and support during confocal microscopy data acquisition, our colleague Aaron Reupert and our former students Florian Baumgardt and Christoph Dittmann for assistance during beamtime experiments.

SUPPLEMENTARY MATERIAL

The Supplementary Material for this article can be found online at: https://www.frontiersin.org/articles/10.3389/fmats.2020.00173/full#supplementary-material

REFERENCES

Abaqus 2016 Online Documentation (2015). *Dassault Systèmes.* Available online at: http://abaqus.software.polimi.it/v2016/ (accessed March 5, 2020).

Bakai, A. S., and Fischer, E. W. (2004). Nature of long-range correlations of density fluctuations in glass-forming liquids. *J. Chem. Phys.* 120, 5235–5252. doi: 10.1063/1.1648300

Baral, P., Guillonneau, G., Kermouche, G., Bergheau, J. M., and Loubet, J. L. (2019). A new long-term indentation relaxation method to measure creep properties at the micro-scale with application to fused silica and PMMA. *Mech. Mater.* 137:103095. doi: 10.1016/j.mechmat.2019.103095

Benzine, O., Bruns, S., Pan, Z., Durst, K., and Wondraczek, L. (2018). Local deformation of glasses is mediated by rigidity fluctuation on nanometer scale. *Adv. Sci.* 5:1800916. doi: 10.1002/advs.201800916

Brüning, R., and Cottrell, D. (2003). X-ray and neutron scattering observations of structural relaxation of vitreous silica. *J. Non Cryst. Solids* 325, 6–15. doi: 10.1016/S0022-3093(03)00318-1

Brüning, R., Levelut, C., Faivre, A., LeParc, R., Simon, J. P., Bley, F., et al. (2005). Characterization of the glass transition in vitreous silica by temperature scanning small-angle X-ray scattering. *Europhys. Lett.* 70, 211–217. doi: 10.1209/epl/i2004-10481-1

Brüning, R., Levelut, C., Parc, R. L., Faivre, A., Semple, L., Vallee, M., et al. (2007). Temperature scanning small angle x-ray scattering measurements of structural relaxation in type-III vitreous silica. *J. Appl. Phys.* 102, 083535–083539. doi: 10.1063/1.2799940

Bruns, S., Johanns, K. E., Rehman, H. U. R., Pharr, G. M., and Durst, K. (2017). Constitutive modeling of indentation cracking in fused silica. *J. Am. Ceramic Soc.* 100, 1928–1940. doi: 10.1111/jace.14734

Bruns, S., Petho, L., Minnert, C., Michler, J., and Durst, K. (2020a). Fracture toughness determination of fused silica by cube corner indentation cracking and pillar splitting. *Mater. Des.* 186:108311. doi: 10.1016/j.matdes.2019.108311

Bruns, S., Uesbeck, T., Tarragó Aymerich, M., Fuhrmann, S., Wondraczek, L., de Ligny, D., et al. (2020b). Indentation densification of fused silica assessed by raman spectroscopy and constitutive finite element analysis. *J. Am. Ceramic Soc.* 103, 3076–3088. doi: 10.1111/jace.17024

Cornet, A., Martinet, C., Martinez, V., and Ligny, D. (2019). Evidence of polyamorphic transitions during densified SiO_2 glass annealing. *J. Chem. Phys.* 151:164502. doi: 10.1063/1.5121534

de Macedo, G., Sawamura, S., and Wondraczek, L. (2018). Lateral hardness and the scratch resistance of glasses in the Na_2O-CaO-SiO_2 system. *J. Non Cryst. Solids* 492, 94–101. doi: 10.1016/j.jnoncrysol.2018.04.022

Deschamps, T., Kassir-Bodon, A., Sonneville, C., Margueritat, J., Martinet, C., de Ligny, D., et al. (2012). Permanent densification of compressed silica glass: a Raman-density calibration curve. *J. Phys. Condensed Matter* 25:025402. doi: 10.1088/0953-8984/25/2/025402

Deschamps, T., Martinet, C., Bruneel, J. L., and Champagnon, B. (2011). Soda-lime silicate glass under hydrostatic pressure and indentation: a micro-Raman study. *J. Phys. Condensed Matter* 23:035402. doi: 10.1088/0953-8984/23/3/035402

Elliott, S. R. (1991). Origin of the first sharp diffraction peak in the structure factor of covalent glasses. *Phys. Rev. Lett.* 67, 711–714. doi: 10.1103/PhysRevLett.67.711

Fischer, E. W., and Dettenmaier, M. (1978). Structure of polymeric glasses and melts. *J. Non Cryst. Solids* 31, 181–205. doi: 10.1016/0022-3093(78)90104-7

Gadelrab, K. R., Bonilla, F. A., and Chiesa, M. (2012). Densification modeling of fused silica under nanoindentation. *J. Non Cryst. Solids* 358, 392–398. doi: 10.1016/j.jnoncrysol.2011.10.011

Gamcová, J., Mohanty, G., Michalik, Š., Wehrs, J., Bednarčík, J., Krywka, C., et al. (2016). Mapping strain fields induced in Zr-based bulk metallic glasses during in-situ nanoindentation by X-ray nanodiffraction. *Appl. Phys. Lett.* 108, 031907. doi: 10.1063/1.4939981

Gerbig, Y. B., and Michaels, C. A. (2020). *In-situ* Raman spectroscopic measurements of the deformation region in indented glasses. *J. Non Cryst. Solids* 530:119828. doi: 10.1016/j.jnoncrysol.2019.119828

Golubkov, V. V. (1996). Features of structure and its relaxations in alkali borate glasses. *Glass Phys. Chem.* 22, 186–195.

Golubkov, V. V., Vasilevskaya, T. N., and Porai-Koshits, E. A. (1980). SAXS study of the structure of glasses containing no modifying oxides. *J. Non Cryst. Solids* 38-39, 99–104. doi: 10.1016/0022-3093(80)90401-9

Greaves, G. N. (1985). EXAFS and the structure of glass. *J. Non Cryst. Solids* 71, 203–217. doi: 10.1016/0022-3093(85)90289-3

Greaves, G. N., Fontaine, A., Lagarde, P., Raoux, D., and Gurman, S. J. (1981). Local structure of silicate glasses. *Nature* 293, 611–616. doi: 10.1038/293611a0

Greaves, G. N., Wilding, M. C., Kargl, F., and Hennet, L. (2008). Liquids, glasses, density fluctuations and low frequency modes. *Adv. Mat. Res.* 39-40, 3–12. doi: 10.4028/www.scientific.net/AMR.39-40.3

Hammersley, A. P., Svensson, S. O., Hanfland, M., Fitch, A. N., and Hausermann, D. (1996). Two-dimensional detector software: from real detector to idealised image or two-theta scan. *High Press. Res.* 14, 235–248. doi: 10.1080/08957959608201408

Hilke, S., Rösner, H., Geissler, D., Gebert, A., Peterlechner, M., and Wilde, G. (2019). The influence of deformation on the medium-range order of a Zr-based bulk metallic glass characterized by variable resolution fluctuation electron microscopy. *Acta Mater.* 171, 275–281. doi: 10.1016/j.actamat.2019.04.023

Huang, B., Ge, T. P., Liu, G. L., Luan, J. H., He, Q. F., Yuan, Q. X., et al. (2018). Density fluctuations with fractal order in metallic glasses detected by synchrotron X-ray nano-computed tomography. *Acta Mater.* 155, 69–79. doi: 10.1016/j.actamat.2018.05.064

Huo, L. S., Zeng, J. F., Wang, W. H., Liu, C. T., and Yang, Y. (2013). The dependence of shear modulus on dynamic relaxation and evolution of local structural heterogeneity in a metallic glass. *Acta Mater.* 61, 4329–4338. doi: 10.1016/j.actamat.2013.04.004

Januchta, K., Youngman, R. E., Goel, A., Bauchy, M., Logunov, S. L., Rzoska, S. J., et al. (2017). Discovery of ultra-crack-resistant oxide glasses with adaptive networks. *Chem. Mater.* 29, 5865–5876. doi: 10.1021/acs.chemmater.7b00921

Johnson, K. L. (1970). The correlation of indentation experiments. *J. Mech. Phys. Solids* 18, 115–126. doi: 10.1016/0022-5096(70)90029-3

Kassir-Bodon, A., Deschamps, T., Martinet, C., Champagnon, B., Teisseire, J., and Kermouche, G. (2012). Raman mapping of the indentation-induced densification of a soda-lime-silicate glass. *Int. J. Appl. Glass Sci.* 3, 29–35. doi: 10.1111/j.2041-1294.2012.00078.x

Kato, Y., Yamazaki, H., Yoshida, S., Matsuoka, J., and Kanzaki, M. (2012). Measurements of density distribution around vickers indentation on commercial aluminoborosilicate and soda-lime silicate glasses by using micro Raman spectroscopy. *J. Non Cryst. Solids* 358, 3473–3480. doi: 10.1016/j.jnoncrysol.2012.04.035

Kermouche, G., Barthel, E., Vandembroucq, D., and Dubujet, P. (2008). Mechanical modelling of indentation-induced densification in amorphous silica. *Acta Mater.* 56, 3222–3228. doi: 10.1016/j.actamat.2008.03.010

Kilymis, D., Faivre, A., Michel, T., Peuget, S., Delaye, J.-M., Delrieu, J., et al. (2017). Raman spectra of indented pristine and irradiated sodium borosilicate glasses. *J. Non Cryst. Solids* 464, 5–13. doi: 10.1016/j.jnoncrysol.2017.03.012

Koike, A., and Tomozawa, M. (2007). IR investigation of density changes of silica glass and soda-lime silicate glass caused by microhardness indentation. *J. Non Cryst. Solids* 353, 2318–2327. doi: 10.1016/j.jnoncrysol.2007.04.006

Krywka, C., Keckes, J., Storm, S., Buffet, A., Roth, S. V., Döhrmann, R., et al. (2013). Nanodiffraction at MINAXS (P03) beamline of PETRA III. *J. Phys. Conference Series* 425:072021. doi: 10.1088/1742-6596/425/7/072021

Krywka, C., Neubauer, H., Priebe, M., Salditt, T., Keckes, J., Buffet, A., et al. (2012). A two-dimensional waveguide beam for X-ray nanodiffraction. *J. Appl. Crystallogr.* 45, 85–92. doi: 10.1107/S0021889811049132

Levelut, C., Faivre, A., Le Parc, R., Champagnon, B., Hazemann, J. L., David, L., et al. (2002). Influence of thermal aging on density fluctuations in oxide glasses measured by small-angle X-ray scattering. *J. Non Cryst. Solids* 307-310, 426–435. doi: 10.1016/S0022-3093(02)01504-1

Levelut, C., Faivre, A., Le Parc, R., Champagnon, B., Hazemann, J. L., and Simon, J. P. (2005). In situ measurements of density fluctuations and compressibility in silica glasses as a function of temperature and thermal history. *Phys. Rev. B* 72:224201. doi: 10.1103/PhysRevB.72.224201

Levelut, C., Le Parc, R., Faivre, A., Brüning, R., Champagnon, B., Martinez, V., et al. (2007). Density fluctuations in oxide glasses investigated by small-angle X-ray scattering. *J. Appl. Crystallogr.* 40, 512–516. doi: 10.1107/S0021889807000507

Li, W. D., Gao, Y. F., and Bei, H. B. (2015). On the correlation between microscopic structural heterogeneity and embrittlement behavior in metallic glasses. *Sci. Rep.* 5:15. doi: 10.1038/srep14786

Limbach, R., Kosiba, K., Pauly, S., Kühn, U., and Wondraczek, L. (2017). Serrated flow of CuZr-based bulk metallic glasses probed by nanoindentation: role of the activation barrier, size and distribution of shear transformation zones. *J. Non Cryst. Solids* 459, 130–141. doi: 10.1016/j.jnoncrysol.2017.01.015

Limbach, R., Poletto Rodrigues, B., and Wondraczek, L. (2014). Strain-rate sensitivity of glasses. *J. Non Cryst. Solids* 404, 124–134. doi: 10.1016/j.jnoncrysol.2014.08.023

Molnár, G., Kermouche, G., and Barthel, E. (2017). Plastic response of amorphous silicates, from atomistic simulations to experiments – a general constitutive relation. *Mech. Mater.* 114, 1–8. doi: 10.1016/j.mechmat.2017.07.002

Ozhovan, M. I. (2006). Topological characteristics of bonds in SiO_2 and GeO_2 oxide systems upon a glass-liquid transition. *J. Exp. Theor. Phys.* 103, 819–829. doi: 10.1134/S1063776106110197

Perriot, A., vandembroucq, D., Barthel, E., Martinez, V., Grosvalet, L., Martinet, C., et al. (2006). Raman microspectroscopic characterization of amorphous silica plastic behavior. *J. Am. Ceramic Soc.* 89, 596–601. doi: 10.1111/j.1551-2916.2005.00747.x

Pierre, A., Uhlmann, D. R., and Molea, F. N. (1972). Small-angle X-ray scattering study of glassy GeO_2. *J. Appl. Crystallogr.* 5, 216–221. doi: 10.1107/S0021889872009227

Poletto Rodrigues, B., Limbach, R., Buzatto de Souza, G., Ebendorff-Heidepriem, H., and Wondraczek, L. (2019). Correlation between ionic mobility and plastic flow events in $NaPO_3$-NaCl-Na_2SO_4 glasses. *Front. Mater.* 6:128. doi: 10.3389/fmats.2019.00128

Porod, G. (1982). "General theory," in *Small Angle X-ray Scattering,* eds O. Glatter and O. Kratky. (London, UK: Academic Press), 17–51.

Rathje, J., and Ruland, W. (1976). Density fluctuations in amorphous and semicrystalline polymers. *Colloid Polym. Sci.* 254, 358–370. doi: 10.1007/BF01384035

Reibstein, S., Wondraczek, L., de Ligny, D., Krolikowski, S., Sirotkin, S., Simon, J. P., et al. (2011). Structural heterogeneity and pressure-relaxation in compressed borosilicate glasses by in situ small angle X-ray scattering. *J. Chem. Phys.* 134:204502. doi: 10.1063/1.3593399

Roe, R. J., and Curro, J. J. (1983). Small-angle x-ray scattering study of density fluctuation in polystyrene annealed below the glass transition temperature. *Macromolecules* 16, 428–434. doi: 10.1021/ma00237a018

Rouxel, T., Ji, H., Hammouda, T., and Moréac, A. (2008). Poisson's ratio and the densification of glass under high pressure. *Phys. Rev. Lett.* 100:225501. doi: 10.1103/PhysRevLett.100.225501

Sawamura, S., Limbach, R., Wilhelmy, S., Koike, A., and Wondraczek, L. (2019). Scratch-induced yielding and ductile fracture in silicate glasses probed by nanoindentation. *J. Am. Ceramic Soc.* 102, 7299–7311. doi: 10.1111/jace.16679

Sawamura, S., and Wondraczek, L. (2018). Scratch hardness of glass. *Phys. Rev. Mater.* 2:092601. doi: 10.1103/PhysRevMaterials.2.092601

Sonneville, C., Mermet, A., Champagnon, B., Martinet, C., Margueritat, J., de Ligny, D., et al. (2012). Progressive transformations of silica glass upon densification. *J. Chem. Phys.* 137:124505. doi: 10.1063/1.4754601

Tan, C. Z., and Arndt, J. (1999). X-ray diffraction of densified silica glass. *J. Non Cryst. Solids* 249, 47–50. doi: 10.1016/S0022-3093(99)00245-8

Tanabe, Y., Müller, N., and Fischer, E. W. (1984). Density fluctuation in amorphous polymers by small angle X-ray scattering. *Polym. J.* 16, 445–452. doi: 10.1295/polymj.16.445

Tran, H., Clément, S., Vialla, R., Vandembroucq, D., and Rufflé, B. (2012). Micro-Brillouin spectroscopy mapping of the residual density field induced by Vickers indentation in a soda-lime silicate glass. *Appl. Phys. Lett.* 100:231901. doi: 10.1063/1.4725488

Warren, B. E., Krutter, H., and Morningstar, O. (1936). Fourier analysis of X-ray patterns of vitreous SiO_2 and B_2O_3. *J. Am. Ceramic Soc.* 19, 202–206. doi: 10.1111/j.1151-2916.1936.tb19822.x

Watanabe, T., Saito, K., and Ikushima, A. J. (2003). Fictive temperature dependence of density fluctuation in SiO_2 glass. *J. Appl. Phys.* 94, 4824–4827. doi: 10.1063/1.1608477

Wiegand, W., and Ruland, W. (1979). "Density fluctuations and the state of order of amorphous polymers," in Anwendungsbezogene physikalische Charakterisierung von Polymeren, insbesondere im festen Zustand, eds

E.W. Fischer, F.H. Müller and R. Bonart. (Darmstadt: Steinkopff), 355–366. doi: 10.1007/BFb0117367

Winterstein-Beckmann, A., Möncke, D., Palles, D., Kamitsos, E. I., and Wondraczek, L. (2014a). Raman spectroscopic study of structural changes induced by micro-indentation in low alkali borosilicate glasses. *J. Non Cryst. Solids* 401, 110–114. doi: 10.1016/j.jnoncrysol.2013.12.038

Winterstein-Beckmann, A., Möncke, D., Palles, D., Kamitsos, E. I., and Wondraczek, L. (2014b). A Raman-spectroscopic study of indentation-induced structural changes in technical alkali-borosilicate glasses with varying silicate network connectivity. *J. Non Cryst. Solids* 405, 196–206. doi: 10.1016/j.jnoncrysol.2014.09.020

Wondraczek, L., and Behrens, H. (2007). Molar volume, excess enthalpy, and prigogine-defay ratio of some silicate glasses with different (P,T) histories. *J. Chem. Phys.* 127:154503. doi: 10.1063/1.2794745

Wondraczek, L., Sen, S., Behrens, H., and Youngman, R. E. (2007). Structure-energy map of alkali borosilicate glasses: effects of pressure and temperature. *Phys. Rev. B* 76:014202. doi: 10.1103/PhysRevB.76.014202

Wu, J., Deubener, J., Stebbins, J. F., Grygarova, L., Behrens, H., Wondraczek, L., et al. (2009). Structural response of a highly viscous aluminoborosilicate melt to isotropic and anisotropic compressions. *J. Chem. Phys.* 131:104504. doi: 10.1063/1.3223282

Yang, Y., Ye, J. C., Lu, J., Wang, Q., and Liaw, P. K. (2010). Revelation of the effect of structural heterogeneity on microplasticity in bulk metallic-glasses. *J. Mater. Res.* 25, 563–575. doi: 10.1557/JMR.2010.0058

Yoshida, S., Nguyen, T. H., Yamada, A., and Matsuoka, J. (2019). *In-situ* raman measurements of silicate glasses during vickers indentation. *Mater. Trans.* 60, 1428–1432. doi: 10.2320/matertrans.MD201901

Yoshida, S., Nishikubo, Y., Konno, A., Sugawara, T., Miura, Y., and Matsuoka, J. (2012). Fracture- and indentation-induced structural changes of sodium borosilicate glasses. *Int. J. Appl. Glass Sci.* 3, 3–13. doi: 10.1111/j.2041-1294.2011.00077.x

Zeilinger, A., Todt, J., Krywka, C., Müller, M., Ecker, W., Sartory, B., et al. (2016). *In-situ* observation of cross-sectional microstructural changes and stress distributions in fracturing TiN thin film during nanoindentation. *Sci. Rep.* 6:22670. doi: 10.1038/srep22670

Zhu, F., Song, S. X., Reddy, K. M., Hirata, A., and Chen, M. W. (2018). Spatial heterogeneity as the structure feature for structure-property relationship of metallic glasses. *Nat. Commun.* 9:7. doi: 10.1038/s41467-018-06476-8

Conflict of Interest: The authors declare that the research was conducted in the absence of any commercial or financial relationships that could be construed as a potential conflict of interest.

frontiers in Materials

ORIGINAL RESEARCH
published: 24 June 2020
doi: 10.3389/fmats.2020.00161

Influence of Vanadium on Optical and Mechanical Properties of Aluminosilicate Glasses

Maria Rita Cicconi[1], Zhuorui Lu[1†], Tobias Uesbeck[1,2], Leo van Wüllen[2], Delia S. Brauer[3] and Dominique de Ligny[1]*

[1] Lehrstuhl für Glas und Keramik, Department Werkstoffwissenschaften, FAU Erlangen-Nürnberg, Erlangen, Germany, [2] Institut für Physik, Universität Augsburg, Augsburg, Germany, [3] Otto Schott Institute of Materials Research, Friedrich Schiller University, Jena, Germany

OPEN ACCESS

Edited by:
Jürgen Horbach,
Heinrich Heine University of Düsseldorf, Germany

Reviewed by:
Sylwester Janusz Rzoska,
Institute of High Pressure Physics (PAN), Poland
Chao Liu,
Wuhan University of Technology, China

***Correspondence:**
Maria Rita Cicconi
maria.rita.cicconi@fau.de

†Present address:
Zhuorui Lu,
Institut de Physique de Nice, Université Côte d'Azur, Nice, France

Specialty section:
This article was submitted to Ceramics and Glass, a section of the journal Frontiers in Materials

Received: 20 March 2020
Accepted: 04 May 2020
Published: 24 June 2020

Citation:
Cicconi MR, Lu Z, Uesbeck T, van Wüllen L, Brauer DS and de Ligny D (2020) Influence of Vanadium on Optical and Mechanical Properties of Aluminosilicate Glasses. Front. Mater. 7:161. doi: 10.3389/fmats.2020.00161

V_2O_5 was introduced up to 9 wt.% in a peralkaline alkaline earth aluminosilicate glass and up to 4.8 wt.% in two sodo aluminosilicate glasses, respectively, a peralkaline and a peraluminous one. This introduction had a strong effect on thermal properties, and in particular, on glass transition and crystallization temperatures of the peraluminous glass, which dropped by 89 K, while a moderate drop of ∼20 K was observed for the two other glasses. Still, the glass stability and the glass-forming ability stayed almost unmodified. The elastic properties measured by Brillouin spectroscopy show a decrease with added Vanadium for the depolymerized alkali earth aluminosilicate and the peraluminous sodo aluminosilicate. In contrast, the elastic properties remained unchanged for the peralkaline composition. Using optical absorption, the proportion of V^{5+}, which is largely dominant, was found to follow the trend predicted using optical basicity considerations. A large photoluminescence emission, centered at ∼560 nm, was found for all glasses, upon excitation in the UV edge at both ∼280 and ∼350 nm. The emission band positions were relatively insensitive to the glass composition, whereas their intensities show variations of one order of magnitude between the sodium peralkaline composition and the calcium depolymerized glass. A too-high concentration of V_2O_5 shows a quenching effect on the emission. Polarized and cross-polarized Raman spectroscopy allowed us to identify the different environments around the $V^{5+}O_4$ tetrahedra. The highly polarizable $V^{5+}O_4$ tetrahedra associated with two non-bridging oxygens, vibrating at 860 cm^{-1}, is proposed to be responsible for the more efficient charge transfer. At the opposite end, the formation of VO_4-AlO_4 units is proposed to quench luminescence properties. Furthermore, we observed that, upon thermal treatment, the optical properties of the glasses are significantly modified without observable structural modifications or evolution of the elastic properties.

Keywords: thermal treatment, redox, cation speciation, optical absorption, glass structure changes, thermal history

INTRODUCTION

Vanadium is a transition element that in glasses can be stable with different speciation. This means that depending on synthesis conditions, bulk chemistry, and total V amount, vanadium ions might be stabilized with oxidation states ranging from the oxidized V^{5+} to V^{4+} to the reduced V^{3+}, each albeit with a different favorite oxygen bonding environment (coordination, bond type) (Johnston, 1965a,b; Schreiber, 1986; Leister et al., 1999). Among the different species, based on cation field strength (CFS) considerations (Dietzel, 1948), vanadium ions can enter in the amorphous network with different roles, namely network formers, modifiers or intermediated. Indeed, both penta- and tetravalent V species could be found in 4-fold coordination ($^{[4]}V^{5+}$, $^{[4]}V^{4+}$) with the $V^{5+}O_4$ tetrahedra having a V = O apex, but also with higher coordination environments, such as tetragonal pyramid ($^{[5]}V^{4+}$) or octahedral coordination (e.g., $^{[6]}V^{5+}$) (Anpo et al., 1980; Dzwigaj et al., 2000; Giuli et al., 2004; Kniec and Marciniak, 2019).

The bulk chemistry is one of the main factors influencing multivalent cation speciation (e.g., for iron, and cerium Mysen and Richet, 2005; Cicconi et al., 2015, 2017), and studies on the influence of chemistry on optical, physical, and mechanical properties of V-doped glasses are surprisingly scarce. This lack of information hampers the possibility of finding applications for this versatile cation. It is important to point out that changes in cation speciation might influence the overall properties of the host glass, and in particular, the physical and optical properties. The latter is particularly important, because changes only limited in the V average redox ratio already can provide a variety of responses in terms of optical properties (electronic configuration varies from $3d^0$ to $3d^2$; e.g., Johnston, 1965a; Anpo et al., 1980; Dzwigaj et al., 2000). And indeed, the color associated with V-bearing glasses usually hampers their use for, e.g., optical applications where colorless transparent materials are required. On the other hand, the several bands achievable in the UV-Vis-NIR regions make this element intriguing for other uses, such as in the case of luminescence nanothermometry, or tunable phosphorous (Gao et al., 2011; Kniec and Marciniak, 2019 and references therein).

Besides the optical properties, V can act as network former cation in glasses, forming the $V^{5+}O_4$ tetrahedral species, similarly to the more famous P^{5+} ions. Like phosphorous, vanadium might have some preferred associations (Na, Fe, or Al for example) in the glass network that influence the network connectivity (Mysen, 1992; Toplis and Dingwell, 1996; Cody et al., 2001; Mysen and Richet, 2005). Furthermore, since vanadium is a transition element, the electronic energy levels are strongly dependent on bond strength, coordination, and kind of first neighbors. Thus, to attain a deep understanding of the correlation between atomic structure and macroscopic properties, a fundamental study of the influence of bulk chemistry and thermal history is required.

With that in mind, we investigated different glasses, either alkali-free or alkali-bearing, and doped them with vanadium up to ∼9 wt.% with the aim of shedding some light on the influence of (i) synthesis conditions, (ii) bulk chemistry, and (iii) thermal history on vanadium speciation and the optical and structural properties of the host glasses.

Alkali-free aluminosilicate glasses and glass-ceramics in the system CaO-MgO-Al_2O_3-SiO_2 are interesting for many applications, because of their dielectric properties and high mechanical and chemical resistance (Shelby, 1985; Toya et al., 2004; Khater, 2010). Here, we selected the Diopside-Anorthite binary system that has a very good glass ability at the eutectic point (1,274°C). For the alkali-bearing glasses, the ternary system Na_2O-Al_2O_3-SiO_2 (NAS) was selected. Sodium in NAS systems acts either as a charge compensator for Al or as a network modifier. In the former case, it influences the local structure and coordination number of Al, whereas in the latter case, it produces non-bridging oxygens. Therefore, in peralkaline composition (Al/Na < 1), Al is mainly in $[AlO_4]$-Na structure since there are enough alkali cations to balance the charge, whereas in peraluminous compositions (Al/Na > 1) aluminum can be easily found in higher coordination (McKeown et al., 1984; Neuville and Mysen, 1996; Xiang et al., 2013).

Glasses were synthetized in air by melt quenching, and portions of the glasses were also thermally treated at a temperature just above Tg for different times. Glasses were investigated at different scale-lengths with various techniques: photoluminescence, optical absorption, and Raman spectroscopy, and mechanical properties were probed by using Brillouin spectroscopy. We verified that the chemistry has a strong influence on the initial vanadium speciation and that the glass thermal properties are affected by vanadium incorporation. Interestingly, we determined that the speciation of vanadium is strongly correlated to the kind of neighbors in the second coordination shell and that variation in the photoluminescence excitation can be associated with the vanadium species observed via Raman spectroscopy. Ergo, variations on the bond strength, oxygen-bonding environment and kind of second neighbors can be correlated (and possibly controlled) when looking in details at the network connectivity.

MATERIALS AND METHODS

Glass Syntheses, Thermal Treatments

Glasses are either in the quaternary system CaO-MgO-Al_2O_3-SiO_2 or in ternary system Na_2O-Al_2O_3-SiO_2, in order to study, respectively, alkali-free and alkali-bearing compositions. Diopside-Anorthite (DiAn) at the eutectic compositions (50 mol% each) have been synthesized starting from dried oxides and carbonated weighed in stoichiometric proportions. The mixed powders were decarbonized at 830°C overnight and then melted in Pt-Rd crucible at 1,450°C for 3 h in air. The melt was cast at room temperature on a brass plate. The obtained glass was finely crushed and melted again in the same conditions. Finally, the homogeneous bubble-free melt was cast in a brass mold and annealed at 600°C, a temperature below their glass transition temperatures (see **Table 1**). A portion of the pristine DiAn glass was finely crushed and doped with different amounts of V_2O_5 (5 wt.% and 10 wt.%). Vanadium-doped samples are labeled DiAn5V and DiAn10V and contain, respectively, 1.7 and 3.5

TABLE 1 | Percentage of mass determined by ICP analysis (wt.%) and the recalculated mol% of the investigated glasses.

Sample	SiO_2	Al_2O_3	MgO	CaO	Na_2O	V_2O_5	V_2O_5 ICP wt%	Density (g/cm^3)	Vm (cm^3/mol)	n_D	Tg (°C)	Tx (°C)	Tm (°C)	Λ
DiAn (wt%)	50.2	15.3	10.6	23.1										
mol%	50.4	9.0	15.8	24.8				2.785 (17)	21.43 (13)	1.593 (0)	742	968, 1,071	1,276	0.60
DiAn5V mol%	49.3	8.9	15.8	24.7		1.3	4.0	2.788 (7)	21.99 (5)	1.609 (0)	728	948, 1,044	1,240	0.60
DiAn10V mol%	48.3	8.7	15.4	24.1		3.5	9.9	2.789 (4)	22.93 (3)	1.621 (0)	703	926, 1,026	1,200	0.61
NA66.10 (wt%)	61.5	16.0			21.9		0							
mol%	66.8	10.2			23.1			2.457 (6)	26.34 (6)	1.501 (1)	523	867		0.58
NAV66.10 mol%	65.5	9.8			22.9	1.8	4.8	2.473 (5)	27.00 (5)	1.522 (2)	514	850		0.59
NA66.18 (wt%)	58.2	27.1			14.0		0							
mol%	66.4	18.2			15.5			2.426 (10)	27.99 (11)	1.504 (3)	814			0.56
NAV66.18 mol%	65.5	17.7			15.0	1.9	4.8	2.432 (9)	28.81 (10)	1.515 (1)	725	1,116		0.57

Section Analytical Methods reports details of the theoretical optical basicity (Λ) calculations.

mol% of V_2O_5. DiAn10V samples were melted at 1,450°C for 4 h and cast at the same condition as the pristine DiAn composition.

The second glass system selected is the alkali-bearing NAS system (Na_2O-Al_2O_3-SiO_2). Two glass compositions, containing different Al amounts, were selected. Indeed, the Al/alkali (Na) ratio was varied, while keeping constant the SiO_2 content, to obtain a peralkaline (Al < alkali) and a peraluminous glass (Al > alkali). The glass stoichiometry is 66 mol% SiO_2-(16.33, 23.33) mol% Na_2O–(18, 10) mol% Al_2O_3. The pristine materials were melted in air at 1,400°C for 2 h, and after quenching and crushing, they were remelted again at 1,500°C for 2 h. The homogeneous melts were fast-quenched by dipping the crucible bottom in water. Portions of the pristine glasses were finely grounded and doped with 5 wt.% vanadium oxide (V_2O_5), then melted and cast under the same conditions used for the pristine glasses. V-free pristine glasses are named NA66.y, with $y = Al_2O_3$ and $Na_2O = 100 - (66 + y)$. V-bearing aluminosilicate glasses are labeled NAV66.y.

Analysis of the base glass compositions was obtained by ICP-MS and are reported in **Table 1**. The molar concentrations were obtained by the renormalization of the weight composition to 100%. Very good agreement is found between the analyzed and nominal compositions of the pristine glasses. For the glass with added V_2O_5, only the Vanadium content was analyzed by ICP-MS. The molar composition was deduced from the measurement of the base glass, taking into account the analyzed amount of V_2O_5. Since the V_2O_5 amount present in the glass is lower than the targeted amount, it is suggested that some volatilization of V occurred during the melting.

Small glasses pieces were double-polished to optical quality with SiC paper until 5 μm and with diamond suspension until 1 μm. Polished samples were used for thermal treatments as well, to reduce surface tension and to avoid induced crystallization. Thermal treatments of all glasses were done in small furnaces with a secondary thermocouple placed directly in contact with the sample edge, to minimize temperature errors. Thermal treated samples are labeled "*samplename*" TT"*x*d" with *x* representing the time (days): e.g., DiAn5VTT3d represents the diopside-anorthite glass doped with 5 wt.% V_2O_5 and thermally treated for 3 days. Thermal treatments have been done for different times and the sample list is reported in **Table 2**, along with glass properties. In the case of DiAn10V, partial crystallization was observed after 3 days at 760°C. Therefore, further heat treatments were done closer to Tg at 735°C.

Analytical Methods

Density was measured by the Archimedes method with water. An average of three to four measurements were done for each sample. The molar volume of the glasses has been calculated according to $V_m = \sum \frac{n_i M_i}{\rho}$, where *n* and *M* are, respectively, the molar fraction and the molecular weight of the oxide *i*, and ρ the glass density. The Refractive Index *n* at the Na-D line and the Abbe number of the polished samples have been measured on an Abbe refractometer. The monobromonapthalene was used as the contact layer between the sample and prism of the refractometer. Thermal properties, i.e. glass transition, the onset of crystallization, and melting temperature, were measured from differential scanning calorimetry (DSC, NETZSCH DSC 404F1) at a constant heating and cooling rate (20 K/min) for DiAn system. For the NAS system, the heating and cooling rates used were, respectively, 30 and 20 K/min.

Absorption spectra were measured using a UV-VIS spectrometer (Lambda 950, Perkin Elmer). All measurements were carried out on polished glasses in the range 1,400 to

TABLE 2 | Thermal treatment (TT) parameters and properties.

Label	TT Temperature (°C)	Time	ΔT (°C)	ρ (g/cm^3)	n_D (error < 0.002)	Abbe
DiAn				2.785 (17)	1.593 (2)	56 (2)
DiAnTT0.5h	774	0.5 h	32	2.786 (5)	1.592	51
DiAnTT1d	774	1 day	32	2.788 (3)	1.598 (9)	57 (1)
DiAnTT3d	774	3 days	32	2.773 (1)		
DiAn5V				2.788 (7)	1.609	47 (3)
DiAn5VTT0.5h	760	0.5 h	32	2.793 (64)		
DiAn5VTT1d	760	1 day	32	2.797 (22)	1.610 (1)	49 (1)
DiAn5VTT3d	760	3 days	32	2.798 (3)	1.607 (1)	47 (1)
DiAn5VTT7d	760	7 days	32	2.800 (7)	1.609	
DiAn5VTT28d	760	28 days	32	2.801 (7)	1.610	
DiAn10V				2.789 (4)	1.621	45 (3)
DiAn10VTT3d760	760	3 days [§]	57			
DiAn10VTT0.5h	735	0.5 h	32	2.797 (27)		
DiAn10VTT1d	735	1 day	32	2.782 (18)		
DiAn10VTT3d	735	3 days	32	2.815 (30)		
DiAn10VTT7d	735	7 days [§]	32	–		
NA66.10				2.457 (6)	1.501 (1)	48 (2)
NA66.10TT3d	555	3 days	32	2.467 (15)	1.502	50 (1)
NA66.10TT7d	555	7 days	32	2.468 (8)	1.506 (1)	52 (1)
NAV66.10				2.473 (5)	1.522 (2)	50
NAV66.10TT3d	546	3 days	32	2.477 (39)	1.521	
NAV66.10TT7d	546	7 days	32	2.486 (11)	1.523	
NA66.18				2.426 (10)	1.504 (3)	60 (2)
NA66.18TT3d	846	3 days	32	2.428 (5)	1.506 (4)	52 (11)
NA66.18TT7d	846	7 days	32	2.424 (3)	1.509	66
NAV66.18				2.432 (9)	1.515 (1)	
NAV66.18TT3d	757	3 days	32	2.435 (16)	1.517 (1)	61
NAV66.18TT7d	757	7 days	32	2.435 (30)	1.517 (1)	61

[§] *The difference between TT temperature and glass transition temperature ΔT, and properties are reported.*
[§] *sample shows partial surface crystallization upon thermal treatment.*

190 nm. In order to avoid artifacts due to the different lamps and detectors, the spectra were collected in three regions, with overlaps of at least 20 nm in between: e.g., 1,400–850 nm, 870–320 nm, and 340–190 nm. Optical emission and excitation spectra (PL) were collected with a spectrofluorometer equipped with double monochromators (Czerny-Turner) in excitation and emission (Fluorolog3, Horiba Jobin Yvon), using a 450 W Xe-lamp as the excitation source (excitation and emission spectral resolution $\leq$ 2 nm). Raman and Brillouin signals have been acquired simultaneously by using the integrated device ARABICA (for details, see Veber et al., 2018). Raman spectra have been collected with a coherent Sapphire single-frequency 488-nm laser (100 mW) as the excitation source and an iHR 320 Horiba monochromator, combined with a Sincerity UV-VIS CCD camera (grating 1,800 gr/mm), in the frequency range of 10 to 1,500 cm^{-1}. The laser was focused on the sample (polished to optical quality) with a microscope (50× objective) and the backscattering signal was collected. Integrated to the 488 nm excitation laser and Horiba Raman spectrometer, there was a Tandem Fabry-Perot interferometer TFP-2 used to collect the Brillouin signal (Veber et al., 2018). Brillouin back scattering data are collected at a scan amplitude of 475 nm (or 449 nm), a 2.5 mm mirror spacing, 450 entrance pinhole, and 700 detector pinholes. Measurements in platelet geometry were done with 5 mm mirror spacing, 450 entrance pinholes, and 700 detector pinholes. Raman data treatment has been carried out with Horiba software Labspec®. Signals have been background–subtracted with a polynomial function and normalized to the total area. Raman spectra have been also acquired in parallel polarized (VV) and cross-polarized (VH) modes.

RESULTS AND DISCUSSION

Glass Chemistry, V Redox State, and Optical Basicity

Glass compositions have been obtained by ICP-MS analysis and are reported in **Table 1**, along with the recalculated mol%. The three glass series studied, even if very different, can be compared using the concept of optical basicity (Λ) developed by Duffy (1996) and references therein. The optical basicity is the mean

magnitude of negative charge carried by the oxygen atoms and is then sensitive to the strength ionic field of the cations to which it is associated (see e.g., Moretti, 2005). It can be calculated according to $\Lambda = \sum_i X_i \times \Lambda_i$, where X_i is the oxide molar fraction, and Λ_i is the theoretical optical basicity of the oxides ($\Lambda CaO = 1.0$, $\Lambda Na_2O = 1.15$, $\Lambda SiO_2 = 0.48$, $\Lambda MgO = 0.78$, $\Lambda Al_2O_3 = 0.6$ (Duffy, 1993). For the ΛV_2O_5, Duffy (1996) proposed a value of 1.04, though we used here the value of 0.65 reported by Lebouteiller and Courtine (1998) and Hamnabard et al. (2012). It can be noticed from the calculated values in **Table 1** that, for our glasses, V content has only a slight effect on the total optical basicity. A general trend of decreasing optical basicity is then given in the order DiAn, NA66.10, NA66.18. Indeed, even if the non-alkali cations have a stronger charge, DiAn composition has a globally lower optical basicity due to its lower silica content. This optical basicity is in the same order as the trend in regards to the bridging oxygen (BO) concentration. From **Table 1**, it can be easily calculated that DiAn contains 68% of BO and that NA66.10, which is peralkaline, has 86% of BO. Since NA66.18 is peraluminous, it is assumed to contain only BO, considering that higher coordinated Al species still act as network formers. All the results will be always discussed further in this order: DiAn, NA66.10, and NA66.18.

V can be stabilized in three possible valences: V^{5+}, V^{4+}, and V^{3+}. It is possible to describe vanadium in glasses according to the two following equilibria (Johnston, 1965a,b):

$$2O^{2-} + 4V^{5+} \leftrightarrow 4V^{4+} + O_2 \quad (1)$$

$$2O^{2-} + 4V^{4+} \leftrightarrow 4V^{3+} + O_2 \quad (2)$$

The optical basicity approach provided also a way to estimate the redox equilibrium of vanadium ions. The ratio V^{4+}/V^{5+} can be calculated by the empirical equation first proposed by Duffy (1993) and later revised by Farah (2008) for aluminosilicates melts of lime or sodium at 1,325°C:

$$\log\left[\frac{V^{4+}}{V^{5+}}\right] = 3.75 - 8.09\Lambda \quad (3)$$

The predicted V^{4+}/V^{5+} ratios are reported in **Table 3**. This ratio should stay relatively insensitive to the total vanadium content as observed by Farah and Brungs (2003), and V^{5+} should be the predominant species (> 86%) in all glasses. DiAn composition is in agreement with experimental data previously reported (Giuli et al., 2004) and with molecular dynamic simulations (Ori et al., 2011). Similarly, in the NAS ternary system, according to Leister et al. (1999), Al-free sodium silicate glasses, synthesized in air, should have ∼96% of V^{5+}. It can also be noticed that glass polymerization increases the number of reduced species, in agreement with the optical basicity concept. V-doped glasses in this study, depending on the presence of alkali earth cation or the Al/Na molar ratio, have distinct colors, highlighting the stabilization of different V oxidation states depending on composition (see **Figure 1**). For NAS glasses, the peralkaline one (NAV66.10) is yellowish, whereas the peraluminous one (NAV66.18) is brownish, indicating a different initial V speciation. To go further in the determination of V valences these colors will be quantified by optical absorption in section Optical Properties.

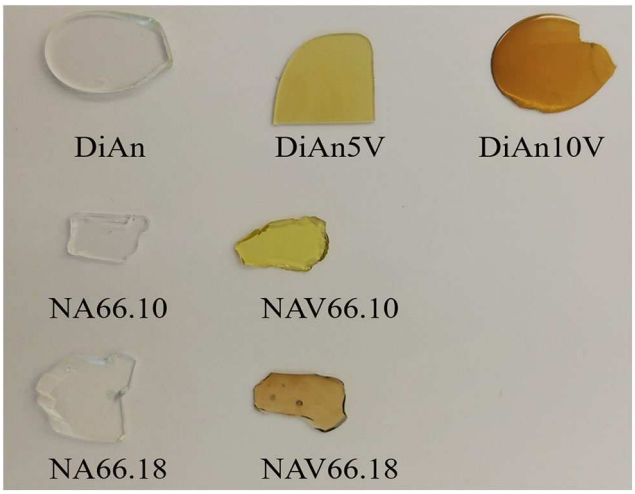

FIGURE 1 | Glasses synthesized in this study. Pristine NA66.10, NA66.18, and DiAn glasses are shown along with the V-doped ones: NAV66.10, NAV66.18, DiAn5V, and DiAn10V.

Glass Physical Properties

The physical and thermal properties of pristine and V-doped glasses are reported in **Tables 1**, **2**. Glass transition temperature values (Tg) were evaluated from DSC curves as well as the onset of crystallization (Tx) and melting temperature (Tm) for the DiAn series. The Tg does not respect the polymerization/optical basicity trend, because even if DiAn glasses are more depolymerized, they have a higher Tg than NA66.10. Indeed, Ca and Mg that are nominally considered network modifiers, have a valence of 2+, which allows them cross-linking species in the glass structure [charge compensator role; e.g., (Cicconi et al., 2016)].

The addition of vanadium induces a strong decrease of Tg for all compositions (see **Table 1**). Even if V acts as a network former, the melting point of V_2O_5 at 690°C is much lower than those of SiO_2 or Al_2O_3. It is then logical that its introduction induces a decrease of Tg. 5 wt.% of V_2O_5 causes only a moderate Tg decrease in the two depolymerized glasses, respectively, of 14°C for DiAn and 9°C for NA66.10, whereas it induces a very significant drop of 89°C in the fully polymerized NA66.18. In the different possible incorporation configurations of Vanadium in the peraluminous NA66.18 glass, one extremely likely may be its association with AlO_2^- tetrahedral units. In such a way, the VO_2^+ tetrahedral and the AlO_2^- tetrahedral will form a neutral $AlVO_4$ unit. Therefore, a part of the network modifiers is not any more charge compensating Al tetrahedral and can create additional non-bridging oxygen (NBO) lowering further the glass transition temperature.

In depolymerized glasses, Tg is driven by the collective breaking of the weakest bonds that are mostly related to the NBO and the modifier cations. In such glasses, the action of V will not

be preponderant. In the polymerized NA66.18 glass, however, V introduces weak points in the strong and very homogeneous (Si, Al) network. The behavior of V here seems to be very similar to the one of another network former, P in aluminosilicate (Mysen and Richet, 2005; Grammes et al., 2020). The DiAn series shows that the evolution of Tg is perfectly linear with increasing V content (see **Table 1**).

Two crystallizations can be detected from the DSC measurement in DiAn series. The evolution of both crystallization temperature Tx is similar to that of Tg. Therefore, the difference between Tg and Tx remains almost constant with V content. This can be understood as a measure of the glass stability (GS). The bigger the difference is between Tx and Tg, bigger is the temperature window in which the glass can be modified without crystallizing. Here the observed constant GS is contradicted by the experimental heat treatment realized since DiAn10V after 3 days at 760°C or 7 days at 735°C, shown crystallization of V_2O_5 on the surface of the samples. No crystallization was observed for the two Na-bearing glasses, as they were thermal treated (TT) 32°C above their Tg for up to 7 days. The eutectic composition DiAn has a very good glass-forming ability (GFA), which can be evaluated in terms of the Hrubÿ parameter $(Tx - Tg)(Tm - Tx)$ (Hrubý, 1972). The addition of vanadium decreases the GFA from ∼1 (DiAn) to 0.74 (DiAn5V). Remarkably, DiAn10V has a higher GFA (0.79) than DiAn5V despite the crystallizations observed. This shows the limitation of using such a parameter (Nascimento et al., 2005). Overall, V has a relatively neutral effect on both GS and GFA.

Density measurements on pristine and thermal treated glasses are reported in **Table 2**. In all cases, introducing around 1.8 mol% of V_2O_5 increases the density slightly, as expected, since V is a heavier element. The molar volume (Vm) of the glasses was deduced from the density measurement and the chemical composition (see Section Analytical Methods). The Vm increased almost linearly for all compositions and can be taken into account by using a near-constant molar partial volume of 63 ± 6 cm^3/mol for V_2O_5. This increase of molar volume is in agreement with the coordination of 4 expected for V and its network former role that opens the atomic structure of the glass. Upon TT, the density of the glasses is not changed. This proves that the effect of the cooling rate on the global glass structures is moderate and not detectable in our case. In the case of the V bearing glasses, no significant variation of the density can be seen. The results of the DiAn series are shown in detail in **Figure 2**. The dispersion of the points and the size of the error bars make it difficult to deduce any clear trend. Therefore, if during the thermal treatment some redox modifications of V took place, its effect on the volume could not be noticed.

Refractive index (n_D) increases with higher V amounts. For the DiAn series, there is almost a linear relationship ($R^2 = 0.98$) between V content and refractive index. This increase can be explained by the higher polarizability of V and/or its action as a network former in which more covalent bonds are involved and/or the possible presence of a double bond V = O. Thermal treatments induce only small variations of the refractive index (see **Table 2**).

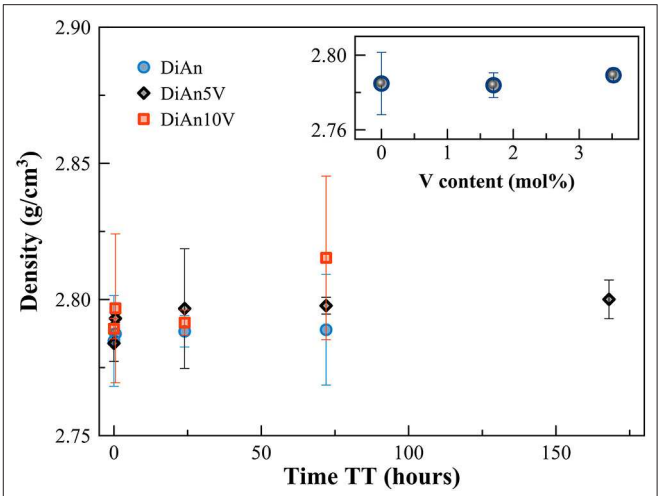

FIGURE 2 | Evolution of density with thermal treatment (TT) time for the pristine and V-doped DiAn glasses. In the inset, the density is reported against the V content (mol%).

Optical Properties

Optical Absorption

The optical absorption spectra of the samples show variations depending on vanadium concentration and thermal treatment in the range 250–1,400 nm (40,000–7124 cm^{-1}) (**Figures 3**, **4**, respectively, for DiAn and NAS glasses). Pristine glasses are colorless and show UV-edges below 300 nm, whereas the colored V-doped samples have UV-edges in the visible range around 400 nm, stopping violet light and giving the characteristic yellowish color (DiAn 5V and NAV66.10). Further shoulders of the UV-edge at 500 nm cutting blue contributions lead to the more brownish colors (DiAn10V and NAV66.18). As can also be seen between DiAn5V and DiAn10V, the total amount of V has a strong effect on the color (**Figure 1**).

The addition of vanadium shifts the UV-edge toward lower frequencies, and this redshift could be partially due to the energy gap between the valence band and conduction band which decreases linearly for higher V_2O_5 amounts (**Figure 3A**). By using a Tauc plot $(\alpha h\upsilon)^{1/2}$ against the photon energy ($h\upsilon$), the UV-edge was estimated in the same manner as for a direct optical band gap energy (**Table 3**). The UV-edge is also partially assigned to charge transfer (CT) bands of V^{5+} (Leister et al., 1999). After TT, all the glasses show a significant evolution of their absorption spectra except for DiAn5V, which stays almost constant (**Figures 3B**, **4B**). The UV-edge decreases for both DiAn samples and stays almost constant for NAV66.10 and NAV66.18. The optical absorptions increase over the full range 500–1,400 nm (2.8–1.0 eV) (as reported in **Table 3**).

Vanadium, having multiple stable valences and different local environments, can induce several bands in the UV-Vis-NIR regions. V^{5+} has a $3d^0$ electronic configuration; thus, only CT bands occur, in or around the UV region. Since CTs have very high extinction coefficients, they are not discernible from the global UV-edge. V^{4+} species ($3d^1$ electronic configuration),

TABLE 3 | Results of the optical absorption and photoluminescence studies.

	$V^{5+}/(V^{4+}+V^{5+})$ From Λ	$\%V^{3+}$	$\%V^{4+}$	$\%V^{5+}$	V^{5+} x 10^3 mol/cm^3	UV-edge (eV)	Em intensity (CPS)
DiAn5V	0.93	0.18	1.42	98.40	1.19	2.86	35,187
DiAn5V TT0.5h		0.34	1.07	98.60	1.20		33,417
DiAn5V TT1d		0.08	1.26	98.66	1.20		32,214
DiAn5V TT3d		0.09	1.26	98.65	1.20	2.60	33,121
DiAn10V	0.93	0.18	2.20	97.62	2.97	2.38	16,744
DiAn10VTT3d		0.50	0.72	98.78	3.03	1.77	16,198
NAV66.10	0.91	2.54	4.60	92.86	1.21	2.74	125,862
NAV66.10TT7d		3.98	7.36	88.66	1.16	2.84	124,877
NAV66.18	0.87	4.82	18.80	76.38	0.98	3.44	43,842
NAV66.18TT7d		7.61	22.44	69.95	0.90	3.44	46,426

Estimated percentage of each single redox species is reported, along with the concentration per volume unit of the oxidized species V^{5+} (mol/cm^3). The results below assumed that the local environment of V did not change significantly with glass composition and that the extinction coefficient of Leister et al. (1999) can be kept constant. UV-edge energies (eV) and intensities of the photoluminescence emission (Em) maxima (counts per second; CPS) are reported as well. In the first column is given the ratio between V^{5+} and V^{4+} calculated from the optical basicity Λ according to Equation [3].

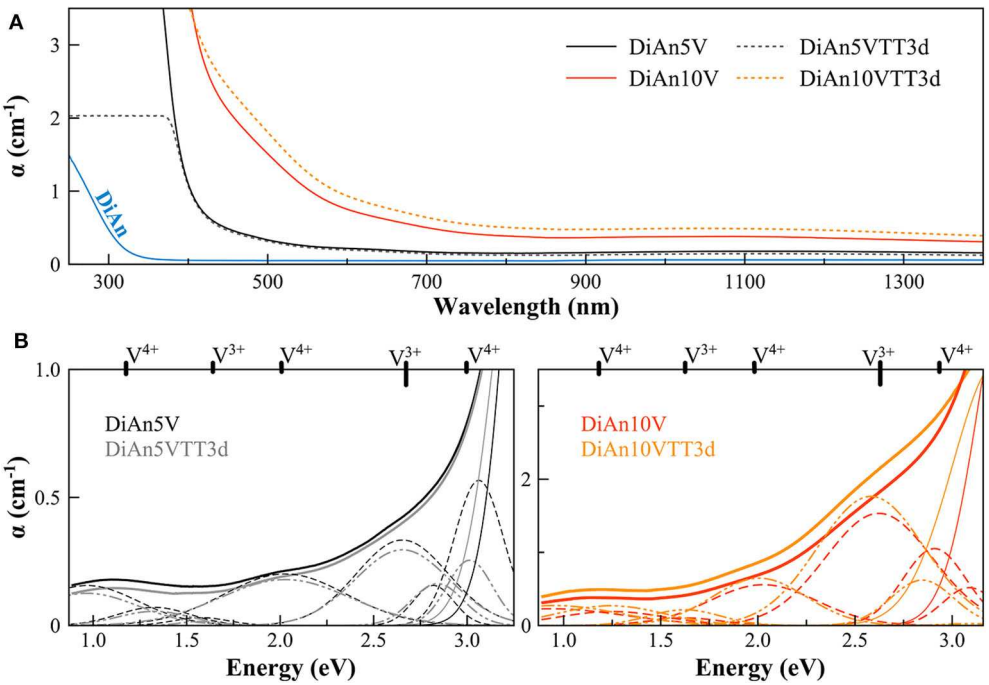

FIGURE 3 | (A) Optical Absorption spectra of pristine and V-doped DiAn glasses, melted in air, or thermally treated (TT). **(B)** Deconvolution of the optical absorption bands for V-doped DiAn glasses and 3-day thermally treated ones (TT3d).

four-fold and six-fold coordinated, should have only one spin-allowed absorption transition. However, in silicate glasses, it has been reported the occurrence of vanadyl VO^{2+} units (V = O p-bond) that yield several *d–d* transitions (Johnston, 1965a; Leister et al., 1999). In **Figures 3**, **4**, *d–d* transitions of V^{4+} (VO^{2+}) occur at ∼ 1,050 nm (∼1.2 eV; $^2T_1 \rightarrow {}^2T_2$), ∼610 nm (∼2.0 eV; $^2T_1 \rightarrow {}^2E$), and ∼420 nm (∼3.0 eV; $^2T_1 \rightarrow {}^2A_1$), and they represent the main bands in the spectra for V-doped glasses. Six-fold coordinated V^{3+} species ($3d^2$ electronic configuration) have bands at ∼700 nm (∼1.8 eV; $^3T_{1g} \rightarrow {}^3T_{2g}$) and ∼460 nm [∼2.7 eV; $^3T_{1g} \rightarrow {}^3T_{1g}$ (P)] (Johnston, 1965a; Leister et al., 1999) and references therein. These assignments are reported on the top of the **Figures 3B**, **4B**.

To go further in the determination of the proportions of the different valence species of V, these different optical absorption bands have been deconvoluted with Gaussian (G) functions (dotted and dashed lines in **Figures 3B**, **4B**). Considering the literature on band assignment and the signal deconvolution, the concentrations of V^{4+} and V^{3+} species have been estimated by considering the intensity of the bands and the molar extinction

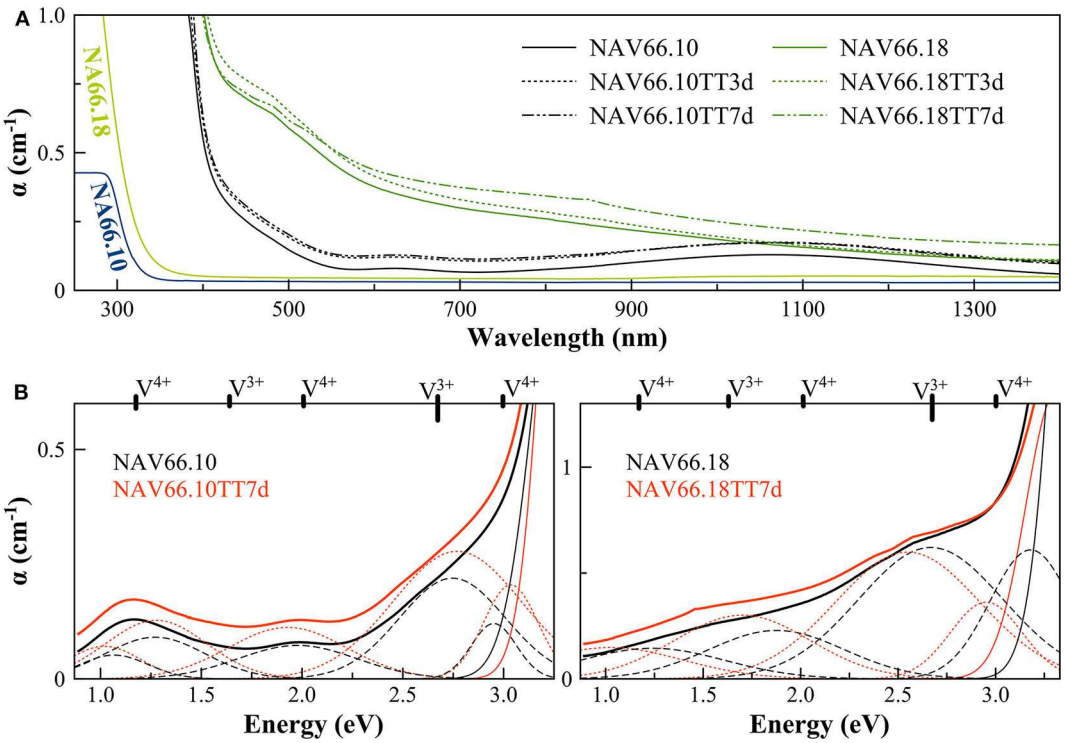

FIGURE 4 | (A) Optical Absorption spectra of pristine and V-doped NAS glasses, melted in air, and thermal treated for 3 (TT3d) and 7 (TT7d) days. **(B)** Deconvolution of the optical absorption bands for V-doped NAS glasses and 7-day thermally treated ones (TT7d).

coefficients reported by Leister et al. (1999). Here, the data treatment was difficult due to the high overlap between the different components and a strong variation of the UV-edge probably due to modification of the V^{5+} local environment and the sensitivity of the CT process to the overall redox conditions. Therefore, only two bands were used to calculate the concentration of the different V species reported in **Table 3**: the band at ∼1.9 eV for V^{4+} and the band at ∼1.6 eV for V^{3+}. The concentration of V^{5+} was deduced from the two previous data considering the total chemically analyzed content of V in the glass from **Table 1**. The proportion of V^{5+} is decreasing in the order of DiAn, NAV66.10, and NA66.18, following the same trend than the one predicted from the optical basicity, see 3.1, reported also in **Table 3**. The best agreement between the optical basicity estimation and those derived from the optical absorption spectra is for the sample NAV66.10, which is very close to the composition used by Leister et al. (1999) to determine the extinction coefficient used, i.e., 66 mol% SiO_2 and 33 mol% Na_2O. It is important to notice that to construct **Table 3**, strong approximations were done. Indeed, it was assumed that the extinction coefficients of all species can be kept constant, i.e., that the local environment of V (oxygen coordination and second neighbors) did not change significantly with glass composition. Knowing the sensitivity of transition metals to the crystal field, it is then not surprising that the results for DiAn and NAV66.18 show more discrepancies.

As can be seen from the data reported in **Table 3**, the thermal treatments change the oxidation states of the different glasses in very different ways. While for DiAn5V, no significant variations are observed, DiAn10VTT3d shows oxidation compared to DiAn10V. On the contrary, for both NAV samples, thermal treatments induced a significant reduction by a decrease of V^{5+} and a strong increase of both V^{4+} and V^{3+} contents. Theoretically, at high temperatures, reduced forms are favored and conversely, low temperatures favor the oxidized ones. Since the glasses were first melted at high temperatures and then thermally treated a little above Tg, in all cases, oxidation of V should be observed. The results here observed, with a reduction in the NAV samples, are very surprising, and no single simple explanation was found at the moment. Another unexpected result is that during the thermal treatment the ratio V^{4+}/V^{3+} stays almost constant within our uncertainties with a ratio of 3. In this paragraph, the optical absorption was only related to V^{4+} and V^{3+}. It is only on the position of the UV edge that variation related to V^{5+} content can be expected. The UV edge here stays almost constant for NAV samples. One can argue that actually, it is not a real redox modification that takes place, but rather changes of the V atomic environment, inducing a variation of the extinction coefficient. The structural evolution around V observed in this study, after several days of thermal treatment, cannot be associated with the typical structural relaxation of glass, which takes only some couple of minutes at Tg. To confirm the observation done by optical

spectroscopy, the study of the photoluminescence can provide complementary information.

Photoluminescence

Photoluminescence (PL) spectra of V-bearing DiAn and NAS glasses are reported in **Figure 5**, and the maximum emission intensities for the different glasses are provided in **Table 3**. The pristine glasses had very weak luminescence due to iron impurities, with intensity by two orders of magnitude lower compared to the V-bearing one and so were omitted here. The excitation spectra were recorded using the intensity of the luminescence at the maximum of the emission spectra (see arrows in **Figures 5B,C**). All spectra shown in **Figures 5B,C** have been normalized to the total area to better discern the differences.

The PL spectra of V glasses show a very broad emission (Em) band centered between 580 and 591 nm, depending on the glass composition. By increasing V content, between DiAn5V and DiAn10V, the maximum of the emission redshifts by 7 nm, and its intensity strongly drops (>50% intensity drop). For alkali-bearing glasses, by going from NAV66.10 to NAV66.18, the maximum of the emission redshifts by 5 nm and its intensity decreases almost by factor 3 (**Figure 5A**). In the latter two glass systems, the amount of vanadium is almost constant; thus, the variations have to be related to the bulk chemistry. The position of the emission maximum and its overall shape does not change significantly during thermal treatment for any sample, whereas the intensity of the emission lines presents small variations depending on the thermal history. Hence, on one hand, bulk chemistry and total V content do not strongly influence the broad emission band position, while on the other hand, the photoluminescence emission intensity shows very strong differences, depending on vanadium content or glass composition.

The broad excitation (Ex) band, split into two discernible contributions: a smaller one at 280 nm, which is the more pronounced in the NAV66.10 series, and the strongest one between ~335 and 350 nm, which presents a shoulder at

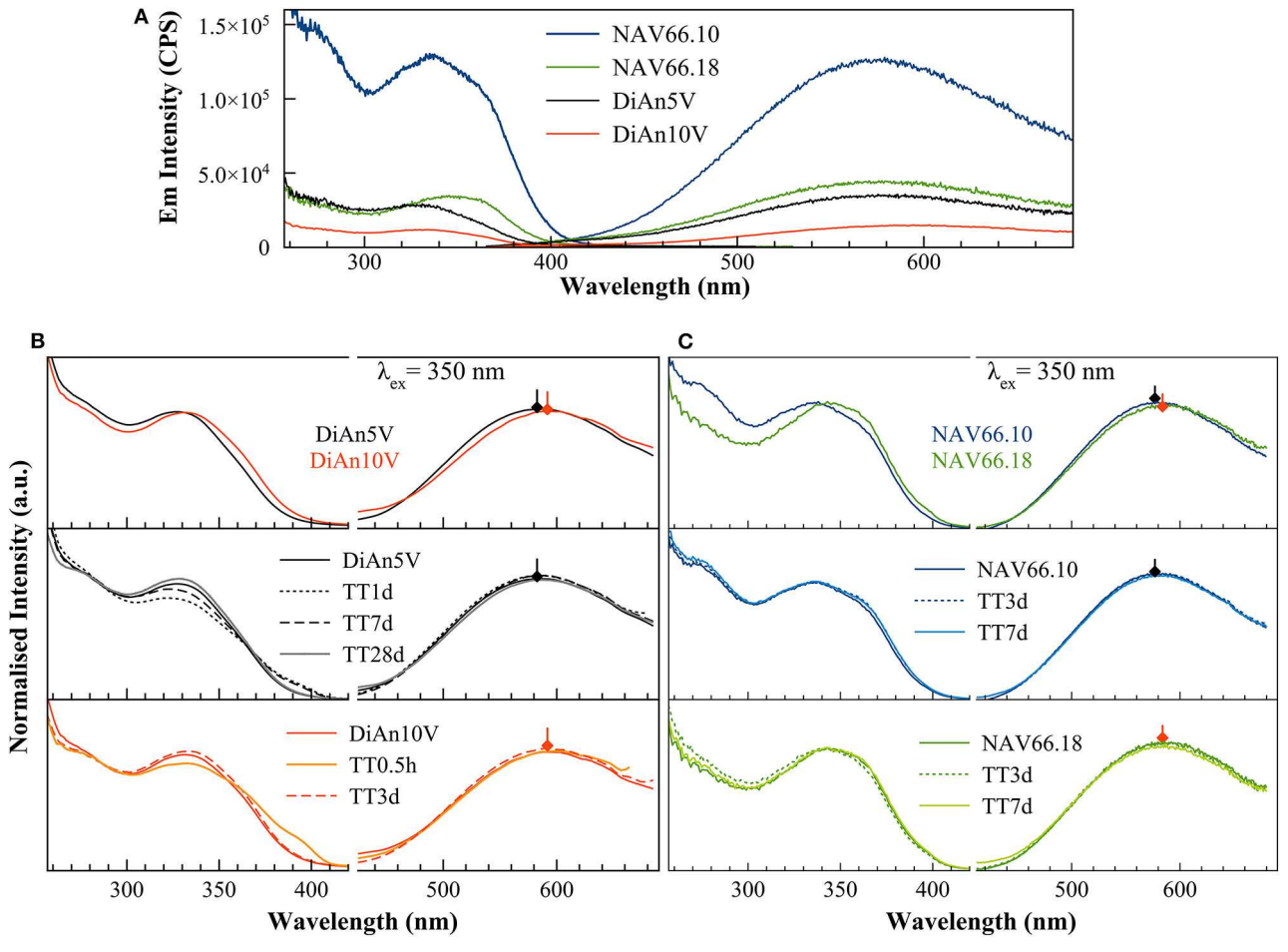

FIGURE 5 | (A) Raw excitation and emission spectra of V-doped DiAn and NAS glasses. There is an intensity drop of the photoluminescence emission depending on the bulk composition. **(B)** Excitation (Ex) and Emission (Em) spectra of V-doped Dian glasses normalized to their total area. The increase of V content induces a redshift of both Ex and Em. TT above 3 days as well-produced changes in the excitation lines. **(C)** Normalized photoluminescence spectra for NAS glasses. The increase of the Al/Na molar content induces a redshift of both Ex and Em bands.

∼360 nm (**Figure 5**). The position of the stronger band redshifts and the relative intensity of the shoulder at 360 nm increases in the order DiAn5V, DiAn10V, NAV66.10, and NAV66.18, following therefore the optical basicity trend. While this stronger band position moves, the peak at 280 nm and the shoulder at ∼360 nm do not change. Thermally treated glasses (**Figures 5B,C**) show variations that are not linear with TT time and differ for each composition. Nevertheless, TT glasses present small differences in the emission intensity and also in the relative intensity of the excitation shoulder at 360 nm. Similar complex behaviors were also observed in the optical absorption spectra in section Optical Absorption.

The excitation spectra can be attributed to CT processes related to V^{5+} groups. These processes involve an electron transfer from the double-bonded O^{2-} to V^{5+} inducing the formation of transitory V^{4+} species from which radiative decay is responsible for the emission (Anpo et al., 1980; Kniec and Marciniak, 2019). Previous studies done on crystalline materials highlighted that the frequency of the oxygen–vanadium charge-transfer excitation band provides information regarding the number of oxygen ligands surrounding vanadium. Indeed, by increasing oxygen coordination around V^{5+} species from 4 to 6, the absorption bands redshift from ∼275 and ∼340 to ∼400 to ∼470 cm^{-1}, as observed for $NaVO_3$ ($^{[4]}V^{5+}$), VPO_4 ($^{[5]}V^{5+}$) and V_2O_5 ($^{[6]}V^{5+}$), respectively (Schraml-Marth et al., 1991; Kornatowski et al., 1995) and references therein.

In our glasses, because of the presence of a split excitation, and because their frequency positions resemble the ones reported for $NaVO_3$ (Schraml-Marth et al., 1991), we assigned the small band at around 280 nm and the main band in the range of 330–360 nm to $\pi(t_{1,2})$ to d(e) oxygen-to-$^{[4]}V^{5+}$ CT transitions with oxygen in apical position (V = O) (Schraml-Marth et al., 1991; Dzwigaj et al., 2000). Other CT transitions at higher wavelengths, as in the case of oxygen-to-octahedral V^{5+} transition, are not present in any of the glasses investigated here. Thus, we can assume that at least two different kinds of $^{[4]}V^{5+}$ species are present in the glasses, that differ according to the distortion of the site, and in turn, according to the first neighbor ligands.

To go further in the link between this CT and the photoluminescence, it could be checked if the emission intensity is correlated to the quantity of V^{5+} previously determined using optical absorption and the extinction coefficient of Leister et al. (1999) (see section Analytical Methods). Since in the photoluminescence spectrometer the excitation is realized in the volume of the sample, it is more appropriate to use the volume concentration of V^{5+} in mol/cm^3, which can be obtained using the density. Such correlation is reported in **Figure 6A**. An overall trend highlights that higher amounts of oxidized species induce lower emission intensity and thus, a quench of the photoluminescence. The reason for this quenching is principally related to self-absorption. However, in the concentration region, the emission intensity of NAV66.10 (represented in light blue in **Figure 6A**) is much higher, suggesting that V^{5+} species contained in this glass have a special configuration enhancing CT processes.

The excitations identified here at 280 and 350 nm correspond to the energy of the UV-edge observed in the optical absorption study. The link between the two observations is confirmed by the very good correlation between the emission intensity and the UV-edge, as shown in **Figure 6B**. The lower energy position of the UV-edge can be correlated with the number of non-bridging oxygen, and to the bond strength (e.g., Hensler and Lell, 1969; Laorodphan et al., 2016), thus the trend observed agrees with depolymerization, and in turn, with the thermal and physical property variations observed for these glasses. However, here again, the sample NAV66.10 that had an exceptionally high photoluminescence emission and an intermediate polymerization falls above the observed correlation. To explain such high emission intensity compared to the other glass compositions, we could take into account the low absorption coefficient in the visible region of the peralkaline NAV66.10 sample, and thus, the possibility of having self-absorption of the fluorescence in all other compositions. All the same, there is not a linear correlation between the absorbance values at 580 nm and PL emission intensity, and the shape of the photoluminescence emission spectra is almost identical for all glasses. Thus, NAV66.18 emission is only marginally lowered by self-absorption. PL emission intensity variations should be explained by other mechanisms, most probably related to V local surrounding. Only further structural observation can help to identify the local structure of V^{5+} responsible for such a high CT capacity.

Glass Structure

In **Figure 7** are reported the parallel (VV) and cross-polarized (VH) Raman spectra of pristine and V-bearing DiAn and NAS glasses. Raman spectra of V-bearing glasses show vibrational modes both related to vanadium and silicon groups that mainly overlap in the frequency range of about 700 to 1,000 cm^{-1}.

The Raman spectrum of the pristine DiAn glass has distinct contributions, typical of a Ca-Mg aluminosilicate glass containing ∼50 mol% SiO_2 (Mysen et al., 1979; Mysen and Richet, 2005). Raman vibrations related to the pristine NAS glasses are discussed in details in (Cicconi et al., 2017). In the pristine aluminosilicate glasses, the main vibrations occurring in the frequency region between 400 and 800 cm^{-1} were assigned to T-O-T intertetrahedral linkages and breathing vibrations of 4- and 3-ring members (defect bands D_1 and D_2; where T represents the tetrahedrally coordinated cation, i.e., Al a/o Si). The main band position decreases as expected with polymerization: 580 cm^{-1} for DiAn, 510 cm^{-1} for NAV66.10, and 490 cm^{-1} for NAV66.18. In the high-frequency region (850–1,300 cm^{-1}) there is the so-called *Q*-range, where vibrations related to Si-O asymmetric stretching can be found. This region shifts to higher frequency with polymerization. Si-O-Si ring and Si-O stretching motions are strongly polarized bands, thus, their intensity drastically decreases when collected as cross-polarized (VH). Indeed, the polarization ratio (PR), that is the intensity ratio between the perpendicular and the parallel components of Raman scattered light $PR = \frac{I_{VV}}{I_{VH}}$ is > 2.5, indicating highly polarized bands.

The Raman spectra of doped DiAn5V and DiAn10V glasses, compared to the pristine one, show additional intense vibration modes, indicating the combined presence of modes both related to the silicate network and to the vanadium ones (marked in

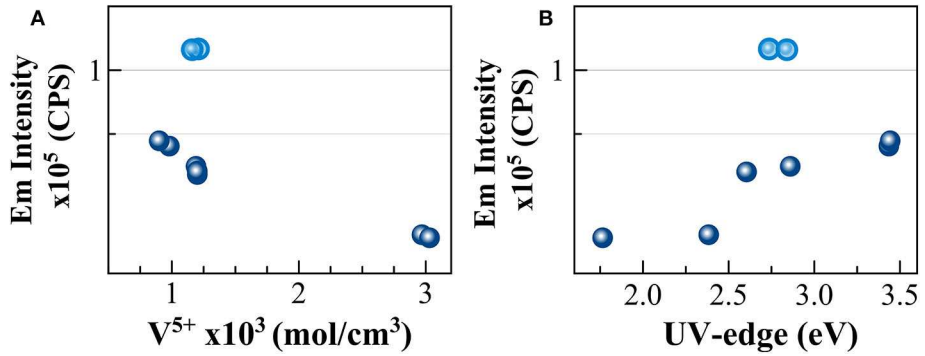

FIGURE 6 | Correlation between the intensity of the photoluminescence emission and **(A)** concentration for volume unit of V^{5+} species and **(B)** UV-edge energy (eV). Light blue circles identify NAV66.10 glasses.

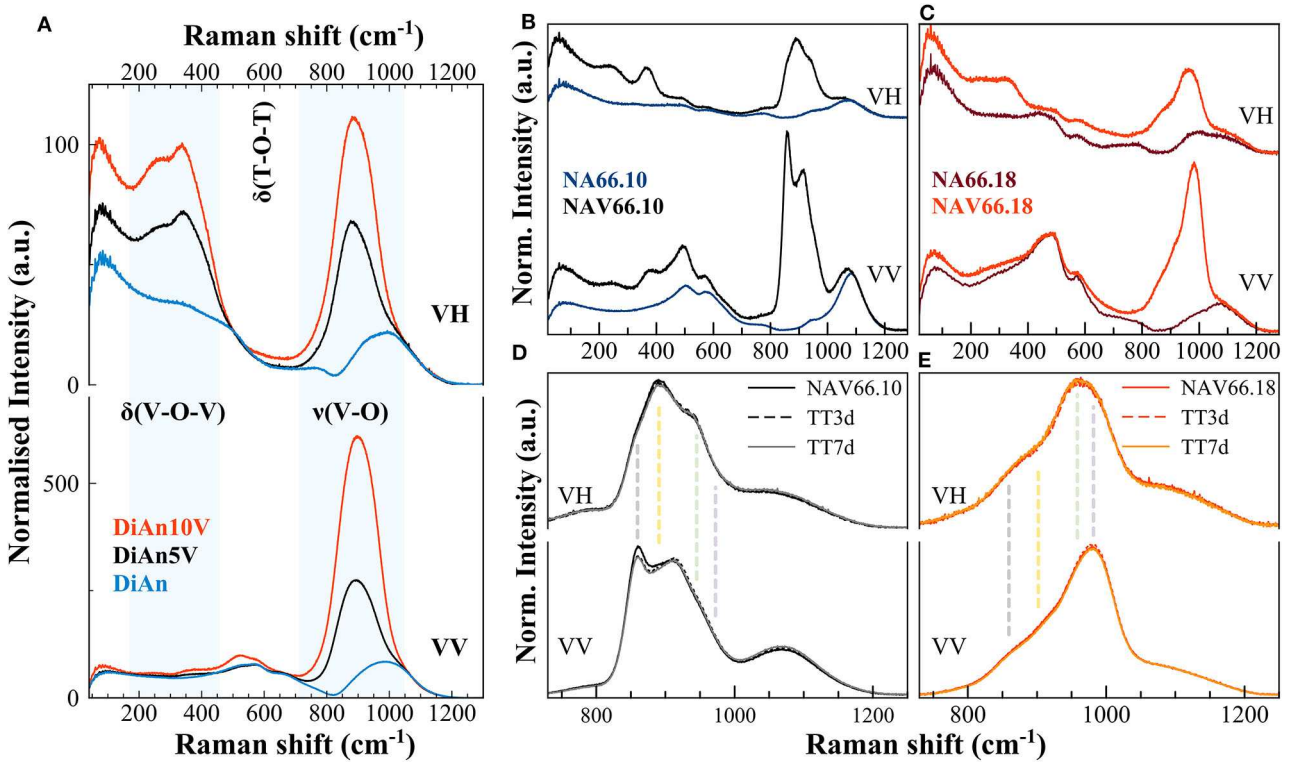

FIGURE 7 | (A–C) Parallel (VV) and cross-polarized (VH) Raman spectra of pristine and V-bearing DiAn and NAS glasses, respectively. Shaded areas highlight the vibrations related to the V networks. Si-O-Si ring and Si-O stretching motions are highly polarized bands; thus, their intensity drastically decreases when collected as cross-polarized. **(D,E)** Raman spectra of V-bearing NAS glasses after thermal treatments above Tg, of 3 (TT3d) and 7 days (TT7d). Vertical dashed lines highlight the different vibrations, each related to distinct V species (see text for details).

Figure 7A). In the low-frequency region (~150–500 cm^{-1}) there are depolarized bands related to bending vibrations of trigonal VO_5 bipyramids (Attos et al., 1997). In the high-frequency portion, above 700 cm^{-1}, a strong asymmetric band rises when vanadium is added, and its intensity increases by increasing V content. This broad band might contain several vibrations, both related to symmetric stretching of V-O-V bonds in penta-coordinated VO_4 groups (tetragonal pyramid $V^{4+}O_5$ at ~885 cm^{-1}), and at least three stretching modes of $V^{5+}O_4$ tetrahedra with a V =O apex between 900 and 1050 cm^{-1} (Attos et al., 1997 and references therein). The broad band partially overlaps with the silica asymmetric stretching modes, making vibrations assignment very difficult, with the presence of V masking most of the contributions of the aluminosilicate network. Precise observation of the silica Main band and of the D_2 band between 500 and 700 cm^{-1}, as well as the region of the Si-O stretching

modes above 1,100 cm^{-1}, present no significant modification. The introduction of up to 4.8 mol% of V_2O_5 does not perturb significantly the aluminosilicate network.

The Raman spectra of alkali-bearing glasses strongly differ as well when containing vanadium (**Figures 7B,C**). However, as for DiAn, in the regions not affected by the vibrations related to V species, the aluminosilicate network remains almost unchanged. In V-doped peralkaline glass (NAV66.10) several prominent features are related to the V network (vertical dashed lines in **Figures 7D,E**). In the low-frequency region, the bending vibrations of trigonal VO_5 bipyramids (∼250 and ∼370 cm^{-1}) are strong, and these bands are highly depolarized (**Figure 7B**). In the high-frequency region, vanadium vibrations are rather well-separated from the silica stretching modes. In the peralkaline glass, the complex nature of the strong vanadium band centered at ∼900 cm^{-1} is undoubtedly discernible, with the split of the main peak in two components. Additionally, another side contribution is clearly visible at 960 cm^{-1}. Moreover, the cross-polarized spectrum of NAV66.10 glass highlights the presence of a depolarized band, centered at ∼893 cm^{-1} (vertical dashed lines in **Figure 7D**). In the peraluminous glass (NAV66.18), the vanadium vibrations in the high frequency (HF) portion are shifted at higher values (maximum at ∼ 980 cm^{-1}) (**Figures 7C,E**). Moreover, the whole band is particularly asymmetric, with the barycenter moved ∼70 cm^{-1} toward higher frequencies. In the low-frequency region, the bending vibrations of trigonal VO_5 bipyramids were shifted at lower frequencies and were broader and weaker compared to the peralkaline glasses, suggesting a different distribution of the vanadium species (**Figure 7C**). Based on studies done on SiO_2 and silicate glasses, the positive anti-symmetrical variation between vanadium low- and high-frequency envelopes, together with the shift toward higher wavenumber of the HF portion, might indicate shorter V–O bond length and higher degrees of polymerization.

Since the majority of vanadium ions are oxidized (V^{5+} > 90%; see **Tables 1**, **3**) the complexity of the vibrations might be explained by the occurrence of several V^{5+} species, with configurations resembling the ones of P^{5+} species. Hence, some assumptions on the possible V–O bonding and first neighbors can be done, commensurate with the glass chemistry and the correspondences with the P^{5+} species. Likely, all Al, Si, and V atoms are exclusively tetrahedrally coordinated, and four-fold coordinated vanadium atoms, depending on the kind of neighbors can have several configurations. For instance, the excessing amount of Na^+ ions in the peralkaline glass could lead to the formation of metavanadate units in which a V^{5+} tetrahedral is connected only by one oxygen to the network. Whereas, the availability of Al ions in the peraluminous glass favors the creation of neutral $AlVO_4$ units by the association of vanadium VO_2^+ tetrahedral units with AlO_2^- ones. Other possible species involve V atoms that are tetrahedrally coordinated to two or three bridging oxygen (BO). This complexity could be represented by using the Q^n-species notation, similarly to the one used to represent Si^{4+} and P^{5+} connectivity. Indeed, Q represents a four-fold coordinated cation, and the apex n denotes the number of BO. In a tetrahedral, the more you have BO, the higher the covalency of the bond is between the central cation and the oxygens. Therefore, the Q^n species vibrate at a higher frequency when n increases.

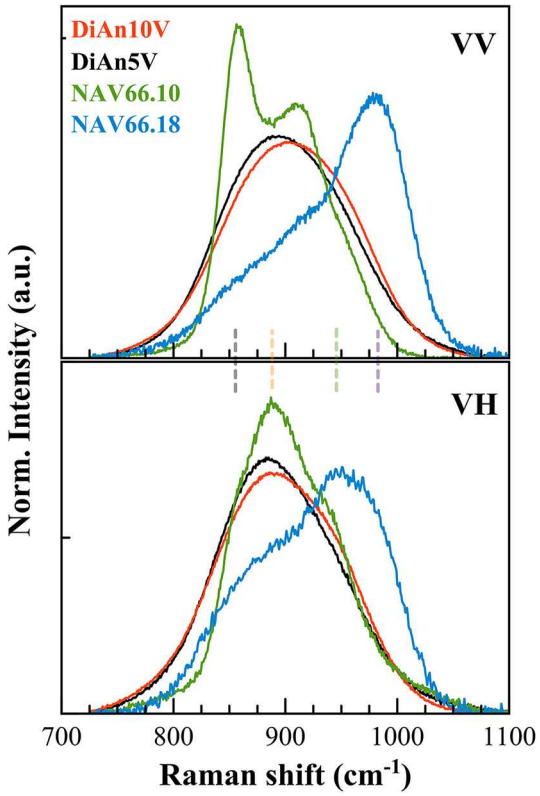

FIGURE 8 | Polarized V signals have been extracted by a direct subtraction of the respective pristine glass signals and normalized on the total area. The extracted spectra highlight the vibrations exclusively coming from V. Four main contributions can be discriminated at ∼855, 890, 960, and 985 cm^{-1} (vertical dashed lines, as in **Figures 7D,E**).

As can be seen in **Figure 7**, the doped glasses are always appearing in excess compared to the respective pristine glasses, because of the strong vanadium vibration modes. It is then possible to extract the signal exclusively coming from the V vibrations by making a direct subtraction of both spectra. The exclusive Vanadium Raman contributions are plotted in **Figure 8** for all glasses (the polarized signals are renormalized to the total area). Here, clearly, the four different contributions can be appreciated in all glasses, albeit with different intensities depending on glass chemistry or vanadium content. In detail, four contributions can be discriminated which are much more evident in the alkali aluminosilicate glasses: at ∼855, ∼890; ∼960, and ∼985 cm^{-1} (vertical dashed lines, as in **Figures 7D,E**). For the DiAn series, only a large envelop embedding the different V species could be observed until now. All the same, despite the broad band, in the subtracted spectra in **Figure 8**, we can observe a shift toward higher frequencies for DiAn10V, from which three considerations can be done: (i) a higher vanadium content induces the increase of the vibration at higher frequencies (∼985 cm^{-1}), at the expenses of the one at ∼890 cm^{-1}; (ii) the position of the dashed lines deduced from the NAS glasses perfectly

reproduce the shoulders observed in DiAn glasses above 850 cm^{-1}; and (iii) a further vibration is present in DiAn5 and DiAn10V glasses, at a lower frequency of ∼815 cm^{-1}.

In order to discriminate the different possible vanadium populations, we used the polarizability of the vibration modes calculated as ratio PR between the parallel and the cross-polarized components after the subtraction and before renormalization. This approach allowed us to evaluate graphically the polarizability (that means the symmetric or asymmetric nature of the vibration) of the different components that are embedded in the broad frequency region between 700 and 1,300 cm^{-1}. **Figure 9** reports the calculated PR of the different V-doped glasses and the probable V^{5+} species associated with each contribution. Indeed, based on the considerations done above and on the extent of the degree of polarizability, four probable Q^n species have been taken into account. By looking at the Raman spectra reported in **Figure 8** and to the PR in **Figure 9**, it is clear that the main peak at ∼850 cm^{-1} in NAV66.10 glass is highly polarized with its PR = 3.4. Likewise, the other intense band centered at 917 cm^{-1} is nearly doubled in parallel polarized spectra. Thus, these two contributions must represent asymmetric V^{5+} species, such as the ones related to Q^1 and Q^3 species. Since the only glass having such sharp prominent features was the peralkaline one, it is rational to assign the band at ∼850 cm^{-1} to Q^1 species connected to Na ions, and the band at ∼917 cm^{-1} to V = O apex of the V^{5+} species. Conversely, in the peraluminous glass, the most prominent feature was at ∼985 cm^{-1}. This vibration is likely related to the association of vanadium with AlO_2^- tetrahedral units. To support this notion, there are two pieces of evidence: (i) this band has a higher frequency position and (ii) the lower polarizability, compared to the V = O apex band. Moreover, NAV66.18 is the only glass with an exceeding amount of aluminum ions compared to network modifiers ones. The V–Al relationship, associated with the creation of NBO in the network could explain the extremely high drop of Tg seen for the peraluminous glass.

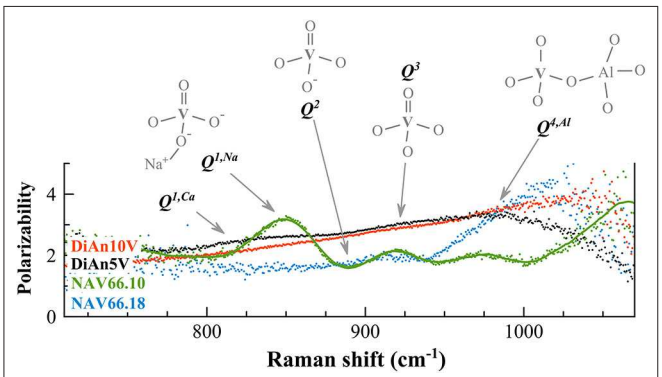

FIGURE 9 | The calculated polarization ratios of the different V-doped glasses (polarizability) allowed us to discriminate the different vibrations in the Raman frequency range between 750 and 1,050 cm^{-1} exclusively related to vanadium. To each contribution is associated the probable V^{5+} species responsible for the vibration. Details of the V species are reported in the text.

V-doped DiAn glasses have a broader band that englobe all possible V-vibration modes, and an almost constant PR = 2.5, from which almost no contributions at 850 and 917 cm^{-1} are distinguishable in **Figure 9**. Only a broad weak band is visible (∼815 cm^{-1}), that might be associated to metavanadate units in which a V^{5+} tetrahedral is connected only by one oxygen to the aluminosilicate network, and has Ca^{2+} ions connected to the NBO ($Q^{1,Ca}$). This uniform behavior can be explained by the lesser localization of the alkali earth cation modifier, compared to Na. Furthermore, it is known on phosphate glasses that the electron of the double bond is not localized giving an identical charge to the apical O and the NBOs (Brow et al., 1995). If that is also the case for V, it is then understandable that the distinction between Q^1, Q^2, and Q^3 species is difficult to make and that a large continuum exists.

This new understanding of the V structure can help us to attempt a better assignment of the atomic environment underlying the V^{5+} CTs noticed in section Photoluminescence. It was observed that this CT was very intense in NAV66.10 and decreased by a factor 2 in NAV66.18 and DiAn5V. The preponderant presence of $Q^{4,Al}$ structure in NAV66.18 is associated with a disappearance of the apical oxygen which prevents the formation of the V^{4+} excited state needed for the CT. Overall NAV66.10 and DiAn5V present both low *n* Q species significantly polarizable. The main structural difference between them is the sharp Q^1 population present only in NAV66.10, which presents simultaneously an apical oxygen, and well-localized NBO. It is reasonable to assert that the CT luminescence observed is associated with these $Q^{1,Na}$ units.

Thermal treated glasses (3 days; label TT33d) show almost no variations in the Raman vibrational bands related to the distribution of apical oxygens and VO_4 units of DiAn glasses. Only the DiAn5V high frequency envelop has a slightly lower VO_4 component, and changes are limited to relative intensities and not on band positions. Thermal treatments of NAV66.10 composition induces small visible structural changes. Deconvolution of the Raman signals in the frequency range 700–1250 cm^{-1} highlights the decrease of the area related to the Q^1 contribution (∼ −8%) after 7 days of thermal treatment. Thermal treatment of the peraluminous sample induces also only small changes depending on the time. After 3 days (TT3d) there is an intensity decrease of the silica D_2 defect line and an intensity increase (∼ +2%) of the band at 980 cm^{-1}. Overall, thermal treatment does not produce visible changes on the aluminosilicate network.

Mechanical Properties

The Brillouin spectra were collected in two different geometries: backscattering and platelet geometry (Kieffer, 2015). In the platelet geometry, both longitudinal and transversal acoustic modes can be observed. Typical Brillouin spectra in platelet and backscattering geometry are given in **Figure 10** for DiAn and NAS samples. The Poisson ratio, ν, can be obtained directly from the ratio between the transverse and longitudinal Brillouin shift. Theoretically, the platelet geometry is enough to get the sound velocities and from them using the determined densities to deduce all the elastic moduli. However, the data then obtained

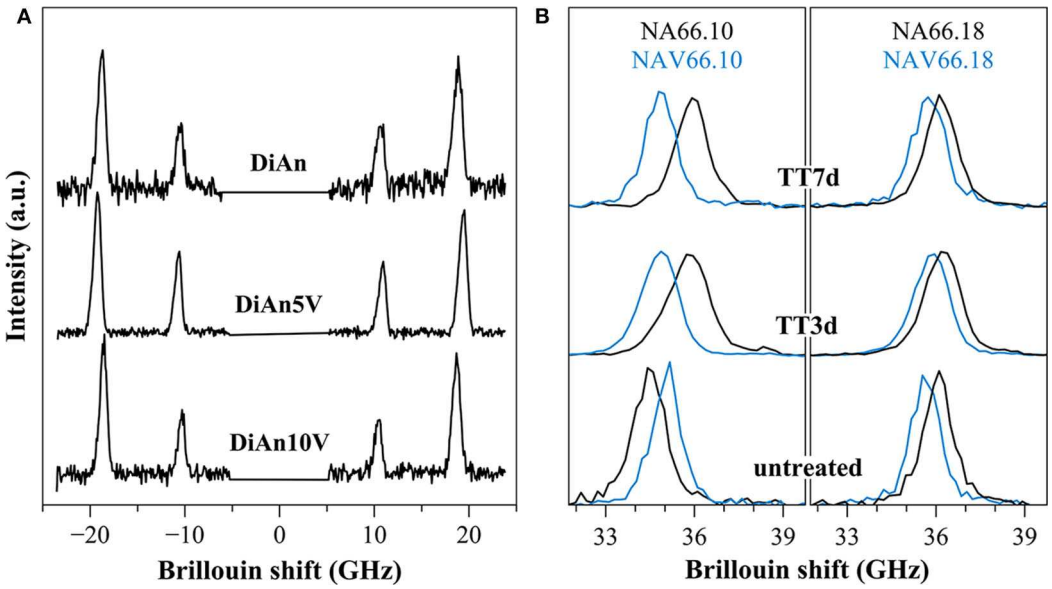

FIGURE 10 | (A) Brillouin spectra for pristine DiAn and V-bearing glasses collected in platelet geometry, where both longitudinal and transversal acoustic modes can be observed. **(B)** Example of Brillouin spectra collected in backscattering geometry for V-free and V-doped NA66.10 and NA66.18 glasses. The evolution of the signals for different thermal treatment times (3 and 7 days) is shown.

TABLE 4 | Elastic properties (GPa) and Brillouin shift (GHz) of all.

	ν	ν *Calc.*	M (GPa)	*M Calc.*	G (GPa)	K (GPa)	E (GPa)	Brillouin shift (GHz)
±	0.004		0.5		0.9	0.8	2.5	0.1
DiAn	0.273	0.261	123.4	111.4	38.5	72.1	98.0	43.7
DiAn5V	0.274	0.261	121.6	111.0	37.9	71.1	96.5	43.5
DiAn10V	0.275	0.261	112.4	110.3	34.9	65.9	88.9	42.4
NA66.10	0.224	0.240	77.0	85.1	27.4	40.5	67.0	34.5
NAV66.10	0.224	0.240	77.3	85.4	27.5	40.7	67.3	35.1
NA66.18	0.215	0.238	82.5	94.1	29.9	42.6	72.7	36.1
NAV66.18	0.214	0.238	79.8	93.6	29.0	41.1	70.5	35.7

The Brillouin shift reported here was obtained in backscattering configuration at 488 nm wavelength and allowed determining the longitudinal modulus M. The Poisson's ratio, ν, is calculated from platelet geometry not reported here. All the other elastic parameters are deduced from M and ν. Calc.: calculated according to the Makishima and Mackenzie (1973) model.

are very sensitive to the angle used, which is difficult to determine with high enough precision. To reduce the uncertainty, the backscattering geometry, where no angle problem can occur, was complementary used. The backscattered Brillouin shifts are reported in **Table 4**. Using the refractive index, corrected at 488 nm using the Abbe number, and the aforementioned backscattered Brillouin shift, the longitudinal modulus M can be determined. Then, by using both ν and M all the elastic parameters are deduced (see **Table 4**). Later in this section, only ν and M will be discussed, since they are the values closest to measurements. The values found are in agreement with previous studies on similar systems (Pönitzsch et al., 2016; Weigel et al., 2016).

Within each series, it can be noticed that ν stays constant, which means that the addition of V or the thermal treatment are not affecting ν. On the contrary, M evolves differently with the addition of V, for each series. In the DiAn series, on average, M decreases by 1.7% for each mol of V_2O_5 added. In the NA66.10, M stays constant with the addition of V. And in what could look surprising, it also decreases by 1.7% for each mol of V_2O_5 added in the NA66.18 series.

Elastic properties have a complex evolution with composition. The model developed by Makishima and Mackenzie (1973) can help us to better understand the evolutions here observed. This model takes into account two parameters: the atomic packing volume and the dissociation energy per unit volume. The packing volume increases with the network polymerization in the order of DiAn, NA66.10. and NA66.18. It increases also with the addition of V_2O_5, following the evolution of the molar volume discussed in section Glass Chemistry, V Redox

State, and Optical Basicity. At the opposite end, the dissociation energy is more sensitive to the elements and especially to the presence of Na, which strongly decreases it. Using this model and the parameters revised by Inaba et al. (2000) theoretical values of both ν and M were calculated and reported in **Table 4**. The values experimental and theoretical significantly differ. The model always overestimates the elastic moduli for the DiAn series and underestimate those for the sodium-bearing glasses. However, the model respects the trend observed, not only between the series, but also with the addition of V_2O_5. Indeed, for both series DiAn and NA66.18, the addition of V induces a decrease of M around 0.25% per V_2O_5 mol added and predict an increase in the case of NA66.10 (see **Figure 11**). The agreement on the trend is very interesting because it underlines the importance of dissociation energy. Its lack of precision shows also its limitation. A similar disagreement was already shown for aluminosilicate glasses (Eagan and Swearekgen, 1978; Inaba et al., 2000; Lin and Liu, 2006; Pönitzsch et al., 2016), and many factors were proposed to explain these disagreements. The calculations can depend a lot on the coefficient use and especially the way to determine properly the atomic packing density (Lin and Liu, 2006; Pönitzsch et al., 2016). The usefulness of the atomic packing density was recently questioned by Zeidler et al. (2014), since the oxygen radius can change a lot. Moreover, the approach of Makishima and Mackenzie only takes into account the mean volumetric values and does not consider the topology of the network. In the case of partially covalent bonds, like in the system investigated here, local intertetrahedral angles have a strong effect on the elastic properties as shown by the non-linear evolution of the Brillouin shift with pressure in sodium aluminosilicate glasses (Sonneville et al., 2013).

No significant variations of the mechanical properties were observed with thermal treatment.

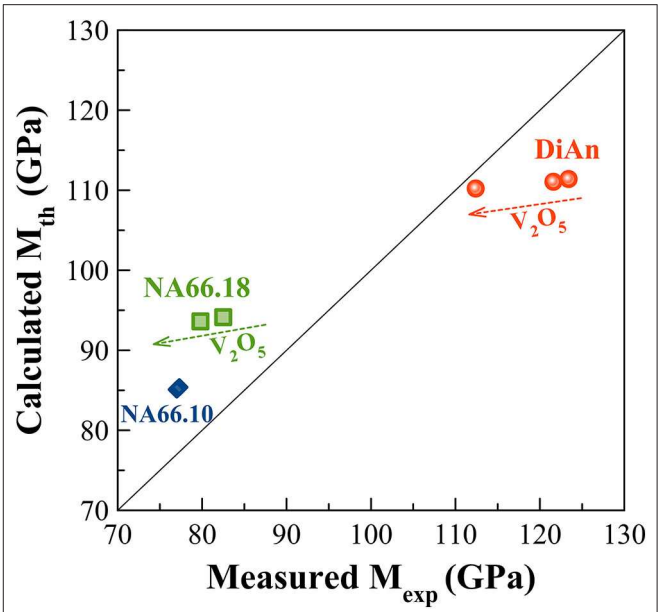

FIGURE 11 | Experimental Longitudinal modulus (M_{exp}) against the Theoretical one (M_{th}) calculated according to the Makishima and Mackenzie (1973) model. The calculated values always overestimate the elastic moduli for the DiAn series and underestimate those for the sodium aluminosilicate glasses. However, the model respects the experimental trends observed not only between the series but also with the addition of V_2O_5.

CONCLUSIONS AND FINAL REMARKS

A large screening of the properties of Vanadium-bearing aluminosilicate glasses was realized through the study of three glasses, having very different network polymerizations. This work complements the very low number of data related to this element in silicates glasses. First of all, we verified that the bulk chemistry (presence of alkali or alkaline-earth ions, Al/Na molar ratio) has a first-order influence on the vanadium speciation, and in turn, on the optical properties. These changes in speciation, evidenced by the different glass colors, were realistically quantified using optical absorption spectroscopy. However, complementary investigations using ESR or XPS spectroscopies would permit to improve the extinction coefficients' reliability.

The average redox state of vanadium and its site symmetry can be modified just above Tg. Thermal treatments induce changes in the vanadium speciation (average oxidation state, bond distances, and oxygen coordination) and on the evolution of V^{3+} V^{4+} and V^{5+} proportions. The variations observed on the vanadium redox state upon thermal treatment are still too narrow in the investigated conditions to produce clear variations on the glass network and the mechanical properties.

Because of the versatility of this element, straightforward structure–property relations are difficult to establish. The structural role of Vanadium needs to be better understood in a more fundamental way. The strong drop in the glass transition temperature, as well as the reduction of the mechanical properties for some compositions, could suggest a modifier role of Vanadium. However, no proof of associated depolymerization of the silicate network could be observed. The Vanadium seems to act as a network former, partially connected to the silica aluminate network. A close observation of the vibrations involving V and their polarizability using Raman spectroscopy shown that V is surrounded by one to four bridging oxygens. The chemistry of the glass has a strong effect on the repartition of these different environments. This new attempt to describe the V network would certainly benefit from complementary NMR studies, or more in general, element selective techniques.

For the photoluminescence properties, the change of chemistry did not affect the wavelength of the large yellow emission of Vanadium, making it a not-easily tunable phosphorous. At the opposite end, its intensity is enhanced dramatically with the presence of Na. The CT mechanism underlying the emission was assigned to four fold coordinated V^{5+} having an apical oxygen (V = O) and surrounded by two non-bridging oxygens.

The addition of V in the sample NA66.10 has shown simultaneously a decrease of the Tg of 20 K, constant glass

stability, and no change of the mechanical properties. This result is very encouraging in view of the efforts currently considered to reduce energy consumption. The introduction of V in the formulation of glass for which transparency is not an issue as reinforcement fibers could be a very promising solution.

DATA AVAILABILITY STATEMENT

The raw data supporting the conclusions of this article will be made available by the authors, without undue reservation.

AUTHOR CONTRIBUTIONS

DL, DB, and LW designed the project, provided funds and supervised the progress. MC, ZL, and TU performed experiments, and data analysis. MC and DL did the data interpretation and wrote the article. All authors contributed to the article and approved the submitted version.

FUNDING

This work was supported by Deutsche Forschungsgemeinschaft (DFG) project PP1594: Topological Engineering of Ultrastrong Glasses.

ACKNOWLEDGMENTS

The authors thank the people of the Glas group WW3 Erlangen for the help and the useful discussions. We would like to thank two reviewers for their constructive comments.

REFERENCES

Anpo, M., Tanahashi, I., and Kubokawa, Y. (1980). Photoluminescence and photoreduction of vanadium pentoxide supported on porous Vycor glass. *J. Phys. Chem.* 84, 3440–3443. doi: 10.1021/j100462a026

Attos, O., Massot, M., Balkanski, M., Haro-Poniatowski, E., and Asomoza, M. (1997). Structure of borovandate glasses studied by Raman spectroscopy. *J. Non Cryst. Solids* 210, 163–170. doi: 10.1016/S0022-3093(96)00596-0

Brow, R. K., Tallant, D. R., Myers, S. T., and Phifer, C. C. (1995). The short-range structure of zinc polyphosphate glass. *J. Non Cryst. Solids* 191, 45–55. doi: 10.1016/0022-3093(95)00289-8

Cicconi, M. R., De Ligny, D., Gallo, T. M., and Neuville, D. R. (2016). Ca neighbors from XANES spectroscopy: a tool to investigate structure, redox, and nucleation processes in silicate glasses, melts, and crystals. *Am. Mineral.* 101, 1232–1235. doi: 10.2138/am-2016-5663

Cicconi, M. R., Giuli, G., Ertel-Ingrisch, W., Paris, E., and Dingwell, D. B. (2015). The effect of the [Na/(Na+K)] ratio on Fe speciation in phonolitic glasses. *Am. Mineral.* 100, 1610–1619. doi: 10.2138/am-2015-5155

Cicconi, M. R., Neuville, D. R., Blanc, W., Lupi, J. F., Vermillac, M., and De Ligny, D. (2017). Cerium/aluminum correlation in aluminosilicate glasses and optical silica fiber preforms. *J. Non Cryst. Solids* 475, 85–95. doi: 10.1016/j.jnoncrysol.2017.08.035

Cody, G. D., Mysen, B., Sághi-Szabó G., and Tossell, J. A. (2001). Silicate-phosphate interactions in silicate glasses and melts: I. A multinuclear (27Al,29Si,31P) MAS NMR and ab initio chemical shielding (31P) study of phosphorous speciation in silicate glasses. *Geochim. Cosmochim. Acta* 65, 2395–2411. doi: 10.1016/S0016-7037(01)00597-X

Dietzel, A. (1948). Glasstruktur und Glaseigenschaften. *Glastechn. Ber.* 22, 41–50.

Duffy, J. A. (1993). A review of optical basicity and its applications to oxidic systems. *Geochim. Cosmochim. Acta* 57, 3961–3970. doi: 10.1016/0016-7037(93)90346-X

Duffy, J. A. (1996). Redox equilibria in glass. *J. Non Cryst. Solids* 196, 45–50. doi: 10.1016/0022-3093(95)00560-9

Dzwigaj, S., Matsuoka, M., Anpo, M., and Che, M. (2000). Evidence of three kinds of tetrahedral vanadium (V) species in vsiβ zeolite by diffuse reflectance UV-visible and photoluminescence spectroscopies. *J. Phys. Chem. B* 104, 6012–6020. doi: 10.1021/jp0000331

Eagan, R. J., and Swearekgen, J. C. (1978). Effect of composition on the mechanical properties of aluminosilicate and borosilicate glasses. *J. Am. Ceramic Soc.* 61, 27–30. doi: 10.1111/j.1151-2916.1978.tb09222.x

Farah, H. (2008). Optical basicity analysis of vanadium-bearing silicate glasses/melts. *J. Am. Ceramic Soc.* 91, 3915–3919. doi: 10.1111/j.1551-2916.2008.02771.x

Farah, H., and Brungs, M. (2003). Oxidation-reduction equilibria of vanadium in CaO-SiO2, CaO-Al2O3-SiO2 and CaO-MgO-SiO2 melts. *J. Mater. Sci.* 38, 1885–1894. doi: 10.1023/A:1023588010572

Gao, G., Meszaros, R., Peng, M., and Wondraczek, L. (2011). Broadband UV-to-green photoconversion in V-doped lithium zinc silicate glasses and glass ceramics. *Opt. Express* 19:A312. doi: 10.1364/OE.19.00A312

Giuli, G., Paris, E., Mungall, J., Romano, C., and Dingwell, D. (2004). V oxidation state and coordination number in silicate glasses by XAS. *Am. Mineral.* 89, 1640–1646. doi: 10.2138/am-2004-11-1208

Grammes, T., Limbach, R., Bruns, S., van Wüllen, L., de Ligny, D., Kamitsos, E. I., et al. (2020). Tailoring the mechanical properties of metaluminous aluminosilicate glasses by phosphate incorporation. *Front. Mater.* 7:115. doi: 10.3389/fmats.2020.00115

Hamnabard, Z., Khalkhali, Z., Qazvini, S. S. A., Baghshahi, S., and Maghsoudipour, A. (2012). Preparation, heat treatment and photoluminescence properties of V-doped ZnOSiO 2B 2O 3 glasses. *J. Lumin* 132, 1126–1132. doi: 10.1016/j.jlumin.2011.12.083

Hensler, J. R., and Lell, E. (1969). "Ultraviolet absorption in silicate glasses," in *Frontiers in Glass Science and Technology, Proceedings Annual Meeting International Commission on Glass*, eds S. Bateson and A. G. Sadler (Toronto, ON), 51–57.

Hrubý, A. (1972). Evaluation of glass-forming tendency by means of DTA. *Czechoslovak J. Phys.* 22, 1187–1193. doi: 10.1007/BF01690134

Inaba, S., Todaka, S., Ohta, Y., and Morinaga, K. (2000). Equation for estimating the Young's modulus, shear modulus and Vickers hardness of aluminosilicate glasses. *Nippon Kinzoku Gakkaishi J. Japan Institute Metals* 64, 177–183. doi: 10.2320/jinstmet1952.64.3_177

Johnston, W. D. (1965a). Optical spectra of the various valence states of vanadium in Na2 O.2SiO2 glass. *J. Am. Ceramic Soc.* 48, 608–611. doi: 10.1111/j.1151-2916.1965.tb14688.x

Johnston, W. D. (1965b). Oxidation-reduction equilibria in molten Na2O.2SiO2 glass. *J. Am. Ceramic Soc.* 48, 184–190. doi: 10.1111/j.1151-2916.1965.tb14709.x

Khater, G. A. (2010). Glass-ceramics in the CaO–MgO–Al2O3–SiO2 system based on industrial waste materials. *J. Non Cryst. Solids* 356, 3066–3070. doi: 10.1016/j.jnoncrysol.2010.02.030

Kieffer, J. (2015). "Brillouin light scattering," in *Modern Glass Characterization.* (Hoboken, NJ: John Wiley & Sons, Inc), 1–51 doi: 10.1002/9781119051862.ch4

Kniec, K., and Marciniak, L. (2019). Different strategies of stabilization of vanadium oxidation states in Lagao3 nanocrystals. *Front. Chem.* 7:520. doi: 10.3389/fchem.2019.00520

Kornatowski, J., Sychev, M., Kuzenkov, S., Strnadová, K., Pilz, W., Kassner, D., et al. (1995). V-Ti and V-AI silicate molecular sieves of MFI topology: synthesis and characteristics. *J. Chem. Soc. Faraday Trans.* 91, 2217–2227. doi: 10.1039/FT9959102217

Laorodphan, N., Pooddee, P., Kidkhunthod, P., Kunthadee, P., Tapala, W., and Puntharod, R. (2016). Boron and pentavalent vanadium local environments in binary vanadium borate glasses. *J. Non Cryst. Solids* 453, 118–124. doi: 10.1016/j.jnoncrysol.2016.10.005

Lebouteiller, A., and Courtine, P. (1998). Improvement of a bulk optical basicity table for oxidic systems. *J. Solid State Chem.* 137, 94–103. doi: 10.1006/jssc.1997.7722

Leister, M., Ehrt, D., von der Gönna, G., Rüssel, C., and Breitbarth, F. W. (1999). Redox states and coordination of vanadium in sodium silicates melted at high temperatures. *Phys. Chem. Glasses* 40, 319–325.

Lin, C. C., and Liu, L. G. (2006). Composition dependence of elasticity in aluminosilicate glasses. *Phys. Chem. Miner.* 33, 332–346. doi: 10.1007/s00269-006-0084-z

Makishima, A., and Mackenzie, J. D. (1973). Direct calculation of Young's moidulus of glass. *J. Non Cryst. Solids* 12, 35–45. doi: 10.1016/0022-3093(73)90053-7

McKeown, D. A., Galeener, F. L., and Brown, G. E. (1984). Raman studies of Al coordination in silica-rich sodium aluminosilicate glasses and some related minerals. *J. Non Cryst. Solids* 68, 361–378. doi: 10.1016/0022-3093(84)90017-6

Moretti, R. (2005). Polymerisation, basicity, oxidation state and their role in ionic modelling of silicate melts. *Ann Geophys.* 48, 583–608. doi: 10.4401/ag-3221

Mysen, B. O. (1992). Iron and phosphorus in calcium silicate quenched melts. *Chem. Geol.* 98, 175–202. doi: 10.1016/0009-2541(92)90184-7

Mysen, B. O., and Richet, P. (2005). *Silicate Glasses and Melts : Properties and Structure*, 1st edn. Berlin: Springer.

Mysen, B. O., Virgo, D., and Scarfe, C. M. (1979). Viscosity of silicate melts as a function of pressure: structural interpretation. *Carnegie Inst Washington Yearbook* 78, 551–556.

Nascimento, M. L. F., Souza, L. A., Ferreira, E. B., and Zanotto, E. D. (2005). Can glass stability parameters infer glass forming ability? *J. Non Cryst. Solids* 351, 3296–3308. doi: 10.1016/j.jnoncrysol.2005.08.013

Neuville, D. R., and Mysen, B. O. (1996). Role of aluminium in the silicate network: *in situ*, high-temperature study of glasses and melts on the join SiO2-NaAlO2. *Geochim. Cosmochim. Acta* 60, 1727–1737. doi: 10.1016/0016-7037(96)00049-X

Ori, G., Montorsi, M., Pedone, A., and Siligardi, C. (2011). Insight into the structure of vanadium containing glasses: a molecular dynamics study. *J. Non-Crystalline Solids* 357:2571–2579. doi: 10.1016/j.jnoncrysol.2011.02.002

Pönitzsch, A., Nofz, M., Wondraczek, L., and Deubener, J. (2016). Bulk elastic properties, hardness and fatigue of calcium aluminosilicate glasses in the intermediate-silica range. *J. Non Cryst. Solids* 434, 1–12. doi: 10.1016/j.jnoncrysol.2015.12.002

Schraml-Marth, M., Wokaun, A., Pohl, M., and Krauss, H. L. (1991). Spectroscopic investigation of the structure of silica-supported vanadium oxide catalysts at submonolayer coverages. *J. Chem. Soci. Faraday Trans.* 87, 2635–2646. doi: 10.1039/ft9918702635

Schreiber, H. D. (1986). Redox processes in glass-forming melts. *J. Non Cryst. Solids* 84, 129–141. doi: 10.1016/0022-3093(86)90770-2

Shelby, J. E. (1985). Formation and properties of calcium aluminosilicate glasses. *J. Am. Ceramic Soc.* 68, 155–158. doi: 10.1111/j.1151-2916.1985.tb09656.x

Sonneville, C., De Ligny, D., Mermet, A., Champagnon, B., Martinet, C., Henderson, G. H., et al. (2013). *In situ* Brillouin study of sodium alumino silicate glasses under pressure. *J. Chem. Phys.* 139:074501. doi: 10.1063/1.4818335

Toplis, M. J., and Dingwell, D. B. (1996). The variable influence of P2O5 on the viscosity of melts of differing alkali/aluminium ratio: implications for the structural role of phosphorus in silicate melts. *Geochim. Cosmochim. Acta* 60, 4107–4121. doi: 10.1016/S0016-7037(96)00225-6

Toya, T., Tamura, Y., Kameshima, Y., and Okada, K. (2004). Preparation and properties of CaO–MgO–Al2O3–SiO2 glass-ceramics from kaolin clay refining waste (Kira) and dolomite. *Ceramics Int.* 30, 983–989. doi: 10.1016/j.ceramint.2003.11.005

Veber, A., Cicconi, M. R., Reinfelder, H., and de Ligny, D. (2018). Combined differential scanning calorimetry, raman and brillouin spectroscopies: a multiscale approach for materials investigation. *Anal. Chim. Acta* 998, 37–44. doi: 10.1016/j.aca.2017.09.045

Weigel, C., Le Losq, C., Vialla, R., Dupas, C., Clément, S., Neuville, D. R., et al. (2016). Elastic moduli of XAlSiO4 aluminosilicate glasses: effects of charge-balancing cations. *J. Non Cryst. Solids* 447, 267–272. doi: 10.1016/j.jnoncrysol.2016.06.023

Xiang, Y., Du, J., Smedskjaer, M. M., and Mauro, J. C. (2013). Structure and properties of sodium aluminosilicate glasses from molecular dynamics simulations. *J. Chem. Phys.* 139:044507. doi: 10.1063/1.4816378

Zeidler, A., Salmon, P. S., and Skinner, L. B. (2014). Packing and the structural transformations in liquid and amorphous oxides from ambient to extreme conditions. *Proc. Natl. Acad. Sci. U.S.A.* 111, 10045–10048. doi: 10.1073/pnas.1405660111

Conflict of Interest: The authors declare that the research was conducted in the absence of any commercial or financial relationships that could be construed as a potential conflict of interest.

frontiers in Materials

ORIGINAL RESEARCH
published: 28 July 2020
doi: 10.3389/fmats.2020.00189

Influence of Al_2O_3 Addition on Structure and Mechanical Properties of Borosilicate Glasses

Sebastian Bruns[1]*, *Tobias Uesbeck*[2,3]*, *Dominik Weil*[1], *Doris Möncke*[4], *Leo van Wüllen*[3], *Karsten Durst*[1] and *Dominique de Ligny*[2]

[1] Physical Metallurgy, Technical University Darmstadt, Darmstadt, Germany, [2] Institute of Glass and Ceramics, Friedrich-Alexander-University Erlangen-Nürnberg, Erlangen, Germany, [3] Institute of Physics, Augsburg University, Augsburg, Germany, [4] Inamori School of Engineering at the New York State College of Ceramics, Alfred University, Alfred, NY, United States

Alkali-borosilicate glasses are one of the most used types of glasses with a high technological importance. In order to optimize glasses for diverse applications, an understanding of the correlation between microscopic structure and macroscopic properties is of central interest in materials science. It has been found that the crack initiation in borosilicate glasses can be influenced by changes in network interconnectivity. In the NBS2 borosilicate glass system ($74.0SiO_2$-$20.7B_2O_3$-$4.3Na_2O$-$1.0Al_2O_3$ in mol%) two subnetworks are present, i.e., a silicate and a borate network. Increasing cooling rates during processing were found to improve glasses crack resistance. Simultaneously, an increase in the network interconnectivity accompanied by an increasing capacity for densification were noticed. Their individual contribution to the mechanic response, however, remained unclear. In the present study the borosilicate glasses were systematically modified by addition of up to 4.0 mol% Al_2O_3. Changes in the network connectivity as well as the short- and medium-range order were characterized using Raman and NMR spectroscopy. Both the Raman and the ^{11}B NMR results show that four-fold-coordinated boron is converted into three-fold-coordination as the Al_2O_3 content increases. Additionally, ^{27}Al NMR experiments show that aluminum is dominantly present in four-fold coordination. Aluminum-tetrahedra are thus charge balanced by sodium ions and incorporated into the silicate network. Finally, nanoindentation testing was employed to link the inherent glass structure and its network configuration to the mechanical glass response. It was found that the glass softens with increasing Al_2O_3 content, which enhances the crack resistance of the borosilicate glass.

Keywords: spectroscopy, Raman, Brillouin, NMR, mechanical testing, glass structure, indentation

OPEN ACCESS

Edited by:
Lothar Wondraczek, Friedrich Schiller University Jena, Germany

Reviewed by:
Satoshi Yoshida, Asahi Glass, Japan
Morten M. Smedskjaer, Aalborg University, Denmark

***Correspondence:**
Sebastian Bruns
s.bruns@phm.tu-darmstadt.de
Tobias Uesbeck
tobias.uesbeck@physik.uni-augsburg.de

Specialty section:
This article was submitted to Ceramics and Glass, a section of the journal Frontiers in Materials

Received: *10 January 2020*
Accepted: *22 May 2020*
Published: *28 July 2020*

Citation:
Bruns S, Uesbeck T, Weil D, Möncke D, van Wüllen L, Durst K and de Ligny D (2020) Influence of Al_2O_3 Addition on Structure and Mechanical Properties of Borosilicate Glasses. Front. Mater. 7:189. doi: 10.3389/fmats.2020.00189

INTRODUCTION

Nowadays oxide glasses are important structural and functional components. The variety of possible applications places different demands on the material. While glass fibers are intended to be stiff, glass used for protective screens needs to be rather flexible (Gross and Price, 2017; Januchta et al., 2019b). The reliability of glass, however, is usually limited by brittle fracture. Approaches to design damage resistant glass are of high scientific significance (Wondraczek et al., 2011); ranging

from local ion implantation (Price et al., 2009; Gross and Price, 2017) over compositional design (Malchow et al., 2015; Rosales-Sosa et al., 2016; Januchta et al., 2019b) to changes in the thermal history (Malchow et al., 2015; Zehnder et al., 2017a). Multi-component alkali-borosilicate glasses represent a widely used type of special glasses with a high technological importance. Low alkali glasses, for instance, exhibit a low thermal expansion coefficient and a relatively high softening temperature. They are highly resistant against thermal shock, chemically resistant, and exhibit a high hardness as well as good optical properties. This makes them suitable for a wide range of applications, such as for substrates in electronic devices or as household and laboratory ware (Ellison and Cornejo, 2010; Mauro, 2014; Smedskjaer et al., 2014). They are used for toxic and nuclear waste immobilization but also in high performance optics (Ehrt, 2000; Rouxel, 2007). A general understanding of the correlation between the network structure and the mechanical response is essential to tailor enhanced properties in multi-component alkali poor borosilicate glasses (Kurkjian et al., 2010; Wondraczek et al., 2011; Mauro, 2014).

Glass processing (thermal history and pressure) and chemical alterations can strongly influence the structure in boron-containing glasses. In this context, the coordination of boron can change from three-fold BO_3 (B^{III}) to four-fold $[BO_4]^-$ (B^{IV}) units. Thereby, differences in the structural homogeneity of the glass are introduced (Dell et al., 1983; Möncke et al., 2003, 2006; Wondraczek et al., 2007, 2010). The network structure of borosilicate glass can be investigated based on experimental ^{11}B NMR results (Dell et al., 1983; Wondraczek et al., 2007). The model by Dell and Bray (Yun and Bray, 1978; Yun et al., 1979; Dell et al., 1983) describes the mechanism behind the creation of non-bridging oxygen atoms (nbO) and thereby the structural evolution of the glass when alkali cations are added. The values of R and K, defined as $[Na_2O]/[B_2O_3]$ and $[Si_2O]/[B_2O_3]$, are especially helpful for predicting structural changes with chemical variation. Nevertheless, it has to be considered that the model of Bray and Dell exhibits some limitations. The model predicts complete phase separation for binary borosilicate glasses, whereas Wang and Stebbins (1998) and Martens and Müller-Warmuth (2000) were able to show that there is a considerable mixing of B_2O_3 and SiO_2 networks. With increasing amount of modifier oxides, neutral trigonal BO_3-units are transformed into charged $[BO_4]^-$ units. Thereby, planar units (B^{III}) are transformed into tetrahedral units (B^{IV}) reinforcing the three-dimensionality of the glass network. As a consequence, the network structure is strengthened (Biscoe and Warren, 1938; Vogel, 1994). In contrast to silica glass, where the network depolymerizes continuously as the network modifier content increases (and the share of nbO increases), borosilicate glasses behave differently. The network connectivity in borosilicate glasses initially increases, which strengthens the glass. At a certain point, when R reaches a value of 0.5, the behavior changes and a further increase of the modifier oxide concentration leads to the formation of nbO on trigonal borate and/or silicate tetrahedra (Milberg et al., 1972; Möncke et al., 2003; Winterstein-Beckmann et al., 2014a). In low-R glasses, where R is smaller than 0.5, the fraction of four coordinated boron N_4 can be approximated to equal to R (Möncke et al., 2003; Winterstein-Beckmann et al., 2013; Januchta et al., 2019b). In this range the *R*-value of 0.2 defines the line of boron oxide anomaly at which many material properties exhibit extrema (Möncke et al., 2003; Winterstein-Beckmann et al., 2014a). Those features make borosilicate glasses a very interesting system to study the link between structural alterations to the mechanical response (Winterstein-Beckmann et al., 2014a,b; Malchow et al., 2015; Zehnder et al., 2017a,b).

Instrumented (nano-)indentation testing has become a widely used tool to investigate the deformation mechanisms of glass, as it activates a variety of possible responses: elastic contact, inelastic shear flow, densification and cracking (Rouxel, 2015; Yoshida et al., 2016; Januchta and Smedskjaer, 2019; Yoshida, 2019). Whereas, indentation-based methods to asses fracture toughness and their applicability to oxide glasses is controversially discussed in the literature (Bruns et al., 2017, 2020; Rouxel and Yoshida, 2017; Yoshida, 2019), indentation testing remains one of the best solutions to compare glasses in terms of critical loads for crack initiation (Wada et al., 1974; Kato et al., 2010; Yoshida, 2019). Significant shifts in crack resistance have been observed upon chemical variations (Kato et al., 2010; Barlet et al., 2015; Malchow et al., 2015), different thermal histories (Malchow et al., 2015; Zehnder et al., 2017a), or upon compression (Januchta et al., 2017). Enhanced crack initiation loads were often referred to excess free volume and enhanced densification contribution to the deformation process (Kato et al., 2010; Januchta et al., 2017; Yoshida, 2019).

The sodium borosilicate glass NBS2 exhibits a composition (74 SiO_2-20.7 B_2O_3-4.3 Na_2O-1.0 Al_2O_3 mol%) which places the glass directly on the line of the boron oxide anomaly (Möncke et al., 2006). The glass exhibits some interesting features, i.e., that the network structure can be influenced by the thermal history of the glass (Möncke et al., 2003, 2006, 2015b). Small pieces of quenched NBS2 exhibits superior fracture properties, which have been attributed to changed subnet connectivity and the larger extent of free volume (Malchow et al., 2015). Quenching, however, limits both sample size and reproducibility. In general, quenching suppresses phase separation by freezing the high temperature configuration of the glass (Möncke et al., 2003, 2006, 2015b). Al_2O_3 can be added for a similar purpose to the sodium borosilicate glass, namely to overpass the miscibility gap (Möncke et al., 2003).

In the present study, a larger fraction of Al_2O_3 is added to the NBS2 glass composition. The effect of Al_2O_3 addition on the network structure and the mechanical response is investigated and compared to quenching effects. Elastic-plastic properties from indentation testing and Brillouin spectroscopy are correlated to short- and midrange structural changes measured by Raman and $^{11}B/^{27}Al$ solid-state NMR. Finally, the fracture behavior is investigated using high load nanoindentation.

EXPERIMENTAL PROCEDURES

Glass Melting/Preparation

NBS2 borosilicate glasses with increasing Al_2O_3 content were prepared in 50 g batches using standard melt cooling methods.

The NBS ratio (74 SiO_2-20.7 B_2O_3-4.3 Na_2O mol%) was kept constant while the Al_2O_3 content was successively increased from 1.0 to 4.0 mol%. The starting materials SiO_2 (Sigma Aldrich, 99% p.a.), H_3BO_3 (Roth, ≥99.8%), Na_2CO_3 (Sigma Aldrich ≥99.5%) and Al_2O_3 (Sigma Aldrich) were mixed and dried for approximately 12 h at 400°C in a covered platinum-rhodium crucible. Glass melting was performed in a platinum crucible at 1,100°C (heating rate of ∼20 K/min) with a dwell time of 30 min in order to evaporate CO_2. In the next step the temperature was increased to 1,500°C with a heating rate of ∼10 K/min. The temperature was kept constant for 60 min with a closed lid to avoid possible evaporation. After this step the temperature was increased to 1,600°C and held constant for another 45 min. Just before pouring the glass onto a brass block the furnace was raised to 1,650°C to improve the flow properties. Finally, the samples were crushed and molten one more time to ensure a homogeneous mixture. During cooling the melt was first poured into a preheated graphite mold (500°C) which was slowly cooled down to room temperature with a cooling rate of about 30 K/h. These samples are referred to as "furnace cooled" (fc). Additionally, samples of each composition were fast cooled by quenching in water, in the order of 200°C/s, hence they are referred to as "quenched" (qu). The henceforth discussion refers to the "furnace cooled" condition if the cooling rate is not specified. The sample containing 4.0 mol% Al_2O_3 was too viscous to pour, so the melt was transferred with the crucible in the preheated furnace and cooled down to room temperature. Subsequently the sample was drilled out of the crucible.

Densities were measured by the Archimedes method in toluene. At least 5 pieces between 0.1 and 1.0 g of weight were used and the mean and standard deviation of the results are given in **Table 3**. ICP-OES (Inductively Coupled Plasma—Optical Emission Spectrometry) was performed to analyze the chemical composition. **Table 1** summarizes the glass compositions. It is shown that the determined proportion of B_2O_3 is ∼5 mol% higher than the intended weighed amount. Simultaneously the SiO_2 content is also ∼5 mol% lower than intended. A typical error source for quantitative analysis by ICP-OES is incomplete dissolution of borosilicate glasses, where silica is known to be easily be underrepresented in solution. Unfortunately, the light element boron is hard to quantify with SEM-EDX (Scanning Electron Microscope—Energy Dispersive X-ray Spectroscopy) or XRF (X-ray Fluorescence Spectroscopy). The negligible loss of volatile boron from the melt was however confirmed by the measured B/Al-ratio, which was close to the expected values. A systematic, near constant loss of sodium ions during melting is however revealed by quantitative analysis. Since the sodium concentration remains constant, the discussion of the competing efforts of aluminate and borate units for the modifier oxide on structure and properties is not affected by the deviation from the nominal composition. Since effects of Al_2O_3 addition are of prime interest in the present study the samples are labeled according to their Al_2O_3 content. The nominal compositions were used in the manuscript henceforth in order to keep labeling simple.

Nanoindentation Testing

Nanoindentation testing was performed using a Keysight[1] G200 nanoindenter. The indentation tests were executed under air-conditioned laboratory conditions (humidity in the range of 33%) at room temperature using a Synton-MDP[2] Berkovich pyramidal indenter as default tip geometry. Tip area function and machine compliance were calibrated on a commercial fused silica reference sample according to the procedure of Oliver and Pharr (1992). Indentation testing was performed in continuous stiffness mode (CSM) a constant strain rate $\dot{\varepsilon}$ of 0.05 s^{-1}. In CSM mode the loading cycle is superimposed with a 2 nm amplitude displacement oscillation at 45 Hz, which allows to record hardness H and indentation modulus E_I as a function of penetration depth. Hardness and modulus values were averaged in a depth range between 500 and 2,000 nm using at least 9 performed indentations. In this depth range, both hardness and modulus exhibit a depth independent, constant value.

Indentation fracture was studied in high load mode with a default step size of 1 N and a maximum loading of 10 N using a constant loading rate of 0.1 N/s. This study also included sharper three-sided pyramidal tips having centerline-to-face angles of 50° and 35.26° (Cube Corner) as well as a four-sided Vickers pyramid.

Solid State NMR

Single resonance MAS-NMR (Magic Angle Spinning—Nuclear Magnetic Resonance) spectra were recorded at 7.0 and 11.7 T using a Bruker Avance III 300 MHz spectrometer and a Varian VNMRs 500 NMR spectrometer. Single pulse ^{27}Al and ^{11}B spectra were measured in commercial MAS-NMR probes using 4 mm and 1.6 mm rotors. The operation conditions are specified in **Supplementary Table 1**. Chemical shifts are reported relative to an aqueous solution of 1 M $Al(NO_3)_3$ ($\delta_{iso} = 0$ ppm) and a 1 M H_3BO_3 solution ($\delta_{iso} = 0$ ppm). ^{11}B triple-quantum (TQ)-MAS-NMR spectra were measured at 11.7 T at a spinning speed of 25.0 kHz using the three-pulse zero-filtering sequence (Medek et al., 1995). The hard excitation and reconversion pulses were 1.0 and 4.0 μs long. The third soft detection pulse had a duration of 10 μs and the relaxation delay was 5 s. The program DMFit was used to analyze the spectra (Massiot et al., 2002).

Raman/Brillouin

Polished glass plates (co-planar for platelet Brillouin) were used for Raman and Brillouin spectroscopic studies. Raman spectra were obtained in the range from 100 to 1,600 cm^{-1} with a Thermo Nicolet Almega XR Raman using a 532 nm laser excitation. To achieve a good spectral resolution each spectrum was collected with 5 scans of 120 s exposure time with a 50x objective. The spectra were background corrected with a polynomial function and normalized to the total area using the LabSpec® software by HORIBA Scientific.

Brillouin spectra in backscattering (180°) and platelet (45°) geometries were measured with an Associated Raman Brillouin Calorimetry (ARABICA) set up (Veber et al., 2017). The samples

[1]Keysight Technologies, Inc., Santa Rosa, CA, United States.
[2]Synton-MDP AG, Nidau, Switzerland.

TABLE 1 | Nominal and measured compositions of the glasses under investigation.

Glass	SiO_2 [mol%]		B_2O_3 [mol%]		Na_2O[mol%]		Al_2O_3 [mol%]	
	Nominal	ICP-OES	Nominal	ICP-OES	Nominal	ICP-OES	Nominal	ICP-OES
1.0% Al	74.00	69.75	20.70	25.59	4.30	3.32	1.00	1.33
1.5% Al	73.62	68.34	20.60	26.35	4.28	3.47	1.50	1.82
2.0% Al	73.25	68.60	20.49	25.77	4.26	3.34	2.00	2.28
4.0% Al	71.76	68.22	20.07	24.57	4.17	3.40	4.00	3.81

were excited with a 488 nm laser with 100 mW. The mean of the Anti-Stokes and the Stokes peak positions were used. For the platelet measurements, polished and coplanar thin samples were measured under a 45° angle. The Poisson's ratio (ν) can be directly calculated from the ratio between the longitudinal and transversal mode peak positions. For the backscattered measurements the laser beam was focused with a microscope (50x objective) at roughly 10 μm below the surface. The refractive index n was measured at 488 nm using an Abbé refractometer. From the backscattering measurement and using the sample refractive index and density the longitudinal modulus M was estimated. Then all the other elastic moduli: Young's (E), Shear (G), and Bulk (K) can be determined (Polian, 2003; Reibstein et al., 2011). Coupling the two geometries reduce very significantly the uncertainties which were evaluated by error propagation.

RESULTS

The Effect of Al_2O_3 Addition on the Glass Structure

Structural changes in the NBS2 borosilicate glass upon Al_2O_3 addition were studied using both NMR and Raman spectroscopy. Alterations of the Raman spectra with increasing Al_2O_3 amount are shown in **Figure 1** for the "furnace cooled" series.

Raman Spectroscopy

Four dominant regions which can be associated with structural changes can be distinguished in the Raman spectra. The small shift to higher wave numbers with increasing Al_2O_3 amount in the silicate network deformation mode (200–620 cm^{-1}) can be associated with a change of the ring size in the silicate sub-network or a small decrease of the mean angle between tetrahedra. The small band at about 600 cm^{-1} increases slightly with increasing Al_2O_3 content, which indicates the presence of three membered silicate rings. The region between 700 and 850 cm^{-1} shows the typical breathings modes for boroxol (805 cm^{-1}) and borate rings with one or two four-fold coordinated boron units (∼770 and 760 cm^{-1}). As observed in **Figure 1C** the boroxol ring band increases with increasing Al_2O_3 amount whereas the amount of four-fold coordinated boron decreases and finally vanishes for the sample with 4.0 mol% Al_2O_3. This indicates that sodium favors aluminum instead of boron for charge compensation. Hence, Al takes the role of an additional network former in the glasses.

The stretching vibrations of the Si-O (in fully polymerized Q^4 units, silicate tetrahedra with 4 bridging oxygen atoms) and mixed Si-O-B bonds can be seen in the region between 950 and 1,250 cm^{-1} (**Figure 1D**).

All modes intensities increase with increasing Al_2O_3 content, while the intensity of the high energy side of Q^4 modes increases faster than the lower energy bands of the same Si-O stretching envelop-modes. The observed variations might reflect a change of connectivity from Si-O-B^{III} to Si-O-Al^{IV}. In the region of highest frequency (between 1,250 and 1,600 cm^{-1}) no significant changes with Al variation can be observed. B^{III}-O stretching modes of rings are weaker in relative intensity than the ring breathing modes observed at 750–800 cm^{-1} and the small variations of ring B^{III}-O vs. non-ring B^{III}-O populations upon Al_2O_3 addition (see NMR section here below) do not result in significant changes of the high frequency envelop.

NMR Spectroscopy

NMR spectroscopy can be used to study the local environments of individual elements and helps in the unambiguous assignment of Raman bands and thus the verification of the Raman results. **Figure 2** shows the ^{27}Al MAS-NMR spectra (Magic Angle Spinning) of the furnace cooled series. Only the central transition of the ^{27}Al nuclear spins ($I = 5/2$) is observed in these spectra. The spectra show the typical asymmetric line shapes which are centered at around 45 ppm. This suggests that most of the Al is four-fold coordinated while the relative broad line shapes can be explained by a broad distribution of the existing quadrupole parameters. These findings correspond well to observations on charge balanced sodium aluminosilicate glasses in the literature (Eckert, 1992, 1994; Eden, 2015). For the investigated glasses, the chemical shift indicates that aluminum must be fully present as negatively charged $[AlO_4]^-$ units. The $[AlO_4]^-$ is charge balanced by positive charged sodium ions in order to achieve charge neutrality in the glass. Thus, Al is completely incorporated into the polymerized glass network.

The effect of Al_2O_3 addition on the ^{11}B MAS-NMR spectra is shown in **Figure 3A**. The spectra (solid lines) can generally be deconvoluted into two distinct types of line shape components. One belongs to four-fold coordinated boron (B^{IV}, Gaussian line near 0 ppm) and the broader one is correlated to three-fold coordinated boron (two anisotropic line shapes between δ_{iso} = 17 and 13 ppm) arising from interactions of the nuclear electric quadrupole moment of the ^{11}B with electrostatic field gradients created by the trigonal planar bonding geometry of three-coordinate boron (B^{III}) species. Due to the different

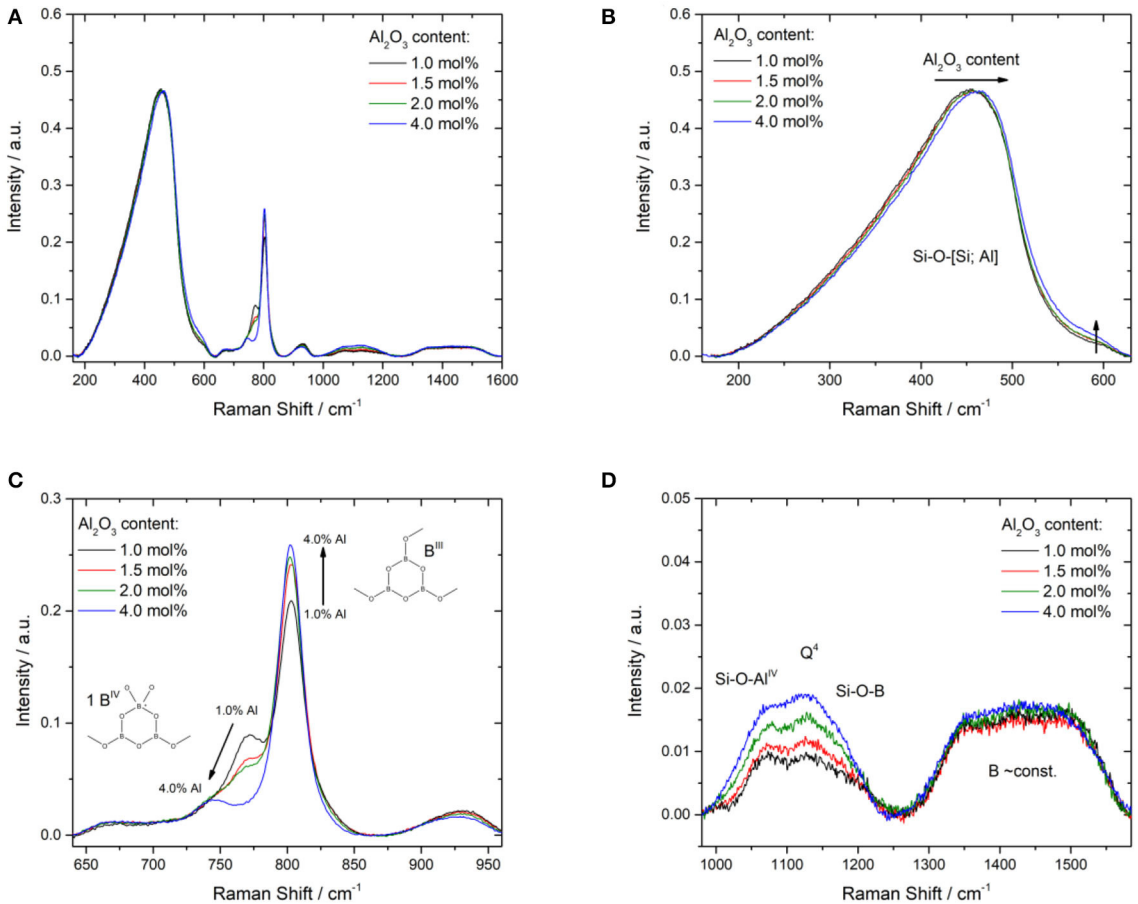

FIGURE 1 | (A) Area normalized Raman spectra of NBS2 glasses with changing Al_2O_3 amount. Enlarged details show the silicate deformation modes **(B)** between 150 and 650 cm^{-1}, the borate and boroxol ring modes **(C)** between 675 and 850 cm^{-1}, and **(D)** stretching modes of borate tetrahedra at 920 cm^{-1}, Si-O stretching modes between 950 and 1,250 cm^{-1}, and of trigonal borate entities between 1,250 and 1,600 cm^{-1}.

environment, the broad resonance in the range 18–2 ppm can be divided into two signal components typical for boron. The broad signal consists of two signal components with a characteristic line shape for the central m = ½ <-> m = −½ transition of a spin-3/2 ^{11}B nuclear isotopes that can be assigned to the B^{III}. Martens et al. assigned in binary borosilicate glasses the signal near 17 ppm to boroxol rings. They assigned the signal near 13 ppm, found in high silicate borosilicate glasses, to boron atoms in mixed borosilicate phase (Martens and Müller-Warmuth, 2000). van Wüllen and Schwering (2002) extended this model and assigned the signal close to 17 ppm to boroxol rings in a borate-like network and the signal near 13 ppm as a superposition of B^{III} units in a borate environment and B^{III} units in a borosilicate environment. Previous studies on this glass system were also able to prove a spatial proximity of the B^{III} and B^{IV} to Si by 2D $^{11}B/^{29}Si$ correlation experiments (Du and Stebbins, 2003; Möncke et al., 2015a). In the literature, a chemical shift of about 0 ppm for the B^{IV}-units is attributed to tetrahedral borate units where one B-atom is connected to 3 silica and 1 boron group. A quantitative deconvolution of the line shape allows to determine the fraction of both boron species (MacKenzie and Smith, 2002). All line shape parameters used for fitting the spectra are listed in **Supplementary Table 2**. For the glass with the lowest Al_2O_3 content the highest fraction of B^{IV} at 12% is measured. With increasing Al content, the amount of B^{IV} decreases (**Figure 3B**).

For the three-coordinated boron species the low value of the electric field gradient asymmetry parameter (0.25 ± 0.03) indicates a species close to axial symmetry such as the one known for neutral trigonal coordinated boron, B^{III}. As expected from the composition, anionic meta- or pyroborate groups for which asymmetry parameters close to 0.5 are expected (Stebbins et al., 2000) can be ruled out since their typical line shapes are not visible in the recorded spectrum. A closer look at the data indicates that there are two distinct types of B^{III} species present in the MAS-NMR spectra, showing different chemical shifts. A ^{11}B-MQMAS (Multi Quantum MAS) experiment was performed on one sample (2.0 mol% Al_2O_3) in order to verify this observation. The MQMAS allows to resolve the previously overlapping signals into two isolated line shapes by selective investigation of the multi quantum transitions (here triple quantum). A representative

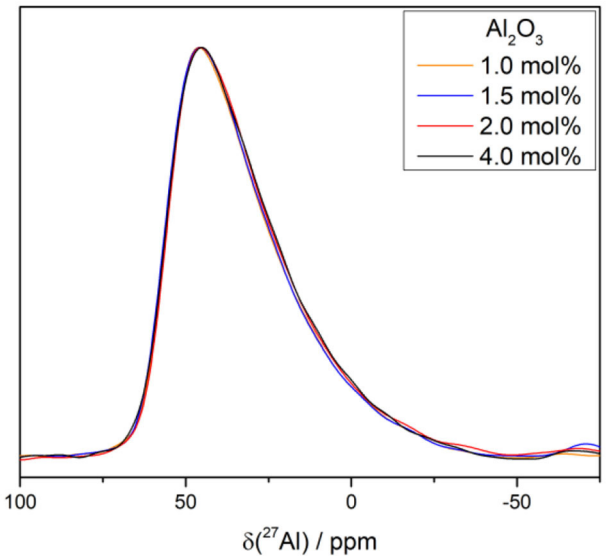

FIGURE 2 | ^{27}Al MAS-NMR spectra of the furnace cooled NBS2-Glasses at 300 MHz.

deconvolution is shown in **Figure 3A** (dotted lines) and for a typical ^{11}B-MQMAS as presented in **Figure 3C**. The dominant species near 17 ppm can be characterized with B^{III} units showing connectivity with other boron species whereas the B^{III} groups close to 13 ppm indicate B^{III} units taking part in non-ring structures like B-O-Si linkages (Möncke et al., 2015b).

The deconvolution results from the NMR investigation are summarized in **Figure 3B** and **Supplementary Data**. The original Dell and Bray model (R) (Dell et al., 1983) does not consider the incorporation of Al_2O_3 in the glass structure. For our compositions since K is 3.6, R-values express directly N_4 and remain constant at 0.21, showing that there should be no change in boron coordination. The NMR results disprove this simplification. If now the sodium fraction mobilized to compensate the aluminum is taken into account, a modified fraction of four-coordinated boron R' can be evaluated according to Januchta et al. (2019b).

$$R' = N_{4Charge\ compensation} = \frac{[Na_2O] - [Al_2O_3]}{[B_2O_3]} \quad (1)$$

Here it is evident that the proportion of B_4 decreases with increasing amount of Al whereas the share of B^{III} increases (**Table 2**). This view agrees well with the ^{11}B-NMR results where the fraction of four coordinated boron N_4 decreases with increasing fraction of Al_2O_3. The analysis of the ^{11}B NMR further shows that the proportion of B^{III} in non-ring configuration seems to remain constant, which indicates a reduction of the B^{IV}-O-Si linkage.

The Effect of Quenching on the Glass Structure

The effect of the thermal history on the network structure can be investigated comparing Raman spectra of a quenched and a furnace cooled sample (**Figure 4A**). The spectrum can be divided into four regions (see for comparison Möncke et al., 2015a). The small shift to higher values in the silicate network deformation mode (200–620 cm^{-1}) for the quenched sample can also be associated with a decrease of the inter-tetrahedral angle due to an increasing amount of smaller sized rings and/or an evolution of the Si-O-B connectivity. In the region between 700 and 850 cm^{-1} the typical modes for borate and boroxol rings can be observed. The borate peak loses intensity with increasing cooling rate (red arrow); a similar effect as observed by Al_2O_3 addition (blue arrow). The fraction of boroxol rings, in turn, behaves anti proportional to the effect of Al_2O_3 addition and decreases also with increasing cooling rate. In the region between 1,000 and 1,200 cm^{-1} which is associated with the bond stretching Si-O, Al-O, and B-O, a higher quenching rate has the same effect than the addition of Al with an increase of the contribution at 1,030 cm^{-1}. In the region between 1,250 and 1,600 cm^{-1} a slight decrease of the signal intensity around 1,500 cm^{-1} can be observed for the temperature treated sample. This decrease can be assigned to an increase of N_4 at higher cooling rate. Möncke et al. found the same trends in their investigations of the influence of the thermal history within this glass system. The increase of the mixed Si-O-B band at about 1,150 cm^{-1}, however, has not been observed in the present study (Möncke et al., 2015a). Those results show that a faster cooling rate results in a different glass network within or between the first coordination spheres. NMR supports those findings. All the recorded spectra (**Supplementary Figure 1**) are very similar. **Figures 4B,C** show the ^{11}B NMR and ^{27}Al NMR spectra of the 1.0 mol% Al quenched glass sample. From the ^{11}B spectra a change in the range of the B^{III} units can be observed. The proportion of B^{III} non-ring units is more pronounced compared to the B^{III} ring units. For the signal which can be assigned to the B^{IV} units a slight shift from 0.3 ppm to a higher chemical shift can be detected. This indicates a higher interconnectivity between the borate and silicate network in the quenched glasses. It is consistent with the results found in the Raman spectra and the literature (Möncke et al., 2006; Malchow et al., 2015). In the ^{27}Al NMR spectrum the linear shape remains constant and only a slight shift from 2 to 3 ppm to lower values is visible upon quenching. This means that the Al coordination is not affected by the cooling rate and that the bond Al-O is only slightly affected by the structural modifications mainly taking place in the vicinity of boron atoms. The proportion of B^{III} and B^{IV} is constant with increasing cooling rate, which is different from other borosilicate glasses (Angeli et al., 2012).

The Mechanical Properties

The mechanical properties of the NBS2 glass series are studied using nanoindentation and Brillouin spectroscopy. Brillouin spectroscopy allows to determine elastic material properties such as Young's modulus E, bulk modulus K, shear modulus G, P-wave

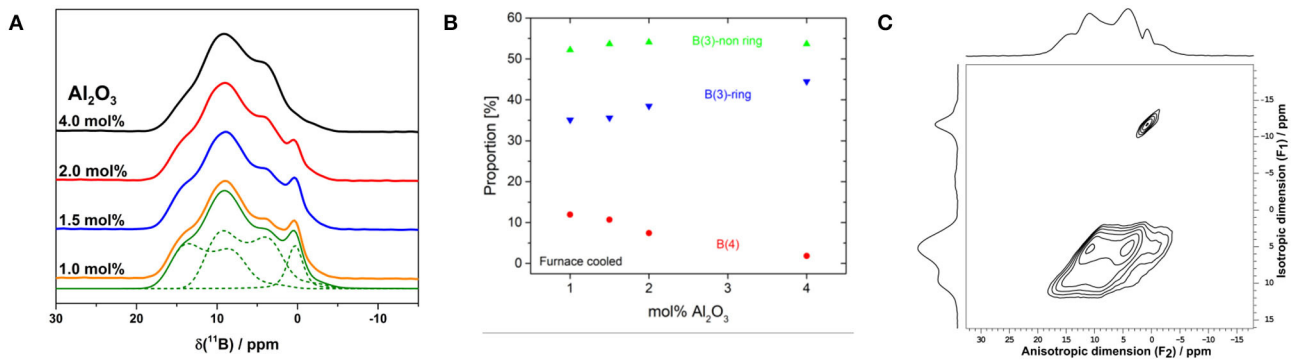

FIGURE 3 | (A) ^{11}B MAS-NMR at 500 MHz. The figure shows the evolution of three boron bands (two for three-fold coordinated and one for four-fold coordinated boron). Solid lines show the MAS spectra and the dotted lines show a typical deconvolution of ^{11}B NMR spectra using Multi Quantum MAS. The first dotted line with two peaks ranging from 18 to 5 ppm is assigned to B^{III} ring, the second line from 13 to 2 ppm to B^{III} non-ring and the third dotted line with a Gaussian shape centered at 0 ppm to B^{IV}. **(B)** The boron ring configuration according to ^{11}B-MAS NMR results for the furnace cooled glasses. **(C)** ^{11}B MQMAS-NMR-Spectra of the sample with 2.0 mol% Al_2O_3. Deconvolution of the three spectra in isolated signals.

TABLE 2 | The fraction of tetragonal boron: $N4_{NMR}$ are the results from NMR deconvolution.

NBS2 glass	$N4_{NMR}$	$R' = N_{4Charge\ compensation}$	$R = N_4$
1.0 mol% Al	0.12 ± 0.03	0.16 ± 0.02	0.21
1.5 mol% Al	0.11 ± 0.03	0.13 ± 0.02	0.21
2.0 mol% Al	0.07 ± 0.03	0.11 ± 0.02	0.21
4.0 mol% Al	0.02 ± 0.03	0.01 ± 0.02	0.21

For comparison the Dell and Bray model is applied for the nominal glass composition without the consideration of Al_2O_3 in that case, R gives the theoretical amount of B^{IV}. If Al_2O_3 is assumed to mobilize as charge compensator a fraction of the Na then a modified R factor called here R′ can be calculated (see text for more details).

modulus M, and Poisson's ratio ν if the density is known. For this purpose, density ρ was determined according to the principle of Archimedes. The determined parameters are summarized in **Table 3**. Both density and elastic properties slightly decrease with quenching rate. The addition of Al has no significant effect on density. The Poisson's ratio within the error bars remains constant for all the samples.

Nanoindentation testing probes the elastic-plastic material behavior and reveals that Young's modulus E values match the absolute values determined by Brillouin spectroscopy surprisingly well (**Table 3**). Moreover, the values obtained for the conventional NBS2 glass (containing 1 mol% Al_2O_3) agree well with the literature (Limbach et al., 2015). With an increased Al_2O_3 amount both hardness and modulus decrease (**Figure 5**). This tendency can be observed in furnace cooled as well as quenched glass. For a single glass composition an increasing cooling rate (quenching) results in lower H and E values, an observation supported by the literature (Ito and Taniguchi, 2004; Deng and Du, 2018). For the conventional NBS2 glass quenching interestingly has a similar effect on H and E as the addition of further 3.0 mol% Al_2O_3. This similitude is very interesting because it will allow us to analyze the structural modifications at iso elastic properties. Later on, in the discussion we will systematically compare these three key conditions: furnace cooled 1.0 mol% Al_2O_3, quenched 1.0 mol% Al_2O_3 and furnace cooled 4.0 mol% Al_2O_3.

The fracture behavior was studied with high load nanoindentation using various tip geometries. For Berkovich indentation the furnace cooled NBS2 glass (1 mol% Al_2O_3) shows mainly radial and conical cracking (**Figure 6A**). The crack systems occur mixed even for similar loading, so no clear trend could be observed.

Quenching the NBS2 glass (1.0 mol% Al_2O_3) to room temperature leads to a strongly stochastic cracking behavior and a significant increase in chipping and mixed fracture where many crack systems are active simultaneously (**Figure 6B**). Pure radial cracking does not appear at all while pure cone cracking can be observed to a very small amount.

The addition of Al_2O_3, in turn, unifies the crack pattern (**Figure 6C**). The 4.0 mol% Al_2O_3 containing NBS2 glass shows mainly edge cracks and lateral bright shining traces in the vicinity of the contact. When those cracks propagate to the surface they lead to chipping. Edge cracks are likely introduced by the tensile component, accompanied with sink-in upon loading, and typically penetrate only straight down to a very small depth (Mound and Pharr, 2019). Occasionally chipping can be observed, even at smaller loads.

Switching indenter geometries from the rather blunt Berkovich to the sharp cube corner tip unifies the cracking behavior within the NBS2 series. Radial cracking becomes predominant with increasing indenter sharpness, which is in good accordance with the literature (Gross, 2012; Bruns et al., 2020). However, cube corner indentation is usually accompanied with traces of chipping and, depending on the degree of chipping, the indentations show significant differences in radial crack extension (**Figure 6D**), ruling out a quantification of cracking according to Lawn et al. (1980).

The estimate of a fracture probability, however, allows to investigate qualitatively the cracking behavior of the borosilicate glass in terms of damage resistance value. In contrast to the

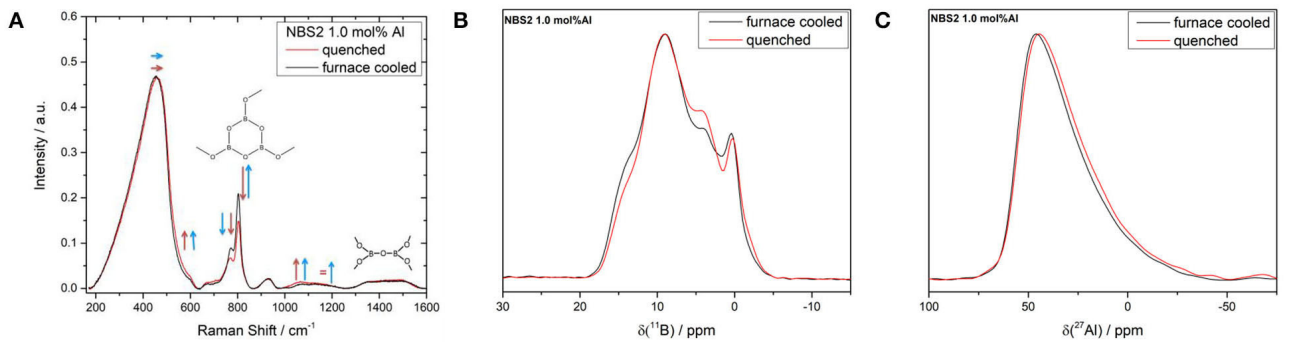

FIGURE 4 | (A) Thermal history effect on the glass structure obtained by Raman spectroscopy. Red arrows indicate changes by quenching while the blue arrows indicate changes upon Al_2O_3 addition for comparison. **(B)** ^{11}B-MAS NMR and **(C)** ^{27}Al-MAS NMR spectrum of a furnace cooled and quenched sample.

TABLE 3 | Density and mechanic properties of the investigated NBS2 glass series obtained by Brillouin spectroscopy and nanoindentation testing.

Al_2O_3 [mol%]	ρ [g/cm^3]	Brillouin shift Backscattering [GHz]	Brillouin shift Platelet transv./long. [GHz]	M [GPa]	ν	G [GPa]	K [GPa]	$E_{Brillouin}$ [GPa]	$E_{Indentation}$ [GPa]	H [GPa]
1.0	2.131 ± 0.006	30.62 ± 0.05	14.92 ± 0.02/8.86 ± 0.01	55.1 ± 0.4	0.228 ± 0.005	19.4 ± 0.4	29.2 ± 0.5	47.7 ± 0.7	47.6 ± 0.4	5.99 ± 0.04
1.0 qu.	2.122 ± 0.006	29.99 ± 0.05	14.43 ± 0.03/8.53 ± 0.03	52.9 ± 0.4	0.232 ± 0.005	18.4 ± 0.4	28.3 ± 0.5	45.4 ± 0.7	46.0 ± 0.2	5.64 ± 0.05
1.5	2.133 ± 0.010	30.60 ± 0.05	14,74 ± 0.01/8.73 ± 0.01	55.1 ± 0.6	0.230 ± 0.005	19.3 ± 0.5	29.4 ± 0.8	47.6 ± 1.2	47.5 ± 0.3	5.88 ± 0.04
1.5 qu.	2.132 ± 0.004	29.65 ± 0.05	14.52 ± 0.06/8.55 ± 0.03	51.9 ± 0.4	0.235 ± 0.005	18.0 ± 0.4	28.0 ± 0.5	44.5 ± 0.7	–	–
2.0	2.130 ± 0.002	30,41 ± 0.05	14.71 ± 0.03/8.69 ± 0.02	54.5 ± 0.3	0.232 ± 0.005	19.0 ± 0.4	29.1 ± 0.6	46.8 ± 0.8	46.1 ± 0.1	5.72 ± 0.04
2.0 qu.	2.124 ± 0.012	29,74 ± 0.05	14.41 ± 0.05/8.47 ± 0.03	52.0 ± 0.8	0.236 ± 0.005	18.0 ± 0.5	28.0 ± 0.7	44.4 ± 1.0	43.7 ± 0.2	5.32 ± 0.03
4.0	2.137 ± 0.004	30.35 ± 0.05	14.52 ± 0.04/8.59 ± 0.06	54.3 ± 0.2	0.235 ± 0.005	18.8 ± 0.3	29.2 ± 0.4	46.4 ± 0.6	45.5 ± 0.2	5.59 ± 0.02

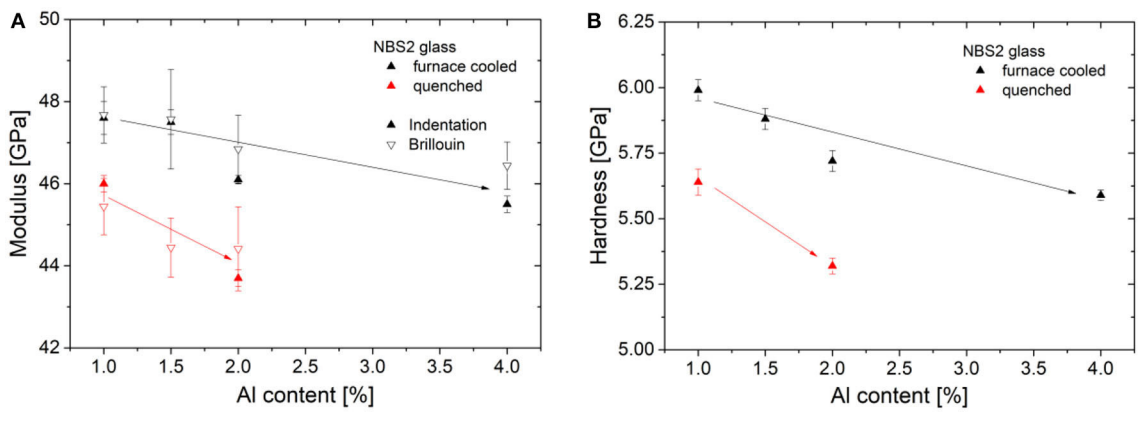

FIGURE 5 | (A) Young's modulus and **(B)** Hardness from nanoindentation testing (solid symbols). An estimate of Young's modulus from Brillouin spectroscopy is shown as open symbols. The thermal history, furnace cooled or quenched, is indicated by black or red color, respectively.

concept of Wada et al. (1974) and Kato et al. (2010), different crack systems are not differentiated in the present study. In this manner, the number of indents showing cracking N_{crack} was related to the total number of indentations N_{total} for a given indentation load.

Fracture probabilities were calculated for all examined indenter geometries, those for Vickers and cube corner tip geometry are shown in **Figure 7**, while Berkovich and 50° are provided as **Supplementary Data**. The rather blunt Berkovich or Vickers indenter exhibit huge scatter within the individual series, likely caused by the variety of the active crack system. The huge differences in crack morphology among the glasses complicates a further comparison. However, using the sharper cube-corner indenter, with a decreasing indenter centerline-to-face angle, the fracture probability is better defined and the scatter decreases. The profiles can be fitted with a sigmoidal function

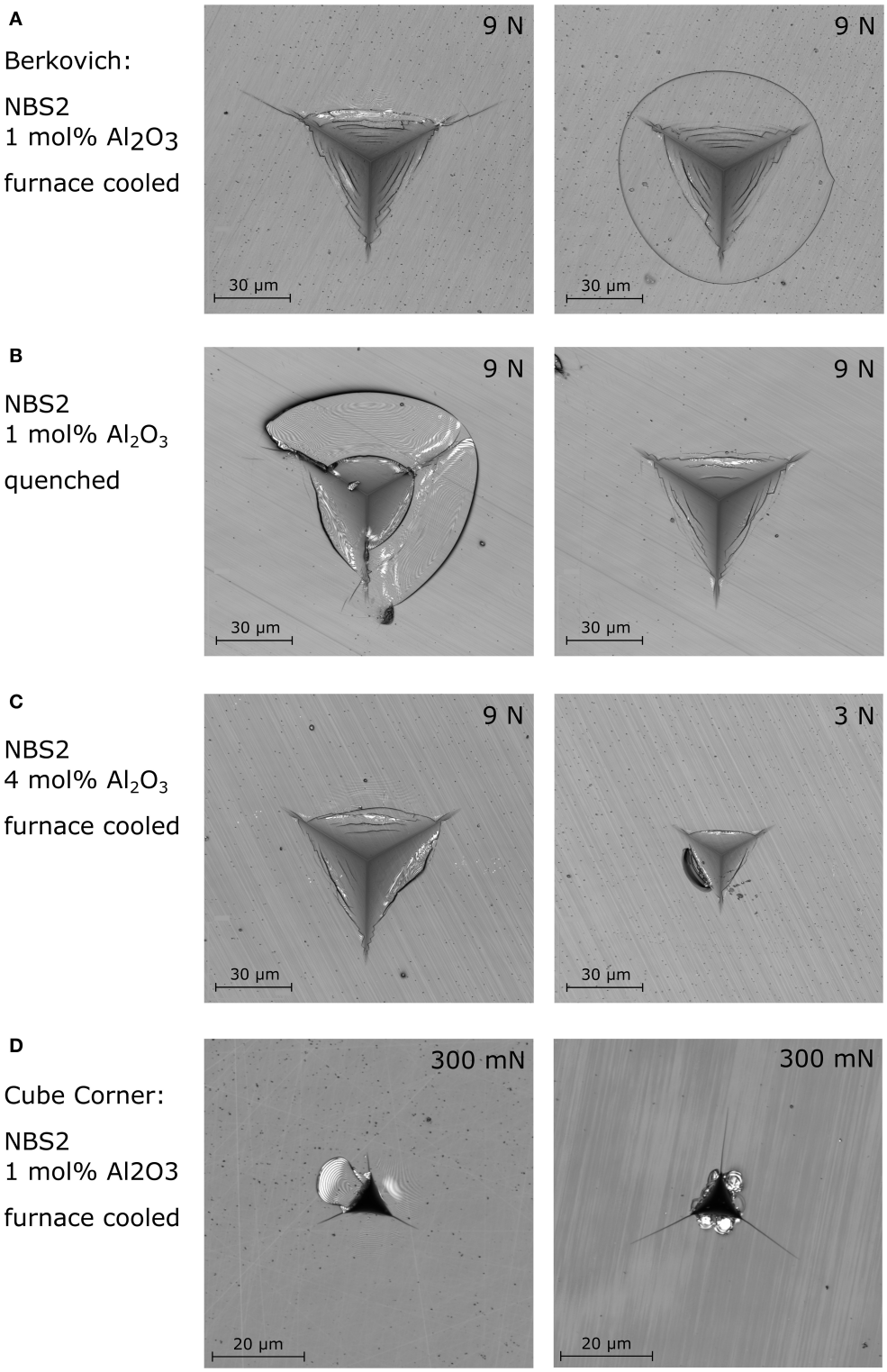

FIGURE 6 | Indentation cracking upon Berkovich indentation in **(A)** furnace cooled and **(B)** quenched NBS2 glass containing 1 mol% Al_2O_3 as well as **(C)** in furnace cooled NBS2 with a larger Al_2O_3 content of 4 mol%. **(D)** Cube corner indentation cracking in conventional furnace cooled NBS2 glass. Even though the loading is equal in both cases, the radial crack length scatters from 11.8 ± 0.8 µm (left) to 21.4 ± 0.4 µm (right), depending on the extent of chipping.

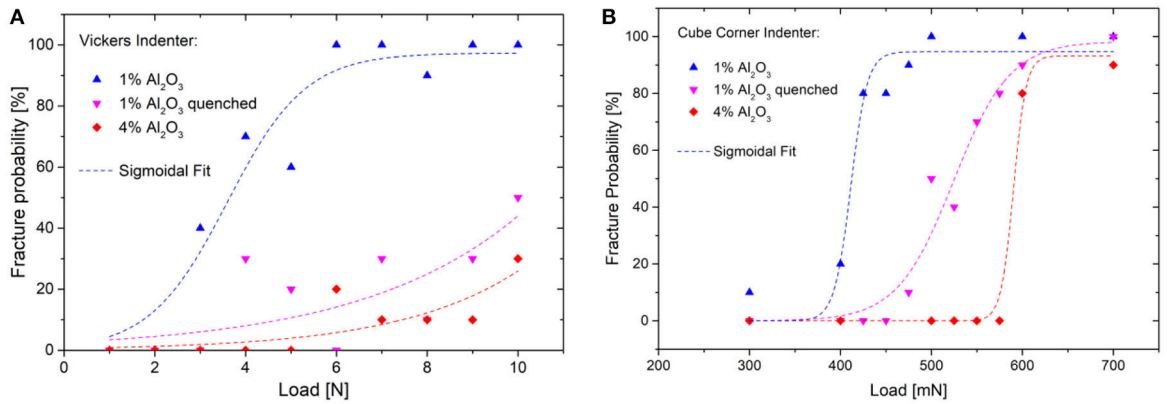

FIGURE 7 | Fracture probability of the NBS2 glass series for **(A)** Vickers and **(B)** Cube Corner nanoindentation.

TABLE 4 | Fracture initiation load in N, determined with sigmoidal fits from fracture probability plots (**Figure 7**).

NBS2 glass	Fracture initiation load [*N*]		
	Vickers (4-sided)	50° (3-sided)	Cube corner (3-sided)
1.0 mol% Al	3.65	0.62	0.41
1.0 mol% Al, quenched	≈10.0	3.27	0.53
4.0 mol% Al	>10.0	3.27	0.59

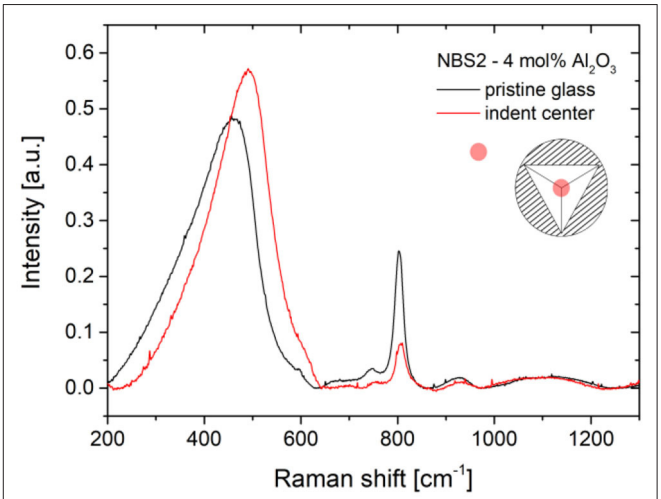

FIGURE 8 | Changes in the area normalized Raman spectra induced by indentation in furnace cooled NBS2 glass (4 mol% Al_2O_3). The black curve represents the pristine condition while the red curve is measured at indent center.

to determine a fracture initiation load, which is here defined as the corresponding load for 50% fracture probability. For the Berkovich geometry, scatter was too high to allow a sigmoidal fit, hence this tip geometry is not listed in **Table 4**.

For all examined indenter geometries, the furnace cooled NBS2 glass containing 1.0 mol% Al_2O_3 exhibits the lowest cracking threshold value. Quenching shifts the threshold values toward higher loads as reported in the literature (Malchow et al., 2015). In a similar manner the fracture initiation loads shifts, with the addition of Al_2O_3 further. Especially for sharper tip geometries, the 4.0 mol% Al_2O_3 containing NBS2 glass exhibits even slightly larger threshold values as samples prepared under the quenched condition.

In the literature, enhanced fracture properties of the quenched state were attributed to an increased interconnectivity between the borate and silicate subnetworks (shown by a small negative shift of 0.3 ppm of the B^{IV} unit from furnace cooled to quenched glass), but also to the smaller packing density and the accompanied larger densification ability provided by the glass prepared under quenching conditions (Malchow et al., 2015). To further elucidate these effects, the glass structure of the three key conditions is analyzed by Raman spectroscopy, comparing spectra at indent center to those of pristine glass (**Figure 8**).

Deformation is accompanied with a significant shift and intensity increase of the deformation band below 600 cm^{-1}, which is called main band in pure SiO_2 glass (**Figure 8**). The boroxol and borate ring breathing bands, in turn, decrease in intensity. This tendency was observed for all three key conditions (1.0 mol% Al_2O_3 furnace cooled and quenched, as well as 4.0 mol% Al_2O_3 furnace cooled). The comparison of the remaining spectra is provided as **Supplementary Data**. The deformation band shift is analyzed according to the procedure proposed by Deschamps et al. (2011, 2013) by defining a half integral main band centroid σ as a measure for the main band position. They established a linear relationship between the band shift Δσ and densification $\Delta\rho/\rho_0$ according to:

$$\frac{\Delta p}{p}\,[\%] = m \times \Delta\sigma \tag{2}$$

To the best of the author's knowledge a correlation factor m for borosilicate glasses has not been determined yet. Deschamps et al.

TABLE 5 | Raman study of the deformation process present during indentation.

NBS2 glass	$\sigma_{pristine}$ [cm^{-1}]	σ_{center} [cm^{-1}]	$\Delta\sigma$ [cm^{-1}]	Densification [%]*
1.0 mol% Al	424	467	43	8.6
1.0 mol% Al qu.	430	470	40	8
4.0 mol% Al	430	469	39	7.8

*Raman spectroscopy was performed in indent center and for comparison in the unaffected base material. *Densification is determined using a correlation factor for SiO_2, which may not be applicable to borosilicate glasses.*

(2011, 2013) established a correlation factor m = 0.2% cm for pure SiO_2 which was used in this study instead. The densification deduced and shown in **Table 5** is then only given an order of magnitude but reflects well the trend between the differences.

All glasses exhibit comparable σ values at the center of the indent. A small difference can be observed for the pristine glass. Here the conventional NBS2 glass is located at 424 cm^{-1}, while the quenched and the 4.0 mol% Al_2O_3 containing glass are located at 430 cm^{-1}. This offset corresponds to the shift of the deformation band found in **Figures 1B**, **4**, and the variation of intensity of the D2 band causing a little larger $\Delta\sigma$.

DISCUSSION

With increasing the content of Al_2O_3 within the sodium borosilicate glass, the boroxol amount increases at the cost of B^{IV} units. This tendency can be observed with both spectroscopical methods used in the present study, Raman (**Figure 1**) and NMR (**Figure 3**) spectroscopy. Most likely Al is inserted into a former B^{IV}-O-Si bridge. Thereby B^{IV} is transformed into a B^{III} unit and Aluminum takes the role as network former, linking Si and B subnetworks. The ^{27}Al MAS-NMR spectra further indicate that the structure within the present glasses is dominated by a four-fold coordination of Al, described as $[AlO_4]^-$ units, which is charge compensated by Na^+ (**Figure 9**). The tendency of boron to form a four-fold coordination depends strongly on the glass composition (Dell et al., 1983), i.e., the type and availability of network modifier species (Kim and Bray, 1974; Angeli et al., 2010), and in the given sodium borosilicate glass, B^{IV} seems to form only with the modifier cations remaining after Al-modification. This behavior is in good accordance with the literature as it has also been observed in other alumino borosilicate glasses (Osipov et al., 2016; Frederiksen et al., 2018; Bradtmüller et al., 2019). As Al is preferred for charge compensation of the Na^+ species, the formation of $[AlO_4]^-$ units indirectly influences the boron modification, which is then limited by the remaining fraction of Na^+. In our modification of the Dell and Bray model (Equation 1) the concentration of B^{IV} units is predicted by taking this behavior into consideration. The experimental N_4-NMR values are only slightly lower than those delivered by our prediction (Equation 1), which might be ascribed to some loss of sodium ions during melting.

Based on those results a structural model for the incorporation of Al_2O_3 in the structure of the sodium borosilicate glass NBS2 can be developed (**Figure 9**).

With regard to the mechanical properties, those structural changes were found to go hand in hand with a softening, as seen in a reduction of the elastic modulus and hardness. Both effects can be attributed to the increasing amount of more flexible trigonal borate units, which softens the network due to its planar nature, leading to a larger free volume for B^{III} and a subsequently reduced stiffness of the glass network (Eagan and Swearekgen, 1978; Inaba et al., 1999; Januchta et al., 2019b). Moreover, both quenching and the alumina addition shifts the fracture initiation load toward higher values for all examined tip geometries (**Figure 7**). An investigation of deformation-induced Raman band shifts upon indentation was performed on the two extreme cases in order to elucidate whether the enhanced fracture initiation behavior can be attributed to significant changes in the predominant deformation process. The study, however, reveals $\Delta\sigma$ values in a similar range, so no significant change in densification ability of the glasses occurred. Hence, the enhanced crack resistance of the 4 mol% Al_2O_3 glass cannot be attributed to densification. This observation is in agreement with a recent study on alumino borosilicate glasses by Januchta et al. (2019a), who neither found a direct correlation between the fracture initiation resistance and densification. The significant changes in the fraction of boroxol and borate rings upon indentation rather indicate that those units have played a significant role during deformation. The Raman study on the pristine glasses has shown that glasses with larger Al_2O_3 content exhibit a larger share of planar B^{III} units (**Figure 1**). It is well-known in the literature that the reduced three dimensionality of the boron network favors shear deformation (Yoshida et al., 2009; Januchta and Smedskjaer, 2019). In a similar manner the intensity of the band related to planar B^{III} rings (750–800 cm^{-1}) is greatly reduced during indentation (**Figure 8**). Glasses with high Al_2O_3 content exhibit more planar boroxol units, hence, a shear softening effect becomes visible, which manifests in a reduced glass hardness (**Figure 5**), similar as found in comparable glass systems in literature (Januchta et al., 2019a,b). Januchta et al. (2019b) discusses a correlation between cracking and the boron configuration. While the crack front has to break B-O bonds if boron is arranged in rigid tetrahedra, bond breakage might be avoided if trigonal boron arranges in planar rings. It can be imagined that adjacent borate rings can be separated without the need of breaking any bond. Thus, the enhanced fracture initiation properties of NBS2 glasses with high Al_2O_3 are likely to be attributed to the larger share of trigonal boron present in those glasses. For the quenched glasses the Raman study at indent center exhibits a strong intensity decrease of the band related to planar B^{III} rings (750–800 cm^{-1}). This indicates that those structural units are involved in deformation. Moreover, the band related to B^{IV} units (∼770 and 760 cm^{-1}) is more intense in this qu 1 mol% Al_2O_3 glass compared to the fc 4 mol% Al_2O_3 configuration. A significant intensity decrease of this B^{IV} band upon deformation can be observed there, too. Unfortunately, the given dataset does not allow for a final conclusion. It is, however, natural that the structural change induced by quenching is different from that induced by an addition of Al_2O_3. It is therefore normal that the deformation of these glasses is different to a certain extent even though E, H, and the fracture initiation properties point in a similar direction.

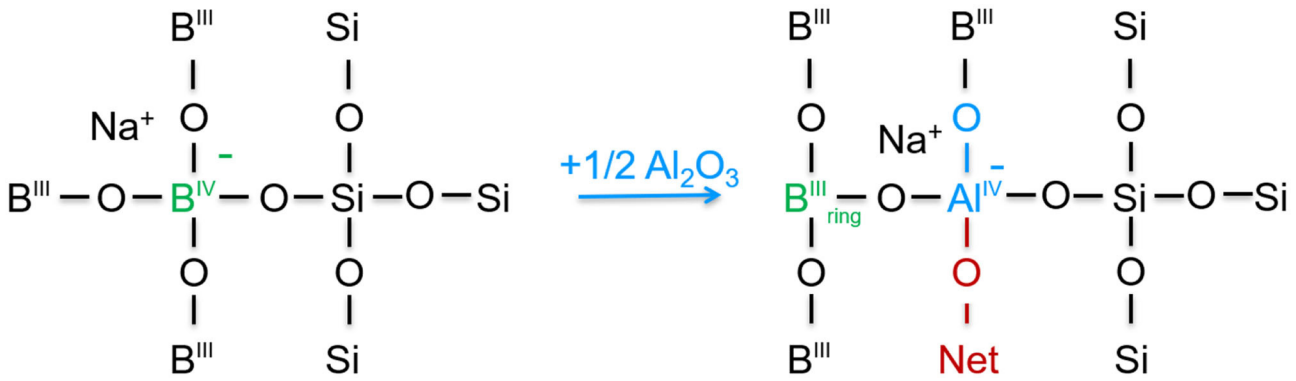

FIGURE 9 | Structural change upon ½ Al_2O_3 addition in the NBS2 sodium borosilicate glass. The ½ O is shared with the network Net represented in red. The B^{IV} changed to a B^{III}_{ring} represented in green here.

Even if elucidating the exact superstructural units connecting aluminate, borate and silicate is a very difficult task and remains therefore speculative, some improvement of the global connectivity can be observed in both quench and Al enriched samples. In the earlier studies on the influence of the annealing rate on the mechanical properties of NBS2, the intermediate range order and connectivity between borate and silicate units were given much focus. Quenching improved the interconnectivity of borate and silicate units in this low alkali borosilicate glass. Indeed, it was shown that trigonal borate had a higher tendency to bond to silicate than tetrahedral borate. Differently, alumina is known to reduce the tendency of phase separation. Its addition helps to close the immiscibility gap, increases the fraction of trigonal borate and therefore increases overall the interconnectivity between network formers. Hence, if it is too complex to attribute the enhanced fracture initiation properties to certain structural units, the interconnectivity between network formers seems to play a central role in both cases.

Finally, it is worth noting that an enhanced fracture initiation load does not correspond to a higher fracture toughness, which describes the critical stress intensity factor for crack growth (Rouxel and Yoshida, 2017; Januchta et al., 2019a). Concerning the fracture toughness, it is even disadvantageous if the crack can surpass certain structural units (e.g., boroxol rings) and has to break less bonds on its way through the material (Januchta et al., 2019b). As the fracture toughness is directly linked to bond strength and packing density, similar to the elastic modulus, it is expected to correlate with E (Rouxel, 2017; Januchta et al., 2019a). In this manner the decrease in the elastic modulus indicates a fracture toughness reduction for the NBS2 glass with higher alumina content and after quenching.

CONCLUSION

The addition of Al_2O_3 is a promising approach for improving the crack initiation loading NBS2 sodium borosilicate glass and, hence, for replicating the effect quenching has on the mechanical properties in this system. In general, both approaches of Al_2O_3 addition and quenching aim to prevent phase separation of the boron and silica subnetworks. Increasing the Al_2O_3 content from 1.0 to 4.0 mol% results in more Al-ions acting as network former linking Si to B units, while four-fold coordination ensures charge compensation sites for Na^+. It is obvious that quenching increases the network interconnectivity differently, since the share of Al_2O_3 is constant. Even though quenching and Al-additions lead to the formation of different network structures within the glass, the effect on the mechanical response is comparable and both the modified NBS2 glass with the highest Al_2O_3 content of 4.0 mol% and the quenched state of the conventional NBS2 glass (1.0 mol% Al_2O_3) exhibit remarkably similar modulus and hardness values. The fracture initiation load shifts toward higher loads following both approaches. The different network structures forming upon Al_2O_3 addition and quenching, however, manifest in differences in the crack pattern. While under the quenched condition a variety of crack systems is activated due to local variations in the glass structure, the addition of Al_2O_3 unifies the crack pattern and reduces scatter in the fracture probability plots (**Figure 7**). In this manner, Al_2O_3 represents a more reliable approach for improving the fracture initiation behavior of borosilicate glass.

While in the literature the improvement of fracture properties is often attributed to a more pronounced densification ability of the enhanced glass (Malchow et al., 2015), recent studies question whether densification alone can enable such significant improvements (Bruns et al., 2017). Raman investigations along indents reveal comparable band shifts for all examined glasses within the present study. Those results clearly show that the gain in fracture initiation cannot be attributed to densification effects alone. The decrease in hardness rather indicates a shear softening accompanied with a smaller driven force for crack initiation in the glasses with improved fracture behavior.

DATA AVAILABILITY STATEMENT

All datasets generated for this study are included in the article/**Supplementary Material**.

AUTHOR CONTRIBUTIONS

DM, DL, and KD developed the basic idea for the presented project. TU produced the glasses and carried out and evaluated the spectroscopic investigations. SB and DW carried out and evaluated mechanical measurements, the theoretical simulations, evaluation and analysis of the data, and contributed ideas. DM, DL, KD, and LW supported TU. All authors worked together in interpreting and linking the measurement results. All authors have discussed the results and collaborated on the manuscript.

FUNDING

Financial support from the German Science Foundation DFG through the priority program 1594 Topological Engineering of Ultra-Strong Glasses (DU 424/8-2 and MO 1375/3-2) was gratefully acknowledged.

SUPPLEMENTARY MATERIAL

The Supplementary Material for this article can be found online at: https://www.frontiersin.org/articles/10.3389/fmats.2020.00189/full#supplementary-material

REFERENCES

Angeli, F., Charpentier, T., De Ligny, D., and Cailleteau, C. (2010). Boron speciation in soda-lime borosilicate glasses containing zirconium. *J. Am. Ceram. Soc.* 93, 2693–2704. doi: 10.1111/j.1551-2916.2010.03771.x

Angeli, F., Villain, O., Schuller, S., Charpentier, T., de Ligny, D., Bressel, L., et al. (2012). Effect of temperature and thermal history on borosilicate glass structure. *Phys. Rev. B* 85:054110. doi: 10.1103/PhysRevB.85.054110

Barlet, M., Delaye, J.-M., Charpentier, T., Gennisson, M., Bonamy, D., Rouxel, T., et al. (2015). Hardness and toughness of sodium borosilicate glasses via Vickers's indentations. *J. Non Cryst. Solids* 417–418, 66–79. doi: 10.1016/j.jnoncrysol.2015.02.005

Biscoe, J., and Warren, B. E. (1938). X-ray diffraction study of soda-boric oxide glass. *J. Am. Ceram. Soc.* 21, 287–293. doi: 10.1111/j.1151-2916.1938.tb15777.x

Bradtmüller, H., Uesbeck, T., Eckert, H., Murata, T., Nakane, S., and Yamazaki, H. (2019). Structural origins of crack resistance on magnesium aluminoborosilicate glasses studied by solid-state NMR. *J. Phys. Chem. C* 123, 14941–14954. doi: 10.1021/acs.jpcc.9b03600

Bruns, S., Johanns, K. E., Rehman, H. U. R., Pharr, G. M., and Durst, K. (2017). Constitutive modeling of indentation cracking in fused silica. *J. Am. Ceram. Soc.* 100, 1928–1940. doi: 10.1111/jace.14734

Bruns, S., Petho, L., Minnert, C., Michler, J., and Durst, K. (2020). Fracture toughness determination of fused silica by cube corner indentation cracking and pillar splitting. *Mater. Design* 186:108311. doi: 10.1016/j.matdes.2019.108311

Dell, W. J., Bray, P. J., Xiao, S. Z. (1983). 11B NMR studies and structural modeling of Na_2O-B_2O_3-SiO_2 glasses of high soda content. *J. Non Cryst. Solids* 58, 1–16. doi: 10.1016/0022-3093(83)90097-2

Deng, L., and Du, J. (2018). Effects of system size and cooling rate on the structure and properties of sodium borosilicate glasses from molecular dynamics simulations. *J. Chem. Phys.* 148:024504. doi: 10.1063/1.5007083

Deschamps, T., Kassir-Bodon, A., Sonneville, C., Margueritat, J., Martinet, C., de Ligny, D., et al. (2013). Permanent densification of compressed silica glass: a Raman-density calibration curve. *J. Phys. Condens Matter.* 25:025402. doi: 10.1088/0953-8984/25/2/025402

Deschamps, T., Martinet, C., Bruneel, J. L., and Champagnon, B. (2011). Soda-lime silicate glass under hydrostatic pressure and indentation: a micro-Raman study. *J. Phys. Condens. Matter.* 23:035402. doi: 10.1088/0953-8984/23/3/035402

Du, L.-S., and Stebbins, J. F. (2003). Solid-state NMR study of metastable immiscibility in alkali borosilicate glasses. *J. Non Cryst. Solids* 315, 239–255. doi: 10.1016/S0022-3093(02)01604-6

Eagan, R. J., and Swearekgen, J. (1978). Effect of composition on the mechanical properties of aluminosilicate and borosilicate glasses. *J. Am. Ceram. Soc.* 61, 27–30. doi: 10.1111/j.1151-2916.1978.tb09222.x

Eckert, H. (1992). Structural characterization of noncrystalline solids and glasses using solid state NMR. *Prog. Nucl. Magn. Reson Spectrosc.* 24, 159–293. doi: 10.1016/0079-6565(92)80001-V

Eckert, H. (1994). "Structural studies of noncrystalline solids using solid state NMR.: new experimental approaches and results," in *Solid-State NMR IV Methods and Applications of Solid-State NMR* (Berlin; Heidelberg: Springer), 125–98. doi: 10.1007/978-3-642-79127-7_3

Eden, M. (2015). "^{27}Al NMR studies of aluminosilicate glasses," in *Annual Reports on NMR Spectroscopy*, *Vol. 86* (Waltham, MA; San Diego, CA; London; Oxford: Elsevier), 237–331. doi: 10.1016/bs.arnmr.2015.04.004

Ehrt, D. (2000). Structure, properties and applications of borate glasses. *Glass Technol.* 41, 182–185.

Ellison, A., and Cornejo, I. A. (2010). Glass substrates for liquid crystal displays. *Int. J. Appl. Glass Sci.* 1, 87–103. doi: 10.1111/j.2041-1294.2010.00009.x

Frederiksen, K. F., Januchta, K., Mascaraque, N., Youngman, R. E., Bauchy, M., Rzoska, S. J., et al. (2018). Structural compromise between high hardness and crack resistance in aluminoborate glasses. *J. Phys. Chem. B* 122, 6287–6295. doi: 10.1021/acs.jpcb.8b02905

Gross, T. M. (2012). Deformation and cracking behavior of glasses indented with diamond tips of various sharpness. *J. Non Cryst. Solids* 358, 3445–3452. doi: 10.1016/j.jnoncrysol.2012.01.052

Gross, T. M., and Price, J. J. (2017). Vickers indentation cracking of ion-exchanged glasses: Quasi-static vs. dynamic contact. *Front. Mater.* 4, 1–14. doi: 10.3389/fmats.2017.00004

Inaba, S., Fujino, S., and Morinaga, K. (1999). Young's modulus and compositional parameters of oxide glasses. *J. Am. Ceram. Soc.* 82, 3501–3507. doi: 10.1111/j.1151-2916.1999.tb02272.x

Ito, S., and Taniguchi, T. (2004). Effect of cooling rate on structure and mechanical behavior of glass by MD simulation. *J. Non Cryst. Solids* 349, 173–179. doi: 10.1016/j.jnoncrysol.2004.08.180

Januchta, K., Liu, P., Hansen, S. R., To, T., and Smedskjaer, M. M. (2019a). Indentation cracking and deformation mechanism of sodium aluminoborosilicate glasses. *J. Am. Ceram. Soc.* 103, 1656–1665. doi: 10.1111/jace.16894

Januchta, K., and Smedskjaer, M. M. (2019). Indentation deformation in oxide glasses: quantification, structural changes, and relation to cracking. *J. Non Cryst. Solids X* 1:100007. doi: 10.1016/j.nocx.2018.100007

Januchta, K., To, T., Bødker, M. S., Rouxel, T., and Smedskjaer, M. M. (2019b). Elasticity, hardness, and fracture toughness of sodium aluminoborosilicate glasses. *J. Am. Ceram. Soc.* 102, 4520–4537. doi: 10.1111/jace.16304

Januchta, K., Youngman, R. E., Goel, A., Bauchy, M., Logunov, S. L., Rzoska, S. J., et al. (2017). Discovery of ultra-crack-resistant oxide glasses with adaptive networks. *Chem. Mater.* 29, 5865–5876. doi: 10.1021/acs.chemmater.7b00921

Kato, Y., Yamazaki, H., Yoshida, S., and Matsuoka, J. (2010). Effect of densification on crack initiation under Vickers indentation test. *J. Non Cryst. Solids* 356, 1768–1773. doi: 10.1016/j.jnoncrysol.2010.07.015

Kim, K. S., and Bray, P. J. (1974). B^{11} NMR studies of glasses in the system MgO-Na_2O-B_2O_3. *Phys. Chem. Glasses* 15, 47–51.

Kurkjian, C. R., Gupta, P. K., and Brow, R. K. (2010). The strength of silicate glasses: what do we know, what do we need to know? *Int. J. Appl. Glass Sci.* 1, 27–37. doi: 10.1111/j.2041-1294.2010.00005.x

Lawn, B. R., Evans, A. G., and Marshall, D. B. (1980). Elastic-plastic indentation damage in ceramics - the median-radial crack system. *J. Am. Ceram. Soc.* 63, 574–581. doi: 10.1111/j.1151-2916.1980.tb10768.x

Limbach, R., Winterstein-Beckmann, A., Dellith, J., Möncke, D., and Wondraczek, L. (2015). Plasticity, crack initiation and defect resistance in alkali-borosilicate glasses: from normal to anomalous behavior. *J. Non Cryst. Solids* 417–418, 15–27. doi: 10.1016/j.jnoncrysol.2015.02.019

MacKenzie, K. J., and Smith, M. E. (2002). *Multinuclear Solid-State Nuclear Magnetic Resonance of Inorganic Materials*. Oxford: Elsevier.

Malchow, P., Johanns, K. E., Möncke, D., Korte-Kerzel, S., Wondraczek, L., and Durst, K. (2015). Composition and cooling-rate dependence of plastic deformation, densification, and cracking in sodium borosilicate

glasses during pyramidal indentation. *J. Non Cryst. Solids* 419, 97–109. doi: 10.1016/j.jnoncrysol.2015.03.020

Martens, R., and Müller-Warmuth, W. (2000). Structural groups and their mixing in borosilicate glasses of various compositions – an NMR study. *J. Non Cryst. Solids* 265, 167–175. doi: 10.1016/S0022-3093(99)00693-6

Massiot, D., Fayon, F., Capron, M., King, I., Le Calvé, S., Alonso, B., et al. (2002). Modelling one- and two-dimensional solid-state NMR spectra. *Magn. Reson. Chem.* 40, 70–76. doi: 10.1002/mrc.984

Mauro, J. C. (2014). Grand challenges in glass science. *Front. Mater.* 1:20. doi: 10.3389/fmats.2014.00020

Medek, A., Harwood, J. S., and Frydman, L. (1995). Multiple-quantum magic-angle spinning NMR: a new method for the study of quadrupolar nuclei in solids. *J. Am. Chem. Soc.* 117, 12779–12787. doi: 10.1021/ja00156a015

Milberg, M. E., O'Keefe, J. G., Verhelst, R. A., and Hooper, H. O. (1972). Boron coordination in sodium borosilicate glasses. *Phys. Chem. Glasses* 13, 79–84.

Möncke, D., Ehrt, D., Eckert, H., and Mertens, V. (2003). Influence of melting and annealing conditions on the structure of borosilicate glasses. *Phys. Chem. Glasses* 44, 113–116.

Möncke, D., Ehrt, D., Tricot, G., and Kamitsos, E. I. (2015a). Connectivity of borate and silicate groups in a low-alkali borosilicate glass by vibrational and 2D NMR spectroscopy. *J. Chem. Technol. Metallurgy* 50, 381–386.

Möncke, D., Ehrt, D., Varsamis, C. P. E., Kamitsos, E. I., and Kalampounias, A. G. (2006). Thermal history of a low alkali borosilicate glass probed by infrared and Raman spectroscopy. *Glass Technol. Eur. J. Glass Sci. Technol. A* 47, 133–137.

Möncke, D., Tricot, G., Winterstein-Beckmann, A., Wondraczek, L., and Kamitsos, E. I. (2015b). On the connectivity of borate tetrahedra in borate and borosilicate glasses. *Phys. Chem. Glasses Eur. J. Glass Sci. Technol. B* 56, 203–211. doi: 10.13036/1753-3562.56.5.203

Mound, B. A., and Pharr, G. M. (2019). Nanoindentation of fused quartz at loads near the cracking threshold. *Exp. Mech.* 59, 369–380. doi: 10.1007/s11340-018-00446-3

Oliver, W. C., and Pharr, G. M. (1992). An improved technique for determining hardness and elastic-modulus using load and displacement sensing indentation experiments. *J. Mater. Res.* 7, 1564–1583. doi: 10.1557/JMR.1992.1564

Osipov, A. A., Eremyashev, V. E., Mazur, A. S., Tolstoi, P. M., and Osipova, L. M. (2016). Coordination state of aluminum and boron in barium aluminoborate glass. *Glass Phys. Chem.* 42, 230–237. doi: 10.1134/S1087659616030111

Polian, A. (2003). Brillouin scattering at high pressure: an overview. *J. Raman Spectrosc.* 34, 633–637. doi: 10.1002/jrs.1031

Price, J. J., Glaesemann, G. S., Clark, D. A., Gross, T. M., and Barefoot, K. L. (2009). "69.3: a mechanics framework for ion-exchanged cover glass with a deep compression layer," in *SID Symposium Digest of Technical Papers*, *Vol. 40*, 1049–1051. doi: 10.1889/1.3256467

Reibstein, S., Wondraczek, L., de Ligny, D., Krolikowski, S., Sirotkin, S., Simon, J. P., et al. (2011). Structural heterogeneity and pressure-relaxation in compressed borosilicate glasses by in situ small angle X-ray scattering. *J. Chem. Phys.* 134:204502. doi: 10.1063/1.3593399

Rosales-Sosa, G. A., Masuno, A., Higo, Y., and Inoue, H. (2016). Crack-resistant Al_2O_3-SiO_2 glasses. *Sci. Rep.* 6:23620. doi: 10.1038/srep23620

Rouxel, T. (2007). Elastic properties and short-to medium-range order in glasses. *J. Am. Ceram. Soc.* 90, 3019–3039. doi: 10.1111/j.1551-2916.2007.01945.x

Rouxel, T. (2015). Driving force for indentation cracking in glass: composition, pressure and temperature dependence. *Philos. Trans. A Math. Phys. Eng. Sci.* 373, 1–26. doi: 10.1098/rsta.2014.0140

Rouxel, T. (2017). Fracture surface energy and toughness of inorganic glasses. *Scr. Mater.* 137, 109–113. doi: 10.1016/j.scriptamat.2017.05.005

Rouxel, T., and Yoshida, S. (2017). The fracture toughness of inorganic glasses. *J. Am. Ceram. Soc.* 100, 4374–4396. doi: 10.1111/jace.15108

Smedskjaer, M. M., Youngman, R. E., and Mauro, J. C. (2014). Principles of Pyrex® glass chemistry: structure–property relationships. *Appl. Phys. A* 116, 491–504. doi: 10.1007/s00339-014-8396-1

Stebbins, J. F., Zhao, P., and Kroeker, S. (2000). Non-bridging oxygens in borate glasses: characterization by ^{11}B and ^{17}O MAS and 3QMAS NMR. *Solid State Nuclear Magnet. Reson.* 16, 9–19. doi: 10.1016/S0926-2040(00)00050-3

van Wüllen, L., and Schwering, G. (2002). ^{11}B-MQMAS and ^{29}Si-^{11}B double-Resonance NMR studies on the structure of binary B_2O_3-SiO_2 glasses. *Solid State Nucl. Magn. Reson.* 21, 134–144. doi: 10.1006/snmr.2002.0054

Veber, A., Cicconi, M. R., Reinfelder, H., and De Ligny, D. (2017). Combined differential scanning calorimetry, Raman and Brillouin spectroscopies: a multiscale approach for materials investigation. *Analyt. Chim. Acta* 998:37–44. doi: 10.1016/j.aca.2017.09.045

Vogel, W. (1994). *Glass Chemistry, 2nd edn,* Vol. 14. Berlin; Heidelberg: Springer, 464. doi: 10.1007/978-3-642-78723-2

Wada, M., Furukawa, H., and Fujita, K. (eds.). (1974). Crack resistance of glass on Vickers indentation. *Proc. Int. Congr. Glass* 11, 39–46.

Wang, S., and Stebbins, J. F. (1998). On the structure of borosilicate glasses: a triple-quantum magic-angle spinning ^{17}O nuclear magnetic resonance study. *J. Non Cryst. Solids* 231, 286–290. doi: 10.1016/S0022-3093(98)00703-0

Winterstein-Beckmann, A., Möncke, D., Palles, D., Kamitsos, E. I., and Wondraczek, L. (2013). Structure–property correlations in highly modified Sr, Mn-borate glasses. *J. Non Cryst Solids* 376, 165–174. doi: 10.1016/j.jnoncrysol.2013.05.029

Winterstein-Beckmann, A., Möncke, D., Palles, D., Kamitsos, E. I., and Wondraczek, L. (2014a). Raman spectroscopic study of structural changes induced by micro-indentation in low alkali borosilicate glasses. *J. Non Cryst. Solids* 401, 110–114. doi: 10.1016/j.jnoncrysol.2013.12.038

Winterstein-Beckmann, A., Möncke, D., Palles, D., Kamitsos, E. I., and Wondraczek, L. (2014b). A Raman-spectroscopic study of indentation-induced structural changes in technical alkali-borosilicate glasses with varying silicate network connectivity. *J. Non Cryst. Solids* 405, 196–206. doi: 10.1016/j.jnoncrysol.2014.09.020

Wondraczek, L., Krolikowski, S., and Behrens, H. (2010). Kinetics of pressure relaxation in a compressed alkali borosilicate glass. *J. Non Cryst. Solids* 356, 1859–1862. doi: 10.1016/j.jnoncrysol.2010.06.009

Wondraczek, L., Mauro, J. C., Eckert, J., Kühn, U., Horbach, J., Deubener, J., et al. (2011). Towards ultrastrong glasses. *Adv. Mater.* 23, 4578–4586. doi: 10.1002/adma.201102795

Wondraczek, L., Sen, S., Behrens, H., and Youngman, R. E. (2007). Structure-energy map of alkali borosilicate glasses: effects of pressure and temperature. *Phys. Rev. B* 76:014202. doi: 10.1103/PhysRevB.76.014202

Yoshida, S. (2019). Indentation deformation and cracking in oxide glass – toward understanding of crack nucleation. *J. Non Cryst. Solids X* 1:100009. doi: 10.1016/j.nocx.2019.100009

Yoshida, S., Hayashi, Y., Konno, A., Sugawara, T., Miura, Y., and Matsuoka, J. (2009). Indentation induced densification of sodium borate glasses. *Phys. Chem. Glass.* 50, 63–70.

Yoshida, S., Wada, K., Fujimura, T., Yamada, A., Kato, M., Matsuoka, J., et al. (2016). Evaluation of sinking-in and cracking behavior of soda-lime glass under varying angle of trigonal pyramid indenter. *Front. Mater.* 3:54. doi: 10.3389/fmats.2016.00054

Yun, Y., and Bray, P. (1978). Nuclear magnetic resonance studies of the glasses in the system Na_2O-B_2O_3-SiO_2. *J. Non Cryst. Solids* 27, 363–380. doi: 10.1016/0022-3093(78)90020-0

Yun, Y. H., Feller, S. A., and Bray, P. J. (1979). Correction and addendum to Nuclear Magnetic-Resonance studies of the glasses in the system Na_2O-B_2O_3-SiO_2. *J. Non Cryst. Solids* 33, 273–277. doi: 10.1016/0022-3093(79)90055-3

Zehnder, C., Bruns, S., Peltzer, J. N., Durst, K., Korte-Kerzel, S., and Möncke, D. (2017a). Influence of cooling rate on cracking and plastic deformation during impact and indentation of borosilicate glasses. *Front. Mater.* 4:5. doi: 10.3389/fmats.2017.00005

Zehnder, C., Peltzer, J.-N., Gibson, J. S. K. L., Möncke, D., and Korte-Kerzel, S. (2017b). Non-Newtonian flow to the theoretical strength of glasses via impact nanoindentation at room temperature. *Sci. Rep.* 7:17618. doi: 10.1038/s41598-017-17871-4

Conflict of Interest: The authors declare that the research was conducted in the absence of any commercial or financial relationships that could be construed as a potential conflict of interest.

frontiers in Materials

ORIGINAL RESEARCH
published: 14 August 2020
doi: 10.3389/fmats.2020.00268

Automated Analysis of Slow Crack Growth in Hydrous Soda-Lime Silicate Glasses

Philipe Kiefer[1], Martin Maiwald[1], Joachim Deubener[1], Robert Balzer[2], Harald Behrens[2], Tina Waurischk[3], Stefan Reinsch[3] and Ralf Müller[3]*

[1] Institute of Non-Metallic Materials, Clausthal University of Technology, Clausthal-Zellerfeld, Germany, [2] Institute of Mineralogy, Leibniz University Hannover, Hanover, Germany, [3] Federal Institute of Materials Research and Testing (BAM), Berlin, Germany

To explore the impact of ambient and structural water on static fatigue, the initiation and growth of 3279 Vickers induced median radial cracks were automatically recorded and analyzed. We find that humidity is more efficient in initiating cracks and promoting their growth than water, which is dissolved in the glass structure. In particular for slow crack growth ($< 3 \times 10^{-6}$ m s^{-1}), tests in dry nitrogen showed a considerable decrease in the crack growth exponent with increasing water content of the glasses. On the other hand, if tests were performed in humid air, the crack growth exponent was independent of the water content of the hydrous glasses, while stress intensity decreased slightly. These observations indicate that water promotes the processes at the crack-tip regardless of its origin. However, ambient water is more efficient.

Keywords: slow crack growth, automated analysis, hydrous glass, Vickers indentation, indentation fracture toughness

OPEN ACCESS

Edited by:
Ashutosh Goel,
Rutgers, The State University of New Jersey, United States

Reviewed by:
John Matthewson,
Rutgers, The State University of New Jersey, United States
Timothy Michael Gross,
Corning Inc., United States

****Correspondence:***
Joachim Deubener
joachim.deubener@tu-clausthal.de

Specialty section:
This article was submitted to Ceramics and Glass, a section of the journal Frontiers in Materials

Received: *24 February 2020*
Accepted: *20 July 2020*
Published: *14 August 2020*

Citation:
Kiefer P, Maiwald M, Deubener J, Balzer R, Behrens H, Waurischk T, Reinsch S and Müller R (2020) Automated Analysis of Slow Crack Growth in Hydrous Soda-Lime Silicate Glasses. Front. Mater. 7:268. doi: 10.3389/fmats.2020.00268

INTRODUCTION

Water is omnipresent at glass surfaces. In particular at the crack-tip, where vapor and liquid water (due to capillary condensation) can react with the stressed glass network. However, the glass-water interaction is complex and not adequately understood, although the control of such the environmental reactions at the crack-tip is essential for improving the practical strength and the endurance limit of glassy products.

The basic idea of studying hydrous glasses is to create a situation where water species (hydroxyl groups and water molecules) are already present in the glass structure and to confront them with environmental water molecules reacting at the crack-tip. This approach requires several steps. Firstly, water-containing glasses must be synthesized to shed light on the influence of dissolved H_2O on the glass structure. The structural effects depend on composition as was shown by previous studies on borate (Bauer et al., 2015), borosilicate (Bauer et al., 2017; Behrens et al., 2018), silicoborate (Balzer et al., 2019b), phosphate (Balzer et al., 2019a), aluminosilicate (Balzer et al., 2020), and soda-lime silicate glasses (Kiefer et al., 2019). Secondly, volumetric and mechanical properties of hydrous glasses need to be investigated. Due to their technical importance, these investigations were carried out on soda-lime silicate glasses (Kiefer et al., 2019). For a microscope slide glass, it was found that density, elastic moduli and Vickers hardness decrease with increasing water content, whereas the Poisson's ratio and the water content of the hydrous glasses are positively correlated. On the one hand, the trends reported by previous work reflect the non-linear change in the concentrations of hydroxyl groups and water molecules in the glasses. On the other hand,

the properties were found to be environmentally sensitive, if the glass surface was involved, e.g., during indentation hardness measurements. It was observed that for dry glasses in humid atmospheres and for hydrous glasses in dry atmospheres, the indent size changed with the duration of the indentation, indicating that water was capable to relax stressed bonds in both scenarios. Particularly, the response times of water species coming from the environment and those being dissolved in the glass structure were found to be effectively equal. Recently, the hydrous glass approach was applied to capture crack growth in a nominal dry (0.13 mol% H_2O) and a hydrous microscope slide glass (17.08 mol% H_2O) using the double cantilever beam (DCB) technique (Waurischk et al., 2020). Under vacuum, crack propagation rates $> 10^{-7}$ m s^{-1} in the hydrous glass were shifted to higher stress intensity, whereas under humid environment (air) crack propagation rates of the hydrous glass were shifted to lower stress intensity with respect to the dry glass. The apparent toughening effect of the dissolved water in the glass under vacuum was explained by higher energy dissipation during fracturing. Water-related internal friction bands observed in dynamic-mechanical spectroscopy studies (Reinsch et al., 2013; Waurischk et al., 2020) supported this idea. With respect to the behavior in air, it was suggested that the dissipation mechanism was overwhelmed by environmental water, which led to the weakening, i.e., a decrease in stress intensity (Waurischk et al., 2020).

With this background, the hydrous glass approach was employed in this study with respect to the sub-critical growth of Vickers induced median radial cracks. A series of 5 microscope slide glasses with water contents ranging from 0.75 to 17.08 (mol%) was tested in two different environments (dry N_2 gas and air) to explore water-dependent effects. In spite of the limitations due to unknown amplitude of the residual stress field in this case, the technique of indentation allowed, in principle, automated experiments as well as automated data processing and analysis (Kiefer et al., 2020). Thus, to demonstrate statistical significance, the growth of in total 3279 cracks was recorded (= 6.165 million frames) and automatically analyzed to determine the mean crack length within the first minute of propagation of each glass with high accuracy.

EXPERIMENTAL

Preparation of Hydrous Glasses

Samples of hydrous soda-lime silicate glasses from a previous study were used (Kiefer et al., 2019). These were synthesized from commercial microscope slides (MSG) with a molar composition $SiO_2/Na_2O/CaO/MgO/Al_2O_3/K_2O/(Fe_2O_3/TiO_2)$ = 73.2/13.3/6.6/6.2/0.5/0.2/(0 +) as analyzed by X-ray fluorescence (Axios, PANalytical). Oxides in parentheses were present in a nominal molar amount < 0.05. Hydration was performed using an internally heated pressure vessel (IHPV) in which welded Pt-capsules were placed. Samples were heated to 1673 K at a pressure of 500 MPa for 20 h. The Pt-capsules were filled with powder of the crushed MSG glass and the required amount of water. Details of the hydration procedure using the IHPV apparatus were provided in Berndt et al. (2002). The water contents were analyzed using Fourier transformed infrared spectroscopy and Karl-Fischer-titration. The results of these characterizations were published in Kiefer et al. (2019). Two platelets of $\sim 20 \times 5 \times 1$ mm^3 in size with diamond polished surfaces (< 1 μm) were prepared from each hydrated glass for Vickers indentation. The glasses were labeled 0W-MSG500 (0.75; 0), 1W-MSG500 (3.15; 0.214), 2W-MSG500 (5.89; 0.374), 4W-MSG (11.62; 0.605), and 6W-MSG500 (17.08; 0.739). The names refer to the nominal water content in wt% and the synthesis pressure in MPa, e.g., 4W-MSG500 = 4 wt% water, 500 MPa. The first value in parentheses behind the name indicates the analyzed water content in mol%, while the second value is the ratio $c_{H2O}/(c_{OH} + c_{H2O})$ where c_{H2O} and c_{OH} represent the contents of water dissolved as molecules and hydroxyl groups, respectively, in the glass structure (Kiefer et al., 2019).

Automated Data Processing of Vickers Induced Crack Growth

To initiate radial crack growth in the hydrous glass samples, the surfaces were indented with a Vickers diamond under a fixed load of 17.66 N using a universal hardness-testing machine (ZHU 2.5, Zwick&Roell, Ulm, Germany). The automated protocol included a loading and unloading step of 5 s each [resulting in an (un)loading rate of ± 3.53 N s^{-1}] and a dwell time of 15 s (**Figure 1**). Crack initiation and propagation were observed through a long distance objective at a magnification of 20x (N PLAN L, Leica, Wetzlar, Germany) of an inverted microscope (DM-ILM, Leica, Wetzlar, Germany) and recorded with a 5.3 megapixel CMOS sensor of a monochrome camera (PL-D725MU-T, PixelINK, Ottawa, Canada). The microscope was positioned directly below the hardness tester and the tip of the Vickers diamond was aligned to be parallel to the optical axis of the microscope. To increase the stiffness of the experimental setup, a steel plate with a thickness of 20 mm replaced the original microscope table. For each of the 62–143 indents per sample a video was recorded at an acquisition rate of 30 frames per second for durations of 60 s (= 1800 frames) or 65 s (= 1950 frames). The start of the image acquisition was triggered by a LabView script at the beginning of the unloading ramp (t = 0). The videos were recorded without any compression as.seq files using the TroublePix software (Norpix, Montreal, Canada). Decomposition of the videos into single Tagged Image File Format (.tiff) files was carried out using the BatchProcessor software (Norpix, Montreal, Canada). Each.tiff image was automatically analyzed via a self-written MatLab code (Mathworks, Natick, MA, United States) that was capable to measure the Euclidean distance between the center of the indent and the tip of the corner cracks for each crack of the single images. The detection of the crack tip was performed using the gray scale values. Lengths determined by the automated analysis were in excellent agreement (< 2 μm) with scanning electron microscope (SEM) measurements.

To study the impact of humidity, the measurements with the above setup were carried out in two different environments. On the one hand, the indentations were conducted in a glovebox

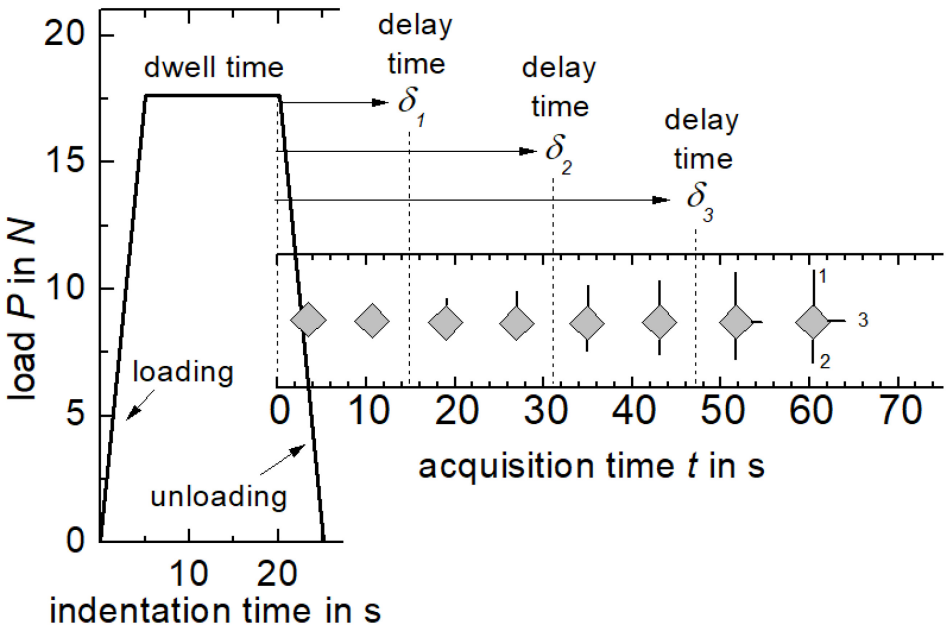

FIGURE 1 | Scheme of the load-time curve of the Vickers indentation. Automated image acquisition was triggered at the start of the unloading ramp. Radial cracks at the corner of the indent were observed to grow after a delay time δ.

(labmaster130, MBraun, Garching, Germany) providing a dry nitrogen atmosphere with a H_2O partial pressure $p_{H2O} \leq 30$ Pa at 25°C. On the other hand, the second platelet of each specimen was measured in a cleanroom with a constant humidity of p_{H2O} = 942 Pa at 18°C. Humidity in the glovebox was monitored with a dew point sensor (Michell Instruments, Easydew EA2-TX, Ely, United Kingdom) connected to a data logger (Ahlborn, Almemo 8590-9, Holzkirchen, Germany). In the cleanroom humidity was monitored using a FHAD462 sensor connected to an Almemo 2470-2S data logger (both Ahlborn, Holzkirchen, Germany).

TABLE 1 | Total number of cracks initiated after 60 s (N_{60s}) and 65 s (N_{65s}), number of indents (z) and the probability of crack initiation F_{60s} and F_{65s}.

Glass	Vapor pressure p_{H2O} = 30 Pa			Vapor pressure p_{H2O} = 942 Pa		
	N_{60s}	z	F_{60s}	N_{65s}	z	F_{65s}
0W-MSG500	183	62	0.736	402	126	0.796
1W-MSG500	294	121	0.606	339	111	0.762
2W-MSG500	324	135	0.599	339	118	0.717
4W-MSG500	259	135	0.479	370	121	0.763
6W-MSG500	467	143	0.815	302	92	0.819

RESULTS

Table 1 summarizes the total number of median radial cracks that were initiated during Vickers indentation and counted at the end of the video acquisition of the series in dry environment after 60 s and of the series in humid environment after 65 s, respectively. Representative images of Vickers induced cracks and their growth by video capturing were presented in a previous paper (Kiefer et al., 2020). According to Wada et al. (1974), the probability of crack initiation was determined by the crack number-to-corner number ratio, with 4 corners per indent z of the Vickers diamond. Inspection of **Table 1** reveals that the probability of crack initiation is higher for each glass when tested under the humid conditions of the cleanroom. Under the dry conditions of the glovebox, the frequency of initiated cracks first decreases with the water content to about 48% (4W-MSG500) and then increases to ∼82% for the glass with the highest water content. Under humid conditions, the probability of crack initiation does not depend significantly on the water content of the glass.

In order to analyze a possible delay in crack initiation in more detail, cumulative frequency functions $F(\delta)$ were generated for each glass (**Figure 2**). This was done by arranging the delay of each crack in ascending order ($\delta_1 \leq \delta_2 \leq \delta_3 \leq \cdots \leq \delta_N$, the minimum first and the maximum last) followed by relating its rank number R_i to the total number of possible cracks ($4z$). With the commonly used median rank approximation of Benard and Bosi-Levenbach (Benard and Bosi-Levenbach, 1953) one has:

$$F(\delta) = \frac{R_i(\delta_i) - 0.3}{4z + 0.4} \quad \text{for } i = 1, \ldots, 4z \tag{1}$$

For example, $F = (1-0.3)/(4 \times 62 + 0.4) = 0.0028$ for the first crack (δ = 1.03 s) of 0W-MSG500 (p_{H2O} = 30 Pa), while $F = (183-0.3)/(4 \times 62 + 0.4) = 0.736$ for the latest crack (δ = 59.87 s). Under humid conditions, crack

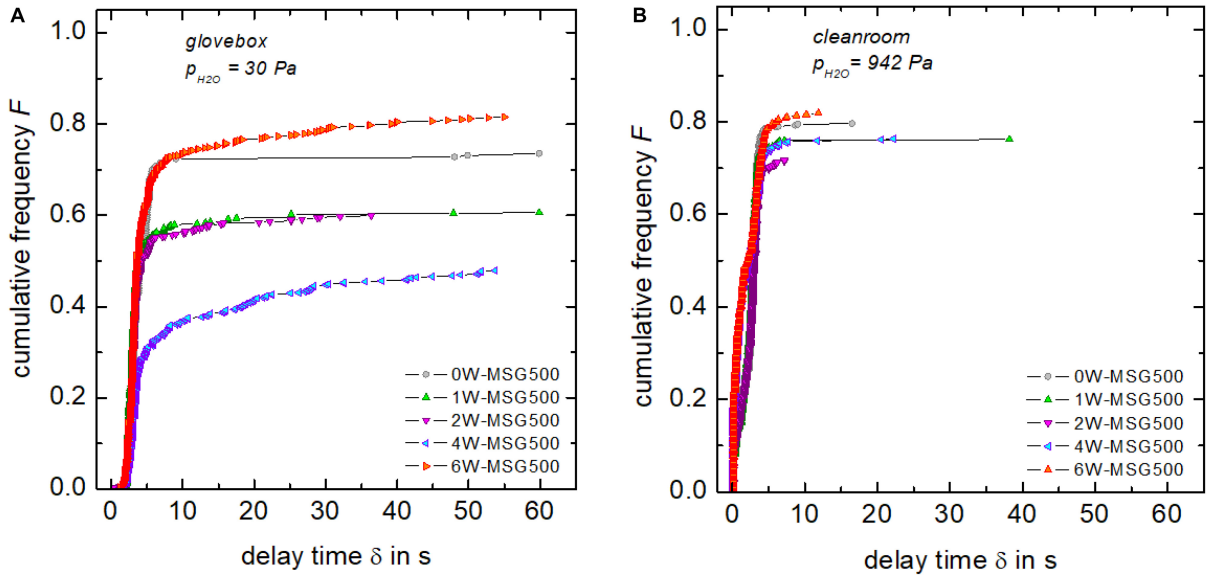

FIGURE 2 | Cumulative frequency distribution $F(\delta)$ of the number of initiated cracks tested in dry **(A)** and humid **(B)** environments. Lines connecting data points are intended as visual guides.

initiation for all glasses occured almost completely while unloading ($\delta < 5$ s). When tested in dry nitrogen gas, differences in the temporal evolution of crack initiation between the nominally anhydrous and hydrous glasses were evident. With increasing water content, crack initiation becomes increasingly delayed and often occurs after unloading is completed ($\delta > 5$ s). In summary, **Figure 2** clearly shows that humidity shortens the delay time.

In order to analyze crack growth in detail, the propagation time ($t-\delta$) was calculated by subtracting the delay δ from the acquisition time t for each crack. **Figure 3** primarily shows that the crack length strongly depend on the H_2O partial pressure, which has been noted already in previous studies (Benbahouche et al., 2012; Striepe et al., 2013). After 55 s, cracks have reached about 70–120 μm under dry conditions, whereas in the humid environment, crack lengths in the range 100–160 μm were detected. Further, large differences in the initial propagation rates from crack to crack are evident, leading to a broad distribution of crack lengths already shortly after their initiation (<5 s). This feature underlines the demand of analyzing crack propagation using large data sets with $N > 200$ (Kiefer et al., 2020).

Figure 4 exemplarily shows cumulative distribution functions of the crack length c_{50s} ($t-\delta = 50$ s). Cumulative frequency analyses using CumFreq[1] software indicated that c_{50s} were consistent with a Weibull distribution for all glasses and environments. Two-parameter Weibull distributions $\{F = 1-\exp[-(c_{50s}/c_m)^{\beta}]$ with scale parameter c_m and shape parameter $\beta\}$ were fitted using the OriginPro 2019 software (OriginLab, Northampton, MA, United States) with median-rank regression (MRR) and maximum likelihood estimators (MLE). For MRR, data series were generated by arranging the length c_{50s} of each crack in ascending order while simultaneously relating its rank number R_i to the total number N of observed cracks. For $F(c_{50s})$ one has:

$$F(c_{50s}) = \frac{R_i(\delta_i) - 0.3}{N + 0.4} \quad \text{for } i = 1, \ldots, N \tag{2}$$

MLE does not make use of data sorting, which could lead to self-correlation of the data. In this case, data points in **Figure 4** were plotted according to median ranks and the lines according to the MLE solutions. Graphs of the confidence interval of **Figure 4** were used to give preference for either MRR or MLE solutions. Results of the fitting procedure were compiled in **Table 2**. These fitted Weibull distributions were found to be negatively skewed and of small tail. It is noteworthy that independent from the fitting procedure a few short and long cracks outside the 95% confidence interval are present in most hydrous glasses (**Figure 4B**). One should note that a more rigorous analysis of fracture data requires unbiassing factors, which must be calculated for any specific Weibull distribution, see e.g., ASTM C1239 – 06a. The unbiased MLE treatment improves the size of the confidence intervals, whereas for large datasets it affects only marginally the fit parameters c_m and β.

Distributions of randomly selected propagation times indicated that the small skewness of the Weibull distributions of **Figure 4** is typical, i.e., -K is nearly constant (0.39–0.42). Hence, the mean length c_{av} instead of the modal length c_m of cracks was taken to simplify the evaluation of the crack propagation rate within these limits. **Figure 5** shows that the crack growth is largely influenced by the humidity. After 50 s of propagation, cracks have reached mean lengths in the range of 90–104 μm at low H_2O partial pressure and 125–139 μm under higher p_{H_2O}.

[1]www.waterlog.info/cumfreq.htm

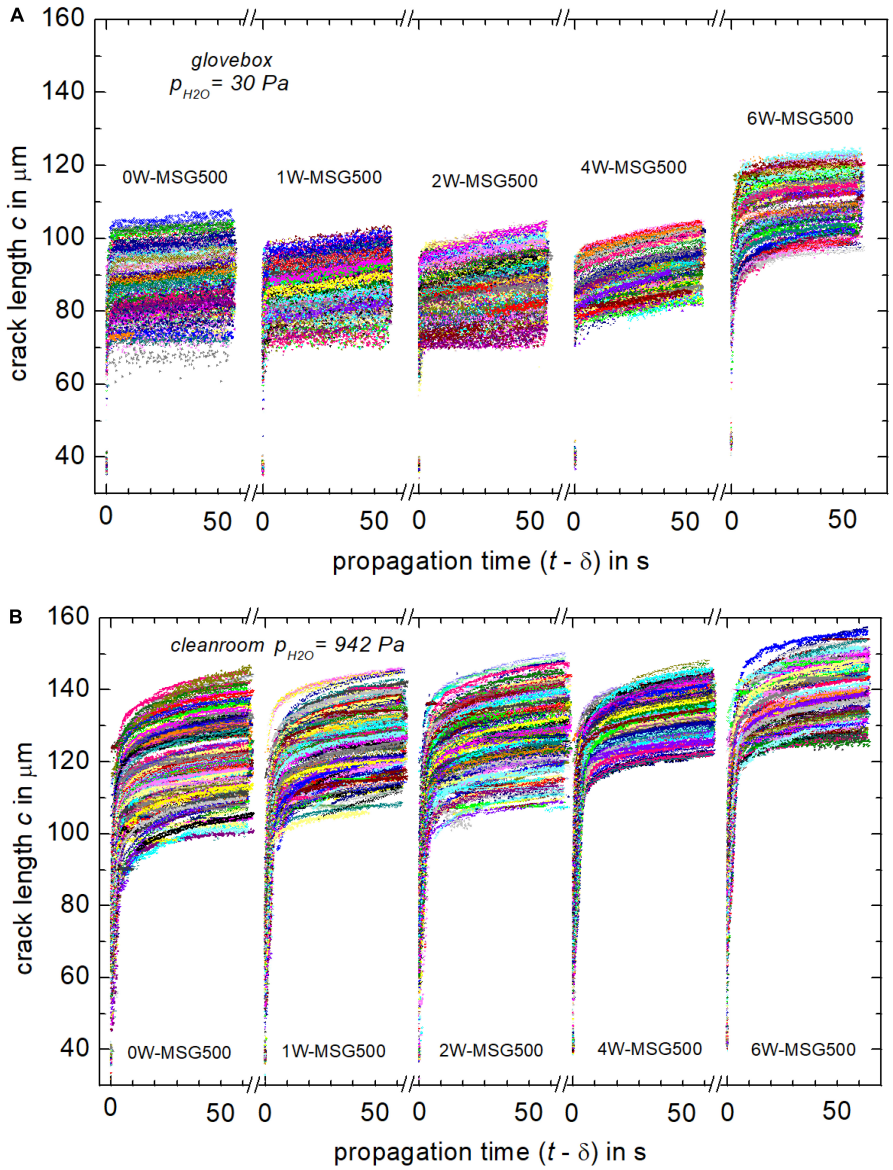

FIGURE 3 | Length vs. propagation time of cracks grown in hydrous glasses in 30 Pa partial pressure of H_2O **(A)** and in 942 Pa partial pressure of H_2O **(B)**.

Within the two series, a trend of longer cracks at higher water contents of the glasses is evident.

A two-phase exponential growth model was used to describe the dependence of average crack length on propagation time since a single-phase power-law (Dériano et al., 2004; Striepe et al., 2013; Striepe and Deubener, 2013; Pönitzsch et al., 2016; Kiefer et al., 2020) noticeably overestimates the early stage $(t-\delta) \leq 5$ s of most tests in higher humidity. The fitting procedure was carried out for c_{av} data of each glass and testing environment of **Figure 5**, which resulted in smoothed crack length data of the form:

$$c_{av} = c_{\infty} + S_1 exp\left[-\frac{(t-\delta)}{t_1}\right] + S_2 exp\left[-\frac{(t-\delta)}{t_2}\right] \quad (3)$$

where c_{∞}, S_1, t_1, S_2 and t_2 are adjustable parameters. The mean crack propagation rate v_{av} was derived by taking the first derivative with respect to the propagation time:

$$v_{av} = \frac{dc_{av}}{dt} = -\frac{S_2}{t_2} exp\left[-\frac{(t-\delta)}{t_2}\right] - \frac{S_1}{t_1} exp\left[-\frac{(t-\delta)}{t_1}\right] \quad (4)$$

DISCUSSION

Figure 2 highlights the environmental sensitivity of crack delay times. To check if an additional influence of the water speciation on crack delay is present, crack initiation probabilities for δ = 1, 2, 3, 6, and 60 s were extracted from **Figure 2** and plotted vs. the

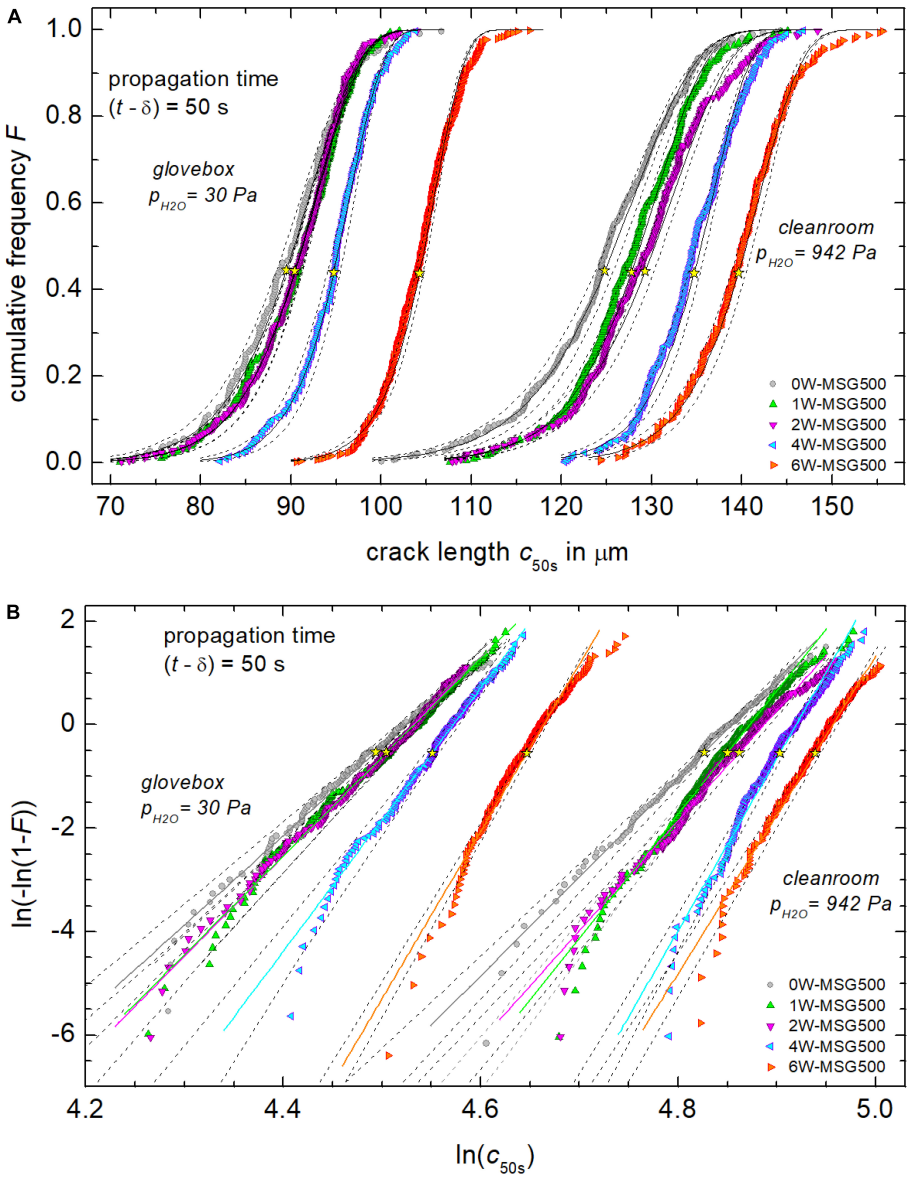

FIGURE 4 | Cumulative frequency F of the crack length c_{50s} in dry and humid environments **(A)**. Part **(B)** shows corresponding Weibull plots of cumulative frequencies. Solid lines are the best fit (MMR and MLE) through the data with parameters compiled in **Table 2**, while dotted lines are 95% confidence intervals. Yellow stars indicate the mean crack length c_{av}.

TABLE 2 | Scale parameter c_m, shape parameter β, skewness parameter K, standard deviation σ, and mean length c_{av} of Weibull distributed crack lengths c_{50s} (propagation time $t-\delta$ = 50 s). The skewness parameter K calculates as $K = (c_{av}-c_m)/\sigma$. Weibull distributions were fitted using median-rank regression (MRR) and maximum likelihood estimators (MLE).

Glass	Vapor pressure p_{H2O} = 30 Pa						Vapor pressure p_{H2O} = 942 Pa					
	c_m (µm)	β	-K	σ (µm)	c_{av} (µm)	Method	c_m (µm)	β	-K	σ (µm)	c_{av} (µm)	Method
0W-MSG500	92.26	17.23	0.39	6.40	89.46	MRR	128.32	19.08	0.39	8.09	124.77	MRR
1W-MSG500	93.04	19.08	0.39	5.87	90.47	MLE	130.69	23.89	0.41	6.66	127.75	MRR
2W-MSG500	92.94	19.31	0.39	5.80	90.39	MLE	132.57	21.32	0.40	7.53	129.26	MRR
4W-MSG500	96.76	25.43	0.41	4.65	94.71	MLE	136.95	33.28	0.42	5.08	134.70	MRR
6W-MSG500	106.04	32.34	0.42	4.05	104.25	MRR	142.15	30.67	0.42	5.71	139.62	MRR

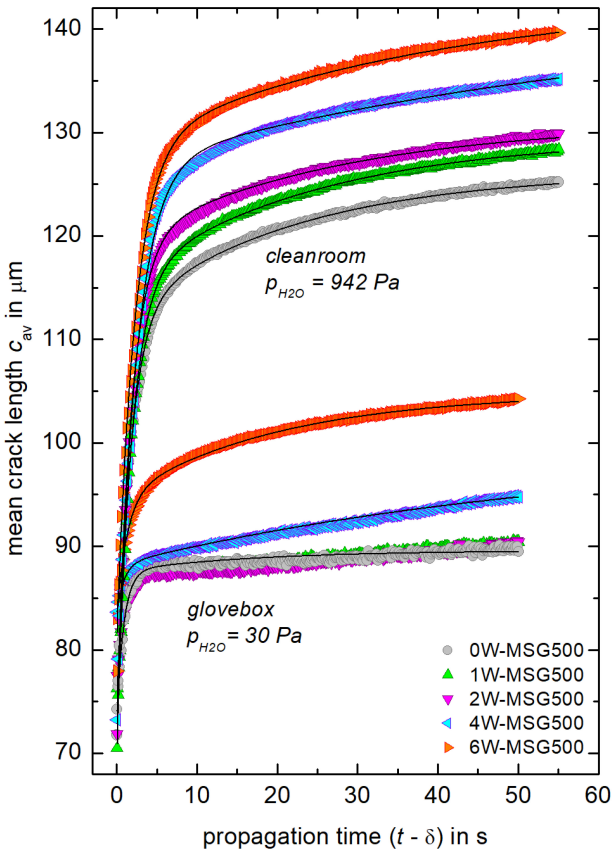

FIGURE 5 | Mean crack length c_{av} as a function of the propagation time ($t-\delta$). Solid lines are best representation of data as fitted by Equation (3) with R^2 = 0.977–0.999.

ratio of dissolved water molecules to total water content of the hydrous glasses (**Figure 6**). On one hand, **Figure 6** shows that the influence of the water speciation is almost constant with time, i.e., the crack initiation probability develops almost uniformly. On the other hand, **Figure 6A** indicates a lower probability of crack initiation of glasses in which dissociated H_2O and water molecules are present in equal fractions. The latter would imply that OH-groups delay cracking while water molecules speed up cracking. Reasons for this compositional effect need to be addressed in a future work. However, one has to note that similar patterns have been found for density and mechanical properties of hydrous glasses, where OH initiated an increase in the elastic moduli, whereas the trend caused by water molecules was the opposite (Kiefer et al., 2019). Further, one has to stress that this analysis is limited to a time maximum of 1 min, which rules out effects taking place during longer observation times. For instance, Bechgaard et al. (2018) reported that initiation of radial cracks in calcium aluminosilicate glasses was shorter when tested in humid atmospheres, but proceeded within 24 h after indentation.

The stress intensity K_I at the tip of median radial cracks, which are induced by Vickers indentation, can be approximated as (Lawn and Fuller, 1975; Marshall and Lawn, 1977; Lawn and Marshall, 1979; Ponton and Rawlings, 1989; Li et al., 1989; Ghosh et al., 1991):

$$K_I = \chi P c^{-m} \tag{5}$$

with χ = residual stress factor, P = load and, m = crack length exponent. A recent attempt to calibrate K_I of 185 single cracks revealed that χ and m are broadly distributed. Mean values and standard deviations of the m and χ distributions were 1.47 ± 0.44 and 0.052 ± 31.3, respectively (Kiefer et al., 2020). The value of the mean exponent (1.47 ≈ 3/2) confirmed theoretical considerations for a point loading indenter (Lawn and Fuller, 1975; Marshall and Lawn, 1977; Lawn and Marshall, 1979). In contrast, the value of the residual stress factor χ is specific and accounts for the elastic-plastic properties of the glass, the angular position along the crack front and the environmental condition of the fatigue experiment. As humidity levels and glass compositions of this study differ from that of Kiefer et al. (2020), χ = 0.052 is not applicable here and χ remains a tuneable parameter. If one assumes that the residual stress factor χ scales with the square root of the Young's modulus-to-hardness ratio $(E/H_V)^{1/2}$ (Anstis et al., 1981; Miyoshi, 1985) and setting $\chi_B = \chi(E/H_V)^{-1/2}$, Equation (5) can be rewritten as:

$$\frac{K_I}{\chi_B} = \left(\frac{E}{H_V}\right)^{1/2} P c_{av}^{-3/2} \tag{6}$$

The calibration factor χ_B accounts now mainly for the environmental reactions at the crack-tip. Thus, an interrelation between stress intensity K_I/χ_B and the mean crack propagation rate v_{av} can be established by plotting v_{av} calculated with Equation (4) vs. the right-hand side of Equation (6). For the determination of K_I/χ_B, Young's modulus E of each hydrous glasses was taken from a previous study (Kiefer et al., 2019) and hardness was calculated using the mean value of the half diagonal length a of the Vickers indent as recorded for $t < \delta$. For instance, see data points at t-δ ≈ 0 of **Figure 2A** for a, while Vickers hardness is $H_V = P/(2.157 \times 10^{-3}\ a^2)$ in units of H_V (GPa), P (N), and a (µm). **Figure 7** shows that in this Wiederhorn diagram (Wiederhorn, 1967, 1974), humidity clearly shifts the lines toward lower stress intensity values and within the two series, K_I/χ_B decreases with increasing water content of the glasses. **Figure 7** also displays that the slope n [$n = \lg(v_{av})/\lg(K_I/\chi_B)$] of the lines is affected by the testing conditions. For the series tested under high p_{H2O} (942 Pa), it is found that n = 20–27, whereas for the glasses tested in low humidity, n increased from 23 to 88 with decreasing water content (**Table 3**). Noticeably, the hydrous glass 4W-MSG500 shows two segments. A first segment at the early stage of the crack propagation ($v_{av} > 2 \times 10^{-7}$ m s^{-1}) of n = 68 and a second segment at the later stage of n = 16. Values of n in the range between 16 and 27 were reported for crack growth, which is controlled by the reaction of water molecules of the environment with the glass at the crack-tip (so called stage I reactions) (Wiederhorn, 1967, 1974; Gehrke et al., 1987). In contrast, higher values are typical for water-independent crack propagation (stage III reactions) (Wiederhorn, 1967, 1974;

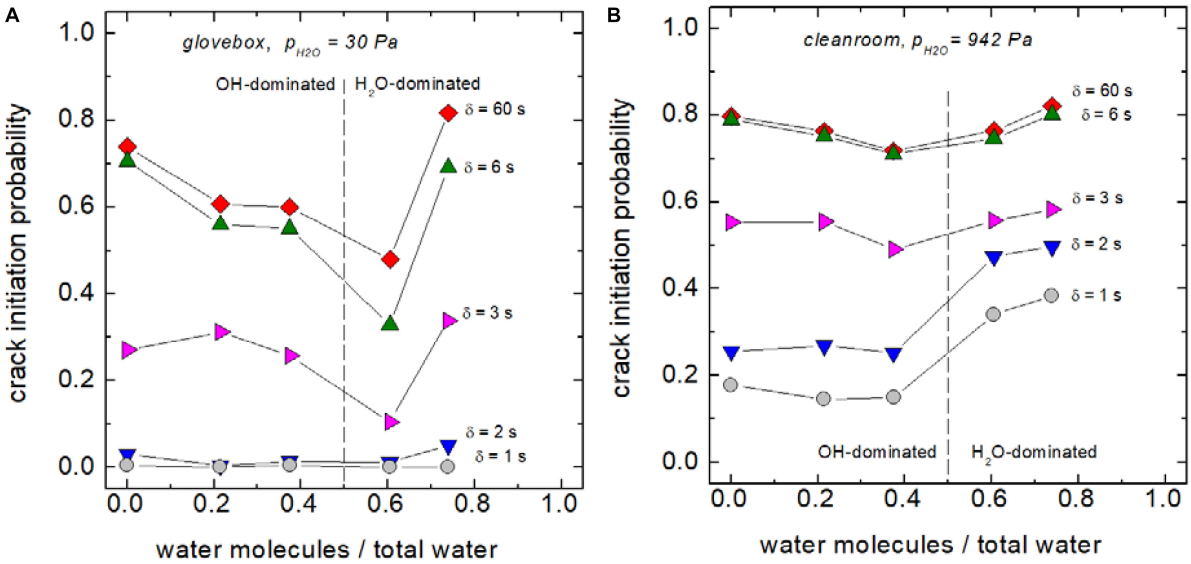

FIGURE 6 | Temporal evolution of the crack initiation probability as a function of the water speciation in low **(A)** and high **(B)** humidity.

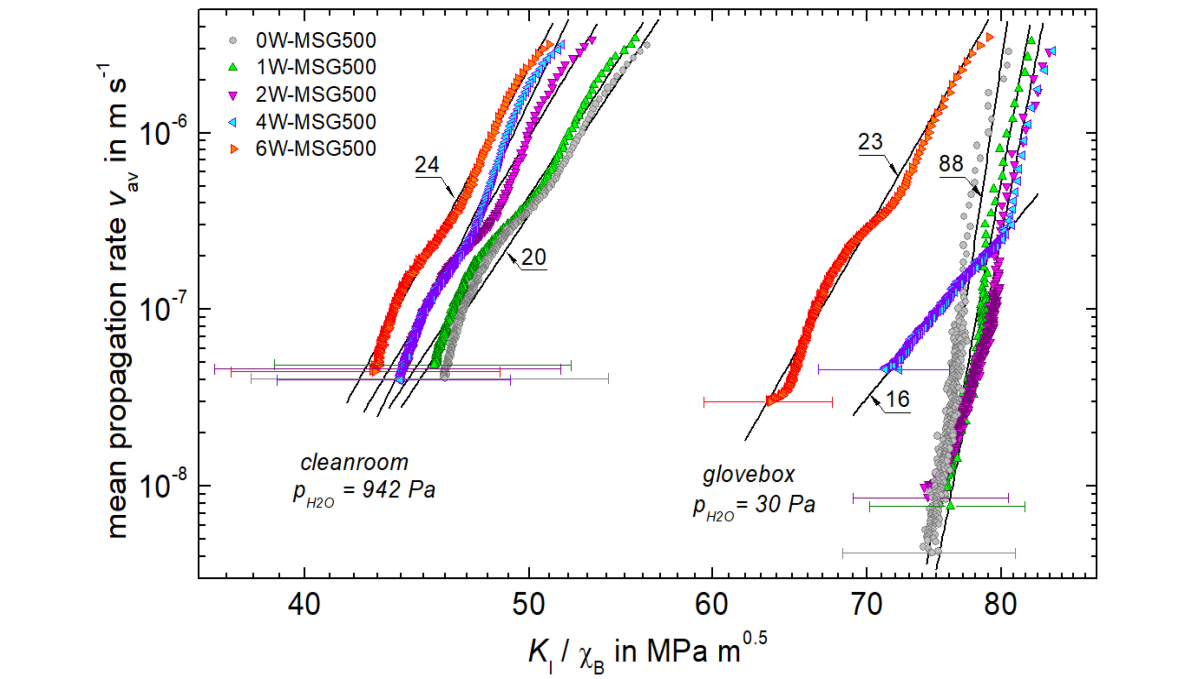

FIGURE 7 | Mean crack propagation rate v_{av} vs. uncalibrated stress intensity K_I/χ_B. Lines of slope n (as indicated) are best linear fits through data. Error bars show standard deviation of the crack length distributions of **Table 2**.

Wiederhorn and Johnson, 1974; Gehrke et al., 1987). Based on this classification, one can assign 0W-MSG500, 1W-MSG500, and 2W-MSG500 to stage III reactions at low p_{H2O} of the glove box (30 Pa), while the more hydrous glasses 4W-MSG500 (at least at low propagation rates) and 6W-MSG500 show already stage I reactions. This implies that for hydrous glasses of high water contents, dissolved water promotes crack growth in a similar way as water molecules originating from the gas phase. One explanation for this would be that water readily escapes from the freshly fractured surface of hydrous glasses increasing the p_{H2O} of the vapor at the crack tip similar to the stress-induced emission of sodium during the fracture of anhydrous soda-lime silicate glass (Lanford et al., 1979). This effect was related to the local stress increase during crack propagation and can result in

TABLE 3 | Crack growth exponent n of the equation $v_{av} = A(K_I/\chi_B)^n$ and $v = AK_I^n$ of Vickers induced and DCB cracks in soda-lime silicate glasses, respectively.

References		**Waurischk et al., 2020**	**Wiederhorn, 1967**	**Wiederhorn, 1967**	**This work**	**Waurischk et al., 2020**	**This work**	**Waurischk et al., 2020**	**Wiederhorn, 1974**	**Wiederhorn, 1967**	**Wiederhorn, 1974**
p_{H2O} (Pa)		**10^{-6}**			**30**	**661**	**942**	**1132**			
T (°C)		**23**	**25**	**25**	**25**	**23**	**18**	**23**			
RH (%)		**≈10^{-8}**	**0.017**	**0.2**	**1**	**24**	**45**	**40**	**50**	**100**	**liq. H_2O**
Glass	**x_{H2O} (mol%)**										
SLS[a]	≈0.1		91 ($v > 2 \times 10^7$) 27 ($v < 2 \times 10^7$)	25					18.1 ± 1.6	21	16.4 ± 0.8
0W-MSG0	0.13	148				16 ± 1		16 ± 1			
0W-MSG500	0.75				88 ± 2		20 ± 1				
1W-MSG500	3.15				72 ± 2		20 ± 1				
2W-MSG500	5.89				68 ± 2		22 ± 1				
4W-MSG500	11.62				68 ± 2 ($v > 2 \times 10^7$) 16 ± 1 ($v < 2 \times 10^7$)		27 ± 1				
6W-MSG500	17.08	16			23 ± 1	14 ± 3	24 ± 1				

To assure comparability with data of previous studies, n was collected from Refs. (Wiederhorn, 1974; Gehrke et al., 1987; Waurischk et al., 2020) for crack propagation rates in the range 10^{-8}–10^{-5} m s^{-1} only. Key:
[a]*Soda-lime silicate (SLS) glass of different compositions.*

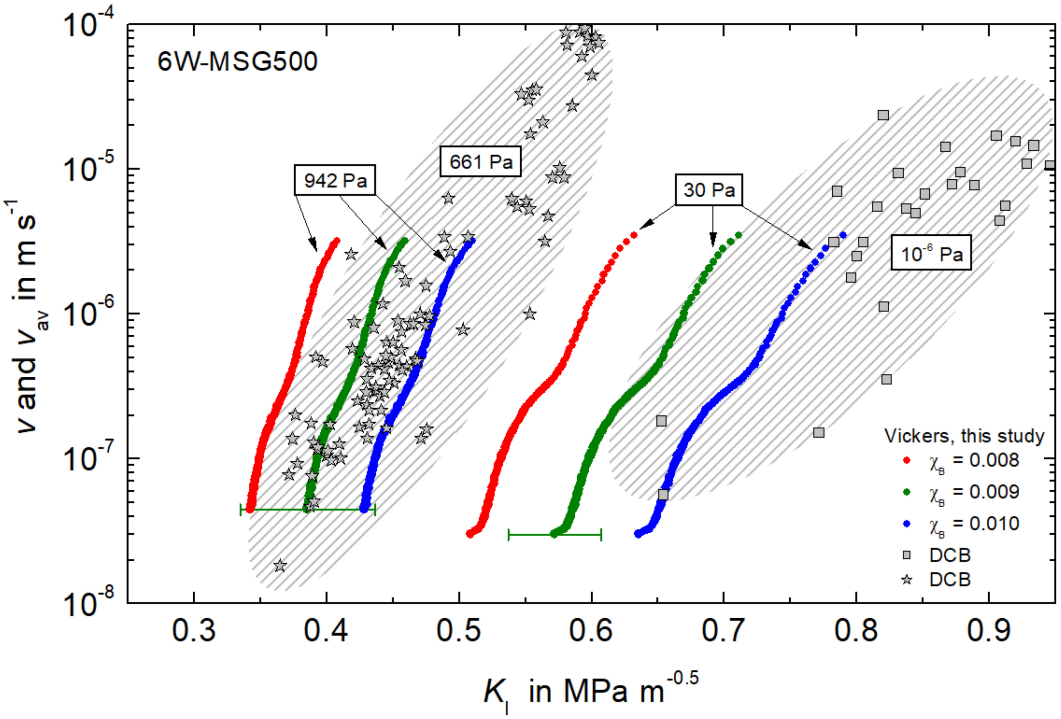

FIGURE 8 | Mean crack propagation rate v_{av} (N = 259 and 370) and crack propagation rates v of single cracks (stress calibrated DCB specimens) of the hydrous glass 6W-MSG500. Stress intensities K_I of the Vickers induced v_{av} data of this study are shown for χ_B = 0.008 (red dots), 0.009 (green dots) and 0.010 (blue dots). Partial pressure of H_2O as indicated. DCB data from Waurischk et al. (2020). Error bars show standard deviation of the crack length distributions of **Table 2**.

an increased sodium concentration at the fractured surface, thus triggering local glass corrosion (Célarié et al., 2007). Another explanation would favor friction of an adhesive water film that is formed by allocated water at the surfaces near to the crack-tip (Wondraczek et al., 2006), which would drop the precondition of water evaporation from the hydrous glass surface into the vapor phase. However, more research is needed to provide new evidence in support of these explanatory attempts.

Figure 7 shows that the calibration factor χ_B is close to 0.01 as the critical stress intensity K_{IC} is about unity for dry and hydrous soda-lime silicate glasses (Wiederhorn, 1974; Gehrke et al., 1987; Waurischk et al., 2020). However, the true value of χ_B of the individual glasses is still unknown and for its determination a calibration procedure has to be applied (Quinn and Bradt, 2007; Marshall et al., 2015; Kiefer et al., 2020). **Figure 8** shows such an attempt for 6W-MSG500, as for this glass stable crack growth in air and vacuum was studied earlier using double cantilever beam geometry (DCB) (Waurischk et al., 2020). Due to the large scatter in the DCB data, however, reconciliation of both data sets while respecting the order of decreasing K_I with increasing humidity is difficult and it does not result in more precise identification of χ_B.

CONCLUSION

Automated recording and analysis of a large number of Vickers induced cracks is a promising route to determine the crack growth exponent with higher accuracy. Water is found to promote slow ($<3 \times 10^{-6}$ m s^{-1}) crack growth independently of its origin. However, water molecules of the environment are more efficient in reducing stress intensity than dissolved water species of the glass structure. When tested in low partial pressure of H_2O, hydrous glasses show a noticeable decrease in the crack growth exponent, which is assumed to be caused by an energy dissipation step.

DATA AVAILABILITY STATEMENT

The datasets generated for this study are available on request to the corresponding author.

AUTHOR CONTRIBUTIONS

PK, MM, RB, and JD produced the manuscript. JD, HB, TW, SR, and RM contributed to the critical revision and direction of the manuscript. All authors contributed to the article and approved the submitted version.

FUNDING

We gratefully acknowledge financial support by the Deutsche Forschungsgemeinschaft (DFG) by the priority program SPP 1594.

REFERENCES

Anstis, G. R., Chantikul, P., Lawn, B. R., and Marshall, D. B. (1981). A critical evaluation of indentation techniques for measuring fracture toughness: I direct crack measurements. *J. Am. Ceram. Soc.* 64, 533–538. doi: 10.1111/j.1151-2916.1981.tb10320.x

Balzer, R., Behrens, H., Reinsch, S., and Fechtelkord, M. (2019a). Structural investigation of hydrous phosphate glasses. *Phys. Chem. Glass. Eur. J. Glass Sci. Technol. B* 60, 49–61. doi: 10.13036/17533562.60.2.041

Balzer, R., Behrens, H., Schuth, S., Waurischk, T., Reinsch, S., Müller, R., et al. (2019b). The influence of H2O and SiO2 on the structure of silicoborate glasses. *J. Non Cryst. Solids* 519:119454. doi: 10.1016/j.jnoncrysol.2019.05.030

Balzer, R., Behrens, H., Waurischk, T., Reinsch, S., Müller, R., Kiefer, P., et al. (2020). Water in alkali aluminosilicate glasses. *Front. Mater.* 7:85. doi: 10.3389/fmats.2020.00085

Bauer, U., Behrens, H., Fechtelkord, M., Reinsch, S., and Deubener, J. (2015). Water- and boron speciation in hydrous soda-lime-borate glasses. *J. Non Cryst. Solids* 423–424, 58–67. doi: 10.1016/j.jnoncrysol.2015.05.004

Bauer, U., Behrens, H., Reinsch, S., Morin, E. I., and Stebbins, J. F. (2017). Structural investigation of hydrous sodium borosilicate glasses. *J. Non Cryst. Solids* 465, 39–48. doi: 10.1016/j.jnoncrysol.2017.03.023

Bechgaard, T. K., Mauro, J. C., and Smedskjaer, M. M. (2018). Time and humidity dependence of indentation cracking in aluminosilicate glasses. *J. Non Cryst. Solids* 491, 64–70. doi: 10.1016/j.jnoncrysol.2018.04.009

Behrens, H., Bauer, U., Reinsch, S., Kiefer, P., Müller, R., and Deubener, J. (2018). Structural relaxation mechanisms in hydrous sodium borosilicate glasses. *J. Non Cryst. Solids* 497, 30–39. doi: 10.1016/j.jnoncrysol.2018.05.025

Benard, A., and Bosi-Levenbach, E. C. (1953). The plotting of observations on probability paper. *Stat. Neerl.* 7, 163–173.

Benbahouche, S., Brient, A., Rouxel, T., and Sangleboeuf, J.-C. (2012). Effect of water corrosion on cracks and Vickers imprints in glass. *Int. J. Fracture* 175, 199–206. doi: 10.1007/s10704-012-9712-4

Berndt, J., Liebske, C., Holtz, F., Freise, M., Nowak, N., Ziegenbein, D., et al. (2002). A combined rapid-quench and H2-membrane setup for internally heated pressure vessels: description and application for water solubility in basaltic melts. *Am. Mineral.* 87, 1717–1726. doi: 10.2138/am-2002-11-1222

Célarié, F., Ciccotti, M., and Marlière, C. (2007). Stress-enhanced ion diffusion at the vicinity of a crack tip as evidenced by atomic force microscopy in silicate glasses. *J. Non Cryst. Solids* 353, 51–68. doi: 10.1016/j.jnoncrysol.2006.09.034

Dériano, S., Jarry, A., Rouxel, T., Sangleboeuf, J. C., and Hampshire, S. (2004). The indentation fracture toughness (KC) and its parameters: the case of silica-rich glasses. *J. Non Cryst. Solids* 344, 44–50. doi: 10.1016/j.jnoncrysol.2004.07.021

Gehrke, E., Ullner, C., and Hähnert, M. (1987). Correlation between multistage crack-growth and time-dependent strength in commercial silicate-glasses: 1. influence of ambient media and types of initial cracks. *Glastechn. Ber. Glass Sci. Technol.* 60, 268–278.

Ghosh, A., Kobayashi, A. S., Li, Z., Henager, C. H., and Bradt, R. C. (1991). *Vickers Microindentation Toughness of a Sintered SiC in the Median-Crack Regime, No. PNL-SA-16927*. Richland, WA: Pacific Northwest Lab.

Kiefer, P., Balzer, R., Deubener, J., Behrens, H., Waurischk, T., Reinsch, S., et al. (2019). Density, elastic constants and indentation hardness of hydrous soda-lime-silica glasses. *J. Non Cryst. Solids* 521:119480. doi: 10.1016/j.jnoncrysol.2019.119480

Kiefer, P., Deubener, J., Müller, R., and Behrens, H. (2020). Statistical analysis of propagation rates of indentation-induced radial cracks in soda-lime-silica glass. *J. Non Cryst. Solids* 527:119739. doi: 10.1016/j.jnoncrysol.2019.119739

Lanford, W. A., Davis, K., Lamarche, P., Laursen, T., Groleau, R., and Doremus, R. H. (1979). Hydration of soda-lime glass. *J. Non Cryst. Solids* 33, 249–266.

Lawn, B. R., and Fuller, E. R. (1975). Equilibrium penny-like cracks in indentation fracture. *J. Mater. Sci.* 10, 2016–2024. doi: 10.1007/bf00557479

Lawn, B. R., and Marshall, D. B. (1979). Hardness, toughness, and brittleness: an indentation analysis. *J. Am. Ceram. Soc.* 62, 347–350. doi: 10.1111/j.1151-2916.1979.tb19075.x

Li, Z., Ghosh, A., Kobayashi, A. S., and Bradt, R. C. (1989). Indentation fracture toughness of sintered silicon carbide in the Palmqvist crack regime. *J. Am. Ceram. Soc.* 72, 904–911. doi: 10.1111/j.1151-2916.1989.tb06242.x

Marshall, D. B., Cook, R. F., Padture, N. P., Oyen, M. L., Pajares, A., Bradby, J. E., et al. (2015). The compelling case for indentation as a functional exploratory and characterization tool. *J. Am. Ceram. Soc.* 98, 2671–2680. doi: 10.1111/jace.13729

Marshall, D. B., and Lawn, B. R. (1977). An indentation technique for measuring stresses in tempered glass surfaces. *J. Am. Ceram. Soc.* 60, 86–87. doi: 10.1111/j.1151-2916.1977.tb16106.x

Miyoshi, T. (1985). Study on evaluation of KIC for structural ceramics. *Trans. Jpn. Soc. Mech. Eng. Ser. A* 51, 2489–2497.

Pönitzsch, A., Nofz, M., Wondraczek, L., and Deubener, J. (2016). Bulk elastic properties, hardness and fatigue of calcium aluminosilicate glasses in the intermediate-silica range. *J. Non Cryst. Solids* 434, 1–12. doi: 10.1016/j.jnoncrysol.2015.12.002

Ponton, C. B., and Rawlings, R. D. (1989). Vickers indentation fracture toughness test, part 1: review of literature and formulation of standardised indentation toughness equations. *Mater. Sci. Technol.* 5, 865–872. doi: 10.1179/mst.1989.5.9.865

Quinn, G. D., and Bradt, R. C. (2007). On the Vickers indentation fracture toughness test. *J. Am. Ceram. Soc.* 90, 673–680. doi: 10.1111/j.1551-2916.2006.01482.x

Reinsch, S., Müller, R., Deubener, J., and Behrens, H. (2013). Internal friction of hydrated soda-lime-silicate glasses. *J. Chem. Phys.* 139:174506. doi: 10.1063/1.4828740

Striepe, S., and Deubener, J. (2013). Effect of lithium-to-magnesium ratio in metaphosphate glasses on crack-tip condensation and sub-critical crack growth. *J. Non Cryst. Solids* 375, 47–54. doi: 10.1016/j.jnoncrysol.2013.04.063

Striepe, S., Deubener, J., Smedskjaer, M. M., and Potuzak, M. (2013). Environmental effects on fatigue of alkaline earth aluminosilicate glass with varying fictive temperature. *J. Non Cryst. Solids Solids* 379, 161–168. doi: 10.1016/j.jnoncrysol.2013.08.005

Wada, M., Furukawa, H., and Fujita, K. (1974). "Crack resistance of glasses on knoop scratch test," in *Proceedings of the X Int. Congr. Glass, vol. 11, Ceram. Soc*, eds M. Kunugi, M. Tashiro, and N. Soga (Kyoto), 39–46.

Waurischk, T., Müller, R., Reinsch, S., Kiefer, P., Deubener, J., Balzer, R., et al. (2020). Crack growth in hydrous soda-lime silicate glass. *Front. Mater.* 7:66. doi: 10.3389/fmats.2020.00066

Wiederhorn, S. M. (1967). Influence of water vapor on crack propagation in soda-lime glass. *J. Am. Ceram. Soc.* 50, 407–414. doi: 10.1111/j.1151-2916.1967.tb15145.x

Wiederhorn, S. M. (1974). "Subcritical crack growth in ceramics," in *Fracture Mechanics of Ceramics*, Vol. 2, ed. R. C. Bradt (New York: Plenum Press), 613–646. doi: 10.1007/978-1-4615-7014-1_12

Wiederhorn, S. M., and Johnson, H. (1974). Fracture of glass in vacuum. *J. Am. Ceram. Soc.* 57, 336–341.

Wondraczek, L., Dittmar, A., Oelgardt, C., Célarié, F., Ciccotti, M., and Marlière, C. (2006). Real-time observation of a non-equilibrium liquid condensate confined at tensile crack tips in oxide glasses. *J. Am. Ceram. Soc.* 89, 746–749. doi: 10.1111/j.1551-2916.2005.00765.x

Conflict of Interest: The authors declare that the research was conducted in the absence of any commercial or financial relationships that could be construed as a potential conflict of interest.

frontiers in Materials

ORIGINAL RESEARCH
published: 28 August 2020
doi: 10.3389/fmats.2020.00223

Creep Deformation of a Cu-Zr Nanoglass and Interface Reinforced Nanoglass-Composite Studied by Molecular Dynamics Simulations

Constanze Kalcher, Omar Adjaoud and Karsten Albe*

Materials Modelling Division, Institute of Materials Science, Technische Universität Darmstadt, Darmstadt, Germany

Using molecular dynamics simulations, we compare the creep properties of a homogeneous $Cu_{64}Zr_{36}$ metallic glass, a nanoglass with the same nominal composition, and a nanoglass-crystal composite, where the amorphous grain boundary phase has been reinforced with the high-temperature stable Cu_2Zr Laves phase. While the nanoglass architecture is successful at preventing shear band formation, which typically results in a brittle failure mode at room temperature and conventional loading conditions, we find that the high fraction of glass-glass grain boundary phase therein is not beneficial to its creep properties. This can be amended by reinforcing the glass-glass interphase with a high-temperature stable crystalline substitute.

Keywords: metallic glass, grain interfaces, creep, molecular dynamics, nanoglass

OPEN ACCESS

Edited by:
Jürgen Horbach,
Heinrich Heine University of Düsseldorf, Germany

Reviewed by:
Paulo Sergio Branicio,
University of Southern California, United States
Haizheng Tao,
Wuhan University of Technology, China

****Correspondence:***
Constanze Kalcher
kalcher@mm.tu-darmstadt.de

Specialty section:
This article was submitted to Ceramics and Glass, a section of the journal Frontiers in Materials

Received: *21 March 2020*
Accepted: *19 June 2020*
Published: *28 August 2020*

Citation:
Kalcher C, Adjaoud O and Albe K (2020) Creep Deformation of a Cu-Zr Nanoglass and Interface Reinforced Nanoglass-Composite Studied by Molecular Dynamics Simulations. Front. Mater. 7:223. doi: 10.3389/fmats.2020.00223

1. INTRODUCTION

Nanoglasses (NGs) are amorphous materials with microstructural features analogous to nanocrystalline materials; they consist of glassy grains connected by glass-glass interfaces (Jing et al., 1989; Fang et al., 2012). The interfaces are characterized by an excess volume (Jing et al., 1989; Şopu et al., 2009; Fang et al., 2012), a defective short range order (Ritter et al., 2011), and a different composition than the glassy grains (Adjaoud and Albe, 2016, 2018). NGs are typically synthesized by cold-compaction of glassy particles prepared through inert gas condensation (Jing et al., 1989; Fang et al., 2012) or by magnetron sputtering (Chen et al., 2011; Śniadecki et al., 2016).

NGs exhibit enhanced plasticity in comparison to their homogeneous metallic glass (MG) counterparts, which has been observed in *in situ* tensile tests of $Sc_{75}Fe_{25}$ in a transmission electron microscope (Wang et al., 2015). Moreover, molecular dynamics (MD) simulations have shown that the interfaces in NGs promote the nucleation of shear transformation (ST) zones (Argon, 1979; Falk and Langer, 1998; Schuh et al., 2007) and prevent strain localization (Albe et al., 2013; Adibi et al., 2015; Şopu and Albe, 2015). However, this enhanced plasticity usually comes at the expense of the glasses' strength. Both experiments and computer simulations confirmed that the yield strength of a conventional NG is significantly lower than that of MG with an identical chemical composition (Ritter et al., 2011; Şopu and Albe, 2015; Wang et al., 2015).

Several studies of nanolaminate NG-MG composites with planar glass-glass interfaces have shown that these architectures can be used to successfully increase the strength of NG-composites (Sha et al., 2014, 2017; Adibi et al., 2016). In a previous computer simulation study, we showed that instead of using planar interfaces, reinforcing a conventional Cu–Zr NG without the loss of ductility can be realized by strengthening the amorphous grain boundary phase. The latter has been replaced with the high-temperature stable crystalline Cu_2Zr Laves phase. In comparison

to the as–prepared NG, the reinforced NG-composite showed an increased yield strength under conventional tensile testing at room-temperature (Kalcher et al., 2017a). At higher temperatures, especially approaching the glass transition temperature, the influence of the high fraction of glass–crystal interfaces on the mechanical properties of these nanocomposites is, however, still unclear and shall be the focus of this study.

At elevated temperatures and elastostatic loading conditions MG typically show viscoplastic behavior and exhibit creep deformation (Castellero et al., 2008; Yoo et al., 2010; Kassner et al., 2015), carried by homogeneous nucleation of ST zones (Kalcher et al., 2017b). For homogeneous MG matrix composites with crystalline secondary phases, we found that the glass-crystal interfaces can cause severe deterioration of the creep resilience, depending on the shape and percolation of the secondary phase (Kalcher et al., 2017b). This is because weak glass-crystal interfaces exhibit a lower activation barrier for ST activity and act as preferred nucleation sites for the latter. Moreover, from creep simulations of a MG-crystal composite containing nanocrystalline Cu_2Zr precipitates, we could conclude that the macroscopic creep rate is indeed a function of the relaxation state of the glass-crystal interfaces defined by their excess energy (Kalcher et al., 2019).

As opposed to the above described MG-composites, NGs feature an inverse microstructure, i.e., they consist of amorphous glassy grains embedded in a percolating amorphous grain boundary phase or crystalline phase in the case of the NG-composite. Thus, it is not expected that the creep behavior of NGs can be deduced from our previous studies of MG-crystal composites.

2. MATERIALS AND METHODS

In the following section, MD simulations were used to investigate the creep behavior of a $Cu_{64}Zr_{36}$ MG, a NG with the same nominal composition and a grain-boundary reinforced NG composite. The simulation package LAMMPS (Plimpton, 1995) was chosen to perform the MD simulations in conjunction with the Finnis-Sinclair type Cu–Zr potential by Mendelev et al. (2009). A timestep of 2 fs was used in all simulations. In order to control the pressure and temperature a Nosé-Hoover thermostat and Parinello–Rahman barostat were applied. Moreover, periodic boundary conditions were applied in all dimensions.

Virtual synthesis of the three different glass model types, i.e., MG, NG, and NG-composite, required multiple steps: First, a homogeneous MG of composition $Cu_{64}Zr_{36}$ was quenched from the melt with a quenching rate of $\dot{T} = 0.01$ K/ps and subsequently relaxed for 1 ns. To obtain a NG with the same nominal composition, spherical particles cut from this MG model were then used as precursors for simulations of the cold-compaction preparation route described in Adjaoud and Albe (2016): The average diameter of the precursor particles was 7 nm and they were annealed at T_g before a hydrostatic compaction pressure of 5 GPa was applied to consolidate the particles. Moreover, the surface atoms of the virtual precursors

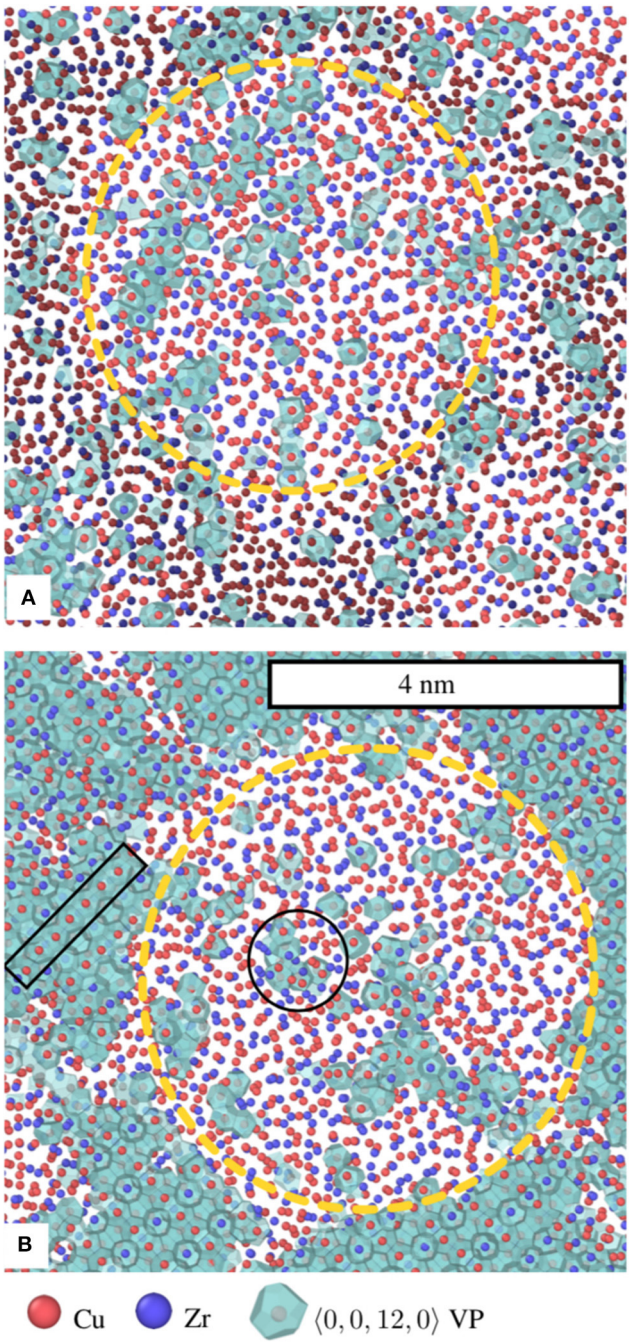

FIGURE 1 | Snapshots of a slice through the **(A)** conventional NG and **(B)** nanoglass-crystal composite, showing two amorphous grains embedded in amorphous interphase and crystalline Cu_2Zr Laves phase, respectively. Copper atoms are depicted in red and zirconium atoms are depicted in blue. The outlines of the grains are indicated with yellow dashed circles. In addition to the atomic configuration, the ⟨0, 0, 12, 0⟩ Voronoi polyhedra present in this structure are shown in light blue. This allows for a distinction to be made between atoms in a glassy grain, and the crystalline interphase, where the Cu-centered ⟨0, 0, 12, 0⟩ polyhedra must form regular chains of face-sharing VP (marked with a black box). Within the glassy grain, the typical clustering into irregular shapes can be observed (marked with a black circle).

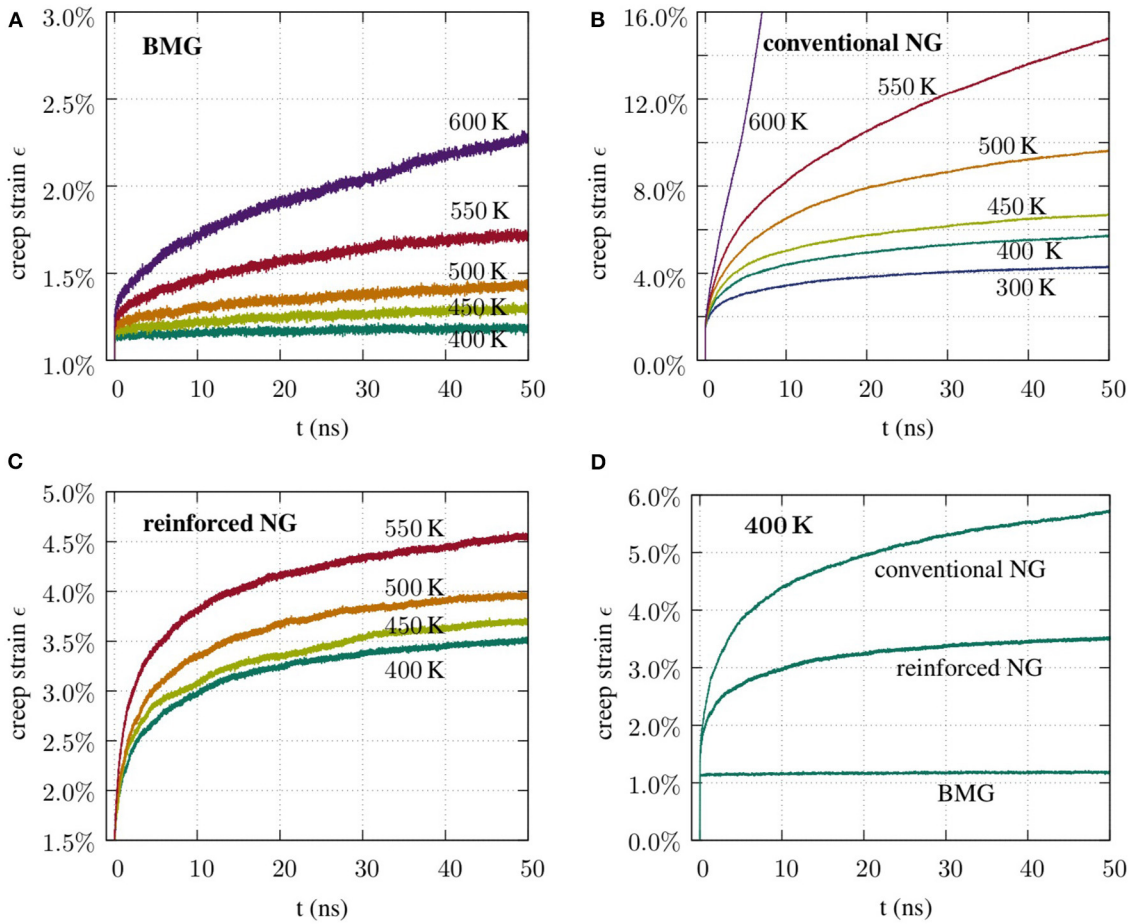

FIGURE 2 | Creep curves under uniaxial elastostatic loading conditions at 750 MPa of **(A)** a homogeneous $Cu_{64}Zr_{36}$ MG, **(B)** a conventional NG with nominal composition $Cu_{64}Zr_{36}$, and **(C)** an interphase reinforced NG-composite. **(D)** For better comparison the 400 K creep curves of each sample type are shown in the same plot.

were marked before compaction. In the finished NG, these atoms form an amorphous grain-boundary phase with an average thickness of about 1 nm. This information was used to define the extent of the grain boundary phase, which allows us to differentiate between the glassy grains and the glassy interface phase that they are embedded in. Finally, this NG was used to generate the reinforced NG composite. The latter has been realized by replacing the grain-boundary interface phase of the as–prepared NG with single crystalline Laves phase C15 Cu_2Zr as described in Kalcher et al. (2017a). More specifically, the replacement procedure has been performed as follows: The glassy grain structure derived from the as–prepared NG sample has been overlaid with a scaled-to-size Cu_2Zr bulk single crystal and all crystal atoms that were found within a 3.6 Å cutoff range of the glass grains have been removed. The resulting composite model was equilibrated at zero pressure and 50 K for 1 ns to allow for relaxation of the artificially created glass–crystal interfaces.

During creep testing the samples were heated up to the target temperature and then a uniaxial load of 750 MPa was instantaneously applied and kept constant for 50 ns. Comparison creep rates were determined from linear fits of the evolution of the creep strain between $t = 25$ ns and $t = 50$ ns. For visualization and analysis of the simulation results, the software OVITO (Stukowski, 2010) was used, which included local deformation analysis using the atomic shear strain measure (Falk and Langer, 1998; Shimizu et al., 2007) and analysis of structural motifs via Voronoi polyhedron statistics (Brostow et al., 1998). A cutoff radius of 5 Å was chosen for computing the per-particle atomic deformation gradient tensor and subsequently the atomic von Mises strain.

3. RESULTS

Figure 1 shows the spatial distribution of the most frequently occurring structural motif, i.e., the Cu-centered $\langle 0, 0, 12, 0\rangle$ Voronoi polyhedra (VP), in the NG and the reinforced NG. An exemplary grain is marked in yellow in both NG samples. As for the pristine NG shown in **Figure 1A**, the $\langle 0, 0, 12, 0\rangle$ VP are homogeneously distributed throughout the glassy grain and

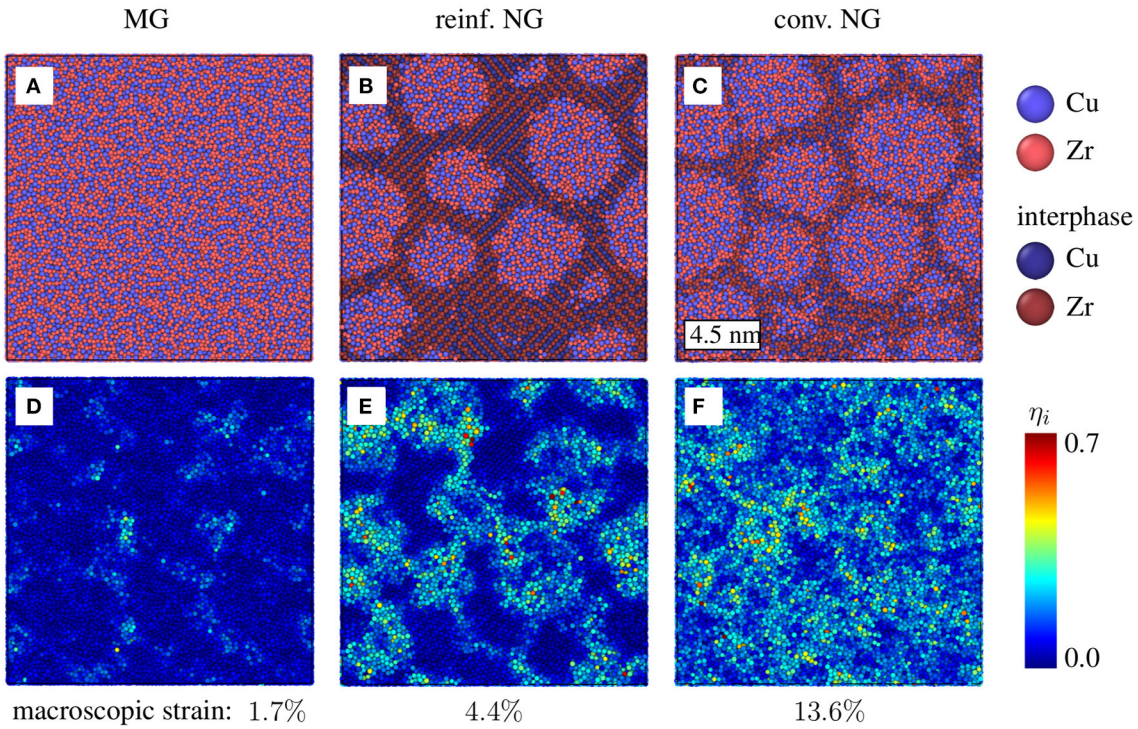

FIGURE 3 | Snapshots of the atomic configurations of the **(A,D)** homogeneous glass, **(B,E)** reinforced NG, **(C,F)** conventional NG samples after 40 ns of creep at 550 K, color coded according to their particle type (top row) and according to the local von Mises strain (bottom row).

also in the interface phase and show the typical interconnection through face and edge sharing, as marked with a black circle in **Figure 1B**. Since the Cu atoms in the regular C15 Cu_2Zr lattice also have a $\langle 0, 0, 12, 0\rangle$ VP coordination, the Laves-type interface in the reinforce NG phase becomes visible in **Figure 1B** as regular arrangement of face-sharing $\langle 0, 0, 12, 0\rangle$ VP strings. Under conventional loading conditions and low temperatures, this NG-composite type has already shown superior mechanical strength as compared to the conventional NG (Kalcher et al., 2017a). We are thus particularly interested in the high-temperature properties of this composite type.

Creep simulations at different temperatures but constant stress have been realized with the above described Laves phase reinforced NG-composite. For comparison, a homogeneous $Cu_{64}Zr_{36}$ glass sample and the cold-compacted NG with the same nominal composition have been probed under the same conditions. Starting with a comparison of the creep behavior of the homogeneous glass and the conventional NG, presented in **Figures 2A,B** it becomes evident, that the NG microstructure promotes creep. Even at room temperature, the conventional NG exhibits viscoelastic creep behavior and reaches a total creep strain of more than 4% after 50 ns elastostatic loading at 750 MPa. Adjaoud and Albe have shown that the cold-compacted NG used in this study, features a defective short-range order in the interphase (Adjaoud and Albe, 2018). Obviously, the activation energy for creep is lowered within the interphase region resulting in an overall increased creep activity. This is also supported by **Figures 3D,F** that depict the local von Mises strain field in the homogeneous glass and the conventional NG after 40 ns of creep deformation. Compared to the homogeneous MG, there is clearly increased ST activity in the whole sample, but even more so in the amorphous grain boundary phase.

The creep compliance of the Laves phase reinforced NG ranges in between those of the homogeneous glass and the conventional NG (see **Figures 2C,D**). The total creep strain reached after 50 ns of creep at $T = 500$ K is 4%, which is less than half the creep strain the conventional NG did reach for that temperature and 2.6% more than observed for the homogeneous glass. The shape of the creep curves of the reinforced NG resemble more closely the shape of the creep curves of the conventional NG, since both feature high creep rates in the initial creep stage.

We performed linear fits to the creep data between $t = 25$ ns and $t = 50$ ns, for comparison of the creep rates in the three different glass types. The data is collected in **Figure 4**, that gives the temperature dependence of the creep rates at constant stress of 750 MPa. As a guide to the eye, a linear fit has been plotted for each data set. For the BMG and the NG, the slopes differ slightly. One reason is that the slope is defined not only by the activation energy for creep but also by the stress dependency. However, since the creep mechanisms, more precisely the ST zones in the NG and BMG, are the same, we can attribute the offset in the creep rates to the different densities of nucleation sites for ST zones in these two systems.

As for the NG composite, it is evident that the temperature dependence of the creep rates between $t = 25$ ns and $t =$

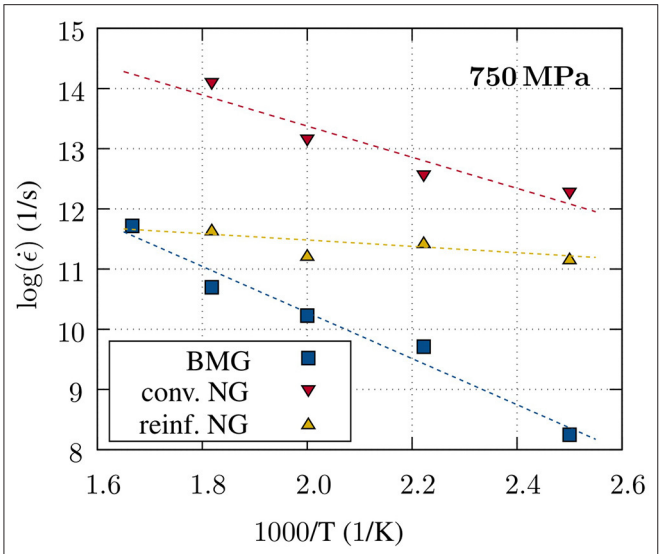

FIGURE 4 | Comparison of the temperature dependence of the fitted creep rates for the three different glass types.

50 ns is not as pronounced as for the other two samples. Especially for higher temperatures, the rates approach those exhibited by the homogeneous glass. An explanation for this can be found in the von Mises strain field of the NG-composite after 40 ns of creep deformation, as shown in **Figures 3B,E**: During creep deformation of the NG-composite, most of the crystalline phase only responds elastically. But the glassy grains embedded therein start to flow. It seems that, at the temperature of 400 K $\leq T \leq$ 550 K, the major fraction of glass phase already participates in the deformation. Thus, the creep rates exhibit a weaker temperature dependence within the testing temperature range. Moreover, at these elevated temperatures, further relaxation of the artificially created Cu_2Zr–MG interfaces is expected. In line with previously presented results obtained for conventional loading conditions (Kalcher et al., 2017a), the reinforcing effect of the Laves phase still prevails under creep conditions at elevated temperatures.

4. DISCUSSION

The behavior of the reinforced NG is not trivial to understand. This issue is rooted in the combination of several different effects. In this context the artificial synthesis procedure of the NG composite warrants further discussion. Assuming that the NG composite constitutes a single crystalline percolating network phase with glassy grains embedded therein, the expectation would be that the creep rates exhibited by such a composite should be lower than the ones observed in the bulk glass. In that case, the creep behavior will be determined by the glass phase, not the crystalline phase. More specifically, the Laves phase would be the load-bearing component, and at the applied stress, would only respond elastically. After this initial elastic response, plastic flow of the glass grains through the nucleation of ST zones should occur until a mechanical equilibrium between both phases is reached again. However, during initial relaxation of the NG composite, the initial percolating Laves network is partially damaged (Kalcher et al., 2017a). The partial amorphization of some ligaments of the crystalline network results in a different stress distribution in the composite, since the glass can also become a load-bearing component when probed under creep conditions. At the same time, there is an increased fraction of activation sites for ST zones with a lower activation energy than in the bulk glass. So creep deformation is also promoted by the presence of less well-relaxed interfaces. For a glass-composite with non-percolating Laves-type inclusions, we have shown that the creep rates significantly depend on the quality of the glass-crystal interfaces present in the composite (Kalcher et al., 2019). Another point to consider is that even though the remaining volume fraction of the intact Laves phase is still quite high (i.e., $f \approx 30\%$) and a large fraction of the composite does therefore not participate in the plastic creep deformation (as visible in **Figures 3D–F**), this is compensated by the high ST activation volume fraction within the glass grains. Consequently, increasing the temperature can not cause a significantly increase in activated ST sites. This could explain the weak temperature dependence in the creep rates exhibited by the NG composite, shown in **Figure 4**.

In summary, by comparing the creep behavior of a $Cu_{64}Zr_{36}$ MG, a NG, and a NG-crystal composite, we showed that the glass-glass interfaces in the cold-compacted NG facilitate activation of ST zones and thus creep. The crystalline continuous Laves-phase network in the NG-composite, on the contrary, successfully reinforced the NG-composite against creep at higher temperatures.

DATA AVAILABILITY STATEMENT

The raw data supporting the conclusions of this article will be made available by the authors, without undue reservation.

AUTHOR CONTRIBUTIONS

CK carried out the simulations, analyzed the data, and wrote the draft manuscript. OA contributed to the conception and design of this study and generated the nanoglass structures. KA supervised the work, reviewed, and edited the manuscript. All authors contributed to the article and approved the submitted version.

ACKNOWLEDGMENTS

The authors acknowledge the financial support of the Deutsche Forschungsgemeinschaft (DFG) through SPP 1594 project 224504410-AL 578/15. The authors gratefully acknowledge the Gauss Centre for Supercomputing e.V. (www.gauss-centre.eu) for funding this project by providing computing time through the John von Neumann Institute for Computing (NIC) on the GCS Supercomputer JUWELS at Jülich Supercomputing Centre (JSC). Computing time was also provided by Technische Universität Darmstadt on the Lichtenberg High Performance Computer.

REFERENCES

Adibi, S., Branicio, P. S., and Ballarini, R. (2016). Compromising high strength and ductility in nanoglass–metallic glass nanolaminates. *RSC Adv.* 6, 13548–13553. doi: 10.1039/C5RA24715B

Adibi, S., Branicio, P. S., and Joshi, S. P. (2015). Suppression of shear banding and transition to necking and homogeneous flow in nanoglass nanopillars. *Sci. Rep.* 5:15611. doi: 10.1038/srep15611

Adjaoud, O., and Albe, K. (2016). Interfaces and interphases in nanoglasses: surface segregation effects and their implications on structural properties. *Acta Mater.* 113, 284–292. doi: 10.1016/j.actamat.2016.05.002

Adjaoud, O., and Albe, K. (2018). Microstructure formation of metallic nanoglasses: Insights from molecular dynamics simulations. *Acta Mater.* 145, 322–330. doi: 10.1016/j.actamat.2017.12.014

Albe, K., Ritter, Y., and Şopu, D. (2013). Enhancing the plasticity of metallic glasses: shear band formation, nanocomposites and nanoglasses investigated by molecular dynamics simulations. *Mech. Mater.* 67, 94–103. doi: 10.1016/j.mechmat.2013.06.004

Argon, A. (1979). Plastic deformation in metallic glasses. *Acta Metall.* 27, 47–58. doi: 10.1016/0001-6160(79)90055-5

Brostow, W., Chybicki, M., Laskowski, R., and Rybicki, J. (1998). Voronoi polyhedra and delaunay simplexes in the structural analysis of molecular-dynamics-simulated materials. *Phys. Rev. B* 57, 13448–13458. doi: 10.1103/PhysRevB.57.13448

Castellero, A., Moser, B., Uhlenhaut, D. I., Torre, F. H. D., and Loeffler, J. F. (2008). Room-temperature creep and structural relaxation of mg-cu-y metallic glasses. *Acta Mater.* 56, 3777–3785. doi: 10.1016/j.actamat.2008.04.021

Chen, N., Frank, R., Asao, N., Louzguine-Luzgin, D., Sharma, P., Wang, J., et al. (2011). Formation and properties of Au-based nanograined metallic glasses. *Acta Mater.* 59, 6433–6440. doi: 10.1016/j.actamat.2011.07.007

Falk, M. L., and Langer, J. S. (1998). Dynamics of viscoplastic deformation in amorphous solids. *Phys. Rev. E* 57, 7192–7205. doi: 10.1103/PhysRevE.57.7192

Fang, J. X., Vainio, U., Puff, W., Würschum, R., Wang, X. L., Wang, D., et al. (2012). Atomic structure and structural stability of $Sc_{75}Fe_{25}$ nanoglasses. *Nano Lett.* 12, 458–463. doi: 10.1021/nl2038216

Jing, J., Krämer, A., Birringer, R., Gleiter, H., and Gonser, U. (1989). Modified atomic structure in a Pd-Fe-Si nanoglass. *J. Non. Cryst. Solids* 113, 167–170. doi: 10.1016/0022-3093(89)90007-0

Kalcher, C., Adjaoud, O., Rohrer, J., Stukowski, A., and Albe, K. (2017a). Reinforcement of nanoglasses by interface strengthening. *Scripta Mater.* 141, 115–119. doi: 10.1016/j.scriptamat.2017.08.004

Kalcher, C., Brink, T., Rohrer, J., Stukowski, A., and Albe, K. (2017b). Interface-controlled creep in metallic glass composites. *Acta Mater.* 141, 251–260. doi: 10.1016/j.actamat.2017.08.058

Kalcher, C., Brink, T., Rohrer, J., Stukowski, A., and Albe, K. (2019). Elastostatic loading of metallic glass-crystal nanocomposites: relationship of creep rate and interface energy. *Phys. Rev. Mater.* 3:093605. doi: 10.1103/PhysRevMaterials.3.093605

Kassner, M. E., Smith, K., and Eliasson, V. (2015). Creep in amorphous metals. *J. Mater. Res. Technol.* 4, 100–107. doi: 10.1016/j.jmrt.2014.11.003

Mendelev, M. I., Kramer, M. J., Ott, R. T., Sordelet, D. J., Yagodin, D., and Popel, P. (2009). Development of suitable interatomic potentials for simulation of liquid and amorphous Cu-Zr alloys. *Philos. Mag.* 89, 967–987. doi: 10.1080/14786430902832773

Plimpton, S. (1995). Fast parallel algorithms for short-range molecular dynamics. *J. Comp. Phys.* 117, 1–19. doi: 10.1006/jcph.1995.1039

Ritter, Y., Şopu, D., Gleiter, H., and Albe, K. (2011). Structure, stability and mechanical properties of internal interfaces in $Cu_{64}Zr_{36}$ nanoglasses studied by MD simulations. *Acta Mater.* 59, 6588–6593. doi: 10.1016/j.actamat.2011.07.013

Schuh, C. A., Hufnagel, T. C., and Ramamurty, U. (2007). Mechanical behavior of amorphous alloys. *Acta Mater.* 55, 4067–4109. doi: 10.1016/j.actamat.2007.01.052

Sha, Z., He, L., Pei, Q., Liu, Z., Zhang, Y., and Wang, T. (2014). The mechanical properties of a nanoglass/metallic glass/nanoglass sandwich structure. *Scripta Mater.* 83, 37–40. doi: 10.1016/j.scriptamat.2014.04.009

Sha, Z.-D., Branicio, P. S., Lee, H. P., and Tay, T. E. (2017). Strong and ductile nanolaminate composites combining metallic glasses and nanoglasses. *Int. J. Plast.* 90, 231–241. doi: 10.1016/j.ijplas.2017.01.010

Shimizu, F., Ogata, S., and Li, J. (2007). Theory of shear banding in metallic glasses and molecular dynamics calculations. *Mater. Trans.* 48, 2923–2927. doi: 10.2320/matertrans.MJ200769

Śniadecki, Z., Wang, D., Ivanisenko, Y., Chakravadhanula, V., Kübel, C., Hahn, H., et al. (2016). Nanoscale morphology of $Ni_{50}Ti_{45}Cu_5$ nanoglass. *Mater. Charact.* 113, 26–33. doi: 10.1016/j.matchar.2015.12.025

Şopu, D., and Albe, K. (2015). Influence of grain size and composition, topology and excess free volume on the deformation behavior of Cu-Zr nanoglasses. *Beilstein J. Nanotechnol.* 6, 537–545. doi: 10.3762/bjnano.6.56

Şopu, D., Albe, K., Ritter, Y., and Gleiter, H. (2009). From nanoglasses to bulk massive glasses. *Appl. Phys. Lett.* 94:191911. doi: 10.1063/1.3130209

Stukowski, A. (2010). Visualization and analysis of atomistic simulation data with ovito- the open visualization tool. *Modell. Simul. Mater. Sci. Eng.* 18:015012. doi: 10.1088/0965-0393/18/1/015012

Wang, X. L., Jiang, F., Hahn, H., Li, J., Gleiter, H., Sun, J., et al. (2015). Plasticity of a scandium-based nanoglass. *Scripta Mater.* 98, 40–43. doi: 10.1016/j.scriptamat.2014.11.010

Yoo, B.-G., Kim, K.-S., Oh, J.-H., Ramamurty, U., and Jang, J.-I. (2010). Room temperature creep in amorphous alloys: influence of initial strain and free volume. *Scripta Mater.* 63, 1205–1208. doi: 10.1016/j.scriptamat.2010.08.034

Conflict of Interest: The authors declare that the research was conducted in the absence of any commercial or financial relationships that could be construed as a potential conflict of interest.

frontiers in Materials

ORIGINAL RESEARCH
published: 06 November 2020
doi: 10.3389/fmats.2020.544660

Mechanical Properties of Glassy Nanopillars: A Comparative, Computational Study of Size Effects in Nanoglasses and Homogeneous Bulk Glasses

Omar Adjaoud and Karsten Albe*

Technische Universität Darmstadt, Fachbereich Material- und Geowissenschaften, Fachgebiet Materialmodellierung, Darmstadt, Germany

We study the mechanical properties of nanoglass (NG) nanopillars with diameters ranging from 4.5 to 54 nm by means of molecular dynamic simulations and compare the results with those obtained for nanopillars prepared from homogeneous glasses. NG nanopillars of two different types of glasses, namely, $Cu_{64}Zr_{36}$ and $Pd_{80}Si_{20}$, were cut from samples prepared by nanoparticle consolidation. The influence of nanopillar diameter on the deformation behavior and strain localization is investigated. Moreover, cyclic loading is used to explore the origin of stress overshoots in the stress–strain curves of NGs. Finally, from the calculated properties, a deformation map for NG and homogeneous glass nanopillars is derived.

Keywords: metallic glass, nanoglass, glass–glass interfaces, nanopillar, mechanical properties, molecular dynamics

OPEN ACCESS

Edited by:
Lothar Wondraczek, Friedrich Schiller University Jena, Germany

Reviewed by:
Saurabh Kapoor, SterliteTechnologies Ltd., India
Paulo Sergio Branicio, University of Southern California, Los Angeles, United States

****Correspondence:***
Omar Adjaoud
adjaoud@mm.tu-darmstadt.de

Speciality section:
This article was submitted to Ceramics and Glass, a section of the journal Frontiers in Materials

Received: *21 March 2020*
Accepted: *22 September 2020*
Published: *06 November 2020*

Citation:
Adjaoud O and Albe K (2020) Mechanical Properties of Glassy Nanopillars: A Comparative, Computational Study of Size Effects in Nanoglasses and Homogeneous Bulk Glasses. Front. Mater. 7:544660. doi: 10.3389/fmats.2020.544660

1 INTRODUCTION

Nanoglasses (NGs) are glassy materials with microstructural features on the nanoscale, which consist of glassy grains connected by glass–glass interfaces (Ivanisenko et al., 2018). These interfaces are characterized by an excess volume (Jing et al., 1989; Şopu et al., 2009), a defective short-range order (SRO) (Ritter et al., 2011), and a different composition as compared with the glassy grains (Adjaoud and Albe, 2016; Wang et al., 2016a; Adjaoud and Albe, 2018). NGs can be synthesized by cold compaction of nanometer-sized metallic glassy particles obtained via inert gas condensation (Jing et al., 1989; Weissmüller et al., 1992; Gleiter, 2008; Fang et al., 2012; Gleiter, 2013; Gleiter et al., 2014; Gleiter, 2016; Nandam et al., 2017; Ivanisenko et al., 2018). Microcompression test revealed considerable plasticity in an $Sc_{75}Fe_{25}$ NG, while the homogeneous glass (HG) with identical composition fails in a brittle manner (Fang et al., 2012). When reducing the sample size to the nanoscale, 15% plastic strain was observed in a 400 nm $Sc_{75}Fe_{25}$ NG nanopillar using *in situ* tensile tests in a transmission electron microscope (Wang et al., 2015). Moreover, a systematic study of nanosized and microsized $Sc_{75}Fe_{25}$ HG and NG pillars by means of compression tests showed that both, yield strength and deformation mode, are size-dependent in HG pillars. These properties, however, are size-independent in the NG pillars (Wang et al., 2016b), which was attributed to the microstructural features present in the NG. Indeed, molecular dynamic (MD) simulations revealed that glass–glass interfaces in NGs act as nucleation sites for shear transformation zones (STZs) and prevent strain localization, which leads to the more homogeneous deformation of NGs as compared with HGs (Şopu et al., 2011; Adibi et al., 2013; Albe et al., 2013; Adibi et al., 2014; Şopu and Albe, 2015; Adjaoud and Albe, 2019; Cheng and Trelewicz, 2019b).

MD simulations were also used in the past to investigate the effect of grain size on the deformation behavior of a 50 nm $Cu_{64}Zr_{36}$ NG nanopillar (Adibi et al., 2015a; Adibi et al., 2016). In these studies, the nanopillar was prepared by cutting a cylinder from an NG produced from an HG using the Poisson–Voronoi tessellation method (Brostow et al., 1978; Finney, 1979; Tanemura et al., 1983). However, this model of an NG underestimates the volume fraction of the interfaces as compared with the NGs prepared by consolidation of nanoparticles (Adjaoud and Albe, 2018; Cheng and Trelewicz, 2019a; Cheng and Trelewicz, 2019b; Adjaoud and Albe, 2019) which is more consistent with the experiment (Fang et al., 2012; Wang et al., 2015; Wang et al., 2016b).

In this work, we report the results of a systematic study on the influence of nanopillar diameter on the mechanical properties of NG and HG nanopillars with various diameters by means of MD simulations. The NG nanopillars were cut from NGs prepared by nanoparticle consolidation (Adjaoud and Albe, 2018). We first investigate the influence of nanopillar diameter on the deformation behavior and strain localization. Then, we examine the effects of nanopillar diameter on Young's modulus and yield stress of NG and HG nanopillars. We finally use the obtained mechanical properties to derive a deformation map for NG and HG nanopillars. In order to see whether the mechanical properties of NG and HG nanopillars depend on the chemical composition, all simulations were done for two different types of NGs and HGs, namely, $Cu_{64}Zr_{36}$ and $Pd_{80}Si_{20}$.

2 METHODOLOGY

MD simulations were carried out using the LAMMPS simulation package (Plimpton, 1995).The interatomic interactions are described by the Finnis–Sinclair-modified-type potential for Cu–Zr (Mendelev et al., 2009) and the embedded atom model potential for Pd–Si (Ding et al., 2012). These potentials have been optimized to predict accurately the structure of liquid and amorphous Cu–Zr and Pd–Si alloys and were successfully applied to Cu–Zr and Pd–Si glasses (Cheng et al., 2013; An et al., 2016; Tang et al., 2018; Adjaoud and Albe, 2019).

First, $Cu_{64}Zr_{36}$ and $Pd_{80}Si_{20}$HGs were obtained by quenching a melt, which was already equilibrated at 2,000 K, to a temperature of about 50 K at a quenching rate of 0.01 K ps^{-1} (Ritter et al., 2011). Next, we prepared $Cu_{64}Zr_{36}$ and $Pd_{80}Si_{20}$ NGs by cold compaction of several glassy spheres with diameters ranging from 6 to 8 nm as described by Adjaoud and Albe, 2018. The resulting NGs have dimensions of about 18 nm × 18 nm × 18 nm, and their microstructure consists of glassy regions connected by glass–glass interfaces. These interfaces are characterized by a defective SRO in a zone with a width of at least 2 nm (Adjaoud and Albe, 2018; Cheng and Trelewicz, 2019a). The resulting $Cu_{64}Zr_{36}$ NG also exhibits locally varying compositions with copper-poor glassy bulk regions ($Cu_{61}Zr_{39}$) and copper-rich interfaces ($Cu_{72}Zr_{28}$) extending over about 1 nm. Similarly, the $Pd_{80}Si_{20}$ NG is made up of $Pd_{78.6}Si_{21.4}$ glassy regions and $Pd_{82.7}Si_{17.3}$ interfaces.

The NGs and HGs were replicated and relaxed in order to construct larger samples. After that, the nanopillars were prepared by cutting a cylinder followed by structural relaxation. The diameters of the nanopillars are ranging from D = 4.5–54 nm, which corresponds to 17 million atoms at maximum. The HG nanopillars have a homogeneous microstructure, while the NG nanopillars have an inhomogeneous microstructure (see **Supplementary Figure S1**). All nanopillars have an aspect ratio (length-to-diameter) of 2, except the nanopillars with D = 4.5 nm which have an aspect ratio of 4. The later aspect ratio is chosen in order to still keep the periodicity in the direction of the axis of the NG nanopillar.

In order to characterize the mechanical properties of NG and HG nanopillars, a series of tensile deformation simulations were performed. The uniaxial tensile load was applied along the axis of the nanopillars, which was chosen in the *z*-direction, with a constant strain rate of 4.10^7 s^{-1} at 50 K. The atomic scale deformation mechanisms were analyzed in terms of the local atomic von Mizes shear strain calculated with the OVITO analysis and visualization software (Stukowski, 2010).

3 RESULTS

3.1 Deformation Behavior and Strain Localization

In NG nanopillars, the glass–glass interfaces as well as the free surface can act as nucleation sites for shear events (Albe et al., 2013). **Figures 1A,B** present the stress–strain curves for $Cu_{64}Zr_{36}$ and $Pd_{80}Si_{20}$ NG nanopillars with an average grain size of d = 7 nm and diameters ranging from D = 4.5–54 nm. It can be seen that the maximum stress, σ_{max}, is higher for $Pd_{80}Si_{20}$ NG nanopillars than for $Cu_{64}Zr_{36}$ NG nanopillars, which is essentially a modulus effect. Apart from σ_{max}, stress–strain curves of $Cu_{64}Zr_{36}$ are similar to those of $Pd_{80}Si_{20}$ with the same nanopillar diameter; both types of NG nanopillars do not show a stress drop upon yielding.

Nanopillars with a diameter smaller than the average grain size (d = 7 nm) exhibit the highest σ_{max}. When D ≥ 9 nm, the stress–strain curves exhibit pronounced strain softening. The onset of strain softening occurs earlier in the large nanopillars: the stress of 36 and 54 nm NG nanopillars starts decreasing at an engineering strain of about 13–15%, in agreement with experimental results on a 400 nm $Sc_{75}Fe_{25}$ NG nanopillar showing about 15% plastic strain (Wang et al., 2015).

Figures 1C,D show the engineering stress–strain curves for the $Cu_{64}Zr_{36}$ and $Pd_{80}Si_{20}$ HG nanopillars with diameters ranging from 4.5 up to 54 nm. The $Cu_{64}Zr_{36}$ and $Pd_{80}Si_{20}$HGs are shown for comparison. It can be seen that the $Cu_{64}Zr_{36}$ HG exhibits a stress drop after the maximum stress, indicating the formation of a critical shear band (Adjaoud and Albe, 2019). The $Pd_{80}Si_{20}$ HG, in contrast, does not show a stress drop, suggesting that the $Pd_{80}Si_{20}$ HG is more ductile than the $Cu_{64}Zr_{36}$ HG. This is in agreement with the bending experiment and compression test on Pd–Si glasses (Yao et al., 2006; An et al., 2016). The nanopillars with smaller diameters, 4.5 nm for $Cu_{64}Zr_{36}$ and up to 9 nm for $Pd_{80}Si_{20}$, show strain softening upon yielding. Nanopillars with larger diameters, D ≥ 9 nm for $Cu_{64}Zr_{36}$ and D ≥ 18 nm for $Pd_{80}Si_{20}$, exhibit a pronounced stress drop and strain softening, while the magnitude of the stress drop is increasing with increasing

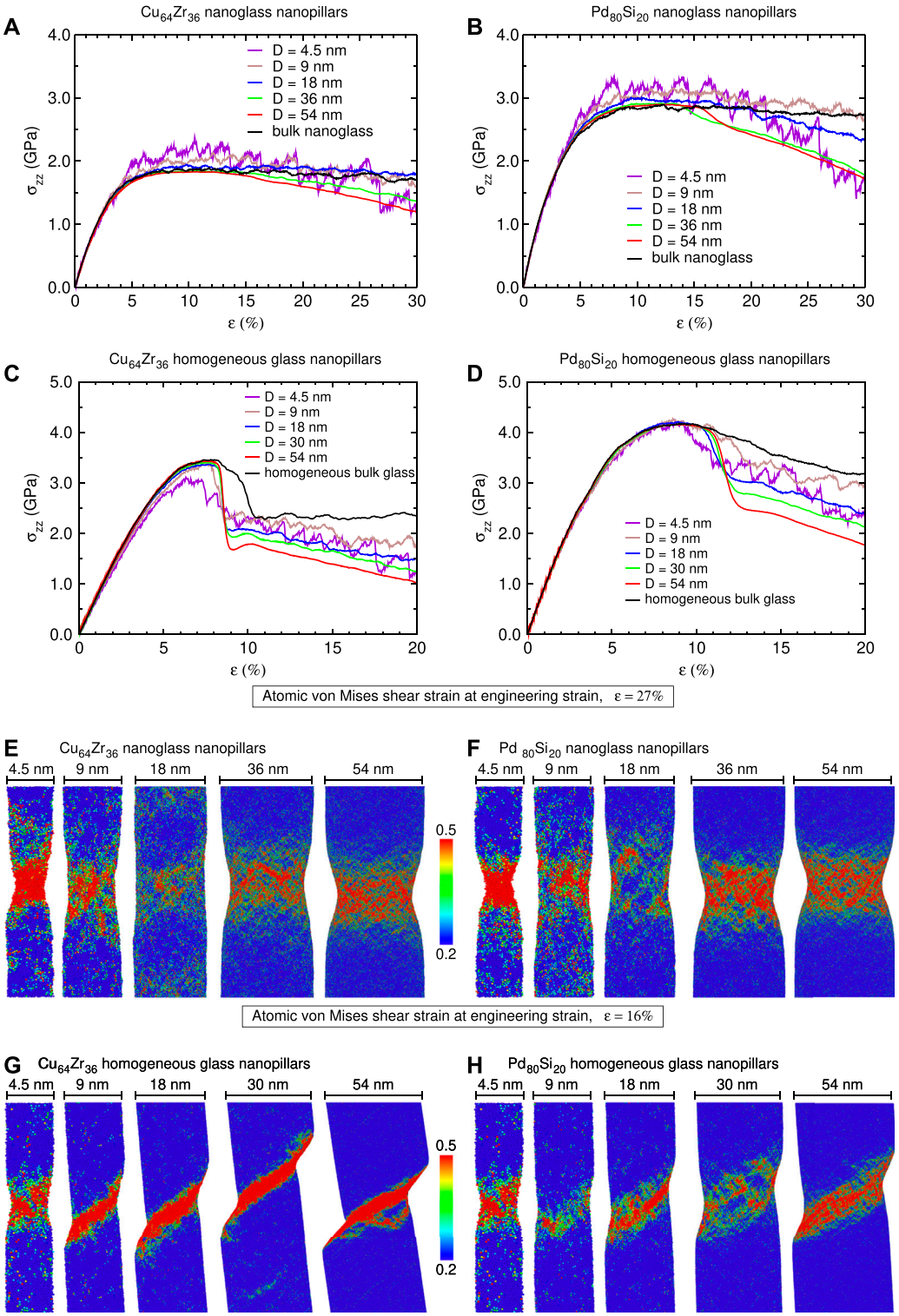

FIGURE 1 | Tensile test of $Cu_{64}Zr_{36}$ and $Pd_{80}Si_{20}$ nanoglass (NG) and homogeneous glass (HG) nanopillars with an average grain size of d = 7 nm and diameters ranging from D = 4.5–54 nm. **(A,B)** Engineering stress–strain curves for NG nanopillars. **(C,D)** Engineering stress–strain curves for HG nanopillars. **(E,F)** Local von Mises shear strain at 27% total strain, showing strain localization in the NG nanopillars. **(G,H)** Local von Mises shear strain at 16% total strain, showing strain localization in the HG nanopillars. Engineering stress–strain curves for HG and NG bulk samples are added for reference; those for $Cu_{64}Zr_{36}$ bulk samples are taken from reference (Adjaoud and Albe, 2019).

nanopillar diameter. This size dependence can be understood in terms of the elastic energy release right after the stress drop, which is proportional to D^2 (Liu et al., 2011). In the case of $Cu_{64}Zr_{36}$ HG nanopillars, strain hardening occurs right after the stress drop at about 9% engineering strain, which is most pronounced in the 30 and 54 nm HG nanopillars. This effect can be explained by the structural relaxation which occurs after the elastic energy release (Ritter and Albe, 2012).

Next, we inspect the strain localization in NG nanopillars. By analyzing von Mises strains, three deformation modes can be defined: (1) pure necking, when the deformation plane is perpendicular to the deformation axis; (2) pure shear banding, when the angle between the deformation plane and the deformation axis is about 40°–60°; and (3) if a nanopillar is not long enough to allow strain localization to occur in a form of necking or shear banding, then von Mises strain distributes over the whole nanopillar which exhibits homogeneous deformation.

Figures 1E,F show the atomic von Mises shear strain at 27% engineering strain for $Cu_{64}Zr_{36}$ and $Pd_{80}Si_{20}$ NG nanopillars. It can be seen that the 4.5 nm nanopillars deform by necking. This necking deformation mode can be explained by the large surface-to-volume fraction which leads to the nucleation of a high number of STZs at the surface of the nanopillar (Albe et al., 2013). The 9 and 18 nm NG nanopillars, where the diameter is about or twice the average grain size, exhibit nearly homogeneous deformation, confirming the weak strain softening observed in the stress–strain curves (see **Figures 1A,B**). When the nanopillar diameter is significantly larger than the average grain size, as in the case of the 36 and 54 nm NG nanopillars, the nanopillars deform again by necking. This is consistent with the strain softening occurring in the stress–train curves. By comparing the $Cu_{64}Zr_{36}$ and $Pd_{80}Si_{20}$ NG nanopillars, it can be seen that the deformation behavior is similar and thus does not depend on the type of the NG nanopillars. Moreover, even after deformation, the interfaces are still characterized by compositional variation (see **Supplementary Figure S2**).

Recent MD studies (Adjaoud and Albe, 2019; Cheng and Trelewicz, 2019b) revealed that the mechanical properties of bulk NG samples are rather independent of the grain size which was attributed to the constant volume fraction of interfaces for NGs with different grain sizes because of the varying interfaces' width. Based on those results, one could expect that the deformation behavior of the NG nanopillars in the present study is grain-size independent as their bulk NGs counterparts. It is interesting to note that a different result was obtained for bulk NGs and NG nanopillars produced by the Poisson–Voronoi tessellation method, which exhibits a grain-size-dependent deformation behavior because the glass–glass interfaces are assumed to have a constant width of 1 nm independent of the grain size (Adibi et al., 2013; Adibi et al., 2015a).

If we compare the NG nanopillars and bulk NG samples of both glasses, we see that bulk NG samples show no strain softening and a homogeneous deformation behavior (Adjaoud and Albe, 2019; Cheng and Trelewicz, 2019b) similar to the 9 nm NG nanopillars (see **Figures 1A,B**).

In order to see whether the necking deformation mode, which is observed in the $Cu_{64}Zr_{36}$ and $Pd_{80}Si_{20}$ NG nanopillars, is related to the presence of glass–glass interfaces or free surface, we inspected the atomic von Mises shear strain in the HG nanopillars which is shown in **Figures 1G,H** at 16% engineering strain. It can be seen that, with smaller diameters, the nanopillars deform by necking, while strain localization in the nanopillars with larger diameters occurs in the form of a shear band. This is in line with previous MD simulation results (Adibi et al., 2015b). Again, because of the large surface-to-volume fraction, the 4.5 nm HG nanopillars deform by necking independent of the chemical composition, similar to the 4.5 nm NG nanopillars. Previous atomistic simulations on $Cu_{64}Zr_{36}$ HGs have shown that a sample thickness of at least 5 nm is needed for shear band formation (Cheng and Ma, 2011).

Comparing the $Cu_{64}Zr_{36}$ HG nanopillars with the $Pd_{80}Si_{20}$ HG nanopillars, we find that the stress drop is steeper and strain localization is more pronounced in the $Cu_{64}Zr_{36}$ HG nanopillars. Moreover, σ_{max} is higher for the $Pd_{80}Si_{20}$ HG nanopillars than for the $Cu_{64}Zr_{36}$ HG nanopillars, similar to NG nanopillars. This difference in the mechanical properties of $Cu_{64}Zr_{36}$ and $Pd_{80}Si_{20}$ HG nanopillars might be attributed to the difference in the chemical and topological SRO. In fact, recent bending experiments and MD simulations have shown that $Pd_{82}Si_{18}$ HG is significantly tougher than $Cu_{46}Zr_{54}$ HG; the higher toughness of the $Pd_{82}Si_{18}$ HG is related to its topological SRO (An et al. 2016). Moreover, our results reveal that the shear-band thickness in the $Pd_{80}Si_{20}$ HG nanopillars is larger than in the $Cu_{64}Zr_{36}$ HG nanopillars (see **Figures 1H,G**). This is consistent with previous experimental and simulation studies which have shown that the shear-band thickness is ranging from 5 to 20 nm or even 200 nm depending on the chemical composition of the metallic glass (Zhang and Greer, 2006; Cao et al., 2009; Murali et al., 2012; Shao et al., 2013; Liu et al., 2017).

Our results show that the main differences between the NG nanopillars and HG nanopillars are maximum stress σ_{max} and the deformation mode: strain localization in the HG nanopillars occurs in the form of a shear band, whereas the NG nanopillars deform by necking or homogeneously, depending on the nanopillar diameter. These results are in agreement with a recent experimental study on the mechanical properties of $Sc_{75}Fe_{25}$ NG and HG nanopillars with diameter of 400 nm using *in situ* tensile tests in a transmission electron microscope (Wang et al. 2015).

3.2 Stress Overshoot during Cyclic Loading

It is known that cyclic loading may significantly affect the deformation behavior of materials. Cyclic loading is usually performed in the elastic regime (Sha et al., 2015;Sha et al., 2017) or in the plastic regime (Zhu et al., 2017; Tang et al., 2018). The cyclic loading of metallic glasses in the plastic regime leads usually to the phenomenon of stress overshoot (Maaß et al., 2012).

In order to investigate the stress overshoot and the remaining plastic deformation in the NG nanopillars in more detail, we performed cyclic loading on the 18 nm $Cu_{64}Zr_{36}$ and $Pd_{80}Si_{20}$ NG nanopillars by unloading them from 15% engineering strain and then reloading them. **Figures 2A,B** present the corresponding

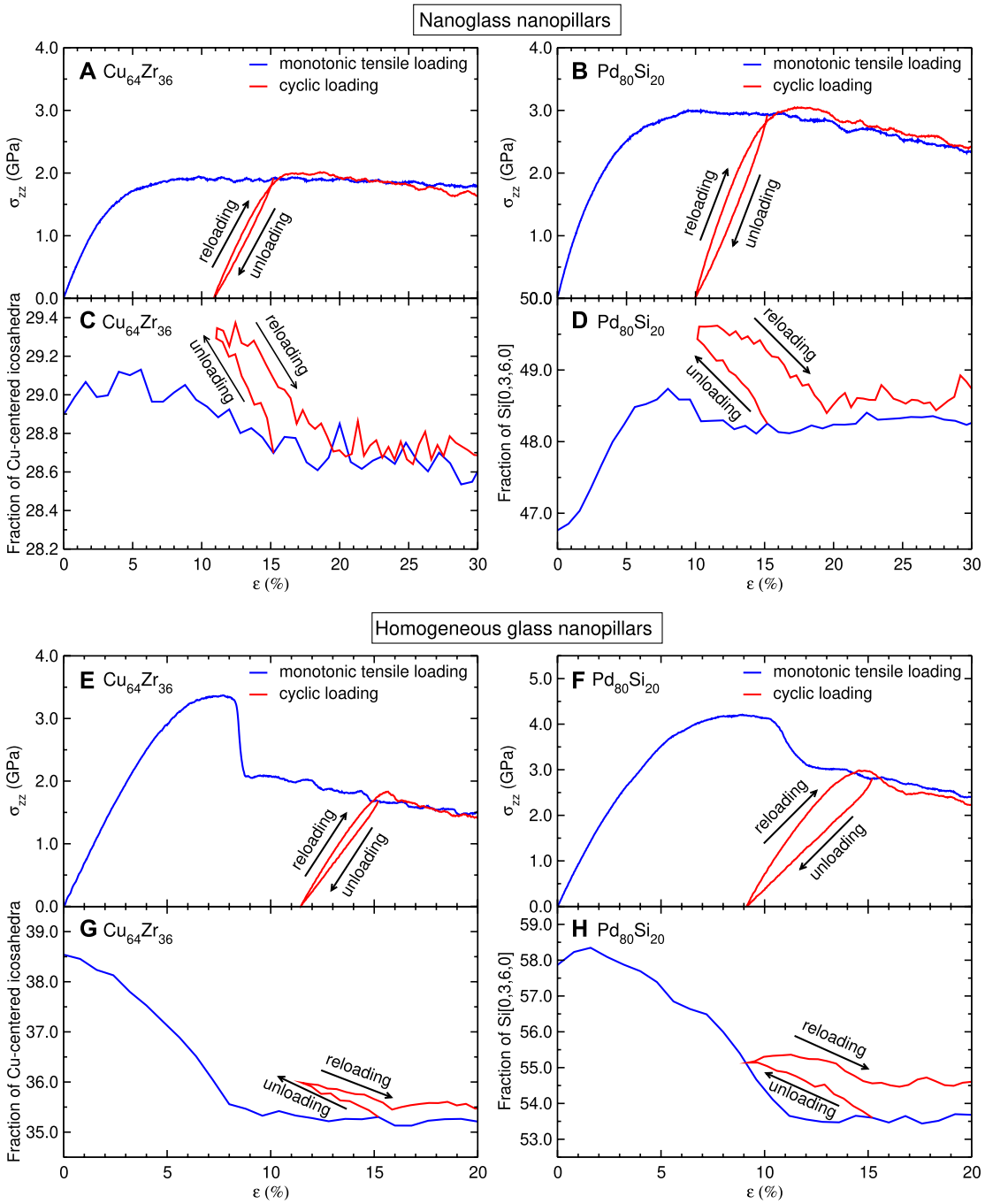

FIGURE 2 | $Cu_{64}Zr_{36}$ and $Pd_{80}Si_{20}$ nanoglass (NG) and homogeneous glass (HG) nanopillars with a diameter of 18 nm under cyclic loading. **(A,B)** Engineering stress–strain curves for NG nanopillars. **(C)** Variation of Cu-centered icosahedra in the $Cu_{64}Zr_{36}$ NG nanopillars, including full icosahedra (index [0,12,0,0]) and disordered icosahedra (indexes [0,2,8,2] and [0,3,6,3]) as a function of the engineering strain. **(D)** Variation of the most prominent Voronoipolyhedra in the $Pd_{80}Si_{20}$ NG nanopillar, Si[0,3,6,0], as a function of the engineering strain. **(E,F)** Engineering stress–strain curves for HG nanopillars. **(G)** Variation of Cu-centered icosahedra in the $Cu_{64}Zr_{36}$ HG nanopillars as a function of the engineering strain. **(H)** Variation of the most prominent Voronoipolyhedra in the $Pd_{80}Si_{20}$ HG nanopillar, Si[0,3,6,0], as a function of the engineering strain. The engineering stress–strain curves for the monotonic loading of 18 nm $Cu_{64}Zr_{36}$ and $Pd_{80}Si_{20}$ NG and HG nanopillars are reproduced for reference.

stress–strain curves during the cyclic loading. In both glasses, the cyclic loading leads to a slight increase of flow stress after reloading caused by structural relaxation: the fractions of the Cu-centered icosahedra in the $Cu_{64}Zr_{36}$ NG nanopillar, including full icosahedra (index [0,12,0,0]) and disordered icosahedra (indexes [0,2,8,2] and [0,3,6,3]) and the most prominent Voronoipolyhedra Si[0,3,6,0] in the $Pd_{80}Si_{20}$ NG nanopillar, significantly increase after the first loading stage

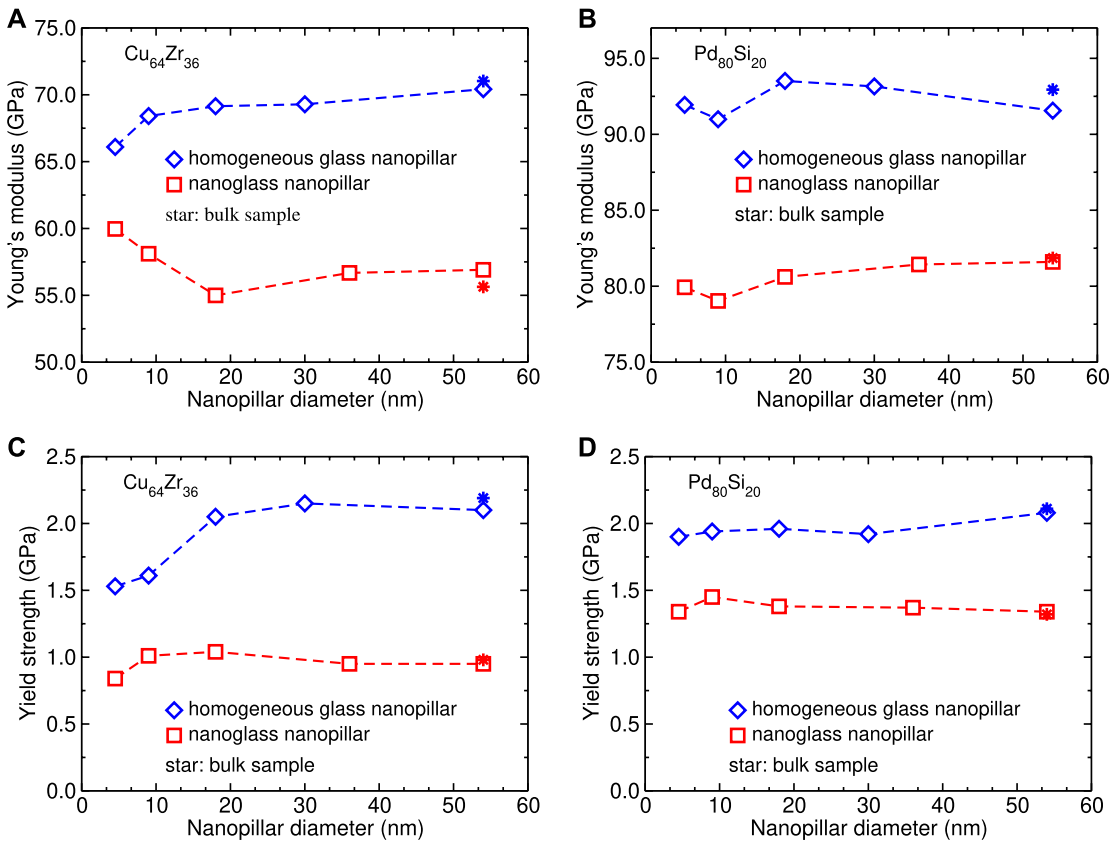

FIGURE 3 | Effect of size on Young's modulus and yield strength of homogeneous glass (HG) and nanoglass (NG) nanopillars. **(A,B)** Young's modulus as a function of the nanopillar diameter for $Cu_{64}Zr_{36}$ and $Pd_{80}Si_{20}$ NG and HG nanopillars. **(C,D)** Yield strength as a function of the nanopillar diameter for $Cu_{64}Zr_{36}$ and $Pd_{80}Si_{20}$ NG and HG nanopillars. The HG and NG bulk samples are added for comparison.

(see **Figures 2C,D**), which indicates that defective interfacial areas are relaxed during the initial stage of plastic deformation.

The correlation between the increase of flow stress and structural relaxation is also observed in the HG nanopillars (see **Figures 2E–H**). However, in the HG nanopillars, the stress increases only in a small region of engineering strains as compared with the NG nanopillars: after the initial stress increases, the stresses of the monotonic tensile loading and the cyclic loading merge together in the $Cu_{64}Zr_{36}$ HG nanopillar, while in the $Pd_{80}Si_{20}$ HG nanopillar, the stress of the cyclic loading is slightly lower than that of the monotonic tensile loading. Moreover, the fractions of the Cu-centered icosahedra in the $Cu_{64}Zr_{36}$ HG nanopillar and the Voronoipolyhedra Si [0,3,6,0] in the $Pd_{80}Si_{20}$ HG nanopillar for the cyclic loading remain higher than those for the monotonic tensile loading after the stress overshoot, indicating the recovery of the local order upon unloading.

These results are in agreement with recent MD simulation results which showed that a cyclic loading after the formation of a shear band in a $Cu_{50}Zr_{50}$ HG leads to structural relaxation, and consequently, a stress increase occurs in the stress–strain curve (Tang et al., 2018). Experiments and theoretical models have shown that this phenomenon depends on temperature, strain rate, and structural relaxation (Kawamura et al., 1997; Lu et al., 2003; Maaß et al., 2012; Jiang et al., 2015; Yang et al., 2019).

3.3 Size Effects on Young's Modulus and Yield Strength

We, next, explore the effect of nanopillar diameter on Young's modulus and yield strength. We obtained Young's modulus from the slope of stress–strain curves at the small strain where the stress is proportional to the strain. We used 0.2% offset strain to calculate the yield strength. **Figures 3A,B** show the calculated Young's moduli as a function of the nanopillar diameter for $Cu_{64}Zr_{36}$ and $Pd_{80}Si_{20}$ NG and HG nanopillars. The HG and NG bulk samples are shown for comparison.

The calculated Young's moduli for $Cu_{64}Zr_{36}$ and $Pd_{80}Si_{20}$ HGs are in agreement with the experimental data which are about 67 GPa for $Cu_{64}Zr_{36}$ (Mendelev et al., 2008) and 94 Gpa for $Pd_{80}Si_{20}$ (Mizubayashi et al., 1998). It can be seen that Young's modulus depends slightly on the nanopillar diameter when $D \leq 9$ nm. However, in the HG, surface stresses are the dominant contribution to this size effect, and the elastic softening of the NG is due to the different elastic contributions of the glass–glass interfaces and the action of surface stresses, which are counteracting. However, the nanopillars with $D \geq 18$ nm show

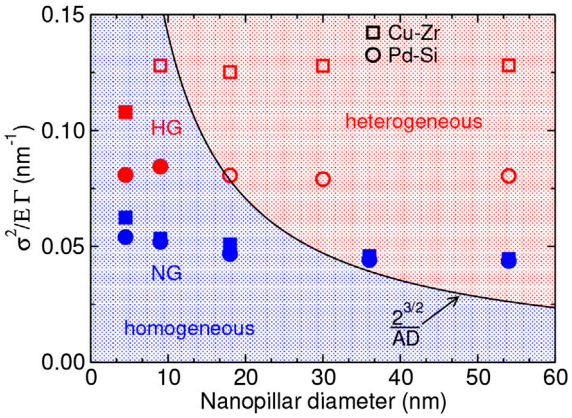

FIGURE 4 | Flow stress normalized by Young's modulus and shear band energy per unit area as a function of the nanopillar diameter at 5% total strain. Red squares and red circles represent $Cu_{64}Zr_{36}$ and $Pd_{80}Si_{20}$ homogeneous glass (HG) nanopillars, respectively. Blue squares and blue circles represent $Cu_{64}Zr_{36}$ and $Pd_{80}Si_{20}$nanoglass (NG) nanopillars, respectively. Open symbols indicate the occurrence of a shear band.

about the same Young's modulus which is close to the value of the bulk samples. Similar behavior is observed for yield strength, see **Figures 3C,D**. Moreover, Young's moduli and the yield strengths of NG nanopillars are clearly lower than those of HG nanopillars. This can be explained by the existence of the glass–glass interfaces in NGs, which act as a source for STZs (Albe et al., 2013). Recently, Wang et al. (2015) investigated the mechanical properties of $Sc_{75}Fe_{25}$ NG and HG nanopillars by using *in situ* tensile tests in a transmission electron microscope and found a similar trend in yield strength: the yield strength of the NG nanopillar is lower than that of the HG nanopillar with identical chemical composition. Strength softening was also observed in $Ni_{78}P_{22}$ NG pillars prepared by the electrodeposition technique (Li et al., 2018).

3.4 Critical Stress

In order to further investigate the difference in deformation modes between the NG and HG nanopillars, we calculated the critical stress required for SB formation (Volkert et al., 2008), $\sigma = \sqrt{2^{3/2}\Gamma E/AD}$, where E is Young's modulus, Γ is the SB energy per unit area, A is the aspect ratio, and D is the diameter of the nanopillar. The values for E are reported in **Figure 3**. For Γ, we used a value of 1.30 J/m^2 for Cu–Zr determined in a previous study (Adjaoud and Albe, 2018) and a value of 2.34 J/m^2 for Pd–Si. We calculated Γ for Pd–Si from the stress–strain curve of the 18 nm $Pd_{80}Si_{20}$ HG nanopillar, using the same method as that for Cu–Zr (Adjaoud and Albe, 2018). Our values for Γ are close to 0.98 ± 0.04 J/m^2 reported in tensile simulation for a $Cu_{50}Zr_{50}$ metallic glass film (Zhong et al., 2015) and 0.56 J/m^2 reported in uniaxial compression experiments for Cu-based and Zr-based metallic glasses (Chen et al., 2010). On the other hand, our calculated Γ values are much smaller than 10 J/m^2 for a Pd-based metallic glass (Volkert et al., 2008) and 9 J/m^2 for a Zr-based metallic glass (Dubach et al., 2009) reported in uniaxial compression experiments. This suggests that the energy Γ depends on the composition of metallic glasses and their processing route.

The predicted critical stress values for the homogeneous glasses (HGs) match very well with the observed deformation modes as shown in **Figure4**. The only exception is the Cu–Zr nanopillar with D = 9 nm. In case of the NG nanopillars, the data fall in the homogeneous regime. The only clear exceptions are the data for the nanopillars with D ≥ 54 nm. Interestingly, the Cu–Zr and Pd–Si NG nanopillars have the same critical stress values. This is consistent with the results in **Figures 1E,F** which show that the deformation modes for the Cu–Zr and Pd–Si NG nanopillars are similar. The relative good agreement with the model prediction is implying that the more homogeneous deformation of NGs can also be understood as a mere modulus effect.

4 DISCUSSION

The results presented above are for nanopillars with diameters up to 54 nm. This size is much smaller than that used in experiment which is about 400 nm (Wang et al., 2015). Sample preparation and mechanical testing in experiments make it difficult to prepare nanopillars with diameters below 100 nm (Shi, 2019). On the other hand, the increase of the nanopillar size in MD simulation leads to the increase of the number of atoms, and this becomes computationally expensive. Although the sample size mismatched between MD simulation and experiment, MD simulation is useful to understand experimental observations (Liontas et al., 2016). From the present MD results, one can see that, for both systems, Cu–Zr and Pd–Si, the 36 and 54 nm NG nanopillars exhibit a similar mechanical behavior. This may be attributed to the small surface-to-volume fraction which leads to the deformation to be dominated by the interfaces rather than by the surface. Indeed, a recent MD simulation study on HG nanopillars has shown that the surface stress becomes less significant when the nanopillar diameter is larger than 30 nm (Zhang et al., 2015). Thus, one could expect that NG nanopillars with diameters larger than 54 nm should show a similar mechanical behavior as the 36 and 54 nm nanopillars.

Present MD simulation results on HG nanopillars show that the transition from necking to shear banding occurs at a diameter between 10 and 20 nm. These results are in agreement with previous MD simulation results which reported that size-independent shear banding until their dimensions approach the shear-band thickness which is about 5–20 nm (Adibi et al., 2016; Liontas et al., 2016; Shi, 2019). This transition appears in experiments at a lager sample diameter, between 100 and 400 nm, as compared with MD simulations (Tian et al., 2016). This difference in the sample size on the change of the deformation mode between experiments and simulations can be related to the different processing and testing conditions (Shi, 2019).

Simulations of NG nanopillars reveal no shear banding: NG nanopillars exhibit necking or homogeneous deformation. Homogeneous deformation occurs in the 9 and 18 nm NG nanopillars, where their length is not long enough to allow strain localization to form necking. Necking deformation mode was also reported in previous MD simulations on the $Cu_{64}Zr_{36}$ NG nanopillars with a diameter of 50 nm (Adibi et al., 2015a; Adibi et al., 2016).

The NG nanopillars studied in the present study are cut from an as-prepared NG. Structural relaxation due to the high compaction rate used in simulation during the preparation of the NG may change the deformation mode. Indeed, a recent study on the compression test of Pd–Si NG nanopillar with a diameter of 36 nm showed a change in the deformation mode from homogeneous deformation to shear banding when the nanopillar is cut from an annealed NG (Nandam et al., 2020). The effect of annealing on the change of the deformation mode was also reported in a recent experiment and simulation study on Zr–Ni–Al nanosized metallic glasses (Liontas et al., 2016).

5 CONCLUSIONS

We have investigated the influence of structure size on the mechanical properties of NG and HG nanopillars with 7 nm grain size and diameters ranging from 4.5 up to 54 nm by means of MD simulations. Simulations were done for two different glasses, namely, $Cu_{64}Zr_{36}$ and $Pd_{80}Si_{20}$, as representatives of metal–metal and metal–metalloid systems, respectively. Different from previous studies, the NGs were produced by consolidation rather than Voronoi tessellation and thus have a more realistic microstructure.

Our results show a clear difference in the deformation mode between NG and HG for the 36 and 54 nm nanopillars, independent of the glass type. While HG nanopillars exhibit a stress drop and strain localization developing in a shear band, NG nanopillars show ductile deformation behavior with softening at larger engineering strains and deformation by necking. The tensile ductility of about 13–15% found in our simulations is in agreement with 15% plastic strain observed for a 400 nm $Sc_{75}Fe_{25}$ NG nanopillar using *in situ* tensile tests in a transmission electron microscope (Wang et al., 2015). HG and NG nanopillars with D = 4.5 nm, where the pillar diameter is smaller than the average grain size d = 7 nm of the NG, deform by necking since the nucleation of STZs on the surface is dominating. In the HG nanopillars with D = 9 and 18 nm, shear banding is more obvious in $Cu_{64}Zr_{36}$ than in $Pd_{80}Si_{20}$. When reducing the NG nanopillar diameter to near or double the average grain size, strain softening appears at the larger engineering strain (>20%). Moreover, structural relaxation after a cyclic loading leads to local recovery, and the stress increases upon reloading.

We determined Young's modulus and yield strengths from stress–strain curves of tensile deformations. We find that both properties are smaller in the NG nanopillars as compared with their homogeneous counterparts in both glasses. From Young's modulus values and the shear band energy, the critical stress for shear band formation is estimated. We find that the predicted critical stress values are quite consistent with the observed deformation modes.

DATA AVAILABILITY STATEMENT

All datasets generated for this study are included in the article and **Supplementary Material**.

AUTHOR CONTRIBUTIONS

OA and KA contributed equally to the conception and design of this study; OA set up and ran the simulations, performed the analysis, and wrote the first draft of the manuscript; KA supervised the work and reviewed and edited the manuscript.

FUNDING

The authors acknowledge the financial support of the Deutsche Forschungsgemeinschaft (DFG) through project no. AL 578/15–2.

ACKNOWLEDGMENTS

The authors gratefully acknowledge the Gauss Centre for Supercomputing e.V. (www.gauss-centre.eu) for funding this project by providing computing time through the John von Neumann Institute for Computing (NIC) on the GCS Supercomputer JUWELS at Jülich Supercomputing Centre (JSC). Computational time was also made available by the Lichtenberg High Performance Computer Cluster at TU Darmstadt.

SUPPLEMENTARY MATERIAL

The Supplementary Material for this article can be found online at: https://www.frontiersin.org/articles/10.3389/fmats.2020.544660/full#supplementary-material.

REFERENCES

Adibi, S., Branicio, P. S., and Ballarini, R. (2016). Compromising high strength and ductility in nanoglass-metallic glass nanolaminates. *RSC Adv.* 6, 13548–13553. doi:10.1039/C5RA24715B

Adibi, S., Branicio, P. S., and Joshi, S. P. (2015a). Suppression of shear banding and transition to necking and homogeneous flow in nanoglass nanopillars. *Sci. Rep.* 5, 15611. doi:10.1038/srep15611

Adibi, S., Branicio, P. S., Liontas, R., Chen, D. Z., Greer, J. R., Srolovitz, D. J., et al. (2015b). Surface roughness imparts tensile ductility to nanoscale metallic glasses. *Extreme Mech. Lett.* 5, 88–95. doi:10.1016/j.eml.2015.08.004

Adibi, S., Branicio, P. S., Zhang, Y.-W., and Joshi, S. P. (2014). Composition and grain size effects on the structural and mechanical properties of CuZr nanoglasses. *J. Appl. Phys.* 116, 043522. doi:10.1063/1.4891450

Adibi, S., Sha, Z.-D., Branicio, P. S., Joshi, S. P., Liu, Z.-S., and Zhang, Y.-W. (2013). A transition from localized shear banding to homogeneous superplastic flow in nanoglass. *Appl. Phys. Lett.* 103, 211905. doi:10.1063/1.4833018

Adjaoud, O., and Albe, K. (2016). Interfaces and interphases in nanoglasses: surface segregation effects and their implications on structural properties. *Acta Mater.* 113, 284. doi:10.1016/j.actamat.2016.05.002

Adjaoud, O., and Albe, K. (2018). Microstructure formation of metallic nanoglasses: insights from molecular dynamics simulations. *Acta Mater.* 145, 322–330. doi:10.1016/j.actamat.2017.12.014

Adjaoud, O., and Albe, K. (2019). Influence of microstructural features on the plastic deformation behavior of metallic nanoglasses. *Acta Mater.* 168, 393–400. doi:10.1016/j.actamat.2019.02.033

Albe, K., Ritter, Y., and Şopu, D. (2013). Enhancing the plasticity of metallic glasses: shear band formation, nanocomposites and nanoglasses investigated by molecular dynamics simulations. *Mech. Mater.* 67, 94–103. doi:10.1016/j.mechmat.2013.06.004

An, Q., Samwer, K., Demetriou, M. D., Floyd, M. C., Duggins, D. O., Johnson, W. L., et al. (2016). How the toughness in metallic glasses depends on topological and chemical heterogeneity. *Proc. Natl. Acad. Sci. U. S. A.* 113, 7053–7058. doi:10.1073/pnas.1607506113

Brostow, W., Dussault, J.-P., and Fox, B. L. (1978). Construction of voronoi polyhedra. *J. Comput. Phys.* 29, 81–92. doi:10.1016/0021-9991(78)90110-9

Cao, A. J., Cheng, Y. Q., and Ma, E. (2009). Structural processes that initiate shear localization in metallic glass. *Acta Mater.* 57, 5146 – 5155. 10.1016/j.actamat.2009.07.016

Chen, C. Q., Pei, Y. T., and De Hosson, J. T. M. (2010). Effects of size on the mechanical response of metallic glasses investigated through *in situ* TEM bending and compression experiments. *Acta Mater.* 58, 189–200. doi:10.1016/j.actamat.2009.08.070

Cheng, B., and Trelewicz, J. R. (2019a). Controlling interface structure in nanoglasses produced through hydrostatic compression of amorphous nanoparticles. *Phys. Rev. Materials.* 3, 035602. doi:10.1103/PhysRevMaterials.3.035602

Cheng, B., and Trelewicz, J. R. (2019b). Interfacial plasticity governs strain delocalization in metallic nanoglasses. *J. Mater. Res.* 34, 2325–2336. doi:10.1557/jmr.2019.101

Cheng, Y. Q., Ding, J., and Ma, E. (2013). Local Topologyvs.Atomic-level stresses as a measure of disorder: correlating structural indicators for metallic glasses. *Mater. Res. Lett.* 1, 3–12. doi:10.1080/21663831.2012.722759

Cheng, Y. Q., and Ma, E. (2011). Intrinsic shear strength of metallic glass. *Acta Mater.* 59, 1800–1807. 10.1016/j.actamat.2010.11.046

Ding, J., Cheng, Y.-Q., Sheng, H., and Ma, E. (2012). Short-range structural signature of excess specific heat and fragility of metallic-glass-forming supercooled liquids. *Phys. Rev. B* 85, 060201. doi:0.1103/PhysRevB.85.060201

Dubach, A., Raghavan, R., Loffler, J., Michler, J., and Ramamurty, U. (2009). Micropillar compression studies on a bulk metallic glass in different structural states. *Scripta Mater.* 60, 567–570. doi:10.1016/j.scriptamat.2008.12.013

Fang, J. X., Vainio, U., Puff, W., Würschum, R., Wang, X. L., Wang, D., et al. (2012). Atomic structure and structural stability of Sc75Fe25 nanoglasses. *Nano Lett.* 12, 458–463. doi:10.1021/nl2038216

Finney, J. L.. (1979). A procedure for the construction of voronoi polyhedra. *J. Comput. Phys.* 32, 137–143. 10.1016/0021-9991(79)90146-3

Gleiter, H. (2008). Our thoughts are ours, their ends none of our own: are there ways to synthesize materials beyond the limitations of today? *Acta Mater.* 56, 5875–5893. doi:10.1016/j.actamat.2008.08.028

Gleiter, H. (2013). Nanoglasses: a new kind of noncrystalline materials. *Beilstein J. Nanotechnol.* 4, 517–533. doi:10.3762/bjnano.4.61

Gleiter, H. (2016). Nanoglasses: a new kind of noncrystalline material and the way to an age of new technologies?. *Small* 12, 2225–2233. doi:10.1002/smll.201500899

Gleiter, H., Schimmel, T., and Hahn, H. (2014). Nanostructured solids - from nano-glasses to quantum transistors. *Nano Today.* 9, 17–68. doi:10.1016/j.nantod.2014.02.008

Ivanisenko, Y., Kübel, C., Nandam, S. H., Wang, C., Mu, X., Adjaoud, O., et al. (2018). Structure and properties of nanoglasses. *Adv. Eng. Mater.* 20, 1800404. doi:10.1002/adem.201800404

Jiang, M. Q., Wilde, G., and Dai, L. H. (2015). Origin of stress overshoot in amorphous solids. *Mech. Mater.* 81, 72–83. 10.1016/j.mechmat.2014.10.002

Jing, J., Krämer, A., Birringer, R., Gleiter, H., and Gonser, U. (1989). Modified atomic structure in a Pd-Fe-Si nanoglass. *J. Non-Cryst. Solids.* 113, 167–170. doi:10.1016/0022-3093(89)90007-0

Kawamura, Y., Shibata, T., Inoue, A., and Masumoto, T. (1997). Stress overshoot in stress-strain curves of Zr65Al10Ni10Cu15 metallic glass. *Appl. Phys. Lett.* 71, 779–781. doi:10.1063/1.119643

Li, F. C., Wang, T. Y., He, Q. F., Sun, B. A., Guo, C. Y., Feng, T., et al. (2018). Micromechanical mechanism of yielding in dual nano-phase metallic glass. *Scripta Mater.* 154, 186–191. doi:10.1016/j.scriptamat.2018.05.050

Liontas, R., Jafary-Zadeh, M., Zeng, Q., Zhang, Y.-W., Mao, W. L., and Greer, J. R. (2016). Substantial tensile ductility in sputtered Zr-Ni-Al nano-sized metallic glass. *Acta Mater.* 118, 270–285. doi:10.1016/j.actamat.2016.07.050

Liu, C., Roddatis, V., Kenesei, P., and Maaß, R. (2017). Shear-band thickness and shear-band cavities in a zr-based metallic glass. *Acta Mater.* 140, 206–216. 10.1016/j.actamat.2017.08.032

Liu, Z., Li, R., Wang, G., Wu, S., Lu, X., and Zhang, T. (2011). Quasi phase transition model of shear bands in metallic glasses. *Acta Mater.* 59, 7416–7424. 10.1016/j.actamat.2011.08.002

Lu, J., Ravichandran, G., and Johnson, W. L. (2003). Deformation behavior of the Zr41.2Ti13.8Cu12.5Ni10Be22.5 bulk metallic glass over a wide range of strain-rates and temperatures. *Acta Mater.* 51, 3429–3443. 10.1016/S1359-6454(03)00164-2

Maaß, R., Klaumünzer, D., Villard, G., Derlet, P. M., and Löffler, J. F. (2012). Shear-band arrest and stress overshoots during inhomogeneous flow in a metallic glass. *Appl. Phys. Lett.* 100, 071904. doi:10.1063/1.3684871

Mendelev, M. I., Kramer, M. J., Ott, R. T., Sordelet, D. J., Yagodin, D., and Popel, P. (2009). Development of suitable interatomic potentials for simulation of liquid and amorphous Cu-Zr alloys. *Phil. Mag.* 89, 967–987. doi:10.1080/14786430902832773

Mendelev, M. I., Ott, R. T., Heggen, M., Feuerebacher, M., Kramer, M. J., and Sordelet, D. J. (2008). Deformation behavior of an amorphous Cu64.5Zr35.5 alloy: a combined computer simulation and experimental study. *J. Appl. Phys.* 104, 123532. doi:10.1063/1.3043587

Mizubayashi, H., Okamoto, T., Koyama, K., and Horiuchi, M. (1998). Dynamic anelastic response of amorphous alloys suggesting collective motions of many atoms. *Acta Mater.* 46, 1257–1264. 10.1016/S1359-6454(97)00283-8

Murali, P., Zhang, Y. W., and Gao, H. J. (2012). On the characteristic length scales associated with plastic deformation in metallic glasses. *Appl. Phys. Lett.* 100, 201901. doi:10.1063/1.4717744

Nandam, S. H., Adjaoud, O., Schwaiger, R., Ivanisenko, Y., Chellali, M. R., Wang, D., et al. (2020). Influence of topological structure and chemical segregation on the thermal and mechanical properties of Pd-Si nanoglasses. *Acta Mater.* 193, 252–260. doi:10.1016/j.actamat.2020.03.021

Nandam, S. H., Ivanisenko, Y., Schwaiger, R., Śniadecki, Z., Mu, X., Wang, D., et al. (2017). Cu-Zr nanoglasses: atomic structure, thermal stability and indentation properties. *Acta Mater.* 136, 181–189. doi:10.1016/j.actamat.2017.07.001

Plimpton, S. (1995). Fast parallel algorithms for short-range molecular dynamics. *J. Comput. Phys.* 117, 1–19. 10.1006/jcph.1995.1039

Ritter, Y., and Albe, K. (2012). Chemical and topological order in shear bands of Cu64Zr36 and Cu36Zr64 glasses. *J. Appl. Phys.* 111, 103527. doi:10.1063/1.4717748

Ritter, Y., Şopu, D., Gleiter, H., and Albe, K. (2011). Structure, stability and mechanical properties of internal interfaces in Cu64Zr36 nanoglasses studied by MD simulations. *Acta Mater.* 59, 6588–6593. doi:10.1016/j.actamat.2011.07.013

Şopu, D., and Albe, K. (2015). Influence of grain size and composition, topology and excess free volume on the deformation behavior of Cu–Zr nanoglasses. *Beilstein J. Nanotechnol.* 6, 537–545. doi:10.3762/bjnano.6.56

Şopu, D., Albe, K., Ritter, Y., and Gleiter, H. (2009). From nanoglasses to bulk massive glasses. *Appl. Phys. Lett.* 94, 191911. doi:10.1063/1.3130209

Şopu, D., Ritter, Y., Gleiter, H., and Albe, K. (2011). Deformation behavior of bulk and nanostructured metallic glasses studied via molecular dynamics simulations. *Phys. Rev. B* 83, 100202. doi:10.1103/PhysRevB.83.100202

Sha, Z., Wong, W. H., Pei, Q., Branicio, P. S., Liu, Z., Wang, T., et al. (2017). Atomistic origin of size effects in fatigue behavior of metallic glasses. *J. Mech. Phys. Solid.* 104, 84–95. doi:10.1016/j.jmps.2017.04.005

Sha, Z. D., Qu, S. X., Liu, Z. S., Wang, T. J., and Gao, H. (2015). Cyclic deformation in metallic glasses. *Nano Lett.* 15, 7010–7015. doi:10.1021/acs.nanolett.5b03045

Shao, Y., Yao, K., Li, M., and Liu, X. (2013). Two-zone heterogeneous structure within shear bands of a bulk metallic glass. *Appl. Phys. Lett.* 103, 171901. doi:10.1063/1.4826117

Shi, Y. (2019). Size-dependent mechanical responses of metallic glasses. *Int. Mater. Rev.* 64, 163–180. doi:10.1080/09506608.2018.1476079

Stukowski, A. (2010). Visualization and analysis of atomistic simulation data with OVITO-the Open Visualization Tool. *Model. Simulat. Mater. Sci. Eng.* 18, 015012. doi:10.1088/0965-0393/18/1/015012

Tanemura, M., Ogawa, T., and Ogita, N. (1983). A new algorithm for three-dimensional voronoi tessellation. *J. Comput. Phys.* 51, 191–207. doi:10.1016/0021-9991(83)90087-6

Tang, C., Laws, K., and Ferry, M. (2018). Atomistic origin of stress overshoots and serrations in a cuzr metallic glass. *Materialia* 1, 121–127. doi:10.1016/j.mtla.2018.04.005

Tian, L., Wang, X.-L., and Shan, Z.-W. (2016). Mechanical behavior of micronanoscaled metallic glasses. *Mater. Res. Lett.* 4, 63–74. doi:10.1080/21663831.2015.1124298

Volkert, C. A., Donohue, A., and Spaepen, F. (2008). Effect of sample size on deformation in amorphous metals. *J. Appl. Phys.* 103, 083539. doi:10.1063/1.2884584

Wang, C., Wang, D., Mu, X., Goel, S., Feng, T., Ivanisenko, Y., et al. (2016a). Surface segregation of primary glassy nanoparticles of Fe90Sc10 nanoglass. *Mater. Lett.* 181, 248–252. doi:10.1016/j.matlet.2016.05.189

Wang, X., Jiang, F., Hahn, H., Li, J., Gleiter, H., Sun, J., et al. (2016b). Sample size effects on strength and deformation mechanism of Sc75Fe25 nanoglass and metallic glass. *Scripta Mater.* 116, 95–99. doi:10.1016/j.scriptamat.2016.01.036

Wang, X. L., Jiang, F., Hahn, H., Li, J., Gleiter, H., Sun, J., et al. (2015). Plasticity of a scandium-based nanoglass. *Scripta Mater.* 98, 40–43. doi:10.1016/j.scriptamat.2014.11.010

Weissmüller, J., Birringer, R., and Gleiter, H. (1992). Nanostructured crystalline and amorphous solids. *Kemi* 77-78, 161–170. doi:10.4028/www.scientific.net/kem.77-78.161

Yang, Z.-Y., Wang, Y.-J., and Dai, L.-H. (2019). Susceptibility of shear banding to chemical short-range order in metallic glasses. *Scripta Mater.* 162, 141–145. 10.1016/j.scriptamat.2018.11.001

Yao, K. F., Ruan, F., Yang, Y. Q., and Chen, N. (2006). Superductile bulk metallic glass. *Appl. Phys. Lett.* 88, 122106. doi:10.1063/1.2187516

Zhang, Q., Li, Q.-K., and Li, M. (2015). Internal stress and its effect on mechanical strength of metallic glass nanowires. *Acta Mater.* 91, 174–182. doi:10.1016/j.actamat.2015.03.029

Zhang, Y., and Greer, A. L. (2006). Thickness of shear bands in metallic glasses. *Appl. Phys. Lett.* 89, 071907. doi:10.1063/1.2336598

Zhong, C., Zhang, H., Cao, Q. P., Wang, X. D., Zhang, D. X., and Jiang, J. Z. (2015). The size-dependent non-localized deformation in a metallic alloy. *Scripta Mater.* 101, 48–51. doi:10.1016/j.scriptamat.2015.01.015

Zhu, B., Huang, M., and Li, Z. (2017). Brittle to ductile transition of metallic glasses induced by embedding spherical nanovoids. *J. Appl. Phys.* 122, 215108. doi:10.1063/1.4997281

Conflict of Interest Statement: The authors declare that the research was conducted in the absence of any commercial or financial relationships that could be construed as a potential conflict of interest.

Advantages of publishing in Frontiers

OPEN ACCESS
Articles are free to read for greatest visibility and readership

FAST PUBLICATION
Around 90 days from submission to decision

HIGH QUALITY PEER-REVIEW
Rigorous, collaborative, and constructive peer-review

TRANSPARENT PEER-REVIEW
Editors and reviewers acknowledged by name on published articles

Frontiers
Avenue du Tribunal-Fédéral 34
1005 Lausanne | Switzerland

Visit us: www.frontiersin.org
Contact us: frontiersin.org/about/contact

REPRODUCIBILITY OF RESEARCH
Support open data and methods to enhance research reproducibility

DIGITAL PUBLISHING
Articles designed for optimal readership across devices

FOLLOW US
@frontiersin

IMPACT METRICS
Advanced article metrics track visibility across digital media

EXTENSIVE PROMOTION
Marketing and promotion of impactful research

LOOP RESEARCH NETWORK
Our network increases your article's readership